FUSION TECHNOLOGY

2007-2008 Activity Report of the Association EURATOM-CEA

(Full Report)

Compiled by : F. LABASSÉ

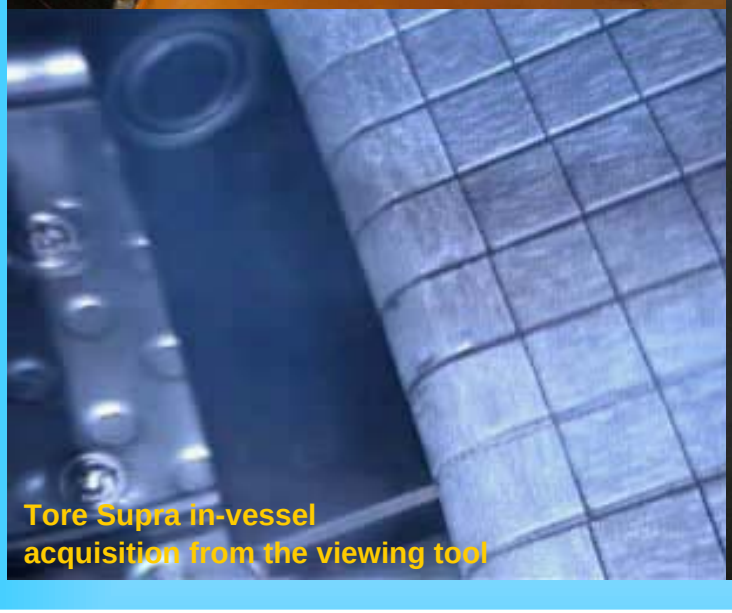

EUR-CEA-FC-1740

ASSOCIATION EURATOM-CEA
CEA/DSM/IRFM
Centre de Cadarache
13108 Saint-Paul-Lez-Durance, France

FUSION TECHNOLOGY

2007-2008 Activity Report of the Association EURATOM-CEA

(full report)

Compiled by : F. LABASSÉ

ASSOCIATION EURATOM-CEA
CEA/DSM/IRFM
Centre de Cadarache
13108 Saint-Paul-Lez-Durance, France

Tel. : 33 - 4 42 25 46 59
Fax : 33 - 4 42 25 64 21
e-mail : dirirfm@cea.fr
Web : http://www-fusion-magnetique.cea.fr

This report is also available on-line at : http://www-fusion-magnetique.cea.fr

This work, supported by the European Communities under the contract of Association between EURATOM and CEA, was carried out within the framework of the European Fusion Development Agreement. The views and opinions expressed herein do not necessarily reflect those of the European Commission

Cover: ***AIA project; CEA development under EFDA workprogramme of a long reach carrier for in-vessel interventions under tokamak ultra high vacuum and temperature conditions. In September 2008, complete demonstration on Tore Supra facility with inner components close inspections and no vessel pollution was performed. This device is ITER-relevant for mini-invasive interventions between pulses required for exploitation and due to the fact that no human intervention will be possible in the tore. In view of future applications, developments of new diagnostics and tools such as vision, leak localisation, surface analysis, diagnostics calibration… are under progress.***

CONTENTS

Diagnostics

Remote Participation

Vessel-In Vessel

Vessel-Blanket and Materials

Plasma Facing Components

Remote Handling

Magnet System and Cryogenics

Tritium Breeding and Materials

Breeding Blanket

Helium Cooled Lithium Lead (HCLL) Blanket

Materials Development

Reduced Activation Ferritic Martensitic (RAFM) Steels

Advanced Materials

Neutron Source

Safety and Environment

System Studies

Power Plant Conceptual Studies (PPCS)

Design Support and Procurement

JET Technology

Vessel-In Vessel

Vessel-Blanket and Materials

Plasma Facing Components

Remote Handling

Tritium Breeding and Materials

Breeding Blanket

Safety and Environment

INTRODUCTION

European research on controlled thermonuclear fusion is carried out in an integrated programme with the objective to develop a safe and economically viable energy source. Part of this programme is driven through the *European Fusion Development Agreement* (EFDA) which provides a framework covering the activities in the field of technology (both Next Step and Reactor) and the collective use of the Joint European Torus (JET). Since 2008, *Fusion For Energy* (F4E) has been in charge of the ITER R&D programme whereas the *"New"* EFDA deals with the European Fusion Physics programme plus long term developments.

This report summarizes activities performed by the Euratom-CEA Association in 2007 and 2008 within the frame of the European Technology Programme (both "EFDA" activities and "Underlying Technology" programme). Activities reported in this document are the continuation of activities implemented in 2006 and 2007. Due to the re-organisation of the European Fusion Institutions in 2008 and the late implementation of the 2008 european programme, tasks implemented in 2008 under "*New*" EFDA are not hereafter reported.

This full report is also available on line at *http://www-fusion-magnetique.cea.fr* In each section, the tasks are sorted out according to the EFDA main fields: Physics, Vessel/In-Vessel, Magnets & Cryogenics, Tritium Breeding Blanket, Materials, Safety & Environment, System Studies, JET technology activities … The Euratom-CEA Association is involved in all these topics.

- CEA activities carried out in the field "***Physics Integration***" are mainly linked to Plasma Edge & Plasma Wall Interaction (PWI), Heating & Current Drive and Diagnostics. A study was devoted to the ELM mitigation/suppression by the use of correction coils. For Plasma Edge & PWI, several tasks were devoted to the study of dust generation mechanisms inside the vessel and necessary associated measurements. For Heating, studies were mainly devoted to the Ion Cyclotron Range of Frequencies (ICRF) antenna developments and to the SINGAP negative ion beam project. Developments on diagnostics, in particular in support to ITER diagnostic design (reflectometry, visible/IR wide angle viewing system, bolometry, magnetic sensors, …) were carried out, together with their integration in the port-plug. Infra Red fibres for thermography applications and laser cleaning methods for diagnostics and mirrors were also studied. Nearly all these activities are carried out in preparation for ITER.

- Plasma Facing Component (PFC) developments, Vacuum Vessel/Blanket activities and Remote Handling studies are carried out in the field "***Vessel/In-Vessel***". The Vacuum Vessel studies were pursued on assembly techniques (hybrid Arc/Laser), qualification of related inspection methods, and also on material database for ITER purposes. On the PFC side, investigations were carried out on dedicated materials, development and optimisation of heterogeneous assembly techniques (HIP) & associated control methods, and specific studies for the divertor (carbon erosion influence on ITER divertor acceptance criteria, Infrared tests of divertor components in SATIR, alternative swirl-tube cooling concept for the ITER divertor). The work performed by the Association in Remote Handling was dedicated to the program called Articulated Inspection Arm (AIA). After the manufacture of the complete AIA robot in 2006, including the deployer and the storage cask, this programme was achieved with the successful tests of the robot under pressure and temperature tokamak operation conditions in Tore Supra. In the mean time, developments on optimisation of components suitable for Fusion RH applications were pursued.

- In the field "***Magnets & Cryogenics***", CEA devoted a major part of its effort to the studies of advanced Nb_3Sn strands for the ITER Toroidal Field (TF) coils, and a prototype full size conductor was tested and qualified. CEA is also involved in ITER PF coils studies: a mock-up, representative of the main features of the coil tail was manufactured, then delivered to JAEA for tests in their CSMC facility. On a long term approach, the Euratom-CEA Association also pursued its investigations on the possible use of high temperature superconductor for future fusion reactors. Studies on ITER cryoplant were also carried out.

- The Field "***Tritium Breeding Blanket***" mainly aimed at preparing Test Blanket Modules (TBM) activities for ITER. On the critical path towards the future operation in ITER of the TBMs, which will be installed and operated as representative modules of the reactor tritium breeding blanket, CEA conducted several complementary studies. First, studies aiming at defining precisely all the necessary steps within the TBM project : design, materials (Eurofer), qualification of assembly (welding),… with regard to the regulation and design codes for both HCPB and HCLL concepts were conducted. Then, other studies focused on the so-called Prototypical Mock-Ups (PMU), which are one of these necessary steps in the development of breeding blankets test modules. After a conceptual design of the PMU in 2006, studies in 2007-2008 focused on the strategy and choices for the detailed design, with the definition of specifications and objectives of the mock-up and test program, for the purpose of an extended qualification. (manufacturing processes, thermohydraulics, thermomechanics, liquid metal technology, etc). Note that the complete demonstration of welding feasibility for the ITER TBMs was successfully achieved, with reduction of stress and distortions to acceptable values.

- On "***Materials"***, CEA maintained during 2007-2008 significant involvement in the development of structural materials for fusion reactor. The main focus was on EUROFER, a reduced activation martensitic steel, including complex welding processes for the DEMO breeding blanket. Post Irradiation Examinations on several reduced activation candidate materials for DEMO were also carried out. Significant work was performed on a long term approach for advanced materials, especially improvement of knowledge on SiC/SiC and tungsten alloys, including irradiation. Further studies on their properties after irradiation will have to be conducted. For purpose of larger knowledge on the materials for fusion applications, the international neutron source project IFMIF is planned. It will be now studied under the "Broader Approach", which is the frame covering the IFMIF project; CEA is of course involved in design studies concerning this facility.

- "***Safety and Environment***" studies realised by CEA covered various subjects such as safety assessment of EU Test Blanket Modules to support ITER licensing projects, feedback experience on components failure on Tore Supra, cryogenic experiments on the EVITA facility, dust measurements and removal techniques, code development and validation (safety studies on hydrogen mitigation and dust explosion in the vaccum vessel or on activated corrosion products).

- Activities in the field "***System studies***" were dedicated, in 2007 and 2008, to various studies for future fusion reactors: studies on breeding blankets (segmentation and maintenance/remote handling issues, multi-module attachment conceptual design); analysis of current profile control in tokamak reactor scenarios using realistic treatment of current drive efficiencies; magnet system outline.

- For direct "***ITER Design Support & Procurement***", studies focused on the development of a Quality Assurance system for the European Domestic Agency for ITER activities, and development of a RAM (Reliability, Availability, Maintenance) and Failure Mode, Effects and (FMEA) Analysis.

- Activities carried out in the Field "***JET technology***" were mainly related in 2007-2008 to PFCs : Tile shaping checking (in particular with regard to heat load) in the frame of the JET ITER-like first wall project; detritiation methods based on laser ablation from carbon materials, together with characterisation of deposited layers and dust measurement. Comparisons between processes for tritium removal from different types of waste were also carried out. Other activities were devoted to the new diagnostic for thermography analysis which produced infrared images of the in-vessel components showing energy deposited on the divertor, on the top limiter and on the outer limiters during ELMs in JET.

Four specific operational divisions of the CEA, located on four sites (see appendix 5), are involved in the Euratom-CEA association fusion technology activities:

- the Nuclear Energy Division (DEN) , for In-vessel component design (first wall, divertor, blanket, …), neutronics, structural materials and safety activities,
- the Technology Research Division (DRT), for activities dedicated to materials (elaboration, assembly) and robotics,
- the Physical Sciences Division (DSM), which includes the *Institute for Magnetic Fusion Research (IRFM)* which operates Tore Supra and is responsible for plasma physics and engineering developments, cryoplant and magnet and plasma facing components activities,
- the Life Sciences Division (DSV), for activities related to the impact of tritium contamination on staff.

The Euratom-CEA programme in Technology also includes specific R&D collaborations done by the French National Centre for Scientific Research (CNRS), Grenoble Institute of Technology (INPG) and Industry on dust generation mechanisms inside the vessel and necessary associated diagnostics, Plasma Facing Components and assembly methods for the vacuum vessel sectors.

Progress in fusion technology is built over the years and this report once again highlights a number of important steps that have been accomplished in many domains. CEA, together with other European Institutions is on the forefront of technological advances which are of prime importance for the success of the ITER construction. The new phase in which its implementation is at stake will need an increased focusing and will be achieved through a new organisation within Europe, mainly through european consortia and alliances, in relation with F4E. On the longer term, progress in technology will gradually improve our vision of an electricity producing reactor and should increase the credibility of fusion energy as a genuine solution for energy production for the future. The authors and the editors should be commended for their dedicated contribution in making this report available.

Gabriel Marbach
Head of Research Unit of the Association Euratom-CEA

EFDA TECHNOLOGY PROGRAMME

CEFDA05-1336
CEFDA07-1700-1578

Task Title: TW5-TPO-ERGITER & TW6-TPO-ELMCONT: RESONANT MAGNETIC PERTURBATION (RMPs) FOR EDGE LOCALIZED MODES (ELMs) SUPPRESSION IN ITER

INTRODUCTION

During the recent design review of ITER, Type I Edge Localised Mode (ELM) control was identified as a high priority task [1]. One of the promising methods to control Type I ELMs is the installation of dedicated coils that achieve this goal by modifying the edge magnetic field, so called Resonant Magnetic Perturbations (RMP) coils. RMPs have been shown to be effective in eliminating Type I ELMs in DIII-D [12] or significantly mitigating them in JET [2]. At present, ELM control by RMP is recommended for ITER since it could increase the lifetime of the ITER divertor by reducing heat and particle fluxes due to Type I ELMs and hence reducing surface erosion [1].
The physics of ELM suppression by RMPs is not completely understood, but rapidly progressing due to great interest of experimentalists, theoreticians and modellers to this ITER-relevant subject. The work on the present Task CEFDA05-1336: TW5-TPO-ERGITER "Magnetic perturbation for ELM suppression in ITER" was done with the aim to finalize the design studies of the optimum set of coils generating Resonant Magnetic Perturbations for Type I ELMs control in ITER. They were based essentially on the empirical criterion and vacuum modelling extrapolated DIII-D experiments to ITER. This was done because the first extrapolations RMP method of ELM control to ITER were mainly based on an empirical criterion and "vacuum" field modelling suggesting that ELMs are suppressed when the edge plasma is ergodized in the pedestal region for r/a>0.9, however up to now it was confirmed only on DIII-D. The objective of the second Task CEFDA07-1700-1578: TW6-TPO-ELMCONT: "Evaluation of ELM control coil configurations in ITER, their compatibility with other field modification systems and evaluation of effects on plasma and power load on PFCs was to estimate mainly the MHD rotating plasma response and braking mechanisms for the RMP coils design optimisation for ITER.
It is known that depending on the plasma parameters and the RMP spectrum, the actual RMP field could be very different compared to vacuum, especially in rotating plasmas where the generation of the current perturbations near rational surfaces could prevent reconnections leading to the effective screening of RMPs [3, 5, 6, 7, 10, 13, 14]. On the other hand it is known from experiment that helical magnetic perturbations can significantly influence the toroidal rotation itself leading to global slowing down of the plasma rotation (braking) [4, 15] or in some cases special cases acceleration was demonstrated [12].
The Neoclassical Toroidal Viscosity (NTV), resulting from the toroidal drag force experienced by the plasma particles moving along field lines distorted by helical magnetic perturbations [4, 15], was proposed as a possible mechanism for the global plasma braking and modelled here for ITER.

2007-2008 ACTIVITIES

During 2007-2008 a large number of possible designs of external or in-vessel coils for ITER were analyzed for the reference scenarios (H-mode, Hybrid and Steady-state) taking into account physical, technical and spatial constraints [5, 6, 13]. The level of stochasticity (Chirikov parameter ~1 at r/a~$\Psi^{1/2}$~0.9) generated by the I-coils in the DIII-D experiments on ELMs suppression were taken as a reference. Designs with a toroidal symmetry n=4 was considered to avoid lower n numbers producing larger central islands (however without screening taken into account), a potential trigger of central MHD. After many possibilities analysed and difficult decisions taken for the changes in the present ITER design, the consensus was reached that the optimum spectrum of RMP coils (small core perturbations and maximal edge perturbations) for all reference scenarios is generated by the in-vessel coils close to plasma. The presently proposed rather flexible in amplitudes and relative phases 9x 3-row RMP coils situated behind blanket modules accepted by ITER are represented on figure 1.
This present design in a big part was influenced by the present physics studies in the framework of these tasks.

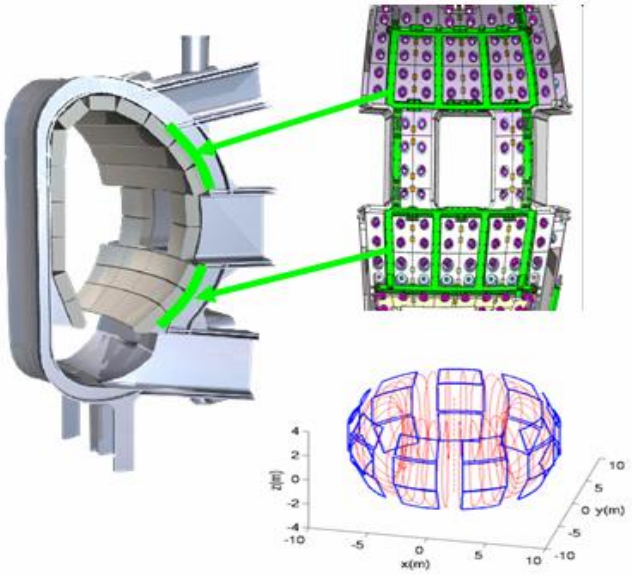

Figure 1: RMP coils in ITER designed to produce n=4 stochastic boundary at the edge (r/a>0.9). Max current 50kAt

During 2007-2008 many features of the plasma response on RMPs were also addressed [7, 8, 13, 14, and 15].
In particular non-linear reduced MHD modelling of the response of a toroidally rotating plasma on Resonant Magnetic Perturbations (RMPs) was done for DIII-D and ITER typical parameters [7, 8]. The non-linear cylindrical reduced MHD (RMHD) code was adapted to take into account toroidal rotation and plasma braking mechanisms such as resonant braking and the Neoclassical Toroidal Viscosity (NTV) calculated for low collisionality regimes ("1/ν" and "ν") [4, 15]. Characteristic time for island formation at zero rotation increases for lower resistivity and for the pedestal top (r~0.9) is roughly estimated ~50ms for DIII-D and ~1500ms for ITER.

The non-resonant helical harmonics $\left(q \neq m/n\right)$ do not produce magnetic islands, penetrate on Alfven–like time, are not screened by plasma rotation, but produce NTV. It was demonstrated that magnetic flux perturbation could be effectively screened by toroidal plasma rotation. This screening is larger for stronger rotation and lower resistivity, hence the central islands are expected to be screened and the pedestal region (r>0.9) is still ergodic in ITER (figure 2a). If the "1/ν" low collisionality regime is dominant, the expected NTV is very strong in ITER and a counter (with respect to the plasma current direction) rotation is predicted for ITER in present study (figure 2b).

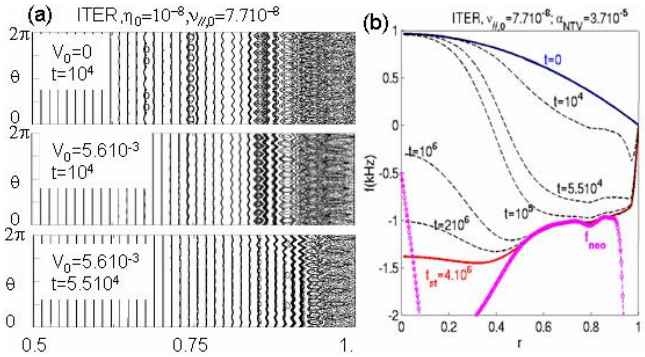

Figure 2: Magnetic topology for typical ITER plasma and rotation parameters without rotation ((a)-top) and with rotation ((a)-mid and (a)-bottom) at different times (in τ_{Alfven}). (b)-Change in rotation profiles with NTV in 1/ν regime for ITER RMP coils. Central islands are screened both by co- and counter rotation

REFERENCES

[1] R. Hawryluk et al Proceedings of 22nd IAEA Conference ,Geneva, Switzerland, 13-18 October, 2008, IT/1-2, submitted to Nuclear Fusion

[2] Y. Liang et al Phys Rev Letters 98 (2007) 265004

[3] R. Fitzpatrick Phys of Plasm 5 (1998) 3325

[4] K. Shaing Phys. Plasm10 (2003) 1443 Phys of Plas 14 (2007) 049903. (Erratum paper)

REPORTS AND PUBLICATIONS

[5] M. Becoulet et al, Nucl. Fusion 47 (2007)1–16

[6] M. Becoulet et al, Nucl. Fusion 48 (2008) 024003

[7] M. Bécoulet, G. Huysmans, E. Nardon, et al 9-13 June, 2008, 35th EPS Conference, Hrsonissos, Crete, Greece, O-4.034

[8] M. Becoulet, G. Huysmans, X. Garbet, E. Nardon, et al 22nd IAEA Fusion Energy Conference, 13-18 October, 2008, Geneve, Switzerland, TH/2-1Ra

[9] M. Bécoulet, E. Nardon, G. Huysmans, W. Zwingmann, P.R. Thomas, M. Lipa, R.A. Moyer, T.E. Evans, V. Chuyanov, Y. Gribov, A. Polevoi, G. Saibene, G. Vayakis, A. Portone, A. Loarte, G. Federici, V. Parail, J. Hastie, C. Gimblett
Final Report on the Task: CEFDA05-1336 TW5-TPO-ERGITER: Design studies of Resonant Magnetic Perturbation (RMP) coils for Type I ELMs mitigation in ITER. Internal report CEA: PHY/NTT-2007.001.

[10] M. Bécoulet, E. Nardon, G. Huysmans, et al Final Report on the EFDA Task: TW7-TPO-ELMCONT "Evaluation of ELM control coil configuration in ITER, effects on plasma and power loads on PFCs" , Internal report CEA: PHY/NTT-2008.007.

[11] Cahyna P, Becoulet M, Panek R, et al. Plasma Phys Reports 345(2008)746

[12] Evans TE, Fenstermacher ME, Moyer RA, et al, Becoulet M., Nucl. Fusion 48 (2008) 024002

[13] E. Nardon, M. Bécoulet, G. Huysmans, et al J Nuclear Metter 363-365(2007)

[14] E. Nardon et al Phys of Plasmas 14(2007), 092501

[15] Shaing KC, Cahyna P, Becoulet M, et al. Phys of Plasmas 15(2008)

TASK LEADER

Marina BECOULET

DSM/IRFM/SIPP
CEA-Cadarache
F-13108 Saint-Paul-lez-Durance Cedex

Tel: 33 4 42 25 74 84
Fax: 33 4 42 25 49 90

e-mail: marina.becoulet@cea.fr

TW6-TPP-BETUNCMOD-D01b

Task Title: MOLECULAR DYNAMICS SIMULATIONS OF MIXED MATERIAL FORMATION AT THE ITER DIVERTOR: REPORT ON THE CONSTRUCTION OF THE POTENTIALS TO STUDY THE INTERACTIONS IN THE Be-C, Be-W AND W-C SYSTEMS IN INTERACTION WHITH D/T AND NOBLE GASES (Ar, Ne, He) TO BE USED IN MOLECULAR DYNAMICS SIMULATIONS

INTRODUCTION

To be suitable for plasma-wall interaction studies, the potentials should allow for chemical bond breaking and reforming without discontinuities in the forces, and include angular terms to describe chemical bonding.

The first step in order to develop molecular dynamics simulation (MD is therefore to build suitable inter-atomic potentials.

The best-adapted starting point is the atom – atom potentials calculated by non-empirical *ab initio* methods such as multi reference configuration interaction (MR-CI) methods or Density Functional theory (DFT) methods. This was the goal of the present part of the EFDA task, the simulations themselves being realize by the others groups (K.Nordlund[1] & M. Probst[2]).

2007-2008 ACTIVITIES

BERYLLIUM – BERYLLIUM INTERACTION

The various available methods were first tested for pure beryllium. It appears from the very special Be electron configuration that MR-CI is the best adapted for the beryllium atom but gives poor results on small atomic clusters. The DFT calculation yields better agreement with experiment concerning the interaction energy as well as atomic distance:

Experiment: $D_e = 944 \pm 25$ cm^{-1} (11. 3 kJ mol^{-1}) Fundamental vibration frequency $\nu_0 = 224 \pm 3$ cm^{-1}	This calculation method: hybrid DFT (B3LYP) $D_e = 16$ kJ mol^{-1} $\nu_0 = 285$ cm^{-1} $R_0 = 2.49$ Å

BERYLLIUM – HYDROGEN AND BERYLLIUM – TUNGSTEN

For these systems, the DFT and MR-CI gave results in reasonably good agreement and since the DFT calculations are less time consuming and easier to perform, my conclusion goes towards DFT method.

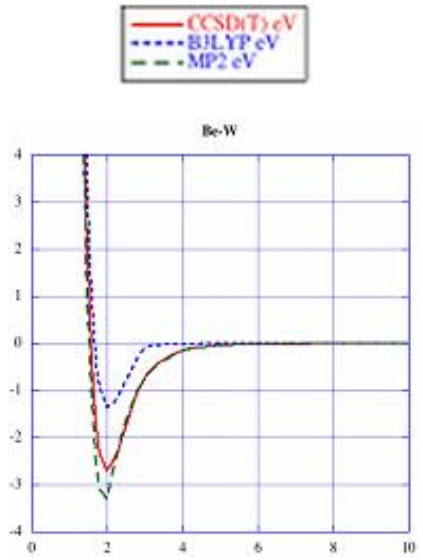

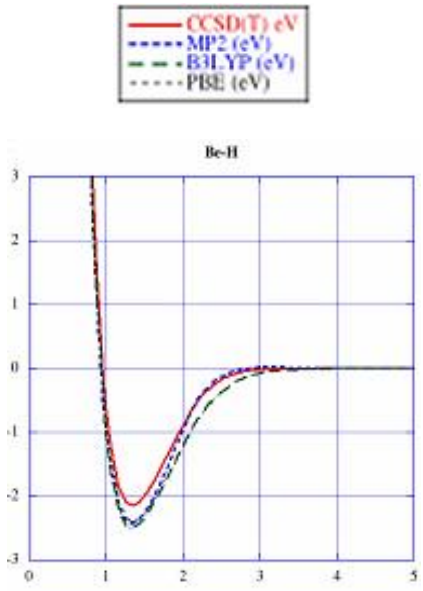

[1] Division of Materials Physics
Department of Physics Helsinki Institute of Physics P.O.Box 4
(Pietari Kalmink.2) 00014 University of Helsinki - Finlande

[2] Institut für Ionenphysik und Angewandte Physik Technikerstr. 25/3
A-6020 Innsbruck - Autriche

He –X POTENTIALS

The DFT functionals commonly used in large calculations, and specialy in solid state the most famous PBE functionnal, are not able to reproduce correctly the very weak interactions such as the dispersion forces. Unfortunately, the rare gas atoms such as helium have a spherical closed electron configuration and their interaction with other atomic or molecular systems is largely dominated by this kind of interactions. Therefore there is no alternative than using MR-CI methods which are very well adapted to that purpose.

Among the MR-CI methods, one of the most largly used is the coupled cluster method (CCSD) which reaches a more description in developping the wave function not only on the electronic ground state but also in introducing a large number of electronic excited states built from the Hartree-Fock determinant using single and double substitution. Consequently, the main issue is to select the excited states and also the electronic state of the associated atom.
The beryllium atom fundamental configuration is $^1\Sigma$, it is unique. The carbon atom lowest electronic states are $^3\Sigma^-$ and $^3\Pi$ and since the associated energies are close, the two states have been calculated. This has been also done for the tungsten electronic states $^5\Sigma^-$ and $^5\Pi$. Helium-helium and hydrogenate-helium are cases less difficult to deal with.

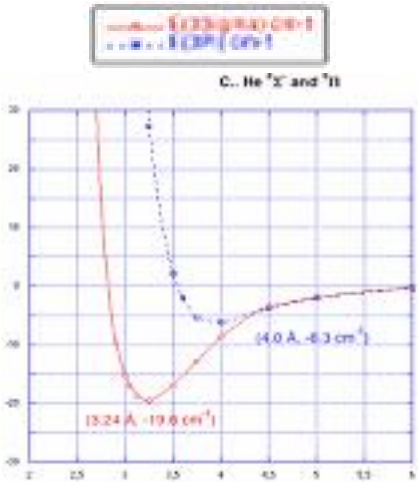

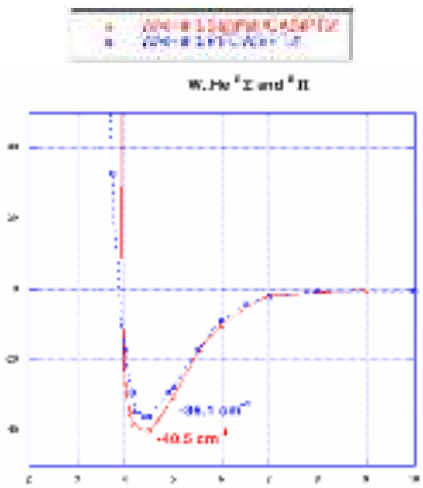

OTHER CALCULATIONS

The other partners of the task do not plan yet to study the case of argon and neon, therefore. These calculations haven't been carriesd out. But, in a less formal way, I performed and delivered to Kai Nordlund number of calculations concerning small beryllium clusters, potential energy surfaces of hydrogen atom approaching the Be(0001) surface, or the BeO(100) surface. Since the Kick-off/progress meeting of task BETUNCMOD in Garching in may 2007, I met Kai in several occasions and our collaboration is still active on this special topic.

TASK LEADER

Alain ALLOUCHE

CNRS-PIIM
UMR CNRS 6633
Centre de Saint Jérôme
Case 232
Avenue Escadrille Normandie – Niémen
13397 Marseille Cedex 20

Tel: 33 4 91 28 85 76
Fax: 33 4 91 28 91 94

e-mail: alain.allouche@univ-provence.fr

TW6-TPP-DUSMEAS-D01a

Task Title: ASSESSMENT OF THE INTEGRATION OF A DUST INJECTOR SYSTEM AND ELECTROSTATIC DUST DETECTOR IN THE TORE SUPRA ENVIRONMENT

INTRODUCTION

In Tokamaks, dusts are produced by the interaction between the plasma (operation and conditioning) and the plasma facing materials. Particles with diameters between 100 nm and 100 µm are considered as dusts. So far, in existing tokamaks, dusts did not represent a major issue both from operational and safety point of view. Nevertheless, the situation will be different in ITER, in particular because of the activation of the materials, the presence of tritium and beryllium.
In ITER Vacuum Vessel (VV), various hazards are linked to dusts: environmental impact in case of dust spreading, production of hydrogen in case of steam ingress and explosion hazard. In order to control the dust hazard, the current ITER strategy is based on a defense in depth approach designed to avoid failures, measure and minimise the dust inventory and to provide reliable confinement systems.
Moreover dusts will have to be monitored in ITER due to operation issues. As a matter of facts, high dust concentration could disturb plasma scenarios in particular when involving high power or could disturb the proper operation of first mirrors for example.
There are thus real needs for quantitative measurement of dusts. Techniques are being developed for assessing dust quantities inside ITER Vacuum Vessel (VV) in between plasmas. But there are also some proposed techniques to be used during plasma operation for time-resolved measurements of dusts.
This last category of techniques must be experimentally investigated in existing tokamaks and it is the purpose of the present task.
The objective of the CEA part is to focus on two main issues related to this problematic:

- Study of the integration of a dust injector system in the Tore Supra (TS) environment,
- Assessment of the integration of an electrostatic dust detector in the Tore Supra environment.

2007-2008 ACTIVITIES

INTEGRATION OF A DUST INJECTOR SYSTEM IN TORE SUPRA

Based on the existing observations performed in TS, it is proposed to consider the following inputs for the definition of a dust injection system in Tore Supra:

- Injection from the top of the machine to take benefit of the gravity will be favoured,
- Particles should remain in the Scrape-Off Layer (SOL) (sufficient life time to be observable),
- Dedicated pulses at controlled power must be performed when injecting calibrated dust to limit the creation of particles by the plasma at the same time,
- Carbon dust should be chosen to avoid plasma disturbance but other materials such as boron should not be excluded,
- The size of the particles to be injected depends on the q/m ratio (charge of the particles when entering the SOL/mass). Based on experience feedback, particles of about 10 µm diameter should be injected,
- About 6 mg of dusts should be injected to have a particle density of about $10^4/cm^3$,
- Moreover conditions related to the temperature (plasma facing components are actively cooled in TS), the pressure (operational pressure about 10^{-5} Pa) and the magnetic field have to be considered while developing such a system.

Several systems of dust injection were studied and assessed for Tore Supra integration during this sub-task. Mainly, vibrating membrane, rotating cylinder, injection of Deuterium pellets seeded with dusts, rotating blade, the DiMES system from DIII-D team, laser material ablation as well as commercial devices [1].

From the review of the techniques used to inject dust for laboratory or Tokamak experiments, the Alcator C-Mod configuration ("dust shaker" coupled to a gas injection) appears to be the most promising for an installation on Tore Supra. Dusts are fed into the hopper, then air is pumped out before operating the piston. The solenoid driven piston allows boron particles to fall from the hopper into the plasma (see figure 1).

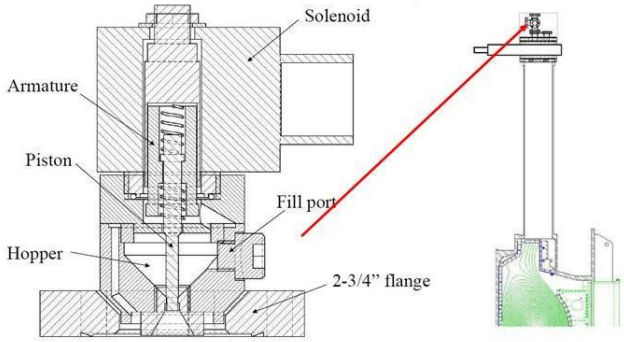

Figure 1: "Dust shaker" and its installation on Alcator C-mod

The same "dust shaker" was used to study the dust transport in the Alcator C-Mod scrape-off layer. In this configuration it was coupled to a gas jet. Boron particles with radius between 40 and 120 µm are injected with a 0.3-0.7 bar puff of helium over 100-300 ms. The gas and the particles are injected through a first pipe of about 5 mm diameter followed by a second one of a lower diameter (existing capillary entering the machine – about 1 mm diameter). It has to be noticed that some dust remain in the pipe after the first puffing and are released by the subsequent puffing. It is thus not possible to know exactly how much dust is injected.
The use of the carrier gas seems the best option to avoid particle agglomerations. The particle trapping on the pipe internal surface remains an issue to determine precisely the amount of injected particles, as it was observed on Alcator C-Mod. Moreover, the injected gas should not lead to significant perturbations of the torus conditions during plasma. A first simulation was performed to assess, in TS conditions, the gas speed after an injection. In this simulation the fluid was injected through a 1 mm diameter tube at 100 m/s. One cm after the injection the speed was reduced by a factor 10.
Moreover, the injected gas should not lead to significant perturbations of the torus conditions during plasma. The injected volume must be negligible in relation to the torus volume in order to avoid disturbance and the maximum quantity was set to 1 Pa.m^3, or 10 ml at 1 bar. Deuterium should be used as carrier gas in order again to limit the perturbations.
At last the "dust shaker" uses a solenoid. A magnetic field shielding will have thus to be foreseen.

Implantation in Tore Supra

The system could be implanted in the vicinity of the flange on top of the one Tore Supra sector (Q5A) where:

- There is room (about 30x40 cm²) for fixing the set-up at about 1.5 m from the flange,
- There is a deuterium reservoir connected to a deuterium bottle. The pressure is slightly higher than the atmospheric pressure,
- There is a vacuum circuit (roughing circuit) operating "on demand" up to primary vacuum (few Pa).

In figure 2, the implantation principle is presented.

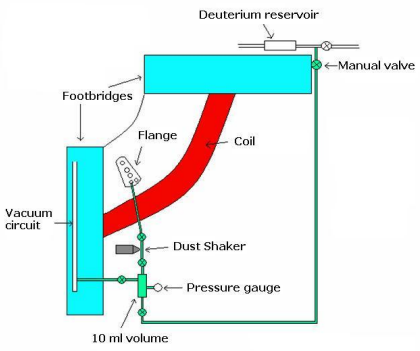

Figure 2: "Dust shaker" implantation principle in Tore Supra

The pre-design was also realised (figure 3).

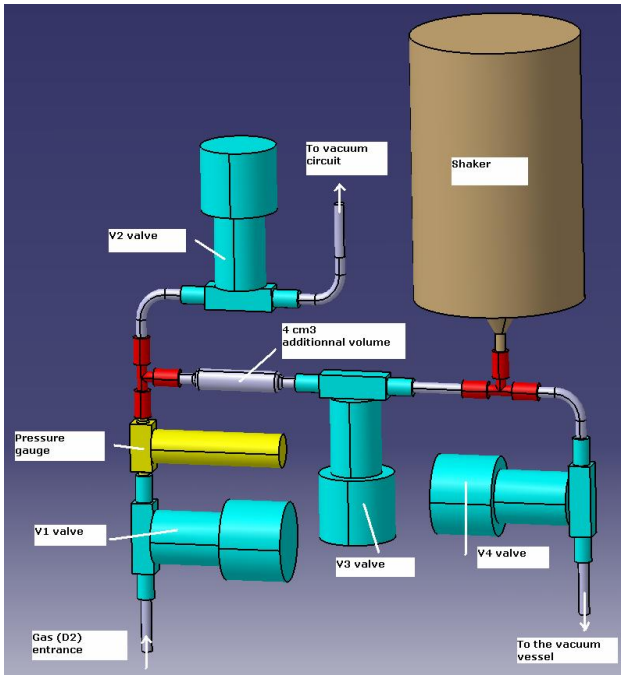

Figure 3: "Dust shaker" Tore Supra pre-design

All the technical components were determined and the dust suppliers contacted. The operating scheme of this dust injector was also prepared.

As a conclusion, this pre-design study showed that calibrated dusts could be injected in Tore Supra at Q5A sector. The system could be based on the use of the dust shaker developed by MIT for Alcator-C Mod. D_2 gas puffing would be used to transport the dust and reduce the agglomeration phenomena. Puffing would be obtained by opening a calibrated volume (10 cm^3) of pipes initially under vacuum. Further design studies are still needed before construction and installation of the system.
Moreover, the injection of calibrated dust could be used to characterize the particle transport within the vacuum vessel via the fast CCD camera. In order to use this injection to calibrate a particle size measurement, a focussed camera (looking at various red plans in figure 4) and an illuminating laser have also to be added.

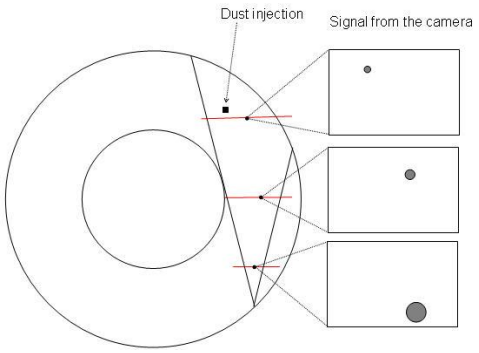

Figure 4: Signal of dust as seen by the camera

A modelling should be also performed to predict the infra-red signal that could be expected by the radiation of particles of 10 µm diameter in the SOL. This modelling

would be then useful for the interpretation of the camera results.

INTEGRATION OF AN ELECTROSTATIC DUST DETECTOR IN TORE SUPRA

Background

This technique, developed by PPPL (USA) is based on two closely interlocking grids (figure 5) of conductive traces on a circuit board that are biased at 30-50 V. When conductive particles land on the energized grid, a transient short circuit occurs and this current pulse can be easily detected by standard nuclear counting electronics. In the case of small particles, two or more adjoining particles could be needed to create the short circuit.
After the short circuit, the particles vaporize in a few seconds restoring the previous voltage standoff. This property was proposed to be used with larger grids in dusty areas to actively control the dust inventory by instantly vaporizing any particles that settle on the grid. The condensation of the vaporized species needs then to be assessed.

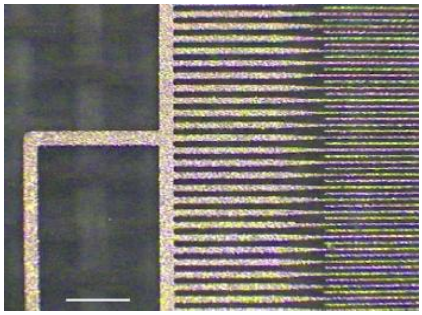

Figure 5: Electrostatic detector. In the active region the width of the trace is 25 µm and the trace spacing is 25 µm. The scale bar corresponds to 500 µm

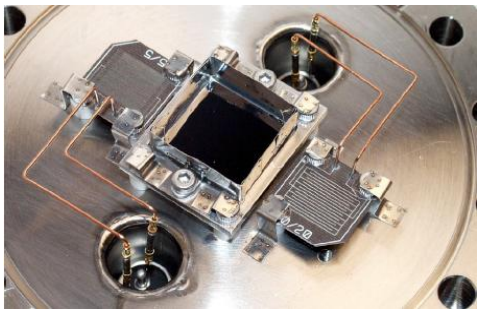

Figure 6: Two grids and reference dust collector mounted on a 15 cm flange for testing in NSTX

This device does not provide an absolute measure of the areal density of dust since it is based on electrostatic and not gravimetric principle. Nevertheless, some correlation was found between recorded counts and particle concentration.
Laboratory tests were performed in air and vacuum with grid spacing from 127 to 254 µm corresponding to a coverage area of 1.2x1.2 cm^2. The particles were scrapped from CFC tile (the count median diameter was calculated from the size distribution to be 2.06 µm). Extra fine grids (25 µm) were used to improve the response of the system to the particles. As a matter of fact, the response is greatly improved with a grid size comparable to the particle size. Thus, a combination of different size grids would extend the dynamic range of the device. Longer "burn-up" times (signal duration) were recorded for larger particles. Therefore, in addition to counting the events caused by to the particles impinging on the grid, this detector can also yield information on the size of the particles from the electrical waveforms. In laboratory the detection threshold, defined as the areal density needed to generate 100 counts, is below 1 µg/cm^2 for particles between 5 and 20 µm. The sensitivity is maximal for the finest particles.
Two grids were installed in NSTX (figure 6) below the outer divertor but a lack of dust signal was observed. This was explained by a level of accumulated dust below the detection limits.

Installation in Tore Supra

Tore Supra is an actively cooled machine and the installation of the electrostatic grid inside the vacuum chamber appears difficult. After discussion with Charles Skinner from PPPL, it was proposed to look at potential locations in the LPT (Limiteur Pompé Toroidal) pumping ducts in order to detect dust transported to this remote area far from the plasma.
The pumping ducts are situated between the LPT and turbo molecular pumps. In figure 7, a drawing of the duct is presented.

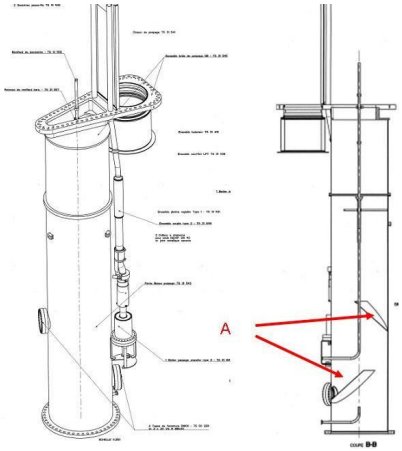

Figure 7: Design of TS pumping dust

The pumping ducts are in TS basement and have thus a relatively easy access. There are such pumping ducts in the 6 sectors of TS. The parts indicated as A in figure 7 are grids designed to collect debris, filings, etc, to protect the pump situated at the bottom of the ducts. It is proposed to fix the detector on the grid at the lower flange (A).

In order to validate the area selection, micro particles sampling was performed in 2008 during the Tore Supra shutdown in 3 different sectors on the lower and upper grids. The pumping ducts have all the same design.
Sampling was performed using conductive adhesive tape (carbon) on top of a Scanning Electronic Microscope

(SEM) support (figure 8). The samples can be directly observed in a SEM. No further preparation is needed.

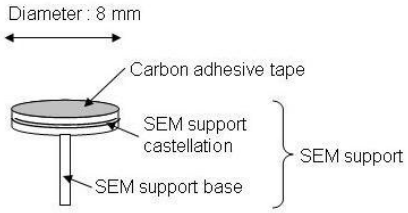

Figure 8: SEM support for dust collection and analysis

In figure 9, a picture of the lower flange is presented where the dust are collected.

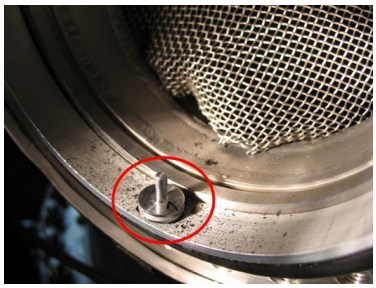

Figure 9: Sampling on Q2B lower flange. The SEM support (in red circle) and the grid installed to collect debris can be seen

The samples were analysed by SEM (shape and size of the particles) and Energy Dispersive Spectroscopy (qualitative analysis of the element present in the sample). One example of the sample recovered can be seen on figure 10.

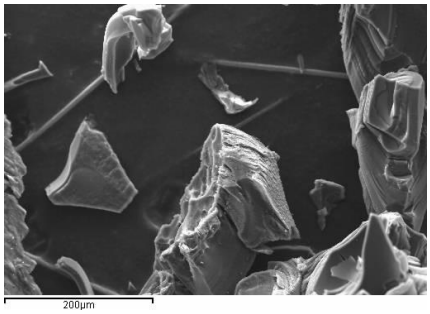

Figure 10: Carbon flake between 40 and 100µm

CONCLUSIONS

Based on these observations, we think that the detector could be installed through the lower flange (easier access) inside one of the pumping ducts observed. There is no gate valve at the top of the pumping ducts. That means that any intervention on this part of the facility must be performed when the vacuum is broken, i.e. during major shutdown. So, if there is a problem on the detector and if some maintenance is needed, the possibility to intervene is really reduced (in practice almost impossible because of the physics programme). The presence of big flakes (larger than the micron sized dust observed on NSTX) will require the installation of a mesh pre-filter above the grid (100 micron mesh to be confirmed), as done for AUG, to prevent them to settle down the electrostatic detector and disturb the measurement. Also having some of the grids with larger spacing, higher voltage, and higher current would increase the ability to tackle large particles, though such a system would be less sensitive. The possibility to have a mosaic of many grids each 1 cm^2 must be further assessed. These could be connected in parallel initially, but if one area becomes permanently shorted then it could be disconnected externally. A potential implantation is presented in figure 11.

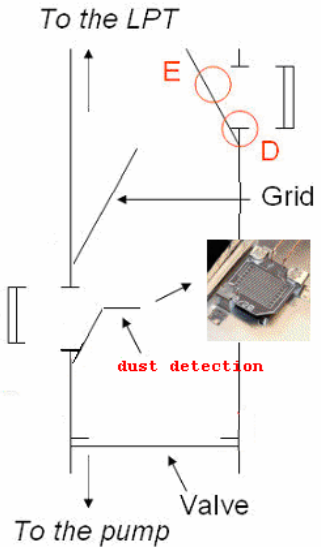

Figure 11: Potential implantation of the electrostatic grid

It has to be noticed that an access in the flange plug should be foreseen to enable particle pumping and collection in case of air ingress and enable a comparison with the dust monitored by the electrostatic grid.
The work started within this task continued in 2008-2009 after the completion of the task TW6-TPP-DUSMEAS. Modified flanges equipped with electrostatic detectors (a mosaic of grids has been chosen) are under fabrication (figure 12) and will be installed on Tore Supra during the 2009 shutdown. These detectors are supposed to give first dust measurements during the next Tore Supra campaign starting end of 2009.

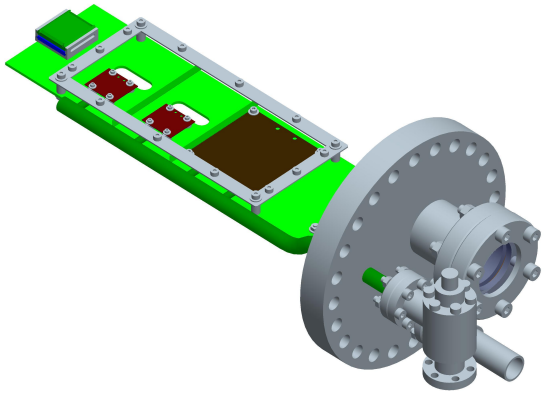

Figure 12: Final design of the Tore Supra detector. The new flange and the set of detectors can be seen

REPORTS AND PUBLICATIONS

[1] "Assessment of the integration of a dust injector system and electrostatic dust detector in the Tore Supra environment." CEA Internal Report CFP/NTT-2007.075 - S. Rosanvallon, T. Boulet and S. Vartanian

TASK LEADER

Christian GRISOLIA and Stéphane VARTANIAN

DSM/IRFM
CEA-Cadarache
F-13108 Saint-Paul-lez-Durance Cedex

Tel: 33 4 42 25 43 78
Fax: 33 4 42 25 44 90

e-mail: christian.grisolia@cea.fr

TW6-TPP-DUSTGEN-D01

Task Title: DUST GENERATION RATES FOR THE PLASMA EDGE/DIVERTOR CONDITIONS EXPECTED FOR THE ITER Q_{DT} = 10 REFERENCE SCENARIO WITH A CFC/W AND W DIVERTOR TARGET AND A Be WALL

INTRODUCTION

Among the carbonaceous fragments usually collected in tokamaks with graphite plasma-facing components, one can observe the presence of spherical nano-sized particulates. Their precursors result from multiple collisions between the reactive carbon atoms and/or between hydrocarbon radicals present in the edge plasma, originating from physical sputtering and chemical erosion.

The understanding of such dust particle formation in tokamak systems is a prerequisite to any attempt to limit or avoid the formation of these particles that may be responsible for undesirable tritium retention and possible pollution of the plasma during the discharge phase.
The study of the formation of such dust particulates is therefore essential for the safe and secure operation of ITER.

2007-2008 ACTIVITIES

MODELLING OF DUST GROWTH

This part of the work has focused on detailed modelling of the electric field structure in the discharge. We divide the discharge into four distinct regions.

The first region is the cathodic sheath, described by a linear electric field model, which gives us the mean energy and incident ion flux impinging on the graphite cathode, and thus the flux of sputtered carbon particles.

The negative glow region is modelled with a Monte-Carlo approach and yields the ionisation source. A transport equation determines the plasma density profile and conditions the electric field build-up in the negative glow region.

The Faraday dark space is described by an ambipolar diffusion equation. Lastly, a classical discharge balance gives the density, the field's axial component and the electron temperature.

All four regions are driven by very different physics. This work gave the full electric field and electron density profiles over the full discharge length (see figure 1).
In particular, the existence of a field reversal region essential trap negatively charged clusters.

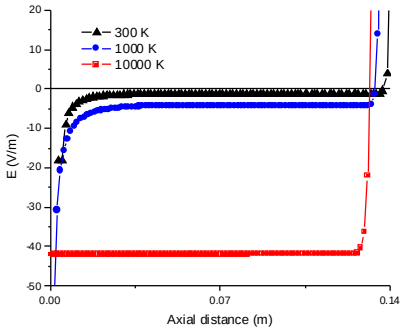

Figure 1: Electric field profiles as functions of the gas temperature

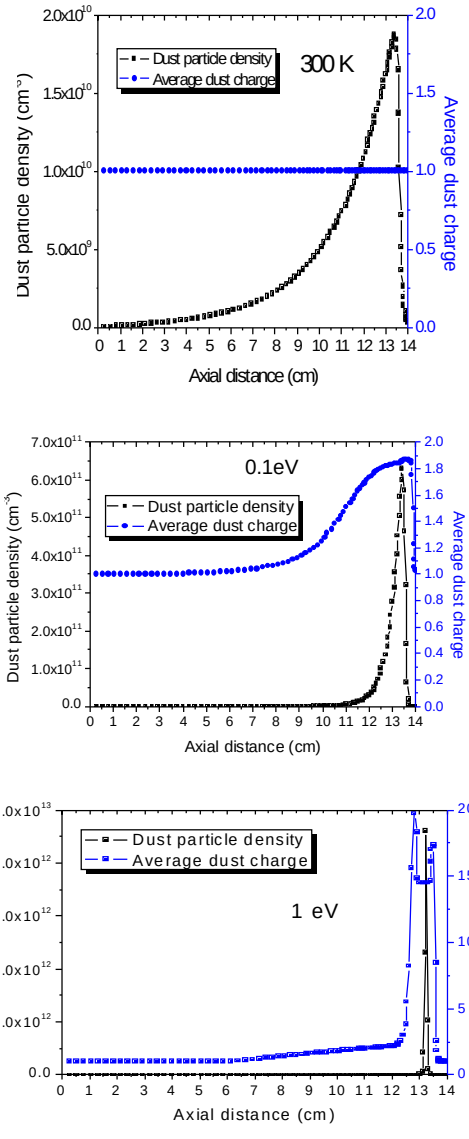

Figure 2: Dust density profiles and charge distribution with increasing gas temperatures

In addition to the electric field model, dust charging effects show a density pile-up of dust particles up to 10 nm in average size, just above the cathodic sheath, with some diffusion and, eventually, escape to the anode once inside Faraday dark space. The non-stationary OML dust charging model includes the kinetics of particle charging with the incoming ion and electron fluxes. The field reversal region maintains the charged dust particles in the cluster growth zone. At 1 eV, we see a local charge minimum at the highest dust density, possibly because of a coagulation rate overestimation, which we attempt to address by describing the dust with a size and charge distribution. Dust density profiles with the full charge model are shown in figure 2 as the gas temperature is increased.

CASIMIR EXPERIMENTAL DEVICE

In parallel, we operated the CASIMIR ("Chemical Ablation, Sputtering, Ionisation, Multi-wall Interaction and Redeposition") device, intended as an ITER dome simulator, to study the formation of eroded carbonaceous compounds (including dust particles), their transport and physico-chemical transformation that may happen in the far SOL of tokamak reactors and/or "parasitic" discharges such as are expected in the ITER divertor dome volume. The main new features installed in 2007 are a mass spectrometer and ion energy analyser as well as a substrate holder which can be both biased and temperature controlled.

We also continued working with an in-house low temperature plasma reactor, developed to simulate some of the plasma/surface processes that can occur under the divertor and in the far scrape-off layer regions of tokamaks. This CASIMIR (Chemical Ablation, Sputtering, Ionization, Multi-wall Interaction and Redeposition) device, envisioned as an ITER divertor dome simulator, aims to address issues related to the chemistry of hydrocarbon erosion products, along with transport, transformation, and re-deposition of these products in parasitic plasma environments, as already observed in different tokamaks and expected in ITER.
We will present here some sample results of measurements of energy distribution functions of hydrogen ions in pure H_2 plasmas or in Ar/H_2 gas mixtures. We were able to detect a shift of the H^+ ion average energy towards higher values when mixed with Ar, likely due to inter-species collision processes.
We also used the mass spectrometer functions to identify the erosion products obtained from the graphite target, heated and biased, again under different plasma gases: H_2, pure Ar, or Ar/H_2 mixtures. The most efficient gas, in terms of erosion yield, has been found to be the Ar/H_2 mixture, which is indicative of synergetic effects between physical sputtering (and creation of dangling bonds at or near the graphite substrate surface) by the bombarding heavier Ar^+ ions followed by chemical erosion from atomic H radicals. The detected hydrocarbons, in the first few minutes of the discharge, remain light (C_xH_y, x<3), as can be seen from the mass spectrum in figure 3 below.

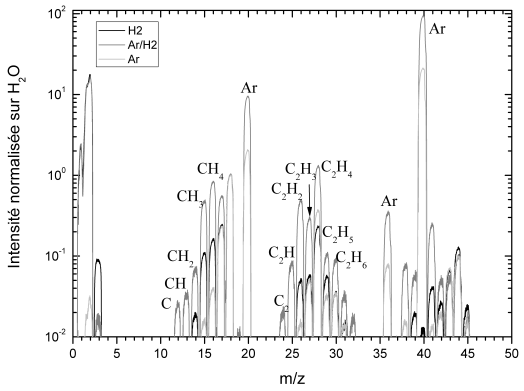

Figure 3: Mass spectra obtained in the CASIMIR erosion chamber for three gas mixtures

In addition, there is a continued effort to develop a PIC (Particle-In-Cell) model of the CASIMIR device, both the erosion chamber plasma and the secondary "parasitic" discharge. This is done in collaboration with the LPPGTS (ENSCP, Paris) and Innsbruck University (Austria). The code boundary conditions were generalized so as to inject several types of positive ions and also deal with the H^- negative ions, which must be handled separately. Currently, the model can compute the space and energy distribution of the positive hydrogen ions (H^+, H_2^+, and H_3^+) inside the CASIMIR erosion chamber (see an example in figure 4), and thus yield the carbon erosion rate of the substrate sample. We are currently working on bettering the model for the H^- negative ions as well as incorporating light hydrocarbons C_xH_y (where $x \leq 3$) such as those detected by mass spectrometry (see previous section) and neutral atoms, molecules and radicals. This will then allow us to estimate the formation rates of the different species and establish the chemical processes at play during the transport phase towards the secondary parasitic discharge and eventual re-deposition. The secondary discharge will also need its own PIC model, since the plasma parameters there are quite different from the erosion chamber plasma.

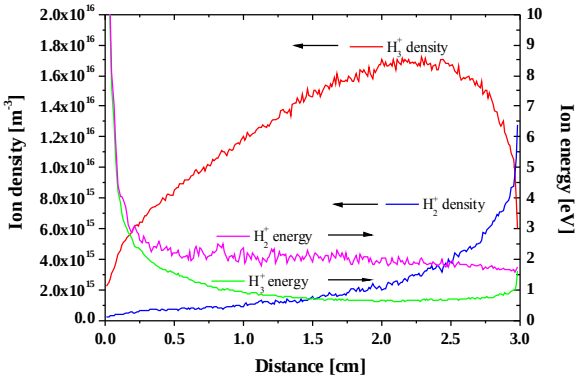

Figure 4: Sample result of density and average energy profiles for H3+ and H2+ ions in CASIMIR. The power injection into the plasma is done on the left at 0 cm and the target is situated on the right at 3 cm

REPORTS AND PUBLICATIONS

X. Bonnin, G. Lombardi, K. Hassouni, A. Michau, F. Bénédic and C. Arnas, Modelling of carbon dust formation by cluster growth in plasmas, J. Nucl. Mater. 363-365, 1190-1194 (2007)

C. Arnas, A. Mouberi, C. Dominique, F. Bénédic, D. Monéger, G. Lombardi, X. Bonnin, K. Hassouni, Ch. Brosset and B. Pégourié, Growth and heating of carbon nanoparticles in sputtering and hydrocarbon discharges, 1st Dust in Fusion Plasmas EPS Workshop, 8-10 July 2007, Warsaw, Poland

C. Arnas, A. Mouberi, K. Hassouni, A. Michau, F. Bénédic, G. Lombardi and X. Bonnin, Nanostructure of carbon dust generated in plasmas of different parameters, 5th International Conference on the Physics of Dusty Plasmas, Ponta Delgada, Azores, May 18th-23rd, 2008

C. Arnas, A. Mouberi, K. Hassouni, A. Michau, G. Lombardi, X. Bonnin, F. Bénédic and B. Pégourié, Carbon dust formation in a cold plasma from cathode sputtering, J. Nucl. Mater. (2009), in press

G. Lombardi, F. Bénédic, K. Hassouni, A. Michau and X. Bonnin, Introduction of a new experimental device for simulating parasitic plasmas such as those expected under the divertor dome, J. Nucl. Mater. (2009), in press

Grisolia, P. Sharpe, J. Winter, C. Arnas, X. Bonnin, S. H. Hong, S. Rosanvallon, M. T. Porfiri, G. Counsell and A. Loarte, Micro-particles in ITER: a comprehensive review, 13th International Conference on Fusion Reactor Materials (ICFRM-13), Nice, France, 10-14 December 2007

X. Bonnin, G. Lombardi, K. Hassouni, A. Michau, F. Duré, F. Bénédic and C. Arnas, Modelling of carbon dust formation by cluster growth in plasmas, 18th International Symposium on Plasma Chemistry, August 26th-31st 2007, Kyoto, Japan

F. Duré, A. Michau, K. Hassouni, X. Bonnin, G. Lombardi, F. Bénédic and C. Arnas, Modelling of carbon dust formation by cluster growth in plasma, 1st Dust in Fusion Plasmas EPS Workshop, 8-10 July 2007, Warsaw, Poland

TASK LEADER

Xavier BONNIN

CNRS – LIMHP, Université Paris 13
99, Avenue J.-B. Clément
F-93430 Villetaneuse

Tel: 33 1 49 40 34 24
Fax: 33 1 49 40 34 14

e-mail: bonnin@limhp.univ-paris13.fr

TW6-TPP-DUSTGEN-D02b

Task Title: EVALUATION OF DUST GENERATION MECHANISMS AT THE ITER SOL AND DIVERTOR PLASMA ANALOGY BETWEEN CLUSTER PRODUCTION BY LASER ABLATION AND DUST GENERATION IN ITER

INTRODUCTION

The objective of this task is related to the estimate of dust production/agglomeration/destruction rates for the plasma edge/divertor conditions expected during ELMs and disruptions for the ITER $Q_{DT} = 10$ reference scenario with a CFC/W and W divertor target and a Be wall.
In the present wok we demonstrated that ITER conditions can be reproduced quite easily by laser-matter interaction with pulsed laser source.
The objectives of the present task were to:

- Upgrade and apply codes developed to study clusters and nanoclusters formation under laser ablation conditions to C material,
- Validate the simulations by laser ablation experiments,
- Extend the codes to plasma-gun conditions in order to compare simulation results and experimental results.

This report describes the main results achieved in relation with the first two objectives. The third objective concerning the extension of the laser ablation codes to plasma gun conditions was not achieved due to difficulties for upgrading ablation codes and consequently through lake of time.

2007-2008 ACTIVITIES

MULTI-SCALE MODELLING OF CLUSTER FORMATION

Multi-scale models based on combinations of atomistic Molecular Dynamics (MD), Direct Simulation Monte Carlo (DSMC) and continuous (hydro dynamical) approaches were performed to study cluster formation both from solid targets and in a gas phase. The developed model allows us to compare the relative contribution of the two channels of the cluster production by laser ablation:
(i) direct cluster ejection from a target under rapid heating, expansion or impact, such as laser interaction, and
(ii) condensation, evaporation and coalescence in a gas phase.

First, we performed both hydrodynamics and molecular dynamics simulations of rapid target decomposition. These simulations demonstrated that clusters can be ejected from the target. Molecular dynamics also provides information about the minimum achievable mean pressure as a function of expansion rate and temperature.
These simulations are used to describe cluster precursors.
Then, additional calculations are performed to study the following evaporation and growth of particles due to collisions in the gas phase. Rapid gas flow expansion and cooling, lead to cluster condensation. In the presence of a background gas, additional collisions with background gas species affect the cluster size distribution. MD simulations are performed until a time delay of 3 ns for a cluster with different initial size and internal temperature, in the presence of a molecular background gas. Simulation results show that the cluster grows with time and the cluster size converges to a constant value dependent on both cluster and gas parameters.
In the presence of a gas with a high density ($2.0 \cdot 10^{19}$ part./cm^3), the size of clusters rapidly increases.
In our simulation, we consider only the following reactions: simple collision, evaporation and condensation processes.

To study the evolution of the cluster, we follow the size of the cluster every 100 ps and the number of cluster particles, which evaporate (low potential energy) and the number of gas monomers, which condensate on the cluster (high potential energy), as shown in figure 1. When cluster grows, the number of particles on its surface with a high potential energy increases. In addition, large clusters have lower potential energy (high negative value) than medium clusters and they grow more rapidly due to the sticking collisions.

We used classical molecular dynamics simulations to investigate material decomposition mechanisms as bond breaking, void nucleation, the formation of new surfaces, etc. These processes are known to be extremely difficult to treat by using conventional continuum approaches. In spite of the wealth of obtained information about the dynamic fragmentation, the practical determining of material decomposition conditions remains challenging.
In particular, problems arise with a simple implementation of these effects in typical finite-element codes, where these conditions are required as a function of calculation parameters (e.g., mean pressure, temperature, expansion rate, geometry, etc) and material properties (bond parameters, potential, etc.).
The present molecular dynamics study is aimed at the better understanding of the material decomposition process by means of a detailed microscopic simulation for a Lennard-Jones (LJ) system. We consider the disintegration of an expanding liquid heated either below or above the critical temperature.
The code allows visualizing the evolution of the mean potential energy per atom of the clusters obtained at different initial strain rates and temperatures. Thus, the

code permits to study void formation, bond-breaking process and free surface cluster formation.

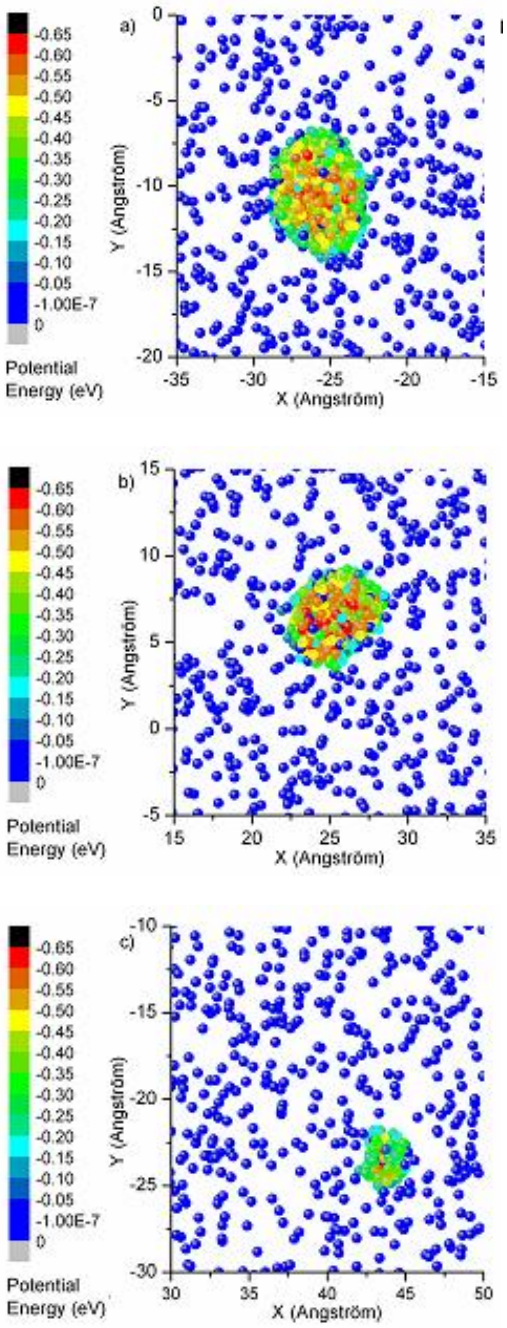

Figure 1: Snapshots from the simulation showing clusters in the presence of a background gas ($1.0 \cdot 10^{19}$ part/cm^3 and at 800 K). The contains (a) 750 particles, (b) 500 particles and (c) 100 particles at the end of simulation (3 ns). The colors correspond to the potential energy. The blue and gray colors represent gas particles (higher potential energy) and black and red colors are for particles inter the cluster (lower potential energy)

The results of the MD simulations are introduced in the DSMC model, which describes the expansion of the plume and then demonstrates the long-timer evolution of the clusters in the plume. With the use of our multi-scale model, we finally investigated the longer-time cluster formation in laser-ablated plumes (carbon targets).

The results show the flow evolution for different cluster groups as a function of their size (figure 2).

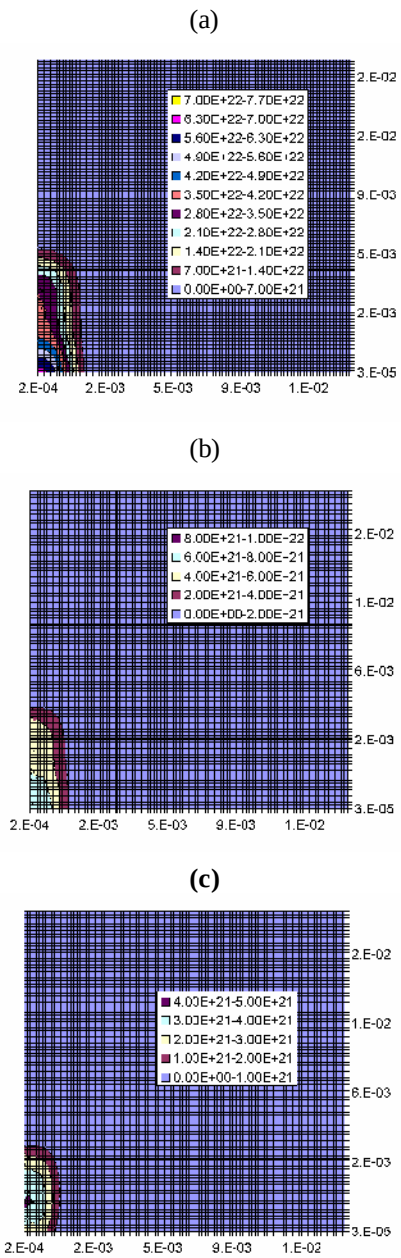

Figure 2: Spatial distribution of carbon cluster density at 1.55 µs after laser picoseconde (12 ps, 8.6 J/cm^2) interaction with a carbon target under vacuum condition. (a) – atoms ; (b) – small clusters (2 to à 10 atoms) ; (c) – big clusters (> 10 atoms)

EXPERIMENTAL STUDY

Characterisation of laser-induced particles

During laser ablation of materials, atoms, electrons, ions and some small aggregates are ejected from the surface with very high velocities (10 to 1000 m.s^{-1}) and react with the surrounding gas. These collisions can lead to aggregation or evaporation processes of particles as it has been shown by the numerical approach. Laser ablation of Tungsten samples and CFC tiles (from Tore Supra) was performed and the ejected dusts (clusters) on a silicon

substrate located in front of the irradiated samples (19mm) were collected.
The laser source was a picosecond Nd-YAG laser emitting at 1064nm wavelength with pulse duration of 50ps.
The experiments were carried out in a chamber under helium (pressure from 2 mbar to 1 bar). Morphological investigations were performed by using Scanning Electron Microscope (SEM JEOL 6320F) to characterize the structure of the deposited layer. Figure 3 shows the influence of the gas pressure on the deposited layer morphology in the case of laser ablation of CFC Tile. At low pressure of Helium the carbon aggregates have sizes of few tens of nanometers. The pressure increase up to 50mbar induces a thicker layer with larger aggregate size, typically 100nm. A further increase of the pressure up to 1bar leads to the disappearing of the aggregates. The layer is thinner and looks like a foam.

(a)

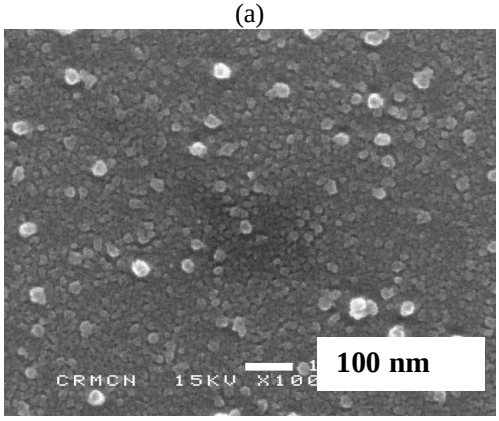

(b)

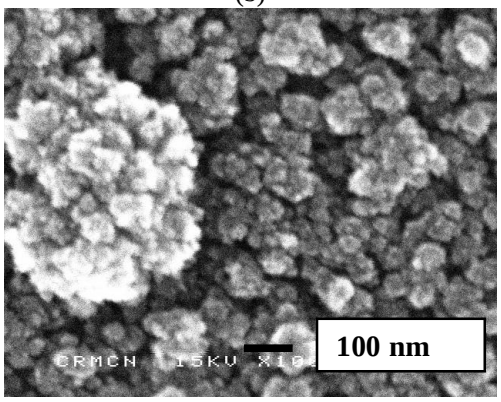

Figure 3: SEM images of dust layer on Si substrate formed by laser ablation of a CFC Tile under 2mbar (a) and 50mbar (b) of Helium.
The substrate was set 19mm from the tile

Comparison with particles formed in plasma induced by other sources

By controlling the plasma parameters and the collection technique, the laser ablation process allow to produce particles over a wide range of characteristics, and then to simulate some of the formation processes occurring in fusion reactors. We were able to reproduce:

- Carbon particles with cauliflower structure produced in Ar DC discharge used to simulate edge plasma of a Tokamak,
- Spherical particles and foam-like aggregates collected in Tore Supra,
- Tungsten layer deposited after plasma gun ablation,
- Tungsten aggregates formed during plasma gun ablation. For this condition the shapes are very similar, but the sizes of the laser-induced cluster are smaller,
- Carbon particles collected from TEXTOR as shown figure 4.

(a)

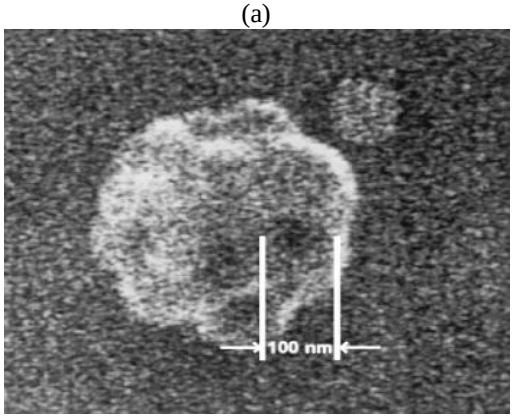

(b)

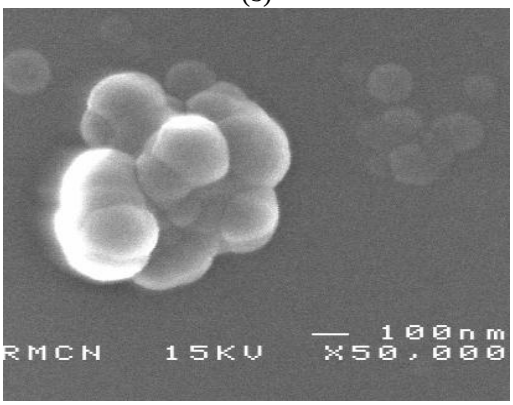

Figure 4: Carbon particles collected from TEXTOR (a), and formed by laser ablation under vacuum (b)

CONCLUSIONS

Both numerical and experimental investigations of the mechanisms of particle formation by laser ablation were performed. The experimental study shows that laser ablation leads to particle formation. This process takes place in the ablation plasma and, as it is described in the modelling part of this report, it is strongly dependant of the plasma characteristics. In particular, the number of collisions allowing the aggregate growth is of prime importance. So, the particle size can be controlled by the surrounding gas pressure and the distance of cluster collection. A higher gas pressure leads to a better confinement and an increase of the collisions. This explains the larger aggregates obtained in the case of an intermediate gas pressure (~ 50mbar). For a gas pressure of 1bar, the plasma expansion is small, and the aggregates cannot move fare away from the target; only atoms and very small aggregates reach the substrate with a very low velocity, and they form a porous layer.

In conclusion this study showed that particles formed by laser ablation have controllable properties and morphology similar to the properties of dust particles formed under ITER conditions. Simulation codes based on Multi-scale models (Molecular Dynamics, Direct Simulation Monte Carlo-hydro dynamical) allow studying clusters/dusts growth and decomposition. Further studies could be developed to simulated cluster formation under plasma gun ablation.

REPORTS AND PUBLICATIONS

[1] T.E. Itina: "Molecular dynamics study of the role of material properties on nanoparticles formed by rapid expansion of a heated target", Applied Surface Science 225, 2009

[2] Gouriet K., Zhigilei L.V., Itina T.E.: « Molecular dynamics study of nanoparticle evolution in a background gas under laser ablation conditions", Applied Surface Science 225, 2009

[3] Gouriet K., Itina T.E., Noel S., et al.: « Formation of nanoparticles by short and ultra-short laser pulses" Conference on High-Power Laser Ablation VII, APR 20-27, 2008 Taos, NM, Proceeding SPIE Vol. 7005, 2008

[4] Hermann J., Noel S., Itina T.E., et al.: "Correlation between ablation efficiency and nanoparticle generation during the short-pulse laser ablation of metals", Laser Physics 18, 2008

[5] Itina T.E.: "Decomposition of rapidly expanding liquid: Molecular dynamics study", Chemical Physics Letters 452, 2008

[6] A.Vatry, M. Naiim Habib, Ph. Delaporte, M. Sentis, D. Grojo, C. Grisolia, S. Rosanvallon: « Experimental investigation on laser removal of carbon particles », Applied Surface Science (2008), doi:10.1016/j.apsusc.2008.09.045

[7] A.Vatry, M. Naiim Habib, Ph. Delaporte, C. Grisolia, D. Grojo, S. Rosanvallon, M. Sentis: "Characterisation of carbon and tungsten micro-particles mobilised by laser irradiation in order to develop an ITER dust removal technique", Accepted for publication in Journal of Nuclear Materials (2008)

TASK LEADER

Marc SENTIS

CNRS-Université de la Méditerranée
Laboratoire LP3 UMR 6182
Parc Scientifique et Technologique de Luminy
163 avenue de Luminy – C.917
F-13288 Marseille Cedex 9

Tel: 33 4 91 82 92 80
Fax: 33 4 91 82 92 89

e-mail: Sentis@LP3.univ-mrs.fr

CEFDA05-1271
CEFDA07-1700-1556

Task Title: TW6-TPHI-ICHDESREW AND TW5-TPHI-ITERDES3: DESIGN OF THE ITER ICRF ANTENNA MECHANICAL DESIGN OF THE ITER ION CYCLOTRON HEATING LAUNCHER BASED ON IN-VESSEL TUNING SYSTEM

INTRODUCTION

The reference design for the ITER Ion Cyclotron Heating (ICH) system established an antenna design based on the resonant double loop concept [1] with conjugate T matching.
This design concept features a circuit with resilient properties regarding strong loading variation due to ELMs. New studies were conducted to improve the existing conceptual design, and to address relevant matters like the electrical performance of the launcher, the matching and the control of the array [2].
On the basis of the issues pointed out by these studies, substantial mechanical modifications were implemented to improve efficiency, reliability and maintenance of the ITER ICH antenna.
This paper described the mechanical design completed during this activity by the joint team from Euratom-CEA Association, ENEA-Frascati and ENEA-Consorzio RFX (Italy), and discussed the main advantages of the proposed array.

2007-2008 ACTIVITIES

ITER ICRH ANTENNA GENERAL DESCRIPTION

The antenna is an array of 24 independents straps separately fed by 24 Vacuum Transmission Line (VTL), each connected to 12 independent T-matching systems and 12 generators.
To minimize cost and ease assembly, qualification and maintenance, a modular approach was privileged. The structure is composed of six modules subdivided in a front and a rear module (figure 1).
Located inside a private vacuum at about 60cm inward from the back flange ensuring the IC plug vacuum boundaries, the 12 T-matching systems are coupled to form the 6 identical rear modules, connected to the 6 front modules that form the antenna radiating face.
A solid port-plug structure, made out of stainless-steel and subdivided in 6 identical drawers, receives the 6 front modules and ensures the connection of the rear ones, thus taking most of the electromechanical forces [3].
Two vacuum-tight barriers, one located close to the back flange and the second one on the back of the rear module ensure the required safety barriers against tritium leakage.

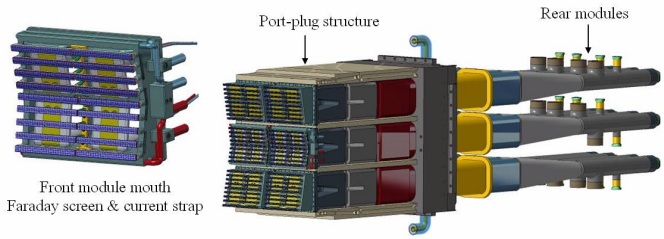

Figure 1: Left: Faraday screen (central module) and current straps. Right: ICRH antenna overall view, showing the six front and rear modules installed inside the port-plug structure (one side plate hidden)

In vessel port-plug and front modules

The front module (figure 2) consists of two resonant circuits, featuring a Faraday Screen (FS) cavity behind which 4 straps are fed by independent RF lines. Except for the FS cavity and the current straps that have to fit the poloidal and toroidal edge profile of the VV, all the module parts are identical and exchangeable. The shapes of the conductors are optimized to reduce the electrical field and make a smooth transition between the strip line geometry of the strap and the coaxial shape of the 20Ω VTL. Besides the electrical properties of this tapered line, the shape presents advantage regarding neutron-streaming compared to a coaxial structure. The rear cylindrical part of the line is hollow to host a RF cavity, where the front part of the matching system will move ensuring a capacitive coupling between the two VTL stages. A vacuum window located at the back of the VTL, with one side connected to the inner coaxial conductor and the other to the outer, make the front structure vacuum-tight. To allow the assembly, the inner and outer conductors are divided in separate sub-parts bolted together, with TIG welded hydraulic connections passing from sub-parts to sub-parts.
To improve the reliability of the in-vessel components, all vacuum-tight joint are welded or brazed. All the parts including the port-plug structure were designed in order to be water-cooled at high pressure and temperature as required by ITER operating conditions. A RF electrical contact was integrated round the vacuum window outer body to allow thermal expansion and protect the ceramic from the disruptive forces. In case of failure, the window design allows the replacement of the faulty component without removing the whole port-plug. Once the 6 front modules fully assembled and tested, they can be independently plugged inside the drawers of the port-plug structure, bolted on the front and vacuum-tight welded on the rear flange of the port-plug.

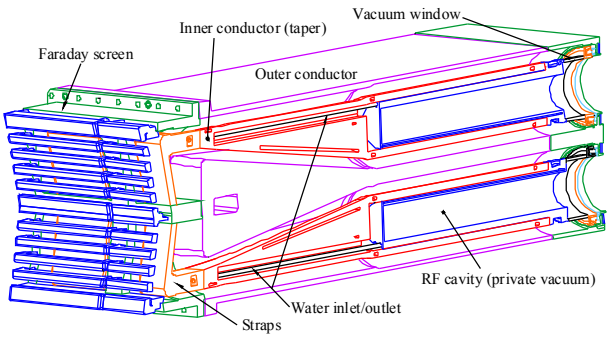

Figure 2: Cut-view of a mid-plane antenna module front part

Rear modules

The rear modules bolted on the back flange of the port-plug complete the in-vessel RF circuit. A Helicoflex® gasket is used to seal the private vacuum, and RF contacts are used to ensure a good electrical continuity between the front and rears structures, and compensate the foreseen discrepancies between the connected parts. Each rear module contains 2 identical tuning system arrays grouped by pair (figure 3).

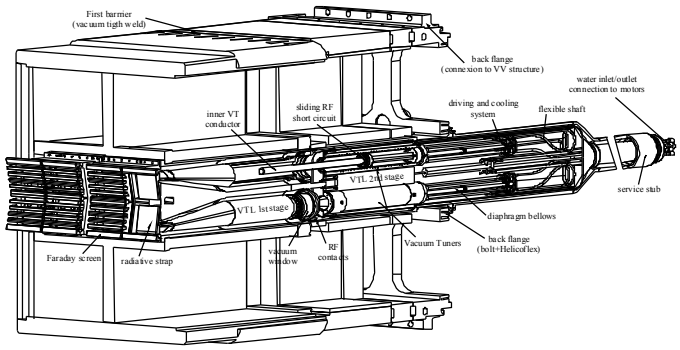

Figure 3: Over-view of a mid-plane antenna module inside the ITER port- plug

A tuning system array consists in series of oval shaped conductors of variable cross-section that form the impedance transformer (going from 2 to 30Ω). Inside this envelop, two tuning systems are mounted one on top of the other. Each element, referred as coaxial vacuum tuner (CVT), consists in a coaxial structure, with an inner conductor of variable length protruding inside the RF cavity made in the VTL first stage. Between the two conductors a contact support can slide independently from the inner conductor, allowing a variation of the depth of the RF cavity located in the VTL second stage.
The movements are guided by bearings and ball screws located in air behind the contact support, isolated from the vacuum by diaphragm bellows. Flexible shafts transmit the rotation through the inner conductor from motors located in air outside the port-plug. All the mechanical components integrated in the design are commercially available standard elements, compatible with heavy-duty cycle, high temperature and high vacuum operation where needed. Like the other components of the antenna, the tuner are fully cooled device, water fed from the rear through a quarter-wavelength service stub.

A specific effort on the design of the second stage of the VTL was made to not only allow in case of failure, a complete withdraw of the component without breaking the primary vacuum, but also a disassembly implying simple mechanical operation. For example, to reduce the operating time the RF contacts used in the tuner are mounted on the outer conductor instead of bolts. The connection with the pressurized feeding lines coming from the power source is made outside the port-plug behind a secondary vacuum window.

CONCLUSIONS

This design was one of the technical options proposed to ITER for the ICRH launcher. The alternative design based an external matching system was preferred to the so-called internal design. However several original features from the internal design became additional ITER design requirements and have been integrated inside the present ITER IC antenna.
The baseline options chosen during the implementation of our design which are now considered in the reference ITER design are:

- A launcher composed of modular elements inserted inside drawers,
- A strong effort in the design made to ease the handling, maintenance and qualification foreseen on the different modular parts,
- A vacuum windows that can be removed without breaking the torus vacuum,
- The use of well-known and improved technologies,
- The design of components like the tapered conductor transition, or the Faraday screen.

Thanks to the great involvement of each partner associated in this task, the design process reached a high level of completeness. Despite, the fact that this design did not succeed to convince ITER, the experience, knowledge, ideas and concepts developed and harvested during this activity will be of great help for the upcoming design of the ITER IC launcher.

Acknowledgements

The fruitful involvement, in the CATIA® drawings, of C. Brun and J.C. Patterlini is gratefully acknowledged.
This work was achieved by the joint team from Euratom-CEA Association, ENEA-Frascati and ENEA-Consorzio RFX (Italy).

REFERENCES

[1] T.L. Owens, F.W. Baity, D.J. Hoffman, ICRF antenna and feed-through development at the Oak Ridge National Laboratory, in Proceedings of the 6th Topical Conference on RF Plasma Heating, 985

[2] Final Report on EFDA contract 04/1129, ITER ICRF antenna and matching system design (Internal matching), April 2005

[3] P.Testoni, F. Cau, P. Sonato, Electromechanical analysis of the ITER Ion Cyclotron antenna structure and components, 24th Symposium On Fusion Technology, 11-15 September 2006, Varsaw, Poland

REPORTS AND PUBLICATIONS

TW6-TPHI-ICHDESREW draft report for sub tasks 1.2 & 2.14 CH/NTT-2007.036 P. Mollard, A. Argouarch

ITER ICRH antenna – Final report on EFDA task TW6-TPHI-ICHDES-REW CH/NTT-2008.001. G. Agarici, A. Argouarch, J.-P. Martins, P. Mollard, K.Vulliez

TASK LEADER

Karl VULLIEZ and Gilbert AGARICI

DSM/IRFM/SCCP/GCHF
CEA-Cadarache
F-13108 Saint-Paul-lez-Durance Cedex

Tel: 33 4 42 25 73 19
Fax: 33 4 42 25 62 33

e-mail: karl.vulliez@cea.fr

CEFDA05-1329

Task Title: TW6-TPHI-ICFS: FARADAY SHIELD MODELLING AND RF SHEATH DISSIPATION

INTRODUCTION

The Faraday shield on the ITER ion cyclotron antenna is a critical component: it is the main plasma-facing component for the antenna and must withstand the same heat loads and disruption effects as the first wall; it shields the inner parts of the antenna from particles; it polarizes the IC wave and prevents the electrostatic field on the current strap from coupling to the plasma.

Experiments on Tore Supra and elsewhere indicate that parts of the antenna structure (e.g., guard limiters) can be heated anomalously in the presence of RF fields and plasma; the standard explanation is that RF-induced sheaths and/or convective cells enhance particle and power transport to these regions, thereby causing the observed high heat load. Considerable modelling of this effect was done in the past. Can a model of these effects be developed and applied to the Faraday shield design for ITER, and what guidance regarding shield geometry can be obtained from these models?

According to specifications in December 2005 the task includes the following activities:

- Use RF electric field maps developed as a part of task TW6-TPHI-ICFS1, static magnetic equilibria supplied by the IT, and current or improved sheath theories to compute the power lost to RF sheaths in different ITER antenna/Faraday shield configurations. Use density profiles in the scrape-off region, supplied by the IT, corresponding to those used to calculate antenna loading for Scenario 4.

- Calculate power deposition profiles on the antenna and surrounding regions for different cases of antenna and Faraday shield geometry. Evaluate the advantages and disadvantages of various geometries, including in particular the case of horizontal and tilted Faraday shield elements, transparent vs. opaque shields and no shield at all for comparison. Consider in particular the case where the antenna is contained completely in a mid-plane port, with the front surface of the Faraday shield being ~ 1 cm behind the first wall.

2007-2008 ACTIVITIES

PRINCIPLE OF RF SHEATH EVALUATION

In their most basic form [7] RF sheath rectification processes can be briefly summarized as follows. ICRF antenna operation drives an oscillating RF potential V_{RF} between the extremities of open magnetic flux tubes, given by $V_{RF} = \int_L E_{//}.dl$, where $E_{//}$ is the RF parallel electric field and integration is along the open field line. As a reaction to this RF potential, and due to the non-linear behaviour of the sheaths at both flux tube extremities, the field line gets biased to a rectified DC potential V_{DC}, which is generally well above typical floating potentials in the Scrape-Off Layer (SOL). Ions accelerated across the high DC potential cause enhanced sputtering and localised high heat fluxes at the field line ends. Moreover the differential biasing of nearby flux tubes creates RF-induced DC E×B particle convection transversally to the field lines [4]. The intense RF-induced DC electric fields could also interact with the H-mode [4].
Calculation is thus performed in several steps:

1°) Evaluate $V_{RF} = \int_L E_{//}.dl$ along every open field line, from computed RF field maps.

2°) Evaluate V_{DC} from V_{RF} on each field line. In the simplest RF sheath model [7], each flux tube is biased independently from its neighbours, to a potential $V_{DC}=|V_{RF}|/\pi$.

3°) Evaluate the density n on each field line. Density is supposed homogeneous along flux tubes so that its determination is a 2D problem transversally to the field lines. Particle transport is due to parallel losses, cross-field diffusion and RF-induced E×B convection, and density balance in steady-state regime reads

$$\mathrm{div}\left[-D_{\perp}\nabla n - n\frac{\nabla V_{DC}\times \mathbf{B}_0}{B_0^2}\right] + \frac{nc_s}{L_{//}} = 0 \qquad (1)$$

where $D_\perp$ is a particle diffusion coefficient, $L_{//}$ is the length of open field lines, c_s is the sound speed = $[k(T_e+T_i)/m_i]^{1/2}$. The 2D density map needs to be computed only in the region affected by convection. This domain is chosen as a rectangular box. In the radial direction, convective cells penetrate from the antenna mouth up to the point where V_{DC} is of the order of kT_e. From Tore Supra measurements, this is of the order of a few skin depths for the Slow Wave [8]. On the other side it was proposed to stop density calculation at the antenna mouth and not to calculate the density inside the box. This is motivated as follows:

- Geometry is complicated, so that precise boundaries of open field lines are not clear.
- Due to complicated geometry, precision of the local RF field might not be guarantied.
- Connection lengths decrease abruptly inside box, leading to fast density decay.

Equation 1 is solved in the simulation box using the CELLS code [1]. As boundary conditions on the plasma side n is fixed to its "unperturbed value". Density is put at 0 on the antenna side, assuming no recycling from chamber walls.

In the poloidal direction the poloidal derivative of the density is supposed to vanish at the limits of the simulation domain (meaning no poloidal convection).

4°) Evaluate ion parallel heat, losses at the extremities of the flus tubes. The particle density outflux is $nL_{//}c_s$ and each ion is accelerated across the sheaths to the energy of eV_{DC}, so that the energy outflux becomes $Q_{//}=enV_{DC}L_{//}c_s$.

PLASMA PARAMETERS

Magnetic equilibrium

The geometry chosen for RF field calculation is a flattened version of the ITER antenna front face. Consistently with this choice a simple magnetic equilibrium is proposed, in which field lines are straight lines parallel to the antenna front face and tilted by a pitch angle of α=15°. The local magnitude of the magnetic field in the antenna vicinity is taken constant at B_0=3.9T, consistently with ITER scenario 2 proposed for computations [9]. Note that since all the geometry is flattened, magnetic field lines are parallel to the antenna front face and no parallel loss is considered on FS rods.

Unperturbed radial profiles

From reference [9], typical SOL radial profiles are available in the zone unaffected by convection. They are shown on figure 1 for ITER scenario 2.

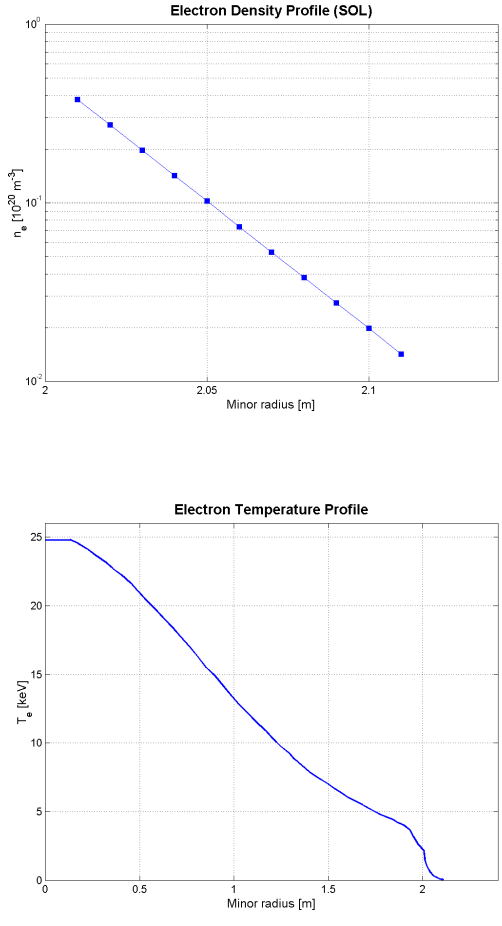

Figure 1: Scenario 2 profiles

Considerable uncertainty remains on these profiles. This, impacts directly on the sheath calculations:

- For given power coupled to the plasma, the magnitude of the RF near fields depends on the antenna coupling resistance, which is quite sensitive to the edge density profile.
- The radial penetration of the slow wave depends on the density at the antenna mouth.
- The local density at the penetration depth roughly determines how many particles are likely to be convected onto the antenna front face.

DEFINITION OF A TARGET MEDIUM FOR RF WAVES

The first step in the simulation process is a 3D mapping of RF near fields in the antenna vicinity. Antenna code HFSS used in this task cannot handle the most general dielectric tensors of magnetized plasmas. The load used for previous test RF field maps was shown to reproduce fairly well the coupling properties of a typical ITER plasma for the fast wave [5]. However, the present task is mainly interested in parallel RF fields, i.e. the slow wave, whose properties are radically different due to the anisotropy of magnetised plasmas. Slow wave is completely absent of the present HFSS medium, since it is isotropic. Simulations should however preserve realistic coupling to the fast wave, which determines the near field amplitude for given coupled power.

A systematic comparison of uniaxial and gyrotropic homogeneous media was made [2]. From this analysis it appears that part of the information about wave propagation is always lost when approximating gyrotropic with uniaxial media. However there is some latitude in choosing what is lost and what is preserved. Based on these considerations the following fall-back solution was proposed to try to get results using HFSS.

- As in "conventional cases" the domain facing the antenna is composed of a "vacuum zone", followed by an isotropic lossy dielectric where the fast wave is damped.
- In the vacuum zone, transverse dielectric constants are still $\varepsilon_\perp$=1. It is proposed to use a highly negative value for the dielectric constant $\varepsilon_{//}$ parallel to (tilted) magnetic field lines, in order to reproduce the high parallel conductivity in the plasma.

The fall-back solution has the following merits :

- Fast wave propagation, being insensitive to $\varepsilon_{//}$, should not be affected by the change of medium, whatever $k_{//}$.
- For perpendicular propagation $k_{//}$=0, suitable for integrating $E_{//}$ over "long field lines"with large toroidal extension (see [3]) a clear decoupling is possible. Propagation properties of the fast wave depend only on elements S and D of the Stix dielectric tensor, while the squared refractive index for the slow wave takes the form

$$N^2=P \qquad (2)$$

The refractive index for the Slow Wave at $k_{//}$=0 is thus well reproduced when $\varepsilon_{//}=P=1-\omega_{pe}^2/\omega_0^2$. From scenario 2 profiles, P~-20000 at the antenna mouth.

For this particular density, the typical evanescence length for the slow wave at $k_{//}=k_y=0$ is typically 6mm. Such rapid decay justifies *a posteriori* the choice of homogeneous plasma parameters near the antenna to represent the Slow Wave. Recent probe measurements on Tore Supra suggest that RF-induced SOL perturbations extend a few centimetres in front of powered antennas, consistently with skin depth estimates [8].
The proposed procedure was never tested previously, and potential drawbacks may arise. The highly anisotropic artificial medium is very demanding for a Finite Element code. The refractive index for the Slow wave is only well reproduced for $k_{//}=0$, whereas other values of $k_{//}$ contribute to the integral of $E_{//}$ over the finite extension of the map. In particular a spurious surface wave is expected for $k_{//}=\varepsilon_{\perp}=1$, which does not exist in the real plasma when $S<0$. Therefore some basic checks should thus be made on the HFSS results:

- Verify that the input impedance matrix, and particularly its real part, are only weakly affected when $\varepsilon_{//}$ is switched from 1 to –20000,
- Check the radial evanescence of the Slow wave,
- Check the absence of surface wave.

LINE INTEGRATED RF FIELD $|V_{RF}|$

Figure 2 shows that close to the antenna $|V_{RF}|$ decreases radially. The observed evanescence length is quantitatively consistent with the predicted dispersion relation for the Slow Wave at $k_{//}=0$. For plane waves this dispersion relation writes $k_x^2+k_y^2=\varepsilon_{//}k_0^2$ with $\varepsilon_{//}$=-20000 and k_0~1.05m^{-1} at 50MHz. The radial decay length $1/|k_x|$ depends on the characteristic poloidal size of the potential structures. For large scale components $k_y=0$ and the decay length is 6.75mm. For poloidal oscillations with a wavelength of 5cm, $k_y=2\pi/0.05=126$m^{-1} and the decay length is 5.15mm. This covers the range of slopes observed close to the launcher. Further away from the antenna $|V_{RF}|$ decreases more slowly.

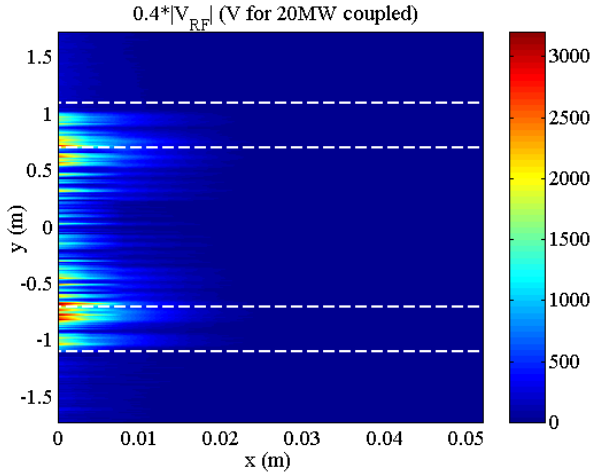

Figure 2: 2D mapping of line-integrated RF field

Close to the antenna $|V_{RF}|$ is maximal in the lower and upper parts of the antenna. Similar poloidal variations were observed experimentally on Tore Supra antennas [8]. Within the simple sheath model adopted for this report, this was attributed to parallel RF currents in the upper and lower edges of the antenna frame [3], [2]. FS bars could also contribute to these return RF currents, which should be avoided in order to reduce sheath potentials. $|V_{RF}|$ is low on magnetic field lines that do not pass in front of the antenna structure (i.e. $|y'|>1.1$m). This suggests that the stripes on the field maps do not contribute too much to the line integral, because of left-right compensations. Note however that the simulated antenna was not recessed in its metallic port, so that parallel RF currents $j_{//}$ cannot develop on the walls above and below the antenna structure.

MAPPING OF DENSITY

Without convection, the computed density is found poloidally homogeneous, as it should. It is also verified that the density e-fold length of the prescribed density profile on figure 1 is correctly recovered with the input parameters chosen in CELLS code. As soon as convection is switched on, poloidal inhomogeneity sets in. However the upper and lower parts of the map are sufficiently far from the antenna to be weakly affected. In regions where convection dominates over other transport processes, iso-density curves tend to align with iso-potential lines. Convection tends to deplete the zones of high potential at the centre of the convective cells. Over-density is observed near the equatorial plane and above major cells. Density perturbations extend radially over a few centimetres, where the slow wave is able to penetrate. The inner part of the simulation is weakly affected.

MAPPING OF HEAT FLUXES

Parallel heat fluxes are estimated from formula $Q_{//}=enV_{DC}c_s$. Within a constant, the 2D map of $Q_{//}$ on figure 3 is the product of the density map by the potential map. Two mappings of $Q_{//}$ were performed, with and without RF-induced density convection. Localised peaks above $Q_{//}$=10MW/m^2 are observed (i.e. 5MW/m^2 on each side of the flux tube). The average flux over the poloidal extension of the field maps and over the first two centimetres in front of the antenna is $\langle Q_{//}\rangle$~2.5MW/m^2.

The poloidal location of the heat fluxes is mainly determined by the antenna geometry. Highest heat fluxes are found in the upper and lower corner zones, where high sheath potentials develop. A local minimum is located near the equatorial plane. The radial extension of the ICRF-perturbed zone is determined by the evanescence of the slow wave at $k_{//}=0$. Significant heat fluxes are found in the first two centimetres in front of the antenna.

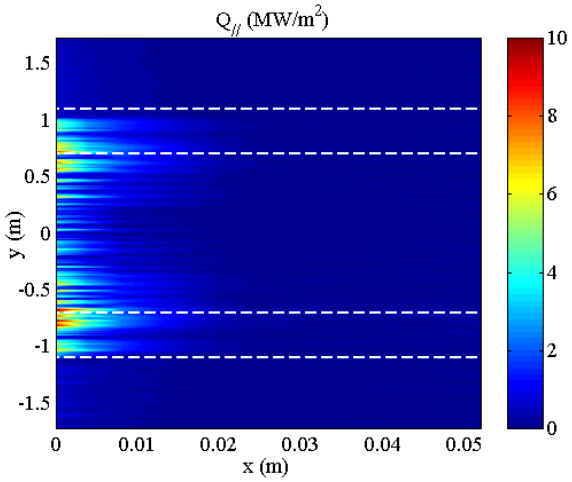

Figure 3: 2D mapping of expected heat loads

The total power lost through the sheaths is the integral of $Q_{//}$ over the 2D simulation domain. For 20MW coupled, spurious losses amount to 94kW without density convection and 88kW with convection, i.e. less than 0.5% of the launched RF power. Losses are lowered with density convection, because zones of high sheath potential at the centre of the convective cells tend to be depleted in density.
It must be finally reminded that the magnitude of $Q_{//}$ depends crucially on the density just in front of wall, which is poorly known so far. In that respect the rapidly decaying density profile on figure 1 is an optimistic assumption. Increased density would indeed mean more ions accelerated into the sheaths, in spite of lower sheath potentials due to better RF coupling. $Q_{//}$ is thus expected to increase with edge density, but more slowly than n_e. The penetration depth of the slow wave (c/ω_{pe}) also scales as $n_e^{-1/2}$.

CONCLUSIONS

In this task the simplest RF sheath model in the literature [7] was applied to "long field lines" in front of a flattened version of the ITER ICRF antenna in slab geometry. Only toroidal phasing [0,π,0,π] was treated. Orders of magnitude were obtained for the rectified sheath potentials (peak values of V_{DC}~4kV for 20MW coupled to the plasma) and parallel heat loads (peak values above $Q_{//}$~10MW/m^2, average $<Q_{//}>$~2.5MW/m^2, for 20MW coupled). Qualitative insight was gained on the 2D (radial/poloidal) topology of RF sheath potentials around the ITER antenna. Heat loads are concentrated where the slow wave can penetrate radially. With the density profiles of scenario 2, this amounts to a few centimetres. Heat loads are located poloidally in box corner zones, where high sheath potentials develop. Comparison with similar modelling on simpler antennas [Colas2005] suggests that such concentration of high potential might be produced by parallel RF currents flowing on the antenna frame and nearby FS rods. That's why it is suggested to reduce $j_{//}$ in further optimisations of the front face design.
Considerable quantitative uncertainty remains at each step of the modelling. Four axis of improvement can be identified.

- 1°) There is no consensus in the community over which sheath model should be used. To simulate the ITER antenna only the simplest model was available at the present time. Active work is under way both to improve sheath models towards more self-consistency, and to constraint the models with more experimental data.

- 2°) The anisotropic load for HFSS is to be considered as a fall-back solution. Although it retains in principle all the information needed for our calculations, it was applied to the ITER antenna without serious prior validation on simpler cases. However the line-integrated $E_{//}$, which is the relevant quantity for our purpose, shows the expected radial and poloidal variations over the simulated domain. It is not clear whether RF field amplitudes are correctly normalized for 20MW coupled, due to changes in the input **S** matrix with respect to "conventional" loads. Powerful antenna codes such as TOPICA [6] are now able to handle complex strap arrays in front of realistic plasmas. This is the easiest way to get rid of the uncertainty.

- 3°) Huge unknowns remain on density and temperature profiles in the far SOL. It must be reminded here that for RF sheaths $Q_{//} \propto \Gamma_{//} \propto nT^{1/2}$. The skin depth for the slow wave scales as $n^{-1/2}$. For given RF power coupled to the plasma, the magnitude of the RF potentials driving sheaths depends on the antenna coupling resistance, i.e. the distance from the straps to some cut-off layer for the Fast Wave.
The density profile used throughout the calculations is an optimistic assumption with respect to heat fluxes. Whatever the quality of the sheath models, as long as the plasma parameters are not accurately determined over the first centimetres in front of the antenna, quantitative results about $Q_{//}$ and slow wave penetration will remain orders of magnitude with 100% error bars.

- 4°) More realism is deserved in the geometry of the simulation. Since all the launching structure was flattened, magnetic field lines are necessarily parallel to the antenna front face and no parallel loss was considered onto FS rods. More generally, all kinds of curvature effect, e.g. FS-FS magnetic connections, field lines intersecting the FS at grazing incidence, are lost from the beginning.
The wall was excluded from HFSS simulations. Since RF parallel currents can develop there, the wall could play a role on the topology of RF near fields. It does play a role on particle screening. More generally there is a poor knowledge about magnetic connections in the far SOL: connexion lengths $L_{//}$, incidence angles… It is even unclear which object is connected to the open field lines over the first centimetres in front of the ITER ICRF antenna.

REFERENCES

[1] M. Bécoulet, et al. Phys. Plasmas, Vol. 9, No. 6, pp. 2619-2632, June 2002

[2] Bobkov V. V. et al AIP CP 933 83–6

[3] L. Colas et al. Nuc. Fus. 45 (2005) 1–16

[4] D.A. D'Ippolito, J.R Myra & al. Phys. Fluids B5 (10), 1993

[5] Ph. Lamalle et al. Nuc. Fus. 46 (2006) 466

[6] V. Lancellotti et al. Nuc. Fus. 46 (2006) S476–S499

[7] Perkins F.W., Nuc. Fus. 29 (4) 1989

[8] L. Colas et al. JNM 363–365 (2007) 555–559

[9] "ITER ICRF Antenna Loading with New Limiter and Plasma" (David Swain and Mark Carter), August 31, 2004

REPORTS AND PUBLICATIONS

[1] 'EFDA Task TW6-TPHI-ICFS2 - Final Report', CEA Internal Report - PHY/NTT-2007.004

[2] 'Approximation of cold magnetized plasmas in the ICRF range of frequencies with a diagonal dielectric tensor', Private communication, November 2006

TASK LEADER

Laurent COLAS

DSM/IRFM/SCCP/GSEM
CEA-Cadarache
F-13108 Saint-Paul-lez-Durance Cedex

Tel: 33 4 42 25 65 32
Fax: 33 4 42 25 62 33

e-mail: laurent.colas@cea.fr

Task Title: TW6-TPHI-ICRFCOORD: CO-ORDINATION OF THE ITER ICRF ANTENNA DESIGN AND R&D ACTIVITIES

INTRODUCTION

The ITER Ion Cyclotron Heating and Current Drive (ICH&CD) system is designed to couple 20MW of power from a single antenna (equivalent to a power density of ~9.3MW/m^2 at the antenna) in the frequency range 40-55MHz for a variety of ITER plasma scenarios. This requirement, together with the need to provide robust coupling in the presence of ELMs, focused attention on the development of an integrated design for the antenna and matching system which will satisfy the ITER performance requirements while operating reliably within the burning plasma environment.

A series of design and R&D activities are underway within the EFDA Technology Workprogramme at present to:
(i) demonstrate that the designs for the internal and external matching concepts can be made compatible with the ITER design;
(ii) develop a complete design of the matching control system, including the handling of arcs within the system, for each concept;
(iii) study the effects of different degrees of optical transparency and of RF sheath dissipation on the antenna Faraday shield design;
(iv) prepare a detailed design for a compact vacuum tuner for the internal matching concept which will satisfy the ITER functional specifications and to construct and test a prototype with the aim of demonstrating its suitability for use in ITER.

The overall aims of the ICRF Co-ordination Task are to ensure that the ongoing physics and engineering analysis on the ITER ICRF antenna, as well as the output from R&D activities, is documented to an acceptable level for the design concept selection and to prepare the framework for the definition of future design and R&D activities. This task is carried out as a collaborative effort between UKAEA (UK), CEA and ERM (B). CEA was in charge of the work package 4.2, dedicated to coordination of the necessary design and R&D analysis, together with relevant documentation that has to be completed in advance of the ITER design.

2007-2008 ACTIVITIES

Beginning 2007, CEA assisted ERM and UKAEA associations (work package 4.1 led by ERM) to complete a list of criteria to be used to assess the two antenna design (Internal matching and External matching). Using this list of criteria, written by ERM, CEA produced a Selection Comparison Document draft in a form that readily allowed comparison to be made between the two designs.

During a meeting held at Ringberg Castle (Germany), April 16-20, 2007, all concerned European associations including also ORNL from the USA collaborated to produce a complete and an agreed Selection Comparison Document.

This final document "Selection Comparison Document" was coordinated by the EURATOM-CEA. It provides the EURATOM-CEA contribution to this task (part 1, 2, 3, 4, 5, 6, and 7 of the sub-task 4.2) [1].

EURATOM-CEA also initiated the work to define the R&D program needed for the ITER ICRH antenna (examples in figures 1 and 2). For that, we produced a R&D Program Document draft. Then, this document has been completed by the collaboration of all the concerned European associations to produce a complete and an agreed R&D Program Document.

EURATOM-CEA also carried out the definition of the requirements for tests and testing facility required for procurement association within the EFDA Task TW6-TPHI-ICHDES-REW- (EFDA 07-1700).

Finally, EURATOM-CEA provided an updated evaluation of the antenna cost, based on latest antenna design (October 2007).

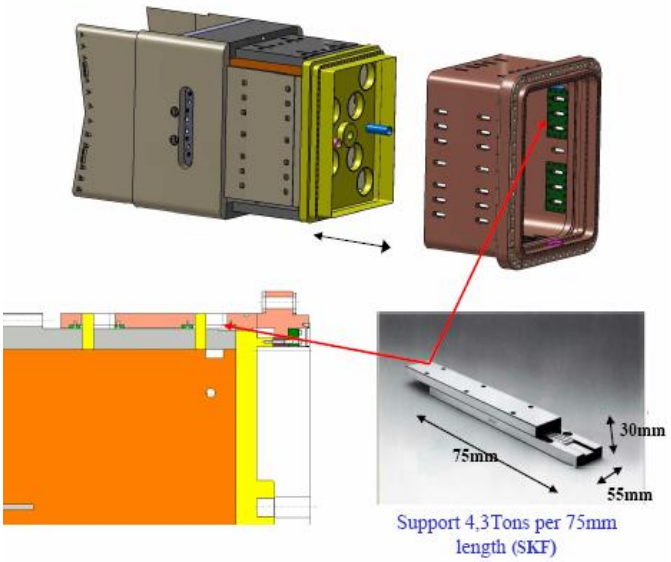

Figure 1: In order to shim the antenna inside the port-plug, specific devices are required to move heavy components (the complete antenna here) up to 45 tons under vacuum in a baked environment. Dedicated R&D programme has been proposed to perform such movement compatible with fusion environment

Figure 2: Several RF tests of components including dedicated mock-ups and full-size prototypes pieces of the ITER IC antenna will be required within the framework of the R&D program. Upgrading of existing test facilities has been proposed to fulfil ITER IC antenna testing programme. Figure 2 show the Tore Supra RF test stand facility. This existing installation is presently limited to the test of components water cooled at low temperature (chilled water below 35°C). Regarding the ITER operating conditions in term of cooling, an upgrade of the test stand is necessary to test water RF components within the ITER specification for the water cooling (100 à 150°C / 20 à 40bars)

REPORTS AND PUBLICATIONS

[1] G.Agarici; Co-ordination of the ITER ICRF Antenna design and R&D Activities EFDA Task TW6-TPHI-ICRFCOORD - (EFDA 06-1409), Final Report CH/NTT-2007.042

TASK LEADER

Gilbert AGARICI and Louis DOCEUL

DSM/IRFM/SIPP/GIPM
CEA-Cadarache
F-13108 Saint-Paul-lez-Durance Cedex

Tel: 33 4 42 25 61 65
Fax: 33 4 42 25 49 90

e-mail: louis.doceul@cea.fr

CEFDA06-1420

Task Title: TW6-TPHI-ICFSDES1: FARADAY SHIELD FOR DESIGN FOR THE ITER ICRF ANTENNA ARRAY

INTRODUCTION

The Faraday shield on the ITER ion cyclotron antenna is one the critical components : It is the main plasma-facing component for the antenna and must withstand the same heat loads and disruption effects as the first wall; it shields the inner parts of the antenna from particles; it polarizes the IC wave and prevents the electrostatic field on the current strap from coupling to the plasma. In addition there will be heat loads from RF losses. The objectives of this task are:

- to advise a Faraday Shield design will withstand heat loads, and disruption forces expected in the ITER burning-plasma environment. Such heat loads shall encompass those specified by the IT (direct radiated power from the plasma, neutron and gamma-ray volume power deposition, and power deposition from ELMs and direct particle bombardment, if any), and also RF loses from RF-sheath effects,
- to investigate possible alternative designs, in particular of a more optically closed FS,
- to develop a detailed plan to fabricate and test a FS element.

2007-2008 ACTIVITIES

A preliminary design of a faraday shield for ITER ICRH antenna is presented here. This design is based on the antenna with internal matching, and its adaptation to the antenna with external matching remains to be evaluated.

PRINCIPLES OF THE GENERAL DESIGN

The design is based on the mechanical structure of the antenna with internal matching. The conception of that design is modular in the sense that the antenna is an assembly of 6 individual modules which are inserted in a port plug (2 horizontal x 3 vertical, figure 1). The design of the 6 modules is globally identical except the front part (faraday shield) and back sections (connections to the stubs).

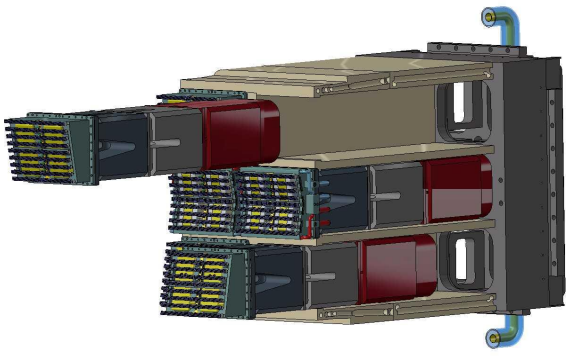

Figure 1: Assembly of the front module in the port plug (lateral plate not shown)

The faraday shield follows this modular logic, which means that:

- Each antenna module has an elementary faraday shield which is assembled onto it (figure 2).

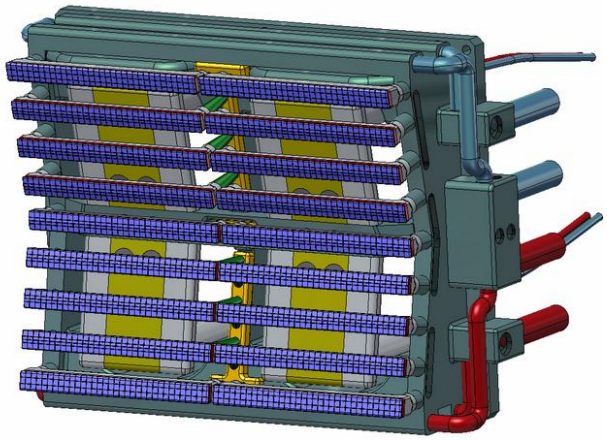

Figure 2: Faraday shield module

The faraday shield module is based on a steel casing (hereafter called the “shield casing”). The shield casing:

- holds the straps and bring the cooling into the antenna internal conductor,
- holds the plasma facing components of the individual modules, the bars.

This structural part is shared between the antenna and the faraday shield and thus acts as interface between the two.

- A specific structure, the frame comes as a superstructure to protect the port plug and the utilities attached onto it. The frame is attached to the port plug from the sides and water fed by it.

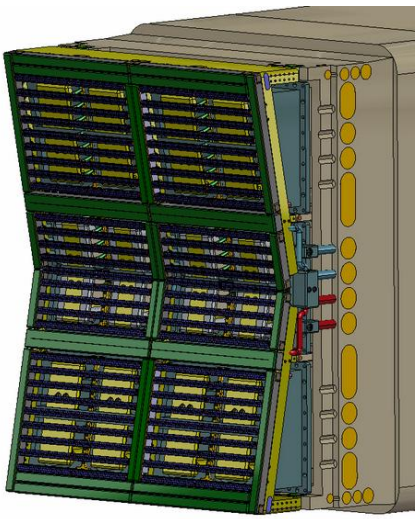

Figure 3: Front view of the antenna with its faraday shield

Both modules and frame are protected from the plasma by plasma facing components (the bars). A faraday shield module needs 18 bars. There are 9 bars in front of the left straps, 9 on the right.
Typical dimension are 340 mm long, 30 mm wide and 22 mm thick.
The frame is also fitted with bars which design is close to the one of the module. Their dimensions are variable to adapt the frame surface. The bar geometry, justification and fabrication is described hereafter.

DESIGN FOCUSED ON FS MODULE BARS

The faraday shield module bars

The constraints imposed by the design [1-4] are that the water has to go and come back within each bar. The cross section needs to be sufficient to have two channels. An arrangement side by side appears preferable, as and arrangement top/bottom would lead to thick bars, which would put the straps farther from the plasma.
The design stems from the design heat flux on the bars, and the principle should follow the same as the first wall. For a surface heat flux of 1- 2 MW/m², the bars are a medium heat flux component, closer to the first wall than to high heat flux components like the start up limiter. It means there is no need to use high conductivity material for the cooling channel, and that stainless tubes should suffice.
The bars are medium heat flux components, protected by beryllium tiles. Structurally, the bars are a sandwich of beryllium, CuCrZr and stainless steel (typical dimension are 340 mm long, 30 mm wide and 28 mm thick). In the current first wall design, the stainless steel cooling channels are completely imbedded into a CuCrZr massive bar, which is then joined to the stainless steel structure. Such a structure does not appear necessary for the FS bars where the heat flux is better known than on the first wall (no transient event) even though the steady state heat flux is 4 times higher. It is then possible to embed the stainless steel cooling tube in a sandwich of both CuCrZr and stainless steel, in a sort of saddle type cross section (figure 4: Bar cross section).That allows for a more robust design.
The cooling channels are made from stainless steel tubes which can be TIG/MIG welded to the structure. That make that no material interface crossed by the water is made of an HIP bond. 10/8 tubes are used for the module bars which have a width of 30 mm.

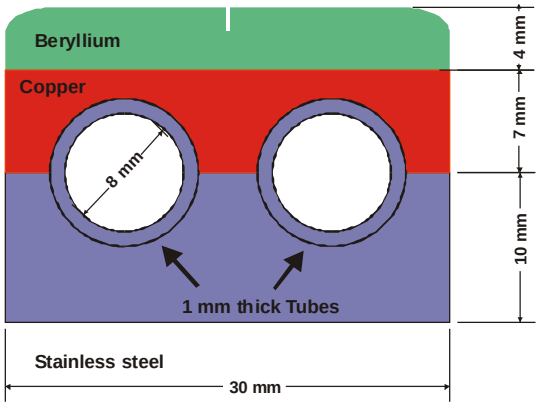

Figure 4: Bar cross section

The bar height is reduced to the smallest value to have the strap closest to the plasma [5]. The beryllium and stainless steel thicknesses are indicative and need optimisation. The design has to care that the minimum curvature radius of the 10/8 SS tube is 20 mm.
That forbids (or at least complicate seriously) a U turn within the bar. Longitudinally, the attachment scheme favours no water inlet or outlet through the septum, so that inlet and outlet are on the same side.

That is also the reason to have two tubes in one bar (see figure 5).

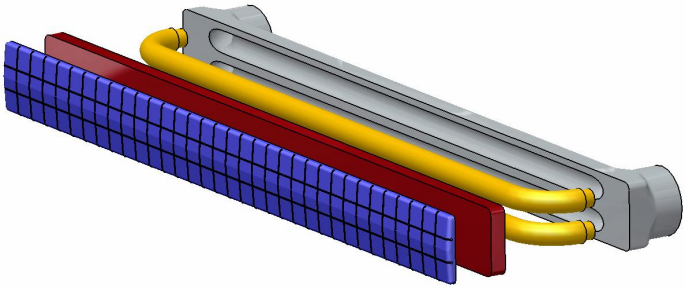

Figure 5: Exploded view of a faraday shield bar

The principle of the attachment of the FS bars to the casing is to have a mechanical clamping on both sides, while having water inlet and outlet on the same side.

DETAILED ANALYSIS

Cooling circuit

Based on preliminary power assessment, the design made a first choice to have 3 bars in series. This repartition is coherent with the 2 x 9 organisation of the bars on a module.
The flow rate is evaluated for an elementary circuit. For a diameter of 8 mm at 3 m/s, the volume flow rate is 0.151 dm^3/s, corresponding to a mass flow rate of 0.143 kg per second.
The total mass flow rate for a complete module is then 0.86Kg/s.
For a single bar of the FS module, the corresponding heating is then :

$$\Delta T = U/(m.Cp) = 22.5\ °C.$$

Three bars are connected in series, meaning that the potential temperature increase may reach 67.5°C. This is on the high and may need reduction. Having no more than two bars in series would greatly complicate the water circuit. It may then be better to go toward a water velocity of 4 m/s during the optimisation phase.

Thermal calculations

The temperature is modeled in the bar for 2 MW/m² and with the following coolant parameters [3]: inlet temperature 100°C, inlet pressure 3 MPa. The vertical symmetry is used so that only a half bar is modeled. The temperature distribution is given figure 6.

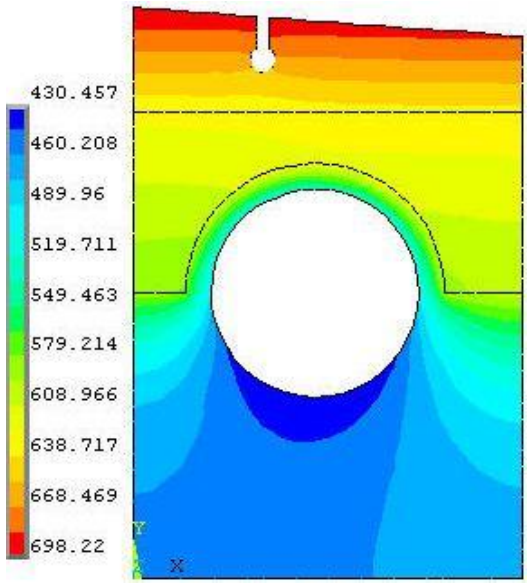

Figure 6: Temperature distribution in the bar (Kelvin)

The maximum surface temperature is 425°C. The beryllium surface has been tentatively shaped, for a λ_q of 1 mm.

Bars stresses

The stresses and strains caused by the differential thermal expansion between the different materials are evaluated in a faraday shield bar. Two steps are evaluated:

- cooling from 800°C to 20°C,
- Heating by a heat flux of 2 MW/m² (including the residual stress obtained during step 1).

The modelling is done in 2D, in generalised plain strains. For the cooling, the stress builds up during the temperature descent from 800°C to 20°C, the temperature distribution in the cross section being uniform.

At 20°C, the stress concentrates at the singular point of the interface between the beryllium tile and the copper heat sink, and reach 243 MPa (figure 7). This value remains tolerable, and this small value compared to other PFC is caused by the fact that the difference of thermal expansion coefficient between copper and beryllium is relatively small (for example compared to carbon to copper).

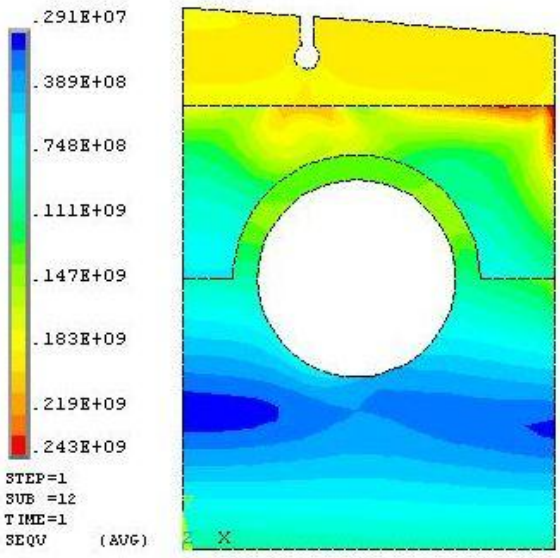

Figure 7: Von Mises stress in the whole structure after cooling

The plastic strain after cooling remains limited, at 0.2 % for the steel structure and 0.6% in the copper (figure 8).

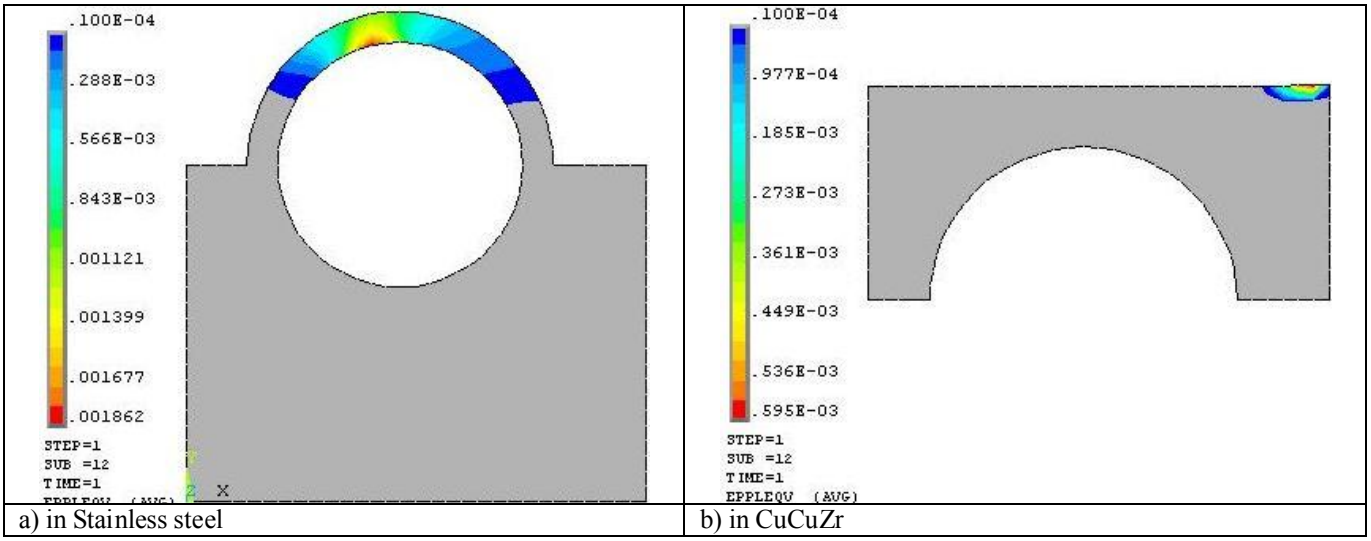

a) in Stainless steel | b) in CuCuZr

Figure 8: Plastic strain in the structural parts after cooling, strainless steel (a) and CuCrZr (b)

The uniform heat flux of 2 MW/m² is then applied. The heat exchange coefficient in the tube is evaluated with the Dittus Boelter correlation to 20400 W/m2/K.
The Von Mises stress remains at 232 MPa, meaning that no additional stress builds in the structure as the results of the heat load (figure 9).

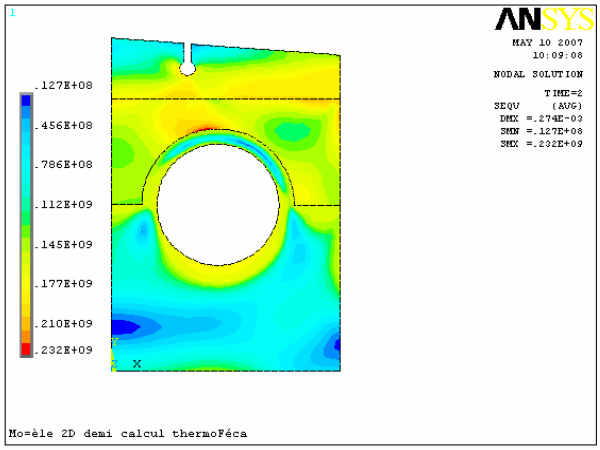

Figure 9: Von mises stress at 2 MW/m²

The plastic strain during heating remains limited, at 0.25 % for the steel structure and 0.1% in the copper As an example 0.25% in steel authorizes 10^5 cycles and 0.1% in CuCrZr more than 10^6 cycles (Raw values without safety margin).
These calculation must next be upgraded by taking into account the longitudinal stresses brought by the clamping of the extremities. These favourable results indicate that the tile-structure bond is unlikely to be the limiting factor of the design.

Whole bar elementary finite element modelling

The stress caused by the thermal dilatation is evaluated for a mean surface heat flux of 1 MW/m² (figure 10).
In this model, beryllium is not present, because it should not influence the stresses (because of the castellations, beryllium tiles bring almost no additional stiffness).

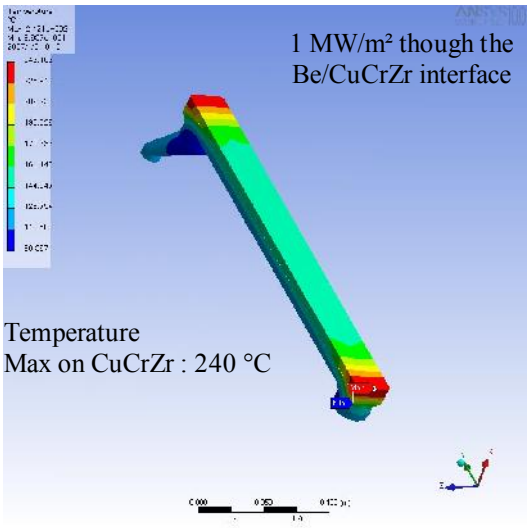

Figure 10: Temperature map on the bar

Obviously, a thermal optimisation need to be done at the bar ends to reduce the temperature in the Be/CuCrZr bonds. This could be done by shaping the surface.

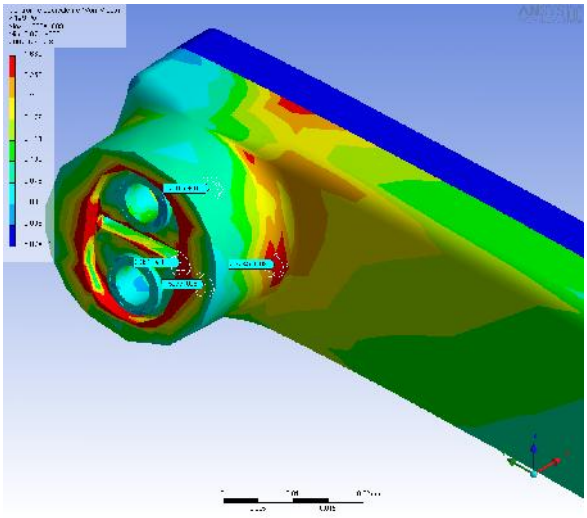

Figure 11: Von Mises stress in the bar connection to the casing

Von Mises Stress across the connection is 150 to 350 MPa (figure 11). This value is a correct first finite element modelling, coherent with initial evaluation of 600 MPa (pure shear in a cylinder at 1 MW/m²). Optimization will allow increasing the margin with respect to 3 SM values (440 MPa at150°C). This calculation shows basically that a 350 mm bar is possible, but that a bar with double the length is likely to be highly constrained and subject to cycle fatigue.

CONCLUSIONS

A faraday shield design was proposed for the ITER ICRH antenna. The main plasma facing element is a bar, whose design is based on the technology of the ITER first wall panels (sandwich of stainless steel, copper chromium and zirconium and beryllium with a stainless steel water liner). The bar is assembled by hot isostatic pressing, and the water tightness is guarantied by TIG welds. A first assessment of the peak beryllium temperature gives 425°C, providing a good margin for resisting the ELMs. A specific feature of the bar is that it is clamped on both sides, to avoid the need for a sliding bond or an electrical connection close to the plasma.

This feature is unique to this plasma facing components, as wall or divertor components allow for thermal expansion through sliding bonds or pinning. Thermomechanical analysis gives reasonable elongation amplitude during cycling (0.1 to 0.25%), which means that the fatigue would be acceptable.

This should however been further analysed and checked on actual mock-ups, which is the aim of the R&D program proposed.

REFERENCES

[1] Detailed Design Description, Ion Cyclotron Heating and Current Drive System. WBS 5.1, G51 DDD 4 01-07-19 W 0.2

[2] Detailed Design Description, First wall design and techniques. G16 DDD 35 R0.1

[3] Detailed Design Description, Cooling loop specifications. N26 DDD 46 R0.2

[4] Detailed Design Description, G16 DDD 2 98-06-2 W 0.5

REPORTS AND PUBLICATIONS

[6] Faraday Shield Design for the Iter ICRF antenna array, Intermediate report for the Task TW6-TPHI-ICFSDES, CFP/NTT-2007.017, May 2007

[7] Faraday Shield Design for the Iter ICRF antenna array, Final report for the Task TW6-TPHI-ICFSDES, CFP/NTT-2007.082, December 2007

TASK LEADER

Raphael MITTEAU and Marc MISSIRLIAN

DSM/IRFM/SIPP/GCFP
CEA-Cadarache
F-13108 Saint-Paul-lez-Durance Cedex

Tel: 33 4 42 25 25 98
Fax: 33 4 42 25 49 90

e-mail: marc.missirlian@cea.fr

CEFDA07-1700-1572

Task Title: TW6-TPHI-RFPFCPOW: EVALUATION OF EXPECTED POWER/PARTICLE FLUXES ON ITER PFCs CAUSED BY LOCAL ACCELERATION OF PARTICLES IN RF FIELDS

INTRODUCTION

The coupling of RF power in tokamak plasma involves implementing a launcher close enough to the plasma in view of the evanescence of the wave in the absence of plasma. This is correlated with the existence of significant RF fields at the plasma edge on closed flux surfaces. It has been experimentally demonstrated that ICRH launching results in sheath rectification phenomena on specific flux tubes, which depends mainly on the antenna arrangement, the plasma density profile at the edge and on the connection patterns. Similarly for LH waves, the large $k_{//}$-parallel part of the spectrum which is of no use for current drive may result in local acceleration of electrons. A large amount of experimental data already exists and many modelling efforts have been undertaken. However, the application to ITER real geometry and design and the lack of a comprehensive inclusion of a scrape-off layer model prevents any attempt to estimate the associated heat and particle fluxes as well as attempts to mitigate such fluxes if they prove to be detrimental.

The main aim of the task is to estimate the parallel fluxes associated with such phenomena in ITER. These fluxes were calculated in view of the actual ITER configuration and with possible design modifications to be envisaged during the design review. Different electron density and temperature profiles in the scrape-off layer (SOL) were considered whenever possible, solutions allowing mitigation of these fluxes will be proposed, including optimisation of the design of specific launcher protections involving ITER plasma facing components. Attention will be given to sustaining the findings with well defined hypotheses, modelling tools and their benchmarking with experimental observations.

In that respect, the work will rely on existing modelling codes and will have to incorporate various hypotheses for the plasma SOL.

The work might also involve possible improvements of the models and in any case will have to describe the ITER geometry as accurately as possible: the magnetic connexions map is of particular relevance for such studies. An assessment of existing experimental data and the production of new data from Tore Supra and JET were carried out.

2007-2008 ACTIVITIES

ICRH PART

The estimate of the heat fluxes associated with radio-frequency (RF) sheath rectification follows a methodology similar to those implemented to interpret TFTR and Tore Supra results, with however more self-consistency and a predictive approach. The three-dimensional (3D) distribution of RF near fields $E_{//RF}$ in front of the ITER antenna was provided by the antenna code TOPICA [1], in absence of sheaths but accounting self-consistently for the plasma in the full-wave solver FELICE [2], contrary to earlier studies. From the RF fields the SEM code [3] was used to estimate a sheath voltage, and CELLS module [4] to evaluate density modifications. Estimation was made delicate by our poor knowledge both of the ITER far SOL and of detailed sheath rectification processes. Uncertainty on input parameters was circumvented by considering four plasma scenarios, covering a broad range of far SOL density profiles. In SEM code each open magnetic flux tube around the ICRF launcher was treated as a symmetric double Langmuir probe connected to a source of oscillating potential $V_{RF} = \int_L \mathbf{E}_{//RF}.\mathbf{dl}$. Nearby flux tubes were coupled by self-consistent transverse exchanges of RF currents via the plasma non-collisional RF conductivity. Due to the non-linear I-V sheath characteristic, the RF solicitation V_{RF} enhances the DC sheath potential V_{DC} on each field line. Differential DC biasing of adjacent flux tubes drives $\mathbf{E}\times\mathbf{B_0}$ plasma convection, which re-distributes the local density. The heat flux at field line ends was finally taken as the Bohm flux times the DC potential. For each plasma scenario (reference scenario 2 and non-inductive scenario 4), an outward convective transport with a radial velocity of 30m/s and 90m/s was assumed leading to the 'short SOL' and 'long SOL' cases, respectively.

A radial/ poloidal map of the parallel heat flux Q// is shown for scenario 2 and [00ππ] phasing on figure 1. For the long SOL case, heat loads are located in poloidal peaks whose distribution is mainly determined by the toroidal phasing. Peaks extend radially where DC potentials can penetrate, i.e. a few centimetres with the density profiles used. For the short SOL case, highest fluxes are found near the separatrix and are present even without RF waves but are enhanced with RF waves.

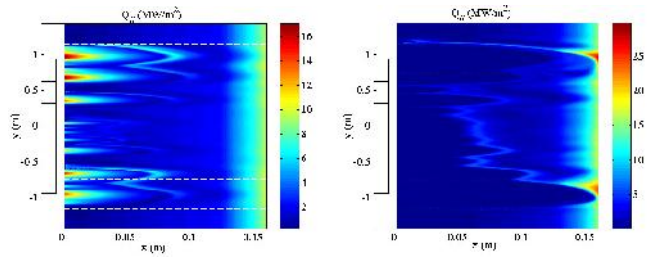

Figure 1: (Radial/poloidal) map of parallel heat fluxes (unit MW/m^2) for scenario 2 with density convection, long SOL (left) and short SOL (right), [00ππ] phasing. Superimposed: vertical cut through ITER antenna structure. Horizontal dashed lines: limits of upper and lower box corner zones

Table 1: Summary of quantitative simulation results

Scenario	2, long SOL			4, long SOL			2, short SOL			4, short SOL		
Phasing	00ππ	0ππ0	0π0π	00ππ	0ππ0	0π0π	00ππ	0ππ0	0π0π	00ππ	0ππ0	0π0π
T_e ; T_i (eV)	11.7 ; 21.6			23 ; 59			11.7 ; 21.6			23 ; 59		
v_{SOL}(m/s)	93			95			28			29		
n_{ant} (m^{-3})	1.1×10^{18}			6.0×10^{17}			5.2×10^{15}			3.9×10^{15}		
P_0 mW/V^2	29.3	20.7	11.5	9.44	6.77	4.67	8.97	6.97	4.85	5.41	4.47	3.6
L_{RF} (mm)	4.1	4.1	4.1	5.6	5.6	5.6	33	33	33	35	35	35
L_{DC} (mm)	39	37	33	42	36	39	50	41	44	54	42	49
V_{DCmax} (kV)	2.0	1.8	2.2	2.6	2.6	4.6	4.3	2.1	2.6	3.5	3.4	5.2
$Q_{//}$ (MW/m^2)	8.1	7.4	8.9	8.9	9.0	16.0	3.2	0.9	2.9	3.2	1.7	3.5
$P_{//0}$ (MW)	1.01			1.23			1.03			1.10		
$P_{//1}$ (MW)	2.18	2.21	2.13	2.48	2.11	3.04	1.97	1.24	1.65	1.98	1.45	1.95
$P_{//2}$ (MW)	1.42	1.60	1.60	1.82	1.62	1.83	1.07	1.01	1.11	1.05	1.09	1.03
ΔP_{sh}(kW)	403	579	582	587	392	**597**	40	-17 !	84	-50 !	-6 !	**-61 !**

Table 1 sums the edge power fluxes $Q_{//}(x,y)$ over the 2D simulation domain. $P_{//0}$ stands for power losses without RF. $P_{//0} \propto n_e T_e^{3/2}$ and is therefore important on dense and hot plasmas. $P_{//1}$ evaluates losses with rectified DC sheath potentials and unperturbed density distribution, for 20MW coupled. As V_{DC} increases in presence of RF power, $P_{//1} > P_{//0}$. $P_{//2}$ was estimated in presence of rectified DC potentials and RF-induced density transport. $\mathbf{E}\times\mathbf{B_0}$ convection tends to deplete the zones of high V_{DC}, so that $P_{//2} < P_{//1}$. Two classes of scenarios emerge from table 1, depending on local density.

On short SOL profiles the power losses $\Delta P_{sh} = P_{//2} - P_{//0}$ attributed to RF sheaths are found small compared to $P_{//0}$. This arises because V_{DC} is only high in regions of low density. In several cases ΔP_{sh} becomes negative: the density depletion over-compensates the increase of DC potential. In long SOL cases, high density penetrates up to the antenna mouth, and the estimated ΔP_{sh} are typically 400-600kW (i.e. 2-3% of 20MW coupled) with full radial broadening. ΔP_{sh} is lost over a small surface of ~0.16m^2.

Infra-red measurements on JET and Tore Supra indicate parallel heat fluxes on the Faraday screen of several MW/m^2 when the electron density near the density is high [5] and these results are consistent with ITER predictions in the large SOL case.

LH PART

On Tore Supra heat fluxes on plasma facing components were investigated with infra-red imaging and RFA measurements. The heat flux scales, as expected, with the RF power (or more exactly with the electric field amplitude) but also with the electron density and temperature measured with Langmuir probes embedded in the launcher [For conditions ensuring good RF coupling ($n_e \sim 3 x n_{cut\text{-}off} = 5x10^{17} m^{-3}$), the heat flux, along the field lines, does not exceed 5MW/m^2 when a RF power density of 25MW/m^2 is launched by an array of 32 waveguides stacked in the toroidal direction. The heat flux can exceed this value when the density at the antenna-plasma interface increases above this optimal density and a scaling law has been established for a wide range of parameters (n_e =0.4-2.0x10^{18}m^{-3}, T_e=11-35eV) as shown on figure 2.

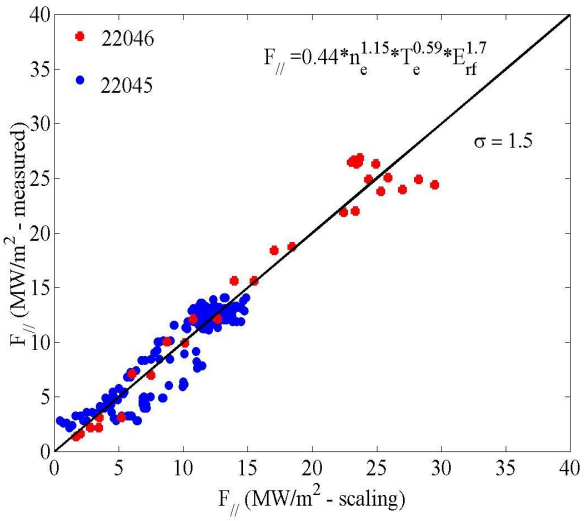

Figure 2: Scaling law of the heat flux on the Tore Supra ergodic divertor tiles. The 2 LH launchers are pulsing and the heat flux deposition on the tiles superimpose. The constant factor has later been revised (Langmuir probe calibration) from 0.44 to 0.36. Emissivity of the surface (B_4C) is supposed to be 1

On JET hot spots on different plasma facing components magnetically connected to the LH antenna (or connected to flux tubes passing in front of the LH antenna) were observed. The heat flux was also estimated from an infra-red camera viewing a poloidal limitor for different plasma positions and LH powers, in L- and H-modes (figure 3). Quadratic power dependence is consistent with Tore Supra results, assuming a linear increase of the density in front of the launcher as inferred from previous measurements on JET with a reciprocating probe [6].

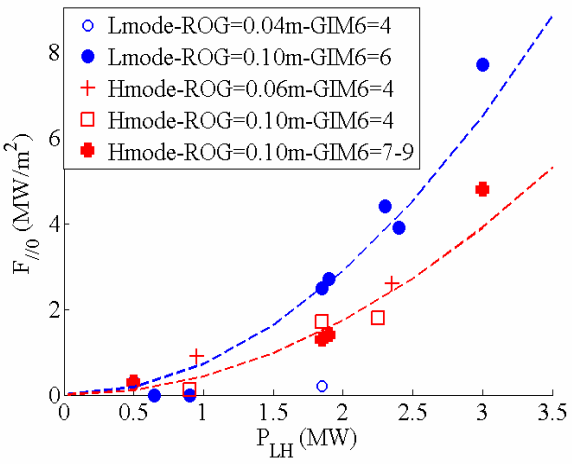

Figure 3: Heat flux $F_{//}$ as a function of the LH power for L mode (blue) and H mode (red) JET plasmas, (pulses 66970 and 68938) for the case d_0=15mm and PF=1.0. Distance between LCFS and the PL (ROG) is varying between 0.05 and 0.10m. The highest heat flux from tile 8 or 9 is here considered. Dashed lines are parabolic fits

Fast electron energy distribution was estimated for the Fully Active Multijunction (FAM, used on JET and Tore Supra) and for the Passive Active Multijunction (PAM, planned for ITER) where the waveguides carrying the LH wave from the generator are separated by passive waveguides terminated at the rear by a short-circuit. Electric Fields are determined by the ALOHA coupling code for both antenna assuming a mower density in the active waveguides of 25MW/m^2. From the electron Green's function determined by launching a group of thermal electrons at one grill end, the dynamics of the electrons is computed for $n_e/n_{cut\text{-}off}$=1 and $n_e/n_{cut\text{-}off}$=3. At the higher density, the average energy of fast electrons is found to be slightly lower for the PAM antenna (340eV) than for the FAM antenna (410eV) as shown on figure 4.

At the lower density, the situation is inversed (340eV for AAM, 600eV for PAM). This result is confirmed by PIC simulations [7], performed for the high density case, giving a more realistic picture of the electric field – edge electron interaction .

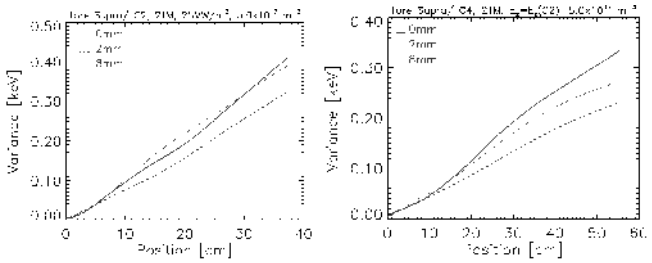

Figure 4: The evolution of edge electron variance along the C2 (left) and C4 (right) grills, at 3x cutoff density ($n_{e,\ grill}$ = 5x10^{17} m^{-3}) for 3 radial positions (antenna is at r=0)

CONCLUSIONS

A simple RF sheath model was applied to open field lines in front of the ITER ICRF antenna to estimate parallel heat fluxes. As observed experimentally quantitative results strongly depend on the local density which is very uncertain on ITER (more than one order of magnitude). Radial broadening of V_{DC} (and heat fluxes) was identified but is thought to be pessimistic and the model should be refined.
A scaling of the parallel heat flux caused by electrons accelerated in the near field of LH antennas is obtained experimentally on Tore Supra. This scaling is consistent with JET measurements in L- and H-mode. Modelling of the electron acceleration by the RF electric field indicates similar average energy for the fast electrons in the case of the FAM (JET/Tore Supra) or the PAM (ITER) antenna.

REFERENCES

[1] V. Lancellotti et al. Nucl. Fusion 46 S476

[2] M. Brambilla Plasma Physics and Controlled Fusion, Vol. 31, No. 5 - 1989

[3] E. Faudot et al. Physics of Plasmas 13 042512 (2006)

[4] M. Bécoulet et al. Phys. Plasmas, Vol. 9, No. 6, June 2002

[5] L. Colas et al. Plasma Phys. Control. Fusion 49 (2007) B35–B45

[6] M. Goniche et al. Plasma Phys. Control. Fusion 51 (2009) 044002

[7] V. Fuchs et al. Nucl. Fusion 43 (2003) 341

REPORTS AND PUBLICATIONS

EFDA Task TW6-TPHI-RFPCROW- ICRF part - Final Report, CEA Report PHY/NTT-2008.008

EFDA Task TW6-TPHI-RFPCROW- LH part - Final Report, CEA Report PHY/NTT-2008.020

TASK LEADER

Marc GONICHE

DSM/IRFM/SCCP
CEA-Cadarache
F-13108 Saint-Paul-Lez-Durance Cedex

Tel: 33 4 42 25 61 95
Fax: 33 4 42 25 62 33

e-mail: marc.goniche@cea.fr

Task Title: SINGAP NEGATIVE ION ACCELERATOR: STUDY OF THE BEAMLET HALO, DARK CURRENTS AND VERIFICATION OF ELECTROSTATIC WITHSTAND CAPABILITY AND TOLERABLE STORED ENERGY IN CASE OF ELECTRICAL DISCHARGES

INTRODUCTION

It was shown in the previous contract TW2-TPHN-NBDES1, that the SINGAP accelerator is an attractive alternative to the ITER reference design the so-called MAMuG (Multi-Aperture, Multi-Grid) accelerator. ITER-relevant good beam optics has been demonstrated and relatively high current densities have been obtained at optimum perveance [1].

As already reported in 2006 we found that the beamlets had a bi-Gaussian power density distribution (90% of the power could be described by a beamlet divergence of ≈4-5 mrad and 10% was in a halo) as opposed to the single Gaussian with 2.5 mrad divergence of the simulation. The fraction of the total power that was seen as a halo varied between <4% while operating at low current densities without Cs to 10% during caesiated high current density operation.

The new contract with EFDA was started in July 2006 in order to focus on three different tasks. The first task is to measure the beam halo and to find a method of how to mitigate it. The second task of the contract concerns the dark current at the SINGAP testbed. The last task is to study the electrical discharge and stored energy in a HV breakdown.

2007-2008 ACTIVITIES

HALO MEASUREMENTS

In the report describing the activities in 2006 we reported that we initially had problems with an instrumental effect in the infrared camera. Once this phenomenon was solved by a re-calibration of the camera we found:

- Real halo < 4% of the total beam power in volume operation (operation without caesium),
- Real halo up to ~10% of the total beam power in caesiated operation.

It is well known (and indeed observed by us during cleaning) that caesium creeps out of the ion source into the accelerator. It is also known for some time that hot neutral H or D atoms (as produced inside the ion source) are converted to negative ions on caesiated surfaces. This means that production of negative ions must take place on these caesium-contaminated accelerator surfaces. Modeling clearly shows that we get wide beam halos if H^- or D^- trajectories are allowed to start from the accelerator grids. It is hypothesized that most of the halo would originate from the plasma grid, as this is the easiest to be reached by hot atoms from the source (atoms would cool down on their way to the downstream parts of the accelerator).

Using the hypothesis described above, it is possible to identify which parts of the plasma grid that transmit trajectories into a halo. These parts are the inside of the aperture (downstream of the meniscus). It was proposed to reduce the halo by machining away the plasma grid downstream of the knife-edge, where the meniscus resides (figure 1). Simulations gave a good beam for this geometry and the experiments were carried out end of 2008.

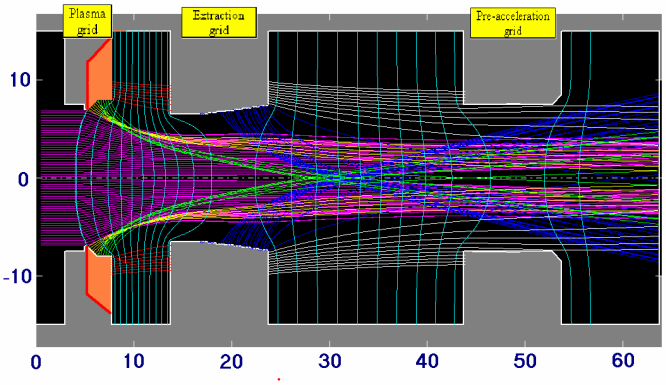

Figure 1: The beam (purple) is originating from the ion source on the left. The negative ions originating from the grid surfaces are shown as green, yellow and red from the plasma grid and blue and white from the extraction grid. The area shown in orange was removed from the downstream side of the plasma grid for the second phase of the experiments

Figure 2 gives the results. Scans in the accelerator voltages, plasma source bias voltage, anode to cathode voltage for the plasma arc and gas pressures have been performed. The so-called "reference shots" have been operated at optimum perveance. They show the lowest halo fraction. All these scans provide a scatter picture. In these, the reference shots have been marked out by the circles and connected by the solid lines.

First the conventional grid was tested in November and December 2008. Then the new grid was made by machining off the orange part of the conventional grid. Any negative ions originating from the downstream side of the plasma grid would thus be intercepted on the extraction grid. The experiments performed in early 2009 show, for the reference shots, a reduction in the halo fraction by about 50% which is consistent with the hypothesis described above.

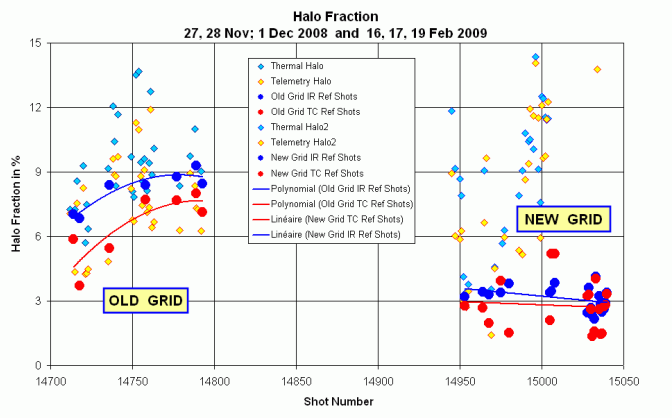

Figure 2: Experimentally measured halo fraction in the beam. Various scans in the accelerator voltages have been performed. The reference shots are the good shots operated at perveance match. Red points have been measured with thermocouples embedded in the target using the telemetry system. The blue points are measured with the infrared camera. The new grid can deliver a beam with half the halo as the old grid

DARK CURRENT

It is found that increasing the voltage in a recently pumped system is opposed by both the appearance of leakage (dark) currents and occasional high voltage (HV) breakdowns. From literature studies we identified 3 likely reasons why the SINGAP testbed had dark currents when applying high voltages:

- Cleanliness had not been respected. Special care should be given to vacuum systems where high voltage is going to be applied. The content of dust should be minimized and all surfaces should be clean and free from loosely bound material. Cleanliness can be improved by allowing vacuum baking in-situ,
- The surfaces seeing HV were not made of correct materials. The cathode should be either made of stainless steel or aluminium with an oxide layer. The anode should be made of stainless steel or titanium,
- The electrical field was not uniform.

In order to address all these issues a new heated cathode structure was built and installed inside the vacuum vessel. This structure allows beam acceleration. It is made up of 6 segments where the stainless steel raw material had been polished and vacuum baked to 950 °C for 1 hour in order to obtain a surface that would outgas as little as possible. The segments were thereafter assembled to one unit inside the vacuum tank. Heater elements were attached to the outside of the cathode structure that allowed a moderate baking (<250 °C) after the structure was assembled.
A new anode structure was also installed. It was made of pre-polished stainless steel and was installed symmetrically inside the cathode structure. The electric field is in this way more uniform than with the previous installation.

The already installed anti-corona screens inside the bushing and the vertical column supporting the horizontal anode structure were removed and vacuum baked in an external vacuum oven at 500°C during 5 hours.

The experimental campaign that followed the installation of the new equipment gave only a few new results. On the positive side we demonstrated that the needed gas pressure to suppress the dark current was reduced to 0.03 Pa. This is now inline with what is anticipated in the ITER NB accelerator.

Several experiments were dedicated to try to identify the cause of the dark current but we could not identify one single source. The only component on the testbed that was not changed for these tests was the HV bushing that forms the boundary between the vacuum tank and the SF6 insulated transmission line. Of the 9 bushing rings, 8 are made of epoxy and one is made of porcelain. In previous experiments done in 2001, we compared the HV holding for the different rings and found that porcelain is far superior to epoxy. We now believe that the problem with dark currents derives from the use of epoxy in the bushing.

A STUDY OF THE ELECTRICAL DISCHARGE AND STORED ENERGY IN A HV BREAKDOWN

The estimated energy that will be dissipated in a breakdown in the ITER neutral beam accelerator is estimated to be 500 J. This energy derives from the stored energy in the last section of the transmission line, the bushing and in the accelerator. These components can not be protected by a snubber. This relatively high level of energy might degrade the voltage holding of the accelerator and cause damage to the acceleration grid surfaces. A new test set-up has therefore been designed to simulate the ITER SINGAP accelerator main accelerator gap in a simplified geometry. In order to obtain 500 J at 1 MV, new capacitors were purchased and will be added at the output of the 1 MV power supply. The voltages withstand before and after breakdowns at different stored energy levels will be assessed.

A modelling of the complete system was done to be able to perform the correct measurements. With this model we could simulate the breakdown between the electrodes and also see the effect of a damper resistor that could be installed in series with the cathode electrode. The modelling indicated which type of instrumentation that was needed to install for the experiments. It also showed that one possibility to reduce the energy dissipated in the arc and cathode/anode electrodes would be to use a damper resistor.

The objective is to study electrical discharges between two electrodes. The tests should simulate the conditions that will be found in the ITER Neutral Beam accelerator. The parameters to vary are:

- The voltage,
- The distance between the electrodes,
- The amount of stored energy,
- Different values of the damper resistor,
- Electrode materials (if needed).

The new equipment that was needed for these experiments can be divided into three categories: the capacitors, the movable electrodes and the instrumentation.

Two sets of capacitors were purchased, one set for breakdown tests at 200kV, to recreate a breakdown between the grids in a MAMUG accelerator, and one set for breakdowns at 1 MV. The latter test is to study a breakdown in the SINGAP case. The capacitors will be installed in a new pressure vessel that is an extension to the present HV transmission line connecting the HV power supply with the SINGAP vacuum vessel. This capacitor tank was designed, built and delivered to Cadarache.

The movable cathode is a system that allows the distance between the electrodes to be modified without breaking the vacuum. This system was also constructed in such a way that the proposed damper resistor could be installed.

Very fast instrumentation is needed for recording of the current and voltage signals. For the temperature measurements we will use a telemetry system with thermocouples for the anode electrode and an IR camera for the cathode electrode. We will also install a very fast CCD camera in order to visualise the arc. All instrumentation is purchased and is available at Cadarache.

This test set-up is under construction and experiments will begin in March 2009. A schematic of the installation for the breakdown experiment is shown in figure 3.

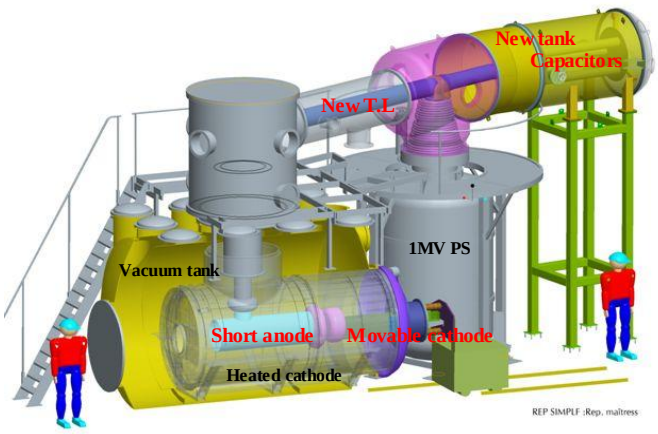

Figure 3: A schematic of the installation for the electrical discharge experiment. The additional capacitors are installed inside the capacitor tank. The distance between the electrodes can be varied by moving the movable cathode. The electrical discharge is done between the electrodes that are attached to the short anode and the movable cathode

CONCLUSIONS

Measurements of the beam halo have been done and we established that the power fraction in the halo is <4 % when no caesium is used in the ion source and it increases to around 10 % when caesium is used to enhance the negative ion production. By removing the material downstream of the meniscus on the plasma grid has reduced the halo fraction, while using caesium, to around 5%.

A new heated cathode structure was designed and was installed during 2007. This structure gave a uniform electric field around the accelerator. It was constructed of pre-polished stainless steel and vacuum baked to reduce the residual gas in the walls. It also incorporates heating elements so that an in-situ baking can be done without breaking the vacuum. The results from the experiments showed that with the new configuration we can hold the same HV as before but at a reduced pressure which is the same as foreseen in the ITER neutral beam accelerator. We have also come to the conclusion that the relatively high dark currents that are found on the Cadarache testbed is due to the use of epoxy in the bushing.

A new test set-up for studying the electrical discharge between the acceleration grids in the ITER SINGAP has been designed and built. This test set-up will demonstrate the voltage withstand before and after a breakdown. The experimental campaign will start in march 2009.

REFERENCES

[1] L. Svensson, D. Boilson, H P L de Esch, R S Hemsworth and A Krylov,"Experimental results from the Cadarache 1 MV test bed with SINGAP accelerators", Nuclear Fusion 46 (2006) S369-S378

[2] A. Masiello et al, European programme towards the 1MeV ITER NB injector, Fusion Eng. Des (2009)

[3] G. Fubiani et al, Analysis of the two accelerator concepts foreseen for the neutral beam injector of the International Thermonuclear Experimental Reactor, Physical Review Special Topics – Accelerators and beams, to be published (2009)

REPORTS AND PUBLICATIONS

H.P.L de Esch et al, Results of the SINGAP neutral beam accelerator experiment at JAEA, Fusion Eng. Des (2009)

H.P.L de Esch et al, Aperture Size Effect on Extracted Negative Ion Current Density, NIBS (2009)

TASK LEADER

Lennart SVENSSON

DSM/IRFM/SCCP/GIDEA
CEA-Cadarache
F-13108 Saint-Paul-lez-Durance Cedex

Tel: 33 4 42 25 61 69
Fax: 33 4 42 25 62 33

e-mail: lennart.svensson@cea.fr

CEFDA06-1429

Task Title: TW6-TPDS-DIASUP1: SUPPORT OF DIAGNOSTIC DESIGN FOR ITER DIAGNOSTIC PORT-PLUG PROCUREMENT, DIAGNOSTIC PORT-PLUG ENGINEERING & INTEGRATION, & DIVERTOR THERMOGRAPHY

INTRODUCTION

ITER requires an extensive set of diagnostic systems to provide several key functions such as protection of the device, input to plasma control systems and evaluation of the plasma performance. These diagnostic systems are to be integrated inside the vacuum vessel of ITER by means of water-cooled stainless steal structure (60t, 2m x 2m x 4m) named port plug structure. The port plug structure must perform basic functions such as providing neutron and gamma shielding, supporting the first wall armour and shielding blanket material, closing the vacuum vessel ports, supporting the diagnostic equipment (see figure 1).

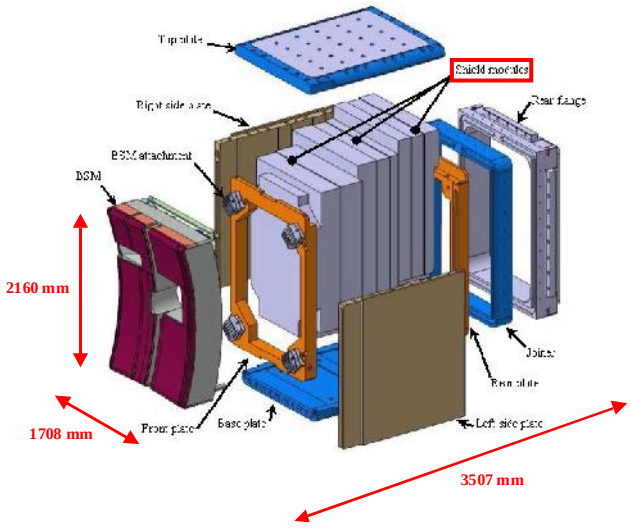

Figure 1: Spread view of the equatorial port plug n°1

The aim of this contract is to support design activities directly related to individual diagnostic procurement package integrated into port plug structure. CEA was in charge to work on the following topics: diagnostic port plug procurement [1], diagnostic port-plug engineering and integration [2], divertor thermography.

2007-2008 ACTIVITIES

DIAGNOSTIC PORT PLUG PROCUREMENT

The aim of the task is to provide a list of specific issues for the procurement of diagnostic port plugs at the ITERO level, and a proposal for the organization at the EU level, taking into account that a general procurement procedure has already been defined at EU level.

The first part of the task consists in providing inputs to the other participants of the task (UKAEA and TEKES) on two specific subjects:

- Review of practice and experience of procurement methods in other relevant projects and organizations. CEA contributes by analysing the procurement methods on the Toroid Magnet system project for the ATLAS detector of LHC at CERN (see figure 2). It mainly focuses on the manufacturing and assembly operations (1998-2007),
- For the assessment of procurement methods, in particular in the areas licensing, reliability and availability requirements, allowable risk and quality assurance and control.

The second part of the task consists in reviewing the assessments and recommendations for methods of procurements for the equatorial port plug made by UKAEA in the framework of this task.

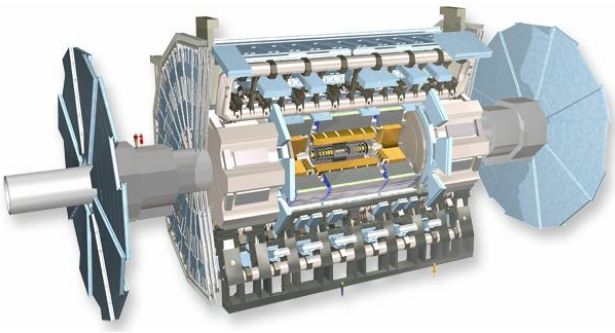

Figure 2: The ATLAS detector

The main problem for collaborative projects like ITER or ATLAS is the communication between the different parties, at each stage of the project.
The different teams must be organized in order to share data and information efficiently. Of course, interfaces management then becomes one of the key to success.
During manufacturing and assembly operations, the most important aspect seems to almost continuously follow the operations, directly on site, with the firm in charge. It is especially important to define all critical operations, and make sure they are correctly handled.
Furthermore, ITER has nuclear aspects. Some recommendations have been expressed in order to obtain an optimum consortium composed of an association and a nuclear engineering company in an integrated interdisciplinary team. The advantage of such a consortium is to gather the expertise and the technological skills of the association and the nuclear know-how of engineering

companies daily involved in the complex systems and construction projects.
Main current projects related to nuclear experimental plants of complex nuclear systems are driven by such a consortium.

DIAGNOSTIC PORT-PLUG ENGINEERING AND INTEGRATION

The requirements expressed in the contract concern engineering activities (FEM analysis, CAD effort, manufacturing, prototyping, remote handling,…). CEA contributed to several equatorial port plug tasks identified and validated during the different meetings held during 2007.

Generic tasks such as CAD methods, calculation methods identification have been performed, with the following results:

- Identification of the calculation rules that should be applied for the design of the port plug.
- Review of the practice of the ITER CATIA methodologies. According to our testing period, associations and partners are recommended to put in place a specific internal work around the understanding of those CAD methods. It can also be useful for persons who will manage CAD data productions within partners to follow an ENOVIA LCA training session in order to understand how works the ITER Product Lifecycle Management system, and so to know specific requirements fixed by it.
- Many points dealing with CAD strategy (protocol of collaboration, exact responsibilities on CAD data management, CATIA methodologies, European CATIA configuration, European CAD manual…) have to be tested from ITER to CEA (through F4E). Installation of the database management system (such as SmarTeam) at CEA will help to improve this process in the future [3].

Performed analysis such as CAD, mechanical studies which validate the proposed version of the shield module equatorial port plug structure [4], and tasks on specific EQPP remote handling and maintenance issues [5]. The main results are:

- Diagnostic Shield Module (DSM) design: the mechanical behaviour of the Diagnostic Shield Module has been validated with respect to the baking conditions (see figure 3). An attachment solution with 5 pins has been designed to sustain the mechanical loads on the DSM during disruption.
  Many studies still have to be performed in order to fully validate this concept: thermal assessment, thermo-mechanical assessment, interfaces with diagnostics, etc.

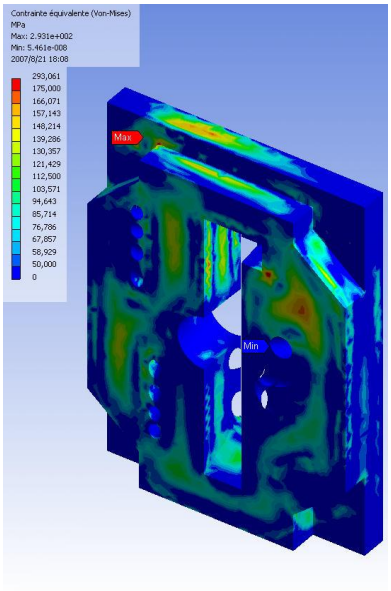

Figure 3: Von Mises Stresses in DSM (293 MPa maxi)

- Diagnostic Shield Module (DSM) remote handling: a first approach of the remote strategy for DSM has been proposed. This work shows a first approach of maintenance of DSM and should be followed by more detailed work in the next years.
- The design of the new flange has been approved and will be integrated into the baseline very soon (see figure 4). The sealing concept is still under discussion: a preferred option has to be selected and some R&D has to start soon. A port rear flange mock-up has been proposed by CEA and GARLOCK during this year, this has to be further detailed in order to have relevant test platform for the features that has to be assessed.

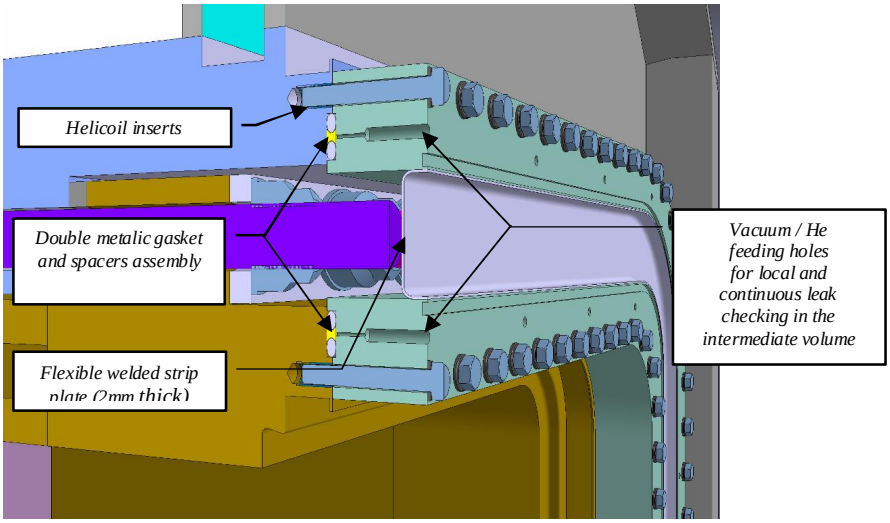

Figure 4: Gasket flange main features

- An assessment of the transfer cask system (see figure 5) has been made in order to identify the possibilities of improvement of the system to help better specify this maintenance system. A gripping tooling has been integrated in the design of the current tractor with regard to the flange and helping cantilever study. This study should be followed by more detailed work.

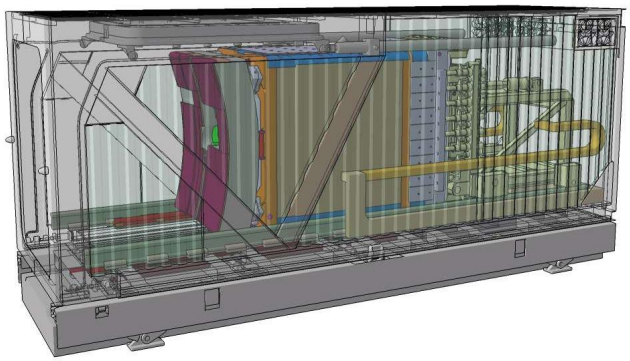

Figure 5: Transfer Cask "In operation"

- With this first study on the port plug interfaces some improvements have been proposed for ensuring a better level of reliability of the transfer operation at the equatorial level. This helping cantilever system has also to be implemented at the upper level in order to ensure a common strategy for the different levels of the tokamak openings.
- These studies have been helping to clarify the port plug main interfaces, but the issues concerning the diagnostic windows and feeder connection/disconnection in the port extension area must be considered in the next steps of the design integration. Also the whole sequence of the preparation of the transfer cask must be assessed in order to identify the relevant requirements induced for the components design definition.

DIVERTOR THERMOGRAPHY

The temperature of the divertor target plates needs to be surveyed to avoid damage. Power deposition is subject of physics studies in ITER. These aims require to measure surface temperatures over a large temperature range (200°C-3600°C) with high spatial resolution (3 mm) and high temporal resolution (2 ms in the range 200°C-1000°C, 20 µs above 1000°C). This can not be provided by the Infrared (IR) instruments in the port plugs but requires an IR diagnostic inside the divertor cassette [6] such an optical system has been designed and implemented in the frame of this contract (see figure 6).

The present solution needs to be adapted to the newest divertor cassette design and the connector between cassette and relay needs to be designed in detail. This work should be accompanied by calculations of the radiation reduction by the front shield. Initial reflection simulation work needs to be intensified. For power deposition calculations it is necessary to determine the thermal characteristics of deposits on the surface.

No additional tools are proposed for this since thermocouples in the target and photothermal methods suffice. We arrive at becoming reasonably confident that with the ensemble of methods proposed here, properly interfaced with each other, it is possible to answer to the ITER requirements even in the case of a change to tungsten as target material. A compromise solution using fibres and conventional elements seems interesting.

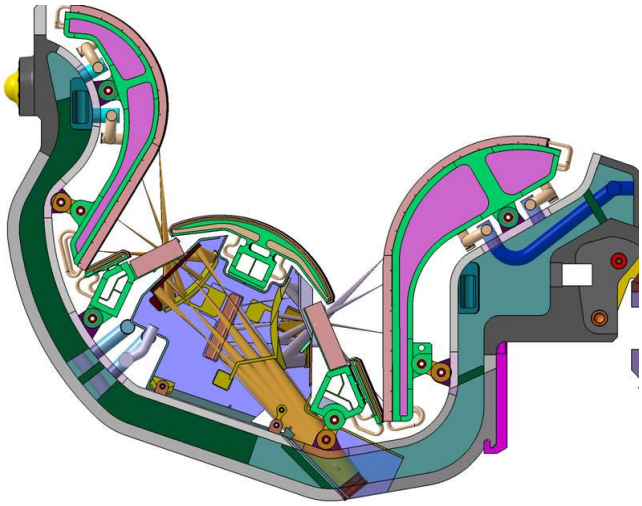

Figure 6: Optical design of the divertor thermography diagnostic

CONCLUSIONS

All the work concerning CEA contribution described in the contract EFDA 06-1429 has been performed and reported.

REPORTS AND PUBLICATIONS

[1] L. Meunier, L. Doceul, 'Diagnostic port plug procurement – Draft Final Report (EFDA Contract 06-1429) D1.2', PEFC/NTT-2007.015 Rev. 0 December 2007

[2] L. Meunier, L. Doceul, J-P. Martins, F. Jullien, 'Engineering assessment of diagnostic port integration on ITER Draft Final Report (EFDA Contract 06-1429 D2.2)', PEFC/NTT-2007.024 Rev. 0 December 2007

[3] F. Jullien, 'Proposition of a collaborative diagnostics integration management for ITER by using digital mock-up, CAD software & PDM system', 25th Symposium on Fusion Technology (2008), to be published in Fusion Engineering and Design

[4] L. Meunier, 'CEA engineering activities on the ITER representative diagnostic port plug EQ#01', 25th Symposium on Fusion Technology (2008), to be published in Fusion Engineering and Design

[5] J.P. Martins,'Study of ITER Equatorial Port Plug handling system and vacuum sealing interface', 25th Symposium on Fusion Technology (2008), to be published in Fusion Engineering and Design

[6] R. Reichle, 'Concept and development of ITER divertor thermography diagnostic', 18th Plasma Surface Interactions in Controlled Fusion Devices (2008), to be published in Journal of Nuclear Materials

TASK LEADER

Louis DOCEUL

DSM/IRFM/SIPP/GIPM
CEA-Cadarache
F-13108 Saint-Paul-lez-Durance Cedex

Tel: 33 4 42 25 61 65
Fax: 33 4 42 25 49 90

e-mail: louis.doceul@cea.fr

CEFDA06-1438-PP1

Task Title: TW6-TPDS-DIADES1: DIAGNOSTIC DESIGN FOR ITER PP1: PLASMA POSITION REFLECTOMETRY

INTRODUCTION

CEA in collaboration with the University of Nancy was in charge of numerical studies and performance evaluation of ITER Plasma Position Reflectometry (PPR). This task was led by IST (Portugal) and also involved CIEMAT (Spain) and ENEA-CNR Milano (Italy).

2007-2008 ACTIVITIES

The main goal of the numerical study led by Université de Nancy, corresponds to define the inputs of simulations, to identify the different phenomena able to introduce an error in the plasma position measurements and to evaluate the performance of the different plasma position reflectometers. Relevant PPR descriptions were also provided to the ENEA_CNR Milano for radiation pattern and reflected power computations. Shaping has a major impact on the reflected signal, in particular for the upper view (gap 5 on figure 1).

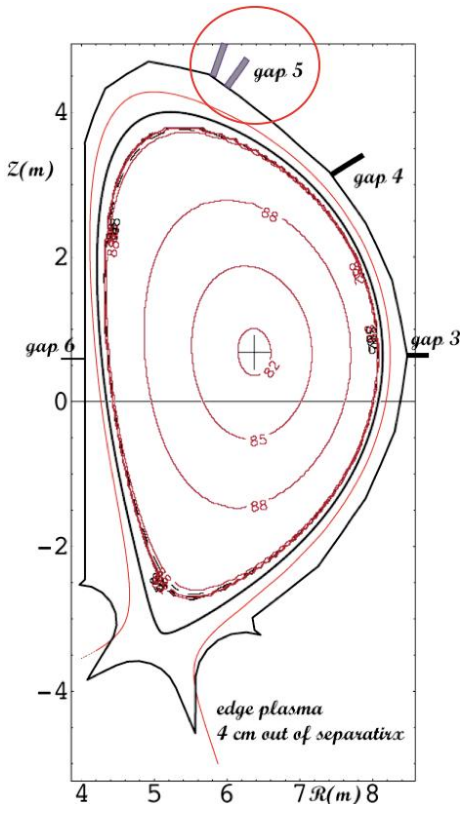

Figure 1: O-mode index contours including relativistic effects with the positions of the different plasma position reflectometers for a scenario type II

To accommodate shaping variation, 2 sets of waveguides are foreseen for the upper view (figure 2).

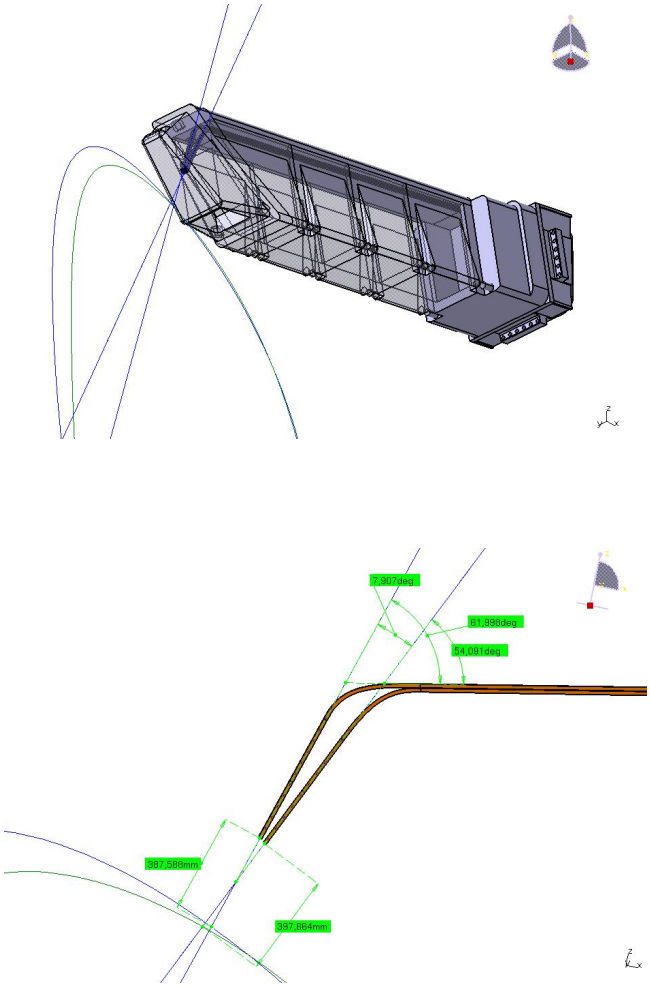

Figure 2: Design of the GAP 5 PPR (top) insertion in the port plug with the add-ons of the curves associated to last closed magnetic surface for the scenarios 2 (center density $10.2 \cdot 10^{19}$ m^{-3}) and 4 (center density $7.25 \cdot 10^{19}$ m^{-3} and (right) the waveguide design satisfying to the recommendation of their optical axis perpendicular to the last closed surface, one for the scenarios type 2 and the other for type 4

One important point corresponds to the evaluation of the role of the poloidal density gradient especially for the top view. As can be seen on figure 3, even if the injection angle is chosen to be normal to the last closed surface (40 GHz), the beam is deflected at other frequencies and it would be necessary to correct this effect to recover the right plasma position. To be more realistic, a 3-D full wave code would be necessary to optimize the shape of the blanket hole surrounding the mouth of the reflectometer antennas to avoid as much as possible the spurious resonances seen with 2D simulations. European Reflectometry Computation Consorsium (ERCC) is in charge of the development of a 3D code that will be able to simulate such effects.

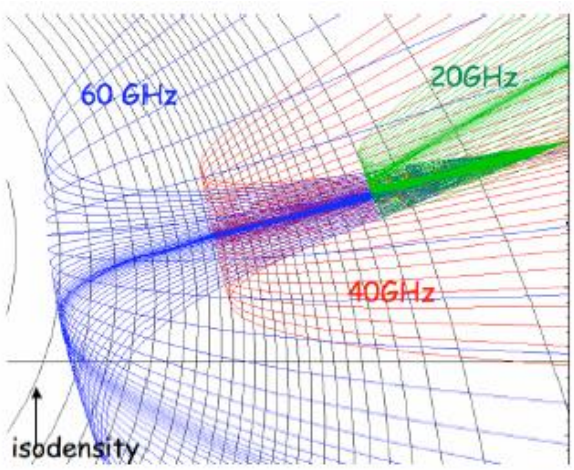

Figure 3: Three different sets of rays for three different frequencies 60 GHz (red), 40 GHz (blue) and 20 GHz (green) for plasma presenting both poloidal density gradient and curvature. The injection angle of the probing beam is optimized for 40 GHz

CONCLUSIONS

Following preliminary results obtained during this task, a list of priority numerical studies was established. The first priority concerns the shaping that has a major impact on the reflected signal, in particular for the upper view (figure 1 Gap 5). Influence of ELM activity was identified as the second priority. Turbulence effects and impact of modes should also be quantified. Other crucial points that were identified are the impact of the various assumptions on plasma parameters.
For example, the accuracy of the measurements depends strongly of the edge density profiles. Moreover, these simulations were done assuming an ideal density profile initialization without taking into account the Doppler shift (without poloidal motion), MHD activity at the edge and plasma fluctuations.
Concerning the performance, the signal to noise (S/N) evaluation is expected to be high (above 35 dB) for all gaps up to 60 GHz if one excludes the reflection losses due to 2 or 3 D effects (aims of future numerical studies). This S/N ratio would be high enough to allow measurements in the microsecond range. S/N ratio remains good up to 75 GHz allowing measurement at slightly higher frequency if necessary.

The work performed in the frame of this task was focused on the Project Plan of Procurement Package 11. Some technical developments were also done, regarding the optical design, the mechanical design, and the integration of Equatorial Port Plug 1. Preliminary analysis of the measurement requirement and of the reachable performances of the Eq Vis/IR system has also started. Stringent issues were raised, and their knowledge will be very helpful for the forthcoming activities.

REPORTS AND PUBLICATIONS

Draft of the Final Report on ITER Plasma position Reflectometry – CEA Internal Report DIAG/NTT – 2008.006 – R. Sabot, S. Heuraux, F. Da Silva, G. Giruzzi

TASK LEADER

Roland SABOT

DSM/IRFM/SCCP/GTTM
CEA-Cadarache
F-13108 Saint-Paul-Lez-Durance Cedex

Tel: 33 4 42 25 61 63
Fax: 33 4 42 25 62 33

e-mail: roland.sabot@cea.fr

CEFDA06-1438-PP11

Task Title: TW6-TPDS-DIADES1: DIAGNOSTIC DESIGN FOR ITER PP11: VISIBLE/IR WIDE ANGLE VIEWING SYSTEM

INTRODUCTION

The European Domestic Agency ("Fusion for Energy") will supply some of the ITER diagnostic systems as part of port-based procurement packages. Procurement Package 11 (PP11) is one of these packages. It consists of Equatorial Port Plug 1 and of two main diagnostics: the Equatorial Visible/InfraRed Wide Angle Viewing System (Eq Vis/IR WAVS) and the Radial Neutron Camera (RNC). In addition, seven other diagnostics (supplied by Europe or other ITER partners) will have to be integrated in Equatorial Port Plug 1. Besides, the Eq Vis/IR WAVS will also be present in three other equatorial port plugs under the responsibility of the United States (Equatorial Port Plugs 3 and 9) and China (Equatorial Port Plug 12).
Task TW6-TPDS-DIADES on Procurement Package PP11 was implemented in order to prepare the future European activities linked to the supply of this package (in terms of timescale, cost...). It was put in place at the end of 2006 with the main objectives to build an integrated Project Plan for the full implementation of PP11, to realize specific design activities on the two main diagnostics, and to tackle the integration issues of the port plug which is included in this package, the Equatorial Port Plug 1.
This task was performed by a cluster of five Euratom Associations: CEA-Cadarache in France (task leader), ENEA-Frascati in Italy, CIEMAT in Spain, HAS in Hungary and IST in Portugal. The part of the work relative to the RNC was ENEA's responsibility, whereas the work on the Eq Vis/IR WAVS was shared between the cluster institutes: establishment of Project Plan by CEA, optical analysis made by CEA and CIEMAT, mechanical/thermal studies by CEA and HAS, neutronic analysis by ENEA and HAS, and study of data acquisition and interfaces with CODAC (COntrol Data Access and Communication) by IST. CEA was also in charge of the study of Equatorial Port Plug 1 integration.
We will give here an overview of the major results obtained by CEA in the frame of this task, regarding the PP11 Project Plan, the technical achievements on the Equatorial Visible InfraRed Viewing System, and the integration of Equatorial Port Plug 1.

2007-2008 ACTIVITIES

PP11 PROJECT PLAN

Objective, scope and overall schedule
The main objective was to build an integrated Project Plan for the full implementation of Procurement Package 11, from preliminary design to commissioning in ITER tokamak. The first step consisted in analysing the PP11 scope which encompasses the full development (from design to integration) of Equatorial Port Plug 1, composed of the port plug, the interspace and the port cell, the full development of the two main diagnostics (from design to integration) : the Equatorial Visible/InfraRed Wide Angle Viewing System and the Radial Neutron Camera, the manufacturing and testing of the Eq Vis/IR WAVS associated to the 3 other Equatorial Port Plugs (3, 9, 12) where this diagnostic is also installed, and the integration in Equatorial Port Plug 1 of seven other diagnostics provided by Europe or other ITER parties (figure 1).

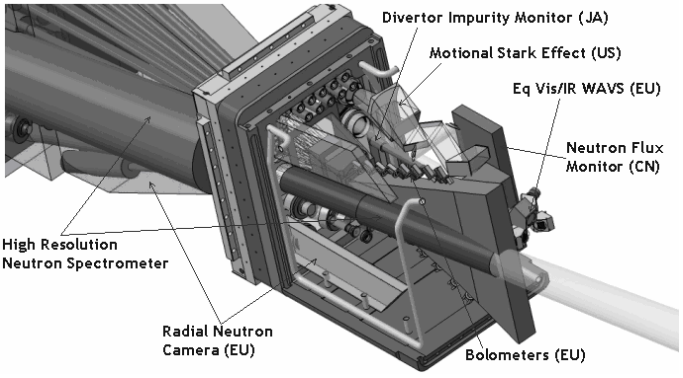

Figure 1 : Diagnostics present in Equatorial Port Plug 1

Regarding the time schedule, the Project Plan spreads over several phases of the project: identification of needs, preliminary design and basic R&D, detailed design and advanced R&D, manufacturing, assembly/test/integration, integration in tokamak, and finally commissioning without plasma. The commissioning with plasma, the tokamak exploitation and the decommissioning are not included in the scope, but their constraints are taken into consideration.

PBS, WBS, time schedule and costing
A breakdown of Procurement Package 11 by "product" (Product Breakdown Structure PBS) was built. Its objective is to identify the main components and to track crucial objects, as the Safety Important Class (SIC) components that play a key role in the machine safety. These SIC components are mainly the objects that form part of the confinement barrier, at the boundary of the vacuum vessel (port plug flange, diagnostics vacuum windows, feedthroughs). These components will have to be particularly taken care of, and will have to meet stringent safety requirements.
A breakdown of PP11 by activity (Work Breakdown Structure WBS) was also done in order to identify the main tasks (Work Packages WPs) and their subtasks.
Taking into account the different tasks of WBS, a time schedule was created for the whole duration of PP11. Due to the length of the project (more than 10 years), only the tasks of the first phases, before the manufacturing, were studied in detail.
On the basis of the WBS tasks, the human resources needed to perform them as well as the material resources (mock-

ups, facilities, diagnostics manufacturing…), an integrated costing was established for each phase of the project. Rather logically, the need in human resources increases during the design phases, decreases during the manufacturing, and increases again for the assembly, tests and integration activities.

Risk Analysis

A preliminary risk analysis for the implementation of PP11 was performed at the end of 2007 by a firm specialised in project management. 60 risks were identified, and are divided into technical risks (linked to design, interfaces, diagnostic performances…) and programmatic risks (relative to organisation, human resources, safety…). It results that 40 % are technical risks, 22 % are linked to the organisation of the project (heaviness of multilayer organisation: IO/F4E/Consortium/Associations, slowness of decision-making process…), 10 % are linked to the safety of the machine (failure of confinement barrier), the remaining 28 % are related to the complexity of the project (manufacturing, machine control, nuclear regulation, human resources, funding…). 85 % of the identified risks are considered as critical, and will have to be monitored by mitigation actions. The critical technical risks of the Eq Vis/IR WAVS are due for a significant part to the quantitative temperature measurement specification in variably reflecting and hostile environment, and will have to be treated by urgent R&D tasks.

TECHNICAL ACHIEVEMENTS OF THE EQUATORIAL VISIBLE/INFRARED WIDE ANGLE VIEWING SYSTEM

Description of diagnostic

The Eq Vis/IR WAVS is an optical system working in visible and infrared with the following main functions : (a) measurement of the plasma facing components (PFC) temperatures (200-3600°C) in the IR (3-5 µm), and (b) study of the plasma-wall interaction in the visible (400-700 nm). Regarding the resolution, the targets to reach are: 3-5 mm for the spatial resolution, 20 µs to 10 ms for the time resolution [1]. As the measurement of PFC temperatures aims at ensuring the machine protection, this diagnostic is mandatory for the tokamak operation, and must be totally reliable. It is composed of three lines of sight (LOS) per equatorial port plug: two horizontal LOS for the view of the first wall and the heating systems, and one vertical LOS for the divertor survey. For each LOS, both visible and IR wavelengths are transported through optical components to the camera sensors located in the port cell, 15 m away from the plasma. Because of the damaging effect of nuclear radiation on materials and coatings in the vicinity of the vacuum vessel, the choice of the optical components is driven by their radiation hardness: only metallic mirrors can be used in the port plug, and refractive components are useable from the port plug flange, where the level of radiation is lower (figure 2) showing also the location of the interspace and the port cell).

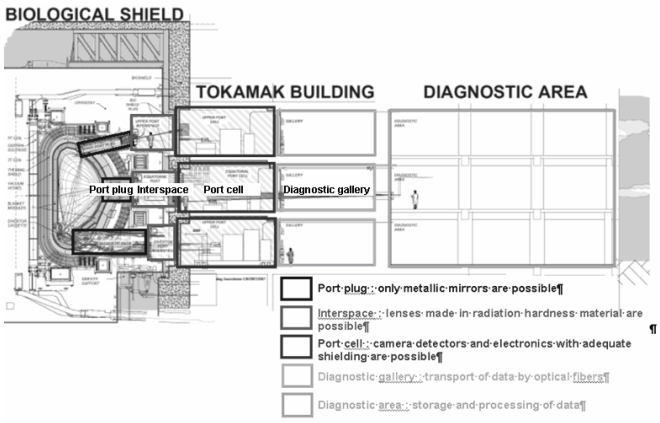

Figure 2 : Breakdown of Eq Vis/IR WAVS from plasma to diagnostic area

Optical design

The Zemax model proposed in a previous study [2] was analysed in order to evaluate the optical performances of the system. In this design, infrared and visible paths have common optical axes from the first mirrors to the camera detectors. The main groups of optical components are for one LOS (figure 3):

- two first mirrors (diameter 150 mm) : the first one is parabolic, the second one is plane; both are very close to the plasma (between 100 and 175 mm behind the first wall),
- two "dog leg" mirrors (plane mirrors with a diameter of 280 mm) folding the beam to reduce the neutron streaming through the port plug,
- a Cassegrain telescope, composed of two conic mirrors (diameters 170 and 45 mm) which reduces the optical beam diameter for the way through the port plug flange,
- four optical relays made of refractive components (lenses with a diameter around 130 mm) for the transport of the light to the camera detectors.

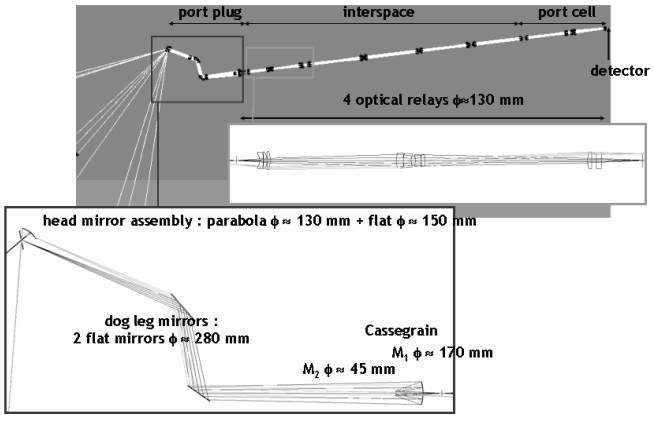

Figure 3 : Main components of one channel of Eq Vis/IR WAVS

In this design, whereas the optical performance of the system could be quite satisfactory for the infrared range, it is unacceptable for the visible. Indeed, because of the separation of wavelengths in the spectral line, the chromatic aberrations cause defocus between the different wavelengths, inducing a severe degradation of the resolution in the visible. This means that the same optical components cannot be used for both visible and IR light along the total optical line. Two solutions are possible: either the two wavelength ranges are separated by a beamsplitter into two parallel beams ("split" solution), or the light is transmitted by two concentric beams ("hollow" solution, with insertion of a small visible Cassegrain before the IR Cassegrain, in order to have concentric visible and IR beams transported by specific lenses). Nevertheless, the "hollow" solution cannot be retained due to the complexity of the optomechanical design, the manufacturing and the alignment. For the "split" solution, there are two possibilities for the beamsplitting : the separation is done either at the end of the optical line, before the camera detector, or as soon as possible after the port plug flange (figure 4). In the first solution, the room occupied by the diagnostic would be minimised, but the correction of chromatic aberrations would be very difficult, and furthermore the material of the lenses before the beamsplitting would have to present good transmission both in IR and visible. The second solution would enable better optical performance, since the two optical paths could be optimized separately (use of specific IR and visible materials, optimization of optical components geometry). Its main drawback is the large space occupied by the diagnostic. The choice between these two solutions will be decided taking into account the optical performance requirements, the results of the material assessment (see later) and the integration constraints.

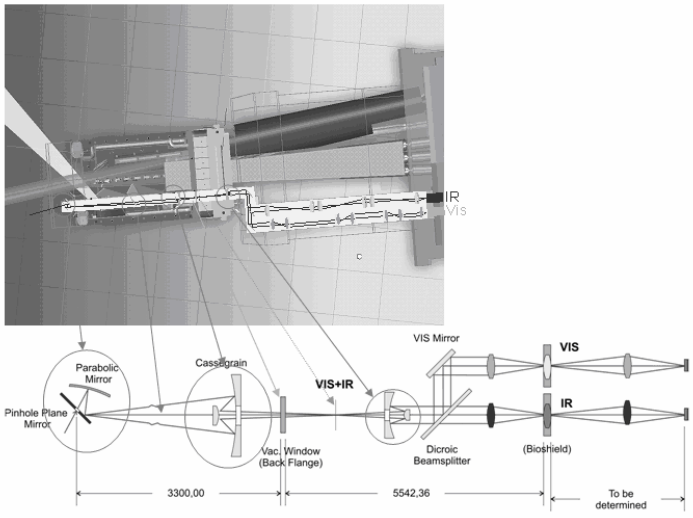

Figure 4 : Eq Vis/IR WAVS: best solution for beamsplitting

Besides, taking into account the characteristics of an IR detector that could be reasonably available in a near future (Sofradir HgCdTe sensor; bicolour 3.4–4.2 µm/4.4–4.8 µm; 640 × 512 pixels, pitch 24 µm [3]), the spatial resolution obtained with such sensor (~16 mm at 6 m) does not meet the current target measurement (see description of diagnostic). So in the future the optical design will be optimized taking into account both the best sensor that could be developed during the design phase, and the best resolution reachable with such sensor, while checking if the present required spatial resolution is really mandatory or can be relaxed.

Several integration issues have also been identified (collision between the three LOS, interferences with other diagnostics). Besides, the periscope mirrors are currently in such locations that the optical lines cross the port plug in both toroidal and poloidal directions, making the integration, alignment and maintenance operations very tricky, or even impossible in some cases. That is why a new integration approach is under study, consisting in inserting the diagnostic into removable cassettes. For this, the optical paths will need to be made as straight as possible along the radial axis, while keeping labyrinths for neutron shielding.

An assessment of the materials for the optical components was performed. For the first mirrors, some R&D tasks are already planned (see further section on "Urgent R&D Tasks"). For the refractive components, the choice of the materials depends, on the one hand, on their transmission capability in the visible, in the IR, or in both ranges, and, on the other hand, on their radiation hardness. Recent neutronic calculations [4] showed that the neutron fluxes just after the port plug flange are very high (10^8 n/cm^2 s). Such radiation level prevents the use of conventional materials transmitting both visible and IR (such as BaF_2 and CaF_2) that would loose their transmission properties by browning in less than 2000 h, unless (a) a sufficient shielding is provided, or (b) the annealing effect of temperature on colouring can be used (at least for CaF_2), or (c) the optical system is stackable. For the visible light transport, some radiation hard materials already exist and are used in nuclear fission facilities (quartz glass KS4, low density material doped with cerium oxide: RS-BK7, RS-LF5, RS-SF6, RS-F2). For the IR transmission, such radiation hard materials are not already available "off-the-shelf". Radiation hardness tests will thus have to be performed on conventional IR materials like Ge, Si, ZnS, ZnSe, and on materials that are transmissive in IR and visible, like MgO and YAG.

Mechanical and thermal design

The mechanical and thermal design of the diagnostic has been improved (figure 5). In particular, the design of the structure (called Head Mirror Assembly) that holds the six first mirrors (two mirrors x three views) was studied. This structure is a parallelepiped-shape box whose walls are actively cooled. The part facing the plasma is protected with a first wall similar to the vacuum vessel one (beryllium + copper alloy CuCrZr). For the thermal calculations, a neutronic loading of 7 MW/m^3 [4] was applied, with a plasma radiation flux of 0.5 MW/m^2. The cooling water temperature is in the range 100–150 °C, and the heat transfer coefficient varies between 10000 and 20000 W/m^2 K, corresponding to a water speed of a few m/s. For the mechanical loads (electromagnetic forces during disruptions), until refined models and analysis are produced, the pragmatic solution is to extrapolate them from the most conservative results to date (scaling factor applied to loads calculated on the Blanket Shield Module : radial moment 0.5 MNm, radial force 700 kN). For the boundary conditions, the assembly is bolted on the first shield module inside the port plug.

A first study was performed in 2007. It was focused on the design of the structure holding the mirrors, the mirrors themselves and their mounting were not taken into account. Two materials gave satisfactory results in terms of thermal

and mechanical behaviours: the copper alloy CuCrZr, and the stainless steel 316 L(N)-IG.

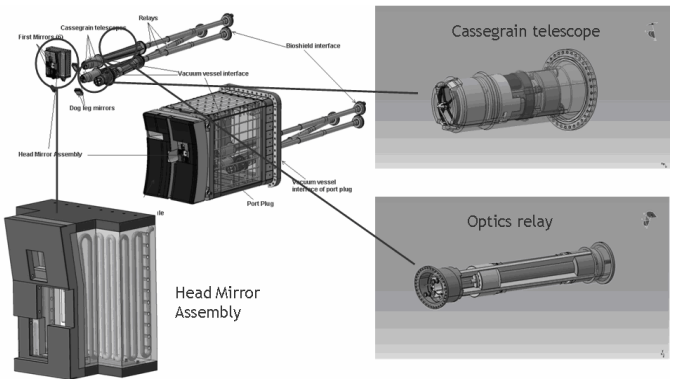

Figure 5 : Overall mechanical design of the Eq Vis/IR WAVS

In a more recent study (figure 6), all the components (except the first wall) were chosen in stainless steel, as this material could be potentially used for the first mirrors, in order to have the most homogeneous behavior as possible, as well as the most pessimistic response from a thermal point of view. To reach acceptable temperatures with this poor thermal conductive material, the cooling system needs to be very dense. The maximum temperatures are located around the aperture of the viewing cones, and reach 600 °C in the beryllium, 270 °C in the CuCrZr and 340 °C in the stainless steel, acceptable values for such materials. Besides, the displacements induced by electromagnetic forces seem rather low (less than 1 mm).

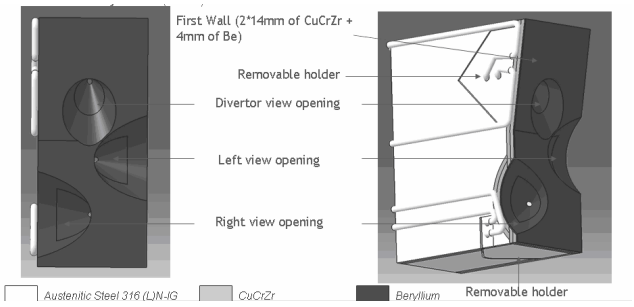

Figure 6 : Design of head mirror assembly

Operational performance analysis

Three operational performance levels of the Eq Vis/IR WAVS can be distinguished : qualitative imaging, calibrated photon source flux measurements, and quantitative temperature power and particle flux measurements. The first level is sufficient for the largest part of operational goals and requires relatively simple hardware (monocolour, no absolute calibration) coupled to cognitive software to detect arcs on antennas, precursors of disruption, ELMs, plasma shape, etc. The achievement of this performance has a relatively low risk level. The second level (medium risk) requires (in metallic environment) multicolour imaging, in-situ calibration and quantitative value oriented data processing (for threshold and feedback operation) as in Tore Supra [5]. The third level (high risk) requires inputs on optical (reflection and emission) and thermal wall conditions (layers, hot spots) and plasma radiation.

Urgent R&D tasks

Radiation hardness testing will have to be made in order to finalize the choice of material and coating for the lenses and freeze the overall optical design architecture. R&D on the first mirrors will also have to be performed : choice of material and coating through the project "PROMISE" (PROtotype of Mirror in Iter Severe Environment), design of a shutter to protect first mirrors from erosion/deposition, possibility of in-situ cleaning, etc.

For the mechanical design, the design of the Head Mirror Assembly will be pursued, with the final objective to build a mock-up of this component and to test it in realistic conditions. Other mechanical components will have to be designed and possibly tested through prototypes, as the systems that will enable to compensate the differential movements between the vacuum vessel and the tokamak building.

For the diagnostic thermography requirements, R&D tasks are needed to evaluate the performances that can be reached in terms of quantitative temperature measurements. The issues of parasitic light due to reflection of hot spots on metallic surfaces and the variable emissivity of surfaces will have to be solved through R&D activities like photonic simulation using a 3D ray-tracing code (project ITERMOD "ITERative Modeling for Optical Design"), and measurement of BRDF on ITER relevant materials. Methods of in-situ calibration will also have to be developed (use of black bodies, photothermal methods, pyroreflectometry [6]). For the data processing, cognitive software will need to be developed for the first performance level, analysis software for multicolour measurements for the second level, and software able to separate signal components for the third level.

INTEGRATION OF EQUATORIAL PORT PLUG 1

Nine diagnostics will have to be integrated in Equatorial Port Plug 1. At the moment, diagnostics are put in place in the port plug without taking into account assembly and maintenance constraints, and regardless of the other diagnostics. Consequently, there are a lot of clashes and inconsistencies and the installation and maintenance of some diagnostics seem difficult (or even impossible). It appears thus as a necessity to try to rationalize the allocation of volume to the different diagnostics in the port plug, taking into account all the environment constraints.

Regarding the Eq Vis/VIS WAVS, its integration in the port plug has to be studied taking into account the constraints of assembly, alignment, maintenance and remote handling. The objective is to integrate the diagnostic in the port plug by using one or several cassettes bolted on the port plug back flange, and these cassettes could be installed and removed from the interspace. In particular, this approach, if possible, would be very useful for the Head Mirror Assembly, for which the maintenance could be done more easily and with a higher frequency than the maintenance of the whole port plug. Another difficulty is due to the location of the Eq Vis/IR WAVS in several equatorial port plugs (#1, 3, 9, 12): even if a standardisation between the four port plugs would be the simplest and less expensive choice, it may be difficult to find an unique

configuration of this diagnostic that is consistent with the available space in the four port plugs.

For the other diagnostics present in Equatorial Port Plug 1, the main goal would be to integrate most of diagnostics with removable cassettes, at least in the port plug. Preliminary contacts with the institutes responsible for the development of these diagnostics were established.
Moreover, the complexity of the integration of Equatorial Port Plug 1 will necessitate a rigorous methodology of CAD data management through the use of a dedicated Product Data Management (PDM) system. This system should be able to manage the evolution of the CAD data provided by the different collaborators, as well as the physical interfaces between CAD models. It should be also consistent with the CAD data management system of ITER Organization (ENOVIA LCA) and the one of Fusion for Energy (SmarTeam). The system should be physically installed at CEA, and would manage all CAD data relative to Equatorial Port Plug 1.

CONCLUSIONS

The work performed in the frame of this task focused on the Project Plan of Procurement Package 11. Some technical developments were also done, regarding the optical design, the mechanical design, and the integration of Equatorial Port Plug 1. Preliminary analysis of the measurement requirement and of the reachable performances of the Eq Vis/IR system has also started. Stringent issues were raised, and their knowledge will be very helpful for the forthcoming activities.

REFERENCES

[1] D. Thomas, A. Costley, N. Nassar, G. Vayakis, 17th HTPD poster, ITER D 2DTR2Ev1.1

[2] D. Guilhem, Y. Corre, A. Géraud, J.-B. Migozzi, E. Thomas, G. Vayakis, et al., ITER wide angle viewing thermographic and visible system, Final report of TW3-TPDS-DIASUP task, EFDA D 2D4ZQC v1.0, August 2007

[3] M. Jouve, Technical point about IR bicolour detectors, New Technologies and Innovative Processing Methods for Imaging in Fusion Devices, JET, 18–20 February 2008

[4] F. Moro, L. Petrizzi, G. Brolatti, B. Esposito, D. Marocco, R. Villari, The ITER RNC: an updated neutronic analysis, Fusion Eng. Des., 2008, in press

[5] D. Guilhem, J.-L. Bondil, B. Bertrand, C. Desgranges, M. Lipa, P. Messina, et al., Tore Supra infrared thermography system, a real steady-state diagnostic, in: 23th SOFT Proc., Fusion Eng. and Design, vol. 74, Issues 1-4, November, 2005

[6] D. Hernandez, J.-M. Badie, F. Escourbiac, R. Reichle, Development of twocolour pyroreflectometry technique for temperature monitoring of tungsten PFC, Fusion Eng. Des. 83 (2008) 672–679

REPORTS AND PUBLICATIONS

S. Salasca et al., CEA Draft Final Report on TW6-TPDS-DIADES Procurement Package 11 - Equatorial Visible/IR Wide Angle Viewing System and Integration of Equatorial Port Plug 1, 2009 (to be published)

S. Salasca et al., Development of equatorial visible/infrared wide angle viewing system and radial neutron camera for ITER, Fusion Eng. Des. (2009), doi:10.1016/j.fusengdes.2008.12.088

M. Davi, Y. Corre, D. Guilhem, F. Jullien, R. Reichle, S. Salasca, et al., Progress of the ITER equatorial vis/IR wide angle viewing system optical design, 17th HTPD Conf., Albuquerque (US), May 2008 (to be published in Rev. Sci. Instr.)

R. Reichle, J.-M. Badie, C. Balorin, S. Carpentier, Y. Corre, M. Davi, et al., in: F.P. Orsitto, et al. (Eds.), Concept and Development of Instruments for ITER Thermography, Burning Plasma Diagnostics, AIP, New York, 2008
.
J.-M. Travère and Tore Supra Team, In-vessel components imaging systems: from the present experience towards ITER safe operation, Fusion Eng. Des., 2008, in press

TASK LEADER

Sophie SALASCA

DSM/IRFM/SIPP/GPIM
CEA-Cadarache
F-13108 Saint-Paul-Lez-Durance Cedex

Tel: 33 4 42 25 77 51
Fax: 33 4 42 25 49 90

e-mail: sophie.salasca@cea.fr

CEFDA06-1438-PP21

Task Title: TW6-TPDS-DIADES1: DIAGNOSTIC DESIGN FOR ITER PP21: BOLOMETRY

INTRODUCTION

The ITER bolometers will be provided by the European Domestic Agency. IPP-Garching (Germany) was task leader for the TW6-TPDS-DIADES – Del. 5 task (Bolometers and Pressure gauges). The CEA collaborated on the subject of the assessment of alternative bolometer concepts (imaging and capacitive bolometers) for integration into ITER and of potentially perturbing effects (e.g. irradiation tests) – some of which had been investigated in an previous EFDA task [1]. Imaging bolometers use a thin metal foil behind a pinhole whose temperature is monitored by an IR camera. Capacitive bolometers make use of the change in capacitance of a capacitor due to temperature changes induced by plasma radiation.

2007-2008 ACTIVITIES

The task started with a Kick-off Meeting 15-16 January 2007 in Garching and the main results were reported in [2]. It had quickly become evident that the capacitive bolometers were not sufficiently advanced to be considered for the present ITER concept and the imaging bolometers were considered to fall outside the scope of the IPP led task. The CEA collaborated with the CNRS-IUSTI (France) on the topic of the analysis of the thermal images measured by imaging bolometers. In 2008, CNRS-IUSTI set up an experiment simulating an imaging bolometer. As source was used a flash lamp with illuminated (2 ms duration) the front face of a thin metal foil through a mask with a random spatial random shape.The temperature of the rear face of the foil was measured with an IR camera.

The temporal and spatial features of the incident heat flux were calculated. The spatial shape of the heat flux (fig. 1a), calculated agrees well with the position and shape of holes in the mask (black lines) and the temporal structure found corresponds well to the excitation (Fig.1b) time by the flash lamp. This could be the starting point for collaboration with the pioneers of this approach [3] on analysis methods using inverse calculation techniques.

The other activity the CEA was involved in was the participation in the preparation of irradiation tests of IPP bolometers at SCK·CEN Mol (Belgium), which are scheduled to take place in 2009.

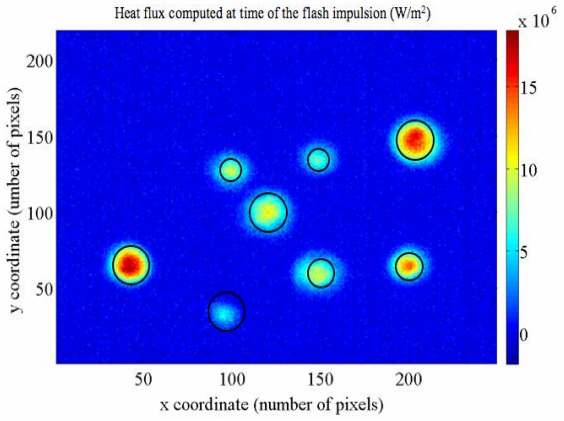

a) Distribution in space of the computed heat flux

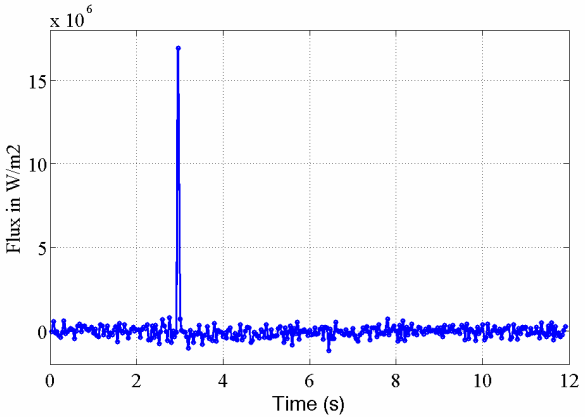

(b) Heat flux computed as a function of time

Figure 1: Heat flux estimated on the surface of a thin foil simulating an imaging bolometer

REFERENCES

[1] CEA DIAG/NTT-2007.011 (2007) & rapport EFDA: Final report for contract EFDA/03-1111 Bolometry CEA: Detailed design analysis of bolometer cameras on the basis of the reference resistive bolometer sensor, R. Reichle, S. Hourcade

[2] The ITER bolometer diagnostic - Status and plans, H. Meister, L. Giannone, LD. Horton, G. Raupp, W Zeidner, G. Grunda, S. Kalvin, U. Fischer, A. Serikov, A. S. Stickel, R. Reichle, Rev. Sci. Instr. 79, 10, 10F511 (2008)

[3] Infrared Imaging Video Bolometer, B.J. Peterson, Rev. Sci. Instr., 71, 10 (2000) 3696

TASK LEADER

Roger REICHLE

DSM/IRFM/SIPP/GCECFP
CEA-Cadarache
F-13108 Saint-Paul-Lez-Durance Cedex

Tel: 33 4 42 25 63 76
Fax: 33 4 42 25 49 90

e-mail: roger.reichle@cea.fr

CEFDA06-1438-PP22

Task Title: TW6-TPDS-DIADES1: DIAGNOSTIC DESIGN FOR ITER PP22: MAGNETIC DIAGNOSTICS: DEVELOPMENT OF A FIBRE OPTIC CURRENT SENSOR SUITABLE FOR ITER

INTRODUCTION

The next generations of thermonuclear fusion reactors should tend towards the burning of thermonuclear fusion plasma in (quasi) steady state conditions. This steady-state operation together with the high radiation level and temperature will challenge the use of the classical inductive magnetic sensors, a key equipment for the operation of the tokamak and the measurement of plasma current. In this context, there is a clear need to look at complementary techniques for the measurement of plasma current and magnetic parameters. One possibility is to use Fibre-Optic Current Sensor (FOCS). The fibre is intrinsically well insulated, insensitive to electromagnetic interference and has a large dynamic range from DC up to about a few MHz making FOCS attractive sensors. The optic fibre itself is a pure silica single mode fibre with an outer diameter of 125µm which makes the sensing device very compact. Nevertheless it is absolutely mandatory to install guiding tubes to protect and guide the fibre. The sensing principle is based on the Faraday effect in silica fibres [1]. The Faraday effect causes the polarization of a linearly polarized light to rotate under the action of an external magnetic field when the wave propagation vector of the interrogating light is aligned with the magnetic field:

$$\beta = V \oint \mathbf{B} \cdot \mathbf{dl} = V \mu_0 I$$

where β is the rotation of the light polarisation, V is the Verdet constant (magneto-optic coefficient) for the fibre material (it is the specific rotation of a material and depends on the light wavelength), *I* is the current flowing in the area defined by the optic fibre.

2007-2008 ACTIVITIES

INTEGRATION OF FOCS IN ITER

In ITER, FOCS was originally foreseen to be integrated in the Toroidal Field Coil (TFC) casing. It was demonstrated that the cryogenic temperature does no favour the operation of the fibre even if the strength of the radiation field is low [2]. Another location was studied between the vacuum vessel and the thermal shield despite the higher radiation field (figure 1). The fibres are inserted into a stainless steel tube of 2 mm diameter which will be anchored on the ITER VV at regular position. A typical loop length around the VV is about 30 meters. Three locations are foreseen distributed over 120° sector (sectors #02, #05 and #08). On each location 4 tubes run in parallel and independently allowing to reach a redundancy of minimum 4 sensors per location. A first bent of about 30 cm at the bottom of the VV will gather all the tubes in one single bundle. A second bent, also of about 30 cm, is then necessary to bring the bundle perpendicular to the VV plane and to enter in the bellows and connection output tube of 6 m long containing also the instrumentation cable. The output tube is equipped with a flange to ensure the vacuum tightness. This flange will be an hybrid separation containing both tight optical and electrical connectors.

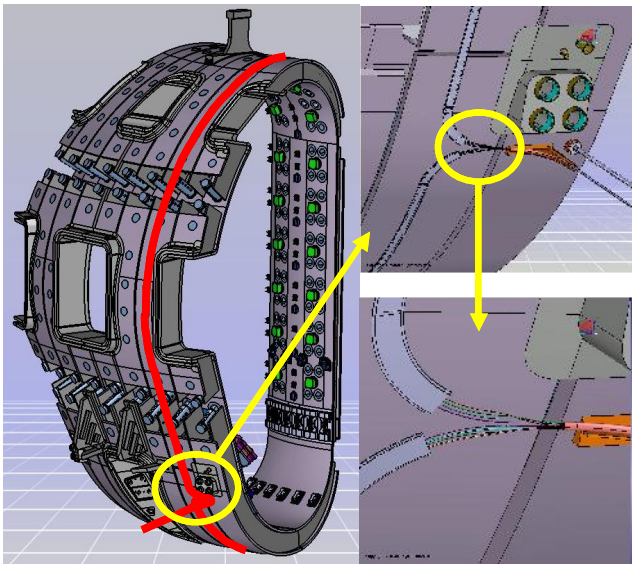

Figure 1: Integration of FOCS in ITER

Gamma radiation test on the fibre up to 5 MGy which is a representative dose for the whole lifetime on the outer ITER vacuum vessel and neutron radiation tests ($2 \cdot 10^{+15}$ n (E>1MeV)/cm^{-2}) were performed [3]. It was found that the magneto-optic coefficient is almost not affected neither by gamma nor neutrons. Thus the sensor performance remains unchanged.

FIRST DEMONSTRATION OF FOCS TECHNOLOGY ON THE TORE SUPRA TOKAMAK

In order to validate the technology of FOCS in a tokamak environment where the current to measure is huge (Ip > 1MA), a FOCS was installed around the Tore Supra vacuum vessel in 2008 in collaboration with SCK-CEN. Two modes of operation were investigated: (i) reflection measurement scheme with a Faraday Rotator Mirror (FRM) put at one extremity of the fibre and (ii) transmission measurement scheme. A laser beam (wavelength=1550nm) is linearly polarized and is launched into the fibre. The change in the polarization ellipse during the plasma discharge is saved in the Tore Supra data base in terms of stokes parameters (or azimuth and elongation of the polarisation ellipse). We clearly observed that the azimuth of the initial linear polarization at the fibre exit is rotated by a certain angle function of the plasma current (figure 2).

The use of the FRM allows to drastically stabilize the polarization states, cancelling the effect of the random fluctuations of the light passing through the fibre. Nevertheless, the polarisation rotation is not univocal with respect to the plasma current. The transmission mode gives linear results but the system would require a day by day calibration.

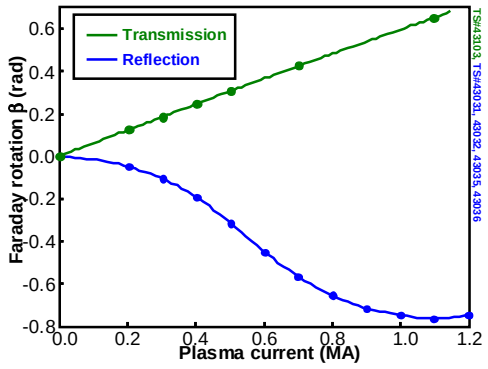

Figure 2: Faraday rotation versus plasma current for the 2 modes of operation: transmission (green) and reflection (blue)

REFERENCES

[1] A.J. Rogers, Optical Fibre Current Measurement, Intern. J. Optoelec., Vol 3, n°5,591-407,1988

[2] B. Brichard EFDA-TW5-IRRCER-Deliverable 9

[3] B. Brichard TW6-TPDS-DIASUP13-Deliverable 1.2

REPORTS AND PUBLICATIONS

Draft Final Report Contract EFDA 06-1438: “Development status of ITER ex-vessel magnetic diagnostic”

Draft Final Report Contract EFDA 06-1438 “Assessment of the equilibrium reconstruction accuracy using ITER magnetic diagnostics”

Draft Final Report Contract EFDA 06-1438 “Overview of ITER Steady State sensors”

Draft Final Report Contract EFDA 06-1438 “Project Plan for ITER ex-vessel magnetic diagnostic”

Ph. Moreau, et al., “Design and performance analysis of ITER ex-vessel magnetic diagnostics”, Fusion Eng. Des. (2009)

TASK LEADER

Philippe MOREAU

DSM/IRFM/STEP/GPAS
CEA-Cadarache
F-13108 Saint-Paul-Lez-Durance Cedex

Tel: 33 4 42 25 36 39
Fax: 33 4 42 25 26 61

e-mail: philippe.jacques.moreau@cea.fr

TW5-TPDC-IRRCER-D03

Task Title: ASSESSMENT OF IR FIBRES FOR THERMOGRAPHY APPLICATIONS, INITIAL GAMMA INDUCED EFFECTS, THEN NEUTRON IRRADIATIONS – FIBRE SELECTION AND PROVISION, DIAGNOSTIC PREPARATION AND MEASUREMENTS

INTRODUCTION

In the course of a study of the feasibility of a divertor thermography diagnostic for ITER [1, 2] the question of radiation hard infrared (IR) fibres had become a topic of interest. Initial tests of a ZrF_4 and hollow waveguide fibres had not given satisfying results [3]. The first ones had darkened already at a dose of 5 kGy, where many MGy would have been the target value and the latter had too high intrinsic transmission losses even before radiation. Neutron irradiation measurements which were initially planned, were therefore considered irrelevant for these fibre types tested initially. Instead it was decided to test a sapphire fibre at high gamma dose.

2007-2008 ACTIVITIES

The CEA provided a sapphire fibre and the SCK-CEN (Mol, Belgium) provided a High Purity Silica Core (HPSC) low OH silica fibre that was tested alongside the sapphire fibre for comparison. Both fibres were irradiated by Co^{60} sources in the BRIGITTE facility of SCK-CEN, which delivers 20 KGy/h of Gamma radiation. Transmission measurements were made before and after irradiation with equipment supplied by the CEA (figure 1).

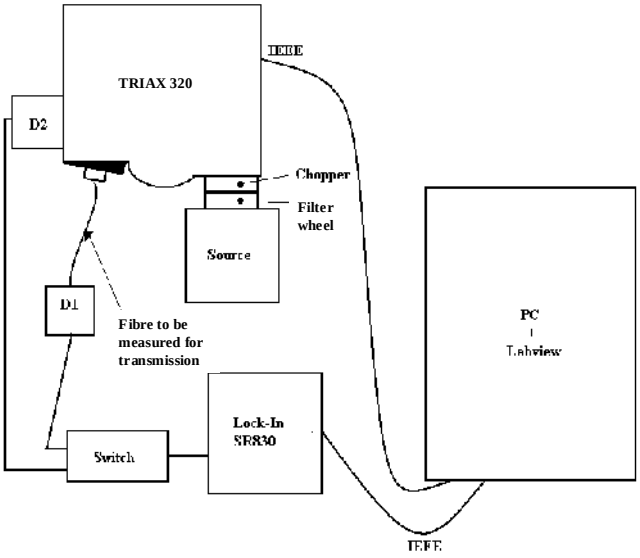

Figure 1: Schema of the experimental setup used to measure the transmission

The equipment consisted of a chopped thermal source, a spectrometer (TRIAX 320) with automatic filter selection to work in different wavelength ranges, IR detectors and synchronous detection equipment which allowed to measure spectrally resolved the transmission in the interesting range of about 1 µm to 4 µm with good signal to noise ratio. The silica fibre was irradiated to a total dose of 500 kGy and the sapphire to a total dose of 2.5 MGy. No significant change in the measured signal was observed (figure 2). For the HPSC fibre the spectral range of strong transmission (more than 50%) extends to 2.3 µm and reaches zero transmission at about 2.7 µm. For the sapphire fibre the 50 % transmission point is reached close to 2.8 µm and the near-zero value transmission point is close to 3.8 µm.

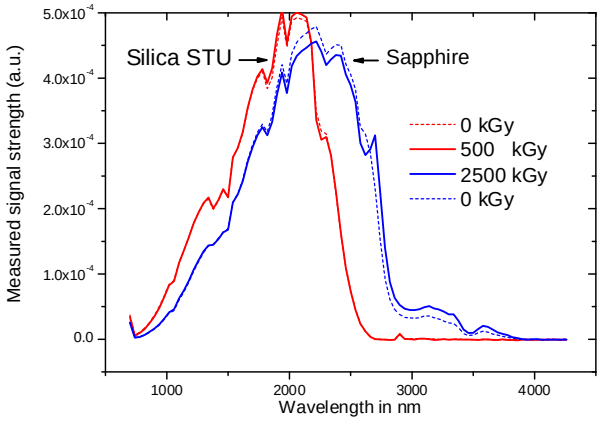

Figure 2: Comparison of the measured signal strength (product of spectral distribution of thermal source light and transmission of the fibres) in a (low OH) HPSC silica fibre (STU) and a sapphire fibre before and after gamma irradiation. The fibres have nearly the same diameter (200 µm for STU, 250 µm for sapphire) and are 2 m long

The draft final report [7] on the task was written together with the SCK-CEN and sent to EFDA for approval beginning 2008. The main results are published [8, 9]. An investigation of the potential overlap in R&D requirements of inertial and magnetic confinement systems has shown that optical fibres are candidates [4], but IR fibres seem so far mainly interesting to magnetic fusion applications. The work was initially done in support of the divertor thermography diagnostic development in Europe. Beginning 2008 negotiations between the Domestic Agencies and ITER led to an attribution of this diagnostic to Japan. This stopped further research on this topic in Europe. Continuation could however become interesting for the midplane visible/infrared TV camera system of ITER, for which Europe is responsible and for which problems of calibration, space and alignment might be overcome by

fibre solutions. In the context of that system, near IR fibres like the HPSC fibre transporting powerful laser light [5] might be used for calibration purposes and sapphire fibres for IR measurements. Another interesting fibre type identified in the course of the investigations are high purity micro-structured fibres, that have the advantage of high radiation resistance potential, since they can be made entirely out of high purity silica glass (figure 3a – 3b) and which can be designed to have also some IR transmission [6].

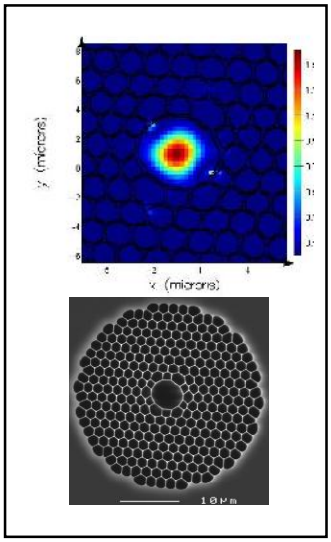

Figure 3a: View of the photonic band gap fibre and the simulation of the light intensity propagation [6]

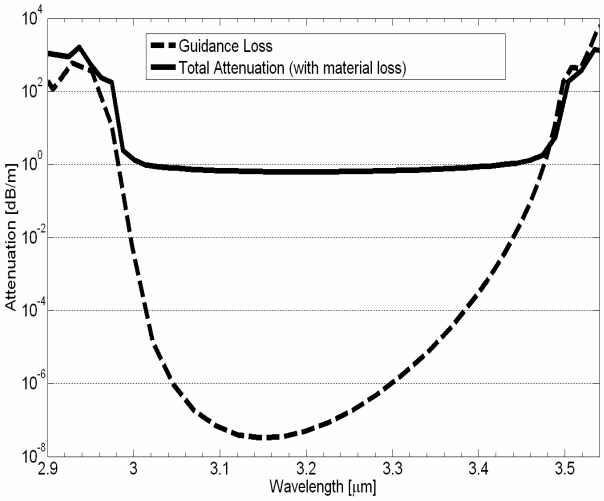

Figure 3b: Calculation of the optical attenuation. The main contribution to optical losses results from the material loss [6]

CONCLUSIONS

The task proved that sapphire fibres are good candidates for IR applications in high gamma radiation environment and confirmed that high purity silica fibres are good candidates for near IR applications in such environment. Micro-structured fibres could become an alternative.

REFERENCES

[1] R. Reichle et al., 'Concept for spectrally resolved ITER divertor thermography with fibres' Proc. 32nd EPS Conf. on Plasma Phys., ECA Vol 29C (2005) P4.083

[2] CEA-Report: DIAG/NTT-2005.019 : 'Evaluation of the potential performance of a spectrally resolving divertor thermography diagnostic for ITER based on a fibre-optics approach; Final report for the EFDA Contract 02-1003 Deliverable 2.3 Thermography – part II : CEA', R. Reichle, S. Henry, J. Miggozzi, E. Thomas, C. Walker (2005)

[3] R. Reichle, B. Brichard, F. Escourbiac, et al. 'Experimental developments towards an ITER thermography diagnostic', Journ. Nucl. Mat. 363-365 (2007) 1466

[4] 'Diagnostic components in harsh radiation environments: Possible overlap in R&D requirements of inertial confinement and magnetic fusion systems', J.L. Bourgade, A.E. Costley, R. Reichle et al. Rev. Sci. Instr. 79, 10F304 (2008)

[5] R. Reichle et al., 'Concept and development of instruments for ITER thermography', in 'Burning Plasma Diagnostics', ed. F.P. Orsitto et al. AIOP, New York 2008

[6] M. Antkoviak, 'Photonic Crystal Fibres with and without inscribed Bragg grating: numerical studies of linear and nonlinear light propagation for specific applications', PhD thesis, Brussels, Belgium: Vrije Universiteit Brussel, (2007)

REPORTS AND PUBLICATIONS

[7] Joint Final report for EFDA Tasks TW4- TPDC-IRRCER D16 (SCK-CEN) and TW5-TPDC-IRRCER D3 (CEA) on irradiation tests of IR optical fibres, R. Reichle, B.Brichard, C. Pocheau, M. Jouve, H. Ooms, S. van Ierschot, S. Martinez, DIAG/NTT-2007.026 (2007)

[8] 'Experimental developments towards an ITER thermography diagnostic', Journal of Nuclear Materials, vol. 363-365, (2007), R. Reichle, B. Brichard, F. Escourbiac, J.-L.Gardarein, D. Hernandez, C. Le Niliot, F. Rigollet, J. Serra

[9] 'Gamma irradiation test of IR optical fibres for ITER thermography', R. Reichle et al., in 'Burning Plasma Diagnostics', ed. F.P. Orsitto et al. AIP, New York 2008

TASK LEADER

Roger REICHLE

DSM/IRFM/SIPP/GCECFP
CEA-Cadarache
F-13108 Saint-Paul-lez-Durance Cedex

Tel: 33 4 42 25 63 76
Fax: 33 4 42 25 49 90

e-mail: roger.reichle@cea.fr

TW6-TPDS-DIADEV-D05d

Task Title: THEORETICAL AND EXPERIMENTAL EVALUATIONS OF LASER CLEANING METHODS FOR DIAGNOSTICS AND MIRRORS

INTRODUCTION

The modeling of laser heating of complex surfaces with and without deposited layers by repetition rate laser pulses was considered. The earlier developed laser heating model [1-2] for complex graphite surfaces heated by nanosecond high repetition rate pulse laser was extended. The simulations were made for sapphire windows and metal surfaces with carbon deposited layer cleaning. In our studies, Nd-YAG laser pulses (1064 nm, 20 kHz repetition rate, 100 ns pulse duration, 1 mJ laser pulses energy) were applied. Different laser fluences were obtained by varying the laser spot radius at the constant laser pulse energy.

2007-2008 ACTIVITIES

Ablation threshold of thin graphite layer deposited on sapphire window

The experiments on laser cleaning of the sapphire surface with a thin graphite layer (150 nm thickness) were made. The carbon layer was demonstrated to be fully removed from the sapphire surface if the applied laser fluence is high enough (several J/cm^2). However, if the laser fluence is below some critical value, a residual very thin layer still remains on the sapphire substrate. It was not possible to remove this very thin residual layer from the sapphire substrate, even if the laser beam with the essentially increased laser fluence was applied. To explain these results, the dependence of laser ablation threshold on the layer thickness for sufficiently thin layers (thinner than the laser wavelength) should be considered. The calculated ablation thresholds versus the layer thickness are presented in figure 1. Laser heating source term in the heat equation for the layer was taken in its exact form without averaging over the electromagnetic field oscillations inside the layer, thus allowing to take into account the interference between the incident beam and the beam reflected from the layer/substrate interface.

From figure 1, a rather deep minimum of ablation threshold takes place for the layer thickness in 100 nm – 3 μm range. For a layer thickness >3 μm, the ablation threshold does not depend on the layer thickness. To find the explanation, the thermal diffusion length during the laser pulse inside the graphite layer was compared with the layer thickness. The thermal diffusion length can be estimated as $l_{TD} \approx 3$ μm. For >3 μm layer thickness, the layer may be considered as a bulk medium on a time scale of a single laser pulse. Thus, for this thickness, the ablation threshold should reach the bulk value and be independent on the layer thickness. If the layer thickness is < 3 μm, the thermal flow is interrupted (at least partially) on the layer/substrate interface, due to a lower thermal conductivity of the sapphire substrate. The heat flow interruption on the layer/substrate interface will increase the layer temperature and, as a result, will decrease the ablation threshold with decreasing the layer thickness until the layer thickness is higher than the laser absorption length (0.2 μm in our case).

With further layer thickness decrease, the laser energy absorption inside the layer will decrease and, as a result, will increase the ablation threshold. The insignificant oscillations of the ablation threshold with varying the layer thickness are attributed to the interference between the incident laser wave and the wave reflected from the layer/substrate interface.

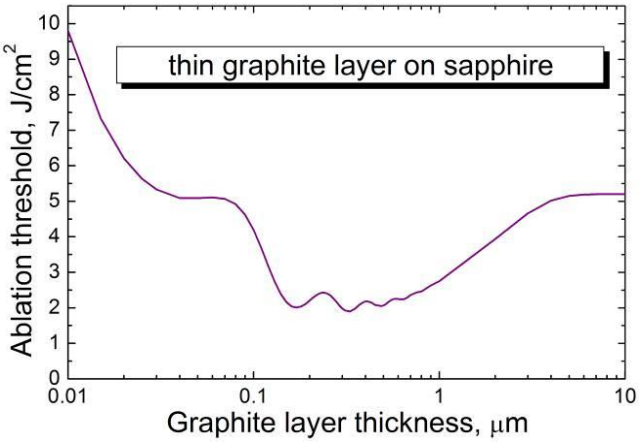

Figure 1: Calculated ablation threshold dependence on the thickness of the graphite layer deposited on the sapphire substrate

Laser heating of metal mirror with a deposited graphite layer

The simulation of laser heating and laser ablation thresholds of carbon layer deposited on the first mirror (molybdenum or molybdenum coated by several micrometers of rhodium) by high repetition rate laser pulses were made. The theoretical temperature profiles for pure molybdenum and rhodium surfaces were obtained (figure 2).

The laser heating temperatures are almost identical, except for the temperature scale. The heat effect of pulse-to-pulse accumulation is low. For the molybdenum surface, the heating temperature is higher, mostly due to its lower reflection coefficient. Under the applied laser conditions, the melting threshold $F_{th}^{(melting)}$ for molybdenum and rhodium are deduced as ≈5 J/cm^2 and 9 J/cm^2, respectively.

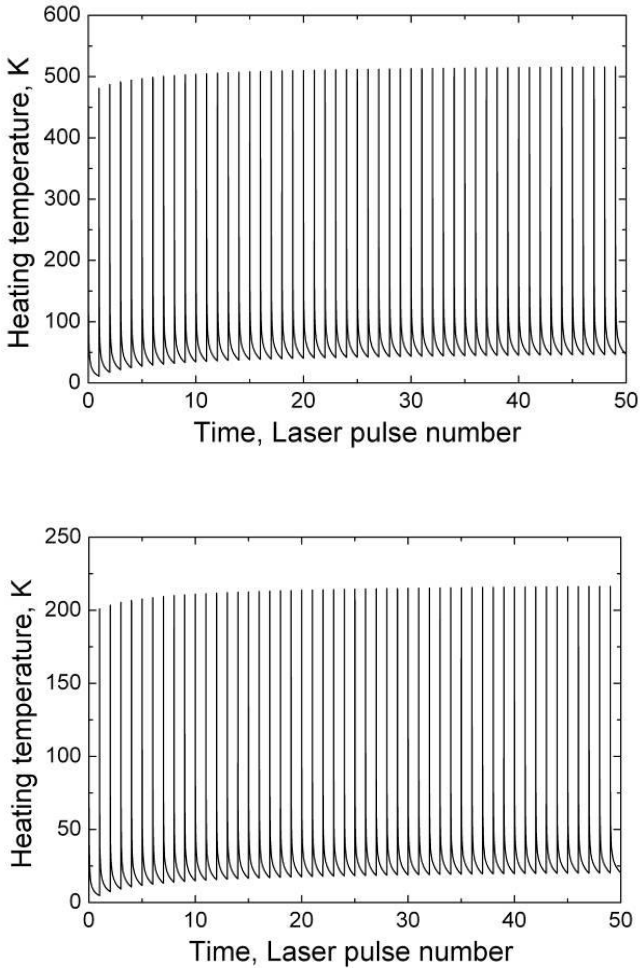

Figure 2: Laser heating profile of the pure molybdenum surface (high panel) and pure rhodium (low panel) F = 1 J/cm^2. 50 laser pulses

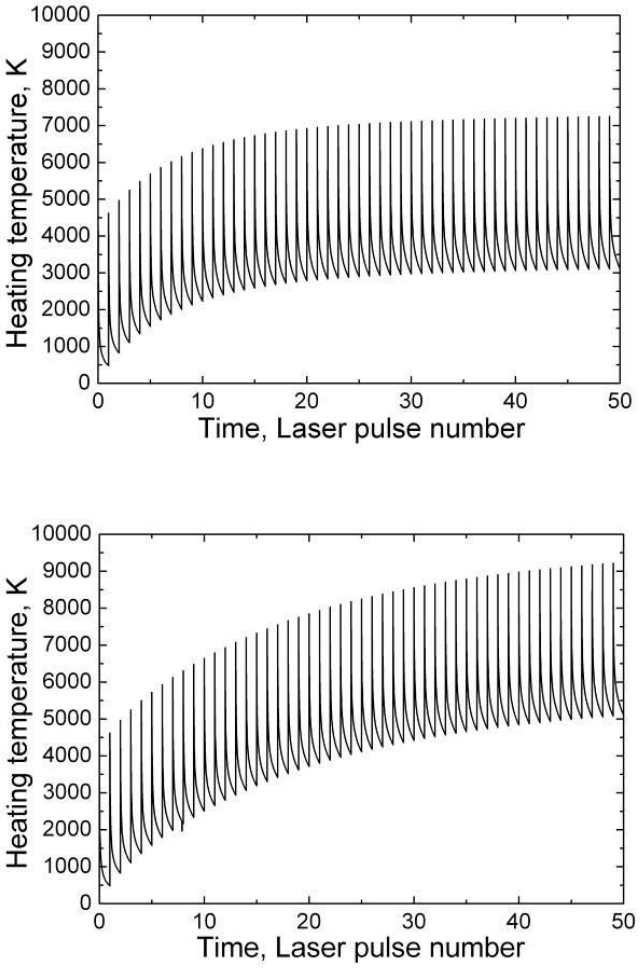

Figure 3: Theoretical heating temperatures for carbon layer (10 μm thickness) deposited on metal surface (molybdenum or rhodium) High panel - perfect heat contact, low panel - intermediate heat contact with h = 60 kW/ (m^2 K). F = 1 J/cm^2. 50 laser pulses

The calculated temperatures for the metal mirror with a deposited carbon layer (10 μm thickness) are presented in figure 3 – figure 6. The properties of the deposited layer were taken as for the TEXTOR deposited carbon layer.

The high and low panels of figure 3 present the results for a perfect and intermediate heat contact of the deposited layer with the metal. When the heating temperature of the layer exceeds the graphite sublimation temperature T_{subl} = 4200 K, the layer ablation should take place. The laser ablation threshold can be easily estimated. For the 50th laser pulse and perfect layer/substrate heat contact, F_{th} = 0.54 J/cm^2. For intermediate heat contact with h = 60 kW/(m^2 K), F_{th} = 0.42 J/cm^2.

Thus, to clean the deposited carbon layer away from the metal Mo-mirror, the laser fluence should be in 0.5 J/cm^2 - 5 J/cm^2 range. In this case, the metal substrate temperature will not exceed the corresponding fusion temperature.

The laser ablation threshold depends on the layer thickness for sufficiently thin layers (figure 4). The ablation thresholds are different for different heat contacts. For sufficiently thin carbon layers (about a few tens of nanometers), the ablation threshold increases with the decrease in the layer thickness. It may be almost the same as the melting threshold for a metal substrate, especially for the perfect layer/metal substrate heat contact (see figure 4e). Thus, it will be difficult to remove completely the carbon deposited layer from the metal mirror surface, including the residual nanometric layer of a good heat contact with the metal substrate. However, this problem is not very important if the layer/substrate heat contact is not perfect. In this case, laser cleaning can provide a complete removal of the carbon layer from the metal mirror surface without the mirror damage.

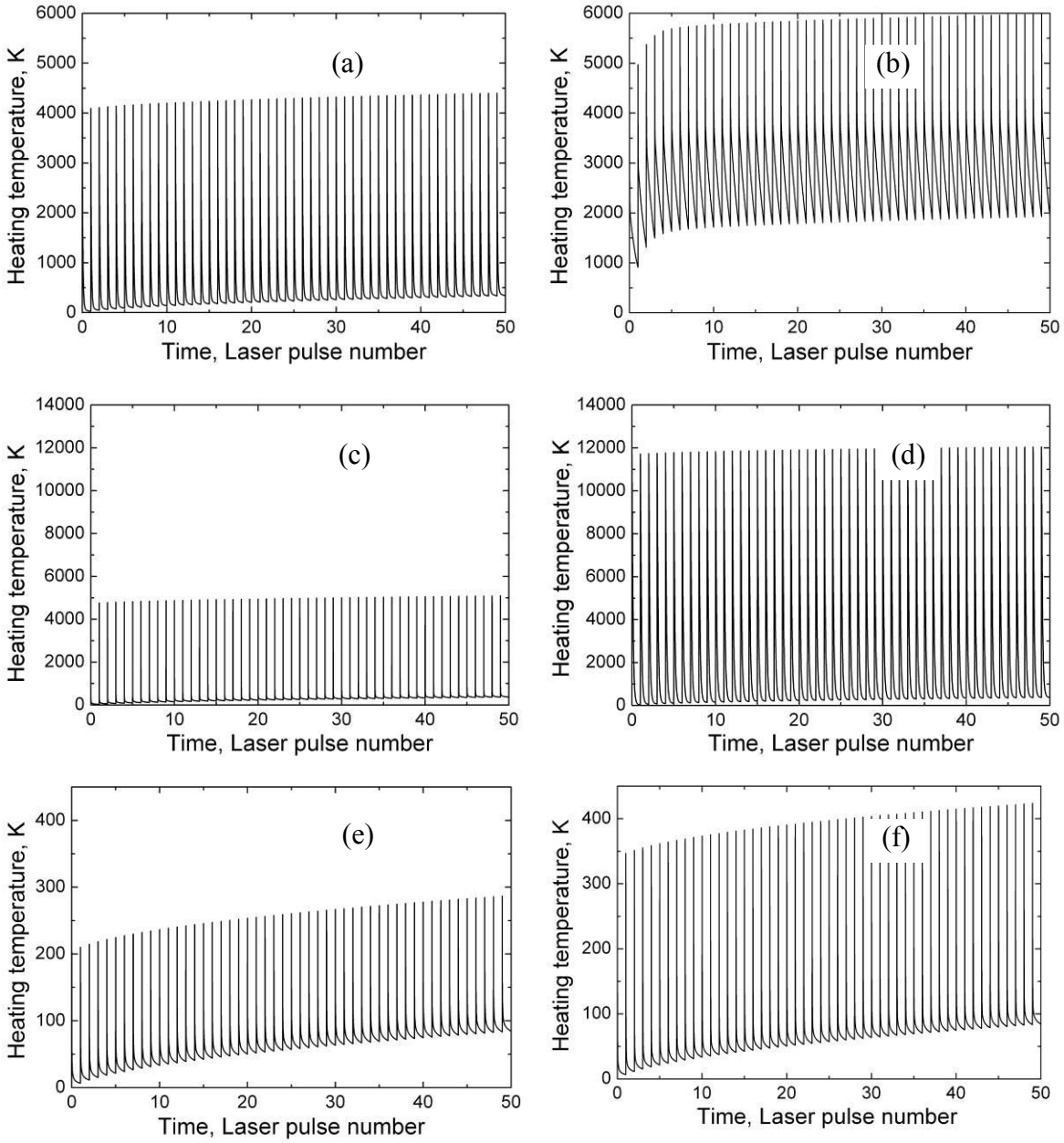

Figure 4: Theoretical heating temperatures for carbon layer deposited on the metal surface (rhodium). Layer thickness – 1 μm (a, b), 100 nm (c, d) and 10 nm (e, f), Left panels (a, c, e) - perfect heat contact, right panels (b, d, f) - intermediate heat contact with h = 60 kW/ (m^2 K). Laser fluence F=1 J/cm^2, 50 laser pulses

CONCLUSIONS

Laser heating model developed for complex graphite surfaces heated by high repetition rate nanosecond laser pulses was extended and applied to the modeling of laser heating of different surfaces (with and without deposited layers) representative for tokamak installations. The simulations were made for nanosecond laser heating and ablation threshold determination for carbon layer deposited on sapphire window and for metal mirror surfaces with carbon deposited layer. The ablation threshold dependence on a thin graphite layer thickness of the sapphire substrate was considered. The restrictions on the laser fluence for the cleaning of metal mirrors from the deposited carbon layer without damaging the metal mirror due to its surface melting were determined.

REFERENCES

[1] A. Semerok, S.V. Fomichev, F. Brygo, P.-Y. Thro, Laser heating of complex graphite surfaces by high repetition rate nanosecond pulses (comparative modelling and experimental studies), CEA report, NT DPC/SCP/06–170–A, 2006

[2] A. Semerok, S.V. Fomichev, J.-M. Weulersse, F. Brygo, P.-Y. Thro, C. Grisolia, Heating and ablation of tokamak graphite by pulsed nanosecond Nd-YAG lasers, J. Appl. Phys. 101, 084916 (2007)

REPORTS AND PUBLICATIONS

[3] A. Semerok, S.V. Fomichev, Simulation of laser cleaning of diagnostic windows and mirrors, CEA report, NT DPC/SCP/2007–249, December 2007

TASK LEADER

Alexandre SEMEROK

DEN/DPC/SCP/LILM
CEA-Saclay
F-91191 Gif-sur-Yvette Cedex

Tel: 33 1 69 08 65 57
Fax: 33 1 69 08 78 84

e-mail: alexandre.semerok@cea.fr

CEFDA06-1376

Task Title: TW5-TPR-RPSUP: SUPPORT TO EFDA REMOTE PARTICIPATION

INTRODUCTION

The EFDA Technology Remote Participation activity provides co-ordination of developments in the infrastructure for remote participation within the Fusion Associations and EFDA.

The task covers Remote Participation technical activities for:

- Exploitation of the JET facilities under EFDA based on JET RP Users' Group recommendations,
- Inter-Association collaborations, in particular the EU Taskforces ITM (Integrated Tokamak Modelling) and PWI (Plasma Wall Interaction),
- Support and Technical Development through EFDA RP technical contact persons,
- Collaborations among Associations, including other organizations involved in fusion research,
- EU Activities within the ITER Framework.

The activity is organized in five broad technical topics:

- Teleconferencing and Telecommunication,
- Remote Experiment Participation,
- Networking and Security Issues,
- Remote facilities including Remote Data and Remote Computer Access,
- Documentation and User Facilities.

2007-2008 ACTIVITIES

All along the task we used the wiki site that we launched in 2006, to put all the information and help the RPTC of the different associations to work together. This useful tool was presented in a poster at the 6th IAEA Technical meeting in Inuyama (Japan).

The activities were focused on Remote Experimentation Participation (REP).
A possible definition of "REP" could be: "all the technical means necessary to allow a remote scientist or engineer to participate, more or less, in an experimental fusion session from his own laboratory, regardless of the distance".
REP must try to give conceptual and technical answers to two big challenges:

- The first, which may be the easier, is to abolish the distance, offering the possibility to operate an experiment regardless of where you are, providing the place is suitably equipped,
- The second one that is more tricky because it embraces a lot of parameters, not only technical but also human, is to manage all the interaction between the actors when they are not in the same place.

To reach these ambitious objectives REP must gather and use together all the tools and techniques usually associated with the different domains of remote participation.
The objective of the works realized during these two years was to study the status of Remote Experimentation (REP) and possibly improve it.

As decided during the kick-off workshop in Riga (Latvia) in 2006 we organized a survey at the beginning of 2007, which was sent to 41 laboratories and which contained a questionnaire on the different topics, including the REP. We got 32 answers.

Concerning the 12 laboratories which operated an experiment 8 proposed more or less services for remote experimentation. These services are mainly remote computer access and remote data access which are the easier services to implement and the most useful at the moment. Only the very small tokamaks like ISTTOK can propose real remote experimentation, with a full control on the tokamak.

Facility/Laboratory	Remote experiment access
ASDEX-Upgrade (IPP Garching, Germany)	Yes
EXTRAP-T2R (VR-KTH, Sweden)	No
FTU (ENEA-Frascati, Italy)	No
ISTTOK (IST)	Yes
JET (EU)	Yes
MAST (UKAEA, UK)	Yes
PSI (FOM, Netherland)	No
RFX (CNR, Italy)	Not yet
TEXTOR (IPP FZ Juelich, Germany)	Yes
TCV, TORPEX (CRPP, Switzerland)	Yes
Tore Supra (CEA, France)	Yes
TJ-II (CIEMAT , Spain)	Yes

Among 41 associations involved in fusion research only 13 of them used services proposed by one or several other laboratories, not always in Europe.

This is rather few. The main reasons are:
- The lack of documentation and promotion on what is proposed,

- The non-standardization of the access method and other features proposed,
- The lack of human motivation (linked to the two above).

So we decided to write a report which could particularly help laboratories which would like to develop REP to their experiment but also those which would like to use services offered to access remotely to an experiment. It derives from the information provided by the associations; on continuous work with Technical Contact Persons ("TCP"), on existing documentation, on the result of the survey carried out on January 2007 and finally on interviews held with people involved in the topic, as providers or users.

This report gives information on the following topics:

- Network,
- Men to computer access,
- Computer to computer access,
- Authentication and authorization,
- Men to men communication,
- Men to remote environment.

We participated with a poster to the 25th Symposium on Fusion Technology (SOFT), [4]. The subject was "Overview of REP" and we had very interesting discussions around it with our colleagues.

Additionally we continued to attend the regular videoconference organised by our German and Hungarian colleagues every two months, so-called VC-TIER (Topic of Interest to EFDA Remote Participation).

REPORTS AND PUBLICATIONS

[1] Support tools for EFDA RP Collaboration (6th IAEA TM June 2007 Inuyama-Japan)

[2] Preliminary report on the progress of the use and expansion or Remote Experiment Participation facilities in Europe (RPTC_0235 - 15/02/2008)

[3] Final report on the status of Remote Experiment Participation Facilities in Europe (RPTC_0243 - 29/04/2008)

[4] Overview of the status of EFDA Remote Experimentation Participation in Fusion Experiments (25th SOFT, 15-19 September 2008, Rostock, Germany)

TASK LEADER

Stéphane BALME

DSM/IRFM/STEP/GICA
CEA-Cadarache
F-13108 Saint-Paul-Lez-Durance Cedex

Tel: 33 4 42 25 47 48
Fax: 33 4 42 25 26 61

e-mail: stephane.balme@cea.fr

CEFDA04-1202

Task Title: TW5-TVV-RFUT: SYNTHESIS OF ULTRASONIC INSPECTION OF THE VACUUM VESSEL WELDED MOCK-UPS FOR ITER: COOPERATION WITH RF

INTRODUCTION

This report concludes the cooperation work between PHOENIX, SINTEZ/ECHO and CEA on the preparation ultrasonic inspection methods for the Splice Plate welds of the proposed ITER vacuum vessel (VV).

This project officially started in September 2005. The kick-off meeting was held in Paris in February 2006. The Final meeting, for results presentation, has been held in Madrid in December 2008.

This report presents the global tasks of the project which are the following: the mock-ups manufacturing [2, 3], the ultrasonic inspection techniques developed for the weld inspection [4 to 7], the round robin trial results [8] and the conclusion drawn.

2007-2008 ACTIVITIES

The main activities during this period were the following:

- The manufacturing of four mock-ups designed by partners involved in the project,
- The round robin trials of the mock-ups manufactured,
- The final meeting for results comparison and discussion of the results obtained by the three involved teams.

MOCK-UPS MANUFACTURING

For this project 4 mock-ups were designed. The geometry of these mock-ups was chosen to take into account some of the realistic configurations of the ITER vacuum vessel inspection welded plates.

Figure 1 presents the schema of the four manufactured mock-ups. In particular, mock-up A is welded planar plates, mock-up B is welded with an angle of 10° between plates, mock-up C is a planar partial welded plates, and mock-up D simulates poloidal rib welded plates. These mock-ups were manufactured with SS316L(N) ITER Grade steel and the coupons were welded using TIG narrow gap process.

The technical specification of the mock-ups is presented in reference [3].

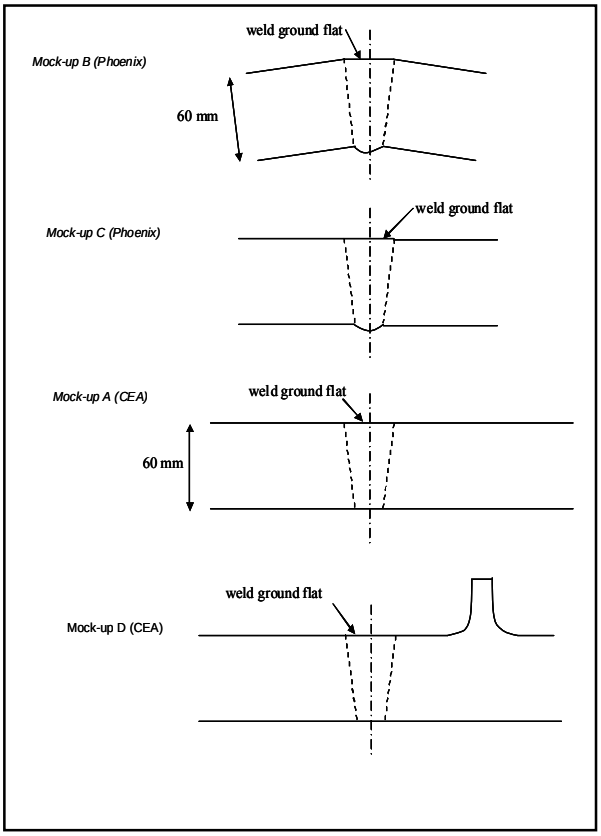

Figure 1: Mock-ups cross section geometry

CALIBRATED DEFECTS INCLUDED

A set of the intentional flaws artificially included in the four mock-ups covers large spectra of defects which could occur during the realistic weld manufacturing process. The specifications for the design of flaws were the following:

- To detect defects immediately after production of weld joint,
- o test the inspections UT systems near the limits of the detection capabilities,
- To compare abilities of systems to detect different types of flaws (lack of fusion in the line of chamfer, centreline cracks, root defects, and incomplete groove weld crow area).

The location of the flaws was distributed across the weld and in the heat affected zone (HAZ). In particular, at root area of the weld were included several flaws since this zone is considered a more critical welded area.

Thus inner breaking defects, embedded flaws and outer breaking defect at surface were included. To carry out these

defects, different fabrication methods were applied, thermal fatigue cracks, solidification cracks and electro-discharge cracks. The sizes of flaws vary between 1x25 mm² and 10x20 mm² located across the HAZ area.

The flaws were designed by PHOENIX and CEA and they were manufactured by TRUEFLAW using proprietary techniques.

CALIBRATION MOCK-UPS

For the inspection of these mock-ups, two calibrations specimens were manufactured. Figure 2 presents the mock-up used by CEA and Sintez and figure 3 the one used by PHOENIX. The matter that constitute both calibration mock-ups is SS316L(N) ITER grade steel.

The mock-up used by the CEA and ECHO contains the following flaws (figure 2):

- Nine drilled holes produced by EDM of 90 cm and Φ= 2 mm. The first hole is at 10 mm from the surface at 130 mm from the side plane.
- Two notches produce by EDM (≈0.2mm opening) of 3 mm and 10 mm high and 20 mm long placed at 120 mm and 200 mm from the opposite side plane and placed in the middle of the block.

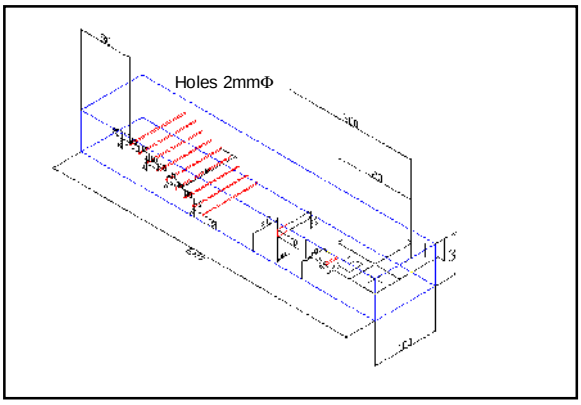

Figure 2: Calibration mock-up

Taking into account the techniques used by PHOENIX (see further), the calibration mock-up is different from the last one described. Figure 3 shows the sketch of this calibration block, in which they are five holes 2mmØ and three notches. The depth of notches included inside is 1.5mm.

Both mock-ups were manufactured by TRUEFLAW cutting a primary piece used for the entire group of mock-ups. The supplier references that the measured uncertainty of flaws is ± 0.2mm.

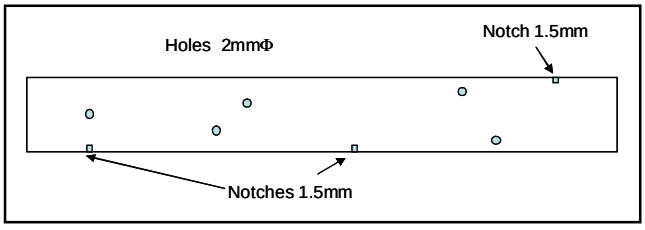

Figure 3: Calibration mock-up for PHOENIX

TECHNIQUES USED FOR INSPECTION

PHOENIX developed a dedicated system for this inspection. The device manufactured is a probe pan in which was installed 14 different transducers types for conventional US techniques, creeping waves, tandem, TOFD (time of flight) and Phased array technique. Thus, PHOENIX implemented these different techniques to intent to detect flaws located in the whole volume of inspection. PHOENIX started testing the different techniques to determine the effectiveness of each one and to find the optimal conditions for the detection. In particular, PHOENIX performed creeping wave technique for the inspection of the border of specimen (surface at root area) and the conventional techniques to inspect the middle thickness of the specimen.

ECHO used the following techniques to cover the volume of inspection : For the area between 45mm and 60mm, ECHO used conventional two-modes (L and S waves) pulse-echo testing with an incidence angle of 41° in austenitic steel the operating frequency was 2.5 MHz with offline two-mode processing. For the area between 0 and 45 mm, ECHO performed two-mode pulse-echo testing with incidence angle in austenitic steel of 56º, the operating frequency was 2.5 MHz with offline data processing. ECHO used also headwave pitch-and-catch testing, the operating frequency was 1.8MHz. ECHO stated a wide directivity pattern allows the inspection of the entire volume of the welded plates.

The CEA used dual probes phased array technique to cover the entire zone of inspection. The frequency of probes used is 2 MHz. For the inspection of the zone near the surface up to 25 mm, the probe wedge generates 60° longitudinal waves focused at 12mm in-depth. Delay laws were calculated to generate longitudinal waves in the axis of the weld. For the inspection of the area between 20mm and 60mm the probe wedge generates L45° longitudinal waves focused at 60 mm in-depth. The delay laws are calculated to generate longitudinal waves between 25° and 60°, focusing at constant radius.

ROUND-ROBIN TRIALS

In order to maximise the benefits, it would have been suitable to perform a complete blind exercise in terms of inspection of flaws. Nevertheless, in the present configuration, it was a partial blind exercise because two mock-ups were designed by PHOENIX and two designed by the CEA. Further, for equity between partners, the specifications of two from four mock-ups were notified to SINTEZ. So, each team knew the intended contents of two of the specimens ("open" mock-ups), but not of the other two ("blind" mock-ups). For each team, the open and blind pairs of mock-ups were different.

In exercises to determine the reliability of an inspection technique, it is customary to reduce the results to a simplified statistical analysis. In such analysis of detection reliability the results are analysed in terms of the numbers of:

- True positives - the indications corresponding to real target flaws (defects detected"),
- False positives - the indications that do not correspond to real target flaws ("false calls"),
- False negatives – the real target flaws without a corresponding indication ("missed defects").

For the present project, such analysis only has very limited value because each team applied his proprietary technique optimising different aspect of the inspection regarding the indications corresponding to the open mock-ups. However, the mock-ups that were open and blind for each team were different:

- The different mock-ups were designed to test different aspects of the possible inspection geometry. For example, mock-up B is intended to represent the possible angular deviation between the two plates, whereas mock-up D allows the influence of a rib near the root-side of the weld to be investigated,
- Two of the mock-ups (B and C) contain a larger population of both intended and unintended defects than mock-ups A and D. This makes it harder to analyse the ultrasonic responses. It is obviously easier if these "difficult" mock-ups are the open specimens.

Since the division of the four specimens into pairs of open and blind specimens was different for each team, each team was faced with a different task.

RESULTS AND DISCUSSION

Synthesis of manufactured flaws detection

The supplier TRUEFLAW manufactured 49 flaws into the four mock-ups. From that set, PHOENIX detected 45/49 flaws, ECHO 43/49 flaws and the CEA 41/49 flaws.

PHOENIX team used conventional techniques, creeping waves, TOFD, tandem and linear phased array techniques to cover the entire volume of inspection. They conclude that linear phased array technique shows enhanced capability to detect flaws in the middle of the volume compared with conventional techniques.

From the different techniques used by PHOENIX creeping waves demonstrate good performances on detecting flaws located at the border of specimen inspected (surface of inspection and root area). The signal to noise ratio is improved in comparison with conventional techniques.

CEA applied dual probe phased array technique showing the ability to detect the majority of flaws to be detected in the entire volume of detection. The probes and the procedure were designed to detect and characterize planar flaws higher than 3 mm. Consequently, limits of the procedure appear for the smallest defects included in specimens, especially near the weld root.

ECHO shows they are able to detect the majority of flaws in the volume inspected using *conventional techniques*. ECHO uses the proprietary algorithms of data treatment to decide if indications can be associated with the flaws to be detected.

Detection of additional indications

The four mock-ups inspected appear to contain defects that were not intended to be present, which are considered "unintentional manufactured". These flaws could be related to the manufacturing process. The manufacturers of the mock-ups used proprietary processes for inserting defects such as thermal fatigue cracks and solidification cracks. It is possible, that the techniques used to insert these flaws have an effect on the local weld structure, so that ultrasonic responses come from the defect created and from regions of metal around the defect.

It has been proposed that the mock-ups be subject to destructive examination, in order to verify whether the locations and dimensions of intended defects are as designed, as well as to investigate the unintended indications. Given the large cost of producing the mock-ups, this course of action is probably inadvisable at this stage of the project.

Synthesis of sizing flaws

In order to characterise flaws, the three partners used the same methods.

For height sizing, the tip diffraction method was used. Nevertheless, if only a single indication is detected, PHOENIX and the CEA judge that the flaws can not be height sized. In that case, ECHO applied a data processing treatment to measure the height of the defect sizing.

For length sizing, the measure is performed using the 6dB drop method from the local maximum.

In order to decide the characteristic of the flaws, the three teams use the image reconstruction of the ultrasonic scan. If the tip diffraction signals are detected, the shape of planar flaws could be recognized. Otherwise, some flaws could reflect from a favourably oriented facet that causes "several signals" detected, in this case, it was characterised as multi-faceted flaws.

In general terms, for the three partners, the majority of flaws are sized in length; nevertheless, the length of the small flaws are over estimated since the size of the beam is measured rather than the length of the flaw. Regarding sizing in height, the performances are different.

In particular, ECHO sized both height and length for 98% of flaws detected. ECHO seems able to measure flaws of about 1.5mm height. Indeed, a specific data processing was used to obtain this performance of results.

PHOENIX and CEA sized in height 65% of the flaws detected. PHOENIX and CEA measure in height only if the

both edges echoes are identified correctly. The accuracy of the resulting height measurement is within 2mm. The flaws sized are those for which height is more than 3mm.

For flaws higher than 3mm and which are not sized, the signal-to-noise ratio is too low to identify tip diffraction for sizing.

Concerning the shape of the flaws, the majority of flaws were characterised as planar even if some of them are volumetric manufactured flaws.

CONCLUSIONS

Inspection results of mock-ups according to three different inspection methods and procedure provide a wide range of interesting results to establish a complete procedure able to fulfill the specification provided by ITER for an inspection during manufacturing. The main conclusions can be drawn:

- The key point is the detection of flaws included in the root area. The signals from the root area are detected in the limit of the amplitude threshold. In fact, a consequence of the high level of noise in the root area is the difficulty to detect small inner breaking flaws; thus a combination of phased array and creeping wave methods can be very useful to optimise the detection in this area,
- For detection of outer defects breaking the surface at the weld cap, creeping waves enhanced the detection performances,
- Solidification cracks and EDM notch are both detected and sized with similar performances. The difficulty in sizing is related to the height of flaws. The resolution of techniques used by PHOENIX and CEA allows sizing flaws higher than 3mm,
- Signal processing algorithms developed by ECHO for conventional techniques could enhance the performances of inspection,
- The quality of the inspection surface plays an important role in the detection since the sensitivity is degraded if the coupling between the sensor and the inspection surface is not constant. Indeed, for mock-up B welded with 10° tilted, increased variability was observed in the amplitude of signals.

REPORTS AND PUBLICATIONS

[1] TW5-TVV-RFUT, CEFDA04-1202 “Comparative assessment of ultrasonic inspection systems for the narrow gap austenitic welds in the ITER vacuum vessel”

[2] Progress report RFUT N°1; technical specifications for RFUT tasks. S§YSSC/06 RT0231/Rev.0 October 2006

[3] Flaws technical specification -CEA/DETECS/ SYSSC/05-385

[4] Automatic ultrasonic system AUGUR –SINTEZ/ECHO Report. 2007

[5] Development of ultrasonic non destructive testing method for the vessel inter-sector weld of ITER: development of dynamic phased array techniques», SISC/03-RT0096/Rev. 0, September 2003

[6] Development of phased array techniques for the inspection of one sided welds in ITER vacuum vessel», SYSSC/04-RT0143/Rev. 0 September 2004

[7] Simulation of phased array technique for qualification of UT methods for one sided welds during VV manufacture - SYSSC/05 RT0167/Rév. 0 October 2005

[8] Inspection of VV welded mock-ups in the frame of RFUT project , final report– SYSSC/07 RT0277/ 2008

TASK LEADER

Jorge TIRIRA

DRT/DETECS/SYSSC/LMC
CEA-Saclay
F-91191 Gif-sur-Yvette Cedex

Tel: 33 1 69 08 40 02
Fax: 33 1 69 08 75 97

e-mail: jorge.tirira@cea.fr

CEFDA06-1477

Task Title: TW6-TVM-LIP4: MODIFICATION OF ITER MATERIALS DOCUMENTS, ASSESSMENT OF MATERIAL DATA AND MAINTENANCE OF A DATABASE

INTRODUCTION

In December 1993, the ITER Joint Central Team (JCT) authorized creation of a Material Properties Handbook (MPH) through a cooperative activity amongst the ITER Parties (Japan, European Union, Russian Federation and US). The goal of this document was to provide the ITER designers with a single reference source of materials data. The last version of the ITER MPH-IV (IDoMS G 74 MA 16 04-02-04 W0.1) was issued as a part of the ITER Final Design Report in 2004. In addition to MPH, ITER JCT authorized creation of an ITER Interim Structural Design Criteria with its associated code qualified materials data in the form of Appendix A. The last major package of this document was issued in 2001.
Since then, MPH and Appendix A documents have been updated with new data generated by ITER partners. With the approach of the construction phase, a greater emphasis has been placed on traceability of materials data and databases, as well as, the increased harmonization between MPH and Appendix A reports in order to satisfy ITER licensing needs.
The current work started with the establishment of files for different nuances of Type 316L(N) steel base metal, including its ITER Grade version (316L(N)-IG)[1] used for fabrication of ITER vacuum vessel. That work is now extended to the weld metals. A first report was issued for weld metal Types 316L and 19-12-2 [1]. This paper presents results for the Type 16-8-2.

2007-2008 ACTIVITIES

MATERIALS

Section IV – Welding, of the RCC-MR and its Appendices [2] provide guidelines for selection and utilization of filler metals for welding of austenitic stainless steels, including the Z2 CND 17-12 grade with controlled nitrogen addition, the steel equivalent to the ITER 316L(N). They include the low carbon grade: 316L for applications at temperatures not exceeding 375°C, and the high temperature grades 19-12-2 and 16-8-2.

Detailed compositions of the above 3 filler metals are given in [1, 2][2]. Although, the nominal operating conditions of ITER, low temperature and low neutron doses, do not necessarily require use of high temperature filler metals, other considerations such as exposures to various fabrication cycles (such as HIPing), application in Blanket.

Test Modules, or future evolution of ITER, require a more comprehensive MPH documentation.

CODES AND MPH PROCEDURES

ITER MPH recommends use of the code data for ITER Structural Design Criteria whenever possible. In fact, in each materials properties handbook file, a clear distinction is made between the available code recommendations and the additional recommendations made as a result of the present work.

RCC-MR [2], ASME [3] and ISDC [4] organize welds into different "Weld Categories" (e.g. A, B, C, D, and E)[3] based on their intended use. The joints are organized in ISDC into different "Weld Types" (I, II, III, IV, V, VI, VII)[4] based on the welding configuration.
The procedure for calculating the tensile strength or the fatigue life of different weld types is based on "knock-down" factors applied to the base material values. These knock-down factors, in addition to material properties differences, also incorporate effects of discontinuities at the joint and factors such as qualification of the welding process and the possibility of weld inspection during and after fabrication.

The number and the type of property sheets used in MPH files vary according to the type of material examined and its intended application. In general, they cover specifications for products, compositions, physical and mechanical properties.

In each property file, the code recommendations are presented first. Then the available materials properties data are collected for different types of welds and analysed, including for the effects of short and long time exposures to high temperatures and the effects of neutron irradiation, see e.g. [5-15]. Finally the results obtained are compared with the code recommendations to see if the safety margins are maintained under ITER service conditions.

RESULTS

For full report the reader is referred to the ITER MPH, here, only a few examples of the analyses performed are presented.

[1] IG stands for Iter Grade, where the specifications for high activation residual elements are more stringent.

[2] 316L (wire for TIG)= 18-20% Cr, 12-14% Ni, 2-3% Mo, 1-2.5% Mn and 0.030% C
19-12-2 (Coated electrode for MA)= 18-19% Cr, 11-12% Ni, 1.9-2.0% Mo, 1.2-1.8% Mn, 0.4-0.7% Si, 0.045-0.055% C
16-8-2 (wire for TIG)= 16-17% Cr, 8-9% Ni, 1.8-2.2% Mo, 1.8-2.5% Mn, 0.030-0.045% C

[3] A= Longitudinal welds in pressure vessel, …,
B= Girth joints in a cylindrical vessel, …,
C= Joints connecting flanges, tube-sheets or flat head to main shell, ….

[4] I= Butt welding, full penetration, two sides accessible, II= idem but backside not accessible, III= Fillet or T weld, …

Tensile Properties

The original data used for establishment of RCC-MR recommendations have been sorted out and analysed according to the filler metal composition, type and position of welds, orientation of specimens, etc. As a result, they show little scatter (reference curves).

When the recent and previous data are plotted, independent of the above considerations, they show a larger scatter but still bound by the minimum curve proposed previously, figure 1.

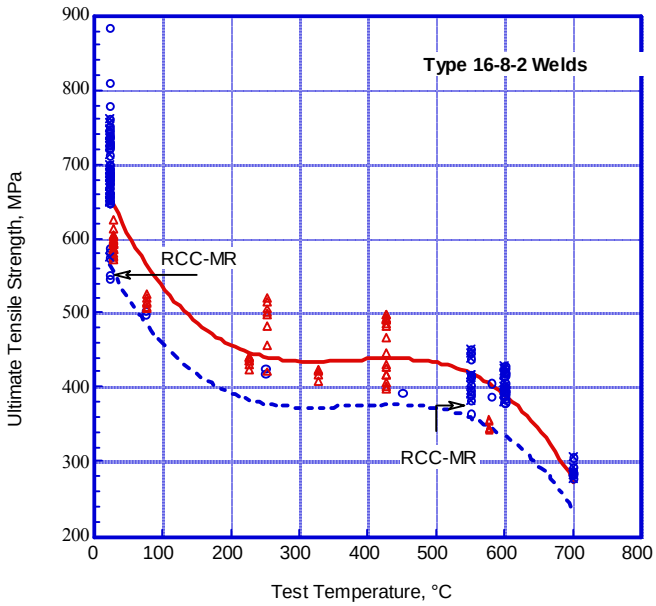

Figure 1: Average and minimum UTS versus temperature for 16-8-2 weld metal independent of welding type and specimen position

It is only when the data from other sources, using different compositions and treatments, are added that the recommended min curve may not apply [8]. However, even in such cases, once the material is irradiated, even to very low doses, it shows significant hardening and properties exceed the minimum values, figure 2.

In addition, S_m of welded joints, from the materials point of view, is governed by the base metal properties and as shown in figure 3, weld metal minimum yield and tensile strengths are significantly higher. Here the materials property coefficient J_m is taken equal to 1. ISDC also recommends the joint efficiency coefficient (n) that includes materials property coefficient, type of weld (I.1, I.2 and I.3) and inspection to be taken as 1, except when inspection is not full, e.g. surface examination after welding is done only on one side (n=0.85).

Creep Properties

RCC-MR recommends knock-down factors J_r and J_t to be applied to base metal stress rupture (S_r) and time dependent stress intensity (S_t). Their exact value depends on the temperature and time of creep. In a table constituted for temperatures from 450 to 675°C and creep rupture times up to 300000 h, they vary from 0.75 to 1, although for most practical applications they are not below 0.8.

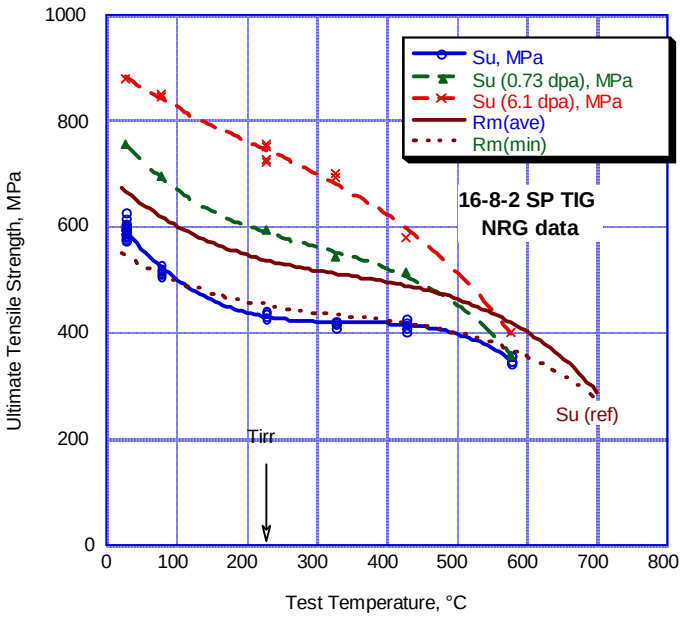

Figure 2: Comparison of ultimate tensile strengths of Type 16-8-2 SP TIG deposit welds [8], before and after irradiation (at 227 °C), with the reference average and minimum ultimate tensile strength (Su or Rm) curves derived for 16-8-2. Notice that filler metals used in [8] are for TIG welding and have a lower carbon content than the reference metal

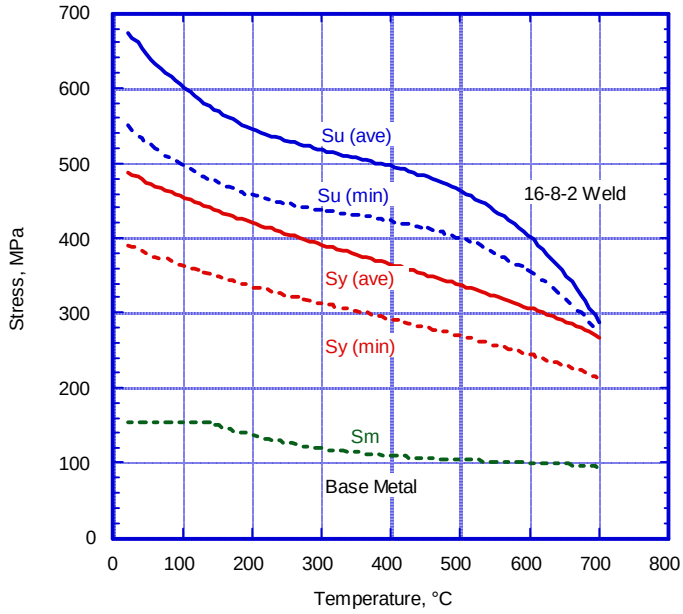

Figure 3: Comparison of S_m derived for 316L(N) base metal with reference curves for average and minimum ultimate (Su) and yield (Sy) strengths of 16-8-2 weld metal

As shown in figure 4, at 550 °C, weld metal creep resistance is lower than the base metal but above the minimum RCC-MR specified values. The figure also shows results for Type 17-8-2 filler metal used in UK. Data on this metal was often combined with those of the 16-8-2 in the early analyses.

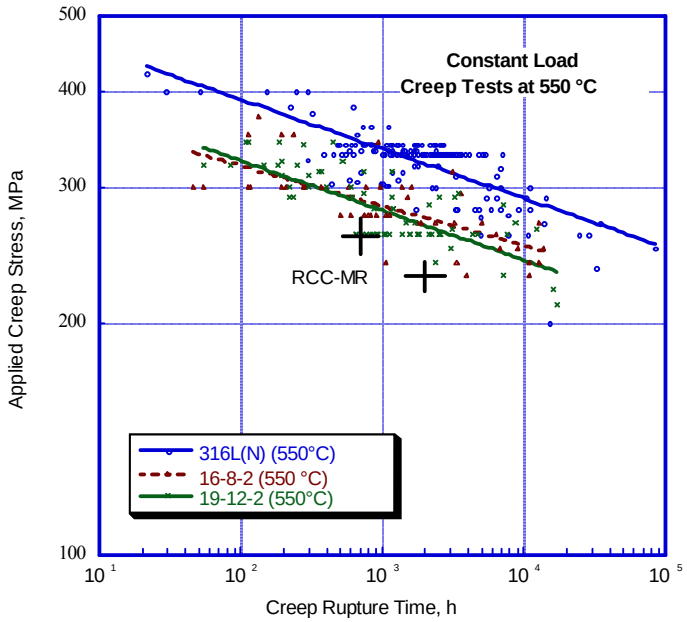

Figure 4: Comparison of Creep rupture strengths of 316L (N) base and weld metals

Reduction factors calculated from figure 4 are in agreement with J_r values recommended during ISDC work, table 1. At 10000 h the calculated coefficient is slightly less than that recommended value.

Table 1: Calculated ratios of weld rupture strength over base metal rupture strength at 550°C compared with J_r coefficients recommended during ISDC work

Time, h	S_r min (base)	S_r (Weld)	Calculated Knock down factor	ISDC Work J_r
10	370	324	0.88	0.84
100	301	271	0.90	0.88
1000	253	224	0.89	0.90
10000	207	182	0.88	0.93

This is probably due to inclusion of additional data in the present work and in any case RCC-MR and ISDC recommendations are regularly verified and if needed updated.

Fatigue Properties

Recommended fatigue strength reduction factor (J_f) in ISDC varies according to the possibility of examinations, surface finishing and type of the welded joint. It is usually 1 but can increase to 1.25 for the types of welds considered in this work.

As shown in figure 5, fatigue properties of Type 316L(N) base and weld metals, as measured through strain-controlled tests, are very close with J_f =1 for results shown.

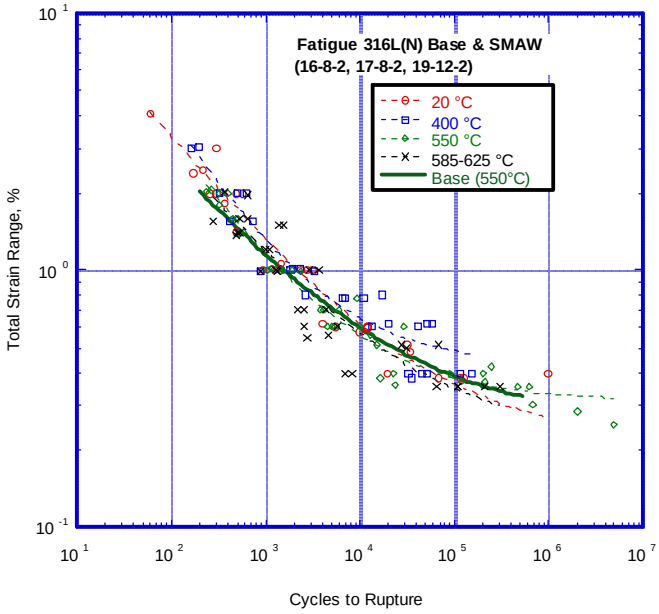

Figure 5: Comparison of fatigue behaviour of 316L(N) base metal at 550 °C with those of its welds (wires 16-8-2, its UK equivalent 17-8-2, and 19-12-2) at temperatures 20 °C through 625 °C (all tests are strain controlled tests)

Fracture toughness

Currently, there is no clear recommendation on the fracture toughness of stainless steel base or weld metals. This is due to the fact that austenitic stainless steels, including their welds, are ductile and exhibit very high toughness. Nevertheless, after irradiation at low temperatures, the toughness of these steels is significantly degraded. In ISDC [4] a tentative proposal has been made for toughness of irradiated weld metal, (table 2) that constitutes the lower bound for the joint. The estimated J_{1C} values for base metal under conditions shown in table 2 are above 250 kJ/m^2.

CONCLUSIONS

Additional analyses performed here confirm ISDC recommendations for treatment of Type 316L(N)-IG weld metals, provided filler metal compositions and welding procedures follow the recommendations made in RCC-MR.

These recommendations are tentatively extended to ITER vacuum vessel where irradiation doses are very low.

Table 2: Estimated variations of minimum fracture toughness with fluence for Type 316L(N) weld metal (ISDC: tentative)

	Un-Irradiated		3 dpa		5 dpa		10 dpa	
	J_{IC} (kJ/m^2)	K_{IC} (MPa-√m)	J_{IC} (kJ/m^2)	K_{IC} (MPa-√m)	J_{IC} (kJ/m^2)	K_{IC} (MPa-√m)	J_{IC} (kJ/m^2)	K_{IC} (MPa-√m)
20-100 °C	300	250	300	250	(80)	(130)	(80)	(130)
250-300 °C	225	205	150	170	80	120	(80)	(120)
400-425 °C	200	190	80	120	80	120	80	120

REFERENCES

[1] A.-A.F. Tavassoli, J. Nucl. Mater. 03 (2007) 260

[2] Design and Construction Rules for Power Generating Stations, Design and Construction Rules for Mechanical Components of the FBR Nuclear Islands, RCC-MR, Section IV Welding, AFCEN, Edition 2002

[3] ASME "Boiler and Pressure Vessel Code", Code Cases, Nuclear Components N-47-24, Class 1 Components in Elevated Temperature Service, Section III Div. 1, 1986

[4] ITER Interim Structural Design Criteria (ISDC), S 74 RE 2 97-02-30 W 1.2, IRB/Welds/Revision 3

[5] A-A. F. Tavassoli, Fusion Engineering and Design 29 (1995) 371-390

[6] T. Forgeron (Fr), A. A. Tavassoli (Fr), J. Wareing (UK), D. Lehmann (Fr), C. Escaravage (Fr), B. Breitling (D), and C. Picker (UK) "Effect Of Thermal Ageing on Mechanical Properties of Type 316L(N) Base and Weld Metals", CEC Study Contract CT-92-0211-F, CEA Report 94

[7] J. L. Puzzolante, M. Scibetta, R. Chaouadi, W. Vandermeulen, "Tensile and Low Cycle Fatigue Properties of Solution annealed Type 316L SS Plate and TIG Weld Exposed to 5 dpa at Low Temperature (42°C)", BLG-821, SCK.CEN, Sept. 1999, (ITER Library Number - SS39, SS50)

[8] J. W. Rensman, J. Boskeljon, M.G.Horsten, M.I.De Vries, "Irradiation Testing of Stainless Steel Plate Material and Weldments, Tensile Properties After 0.5 and 5 dpa at 350K and 500K", report ECN-C-97-088, Oct. 97, (ITER Library Number - SS17)

[9] G. L. Tjoa, J. Boskeljon, D. S. D'Hulst, M. I. de Vries, "Results of Tensile tests on Type 304 and 316 Stainless Steel Plate and Welded joints", Report ECN-I-94-007, Feb. 1994, (ITER Library Number - SS100)

[10] H. Yamada, H. Kawamura,"Qualification of structural materials and joints", Final report on ITER Task T427 JA, Task No G 16 TT fr 97 FJ, May 2001, (ITER Library Number – SSCuJ19)

[11] W. Vandermeulen, W. Hendrix, V. Massaut, J. Van de Velde, and Ch. Raedt, "FAFUMA 1 test results", FT/MOL/90-01, WV/MJW-V, Mol, February 1990, (ITER Library Number - SS87, SS1)

[12] R. Källstrom, B. Josefsson, Y. Haag Y., "Results from Tensile Testing of 316L Plate and Weld Material", Studsvik Nuclear - Report No. Studsvik/M-93/45, April 1993, (ITER Library Number - SS7)

[13] M. G. Horsten, J. Van Hoepen, M. I. de Vries, "Tensile Tests on Plate and Electron-Beam Welded Type 316L(N) Material", ECN, Petten, NL - Report No. ECN-CX-93-112, November 1993, (ITER Library Number - SS9)

[14] A. Rowcliffe, "Irradiation testing of stainless steel and Inconel including welding and rewelding of irradiated materials", Final report on ITER task T214 US Task No G 16 TT fr 75 95-07-04 FU, March 1998, (ITER Library Number - SS29)

[15] H. Sagawa, "Irradiation testing of stainless steel and Inconel including welding and rewelding of irradiated materials", Final report on ITER task T214 JA, Task No G 16 TT fr 73 95-07-04 FJ, June 1998, (ITER Library Number - SS30)

TASK LEADER

Farhad TAVASSOLI

DEN/DMN
CEA-Saclay
F-91191 Gif-sur-Yvette Cedex

Tel. : 33 1 69 08 60 21
Fax : 33 1 69 08 80 70

e-mail : tavassoli@cea.fr

CEFDA06-1482

Task Title: TW6-TVA-IHYB2: INDUSTRIALISATION AND WELD QUALITY ISSUES OF HIGH PRODUCTIVE LASER/ARC HYBRID FOR THICK SECTION WELDING OF ITER GRADE SS MATERIAL

INTRODUCTION

In assembly procedures for ITER, welding is the key joining method to be used. To reach reasonable assembly times especially in the critical applications, the welding method should be very productive. Another point of view is the minimal distortions in order to complete the assembly smoothly and also quality of the welds, in order to avoid expensive and slow repair welding. ITER Vacuum Vessel or other components require enhanced welding technologies.

This task establishes the status of future required work for preparing manufacturing choices and welding and NDT procedures.

2007-2008 ACTIVITIES

FORMER WORK IN HYBRID JOINING AREA

ITER vacuum vessel sectors, (60 mm thick stainless steel), have to be welded on site and hence cost, welding time and distortion issues become critical. The necessity of site welding, together with the complicated geometry of the vessel, set a prerequisite for excellent position welding capabilities. Therefore, Nd:YAG - laser based solutions were judged as potential due to the flexible transmission of laser light via optical fibre.

To reach reasonable assembly times especially in the critical applications, the welding method should be very productive. Secondly, minimal distortions are required in order to complete the assembly smoothly, and thirdly, high quality of the welds is expected to avoid expensive and slow repair welding.

In recent last years, laser welding began to be used for assembly welding of automotive bodies and parts. One restraint is that in laser lap and butt welding, the gap between the lapped sheets must be controlled very tightly. Hybrid welding was mainly introduced in applications where thicknesses allow single pass welding.
In Europe, one shipyard in Germany for one application for flat reinforced panels producing and mainly all car manufacturers have already successfully used this opportunity, by using more than 120 hybrid welding units in production plants.

Hybrid welding means the coupling of the energy of two different energy sources into a common process zone. This means that laser beam and arc interact simultaneously in the same region (plasma and weld pool) and mutually influence the accomplishment of welded joint (figure 1). Synergistic effects from coupling incorporate the increase of penetration and hence welding speed.

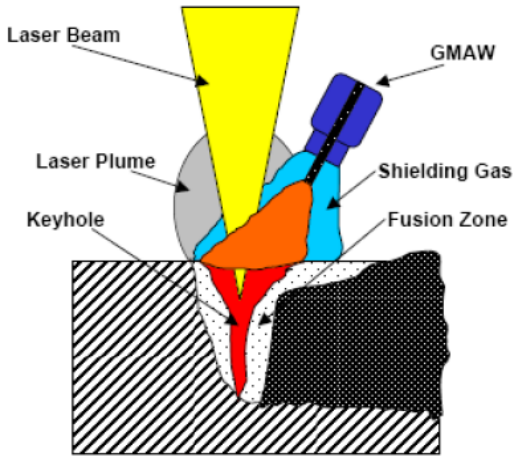

Figure 1: Configuration of laser beam and arc-welding electrode in laser-arc hybrid process

The GMAW arc is also attracted and constricted by the hot spot. This phenomenon was used in order to get the process adaptable inside very narrow grooves. This novel approach, combined with multi-pass techniques, enables a considerable increase in the thickness of the parts to be welded.

Figure 2: Hybrid effect

Experimental works, from different Laboratories, Associations and Institutes, focused on single pass welding. According to the published data, this means plate thicknesses up to 12/16 mm (figure 2). The limiting factor for increasing plate thickness in single pass welding is the power of the laser. For industrial continuous solid state lasers, the maximum available power is in the range of 8 Kilowatts. Main applications on these thicknesses are focused on shipyard industries and pipeline on and offshore (for high strength steels such X80 and X120 dedicated to 500m underwater depth or hydrogen transport).

Figure 3 shows VTT (Finland) welding workstation (3 Kw continuous Nd:YAG Laser). For welding 20mm thickness of AISI 316L (N)-IG ITER-grade by using a THERMANIT 19/15 filler wire material, 6 welding passes are necessary (including cosmetic pass), that means 3.5 to 4mm by pass.

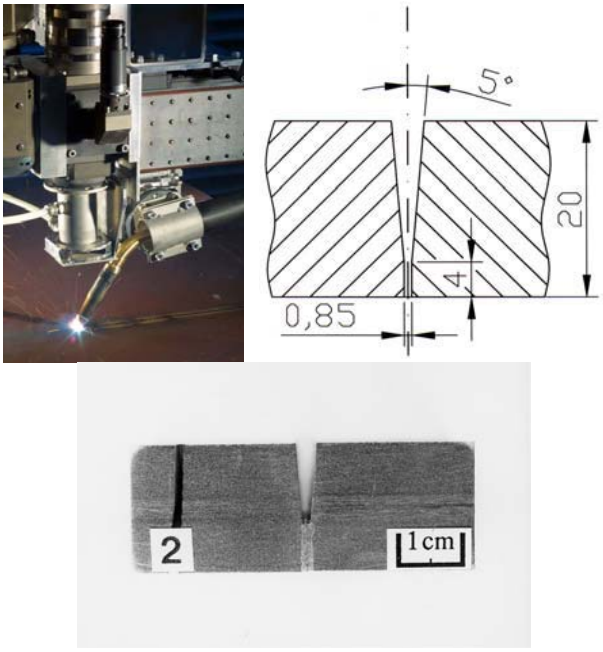

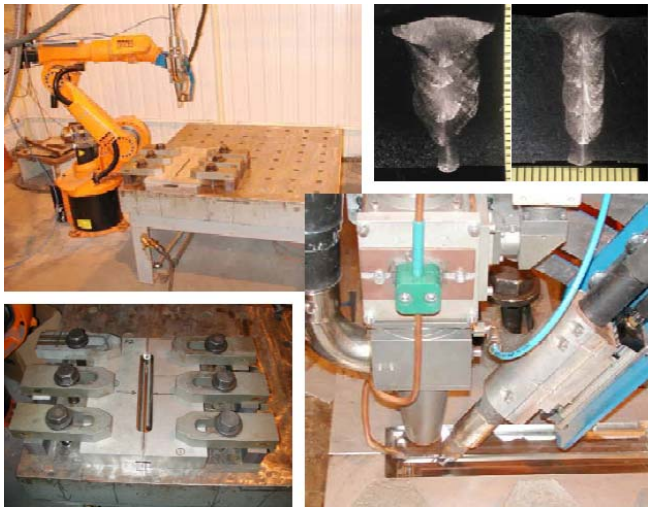

Figure 3: Hybrid welding set-up and results from VTT

The results of welding tests showed that the developed test set-up can produce strains high enough to promote hot cracking in produced test welds. According to welding test results, hot cracking occurred in these rigid weld arrangements (figure 4). The effect of chemical composition of the used parent/filler material and prevailing micro-structure of weld metal on the risk of hot cracking susceptibility are discussed later.

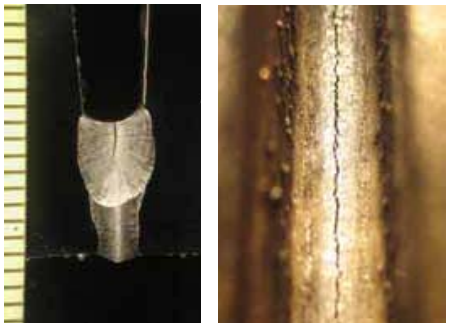

Figure 4: Macro cross-section showing hot cracking propagated into the surface of the first filling pass along the weld length

Exactly, same observations (figure 5) were made in hybrid welds performed in CEA, on the same batch of AISI 316L (N)-IG ITER-grade and THERMANIT 19/15 filler wire. CEA Hybrid process is different from VTT one, and also the chamfer design: 2 to 2.5mm by pass. Bottom chamfer width is 2 times higher in CEA case (6mm), which means a less stressed configuration. However, same conclusions are driven.

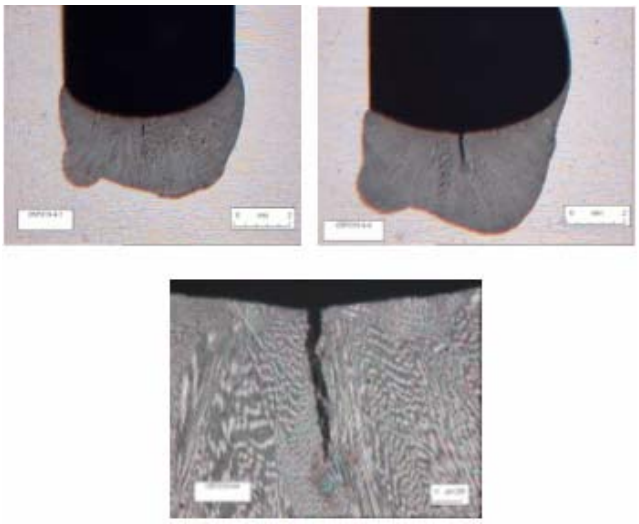

Figure 5: Hybrid cross sections with hot cracks and lack of fusion in weld centreline

In performing the following hybrid welding pass, the longitudinal hot cracks or lack of fusion disappear. These weld defects appear during the 5 first passes, where the stress level is maximum for the welding sequence. It is demonstrated that the main distortions occur till 5 welding passes. Stresses are high, which explains the hot cracks on VTT and CEA hybrid welds. The conclusion is to widen the chamfer bottom to decrease the stress level. Obviously, distortion rate is more important at bottom position rather than top weld position. The second way for avoiding hot cracking phenomena is to limit to a certain level the molten pool volume. It can be recalled the pass thickness for different welding processes:

- NGTIG: 0.8 to 1.2mm,
- CEA Hybrid: 1.8 to 2.5mm,
- VTT Hybrid: 3.5 to 4mm.

CEA developed its hybrid process by adaptation the laser energy combined with the GMA one to perform reasonable, smooth and quiet molten pools at high welding travel speed for distortions reducing, in limiting the welding energy and mastering the cooling rates. It is not at all necessary to try to manage huge molten pool in single pass. Those welding conditions are quite adaptable for performing position welding as overhead (4G) and vertical (3G). Those trends were demonstrated in EFDA Task TW0-LASER-WELD which describes 60mm 316L welding in all positions for laser with cold filler wire. Narrow Gap Hybrid process is not yet performed with real industrial welding tools. CEA prototype is too huge, and not optimized. CEA design work was performed to use the feedback of NGTIG process to get the tool of figure 6. This tool has not been manufactured, but principles and designs are achieved.

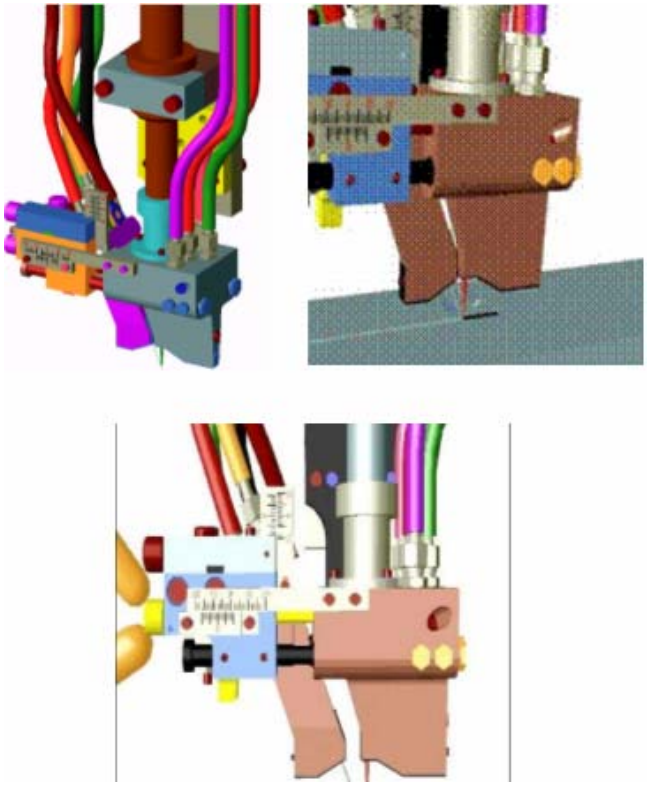

Figure 6: Narrow Gap Hybrid welding tool prototype

Standard Energy Industry such pipe line or GNPL pressure vessels (diameter from 50 to 80m) develop 9 Ni steels and high strength steels (X80, X100, X120) welding technology, from 12 to 60mm thickness with severe joints requirements. Those steels present enhanced metallurgical troubles compare to much easier steels to be welded such 316L stainless steels. Hybrid technology seems to be the only way to master thermal cycles adapted to the material behaviour (figure 7).

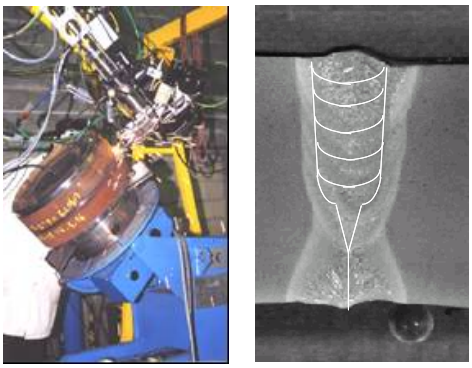

Figure 7: 2G Hybrid welding on 19mm thickness tube (20"diameter) in X80 steel, with 1 root pass and 4 filling passes (2.2mm by welding pass)

Mismatch till 1.5mm of tubes to be welded can be operated with enough mechanical strength. Pores can be thus generated. Sticking defects (figure 8) appears on the chamfer walls.

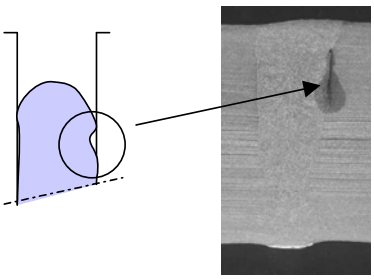

Figure 8: Sticking defects on the chamfer walls

Such defects are generated by a too huge molten pool volume for the filling pass, at a too high welding travel speed. The molten pool did not get an enough time for providing the fusion of the chamfer sidewall. For avoiding these defects, a wide molten pool is waited for getting the chamfer wall fusion with an enough sidewall penetration depth in the range of 1mm, as produced in NGTIG welding. Thus, welding travel speed must be decreased to the conduction mode upper limit, i.e. 0.3 m/min with standard hybrid welding process. No productivity and distortions gain is obtained, in comparison with the NGTIG one: 0.1 m/min.

It explains why the laser beam is divided into two spots (figure 9) located as narrow as possible to the chamfer walls in CEA Hybrid process, to assume the fusion at the sidewall interface and keeping thus a high rate of the welding travel speed.

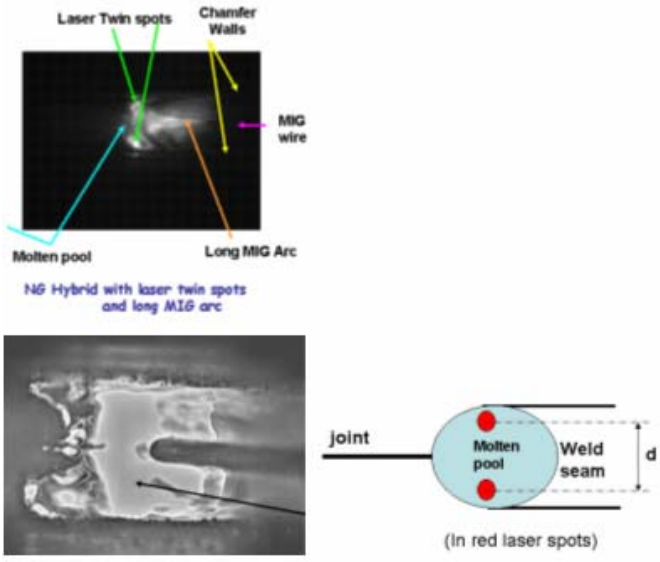

Figure 9: Hybrid with 2 laser spots combined coaxial vision technique

Hybrid welding shares the excellent opportunity to use medium power lasers in the range of 6 kW for thicker sections with laser welding with filler wire. Reduction in necessary laser power means capital cost reductions, but still allows more effective joining than multi-pass arc welding. These observations confirm the interest of penetration depth in the range of 2 to 3mm.

The third action to avoid hot cracks is to modify the filler wire chemical composition. Both parent material and filler wire used, are fully austenitic. It has been noticed the Thermanit 19/15 filler wire, selected for ITER welds at beginning, is not well adapted for performing reference welds. Two criteria very simple to use were applied on DeLong diagram and WRC 1992.

Diagram	Chromium equivalent (Cr_{eq})	Nickel equivalent (Ni_{eq})
DeLong	Cr_{eq} = Cr + Mo + 1.5 Si + 0.5 Nb	Ni_{eq} = Ni + 0.5 Mn + 30 C + 30 N
WRC-1992	Cr_{eq} = Cr + Mo + 0.7 Nb	Ni_{eq} = Ni + 35 C + 20 N + 0.25 Cu

Certain impurity elements like sulphur, phosphorous, silicon, boron, etc. enhance solidification cracking susceptibility in steels. Especially, sulphur (S) and phosphorous (P) is ranked to the most detrimental elements. Sulphur and phosphorous has low solubility in iron, chromium and nickel, which are the three major constituents of stainless steel. These impurities have potential to form low-melting eutectics which appear as liquid eutectic films along the grain boundary and interdendritic regions during the terminal phase of solidification. Combined with high stress level, solidification cracking will occur as a rupture of last solidifying liquid films. Technical discussions with filler wire producers permitted the filler wires selection, given in report [1].

It can be concluded that priority number one is on the process development ending, in particular by the mastering of the thermal field and molten pool. Robust and stiff welding parameters must be set up. Priority number 2 is on position welding development, including the preparation of an industrial hybrid welding tool, which can be delivered by an industrial company. These problems solved, it will be easy to select the proper filler wire, which is a priority number 3 only.

Narrow Gap TIG Welding

The reference welding process for ITER vacuum vessel welding is still yet Narrow Gap TIG welding (figure 10). Looking at process technology, there exists several principles of NGTIG. The filler wire can be fed into the process either preheated or cold (not preheated). In the so-called “hot wire” process, the wire is resistance heated by an additional power source. This has advantages in the increasing the deposition rate. This is made possible by the heated wire which can approach melting before entering the weld pool and does not reduce the temperature of the weld pool a a “cold” wire does. Depending on weld position and process parameters, increased deposition of more 1 kg / h is possible.

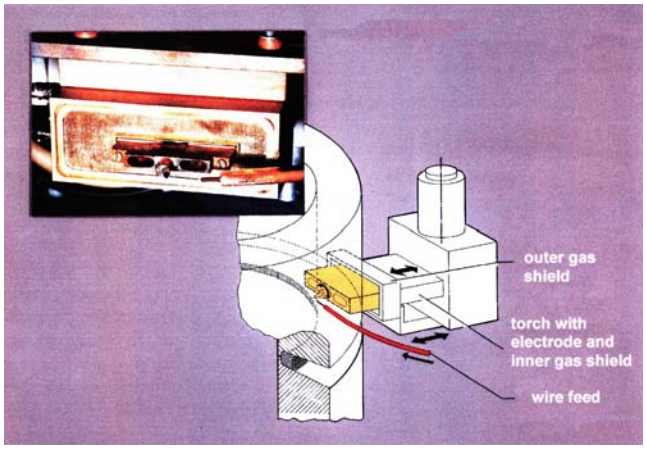

Figure 10: Schematic sketch of TIG Narrow Gap Hybrid welding

The advantages of this well known process are the following:

- process in manufacturing level stage since 30 years (PWR pressure vessel), no more development conducted or expected,
- on site welding process,
- demonstration by Mitsubishi Heavy Industries of a full sector welding sequence (6 month manufacturing),
- fabrication of Superphénix fast breeder reactor (material : 316LN).

Disadvantages:

- pre and post heating necessary during the welding sequence,
- low speed process (below 30 cm/min),
- every 10 weld meters, cleaning of the TIG electrode and before operating, welding and examination of the penetration depth on a test probe,
- high level of distortions.

Different examples of NGTIG tools are presented and hot wire technology, coming from the French company Polysoude in figure 11.

For increasing welding productivity, one solution consists to use tandem technology (figure 12), which is the combination of two NGTIG units on the same carrier or bug. They are located at a maximum distance of 0.5 meter, for keeping the benefit of pre-heating.

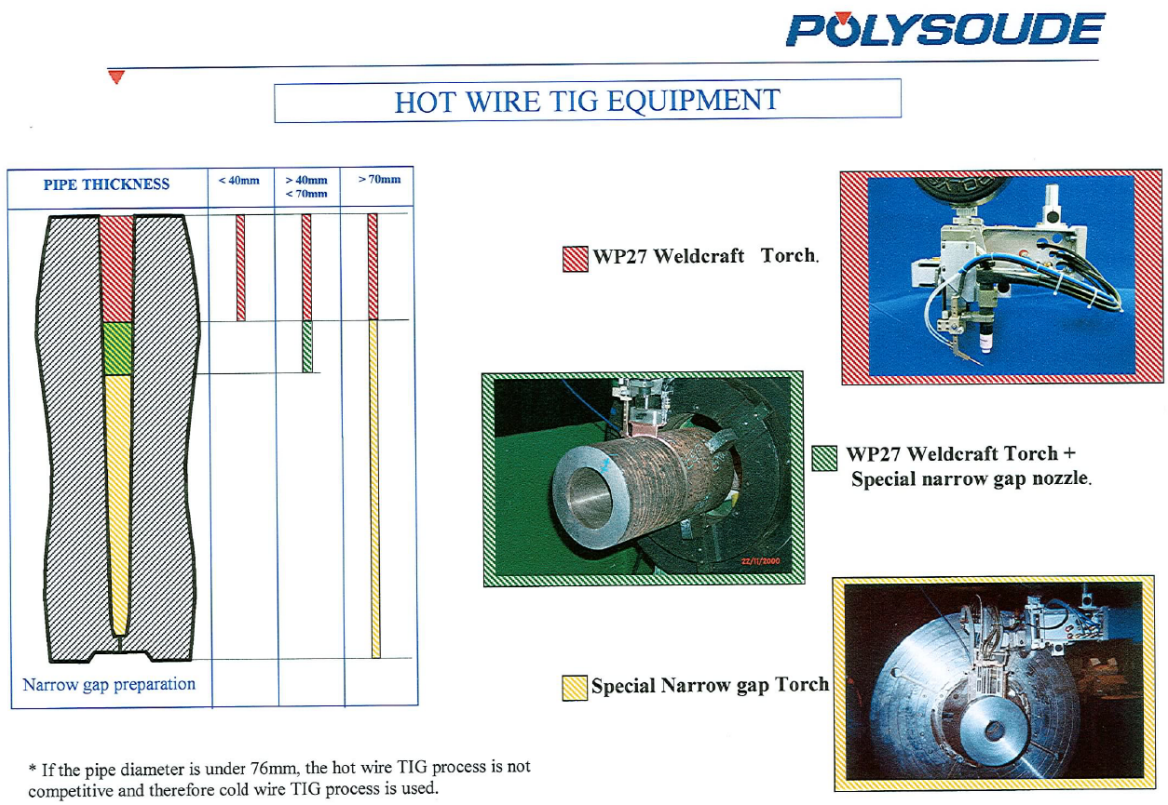

Figure 11: Polysoude Hot Wire NGTIG

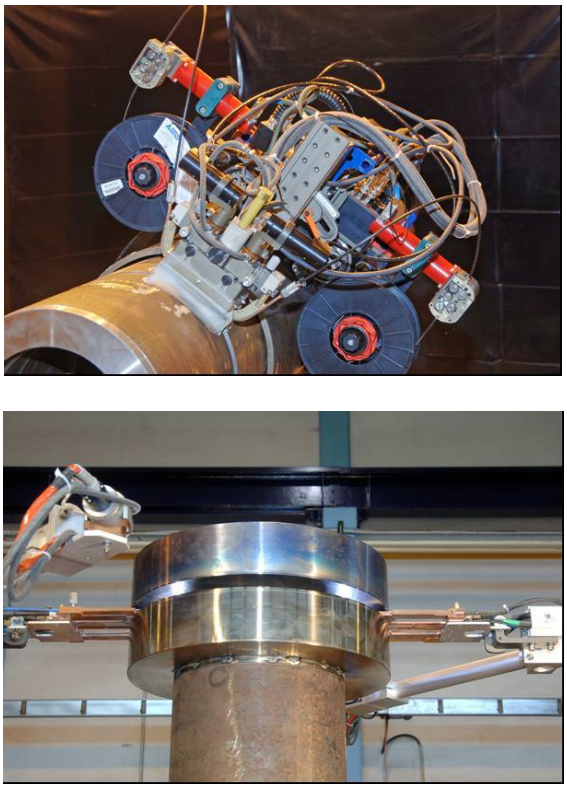

Figure 12: NGTIG tandem

Private discussions with the technical manager of the French company Polysoude (Nantes) brought important technical data. Figure 13 shows chamfer top width related to different steels and welds restraint curve function of chamfer depth and steels.

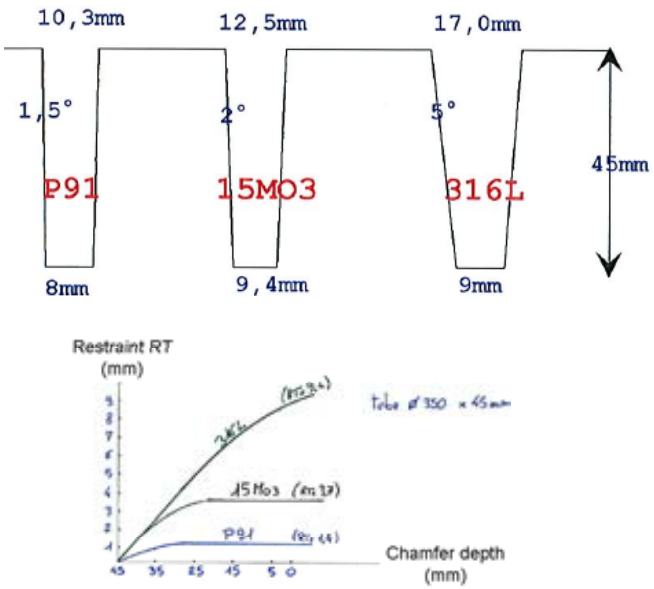

Figure 13: Chamfer top width related to steels and Restraint curves function of chamfer depth and steels

NGTIG process performances

	Cold TIG Narrow Gap	Hot Wire TIG Narrow Gap	Hot Wire TIG Open chamfer
Deposition rate (kg / h) Flat position – 1G	0.6 à 0.7 maxi	Till 1.5	Till 3.0
Deposition rate (kg / h) Position (2G-3G-4G)	0.3 à 0.5	0.8 à 1.2	1 à 1.5
Welding travel speed (mm / min)	50-80	90-120	80-120
Pass thickness (mm) Flat position – 1G	2 à 2.5	2 à 3.5	2 à 3.5
Pass thickness (mm) Position (2G-3G-4G)	1.5 à 2.0	2 à 2.5	2.5 maxi

Chamfer configuration

t: root thickness, L: thickness ½ chamfer, θ: maximum tilt angle, d: maximum, mismatch, J: maximum gap
Welding with one layer by filling pass

	Cold TIG Narrow Gap	Hot Wire TIG Narrow Gap	Hot Wire TIG Open chamfer
t (mm)	1.5 +/- 0.2	2 à 3 +/- 0.2	2 à 2.5 +/- 0.2
L (mm)	3.5	Till 4.5	whatever
θ (mm) (1)	1 à 6°	0 à 6°	10 à 20°
J (mm) (2)	0 – 0.5	0 – 0.5	0 à 0.5
d (mm)	0.75 t	0.75 t	0.75 t

(1): the angle depends on alloy and thickness
(2): gap depends of clamping conditions. Considered below 0.5mm (often 0.3mm)

Other joining processes than NGTIG welding

Figure 14 shows a classification with emphasis on several important welding process characteristics.

submerged arc narrow gap welding	electroslag narrow gap welding	gas-shielded metal arc narrow gap welding		tungsten innert gas-shielded narrow gap welding
process with straightened wire electrode (1P/L, 2P/L, 3P/L)				
process with oscillating wire electrode (1P/L)	process with linearly oscillating filler wire	electrogas process with linearly oscillating wire electrode	MIG/MAG-processes (1P/L,2P/L,3P/L)	process with hot wire addition (1P/L, 2P/L)
process with twin electrode (1P/L, 2P/L)	process with stripshaped filler and fusing feed	electrogas process with bent, longitudinally positioned strip electrode		process with cold wire addition (1P/L, 2P/L)
process with lengthwise positioned strip electrode (2P/L)				
flat position	vertical up position		all welding positions	

Figure 14: Survey of Narrow Gap Welding Techniques

HYBRID QUALIFICATION SET UP

For processing Hybrid joints, the welding set-up has the components shown in figure15. An efficient specific gas shroud device, located at top work piece, was developed for reaching only 70 ppm of oxygen at chamfer bottom and for all welding pass with standard argon bottles. No weld oxidation was observed during the whole chamfer filling. Thus, a complete automatic welding can be processed, due to the lack of brushing and cleaning operation between each welding pass. The gas shroud prototype can be easily reduced in size, quite comparable to NGTIG systems (available) or NGMIG prototypes (in development stage) devices.

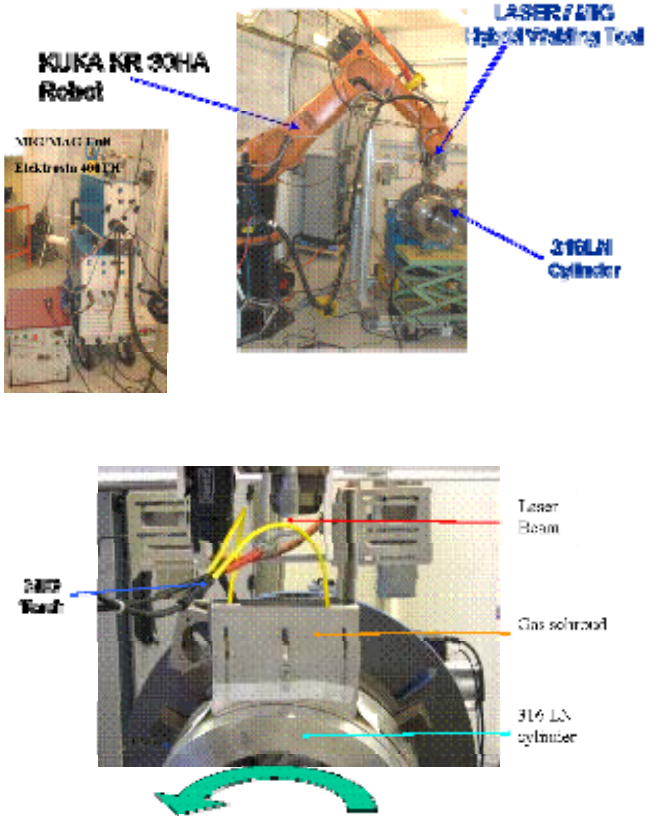

Figure 15: Hybrid welding configuration with on line control device

The more advanced Hybrid process is developed in CEA, only on flat position. It has produced a reference weld by hybrid welding process on reference material AISI 316L (N)-IG ITER-grade and THERMANIT 19/15 filler wire). Mechanical and metallurgical characterizations was completed in 2008, to compare to Narrow Gap TIG Welding process results, performed in other EFDA tasks.

Hybrid welding parameters come from welding developments described in § 2 of the final report [2]:

- Laser power: 4.5 KW,
- MIG power: 5.5 KW,
- Spot diameter: 2.1mm, Twin spots Configuration,
- Gas: Arcal 12 (98 % vol. Argon and 2% vol. CO2), 20 l/min,
- Laser / torch angle: 30°,
- Filler wire speed: 9m/min,
- Welding travel speed: 0.8m/min,

- MIG Voltage: 22.2V and Intensity: 230 A,
- Arc transfer mode: forced short spray,
- 23 filling passes,
- Chamfer top groove width: 9mm.

The quite good running of hybrid welding process is demonstrated in the figure 16 showing welded tubes, diameter 380 mm and 60 mm thickness, in AISI 316L (N)-IG ITER-grade and THERMANIT 19/15 filler wire cylinders. They were characterized upon RCCMR requirements.

Compact and sound welds are produced, with a sidewall penetration depth of 0.8 mm. The same weld quality as NGTIG process has been get. Pores, lack of cracks, compactness, and grain size are in the same range than NGTIG process. The only differences for Narrow Gap Hybrid process are related to the travel speed 8 times higher and deposition rate in the range of 5 kg/hour in comparison to 0.6 kg/hour for NGTIG process.

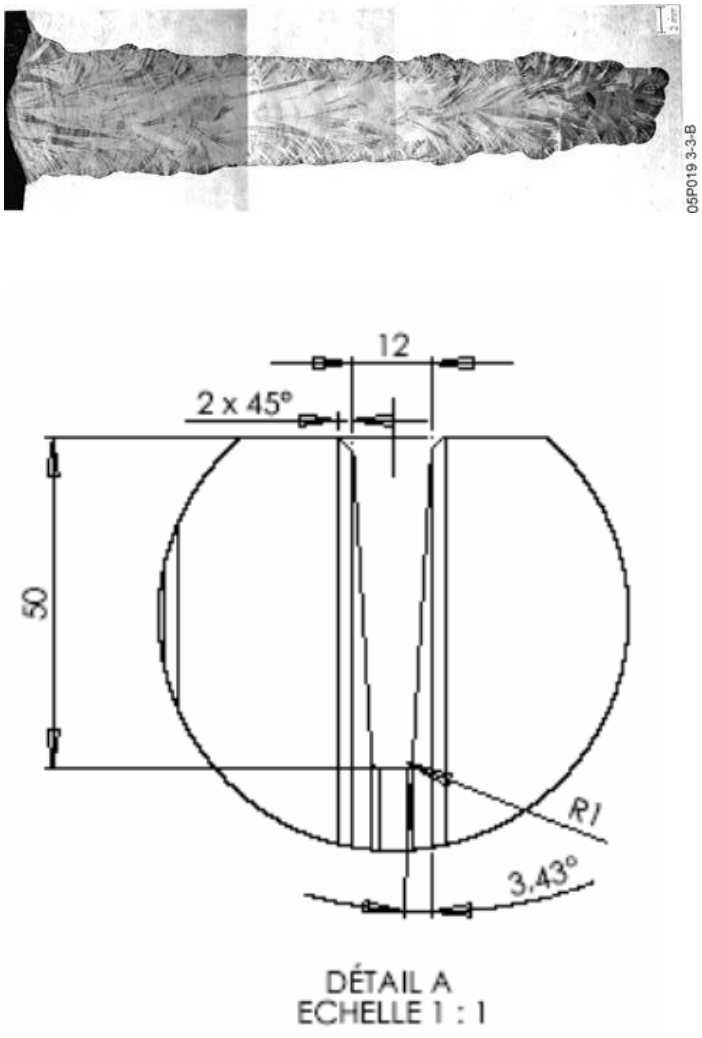

Figure 16: Hybrid welding on 50mm depth chamfer

Macrographs from the weld cross-sections show in Base Material a fully austenitic microstructure with twins and in Fusion Zone an austenitic structure with dendrite solidification. In weld junction, epitaxic growing of grains is observed. In all weld cross sections, no hot cracking is observed. The CEA hybrid process was developed for this target, even if the THERMANIT 19/15 filler wire is not well adapted for welding operating, even for NGTIG process. It confirms that during the multi-pass welding of this study, the following filling pass was overlapped into the previous pass such much that molten metal has “healed” the hot crack underneath. Evaluations from the X-ray radiography and from the welds cross-sectional macrographs seem to support those observations. Both weld metals solidified in primary austenite solidification mode. Fully austenitic microstructure of weld metal is presented in figure 17.

The principal welds defects are mainly some porosity in the fusion zone and in the fusion zone near the weld junction. These porosities are whether spherical or vermiform. Their dimensions are up to about 1.5mm long (vermiform) and up to 1mm diameter (spherical). Defects as lack of fusion (between base material and fusion zone) are linked with porosities. Some of these defects are localised at the junction of two successive passes. These defects, in low number, are located in the same parts of the joint, related to X rays radiography positions. These welds defects, on ongoing zone (200° to 240° from start joint), are explained by process troubles which occurred during the welding phase. In producing the welded tubes, laser spots are manually spaced with the visual control of the CCD camera for each welding pass. They are located just close to the chamfers walls, for assuming their fusion, and thus a sufficient sidewall penetration depth. In tubes welding, miss-adjustments were operated, by too speedy welding. It was paid cash on cross sections. In industrial phase, motorized systems, which could be controlled by a back loop coming from the CCD camera, will drive the process to a full automatic one. These defects will be eliminated by procedures respect and appropriate optical mechanised tools.

Tensile tests

Joint mechanical properties depend also from those of the filler wire in multi-pass joining process. Tensile tests were performed according to an internationally recognised standard (specified in RCCMR code). Joints tensile tests were performed upon the norm NF EN 895 / 1995. Two samples upon 6 broke in the Fusion Zone.
All the tensile samples respect the acceptance criteria of AISI 316L (N)-IG ITER-grade and present higher mechanical strength than this of filler wire itself (figure18). Sticking defects (lack of sidewall penetration depth) were observed on the broken cross section, which explains the fracture. However the reducing rate of samples welded with lack of fusion is quite low with those broken in Base Material: less than 2 %. This point must be kept in mind, with robust welding processes, which present few sidewall lack of fusion. Creep must be assessed. Risk analysis must be run out for a potential qualification. Hybrid joints can be considered with a joint coefficient of 1 for mechanical tests point of view, due to rupture in Base Material. This conclusion was already established on the same welding process with more complex steel in welding consideration: Eurofer steel for TBM (9Cr steel family).

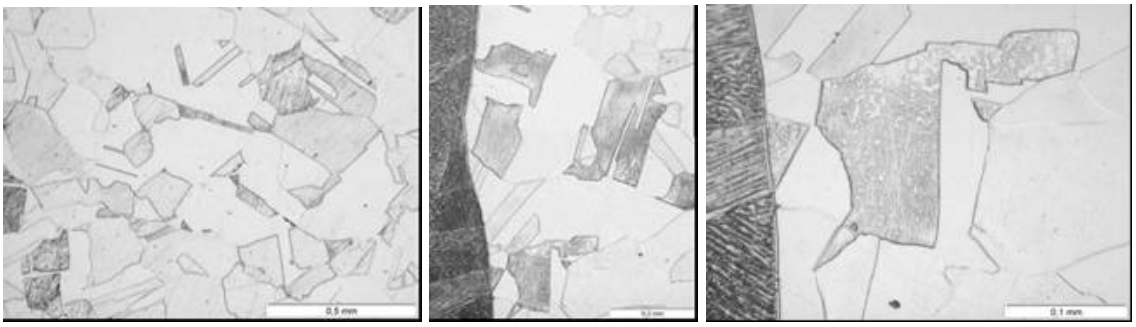

BM: austenic structure with twins dendritic solidification | *Weld junction* | *Weld junction Epitaxic growing*

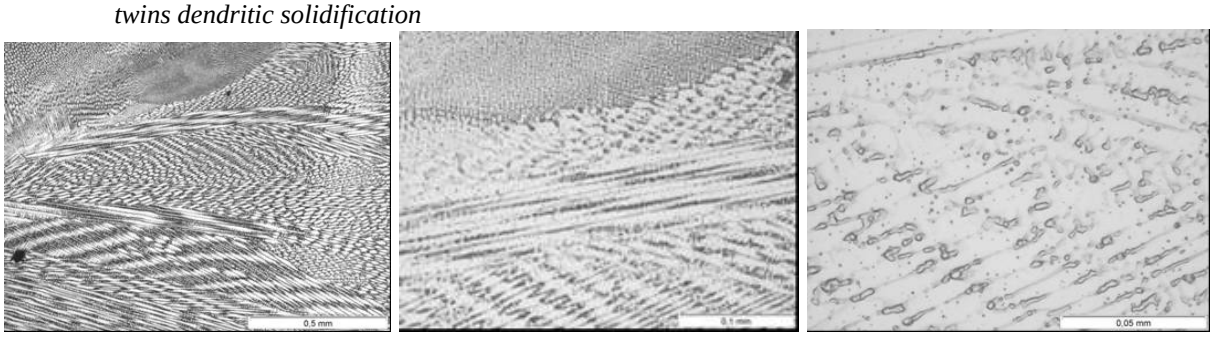

Austenitic structure, dendritic solidification in Fusion Zone

Figure 17: Welds micrographs of Fusion Zone

Repère éprouvette *Specimen mark* *Probenkennzeichen*	θ °C	Dimensions *Sizes* *Abmessungen* mm	So mm²	Lo mm	Rp YS 0,2 % N/mm²	Rm TS N/mm²	A Elong %	Z R of A %	Position cassure *Fracture location* *Bruchlage* MB (1)	 MF (2)	Fm kN	Observations (3) *Remarks* *Bemerkungen*
Tube												
TT1	21	25.01*20.04	501.20			632			X		312.3	
TT2	21	25.06*20.02	501.70			606			X		304.3	
TT3	21	25.01*20.16	504.20			608			X		306.5	
TT4	21	25.08*20.18	506.11			614			X		309.3	
TT5	21	25.03*20.19	505.36			608				X	307.2	
TT6	21	25.05*20.05	502.25			594				X	298.1	

MB : Métal de base
MB : Parent material - MB : Grundwerkstoff

(2) MF : Métal fondu
MF : Weld metal - MF : Schweißgut

(3) Position exacte de la rupture
Exact fracture location - Genaue Lage der Bruchlage

Figure 18: Hybrid welding tensile tests

Bending tests

Joints bending tests were performed upon the norm NF EN 910 / 1996 (Annexe 9). The obtained results (figure 19) show bent angles of 180°, which qualify the hybrid welds for this test.

Impact tests

Joints impact tests were performed upon the norm NF EN 875 / 1995 (Annexe 10). Some values are lower than others (weld junction at 0°C), defects seem to be observed on the broken cross section (figure 20). These tests must be performed again in a sound joint area, NDT controlled.

All the impact samples, except those performed in weld junction at 0°C respect the acceptance criteria of AISI 316L (N)-IG ITER-grade and present higher shear strength than this of filler wire itself. Those tests are just the beginning of a qualification. DBDT curves must be established. RCCMR tests specifications have to be completed.

These results are the beginning of a qualification phase. From providing phase, laboratory notes and welding procedures, RCCMR requirements were respected. Except some observed defects, hybrid joint performances are quite good. On the remaining sound joint areas, it will be useful to continue, in a future work, welds qualification.

Vertical position welding

3G vertical position, groove weld, was evaluated. It must be remembered that alone laser welding with filler wire has been shown possible by some work performed in a former EFDA task: TW0-LASER-WELD. The main conclusions were to limit the penetration depth for each filling welding pass at a maximum value of 2mm and to maintain a welding travel speed above the minimum value of 1.5 m/min. For pipe orbital welding, 5G, 6G and 6GR multiple positions (overhead, vertical and flat) welding are developed or performed on high strength steels (X80 to X120) with thicknesses below 20mm. It illustrates the low difficulty level, except minimum work to perform, to assess this position welding.

Repère éprouvette Specimen mark Probenkennzeichen	Dimensions Sizes - Abmessungen		Conditions de pliage Bending conditions - Biegenbedingungen							
	Largeur : l Width Breite mm	Epaisseur : e Thickness Dicke mm	ø mandrin Ø of mandrel - Biegedommesser		Intervalle entre appuis Loading span - Stützweite		Endroit Face Raupe	Envers Root Wurzel	Côté Side Seite	Angle pliage Bend angle Biegewinkel
			... x e ...x t - ...x e	mm	... x e ...x t - ...x e	mm				
Tube										
PC1	40	10	4	40	6.2	62			x	180
PC2	40	10	4	40	6.2	62			x	180
PC3	40	10	4	40	6.2	62			x	180
PC4	40	10	4	40	6.2	62			x	180

Figure 19: Hybrid welding bending tests

Repère éprouvette Specimen mark Probenkennzeichen	θ °C	Dimensions à fond d'entaille Size of the root of the notch Abmessungen (Prüfquerschnitt) mm	Section à fond d'entaille Section of the root of the notch Kerbquerschnitt mm²	Energie absorbée Absorbed energy Kerbschlagarbeit J	Expansion latérale Lateral expansion Seitliche Ausdehnung mm	Cristallinité Crystallinity % MF	Observations Remarks Bemerkungen
Tube							
MF 1-3	0	10*8	80	296-296-296			
ZL+2 1-3	0	10*8	80	72-64-73			
MF 4-6	-40	10*8	80	112-119-120			
ZL+2 4-6	-40	10*8	80	296-296-296			

Figure 20: Hybrid welding impact tests

Some welding trials on AISI 316L (N)-IG ITER-grade plates (60mm thickness) were processed with Hybrid technology (figure 21).

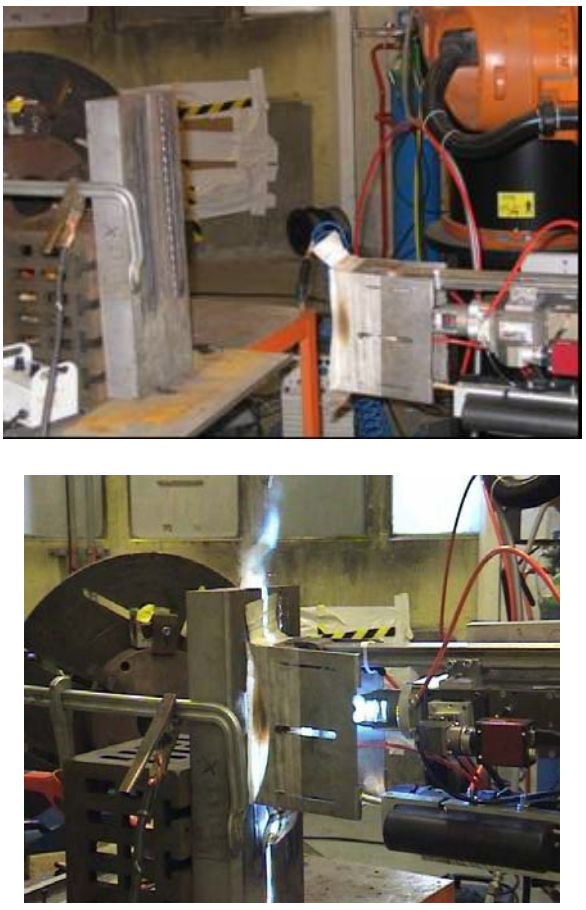

Figure 21: Hybrid welding in vertical position

These preliminary trials confirmed the results of the previous EFDA tasks. Welding is possible and seems to be possible in down hand or up ways. Hybrid process must be simply adapted and developed in this welding position, with low level of technical difficulties. It is encouraging for a future application of this process.

Overhead position welding

Due to lack of time and budget, 4G overhead position, groove weld, was not evaluated. Like vertical position welding, it must be remembered that only laser welding with filler wire has been shown possible by some work performed in a former EFDA task. The main conclusions were to limit the penetration depth for each filling welding pass at a maximum value of 1.5mm and to maintain a welding travel speed above the minimum value of 2 m/min for getting high cooling rates and low size molten pools. Those results let think to low level difficulties for developing and qualifying this welding position. Only time and budgets are necessary.

SUGGESTED HYBRID DEVELOPMENT PROGRAM

Figure 22 illustrates the certification road map, which could be obtained after 4 years from the launching date. If earlier date is expected, 9 months could be saved. An estimation of the overall budget required could be in the range of 1.5 to 2 M€, in first approach.
For ITER manufacturing, the Go no Go date could be established at T0 + 1.5 year.

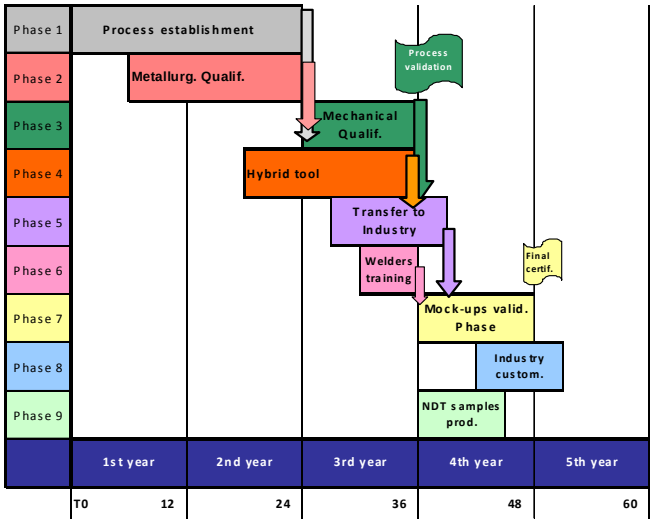

Figure 22: Hybrid welding process qualification road map

PERSPECTIVES

Hybrid technology can be today considered at “stone age” for humanity history. In keeping in mind the molten pool control and solidification mastering, and considering enhance technology in constant progress in laser field and innovative ideas, the road map of figure 23 could be estimated “shy” or conservative. In fact, this welding technology will follow a fast implementation way.

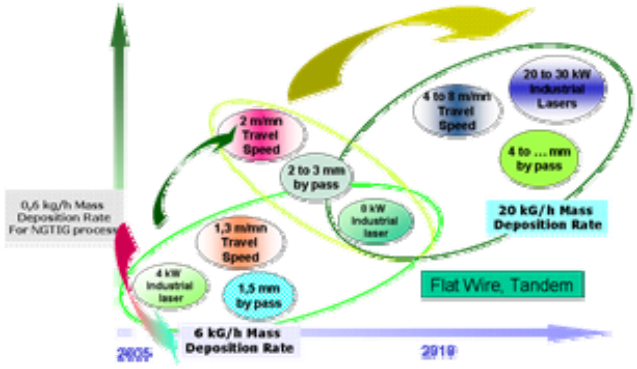

Figure 23: Hybrid welding progress road map

CONCLUSIONS

Narrow Gap Laser MAG Hybrid Welding (NGHW) is expected to be an especially suitable process for manufacturing the vacuum vessel of the next reactor ITER. The hybrid process consists in combining both the MAG process and the laser process with potentially high quality of welds at high productivity in multi-pass operation.
ITER Vacuum Vessel or other components require enhanced welding technologies. The reference one is Narrow Gap TIG Welding, qualified for RCCMR code. This process procures distortions and is quite low for production management (welding travel speed in the range of 0.1 m/min and mass deposition around 0.6 Kg/hour). Trained and certified welders teams are not sufficient in Europe.
These reasons conduct to analyse other joining processes such Hybrid in Narrow Gap situation. This technique is a combination of MAG and Laser process. It procures today an increasing by a minimum factor of 5 the former numbers of TIG process. The negative points of this interesting process are the incomplete development stage, the lack of real industrial tools on the market, the qualification not really started. This report makes the technology status and the estimation of future program for getting the hybrid process certification, which could be obtained in less than 4 years.
As starter of qualification, CEA developed welding tool and manufactured a cylindrical mock-up in 316LN stainless steel. Characterisation of this cylinder under RCCMR code has been performed. Interesting results have been reached. The main objective was to prepare welding developments for process which will be certified in the following F4E tasks, in the target of residual distortions fight.
This report establishes the status of future required work for preparing manufacturing choices and welding and NDT procedures. Key trends were analyzed, to develop Hybrid process for producing quite acceptable distortions. So, this task will prepare the potential future works.
The only conclusion is that Hybrid processing for manufacturing is possible. Costs and efforts must not be wasted, that is the only challenge.

REFERENCES

[1] TW6-TVA-IHYB, “Industrialisation and weld quality issues of high productive laser\arc hybrid for thick section welding of ITER grade SS material”, M. Karhu and V. Kujanpää,
Research report VTT-R-07448-08

REPORTS AND PUBLICATIONS

[2] Industrialisation and weld quality issues of high productive laser/arc hybrid for thick section welding of ITER grade SS material – TW6-TVA-IHYB – Final report, Ph. Aubert, CEA Internal report DM2S/RT/08-0010/A, 14 Dec 08

TASK LEADER

Philippe AUBERT

DEN/DM2S
CEA-Saclay
F-91191 Gif-sur-Yvette Cedex

Tel: 33 1 69 08 37 99
Fax: 33 1 69 08 66 42

e-mail: philippe.aubert@cea.fr

CEFDA07-1700-1542

Task Title: TW6-TVV-TLDES: DESIGN AND MANUFACTURE OF COSMETIC WELDING HEADS ON EB WELDS OF VV SECTORS

INTRODUCTION

One possible method of manufacturing the Vacuum Vessel (VV) sectors consists in Electron Beam (EB) welding inner and outer shells on ribs as well as on the so-called "flexible support housings" (SH).

In order to demonstrate the validity of this method, a scale one mock-up, called VATS as well as a coupon called VACS which reproduce the so-called INBOARD_SEGMENT_A have been manufactured by DCN, La Montagne, France under EFDA contract 06-1908.

The EB welding process creates a burr on the opposite (root) side of the welding gun.

This burr must be removed by autogenous fusion.

The task to be undertaken is to CAD design specific welding heads able to remove by autogenous fusion the EB welding burrs between inner and outer shells to the flexible housings and ribs.
Two different machines are then necessary:

-The SCWT, Small Circular Welding Tool required to cosmetic weld the root side of the e-beam circular (housing) welds,

-The SLWT, Small Linear Welding Tool required to cosmetic weld the root side of the e-beam linear (rib) welds.

The task consists of the following work:

The first stage to be undertaken will cover CAD design of the SCWT, as the main concern is the very tight clearances (40 mm) between housings and shields.

In addition to the CAD design, a mock-up reproducing local conditions of four adjacent flexible housings of the same shell of the so-called INBOARD_SEGMENT_A will also be manufactured.

Two mock-ups SCWT 276 & 190 will be also manufactured in order to demonstrate the possibility of installation and retrieval of the welding head versus the flexible housings.

The mock-up welding head will solely reproduce external dimensions of the proposed CAD welding head and all other peculiarities necessary for the installation and retrieval exercise.

2007-2008 ACTIVITIES

DESIGN CONCEPT OF SCWT (mechanical welding head only)

The SCWT includes the following functions:

- Operation of travel along weld by means of servo-controlled electric motor,
- Possibility of viewing of the area by endoscope over the required distances, also during welding,
- Control of system including position feedback, with the possibility of pre-programmed path or teach and repeat operation,
- Additional possibility of operation of holding of UT probe to all areas,
- Additional possibility of operation of delivery of X-Ray film to all areas.

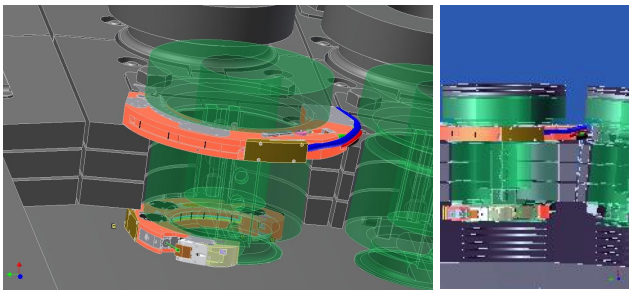

Figure 1: SCWT 276 & 190 in place onto flexible housings (green)

DESIGN CONCEPT OF SLWT (mechanical welding head only)

The SLWT includes the following functions:

- Operation of travel along weld by means of servo-controlled electric motor,
- Operation of travel transverse to weld line by means of servo-controlled electric motor,
- Possibility of viewing of the area by endoscope over the required distances, also during welding,
- Control of system including position feedback, with the possibility of pre-programmed path or teach and repeat operation,
- Traction force for linear travel achieved without additional rails, i.e., by using the features which exist within the structure anyway,
- For the SLWT, the linear travel features to be made adaptable to the whole VV construction, i.e. with greater inter-wall distances,
- Additional possibility of operation of holding of UT probe to all areas,

- Additional possibility of operation of delivery of X-Ray film to all areas.

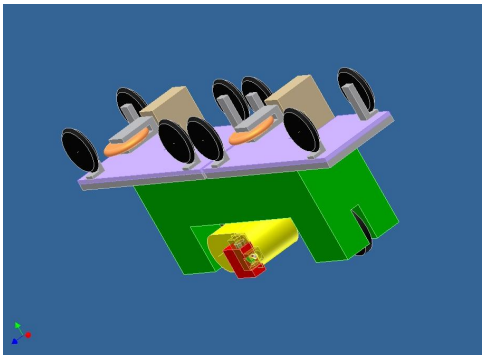

Figure 2: SLWT cart

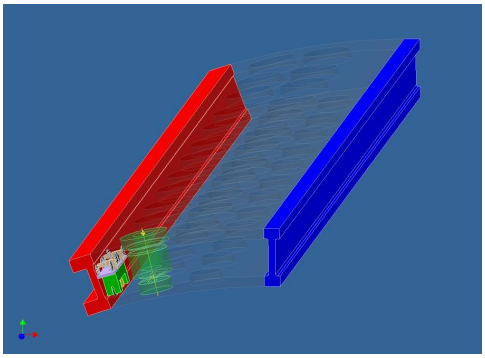

Figure 3: SLWT cart onto INBOARD segment

MOCK-UP JIG

The mock-up jig reproduces at scale one a portion of the inboard segment of four adjacent flexible housings, two housings in place, two holes free for introduction of SCWT. Two mock-ups SCWT 276 and 190 have been produced to demonstrate the installation and retrieval capabilities.

Figure 4: Scale 1 mock-up with 2 flexible housings in place

Figure 5: Introduction of SCWT_190

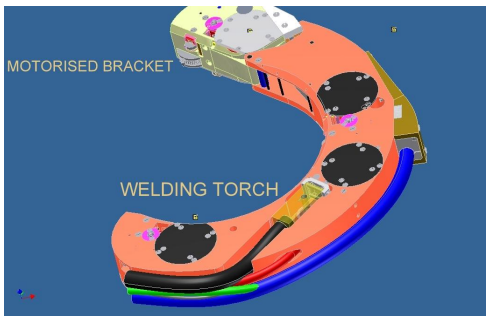

Figure 6: SCWT_190 under CAD view

Figure 7: Intro. Of SCWT_190 though hole

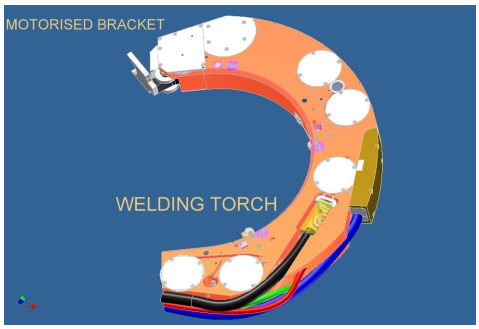

Figure 8: SCWT_276 under CAD view

Figure 9: Operator peeps one's head and shoulder through hole

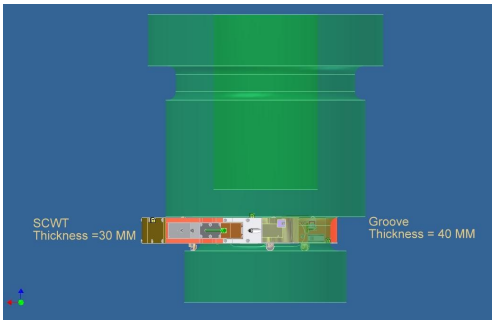

Figure 10: SCWT in place on housing

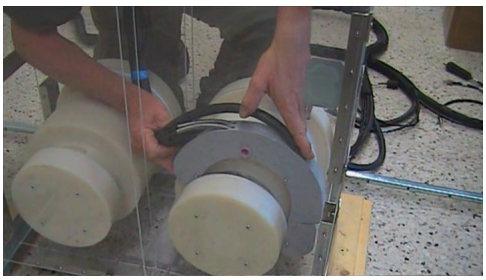

Figure 11: Operator sets SCWT "de visu" within the INBOARD segment

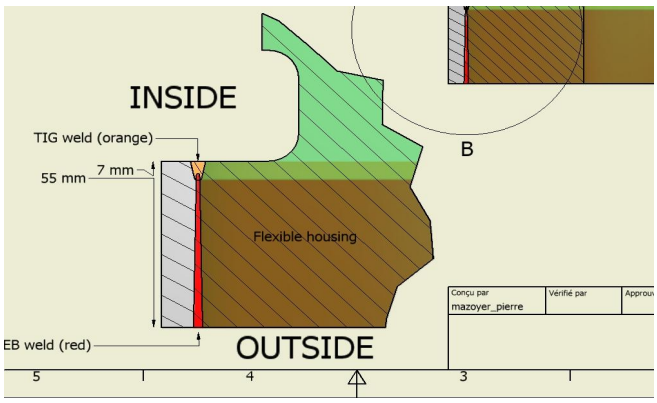

Figure 12

CONCLUSIONS

The installation and retrieval of SCWT machines is quite feasible taking advantage of free holes of the adjacent flexible housings. The possibility for the operator to introduce one's head and shoulder enables to set the SCWT «de visu» on the flexible housing.

The electron beam welding is the likely candidat for most of the welds due to :

- wallthicknesses to be welded,
- minimum deformations request.

Though, as far as flexible housings are concerned, the VACS coupon shows limitations to this welding technique:

- robust parameters as developed for the VACS coupon produce an opposite « burr » of a section roughly 5 by 5 mm which would require much more than 300 A under TIG conditions to be correctly melted,
- the part of the beam which exits from the piece (assumed 30% of the total energy) produces a second weld on the opposite shell which would damage if not destroy the borated steel plates.

Hence, we suggest to promote the EB welding as a blind weld completed by an opposite TIG weld, the combination overcoming the two previous limitations.

Welding Technique	Penetration (mm)	Number of passes	Current (A)	Torch Technique	Technique available
AA_TIG	7	1	200	TIG-double flux	yes
EB	55	1			yes

REPORTS AND PUBLICATIONS

TW6-TVV-TLDES Final Report
Orbital intern Report, March 2008

TASK LEADER

Pierre MAZOYER

ORBITAL
Les Balufiers
F-01540 VONNAS

Tel : 33 4 74 50 13 58
Fax : 33 4 74 50 19 93

e-mail : pierre.mazoyer1@wanadoo.fr

CEFDA07-1700-1623

Task Title: TW6-TVV-LEAKD1: LEAK LOCALISATION FOR IN-VESSEL COMPONENTS

INTRODUCTION

The demands on leak localisation are unique in ITER because of the very sensitive level of leak detection required combined with the environment in which the detection has to be performed. The techniques to be applied to ITER leak detection and localisation have to be selected in the early phase of the project as they may influence component or system design, access to the vacuum chamber and additional procurements. The experience gained in existing devices especially with actively cooled components needs to be used and projected to the ITER case.

The objective of the task was to propose a limited number of techniques which should ideally allow a localisation in the vacuum vessel ideally to within 10 mm of a water leak and to cover the leak range 10^{-7} $Pa.m^3.s^{-1}$ to 10^{2} $Pa.m^3.s^{-1}$ (equivalent He). These need to be ranked according to their potential to find leaks reliably, precisely and speedily as well as their applicability for finding leaks in inaccessible locations. Important considerations for the ranking relates to the environment requirements and to the fact that remote handling should not be required. If not, the priority should be given to techniques with the least demanding remote handling requirements.

2007-2008 ACTIVITIES

The work was performed in collaboration with FZK (Germany). The sub-tasks performed by the CEA were on:

- the critical analysis of the present ITER water cooling circuits and on proposals for improvements,
- the review of experience of water leaks and leak detection in the present fusion devices,
- the proposal for a possible leak detection scheme for ITER pending the results from proof-of-principle tests proposed by FZK.

For the first point, the work was based on the analysis of the ITER documents. It was relative to the blanket modules and divertor. For the blanket, issues come from the fact that:

- there are 3 cooling loops serving the 420 modules, the number of sub-loops is high (92),
- the blanket modules inlet and outlet pipes are situated on top of the machine, which will make more complex the draining and drying processes,
- there is a lack of space available at the upper port level which doesn't allow the implementation of additional valves.

With the present design, only 6 to 9 modules can be segregated. For the divertor, 3 cassettes can be segregated if each sub-loop can be valved-off. Present cooling water circuits configuration is not convenient for the application of pressurization/depressurization cycles, which is a method generally used to identify a leaking circuit. To localize the leaking component, in-vessel local techniques are required.
ITER documents present a survey of potential leak detection and localisation methods (Visible spectroscopy, spiking, accumulation methods, laser methods, leak localisation by movable sensors, He leak testing,…). The visible spectroscopy and laser methods can be seen as diagnostics. They are not presently used on existing devices for this purpose. Their applicability has to be checked and they have to be validated. Spiking method seems adapted to the circuit's configuration, but it requires additional pipes and further work is necessary for the selection of the additives and for the optimisation of the leak localization procedure. It requires a local sniffing method with He or tracer gas and the availability of a snake arm, which should be capable to resist to the in-vessel irradiation.

The review of water leaks experience in present devices is limited. Several teams were contacted, but only information from JET and Tore Supra was available. Both developed procedures for the localisation and the management of a leak on a plasma first wall component. At JET, the localization of the leaking water circuits is achieved by the monitoring of the pressure of the locked-in water for the divertor. For the Neutral Injector box, it is achieved by pressure changes in the water circuits.
At Tore-Supra depressurization/pressurization cycles are applied on each water sub-loop to find the leaking one. But the procedure applied to localize the leaking component is clearly not applicable for ITER, because the access in the vacuum vessel will not be possible to proceed manually a local He sniffing.

CONCLUSIONS

The localization of a leaking component in ITER is specific compared to what is achieved in the existing tokamaks such as JET or Tore Supra. The present water circuits configuration and valves and relief valves arrangement do not allow to apply the methods used on these devices (Pressurization,/Depressurization of sub-loops, monitoring of the pressure in isolated circuits) to identify the leaking sub-loop. Changes are required and were proposed in the final report [1].

With the present water system configuration, it will not be possible to localize the leaking blanket module or divertor cassette.

The proposed spiking method seems convenient to localize the leaking PHTS and sub-loops, but several additives are

required and it has to be checked that there is no connection between the divertor sub-loops via the flow lines. Local measurements are needed to localize the leaking component and a remotely controlled equipment will be necessary. The feasibility of the method has to be validated on two aspects: selection of convenient chemical additives, local detection capacity by an RGA.

The He or tracer gas sniffing method can also be used to localize the leaking component or module, but it requires that the sub-loop identified as leaking has to be drained out and dried and that there is no water remaining in the circuits. For local measurement, the use of a remotely controlled device (such as an inspection arm) and of radiation -hard instrumentation (100+ Gy/h gamma dose rate, 100+ KGy integral dose) are required.

The other methods foreseen (visible spectroscopy, laser methods) are not used presently on existing tokamaks for leak localization. They require development and experimental validation. Their sensibility to detect the leaking sub-loop is not obvious, particularly in the modules located at the interface between two PHTS for the blankets or between two ports for the divertor cassettes.

Their advantage is that they potentially could allow the localization of the leaking component without draining out and drying the circuits, but their capability still must be demonstrated with a proper test programme.

REPORTS AND PUBLICATIONS

[1] EFDA Contract TW6-TVV-LEAK
Deliverable 5, CEA Internal Report
IRFM/STEP/GARV/REF/NTT-2009.003
M. Chantant, J.-C. Hatchressian

TASK LEADER

Michel CHANTANT

DSM/IRFM/STEP/GARV
CEA-Cadarache
F-13108 Saint-Paul-lez-Durance Cedex

Tel: 33 4 42 25 49 80
Fax: 33 4 42 25 44 21

e-mail: michel.chantant@cea.fr

TW6-TVM-BRAZE

Task Title: TESTING OF SILVER FREE BRAZE MATERIALS WITH Be

INTRODUCTION

The objectives of this task are to test the lab-scale silver-free brazing alloys developed in 2005 under TW5-TVM-BRAZE task, to test the industrial ribbons developed in 2006-2007 by INFM Poland under the same task, to perform Be/CuCrZr junctions with them and to characterise these junctions.
In 2006 and 2007, three induction brazing campaigns were performed at AREVA NP in Le Creusot. Results of the third campaign are described here. Beryllium and CuCrZr were joined with two brazing alloys, STEMET 1108 ATM (78.8Cu-11.1Sn-7.7In-2Ni-0.4P in wt.%) and GLIWICE5 (Cu-Sn-In-Ni-Mn alloy), at different temperatures and for different soaking times. Coupons of half of these brazed samples were characterized by optical and scanning electron microscopy. The other half samples were shear tested.

2007-2008 ACTIVITIES

Twelve 25x25mm² samples were brazed under a flowing N_2-5%H_2 atmosphere (table 1). Half of them, all brazed for 5 min at 770°C, were used for shear tests, performed by AREVA NP. The other samples were prepared for metallographic observations by ATMOSTAT. Three temperatures (730°C, 750°C and 770°C) and two plateau durations (1 and 5min) were tested.
Several pictures of the Be/CuCrZr brazed samples are shown on figure 1. All the samples were brazed successfully. In the case of GLIWICE5 alloy, ribbons became mainly oxidized on joints periphery. With STEMET 1108 ATM, several small and shiny droplets of alloy could be seen on joints periphery.

Table 1: Description of the samples brazed during the third campaign

Test Nb	Sample ref.	Alloy used	Temp./Plateau duration	Utilisation
1	Braze36	GLIWICE5	770°C - 5min	Metallography
	Braze37	GLIWICE5	770°C - 1min	Metallography
2	Braze38	GLIWICE5	750°C - 5min	Metallography
	Braze39	GLIWICE5	750°C - 1min	Metallography
3	Braze40	GLIWICE5	730°C - 5min	Metallography
	Braze41	GLIWICE5	730°C - 1min	Metallography
4	Braze42	STEMET 1108 ATM	770°C - 5min	Shear test
	Braze43	STEMET 1108 ATM	770°C - 5min	Shear test
5	Braze44	STEMET 1108 ATM	770°C - 5min	Shear test
	Braze45	GLIWICE5	770°C - 5min	Shear test
6	Braze46	GLIWICE5	770°C - 5min	Shear test
	Braze47	GLIWICE5	770°C - 5min	Shear test

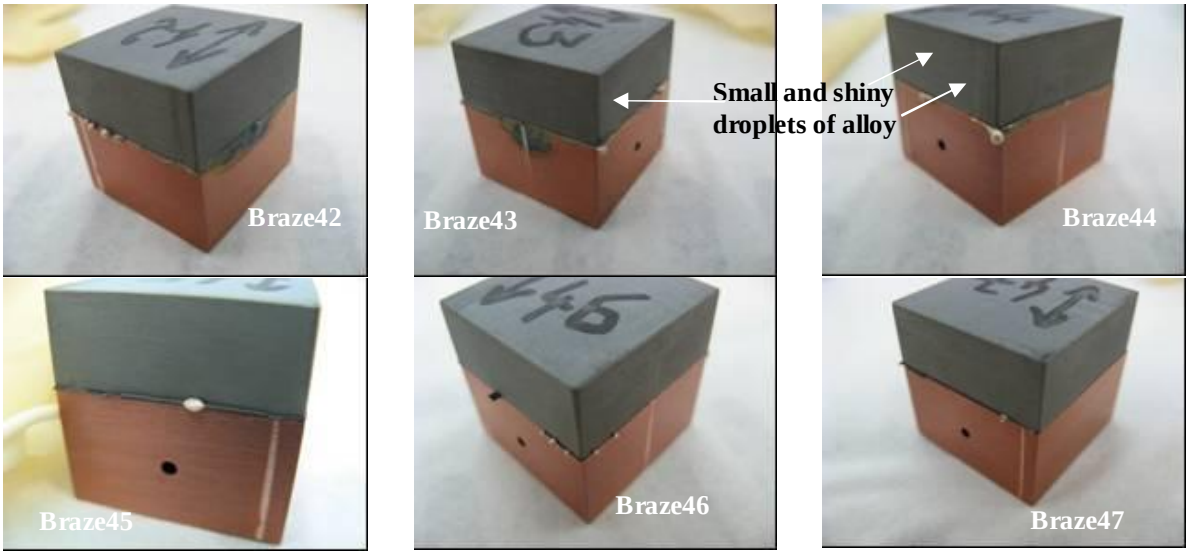

Figure 1: Samples Braze42 to Braze47 after brazing and before shear tests

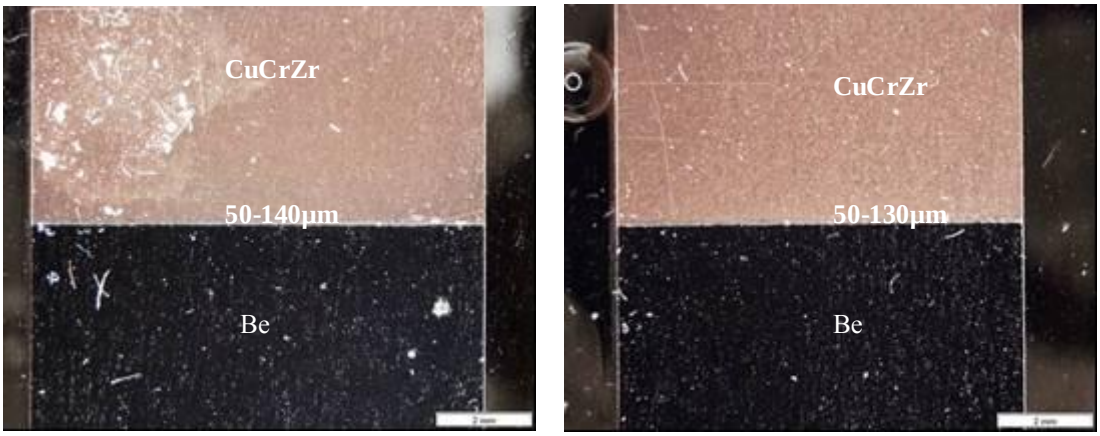

Figure 2: a) Middle and b) Corner of Braze36 (Be/CuCrZr; 770°C/5min; GLIWICE5)

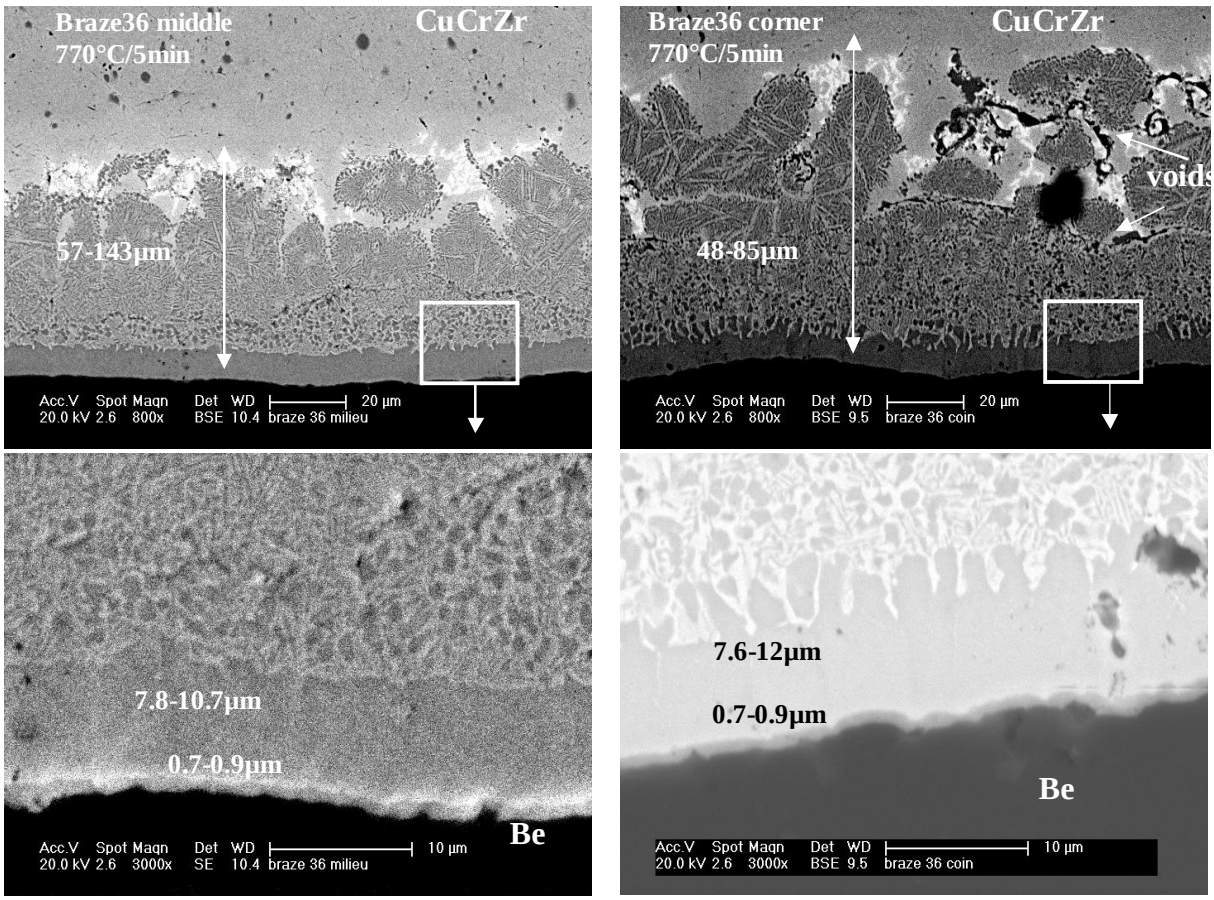

Figure 3: SEM images of Braze36 sample in middle and corner and for two magnifications

METALLOGRAPHIC OBSERVATIONS

For all the samples, the diffusion affected zones are very limited as shown on optical micrographs from Braze36 sample observed in its middle and a corner (figure 2). The total thickness of diffusion-affected zone and reaction layers are around 50-140µm.

SEM observations of Braze36 sample in two areas (middle and corner) are shown on figure 3. Brazed interfaces are composed of two reaction layers, as analysed by microprobe: a 0.5-1µm thick $Be_{2+x}Cu_{1-x}$ layer (δ-phase) close to Be and a 8-12µm thick BeCu (γ-phase) + Cu(Be) layer. Be diffuses also in braze alloy and CuCrZr. The $Be_{2+x}Cu_{1-x}$ layer contains less than 1at.% of oxygen. Several voids are observed in the joints; they could be due to the presence of non-molten oxide on initial ribbons.

Thicknesses of the different layers (diffusion, δ-phase and γ-phase layers) were measured for all the samples in the brazed areas and are given in table 2.

The main effects of temperature and plateau reduction, respectively from 770°C to 750°C and from 5min to 1min, concern the γ-phase BeCu+Cu(Be): a plateau of 1min gives much lower thickness compared to 5min; 750°C

tends to give lower thickness compared to 770°C. There is no measurable effect on δ-phase ($Cu_{1-x}Be_{2+x}$) thickness. Variations on diffusion affected zones are too large within a given sample to give any conclusion on temperature and time effects.

Other observations are the following: 730°C/5min is not sufficient for obtaining good joints. Whatever the temperature, a plateau's duration of 1min is not long enough.

SHEAR TESTS

Results are given in table 3. GLIWICE 5 alloy gave the highest shear strength at 85±2 MPa, versus 73±4 MPa for STEMET 1108 ATM. For both, very small standard deviations are obtained.

Table 2: Thicknesses (in µm) of the different layers

		Braze36 770°C/5min	Braze37 770°C/1min	Braze38 750°C/5min	Braze39 750°C/1min
Middle	Diffusion+reaction	57-143	52-136	55-86	45-100
	Layer $Cu_{1-x}Be_{2+x}$	0.7-0.9	0.4-0.7	0.6-0.9	0.5-0.7
	Layer BeCu + Cu(Be)	7.8-10.7	3.8-7	6.3-9.8	3.8-5.6
Corner	Diffusion+reaction	48-85	43-64	63-82	45-90
	Layer $Cu_{1-x}Be_{2+x}$	0.7-0.9	0.7-0.9	0.5-0.9	0.5-0.6
	Layer BeCu + Cu(Be)	7.6-12	6-8	6.7-9.5	2.8-3.3

Table 3: Shear test results

Sample ref.	Brazing alloy	Temp./Plateau duration	Shear stress (MPa)	Mean value and standard deviation (MPa)
Braze42	STEMET 1108 ATM	770°C – 5min	76	**73 ± 4**
Braze43	STEMET 1108 ATM	770°C – 5min	75	
Braze44	STEMET 1108 ATM	770°C – 5min	69	
Braze45	GLIWICE5	770°C – 5min	84	**85 ± 2**
Braze46	GLIWICE5	770°C – 5min	87	
Braze47	GLIWICE5	770°C – 5min	84	

Pictures of broken samples are shown on figure 4.

Figure 4: Views of brazed samples after shear tests

Surprisingly, the higher shear stresses, obtained with GLIWICE5, correspond to the less homogeneous breaking pattern : ribbons are still visible on tiles, and a grey area is observed in the middle. There is no correlation between the extent of the grey surface and the shear value: in the case of Braze47, the grey surface is very limited, but the

shear value is close to the values obtained for Braze45 and Braze46.

For samples using STEMET 1108 ATM (Braze42, 43 and 44), breaking patterns are 100% grey on each side, indicating an homogeneous reaction.

CONCLUSIONS

Beryllium was successfully induction-brazed to CuCrZr tiles using two Cu-based Ag-free alloys, STEMET 1108 ATM and GLIWICE5. Optical microscope and SEM observations showed good interfaces with limited defects whatever the area observed. Brazed interfaces are composed of two reaction layers, as analysed by microprobe: a 0.5-1µm thick $Be_{2+x}Cu_{1-x}$ layer (δ-phase) close to Be and a 8-12µm thick BeCu (γ-phase) + Cu(Be) layer. Be diffuses also in braze alloy and CuCrZr. A plateau of 1min gives much lower thickness for γ-phase BeCu+Cu(Be) compared to 5min; a brazing temperature of 750°C tends also to give lower thickness compared to 770°C.

Shear tests of Be/CuCrZr brazed samples were performed: GLIWICE 5 alloy gave the highest shear strength at 85±2 MPa, versus 73±4 MPa for STEMET 1108 ATM.

REPORTS AND PUBLICATIONS

Testing of silver free braze materials with Be, Final Report,
Technical Report DTH/DR/2007/67, December 2007

TASK LEADER

Thierry BAFFIE

DRT/DTH/LTH
CEA-Grenoble
17 rue des Martyrs
F-38054 Grenoble Cedex 9

Tel: 33 4 38 78 93 79
Fax: 33 4 38 78 54 79

e-mail: thierry.baffie@cea.fr

TW6-TVM-LEAK

Task Title: INVESTIGATION OF LASER-BASED TECHNIQUES FOR LEAK LOCALIZATION, AND DEMONSTRATION OF A LASER-BASED TECHNIQUE FOR LEAK LOCALIZATION COMPATIBLE WITH ITER REQUIREMENTS

INTRODUCTION

Leak detection and localization is an identified issue during ITER vacuum vessel construction. Indeed, the vessel is wide and high, and the accepted leak rate is very low: 10^{-9}mbar.L/s. This task is aimed at investigating the ability of laser based techniques for leak detection and localisation of the ITER vacuum vessel.
At first, the ITER environment and constrains are studied, together with the leak detection existing techniques. Then the possible laser-based techniques and detection methods are reviewed, their technical limitations described. Finally the leak localization most promising method is demonstrated on the laboratory scale. Additionally the characteristics of leak localization by the selected and demonstrated laser-based technique are summarized.

2007-2008 ACTIVITIES

Bibliographic study on laser based techniques and assessment of their applicability to leak localization within the frame of ITER requirements

Laser-based spectroscopy techniques have been investigated to detect and localize 10^{-8} -10^{-9}mbar.L/s leaks in air, in the aim of ITER sectors leak testing. The leak test has to be achieved along 1 km weld, with a 10 cm spatial resolution and within one week, meaning that measurement plus instrument scanning step is accomplished within 1 minute. Leak test is done at atmospheric pressure in ambient air. Search gas is selected according to ITER leak detection; small molecule, chemically inert, not halogenated.

Few leak characteristics are first calculated and reported in order to establish scientific criteria to select the most suitable technique, in terms of sensitivity and response time. The micro leak is generated by a submicrometer default in the vacuum vessel wall. According to the Poiseuille law, the corresponding leak rate is enhanced with a high upstream pressure. The leaking molecules in the ambient air (room temperature and pressure) are slowly diffusing; the local trace gas concentration in front of the 10^{-9}mbar.L/s leak is about 1 ppbv (10^{10}molecules/cm^3) within 1 cm^3 and 1 second. The trace gas flow is clearly very weak: 10^{-9}mL/s at atmospheric pressure.

Basic laser photon – molecule interaction processes are recalled. Among them, absorption spectroscopy is clearly the most promising for the leak detection application. Then remote laser-based techniques (scanning) are primarily reviewed; but their density measurement detection limit is too high for a local 10^{-8}mbar.L/s leak detection.

Finally, laser absorption techniques involving an analyzing cell are reviewed; sensitivity, response time and compactness are studied. Obviously, CRDS (cavity ringdown spectroscopy) and OF-CEAS (optical feedback cavity enhanced absorption spectroscopy) are suitable techniques for leak detection: indeed sub-ppb detection limit (below 10^{-6}mbar partial pressure) is obtained for some molecules within a second time scale with a compact system having a 10 cm^3 volume analyzing cell. Shortly, these high finesse cavity absorption spectroscopy are promising techniques for local and fast measurement of very weak leaks in ambient air at atmospheric pressure. Performances are expected better with one of these techniques than with the helium mass-spectrometry in sniffing configuration. The implementation of the highly sensitive absorption device is foreseen as a sniffing device moving close to the wall surface, in a configuration very similar to the well-known helium mass spectrometry, with the following benefits:

- absolute measurement (no reference cell needed, no calibration),
- measurement in ambient air, gas circulation is accomplished with a small pump,
- various search gas can be selected, for example a molecule that air does not contain.

Acetylene is suggested.
- the two previous items result in a better leak detection sensitivity for a sniffing configuration in air,
- device compactness and cost-effectiveness.

As a comparison, helium mass spectrometry requires:
- a helium filled reference cell,
- high vacuum in the analyzing chamber, which means a turbo molecular pump and a rotary pump (heavy),
- air contains 5 ppmv helium,
- sniffing configuration sensitivity limited to $5{\cdot}10^{-6}$mbar.L/s, due to the 5 ppmv helium concentration in air (can be slightly improved in laboratory by noise subtraction).

Experimental leak detection by the selected (OF-CEAS) laser-based technique

Laser-based sensing methods have proved to be fast and accurate in measuring low gas concentrations. They are extensively applied to a wide variety of molecules in different fields, including environmental monitoring and industrial process supervision. More sspecifically, Optical Feedback – Cavity Enhanced Absorption Spectroscopy (OFCEAS) – a highly sensitive version of optical absorption technique - is a promising candidate for leak detection. Portable and cost-effective instruments are available (figure 1).

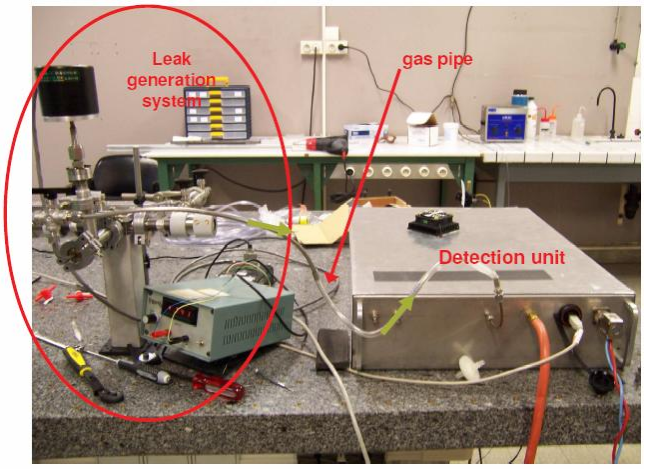

Figure 1: OF-CEAS based methane detector (right) developed by D. Romanini and coworkers, coupled to the leak generation system (left)

A laboratory experiment was undertaken to demonstrate the capability of OF-CEAS to detect a micro-leak down to the 10^{-8}-10^{-9}mbar.L/s range. The experiment was done in collaboration with the LSP, Joseph Fourier University of Grenoble (France), world-wide expert in gas trace detection. Methane was selected trace gas for the experimental demonstration for convenience. A controlled methane leak was generated by successive dilution from $2{\cdot}10^{-7}$mbar.L/s, down to $1{\cdot}10^{-9}$mbar.L/s. The leak gas concentration was successfully measured by OF-CEAS technique down to $4{\cdot}10^{-9}$mbar.L/s. The optical measurement time is about 1 s (single spectra) to 10 s (time-averaging). However the whole demonstration system response is about 40 s (still below 1 minute) due to the large gas pipe volume of the leak generation set-up. This pipe system could be easily optimized.

This demonstrated leak detection in air is 3 orders of magnitude better than the minimum leak rate detectable with helium sniffing mass spectrometry in ambient air at atmospheric pressure.

Though methane was selected for the laboratory demonstration, a search gas more compatible with ITER requirements and no present in air should be chosen for future work. However this demonstration is fully significant because OF-CEAS is not gas specific, and is adaptable to another trace gas by changing the tuneable laser diode and the optical components. Acetylene is an identified (but not unique) candidate: its strong optical absorption line will lead to lower minimum leak rate detection than previously demonstrated with methane, together with a faster response time due to a higher gas flow in the optical cell. Additionally, air does not contain any acetylene (but contains 5 ppmv of Helium and 2 ppmv methane). And this small and chemically inert molecule is suitable for leak detection.

CONCLUSIONS

Extremely weak leak localisation is an issue during ITER vacuum vessel construction and testing.
Current methods have sensitivity limitations. At first remote and local laser based techniques are reviewed to assess their ability to detect and localize leak down to 10^{-7} -10^{-9} mbar.L/s, with a cadence of 1 measurement per minute. Remote techniques are clearly to be not sensitive enough. Sniffing configuration are then studied, implying local measurements. High finesse cavity absorption techniques, cavity ringdown spectroscopy (CRDS) and optical feedback cavity enhanced absorption spectroscopy (OF-CEAS), have proved to be fast and accurate in measuring low gas concentrations, with easily handled systems. These two similar methods are the most promising for rapid micro leak detection in air.
A demonstration experiment was undertaken in collaboration with D. Romanini from Grenoble University involving an OF-CEAS system and a controlled methane leak generation system. The minimum leak detect was as low as $4{\cdot}10^{-9}$mbar.L/s within 40s, a measurement time essentially determined by the leak generation tubing system. This result with methane could be improved in sensitivity and response time by using acetylene, no present in air and suitable as a trace gas for ITER leak localization in air. Sensitivity would be then 3 orders of magnitude better by replacing helium mass spectrometry in a sniffing configuration by OF-CEAS laser technique.

REFERENCES

W. Demtröder “Laser Spectroscopy, basic concepts and instrumentation” third edition 2003, Springer

G. Berden, R. Peeters, and G. Meijer, « Cavity ring-down spectroscopy: experimental schemes and applications, » Int. Rev. Chem., 19, 565-607, 2000

J. Morville, S. Kassi, M. Chenevier, and D. Romanini, « Fast, low-noise, mode-by-mode, cavity-enhanced absorption spectroscopy by diode-laser self-locking, » Appl. Phys.B, 80, 1027-1038, 2005

D. Romanini, M. Chenevier, S. Kassi, M. Schmidt, C. Valant, M. Ramonet, J. Lopez, and M. J. Jost « Optical-feedback cavity-enhanced absorption: a compact spectrometer for real-time measurement of atmospheric methane » Appl. Phys.B, 83, 659-667, 2006

R. J. H. Pearce and M. Wykes, « Consideration of an overall acceptable leak rate for the ITER vacuum vessel sectors and how to achieve an effective test » MPVV3 meeting, Naka, 28th-30th Nov 2006

REPORTS AND PUBLICATIONS

« Investigation of laser-based techniques for ITER leak localization and selection of the most promising method with regards to ITER requirements », I. Debecker, A. Pailloux, NT DPC/SCP 08-257-A, 2008

« Demonstration of laser-based technique for leak detection and localization of ITER vacuum vessel », J. Cousin, A Pailloux, NT DPC/SCP 08-254-A, 2008

TASK LEADER

Agnes PAILLOUX

DEN/DPC/SCP/LILM
CEA-Saclay
F-91191 Gif-sur-Yvette Cedex

Tel: 33 1 69 08 65 92
Fax: 33 1 69 08 78 84

e-mail: agnes.pailloux@cea.fr

Task Title: STORAGE OF STAINLESS STEEL MATERIAL FOR VV

INTRODUCTION

In July 2006, about 85 tons of plates, forgings and tubes of ITER grade SS material, to be used for the manufacturing, welding and inspection mock-ups of the ITER vacuum vessel, were manufactured and delivered to CEA-Saclay for storing phase.

In addition, other type of parts, such filler wire coils, bars and tubes were also sent to CEA-Saclay. These 316 LN IG base materials, coming from different batches, were stored in CEA-Saclay Laboratory, and for some of them shipped to EFDA sub-contractors for sub-components or mock-ups manufacturing. This report makes an overview of performed work in this task.

2007-2008 ACTIVITIES

EFDA described the storage requirements, under the task contract. CEA managed a facility to store the different 316 LN parts in a building in CEA-Saclay laboratory.

FILLER WIRE STORAGE

The second shipping in CEA-Saclay plant concerns 316 LN filler wire diameter 1.2 mm produced by the company MAN DWE Gmbh (Germany): 250 kg of Thermanit 19/15H welding wire, 1.2 mm, wound onto unitary 15 kg coils.

Those coils were stored in CEA-Saclay. 2 coils were already shipped to VTT Lappeenranta (Finland) for performing hot cracking welding tests. In November 2008, all the remaining coils were sent to MAN DWE Gmbh.

316LN plates and forged parts storage

Plates in 60 mm thickness and 59.24 tons weight, produced by ARCELOR MITTAL (Le Creusot, France), were shipped to DCNS (Saint Nazaire, France) for VATS mock-up manufacturing. Some coupons were shipped to CNIM (La Seyne-sur-Mer, France), CEA-Saclay and Cadarache.

§ 1 plate	2550.00 mm x 5000 mm x 60 mm	6 304 Kg
§ 1 plate	2400.00 mm x 2400 mm x 60 mm	2 848 Kg
§ 1 plate	2490.00 mm x 6200 mm x 60 mm	17 582 Kg
§ 1 plate	2400.00 mm x 6000 mm x 60 mm	17 558 Kg
§ 3 plates	2550.00 mm x 5000 mm x 60 mm	18 540 Kg
§ 1 plate	2200.00 mm x 3150 mm x 90 mm	5 030 Kg
§ 1 plate	2400.00 mm x 6200 mm x 60 mm	7 220 Kg
§ 1 plate	2000.00 mm x 3000 mm x 20 mm	960 Kg
§ 1 plate	2000.00 mm x 3000 mm x 60 mm	4 010 Kg

Related to the initial tables of delivering parts, the final situation is the following:

Item						Unit	Pcs and Location	Pds remaining in Saclay
Ref:	PLATE	Pcs	Dia. mm.	Length m.	Width m.	Weight Tons		
A	20 mm for samples	1	20	2.00	3.00	0.96	DCNS	0
B	40 mm for the ribs	1	40	2.00	6.20	3.97	DCNS	0
C	60 mm for the demo shells	2	60	2.40	6.20	7.14	DCNS	0
D	60 mm for the coupon shells	1	60	2.40	2.40	2.76	DCNS	0
E	**60 mm for tube dia 812.8mm**	**1**	**60**	**2.49**	**6.00**	**7.17**	DCNS	0
F1	60mm for process qualification	1	60	2.55	5.00	6.12	DCNS	0
F2	**60mm for Exploform**	**1**	**60**	**2.55**	**5.00**	**6.12**	DCNS	**0**
F3	60mm spare	1	60	2.55	5.00	6.12	DCNS	0
F4	60mm spare	1	60	2.55	5.00	6.12	DCNS	0
G	90 mm for the rib T-pieces	1	90	2.20	3.15	4.99	DCNS	0

Item					Unit	Total	Pcs and Location	Pcs remaining in Saclay
Ref:	Cylindrical Forgings	Pcs	diam.	length	Weight	Weight		
	Unit		mm	mm	Tons	Tons		
C1	**BM shield block**	**5**	**300**	**800**	**0.44**	**2.22**	DCNS	**0**
C2	PS1 cassette housing	5	345	425	0.31	1.56	**Saclay**	5
C3	PS1 flexible housing	50	280	340	0.16	8.22	DCNS	0
C4	PS1 key	16	315	210	0.13	2.06	**Saclay**	16
C5	PS1 Inner ring	16	280	85	0.04	0.66	**Saclay**	16
C6	PS1 tube	16	150	280	0.04	0.62	**Saclay**	16
C7	outer housing	2	300	800	0.44	0.89	**Saclay**	0
C7	outer housing	8	300	800	0.44	3.55	**Saclay**	8
C8	PS1 outer plug	16	195	65	0.02	0.24	**Saclay**	16

Item						Unit	Sub-total	Pcs and Location	Pcs remaining in Saclay
Ref:	Rectangular Forging	Pcs	width	height	length	Weight	Weight		
	Unit		mm	mm	mm	Tons	Tons		
R1	**BM shield block**	**2**	**500**	**1300**	**1500**	**7.65**	**15.31**	**Saclay**	**2**
R2	PS1 manifold support	6	160	190	500	0.12	0.72	**Saclay**	6

MAN DWE Gmbh shipped to SPECITUBES Company (Samer Plant, France) 322 tubes 316 LN IG (12 x 1.0 mm, 1 791.40 Meters), and in CEA-Saclay 1 wooden box with 322 pieces (316 LN IG tube ø12x1.0 mm, 659 kg total) and 1 wooden box with 321 pieces (316 LN IG tube ø12x1.0 mm, 665 kg total).

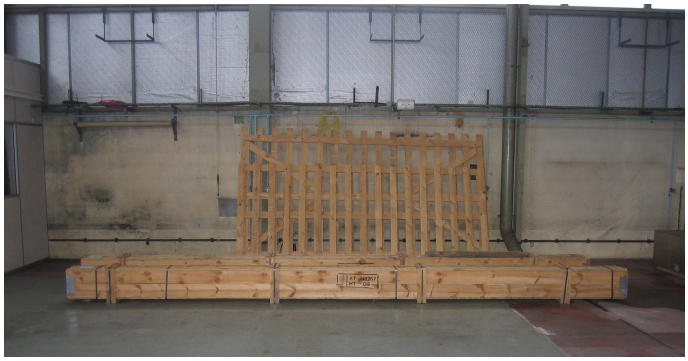

Figure 1: 316 LN IG tube ø 12x1.0 mm, inside 2 wooden boxes with dimensions 6.25 m x 0.36 m x 0.41 m and 1324 kg weight each

MAN DWE Gmbh shipped to Saclay precursors bars : 3 forged round peeled bars ø189 mm -> 2348 kg, 3 forged round peeled bars ø238 mm -> 5422 kg, 3 forged round peeled bars ø267 mm ->5826 kg.

Figure 2: precursor's bars

CONCLUSIONS

316-LN-IG stainless steel storage is effective in CEA-Saclay. Shipments to short term users are performed. Documentation is available through EFDA requirements. This status closes the task.

REPORT AND PUBLICATIONS

TW6-TVV-STORVS Task, Final Report, Ph. AUBERT, CEA Internal Report DEN/DM2S/DIR/RT/08-0004/A, December 2008

TASK LEADER

Philippe AUBERT

DEN/DM2S
CEA-Saclay
F-91191 Gif-sur-Yvette Cedex

Tel: 33 1 69 08 37 99
Fax: 33 1 69 08 66 42

e-mail: philippe.aubert@cea.fr

CEFDA05-1248

Task Title: TW5-TVD-ACCEPT: INFLUENCE OF THE CARBON EROSION ON THE ACCEPTANCE CRITERIA OF THE ITER DIVERTOR

INTRODUCTION

The CFC (Carbon Fibre Composite) monoblocks of the ITER divertor vertical target must sustain high heat fluxes of 10 MW/m^2 during 1000 s (normal operation) and 20 MW/m^2 during 10 s (off normal event).
One can expect erosion instability in normal operation in case of one faulty monoblock besides good ones due to the balanced rate between the various erosion mechanisms at different temperatures [1]. Coherent plasma parameters, which represent the worst cases of erosion in normal operation, have been taken into account to analyse the erosion behaviour of the monoblocks, the aim being to evaluate the eventual impact of these phenomena on the acceptance of the monoblocks (the monoblocks are considered thermo-mechanically compliant to a defect but this compliancy could be drastically reduced by erosion instability).
For that it was decided to investigate a 20% decrease of CFC conductivity or a defect at the CFC/Cu bond.

2007-2008 ACTIVITIES

All the calculations having been completed in 2006 and the intermediate reports published, the year 2007 was dedicated to the closure of the task with the redaction of the final report [1] and a publication at ICFRM conference [2].

CONCLUSIONS

This task has demonstrated the capability to run erosion calculations with both ANSYS (transient calculation) and CAST3M (series of steady states) and has pointed out some erosion instabilities for the studied cases (neighbour monoblock with reduced conductivity or with 90° defects) but without consequence on the acceptance criteria of the CFC monoblocks. Further investigation of critical cases could be however pursued.

REPORTS AND PUBLICATIONS

[1] J. Schlosser, INFLUENCE OF THE CARBON EROSION ON THE ACCEPTANCE CRITERIA OF THE ITER DIVERTOR, EFDA CONTRACT N°05-1248, Final report, CFP/NTT-2007.021, (2007)

[2] J. Schlosser, C. Lowry, B. Riccardi, E. D'Agata, J. Bouvet, M. Merola, Evaluation of the erosion on the CFC tiles of the ITER divertor by means of FE calculations, J. Nucl. Mater. (2009), in press

TASK LEADER

Jacques SCHLOSSER

DSM/IRFM/SIPP/GCFP
CEA-Cadarache
F-13108 Saint-Paul-Lez-Durance Cedex

Tel: 33 4 42 25 25 44
Fax: 33 4 42 25 49 90

e-mail : jacques.schlosser@cea.fr

CEFDA05-1257

Task Title: TW5-TVB-JOINOP: OPTIMIZATION OF Be/CuCrZr HIP JOINING FOR FW PANEL

INTRODUCTION

The ITER blanket-shield concept is a modular configuration mechanically attached to the vessel. It is constituted with Shield modules and First Wall (FW) panels mechanically attached on the shield blocks. A First Wall panel is constituted with a stainless steel support, a copper alloy that acts as a heat sink material and beryllium tiles that act as an armour material against the plasma. 316LN stainless steel, CuCrZr copper alloy and beryllium tiles are assembled together by diffusion welding under Hot Isostatic Pressing (HIP). The CuCrZr/316LN welding is done at 1040°C whereas Be/CuCrZr welding is done at 580°C.

The objectives of this task are to increase the performances of Be/CuCrZr joints under High Heat Flux (HHF) tests and also to improve the manufacturing techniques to satisfy the requirements for series production. To achieve these objectives, several ways have been investigated. They are:

- The anti-diffusion materials to make easier the decanning of the canister in order to reduce the cost of the last machining operations,
- Cleaning products to clean CuCrZr and 316LN materials according to the requirements for series production,
- Interlayers to reduce the formation of brittle intermetallic layers between Be and Cu and increase the performance of Be/CuCrZr joints under HHF operations,
- HIP parameters.

2007-2008 ACTIVITIES

Anti-diffusion materials

To avoid the machining of the beryllium tiles after HIPing, an anti-diffusion material is placed between the top surface of the beryllium tiles and the canister cover. To make easier the decanning operations and reduce its cost, anti-diffusion materials may be used also between the whole mock-up faces and the canister. However, the anti-diffusion material used up to now presents drawbacks such as being crumbly and also source of pollution for the Be/CuCrZr joint. To replace this anti-diffusion material, several new materials have been investigated. Most of them are thin ceramic oxide coatings such as zirconia and alumina. We also tested thin metallic sheets oxidized under air at high temperature during several hours.
The anti-diffusion materials have been tested by manufacturing several CuCrZr/CuCrZr mock-ups as shown in figure 1. The anti-diffusion materials are placed on the bottom and on the lateral faces of two small CuCrZr blocks to make easier their extraction after the HIP cycle. This first verification is completed by mechanical tests to verify the influence of the anti-diffusion material on the impact toughness of CuCrZr/CuCrZr joints.

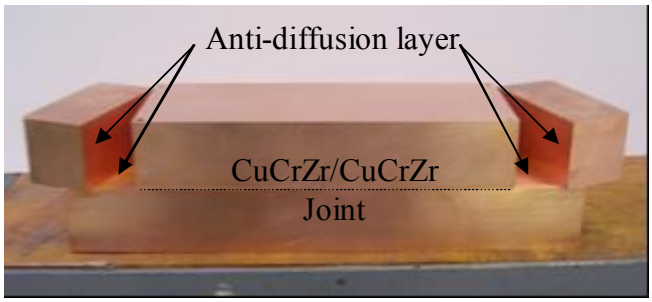

Figure 1: Mock-up constituted with a CuCrZr/CuCrZr joint to test several anti-diffusion layers

Our investigations show that the selected anti-diffusion materials enable easily the extraction of the small CuCrZr blocks. Moreover, the impact toughness of the CuCrZr/CuCrZr joints is similar to the impact toughness of CuCrZr/CuCrZr joints manufactured without anti-diffusion materials (about 75J/cm²). Thus, we conclude that these materials can replace the anti-diffusion sheet used up to now without affecting the fabrication of the Be/CuCrZr joint. This point has been verified definitively by testing one mock-up under High Heat Flux conditions (figure 2).

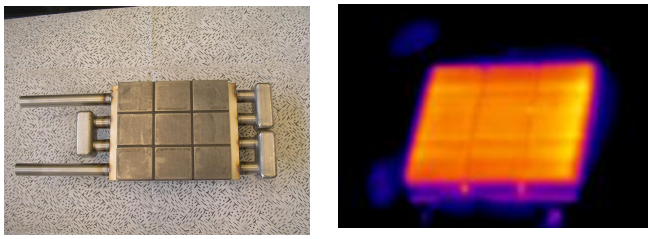

Figure 2: HHF mock-up made with one type of anti-diffusion material (left) and tested under High Heat Flux conditions (right)

Cleaning treatment of CuCrZr and 316LN materials

To replace our laboratory cleaning route by industrial routes which are compatible with the requirement for series production, several industrial cleaning products have been tested to clean CuCrZr alloy and 316LN materials.
Industrial products are mainly constituted by solvent or detergent liquids to degrease the materials and weak or strong acid liquids to remove the native oxide layer at the surface of the materials. A plasma cleaning treatment has been tested also for comparison. To validate industrial products and routes, several CuCrZr/316LN and CuCrZr/CuCrZr joints have been manufactured and tested mechanically. The joints have been manufactured by following a classical 1040°C HIP cycle, a solutionning

treatment at 980°C and an ageing treatment at 480°C. As impact toughness tests are generally the most discriminatory for joint, impact specimens with a U notch centred on the joint have been machined inside the CuCrZr/CuCrZr and CuCrZr/316LN samples. These tests were completed by tensile tests at a strain rate equal to $10^{-4}s^{-1}$. The results of the mechanical tests are presented in figure 5 and figure 6. These results were completed by metallographic examinations and XPS analyses (see [1]).

CuCrZr/316LN and CuCrZr/CuCrZr tensile results are presented in figure 3 and figure 4. In all the cases, the rupture does not occur at the joints but in the CuCrZr part of the tensile samples. It indicates that the cleaning products used in this study enable to make CuCrZr/316LN and CuCrZr/CuCrZr joints which tensile strength is limited by the tensile properties of the CuCrZr aged at 480°C.

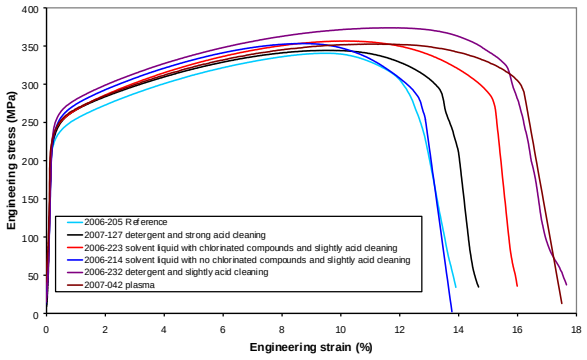

Figure 3: Tensile strength of CuCrZr/316LN joints after industrial and plasma cleaning treatments

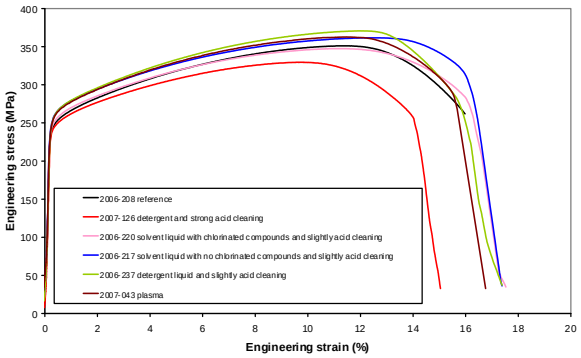

Figure 4: Tensile strength of CuCrZr/CuCrZr joints after industrial and plasma cleaning treatments

CuCrZr/316LN and CuCrZr/CuCrZr impact toughness results are presented in figure 5 and figure 6. In the case of CuCrZr/316LN joints, industrial cleaning products enable to manufacture joints with similar impact toughness compared to our reference cleaning route. A different result appears in the case of CuCrZr/CuCrZr joints where the best results are obtained when CuCrZr pieces are cleaned with plasma. As liquid cleaning is more suitable than plasma cleaning to treat large scale pieces, we proposed to use an industrial route constituted by a detergent and a strong acid liquid. In fact, this route gives slightly lower impact toughness than our reference cleaning route.

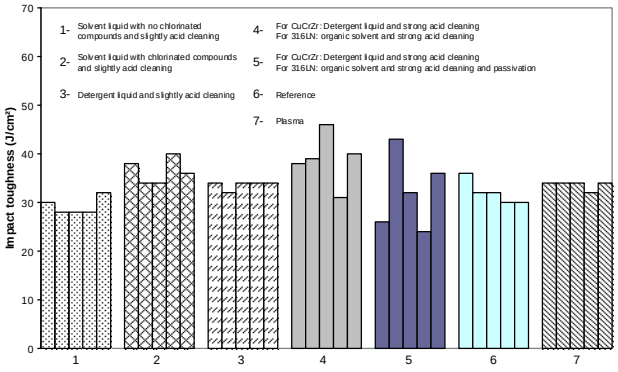

Figure 5: Impact toughness measurements performed on CuCrZr/316LN joints

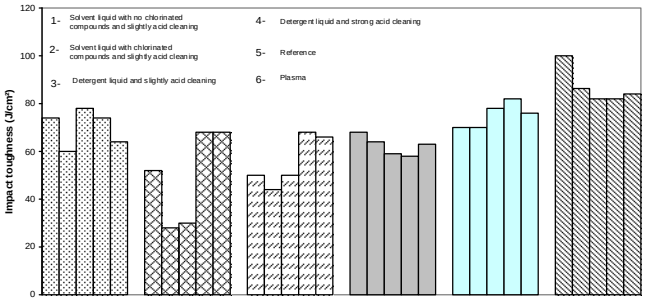

Figure 6: Impact toughness measurements performed on CuCrZr/CuCrZr joints

Interlayers

During the welding process, beryllium reacts with copper to form brittle intermetallic phases. These phases limit the performance of the mock-ups under HHF tests and it is necessary to limit or avoid their formation. To achieve this goal, we tested several metallic interlayers such as Ni, Ti, Cr, Si and Al.

To choose the best interlayers to manufacture two HHF mock-ups, we manufactured 15 small Be/CuCrZr samples by sputtering the interlayers by PVD onto the Be tiles. The diffusion welding process is performed at 580°C as for the fabrication of HHF mock-ups.

After the HIP cycle 25x25x30mm^3 samples are machined from the Be/CuCrZr joints and tested at ambient temperature by applying a rising force on one side of the beryllium tiles whereas the CuCrZr part is fixed inside holding jaws (figure 7). The force measured when the joint breaks enables the calculation of the ultimate strength of the junction R_m. R_m is defined by the ratio between the applied force and the surface area of a beryllium tile.

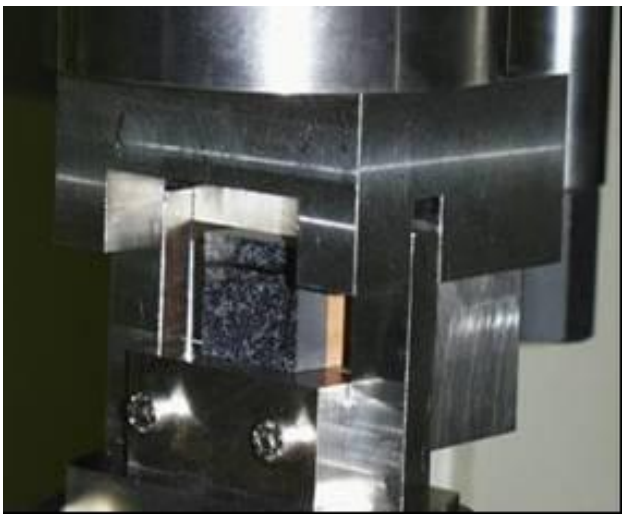

Figure 7: Photograph of a shear test performed on a Be/CuCrZr joint

Results of shear tests are presented in figure 8. On this figure we observe that Cr interlayer enables to manufacture Be/CuCrZr joints with R_m in the range 100-120MPa whereas those manufactured with Al and Ti interlayers present slightly lower strength (80-100MPa). Be/CuCrZr joints manufactured with Ni interlayer broke during the machining of the samples. Results with Si interlayer are uncertain because one sample broke during the machining operation whereas the two other samples present quite good strength of about 110MPa. In these conditions, we decided to manufacture HHF mock-ups with Ti and Cr interlayers. One interlayer-free HHF mock-up was manufactured at the same time to have a reference mock-up.

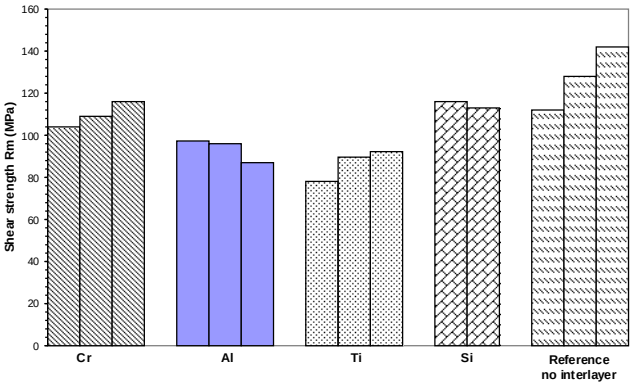

Figure 8: Shear tests results of Be/CuCrZr samples manufactured with Cr, Al, Ti and Si interlayers

The HHF mock-ups are manufactured by welding Be onto CuCrZr at 580°C and under a pressure equal to 140MPa. These parameters are kept constant during two hours before a slow cooling down phase to reach atmospheric pressure and ambient temperature. After the HIP cycle the mock-ups are machined, and the quality of the Be/CuCrZr joints are analysed by making ultrasonic tests (figure 9). Mock-ups manufactured with Cr or Ti interlayers present no defect.

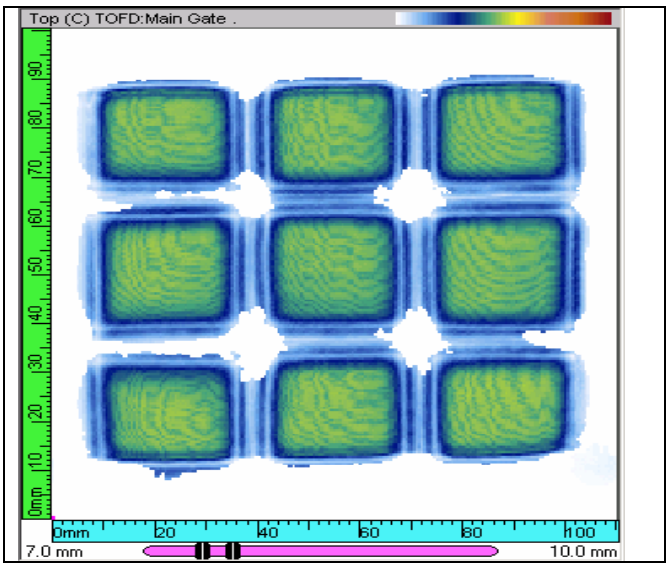

Figure 9: Ultrasonic tests of HHF mock-ups made with Ti and Cr interlayers. No defect is detected in both cases

Figure 10 shows the behaviour of mock-ups made with Ti and Cr interlayers under high heat flux tests. The best performance is obtained with Cr interlayers. A precise examination of the joints is made in the task TW5-TVB-DES2 to understand these results and improve our manufacturing techniques.

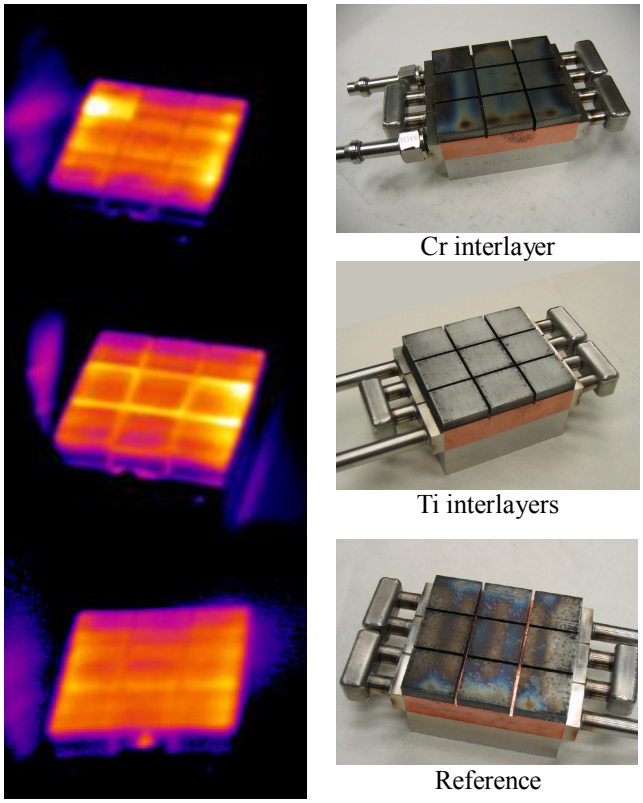

Figure 10: HHF tests of mock-ups made with Cr and Ti interlayers

HIP parameters

To reduce the stress at the Be/Cu joint during the manufacturing process, we modified the standard HIP cycle. The new cycle presents the same temperature and pressure plateau (580°C, 140MPa) as a classical HIP cycle but the variation of the pressure and the temperature during the cooling down phase were modified to put the Be/Cu joint under compression at the end of the HIP cycle. The mock-up manufactured following this new cycle is presented in figure 11. Under High Heat Flux tests, the behaviour of this mock-up is similar to that of a mock-up made with a classical HIP cycle.

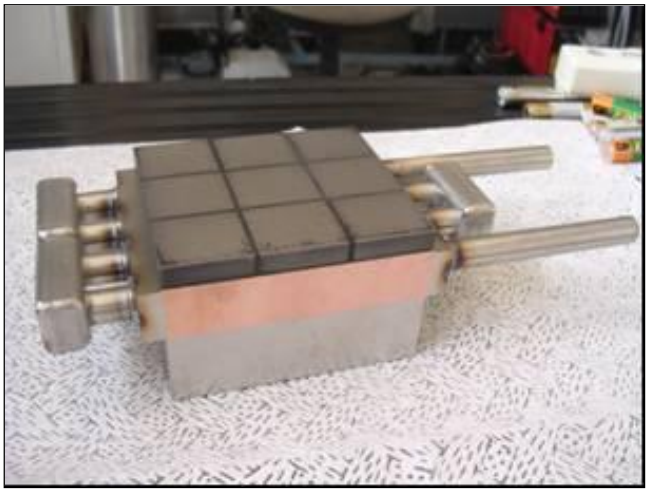

Figure 11: HHF mock-up manufactured with a new HIP cycle

Fabrication of large scale mock-ups for Thermal Fatigue tests

To finish the task TW5-TVB-JOINOP, two large scale mock-ups have to be manufactured. These mock-ups are 250mm long, 110mm width and 90mm height. They are made with nine beryllium tiles which have different sizes. Four tiles are 56x54mm², three tiles are 42x43.3mm² and two tiles are 66x66mm². As for the small scale mock-ups presented above, large scale mock-ups are constituted by a 316LN backing plate and a CuCrZr alloy cooled by 10/12mm 316L tubes. A photograph of the CuCrZr/316LN structure manufactured in 2007 is presented in figure 12.

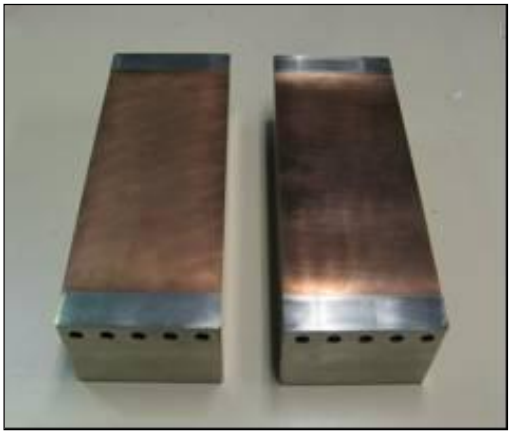

Figure 12: CuCrZr/316LN joint constituting the two large scale mock-up

As the interlayers tested in this programme gave similar results compared to free interlayer mock-ups, the completion of these large scale mock-ups was delayed up to the results of the interlayer study done in the frame of the task TW6-TVB-HIPJOIN.

CONCLUSIONS

Several routes were investigated to enhance the performance of the Be/CuCrZr joints under high heat flux tests and to improve the manufacturing techniques in accordance with the requirement for series production.
Several anti-diffusion materials were tested successfully to replace the material used up to know and placed between the beryllium tiles and the canister. Mock-ups manufactured with the new anti-diffusion material present a good behaviour under HHF tests, thus validating our choice.
Different chemical products have been tested to clean CuCrZr and 316LN materials. Some of them enable to manufacture CuCrZr/316LN and CuCrZr/CuCrZr joints with impact toughness and tensile properties as good as those obtained with our own cleaning route.
To avoid the formation of brittle intermetallic phases between Be and Cu, several metallic interlayers have been tested. Under High Heat Flux tests, Be/CuCrZr joints made with a Cr interlayer present the same behaviour than interlayer-free joints.

REPORTS AND PUBLICATIONS

P.-E. Frayssines, P. Bucci, E. De Vito, E. Rigal , P. Lorenzetto, “Cleaning surface treatments for the fabrication of ITER First Wall panels by HIP” International Conference on Fusion Reactor Materials, Nice, 2007. To be published in Journal of Nuclear Materials (2009), doi:10.1016/j.jnucmat.2008.12.191

P-E. Frayssines, O. Gillia, E. DE Vito, B. Oresic, J-M. Leibold, and A. Montani “Optimisation of Be/Cu alloy HIP joining for first wall panels”, TW5-TVB-JOINOP, final report no. DTH/DL/2007/72

TASK LEADER

Pierre-Eric FRAYSSINES

DRT/LITEN/DTH/LTH
CEA-Grenoble
17 rue des Martyrs
F-38054 Grenoble Cedex 9

Tel : 33 4 38 78 28 59
Fax : 33 4 38 78 54 79

e-mail : pierre-eric.frayssines@cea.fr

CEFDA05-1293

Task Title: TW5-TVD-NDTEST1: UPGRADE OF THE SATIR TEST BED FOR INFRARED THERMOGRAPHIC INSPECTIONS CONSTRUCTION PHASE

INTRODUCTION

The high technology components used in plasma fusion devices, especially high heat flux Plasma Facing Components (PFC), require an efficient power exhaust capability. This characteristic can be only guaranteed by a very high level of quality control through a rigorous inspection method. Among all Non-Destructive Examinations (NDE), active infrared thermography is recognised as a functional inspection technique available today for testing the cooling performance of many structures involved in heat transfer. In 1998 an infrared thermography test bed so-called SATIR (Station Acquisition Traitement Infra Rouge) based on internal thermal excitation was developed by the CEA to assess the acceptability of high heat flux PFC prior to their installation into a fusion machine. It is a functional non-destructive examination, which gives global information about the soundness of the thermal path thus being a fast and economical way to check high heat flux PFC. Within the procurement package of the ITER Divertor (17.P1 17.P2), the SATIR diagnostic has been identified as the basic test to decide upon the final acceptance of the PFC. In order to check the Composite Fiber Carbon monobloc targets, a new SATIR diagnostic concept was calculated and designed in 2006 [1] and has led to the following outcomes:

i) To increase the water velocity inside the tested component (10m/s).
ii) To minimise the test time needed to check each component.

2007-2008 ACTIVITIES

TEST BED DESCRIPTION

The principle of SATIR test is to generate successively a hot and a cold-water front in the cooling channel of the elements, in order to measure the surface temperature evolution. A cooled infrared digital camera is used to detect zones where heat exhaust is not sufficient. Defects like braze voids are detected by a slower temperature response of the surface during transient. Geometry tolerances and the material properties dispersion play a major role in the determination of acceptance criteria. In case of serial control, two components are tested in parallel with a reference. A DTref criterion is defined with respect to the reference. The detailed principle of SATIR facility and DTref Criterion were subject of many papers [2, 3].
Within the work on acceptance criteria task, which was carried out by EU and the ITER International team, SATIR inspection has been identified as the basis test to decide upon the final acceptance of the Divertor PFCs [4].

However, the ITER Divertor PFCs pose new challenges for the following reasons:

The CFC thickness is 2-3 times higher than any existing component manufactured or being manufactured so far either within the ITER project or within domestic projects.

DESCRIPTION OF THE IMPROVEMENTS

The following section presents a description of implemented sub systems (figure 1):

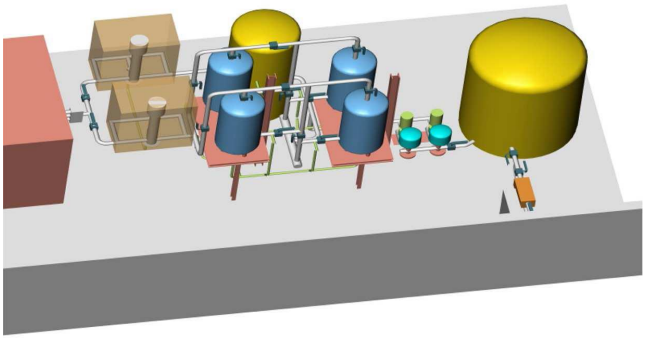

Figure 1: SATIR test bed sub systems

New Heating Sources: The capacity of the new heating source was designed for 8 successive tests on ITER Divertor Qualification Prototype without re-heating; taking into account that normally re-heating is done on line between two tests within time duration of 12min. The total volume is 4 times 0.3m^3 (figure 2). The water heating power is 12KW for each tank for a maximum temperature of 120°C. [Supplier: Charot; Reservoir volume: 0.3m^3; Heating power: 12 KW]

Figure 2: New heating sources

Water Buffer Tank: SATIR test bed has to be freed from the pressure fluctuations induced by the Cadarache building open loop water network (up to ~20% fluctuations measured). This is the main function of the water buffer tank (figure 3), which has the following specifications:
[Supplier: Friedlander; Total volume of 3.75m^3;
Available volume: 3.25m^3, regulated water level by a UT probe; refilling time of 10 min, compatible with water TORE SUPRA network].

Figure 3: Water buffer tank

Feeding pumps: In order to avoid a depressurization of the 2 water sources tanks and a boiling phase in the hot water tanks, a safety device was installed between the buffer tank and the 2 water sources: the feeding pump has the role of rebuilding and maintaining a constant pressure of 5 bars in the network at the inlet of the 2 water sources (figure 4). The safety device consists of 2 parallel pumps with a variable speed controller on each one, and 2 additional bladder tanks. The specification of feeding pumps is the following: [Supplier: Flygt; P_{in}=atmospheric pressure, P_{out}=4-5 bar at nominal=10m^3/h].

Figure 4: Feeding pump: safety device

Scale inhibitor: In order to prevent scale appearing into the heating tanks and pipes, which would reduce the global flow rate and would damage pipes and connectors, an electromagnetic process device (figure 5) was implemented at the inlet of the general water network upstream the water buffer tank. [Supplier: Rimeau Compagny].

Principle: Crystal nucleation sites are forced to appear in the centre of the fluid vein instead of growing on the impurities of pipe walls or tank walls. Crystallization is forced in the aragonite CaCO3 form (orthorhombic, non adherent to wall) instead of the calcite form (rhombohedral), which is responsible for scale.

Figure 5: Electromagnetic process device

In the previous version SATIR test bed possessed a single injection stage at 10 bar shared by the 2 water sources, hot and cold one. Within the framework of this contract, the facility was transformed into 2 independent injection lines, a hot and a cold one, synchronized by an industrial programmable logic controller. This upgrade allows to protect the pumps against the repetitive thermal shocks, which might degrade lifetime. This concept is based on 2 continuously operated pressurized stages where each injection stage is designed to be operated all day long under pressure with the steepest switching injection time in the monoblocks. SATIR process has been simplified using only one thermal shock. The thermographic analysis is done on the unique thermal transient. This allowed to reduce both size of infrared films and requested tests time.

Hot water line: The hot water injection line allows to obtain rapidly a steady state to 100°C (figure 6).
The technical specifications are following: [Supplier: Flygt pump with 9 stages; Performances: flow rate 8 m^3/h, 5 <P< 10 bar].

Figure 6: Hot water injection line

Cold water line: In order to obtain the controlled steepest thermal shock for the cooling cycle, a more powerful pump with PID control was implemented on the cold water line (figure 7). The technical specifications are following: [Supplier: Flygt pump with 12 stages; Performances: 10 m^3/h, 5 <P< 12 bar; P_{in} regulated; Response time < 1s].

Figure 7: Cold water injection line

Pipe diameter: In order to provide enough water flow rate for the both hot and cold sources, the feeding pipes diameter was increased to 2 inches.

Cooling unit: A new cooling unit more reliable and more industrial – using tubular thermal exchanger - will be implemented on SATIR test bed. The technical specifications are following: [Supplier: YORK; Performances: Cooling power=27KW instead of 13KW before; Total volume=1m^3; cooling time after each shot=5 min].

In order to remove the relay control, although it is intrinsically cheap - because the number of servo hydraulic devices to control has significantly increased - an industrial programmable logic controller with a graphic interface (figure 8) was installed. This technology of command control is already used in the frame of TORE SUPRA machine. [Supplier: Schneider; Programming: Platon Company]

Figure 8: Graphic interface of programmable logic controller

TEST BED VALIDATION

ITER Divertor PFC-like experimental test:

2 tubes - Divertor PFC-like (internal diameter 12mm; tube of length 1500mm) - were installed in parallel on the SATIR test bed to assess the maximum value of water flow rate. The maximum water flow rate reached 5.52m^3/h for each tube, corresponding to 13.5m/s. A workable flow rate in order to keep a reasonable reliability of the test bed, was estimated to 4m^3/h for each tube, corresponding to the ITER requirements of 10m/s.

Improvement of the defect detection capability:

This study was carried out on ITER monoblock samples (figure 9). The components were installed on 3 parallel lines. This study was carried out on one ITER CFC monoblock including smallest calibrated defect (position 0° - extension 20°), this CFC sample was tested with 6 water flow rates: 1, 2, 3, 3.5, 4, 5m^3/h.

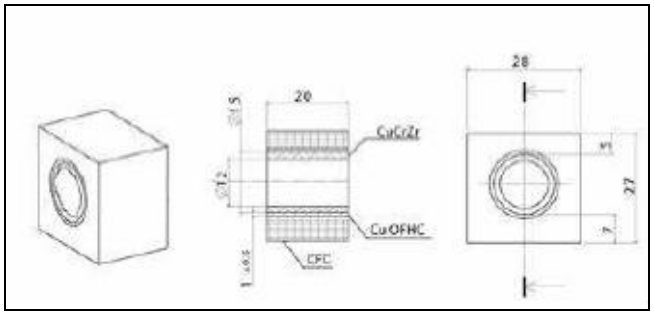

Figure 9: CFC_ITER monoblock samples

The figure 10 clearly shows the water velocity effect on the detection sensitivity for a calibrated defect of 0_20°. A nolinearity phenomenon, for elevated water flow rates, has been observed on this CFC monoblock sample.

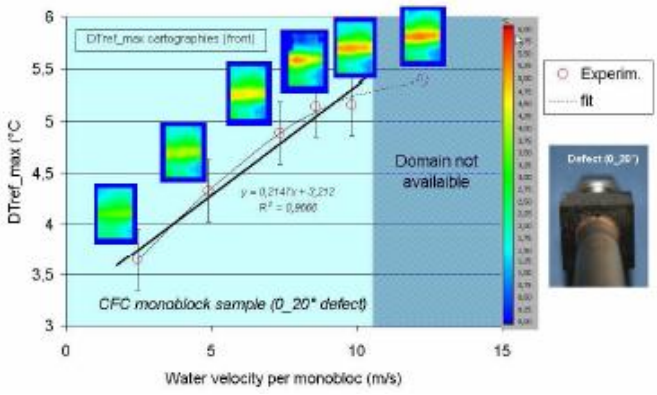

Figure 10: Water velocity effect on the detection sensitivity

The figure 11 presents a cumulated gain of detection performances of ~38% for 10m/s (4m^3/h).

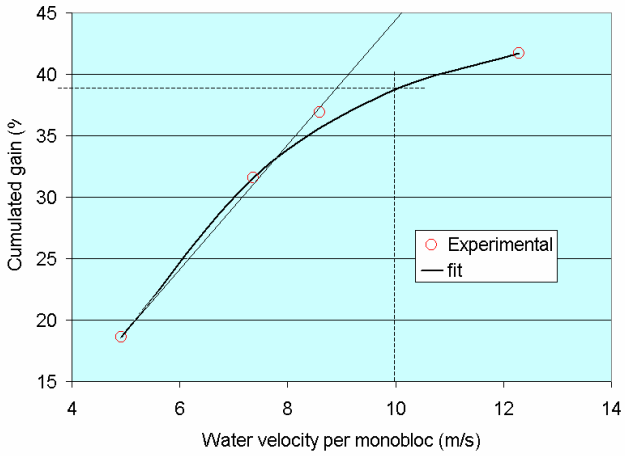

Figure 11: Cumulated gain of detection performances

Figure 12: ITER_SATIR test bed

Minimise the time required to test each component

For the ITER CFC monoblock, the size of infrared films and the requested test time were reduced, respectively 30% and 51% between $1m^3/h$ and $4m^3/h$, considering only one cooling cycle.

Table 1: Experimental conditions for ITER monoblock

ITER_Q	Hot cycle			Cold cycle			Infrared film		
(m^3/h)	Time (s)	Pressure (b)	Temp.(°C)	Time (s)	Pressure (b)	Temp. (°C)	Duration (s)	Size (Mo)	%Gain
1	30	8	101	30	8	25	32	247	0
2	25	8	101	25	8	25	27	210	15
3.5	22	10	98	22	10	25	24	172	30
4	22	10	106	22	10	25	24	172	30
5	15	12	102	15	12	25	18	135	45

CONCLUSIONS

The large modification of SATIR test bed, dedicated to test the ITER Divertor PFCs, is now completed and validated (figure 12). The first assessments of detection performances correspond roughly to the finite elements calculation carried out within the previous studies framework [1].

We can summarize the main results below:

- The increasing of global water flow rate improves in a significant way, the sensitivity of SATIR diagnostic: 38% of improvement with a water velocity of 10m/s ($4m^3/h$) in each ITER element with a better definition of defect contour. For reliability reasons of the SATIR test bed, the global water flow rate will be limited to $8m^3/h$ on 2 lines for the tests on the ITER qualification prototypes.

- In order to reduce the needed test time between each thermal excitation, the water heating power was increased by a factor 6 (2KW to 12KW each). Besides, SATIR operation with only one cycle allowed the reducing of the requested test time of 51%.

REFERENCES

[1] Contract CEFDA 05-1243 “Upgrade of the SATIR test bed for infrared thermographic inspections – Design phase”

[2] “Advanced Qualification Methodology for Actively Cooled High Heat Flux Plasma Facing Components” p.1682-1689, Nucl. Fusion 47 (2007)

[3] “Development of an original active thermography method adapted to ITER plasma facing components control” Fusion Engineering and Design 75-79 (2005) 401-405

REPORTS AND PUBLICATIONS

“An operational non-destructive examination technique for ITER Divertor plasma facing components” – ICFRM-13, 2007, Nice –F

“Evaluation of plasma facing components thermal performance by infrared thermography” – InfraMation 2008, Reno -USA

TASK LEADER

Alain DUROCHER

DSM/IRFM
CEA-Cadarache
F-13108 Saint-Paul-Lez-Durance

Tel : 33 4 42 25 62 24
Fax : 33 4 42 25 43 54

e-mail : alain.durocher@cea.fr

CEFDA05-1308

Task Title: TW5-TVB-DES2: DESTRUCTIVE EXAMINATION OF FIRST WALL PANELS AND MOCK-UPS

INTRODUCTION

ITER First Wall (FW) panels are the innermost part of the ITER reactor. One of their functions is to behave as a protective armour against the plasma. Be tiles, bonded on the plasma facing surface of the panels by Hot Isostatic Pressing (HIP), a welding technique tested for panels fabrication, are supposed to bring such properties. However, Be is known to have a low solubility with a lot of elements (including Cu), which is harmful for the mechanical life of the junctions. It has been proposed to insert interlayers of diverse nature between Be tiles and Cu alloy heat sink substrate, in order to minimize the detrimental effect of interface Be compounds.

In order to point out the effects of the HIP procedure and the High Heat Flux (HHF) tests, scanning electron microscope (SEM), ion beam analyses (IBA) and wave-length dispersion spectroscopy (WDS) have been achieved. This work completes a previous study of a batch of junctions, a number of which did not pass any HHF tests, contrary to the junctions analysed in the present study.

2007-2008 ACTIVITIES

EXPERIMENTAL CONDITIONS

Samples of 1 cm^2 (~1 mm thick) have been extracted from the mock-ups, polished, and protected from air oxidation with a varnish layer. This layer is easily removed with acetone before processing the analyses.

SEM analyses have been achieved on a FEG LEO-1530 microscope (Zeiss company).

IBA observations have been performed in Pierre Süe Laboratory of CEA-Saclay. A Van de Graaf high energy accelerator is used to beam a micro-focussed stream of 3 MeV $^3He^+$ particles onto the samples. The best possible focussing is ~1 µm diam., which is necessary in this study, due to the small size of the junction (optic microscopy shows 5-50 µm thickness depending on the samples).

WDS analyses have been performed on a CAMECA SX50 microprobe equipped with 4 vertical spectrometers. All analyses have been achieved using an energy of 15 kV and a current of 200 nA.

The nuclear reaction used for the detection of Be is $^9Be(^3He^+,p)^{11}B$. Heavier elements are detected using the X-ray emission produced by the electronic interaction occurring between atoms and $^3He^+$ particles.

The analysed areas have different sizes and shapes, depending on the junction appearance near the analysis spot and on the optimization of the acquisition times. The area analysis was chosen to be lower than about 15000 μm^2 to minimize acquisition time, and larger than about 5000 μm^2, to get enough signal for later quantitative processing. The area has always been centered on the Be//Cu junction.
Characteristics of the analysed mock-ups have been summarized in table 1.

Table 1: The analysed mock-ups

Mock-up	Be//Cu junction type	HIP temp.
PH/S-43J	Be/Cr//Cu	580°C
PH/S-44J	Be/Si//Cu	580°C
PH/S-45J	Be/Ti//Cu	580°C
PH/S-46J	Be//Cu (reference junction)	580°C
PH/S-47J	Be//Cu (reference junction with thicker compliant layer than PHS-46J)	580°C
PH/S-54J	Multilayer junction	T1<T2<580°C
PH/S-55J	Multilayer junction	T2
PH/S-62IR	Multilayer junction	580°C
PH/S-64IR	Multilayer junction	580°C
PH/S-17J	Be/Al//Cu	580°C
PH/S-41J	Be/Ti//Cu	580°C

EXPERIMENTAL RESULTS

Interlayer-free Be//Cu junctions

All interlayer-free mock-ups (also called reference junctions) show a small diffusion layer. A SEM image of this reaction zone is presented on figure 1.

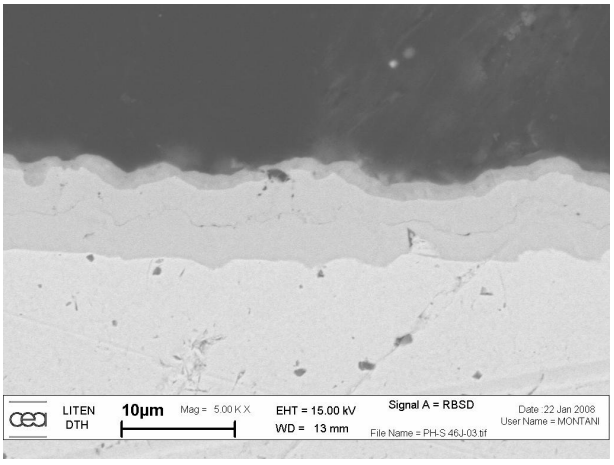

Figure 1: SEM imaging of PH/S-46J

On figure 2, the IBA image shows the same thin layer (10 µm) as observed on figure 1, which is the result of the interaction of Be and Cu, leading to brittle intermetallics. The IBA quantitative results allow to assess that this layer is composed of $BeCu_2$ intermetallics, generated by the HIP process and the HHF tests.

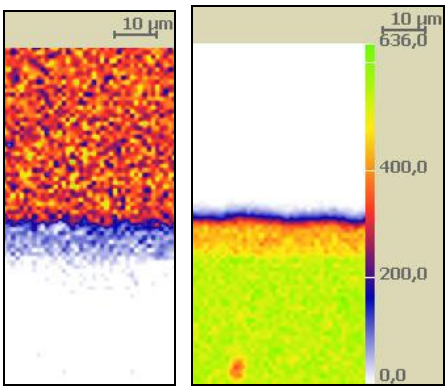

Figure 2: IBA imaging of PH/S-46J Be//Cu junction (to the left, Be and to the right, Cu)

"One compound"-based junctions

Several junctions based on "one element" interlayer have also been characterized: interlayers were either composed of PVD-deposited Cr, Si, Ti or Al.
The precise observation of the junctions shows a wide array of behaviour dependent on the nature of the interlayer.

For example, the Cr-based junction reveals a columnar structure (figure 3) with sharp borders and "channels" going through the layer. Though the columnar structure of the Cr layer does not prevent Cu and Be to be in contact, it does not lead to the same situation as a direct Cu/Be junction. This observation is confirmed by IBA results (figure 4). While there is a "diffusion" of Cu in the Cr interlayer, and of Cr in Be tile, no interaction between Cu and Be can be emphasized. Thus, Be is rather well confined by the Cr layer.

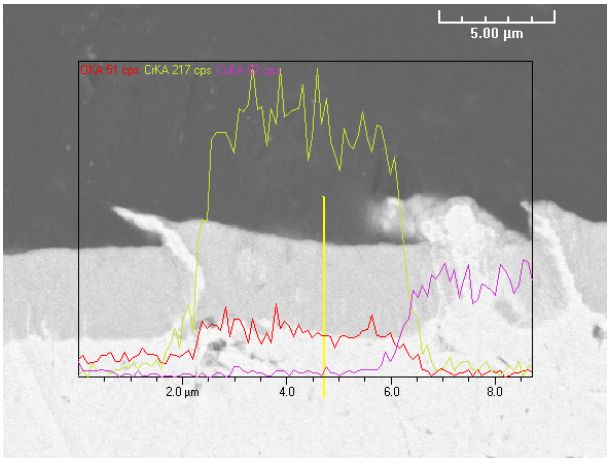

Figure 3: EDS concentration profiles of PH/S-43J junction (red: O, yellow: Cr, purple: Cu)

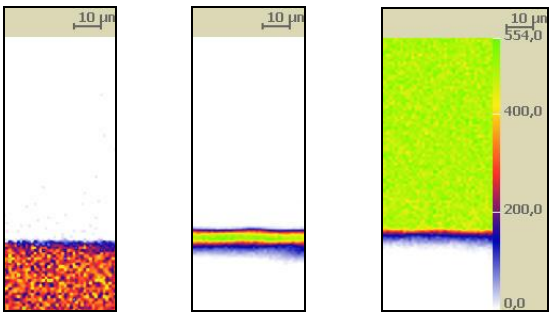

Figure 4: IBA imaging of PH/S-46J Be//Cu junction (to the right, Be, in the centre, Cr and to the right, Cu)

The interface itself contains 9% Be, 64% Cr and 27% Cu. Be is detected in the Cr interface and probably reacted with Cr in the first half of the Cr layer to form a mix of Be and probably $CrBe_{12}$ compounds. Cu is almost not detected in the EDS concentration profile; this may be due to the specific localization of Cu in the Cr layer. Be does not reach the Cu substrate while Cu fills the numerous channels through the Cr layer.
As opposed to the Cr-based junction, the Si junction is wide, as seen on figure 5.

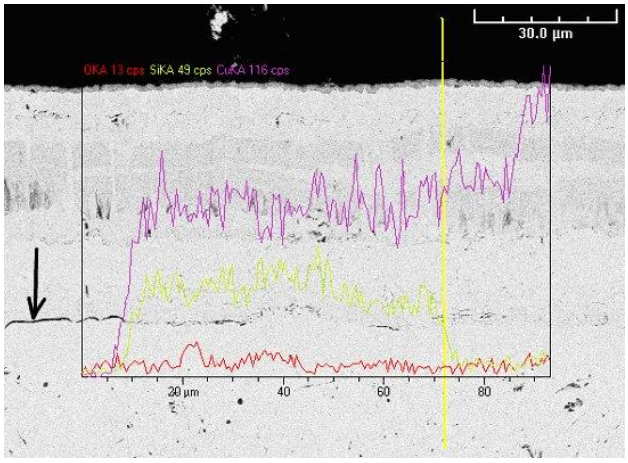

Figure 5: SEM image and concentration profiles of PH/S-44J Be//Cu junction (red: O, yellow: Si, purple: Cu)

We observe a broad diffusion of Be (reaction zone of about 60-70µm) through the junction – as shown in IBA imaging results, on figure 6.

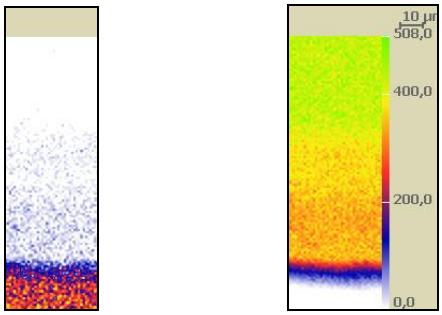

Figure 6: IBA results for PH/S-44J Be//Cu junction (to the right, Be and to the left, Cu)

This reaction zone is the result of the HIP process and the HHF test that heat periodically the Be//Cu interface at high temperature. EDS concentration profiles also show that Si concentration takes two distinct levels (this is also pointed out by the examination of the SEM image). The first one is measured between 0 and 50 µm and the second one is measured between 50 and 70 µm. This result is in good agreement with the IBA concentration profiles on figure 7, showing also two concentration levels for Cu (as Si is a light element it cannot be detected by IBA). A crack is located at the boundary between unaffected Cu and the Si-based layers on the SEM image.

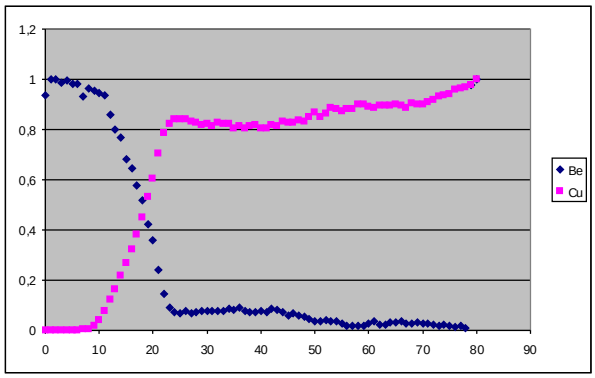

Figure 7: IBA concentration profiles of PH/S-44J junction

Here we can also underline the complementary aspects of both techniques: IBA allows the detection of Be but Si, EDS (at least our equipment) allows the detection of Si except Be.

Another interesting case is the PH/S-41J Ti-based junction. In that case, several reaction zones are clearly observed (figure 8).

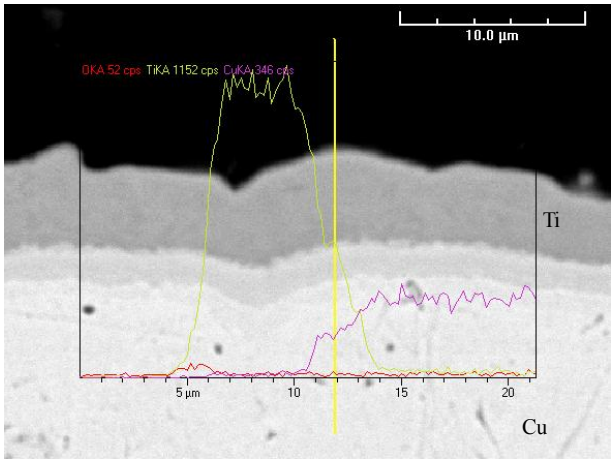

Figure 8: SEM image of the PH/S-41J junction (red: O, yellow: Ti, purple: Cu)

WDS analysis results are presented on figure 9. As stated above no Cu is present near or within the Ti/Be layer. Moreover, it shows that Be has been confined in this region and is not part of the compounds. According to EDS quantitative analyses, it seems that there is a superposition of several Ti_xCu intermetallics, from Ti to Cu, and in particular, Ti_2Cu and Ti_4Cu.

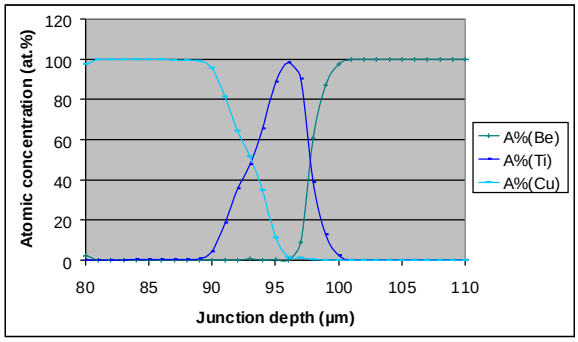

Figure 9: SEM image of the PH/S-41J junction

Multilayer-based junctions

Some junctions have been made by using multiple layers of PVD –deposited materials. The aim of this work was to reduce the amount of Be intermetallics by reducing the HIP temperature.

PH/S-54J, 55J and 62IR - For example, a series of junctions made at three different HIP temperatures have been manufactured and tested and the SEM imaging of these junctions after the HHF tests is shown on figure 10. PH/S-54J and PH/S-55J have similar junction thicknesses, while PH/S-64IR shows a thicker interaction zone. Thinner zones are observed at lower temperatures.

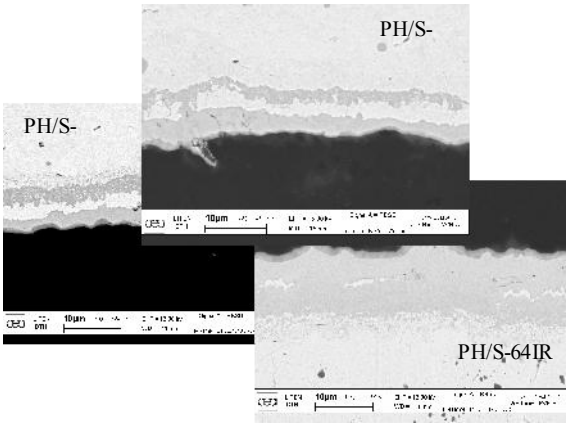

Figure 10: SEM imagse of Cu/Ni based junctions

PH/S-62IR - A SEM image of this junction is shown on figure 11. A columnar structure is observed, as for PH/S-43J junction described above. Some cracks have been formed through the Cr layer, filled either with Cu or unfilled.

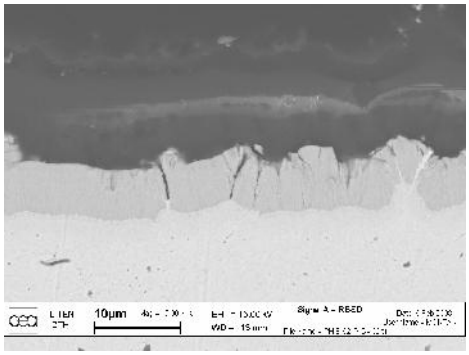

Figure 11: SEM image of the PH/S-62IR junction

CONCLUSIONS

Hipped Be//Cu junctions have been characterized using complementary analyses techniques. SEM, EDS, WDS, combined with ion beam analysis techniques have been confronted all together in order to get the necessary chemical and structural information from the studied junctions. This work demonstrates how it is possible to obtain precise information from Be//Cu junctions by combining the results of the different analyses techniques used in this study and highlights their complementarity.
As far as the results are concerned, the main results obtained on the analysed junctions are given below.
On the reference junctions, the interaction of Be and Cu during the HHF tests leads to a 10 µm thick layer of brittle intermetallics identified as probably $BeCu_2$.
The comparison of PH/S-43J and PH/S-62IR shows that thicker Cr interlayer leads to more defaults, porosity and/or paths in the layer, which may weaken the junction with regards to the HHF tests.
As observed before, Ti-based interlayers are good for Be confinement. In particular, the behaviour of Ti in the PH/S-41J mock-up leads to the formation of thin Ti intermetallic layers with a decreasing Ti ratio while going into the Cu substrate. Even if it is a superposition of a series of definite compounds it looks like a diffusion profile.
The Si-based junction has a large and complex reaction zone of about 60 µm, and Be is detected throughout the whole reaction zone. The observed crack is close to the frontier between this reaction zone involving Si, Cu and Be, and the "unaffected" Cu substrate. This might be due to the difference between physical properties of both layers, e.g. hardness and thermal expansion, and may be confirmed by later hardness measurements.
The observations of the multilayer-based junctions allowed to confirm that a reduction of the HIP temperature favour a reduction of the thickness of the Be-Cu interaction, which is detrimental as far as the Be//Cu welding is concerned.

REPORTS AND PUBLICATIONS

"Destructive examination of first wall panels and mock-ups Be//Cu junction analysis of eight selected mock-ups", Intermediate report, E. De Vito and A. Montani, DTH/DR/2008/58 (april 2008)

ACKNOWLEDGEMENTS

LCPEM laboratory wish as to thank P. Süe Laboratory for the access to IBA facilities, and particularly Dr H. Khodja for the provided help in using the facilities and data processing.

TASK LEADER

Eric DE VITO

DRT/DTH/LCPEM
CEA-Grenoble
17 rue des Martyrs
F-38054 Grenoble Cedex 9

Tel: 33 4 38 78 28 87
Fax: 33 4 38 78 52 73

e-mail: eric.de-vito@cea.fr

CEFDA05-1309

Task Title: TW5-TVB-INMOCK2: MANUFACTURE OF FIRST WALL MOCK-UPS FOR IN-PILE EXPERIMENT

INTRODUCTION

The ITER blanket-shield concept is a modular configuration mechanically attached to the vessel. It is constituted with Shield modules made with stainless steel and First Wall (FW) panels mechanically attached on the shield blocks. A First Wall panel is constituted with a stainless steel support, a copper alloy that acts as a heat sink material and beryllium tiles that act as an armour material against the plasma. 316LN stainless steel, CuCrZr copper alloy and beryllium tiles are assembled together by Hot Isostatic Pressing (HIP).

The objective of this task is to manufacture 15 First Wall mock-ups for irradiation experiments in order to check the effect of neutron irradiation on the strength and fatigue behaviour of the joints constituting a FW panel (316LN/CuCrZr and CuCrZr/Be joints). The fabrication of the 15 mock-ups is divided in two series of 9 and 6 mock-ups. The First set of mock-ups is 130mm long, 56mm wide and 56mm thick. They are manufactured with two 56x56mm² beryllium tiles. The second set of mock-ups is 130mm long, 50mm wide and 56mm thick. They are fabricated with 56x50mm² beryllium tiles. Their fabrication depends mainly on the on-going development work programme of the tasks TW5-TVB-JOINOP and now, TW6-TVB-HIPJOIN.

As several difficulties were encountered during the manufacturing or during the high heat flux tests of the small scale mock-ups fabricated in the frame of the tasks TW5-TVB-JOINOP, the fabrication of all INMOCK mock-ups have been delayed. In this paper, we present only the fabrication and the results of the high heat flux tests of the first series. The second series is almost fabricated and we are waiting for the interlayer results of the task TW6-TVB-HIPJOIN to manufacture the last Be/CuCrZr joints. According to our working plan, all the INMOCK mock-ups will be fabricated before July 09.

2007-2008 ACTIVITIES

MATERIAL SPECIFICATIONS FOR THE FABRICATION OF THE MOCK-UPS

The type and the chemical composition of the main materials used for the fabrication of the INMOCK mock-ups are presented in table 1, table 2 and table 3. 316LN material used to manufacture the mock-ups is a special heat supplied by AREVA whereas CuCrZr alloy is provided by KME Europa.

Table 1: Chemical composition of 316LN stainless steel material

Wt%	C	Ni	Cr	Mo	S	P	Si	Mn	N2
ITER	<0.03	12-12.5	17-18	2.3-2.7	<0.025	<0.035	<0.5	1.6-2	0.06-0.08
316LN	0.027	12.210	17.530	2.455	0.001	0.024	0.305	1.845	0.069

Table 2: Chemical composition of CuCrZr copper alloy

Wt%	Cu	Cr	Zr
ITER	Remainder	0.6-0.8	0.07-0.15
CuCrZr	99.2	0.65	0.11

Table 3: Manufacturer specification for the chemical composition of S65C beryllium grade (from ITER material handbook)

Max (Wt %)	Be	BeO	Al	C	Fe	Mg	Si	Other metal impurities
S65C	99	1.0	0.06	0.1	0.08	0.06	0.03	0.04

FABRICATION PROCESS OF INMOCK MOCK-UPS

Fabrication of the bi-metallic CuCrZr/316LN support

After the machining operations, all the pieces are controlled accurately to verify if their sizes and their mean roughness are under the machining specifications. Then the pieces are thoroughly cleaned and assembled inside a canister.

The standard HIP cycle used to manufacture the bi-metallic support of the mock-ups is presented in figure 1. The diffusion welding plateau is 2 hours long and is made at 1040°C and 140MPa.

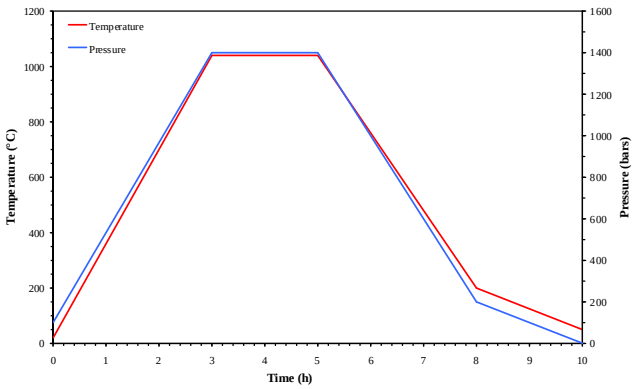

Figure 1: Theoretical HIP cycle to weld by diffusion CuCrZr and 316LN materials

After the HIP cycle, 316LN/CuCrZr supports are submitted to a thermal treatment to restore the CuCrZr mechanical properties. All the mock-ups are heat treated at 980°C during about one hour and cooled quickly at about 60°C/min to freeze the solid solution of Cr and Zr inside the copper matrix. The solutionning heat treatment applied to the first series of INMOCK mock-ups is presented in figure 2 whereas the solutionning heat treatment applied to the second series is presented in figure 3.

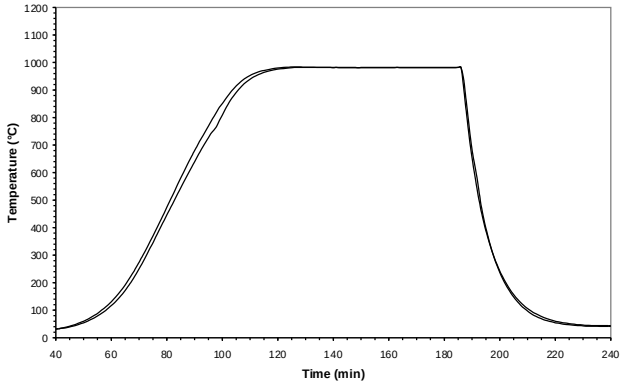

Figure 2: Solutionning heat treatment applied to the first series of INMOCK mock-ups

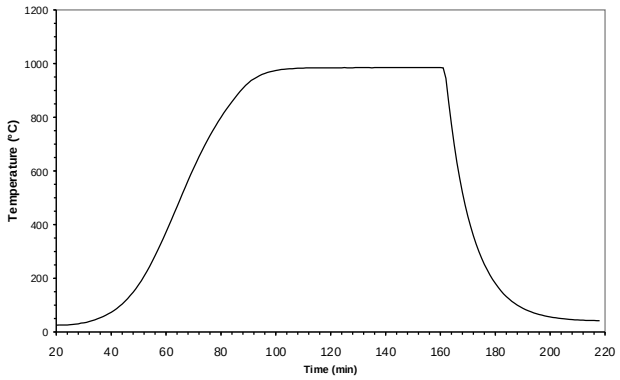

Figure 3: Solutionning heat treatment applied to the second series of INMOCK mock-ups

After the solutionning heat treatment the mock-ups are machined. A photograph showing the second series of INMOCK mock-ups after the machining operation is presented in figure 4.

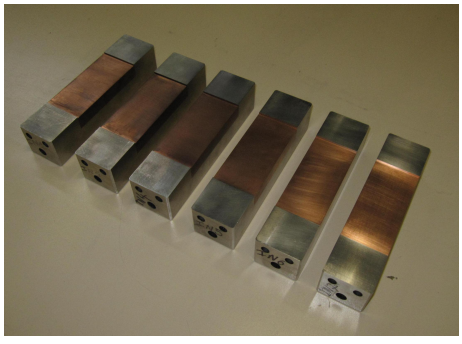

Figure 4: The second series of INMOCK mock-ups after the solutionning heat treatment

Fabrication of Be/Cu joints (first series of mock-ups)

As for the fabrication of CuCrZr/316LN joints, the beryllium tiles and the CuCrZr surfaces are size controlled and thoroughly cleaned before their assembly.

The beryllium tiles and the CuCrZr heat sink alloy are welded by diffusion at 580°C and under 140MPa. These two parameters are kept constant during two hours to obtain a joint with good mechanical properties and also to confer to the CuCrZr alloy mechanical strength that fulfils the ITER requirements [1]. According to the mechanical and high heat flux results obtained in the task TW5-TVB-JOINOP, six INMOCK mock-ups have been manufactured with different interlayers whereas the last three mock-ups of the first series have been made without interlayers to make reference mock-ups. A photograph of these mock-ups after their fabrication is shown in figure 5. The last six mock-ups that shall be fabricated in this task will be fabricated soon according to the interlayer results obtained in the task TW6-TVB-HIPJOIN.

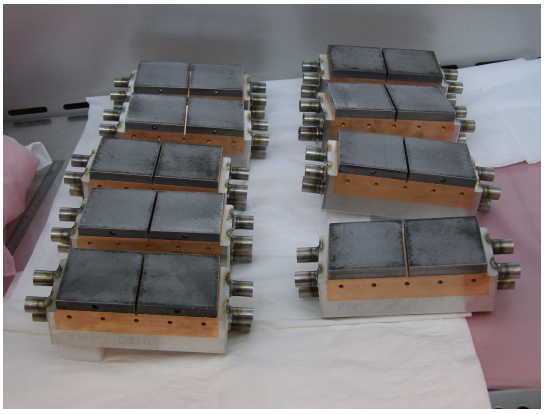

Figure 5: First series of INMOCK mock-ups

After their fabrication, the mock-ups shown in figure 5 have been tested under high heat flux. IR image of one INMOCK mock-up taken during the tests is presented in figure 6. High heat flux tests show that the chosen interlayers have not allowed a significant increase of the mock-up performance. To better understand these results metallographic samples have been machined from the tested mock-ups and analysed by SEM and IBA.

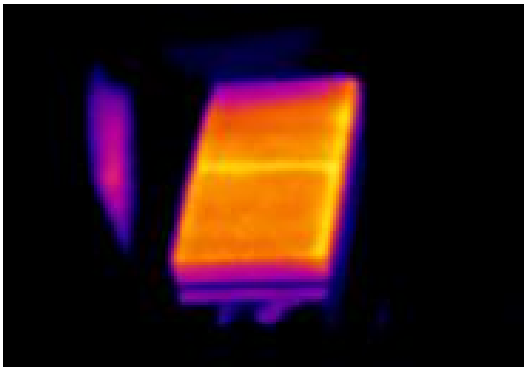

Figure 6: IR image of one INMOCK mock-up during High Heat Flux tests

REFERENCES

[1] K.Oki et al. “Six party qualification program of FW fabrication methods for ITER blanket module procurement”, Fusion Engineering and Design, 2007

REPORTS AND PUBLICATIONS

P-E. Frayssines, J-M Leibold, and B. Oresic, “Manufacture of first wall mock-ups for In-Pile experiments”, EFDA 05-1309, TW5-TVB-INMOCK, final report no. DTH/DL/2007/71

TASK LEADER

Pierre-Eric FRAYSSINES

DRT/LITEN/DTH/LTH
CEA-Grenoble
17 rue des Martyrs
F-38054 Grenoble Cedex 9

Tel: 33 4 38 78 28 59
Fax: 33 4 38 78 54 79

e-mail: pierre-eric.frayssines@cea.fr

CEFDA06-1372

Task Title: TW5-TVD-FABCON: DEVELOPMENT OF FABRICATION CONTROL METHODS FOR THE ITER DIVERTOR

INTRODUCTION

For steady state magnetic thermonuclear fusion devices which need large power exhaust capability, actively cooled Plasma Facing Components (PFCs) were developed. Therefore, the examination and qualification of PFCs became a key issue for actively cooled fusion devices. In order to guarantee the integrity of the components during the required lifetime, the thermal and mechanical behaviour of the PFCs must be assessed. Before the procurement of the ITER Divertor, the examination of the heat sink to armour joints with Non Destructive Techniques (NDT) is an essential topic to be addressed. NDT will also be used to assess the quality of the PFCs and decide upon their acceptability for the ITER machine. In Carbon Fiber Composite (CFC) armoured components defects may be localised at CFC/CuOFHC or CuCrZr/CuOFHC bonding interface. Using two facilities of infrared thermal imaging equipment such as SATIR [1] and LOCKIN [2], a preliminary work already showed the capability of data merging to improve reliability of NDT for PFCs. This experimental study was carried out on flat tiles components for the Wendelstein 7-X Stellarator [3]. The data fusion method makes use of the Dempster-Shafer theory of evidence. New developments were needed to generalise the data merging methodology to Divertor monoblocks designed for ITER. The experimental study was conducted on ITER CFC monoblocks with calibrated defects. For these PFCs, two non-destructive testing techniques were selected: infrared thermography (SATIR test bed) and ultrasonic tests.

2007-2008 ACTIVITIES

MOCK-UP AND NON-DESTRUCTIVE TECHNIQUES DESCRIPTIONS

Mock-up description

Figure 1 shows the mock-up geometry. Carbon Fiber Composite (CFC) NB31mock-ups were manufactured with artificial defects. The CFC conductivity is displayed in table 1. These monoblocks have either CFC/CuOFHC (CFC/Cu) or CuOFHC/CuCrZr (Cu/CuCrZr) joint defects. Defects were manufactured using different techniques: machining (Electro Discharge Machining (EDM) with a wire of 0.3 mm diameter), “stop-off” (uses a coating to avoid joining for defects localised at Cu/CuCrZr interface) or a lack of CFC activation (pre activation brazing alloy is lacking in the defect area for defects localised at CFC/Cu interface).
Definitions of the defect location and of the nomenclature side are presented on figures 1a and 1b.

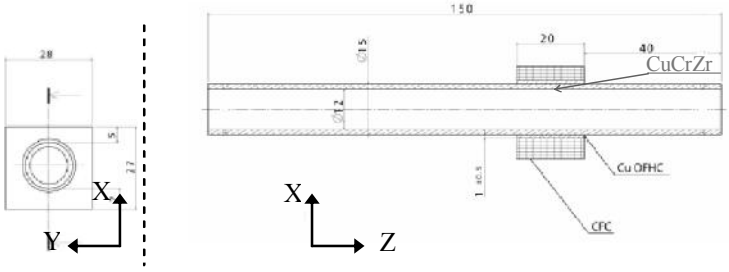

Figure 1a: Mock-up geometry

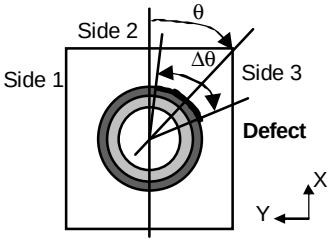

Figure 1b: Nomenclature of sides

Infrared thermography images

Infrared thermography images are obtained using SATIR test bed. SATIR facility is an active Infrared thermography test bed based on the heat transient method. It was developed at the CEA and was used as an inspection functional tool in order to guarantee the actively cooled PFC performances. The description of SATIR facility was the subject of several papers [1]. This test bed is based on the comparison of the surface temperature evolution of the inspected component with a reference one. The temperature difference is called DTref. The armour surface temperature is observed by means of a digital infrared camera (CEDIP JADE II) located in front of the tested PFC. CFC armour is observed from 3 sides (Side 1, side 2 (top view) and side 3). In what follows, Infrared thermography will be called shortly IR.

Ultrasonic images

The figure 2 illustrates the ultrasonic (UT) method performed by CIEMAT-Tecnatom [4, 5]: pulse-echo with normal incidence of UT beam at high frequency with the use of a mirror and immersion in the water. The scanning surface is the inner wall of the cooling tube. Inspection scan is performed with a circular movement with data acquisition every 1° angle and the distance between inspections scan is 1 mm up to 20 mm along Z axis. The presence of defect at one of the two interfaces creates an echo at one of the two fixed temporal windows. The UT amplitude is referred to as Full Screen Height (FSH). The maximum amplitude in the temporal window is chosen as the integrity indicator. FSH is given at CFC/Cu or CuCrZr/Cu interface for each step angle and each step depth.

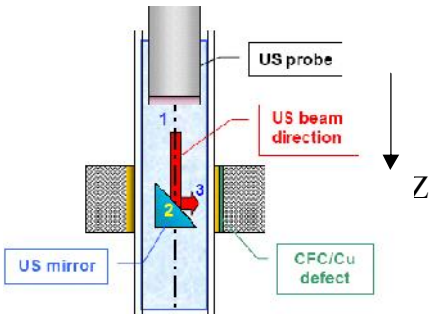

Figure 2: Ultrasonic method

Data merging method

The concept of Data Merging (DM) was developed in order to offer user-friendly machine interfaces and give decision capacities to non-experts in complex multi-sensor environments. This concept was widely used for military applications [6, 7], and then in other domains where the complementarity of the information improves the decision: first for medicine and more recently for NDT [8].

Referential for data combination

The combination of images obtained with IR and UT is made pixel-by-pixel [9] consequently it needs a reconstruction of these images in the same referential. The three sides of monoblock defined on figure 1b represent the common referential. This referential implies to project the UT data on these lateral surfaces. For this projection we took into account the orthotropic behaviour of the thermal dissipation in CFC (table 1). The orthotropic projection was validated and retained.

Table 1: Carbon Fiber Composite NB31 conductivity

Conductivity λ_{xx} (W m^{-1} K^{-1})	323
Conductivity λ_{yy} (W m^{-1} K^{-1})	117

Data Merging Theory

The combination of knowledge-data coming from different NDT sensors is done through the Dempster orthogonal summation rule (1) [10]. For each NDT, this method assigns degrees of confidence, so called "sets of masses" (mxi) to simple hypotheses, or combination of simple hypotheses. The purpose is to calculate the sets of masses after combination of the sources (xi) for each hypothesis (Hi). It is also necessary to introduce the term K for conflict between the NDT data when they are contradictory (2).

$$m(H) = (m_{x_1} \oplus m_{x_2} \oplus \Lambda \oplus m_{x_n})(H) = \frac{\sum_{H_i \cap H_j K \cap H_n = H} m_{x_1}(H_i) \times m_{x_2}(H_j) \times \Lambda \times m_{x_n}(H_n)}{1 - K} \quad (1)$$

$$\text{Where} \quad K = \sum_{H_i \cap H_j K \cap H_n = \varnothing} m_{x_1}(H_i) \times m_{x_2}(H_j) \times \Lambda \times m_{x_n}(H_n) \quad (2)$$

The Dempster-Shafer method adopted is based on decision-making on three hypotheses. The hypothesis H1 characterises the presence of a defect; the hypothesis H2 corresponds to the absence of defect; and the hypothesis H3 corresponds to ignorance, characterising hesitation relative to the nature of the defect.

For each measurement x_i (x_i = DTref or FSH) limits have to be established so that pixels are classified as defective, not defective or unknown (ignorance). Consequently three regions are defined. Each region represents the zone where the majority decision is one of the three hypotheses H1, H2 or H3. In these regions, hypotheses are weighted by the sets of masses. Transitions between these regions are sharp so that decision changes are very abrupt and will be too sensitive to measurement noise. To obtain a more continuous behaviour from the transitions, fuzzy functions are used. Lower (Vus1, Vir1) and upper (Vus2, Vir2) thresholds (figure 3a) are evaluated thanks to the standard deviation (σ) estimation for each NDT. The standard deviation was estimated to 2.38 °C for SATIR, 11 %FSH for ultrasonic test bed in the case of the CFC/Cu interface and 9 %FSH in the case of the Cu/CuCrZr interface (figure 3b). Previous experience enables to set a short ignorance region for SATIR and CIEMAT data (i.e. P1=10; P2=90), meaning that for example when DTref = 7 °C: H1= 90 %, H2 = 10 % and H3=0 %.

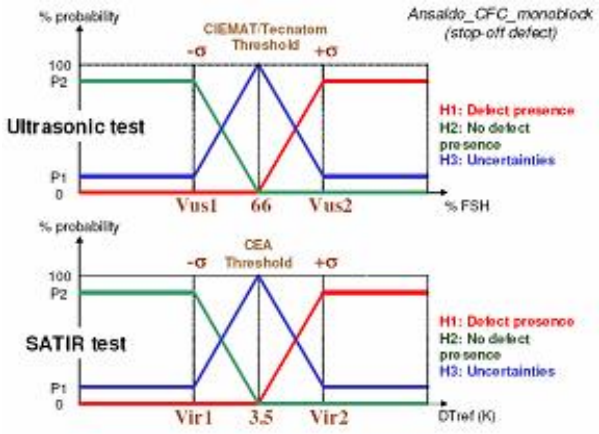

Figure 3a: General description of fuzzy logic and hypothesis regions

SATIR data for CFC/CuOFHC and CuOFHC/CuCrZr					
	Vir1	Limit	Vir2	P1	P2
DTref / °C	1.12	3.5	5.88	0.1	0.9

Ultrasonic data for CFC/CuOFHC					
	Vus1	Limit	Vus2	P1	P2
% FSH	55	66	77	0.1	0.9

Ultrasonic data for CuOFHC/CuCrZr					
	Vus1	Limit	Vus2	P1	P2
% FSH	44	53	62	0.1	0.9

Figure 3b: Corresponding threshold

Definition of the defect zone

To obtain the defect zone we select rectangular areas, which have H1 more than 90% average. Then we select the largest area (size) = ind1 (XA: dimension in angular direction, Z: dimension in monoblock axial direction). We select other areas ind_i if their size is upper than 0.5 x ind1. Areas may be clustered if their distance between them is less than XA/2 and Z/2.

RESULTS AND DISCUSSION

An example of DM for a machined defect at CFC/Cu interface is presented in (figure 4 Left); UT and IR data localises the defect at θ= 45°, Δθ= 65°. The contour shape of defect given by DM leads to θ= 45°, Δθ= 65°.The DM method applied to the machined defects reveals very good results because, in this particular case, results obtained with UT and IR data are excellent. Consequently, the DM study of machined defects presents a minor interest within the development of this method and will not be detailed here.

In what follows we focus on the defects manufactured by means of other techniques which are more relevant to be analysed ("stop-off" and lack of CFC activation). For these types of techniques, table 2 summarises angular position (θ) and extension (Δθ) obtained with UT, IR and results obtained by merging these two NDT techniques. It also presents the percentage of monoblock for which the technique identifies the defect by a position and an extension (Ident / %). In this table we use "-"when a technique does not give any information about the defect.

The majority of defect indications given by DM are obtained when both UT and IR results are valid. In the case of Cu/CuCrZr interface defects, we obtained excellent results with a significant improvement of the defect contour shape (100% of detection with a decreasing of the uncertainty). However, in the particular case of #8CU the parameters of DM were modified to detect a lower relevant signal.

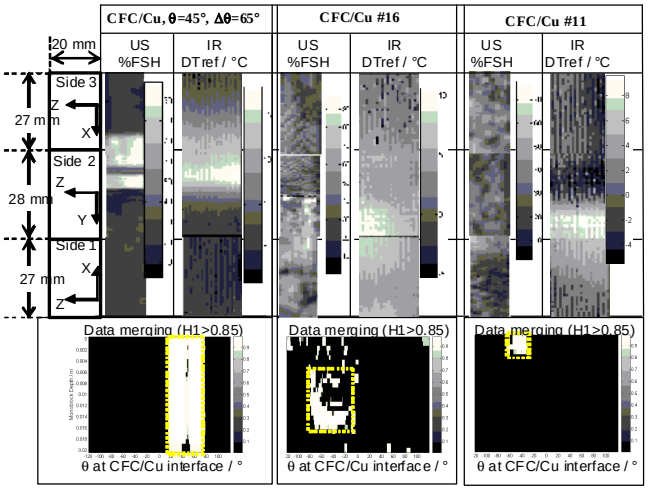

Figure 4: UT (%FSH), IR (DTref / °C) data and data merging results (H1: probability of defect presence) for a monoblock with a calibrated (Left) machined defect at CFC/Cu interface (θ =45°,Δθ =65°), (Middle) lack of CFC activation defect at CFC/Cu interface (#16), (Right) Lack of CFC activation defect at CFC/Cu interface (#11)

In the case of the defect #16 localised at CFC/Cu interface UT localises the defect at θ = -45°, Δθ = 80° and IR localises the defect at θ = -40°, Δθ = 60°. UT and IR give similar results. Data merging of UT and IR data leads to localise the defect at θ = -45°, Δθ = 70°: results are consistent with UT and IR data. The contour shape of the defect is better described than UT and IR cartographies themselves (figure 4 Middle). In the case of the defect #11 localised at CFC/Cu interface (figure 4 Right) UT does not clearly localises the defect whereas IR localises the defect at θ = -45°, Δθ = 40°. Data merging of UT and IR data leads to localise the defect at θ = -45°, Δθ = 30°. DM gives reliable information about the defect due to some indications of defect on UT cartographies (table 2).

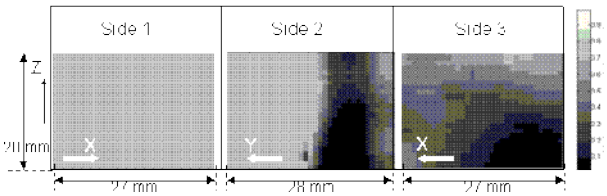

Figure 5: Conflict cartography of the calibrated «stop-off» defect #15 (CFC/Cu interface)

Table 1: For calibrated defect manufactured with "stop-off" or a lack of CFC activation techniques: Defect angular position (θ/°), extension (Δθ/°) and percentage of monoblock for which the technique identifies a defect by a position and/or extension (Ident / %) at CFC/Cu and Cu/CuCrZr interfaces. Defect are identified with ultrasonic (UT), infrared thermography (IR) techniques and data merging analyses (DM)

Defect at CFC/Cu interface	θ / °			Δθ / °		
	UT	IR	DM	UT	IR	DM
	-110	-110	-60	23	20	30
	5	10	5	25	20	25
	15	-	-110	35	-	20
	-	10	0	-.	40	80
	10	0	15	55	45	35
	10	0	10	60	40	60
	5	0	0	60	60	60
	10	10	40	70	60	2
	-50	-45	-45	20	30	20
	-	-45	90	-	30	20
	-	-45	-45	-	40	30
	-35	-45	-35	25	40	30
	-40	-50	-40	25	40	20
	-100	-50	-80	45	60	10
	-	-40	-	-	50	-
	-45	-40	-45	80	60	70
t	75	94	94	75	94	94

Defect at Cu/CuCrZr interface	θ / °			Δθ / °		
	UT	IR	DM	UT	IR	DM
#1Cu	0	0	0	85	40	80
#2Cu	8	5	10	60	30	60
#3Cu	78	70	80	55	30	30
#4Cu	140	-40	-50	50	40	15
#5Cu	-42	-45	-40	85	70	80
#6Cu	56	45	55	102	70	100
#7Cu	-40	-45	-40	110	70	100
#8Cu	-62	-50	-55	147	60	130
Ident / %	100	100	100	100	100	100

In some cases (for example #1), UT and IR give the same position but DM leads to localise the defect at a different position. As DM cartography is obtained with the sum of contributions from UT and IR, theses cases are due to the defect mapping which is different for UT and IR. This is observed when defect areas detected by UT and IR are dissociated threw the monoblock depth.

In the case of CFC/Cu interface defects, the DM detection would be improved if both techniques had the same reliability level. DM gives the same percentage of defect detection as IR data (94%) at the CFC/Cu interface. In general, conflict between UT and IR data leads to invalid conflict DM results (#15). In the case of the defect #15 localised at CFC/Cu interface, IR detects a global indication of thermal imperfection whereas UT does not indicate the presence of defect: in this case the analysis of the defect could reveal localisation in the CFC volume or at the Cu/CuCrZr interface. When looking at the conflict cartography (figure 5), we may say that the defect is localised in CFC volume or at the Cu/CuCrZr interface. A further UT examination at Cu/CuCrZr interface may reveal where the defect localisation is. Thanks to conflict cartography, one of the main advantages of DM is to provide a better definition of the shape of the defect and the defect interface localisation: CFC/Cu, Cu/CuCrZr or in CFC volume.

In order to compare the actual defect with respect to location and extension obtained with UT, IR and DM, destructive examinations were performed at Forschungszentrum Juelich (Germany) on all CFC monoblocks. Monoblocks are cut at 1-2 mm from the front and the rear sides, the two interfaces were then observed. In the case of machined defects, destructive examinations revealed the same position and extension than UT and IR ones.

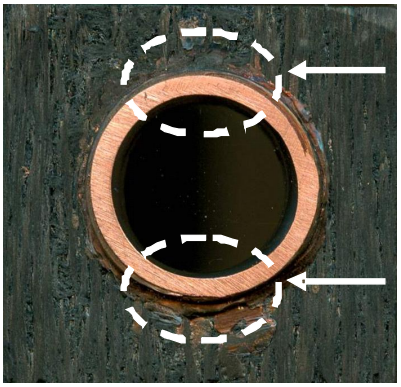

Figure 6: Examination of #2Cu

Figure 6 is a view of #2Cu interfaces manufactured with "stop-off" or lack of CFC technique. The monoblock was cut at 2 mm from the rear side; this picture shows that the definition of the defect given by UT, IR and DM is not consistent with the observed defect. For the "stop-off" and lack of CFC techniques, defect may not be identified or be observed at other location than the one defined with UT or IR technique. This may be due to the fact that defect is not homogeneously located along the monoblock length.

CONCLUSIONS

The data merging method applied to the "machined" defects reveals very good results because, in this particular case, the confidence in both ultrasonic and infrared thermography data is excellent. Data merging applied to defects which were manufactured using "stop-off" or a lack of Carbon Fiber Composite (CFC) activation techniques gives the same percentage of defect detection as IR and UT data. The advantages are that data merging provides a significant improvement of the defect contour shape. Moreover the combining of these two non destructive techniques is a way to obtain more reliable results. Thanks to conflict cartography, data merging leads to a better definition of the defect interface localisation: CFC/CuOFHC, CuOFHC/CuCrZr or in CFC volume. The data merging of several non destructive techniques improves the capability of defect detection, minimizing the global uncertainty. In addition, this study showed that by using the knowledge acquired during the development of each non-destructive inspection method taken separately, it would be possible to implement a process of data combination with fairly reduced training.

REFERENCES

[1] A. Durocher et al., Advanced Qualification Methodology for Actively Cooled High Heat Flux Plasma Facing Components", Nucl. Fusion 47 (2007) 1682-1689

[2] D.T. Wu, G. Busse, Lock-in thermography for nondestructive evaluation of materials, Revue Générale de Thermique 37 (1998) 693-703

[3] A. Durocher, J. Moysan, F. Escourbiac, M. Missirlian, N. Vignal, J. Boscary, Infrared images data merging for plasma-facing component inspection, Fusion Eng. Des. 82 (2007) 1694-1699

[4] M. Garcia, M. Medrano, R. Martinez-Ona, UT inspection of the CFC monoblocks manufactured by PLANSEE, CIEMAT-Tecnatom report, 12/2006, IN-IT-DIV-002

[5] M. Garcia, M. Medrano, R. Martinez-Ona, UT inspection of the CFC monoblocks manufactured by ANSALDO, CIEMAT-Tecnatom report, 09/2007, IN-IT-DIV-005

[6] J. Esteban, A review of data fusion models and architectures: towards engineering guidelines, Neural Comput. Appl. 14 (2005) 273–281

[7] Bloch, Information Combination Operators for Data Fusion: A comparative review with classification, IEEE Trans. Syst. Man Cybern. Part A. 26 (1) (1996) 52–67

[8] X.E. Gros, NDT Data Fusion, Arnold, London (1997)

[9] J. Moysan, A. Durocher, Improvement of the Non-Destructive Evaluation of Plasma Facing Components by Data Combination of Infrared Thermal Images, 9th European Conference on Non-Destructive Testing (2006)

[10] G. Shafer, Int. J. Approx. Reason. 4 (1990) 323–362

REPORTS AND PUBLICATIONS

Development of fabrication control methods for the ITER Divertor, CEA Report CFP/NTT – 2008.007 – 15/4/2008

TASK LEADER

Alain DUROCHER

DSM/IRFM
CEA-Cadarache
F-13108 Saint-Paul-lez-Durance Cedex

Tel: 33 4 42 25 62 24
Fax: 33 4 42 25 43 54

e-mail: alain.durocher@cea.fr

CEFDA06-1373

Task Title: TW6-TVD-ACCREV: DEFINITION OF ACCEPTANCE CRITERIA FOR THE ITER DIVERTOR

INTRODUCTION

The ITER divertor system is aimed at exhausting the alpha particles and reducing the impurity content of the plasma, it consists essentially of two parts: the Plasma Facing Components (PFC) and a massive support structure called cassette body. The cassette body is aimed at supporting the PFC, routing the water coolant into the PFC and providing neutron shielding. The PFC are actively cooled thermal shields devoted to sustain the heat and particle fluxes during steady-state and transient operations. During the PFC manufacturing, tens of thousands of armor/heat sink joints will be produced by the industry, either Carbon Fibre Composite (CFC) or tungsten (W) to copper alloy (CuCrZr) joints [1]. Past experience has proved that statistically, there is a probability to deliver some joints with defects [2, 3].

The purpose of this task is to study the detection and the evolution during operation of calibrated defects artificially implemented on PFC samples, as an experimental basis for the definition of acceptance criteria for the bond armor/heat sink in the frame of industrial manufacturing conditions.

Firstly, the samples with artificial defects are described, then, results of the defects characterization by Non-Destructive Examination (NDE) and high Heat Flux (HHF) testing are presented and discussed.

2007-2008 ACTIVITIES

DESCRIPTION OF SAMPLES

Technology

EFDA procured via industry 108 samples for the study. Two sets were manufactured, each set consisted of: 26 CFC NB31 (SAFRAN trademark) monoblocks, 14 W monoblocks and 14 W flat tiles. For the 3 design options (figure.1), an interlayer of pure Copper (Cu) was used as compliant layer between the armour material and the CuCrZr cooling tube (12/15 mm inner/outer diameter).

The first set was manufactured by PLANSEE SE company, the selected joining technologies were Active Metal Casting (AMC®) for CFC/Cu joint and Hot Isostatic Pressure technique (HIP) for Cu/CuCrZr joint in case of the CFC NB31 monoblock design option [4]; copper casting and HIP for the W monoblock and for the W flat tile options.
The second set was manufactured by ANSALDO Ric.company, the technologies of joining selected for this study were: Pre-Brazed Casting (PBC) for CFC/Cu joint and Hot Radial Pressing technique (HRP) for Cu/CuCrZr joint in case of the CFC NB31 monoblock design option [5];copper casting and HRP for the W monoblock and brazing for the W flat tile options.
Each sample was made of one unique monoblock or 4 flat tiles (figure 2) with reduced armour thickness for HHF testing (4 mm for CFC, 5 mm for W).

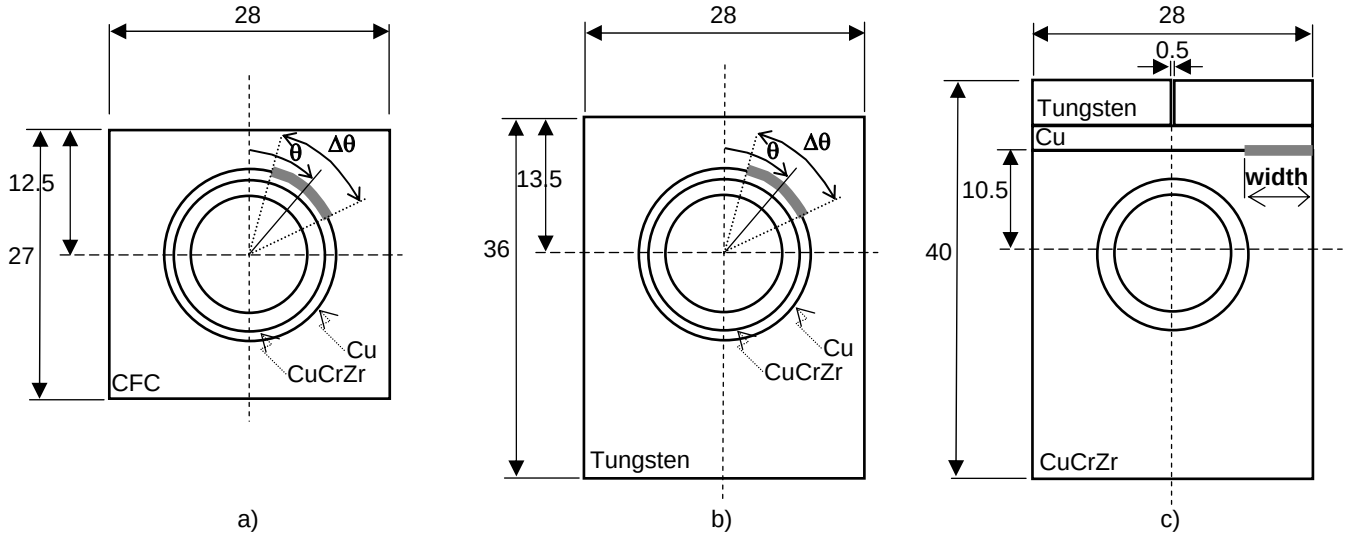

Figure 1: Design of samples with artificial defects a) CFC monoblock; b) W monoblock; c) W flat tile

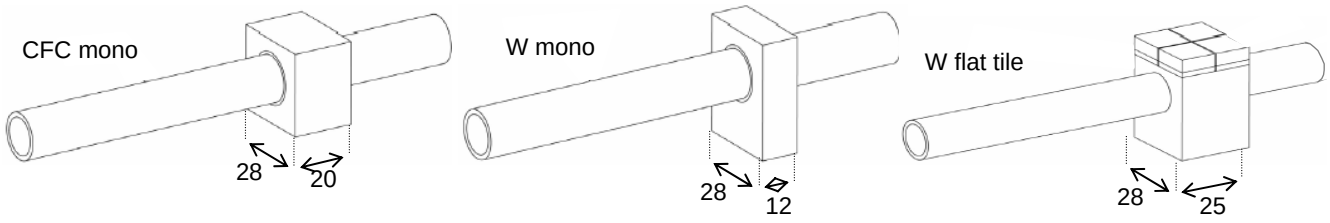

Figure 2: Sketch of samples – Tube length 150 mm

Table 1: Specified artificial defects interface, dimensions and locations

Interface	CFC monoblock	W monoblock	W flat tile
Armour / Cu	θ=0° : Δθ= 20, 35, 50, 65° θ=45° : Δθ= 20, 35, 50, 65°	θ=0° : Δθ= 15, 30, 45°	2, 4, 6 mm (edge)
Cu / CuCrZr	θ=0° : Δθ= 40° θ=45° : Δθ= 20, 40, 60°	θ=0° : Δθ= 15, 30, 45°	2, 4, 6 mm (edge)
	2 samples defect-free	1 sample defect-free	1 sample defect-free

Artificial defects

The artificial defects on PLANSEE samples were implemented by Electro Discharge Machining (EDM) with a wire of 0.3 mm diameter (NB: a first step of 0.5 mm diameter drilling was necessary for monoblock geometry). In case of ANSALDO, the artificial defects on monoblock samples were implemented by preventing the wetting of CFC surface by local lack of pre-brazed casting alloy and by a stop-off coating for defects at W/Cu and Cu/CuCrZr interfaces. For W flat tile geometry the defects at W/Cu and Cu/CuCrZr interfaces were provided by machining and stop off technique, respectively.

During previous studies [6], it was calculated that the defects to be implemented into the CFC samples must respect the following rules of design:

- do not degrade margin to Critical Heat Flux occurrence lower than 1.4;

- do not increase CFC surface temperature higher than 2000°C (to limit erosion) or copper temperature higher than 550°C during normal operation (to avoid crack formation).

Consequently, the calculated maximum acceptable defect in case of CFC monoblock geometry was an extension of 60° angle (Δθ) at a 30° location (θ) at the CFC/Cu interface (see figure 1 for defects definition). In order to study the fatigue behaviour of such range of defects and extending these results to W monoblock geometry and W flat tile geometry, it was decided to manufacture the 108 samples with specified defects dimensions and locations as detailed in table 1.

NON DESTRUCTIVE EXAMINATION

Ultra Sound (US) technique

NDE by US technique was found reliable and accurate in case of W/Cu or Cu/CuCrZr interfaces. For these metallic materials, it can be stated that a defect lower than 2 mm width in case of flat tile geometry or 20° extension in case of monoblock geometry can be reliably detected.
On another hand, the too low acoustic impedance of CFC material impair the possibility to detect reliably the presence of joining defects with such a technique.

SATIR technique

The principle of SATIR technique [7] is based on the detection of a time delay of the surface temperature evolution measured by infrared thermography during a fast decreasing of the water temperature flowing in the cooling tube:
an imperfection at one of the joints or into a material may create a thermal resistance so that the delay increases during the transient thermal regime. This delay is measured by comparison with the thermal behaviour of a "defect-free" reference component. The maximum value of this delay – called DT_ref_max (°C) - is calculated for each pixel on the infrared images. SATIR can be used both for metallic and CFC materials. In this study, the technique was applied to CFC monoblock samples.

Testing protocol

The examination was performed on 3 sides of each sample : a cartography of DT_ref_max was obtained in front side, then the samples were +90° turned for a second examination (right side) and finally turned of -180° (left side) for a third and last examination. A 3D reconstruction can be done as proposed in figure 3.

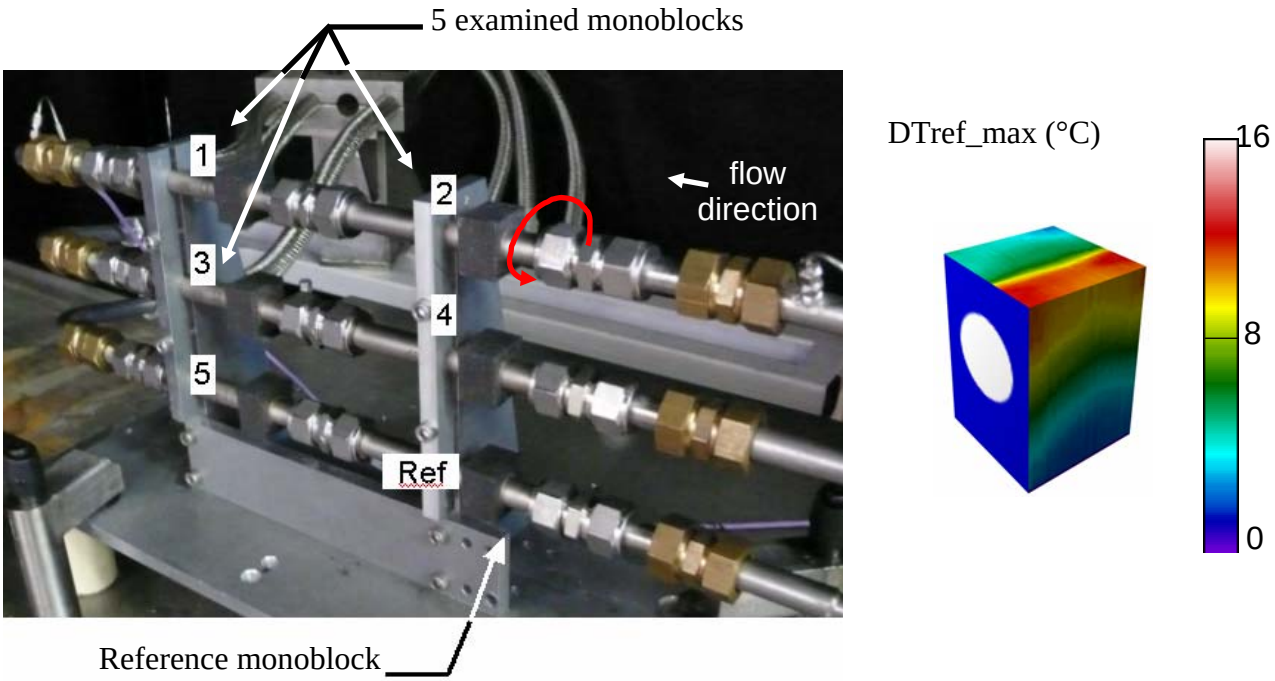

Figure 3: 6 CFC monoblock samples connected to SATIR facility – 3D reconstruction of DTref_max by pixel for one sample

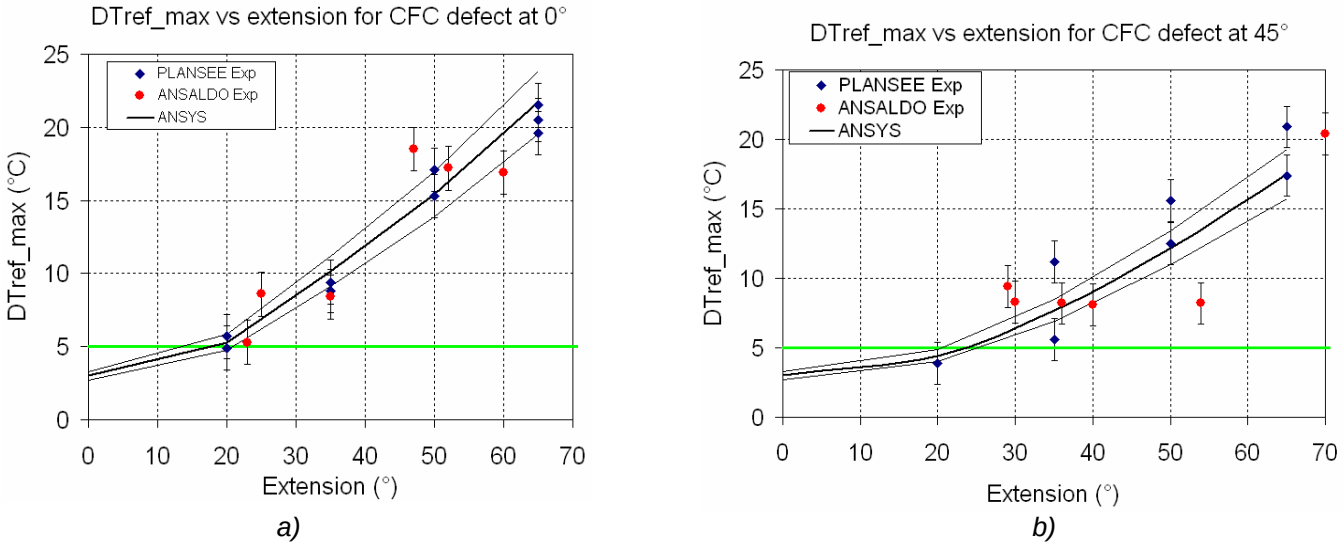

Figure 4: DT_ref_max vs defect extension at CFC/Cu interface a) location 0° - b) location 45°

Results

The maximum value of the DT_ref_max was extracted from the cartography of each block and plotted as a function of defect dimension for a given interface and location. Measurements were obtained on the front side of CFC monoblocks with a defect located at 0° and 45°, CFC interface (figure 4). Measurements were found repeatable with errors bars of +/- 1.5°C. The horizontal line represents the 5°C threshold below which the measurement is considered in the experimental noise. In case of defects at CFC interface, the threshold of detection was found at respectively 20° and 25° extension for locations at 0 and 45° (figure 4a and 4b).

A non-linear ANSYS model was developed to simulate the thermal process of SATIR inspection: 3 curves taking account the CFC thermal properties scattering (+/-5% variation, from [8]) compares satisfactory with experiments from machined defects. In case of defects implemented by preventing the wetting of CFC surface with local lack of pre-brazed casting or by a stop-off coating for defects at W/Cu and Cu/CuCrZr brazed interfaces, it appeared logically that the defects dimensions were not perfectly controlled. In this latter case W/Cu and Cu/CuCrZr interfaces defects dimensions and locations were estimated by US NDE technique. However these estimations are questionable and may partially explain the observed scattering.

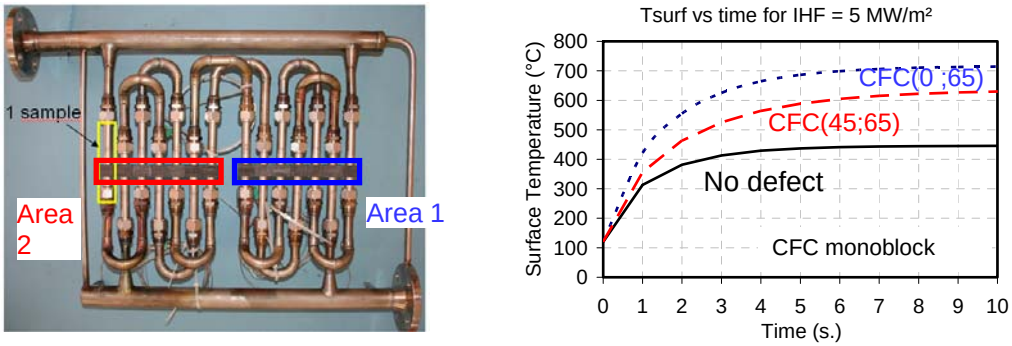

Figure 5: a) Mock-up prepared for HHF testing; b) Calculated thermal behaviour of samples (water cooling conditions 120°C; 35 bar; 12 m/s)

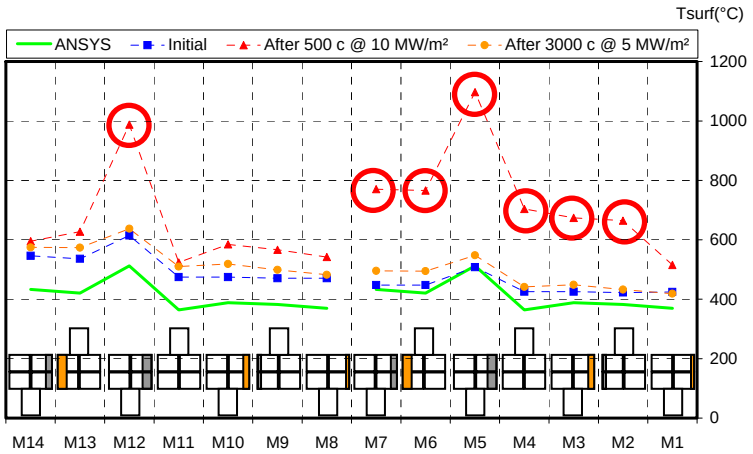

Figure 6: Thermal mapping of 14 W flat tiles

HIGH HEAT FLUX TESTING

Testing protocol

8 mock-ups were prepared for high heat flux (HHF) testing at FE200 facility [9] with a maximum of 14 samples per mock-up (maximum possible with regards to water loop pressure drop and available flow rate) (figure 5a).
Alternative heating was done by the electron beam sweeping: 10 sec on Area 1, 10 sec in Area 2.
The thermal steady-state was reached after typically a few seconds (figure 5b). Selected heat loads on the 8 mock-ups were – from fatigue point of view - relevant with ITER Divertor design values [10]: a first cycling step of 3000 cycles at 10 MW/m² then a second cycling step of 500 cycles at 20 MW/m² on CFC and W monoblocks (resp. 5 and 10 MW/m² on W flat tile), a thermal mapping at 5 MW/m² being performed initially and between each cycling step.

Diagnostic of acceptation

Surface temperature was measured by infrared thermography in order to estimate the thermal impact of a defect propagation on bond or material degradation. During the study it was decided to use the following rule for acceptance criteria: if Max (Tsurf-Twater) increasing of a sample is lower than 30% (unit: °C) from one thermal mapping to the next one, then the sample is declared acceptable. The sample is declared rejected if the increasing is higher than 30%.

Results

For each mock-up, the infrared measurements of first, intermediate and final thermal mapping are reported on the same graph (respectively square, circle and triangle marks). A non-linear ANSYS model is also reported (line) to check the consistency of the initial thermal mapping.
Defect locations and extensions are symbolised on the bottom of the graph for each sample marked M1-M14. Samples rejected are indicated with red circles.

W flat tile

Initial thermal mapping was consistent with ANSYS calculations on ANSALDO Ric samples figure 6. The shift of ~100°C between modeling and measurements on the samples M7 to M14 was attributed to discrepancies on W emissivity. No evidence of overheating was observed during the thermal mapping after 3000 cycles at 5 MW/m². However, after cycling at 10 MW/m² defects propagation was observed for defects dimensions of 2, 4 and 6 mm at W/Cu and Cu/CuCrZr interfaces. Similar results obtained with PLANSEE samples demonstrate that this design is not adapted for cycling fluxes of 10 MW/m².

W monoblocks

Overheating of the largest Cu defect on ANSALDO Ric samples (Monoblock M06, with a 110° extension estimated by NDE US technique) was observed after cycling at 10 MW/m² (figure 7).

None of the other defects propagated, including in the case of PLANSEE samples. This result demonstrates that W monoblock design is suitable for heat fluxes expected at the upper part of the Divertor vertical target.

At 20 MW/m², defects propagation was observed for defects at W/Cu interface with dimensions above 30° extension (with 2 exceptions on W interface at 42° and 52° extension). At Cu/CuCrZr interface, systematic propagation was observed for dimension above (0; 30°). Moreover, overheating was observed for a defect-free sample and 4 blocks among 28 cracked axially from the top of the tube to the center part of the heated side. These results demonstrate that this design is not adapted for cycling fluxes of 20 MW/m².

CFC monoblocks

No evidence of overheating was observed during the thermal mapping after 3000 cycles at 10 MW/m² on the CFC samples (figure 8). After 500 cycles at 20 MW/m², systematic defect propagation was observed for defects at CFC/Cu interface with 65° extension at 0° and 45° position. At 0° position, the CFC/Cu defect of 50° extension (sample #M06) was detected overheated, however it was not confirmed by post-testing metallographic examination after cutting of the block. Additionally, the US-C-scan performed after HHF testing was similar to the US-C-scan obtained before, same observation with SATIR inspection performed after the HHF testing which gave same DT_ref_max than before HHF testing (~15°C). It is assumed that the local overheating observed on the infrared image is an artefact due to the erosion of the surface. This result demonstrates that CFC monoblock design is suitable for heat fluxes expected at the lower part of the Divertor vertical target with reasonable acceptance criteria

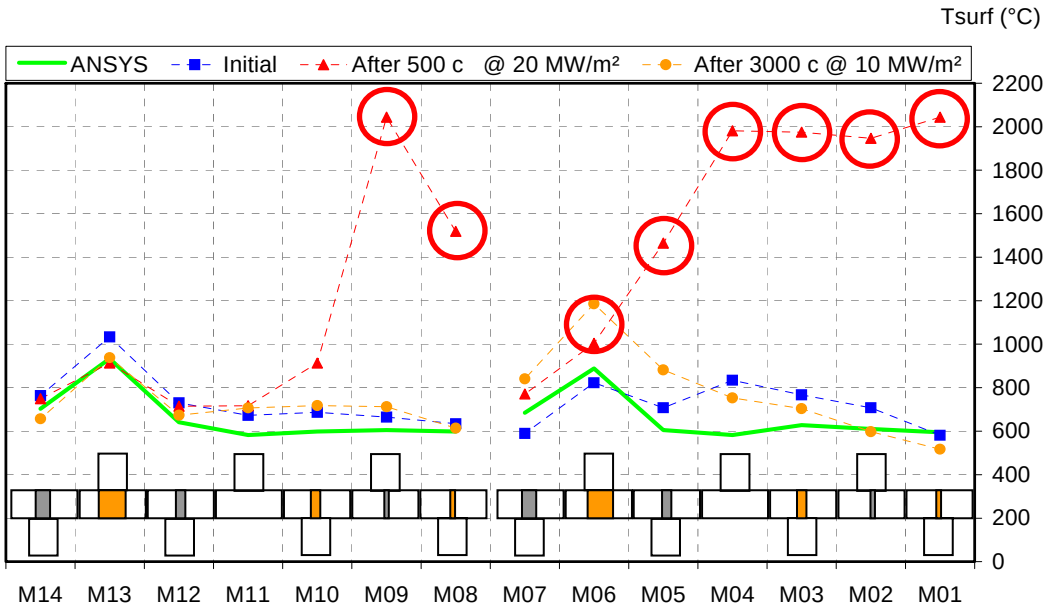

Figure 7: Thermal mapping of 14 W monoblocks

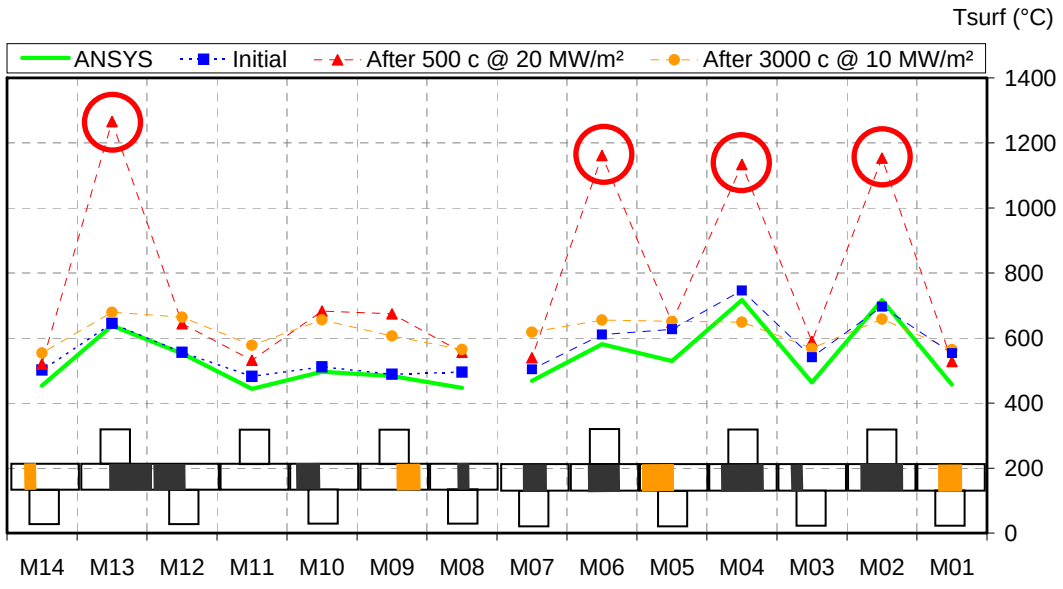

Figure 8: Thermal mapping of 14 CFC monoblocks

CONCLUSIONS

It was observed that current CFC monoblock design option was compatible with the heat loads (up to 20 MW/m²) specified at the lower part of the vertical target, including the presence of armor/heat sink defects (up to 50° extension for a location at 0° or 45°) detectable with NDE techniques developed in Europe (US, SATIR).

The current W monoblock design appeared suitable for the upper part of the vertical target with defect extension up to 50°, but is not adapted for heat flux of 20 MW/m². The studied W flat tile design proved to be compatible with fluxes of 5 MW/m² but unable to sustain cycling fluxes of 10 MW/m² (table 2).
These results give confidence in the European capability to manufacture and characterize the ITER Divertor PFC with the required level of performance.

Table 2: Summary on experimental results - (*) Except cycling steps at 10 and 20 MW/m² (for W flat tile samples and W monoblock respectively)

		Artificial defect				
Design option	Cycling HHF	Location	Interface	Min. detectable SATIR/US	Acceptable during cycling HHF	Propagation or overheating detected
CFC Monoblock	3000 x 10 MW/m² + 500 x 20 MW/m²	0°	CFC/Cu	20° / < 20°	50°	50°
		45°	CFC/Cu	25° / < 20°	50°	65°
		0°	Cu/CucrZr	< 40° / < 20°	40°	no
		45°	Cu/CucrZr	30° / < 20°	60°	no
W Monoblock	3000 x 10 MW/m²	0°	W/Cu	< 20°	45°	no
		0°	Cu/CucrZr	< 20°	45°	no
		0°	W/Cu	< 20°	50°	no
		0°	Cu/CucrZr	< 20°	50°	110°
W Flat tile	3000 x 5 MW/m²	edge	W/Cu	< 2 mm	6 mm	no
		edge	Cu/CucrZr	< 2 mm	6 mm	no
		edge	W/Cu	< 2 mm	6 mm	no
		edge	Cu/CucrZr	< 2 mm	6 mm	no

REFERENCES

[1] R. Tivey, M. Akiba, D. Driemeyer, I. Mazul, M. Merola, M. Ulrickson, Fus. Eng. and Des. 55 (2001) 219-229

[2] J. Schlosser, A. Durocher, T. Huber, P. Garin, B. Schedler, G. Agarici, Fus. Eng. Des. 56-57 (2001) 309-313

[3] M. Missirlian, A. Durocher, A. Grosman, J. Schlosser, J. Boscary, F. Escourbiac, F. Cismondi, Phys. Scr. T128 (2007) 182-188

[4] T. Huber, L. Plöchl, N. Reheis, J.P. Cocat, J. Schlosser, Proc. 16th IEEE/NPSS/SOFE, Champaign, 1995 716–719

[5] E. Visca, S. Libera, A. Mancini, G. Mazzone, A. Pizzuto, C. Testani– Fus. Eng. Des. 82 (2007) 1651-1656

[6] S. Fouquet, J. Schlosser, M. Merola, A. Durocher, F. Escourbiac, A. Grosman, M. Missirlian, C. Portafaix, Fus. Eng. and Des. 81 (2006) 265-268

[7] A. Durocher, F. Escourbiac, A. Grosman, J. Boscary, M. Merola, F. Cismondi, X. Courtois, J.L. Farjon, M. Missirlian, J. Schlosser, R. Tivey, Nuc. Fus. 47 (2007) 1682-1689

[8] I. Berdoyes - Technical note FPTM0426079A – EFDA series production material characteristics NB31 – Snecma propulsion solide

[9] I. Bobin-Vastra, F. Escourbiac, M. Merola, P. Lorenzetto Fus. Eng. and Des. 75-79 (2005) 357-363

[10] Project_Integration Document__PID__ITER_D_2234RH_3_0 from ITER Org

REPORTS AND PUBLICATIONS

[a] Interim report of contract EFDA 06-1373: monitoring and analysis of divertor components tested at FE200 – CFP/NTT-2007.037 – F. Escourbiac

[b] Spécifications techniques pour la maquette W_flat_tile_A à tester au FE200 CFP/NTT-2006.038 – F. Escourbiac

[c] Spécifications techniques pour la maquette W_ mono _A à tester au FE200 CFP/NTT-2007.013 – F. Escourbiac

[d] Spécifications techniques pour la maquette CFC_mono_P1 à tester au FE200 CFP/NTT-2007.020 – F. Escourbiac

[e] Screening and fatigue tests on a CFC_mono_P1 component (CEA94 – EFDA 06/999) NTCF-F IBV R/07.945 A– I. Bobin-Vastra

[f] Spécifications techniques pour la maquette CFC_mono_P2 à tester au FE200 CFP/NTT-2007.045 – F. Escourbiac

[g] Spécifications techniques pour la maquette CFC_mono_A1 à tester au FE200 CFP/NTT-2007.069 – F. Escourbiac

[h] Spécifications techniques pour la maquette CFC_mono_A2 à tester au FE200 CFP/NTT-2007.078 – F. Escourbiac

[i] Spécifications techniques pour la maquette W_mono_P à tester au FE200 CFP/NTT-2008.011 – F. Escourbiac

[j] Spécifications techniques pour la maquette W_flat_tile_P à tester au FE200 CFP/NTT-2008.020 – F.Escourbiac

[k] Rapport d'inspection SATIR des Monobloc CFC Ansaldo avant FE200 EFDA Contract 06-1373 on Acceptance criteria for ITER Divertor PFC - CFP/NTT-2007.062 (2007)- N. Vignal

[l] Rapport d'inspection SATIR des Monobloc CFC Plansee P2 avant FE200 EFDA Contract 06-1373 on Acceptance criteria for ITER Divertor PFC - CFP/NTT-2007.064 (2007)- N. Vignal

[m] Rapport d'inspection SATIR des Monobloc CFC Plansee P1 avant /après FE200 EFDA Contract 06-1373 on Acceptance criteria for ITER Divertor PFC - CFP/NTT-2007.063 (2007)- N. Vignal

[n] SATIR inpection report of mock-up CFC_MONO_P2 after FE200 testing EFDA Contract 06-1373 on Acceptance criteria for ITER Divertor
PFC - CFP/NTT-2007.066 (2007)- N. Vignal

[o] SATIR inpection report of mock-up CFC_MONO_A 1 and A2 after FE200 testing EFDA Contract 06-1373 on Acceptance criteria for ITER Divertor
PFC - CFP/NTT-2008.016(2008) - N. Vignal

[p] Final report of contract EFDA 06-1373: monitoring and analysis of divertor components tested at FE200
CFP/NTT-2008.019 – F. Escourbiac

[q] Experimental activity on the definition of acceptance criteria for the ITER Divertor plasma facing components Proceedings SOFT2008 – To be published in Fusion Engineering and Design - F. Escourbiac, S. Constans, N. Vignal, V. Cantone, M. Richou, A. Durocher, B. Riccardi, I. Bobin, J.L. Jouvelot, M. Merola

TASK LEADER

Frédéric ESCOURBIAC

DSM/DRFC/SIPP
CEA-Cadarache
F-13108 Saint-Paul-Lez-Durance

Tel : 33 4 42 25 44 00
Fax : 33 4 42 25 49 90

e-mail : frederic.escourbiac@cea.fr

Task Title: TW6-TVD-SATIR: SATIR TESTS OF VERTICAL TARGET QUALIFICATION PROTOTYPES

INTRODUCTION

A prequalification phase is needed for the critical procurement packages shared by multi-party, including the Divertor plasma-facing components (PFC). PFC which will be installed in the ITER Divertor, require a heat flux removal capability in the range 5-10 MW/m² in thermal steady-state conditions and up to 20MW/m² in transients. Well in advance of the assumed start of the procurement, each ITER Party should first demonstrate its technical capability to carry out the procurement with the required quality, and in an efficient and timely manner [1]. This is achieved via the successful manufacturing and testing of medium-size "Qualification Prototypes" (QP) made of three HHF units. HHF units have a Composite Fibre Carbon (CFC) monoblock part and a tungsten part with either monoblock or flat tile geometry. The Party is "qualified" if at least 2 of the QP meet the acceptance criteria and at least one withstands the high heat flux qualification tests. Nowadays, the technical specifications, for the procurement of ITER Divertor components, state that all copper interlayer on CFC armour must be subjected to 100% infrared thermographic examination. An original infrared thermography technique, named SATIR (French acronym for Station Acquisition et Traitement InfraRouge) based on thermal transient method was developed by CEA in order to evaluate the manufacturing process quality control of PFC. The SATIR inspection is considered a key non-destructive testing technique to assess the final quality of the joints between the CFC monoblock and the cooling tube [2]. The aim of this study was to analyse the SATIR inspections results performed on Divertor HHF units manufactured by European industry and to propose a decision on the acceptance of these HHF units with reference to the acceptance criteria defined by ITER Organization (IO).

2007-2008 ACTIVITIES

DESCRIPTION OF HIGH HEAT FLUX UNITS

Three batches of HHF units manufactured by PLANSEE Company and ANSALDO Ricerche were received at CEA-Cadarache. The CFC monoblock part of HHF unit is straight and consists of eleven CFC tiles, possibly separated by a 0.5 mm gap. Each of them has an axial length of 19.5 mm (or 20 mm if no gap is foreseen) and a width of 28 mm. To reduce the joint interface stress, a pure copper interlayer is envisaged between the CFC and W armour and the CuCrZr heat sink. The thickness of this interlayer is about 0.5-1.0 mm and 1.5 mm for the monoblock and flat tile geometry, respectively. The cooling tube (12/15 mm ID/OD) is made of CuCrZr. A steel/CuCrZr tube-to-tube transition joint shall be foreseen prior to welding the tube onto the steel supporting structure. A twisted tape, with a twist ratio of 2, is inserted into the straight part of the cooling tube. It is made of pure Cu and has a rectangular cross-section of 0.8x12 mm². Its aim is to increase the critical heat flux limit of the water coolant and, to a lesser extent, to increase the heat transfer coefficient. The tape is kept in position by the 316L tube, which is joined to the cooling tube of the prototype via a sleeve, typically made of nickel alloy, which is welded onto the facing ends of the CuCrZr and 316L tubes (figure 1). The SATIR inspection is performed on HHF units prior to the insertion of the twisted tape and prior the assembly of the components onto a steel support structure, only the CFC part of HHF units was tested and analysed.

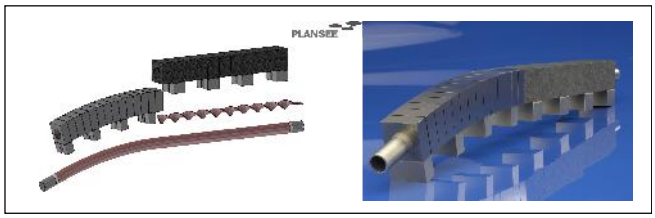

Figure 1: ITER prototype component manufactured by EU industry

PRINCIPLE OF SATIR INSPECTION

The test bed consists of two pressurized independent injection lines synchronized by an industrial programmable logic controller. The HHF units are heated in steady state conditions at 98 °C ±3 °C by means of a hot water flow and then cooled down to 5 °C ±3 °C by means of a cold water flow at 10 $m.s^{-1}$ ±0.5 $m.s^{-1}$. The principle of SATIR test is based on the detection of a time delay of the surface temperature evolution measured during an abrupt variation of the water temperature flowing in the cooling tube during the thermal transient. This delay is measured in comparison to the thermal behaviour of a "defect-free" reference component. The HHF units are tested in parallel with a chosen reference component and a DTref_max criterion was defined as maximum of the transient temperature difference with respect to this reference (figure 2).

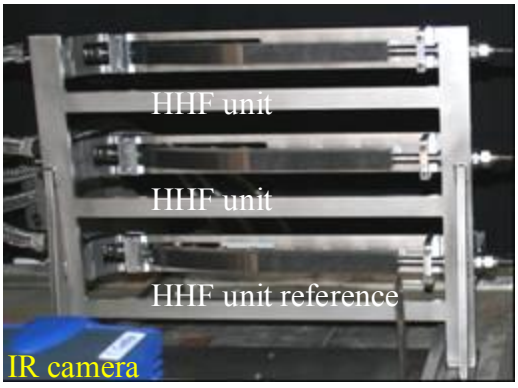

Figure 2: View of tested HHF units on SATIR test bed using specific rotated mounting

Thermal responses of the three sides of a HHF unit are measured (Left, Top, and Right) (figure 3).

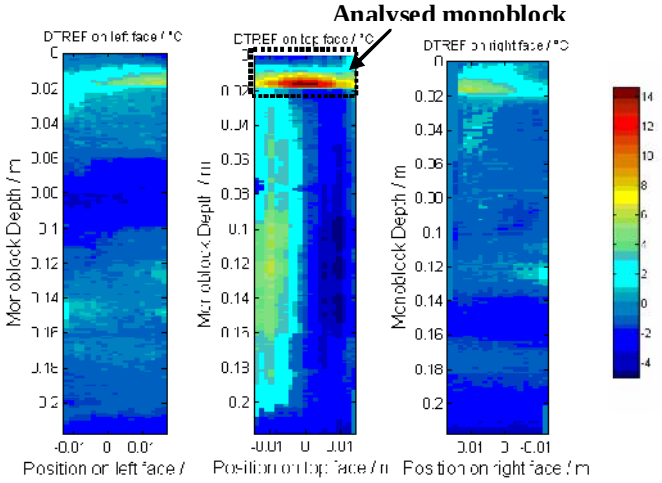

Figure 3: DTref Cartography on the three sides of one HHF unit (SATIR test using a reference component)

In order to correct the emissivity of the measured surface, a normalization algorithm has been developed at the CEA and allowed the detection threshold to be reduced. In fact, both the normalization processing and the DTref_max pixel by pixel allowed a significant improvement of the spatial localization and the detection sensitivity [3, 4]. The physical relation between this DTref_max and the size of defect was established both by means of finite element modelling, taking into account physical properties variation of material and the background noise of the test bed, and by means of tests on samples with calibrated defects defined in the framework of the acceptance criteria study.

DEFINITION OF ACCEPTANCE CRITERIA

Preliminary to this activity on HHF units, a comprehensive study was launched in order to define acceptance criteria for the Divertor PFC with regards to thermo mechanical fatigue. This study consisted in particular in the manufacturing, SATIR inspection and fatigue tests at FE200 (high heat flux facility located at Le Creusot – France) of 54 CFC monoblock samples with artificial defects, axially crossing over the monoblock ("called in the text "Acceptance Criteria samples" or "AC samples") (figure 4).

In the past, the experience of the Fusion community showed that the most critical part of a PFC was the armour to heat sink joint, therefore, maximum dimensions of an acceptable defect at the interfaces of bonding appeared to be relevant criteria with regards to thermomechanical fatigue.

Consequently, crossing strip shape imperfections from 20° to 60° extension ($\Delta\theta$2D) at various positions (θ) were introduced on monoblock design by direct machining (*artificial defect P*) or others techniques (*artificial defect A*). As a first step, AC samples were inspected by transient infrared thermography SATIR technique. Detection of the imperfections on CFC monoblock geometry was found reliable with a limited uncertainty. In particular it was found that defect with an extension above 25° could be detected at the interface CFC/copper, with a SATIR inspection on the 3 sides of each monoblock (figure 5). It was established that a defect at the Copper/CuCrZr interface can be detected with an extension higher or equal to 30°, whatever the position. Experimental errors bars were estimated on the DTref_Max during the SATIR inspections. It was measured with an error margin of ±1.5°C due to the uncertainties of infrared measurement. It was stated that DTref_Max measurements less than 5°C were not significant.

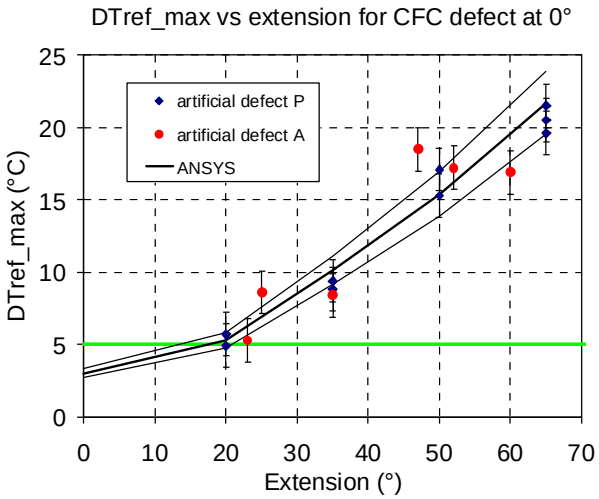

Figure 5: Experimental validation of the thermal model: position 0°; L= Lmonoblock (AC samples)

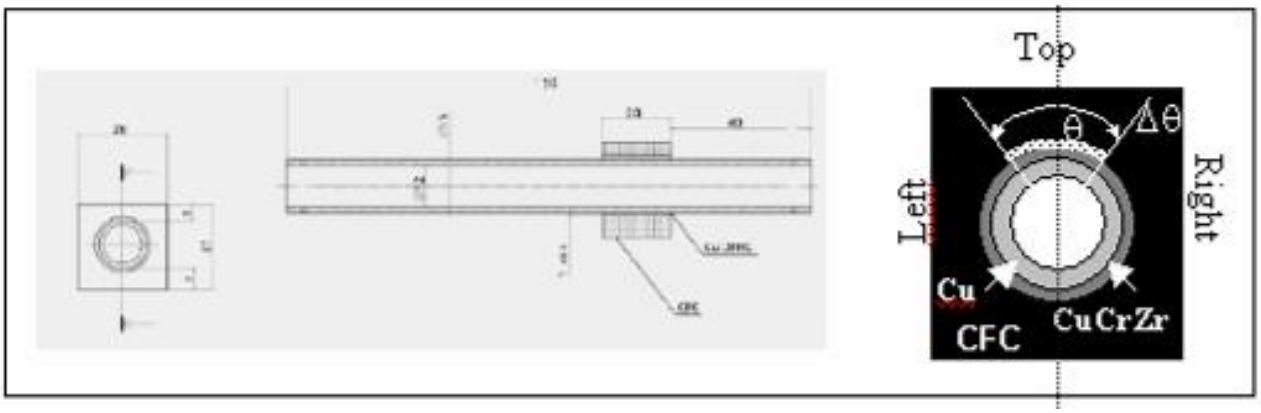

Figure 4: Acceptance Criteria samples geometry and definition of defect extension ($\Delta\theta$2D) and position (θ)

Secondly, the samples were high heat flux tested following a program relevant with the lifetime of the Divertor PFC into the ITER machine: 3000 pulses at 10 MW/m² plus 500 pulses at 20 MW/m² for CFC monoblock concept. For each artificial defect, propagation or stability during the fatigue testing was assessed. It appeared through this study that defects at the cylindrical interface CFC to Copper, which propagate during fatigue, are detectable with SATIR NDE technique.

Finally, post mortem destructive metallographic examination has been launched to confirm the defect propagation due to thermal fatigue testing. On the basis of experimental results detailed in [5] the following acceptance criteria was proposed by IO: defects extension smaller than 50° at CFC/Cu interfaces (40° for Cu/ CuCrZr interfaces) could sustain cycling at 20 MW/m² (table 1).

Table 1: Specification of acceptance criteria for the CFC/Cu and Cu/CuCrZr joints of the ITER CFC monoblocks

	Thermomechanical fatigue	CFC/Copper		Copper/CuCrZr	
		$\Delta\theta_{2D}^{lim}$	θ	$\Delta\theta_{2D}^{lim}$	θ
Criterion 1	Maximum acceptable defect (none)	50° 60°	±45° > ±45°	40°	Whatever the position
Criterion 2	Maximum acceptable defect (less than 28%)	40° 50°	±45° > ±45°	30°	Whatever the position

INSPECTION METHODOLOGY OF HHF UNITS

CFC grades (provided by SAFRAN Group) and thickness of monoblocks are different for the samples and the HHF units of QP: NB31, 4.5 mm for AC samples, respectively NB41, 7 mm for HHF units. However it is assumed that the thermo mechanical fatigue behaviour of AC samples and HHF units are comparable. Consequently, with regards to SATIR inspection, a model was developed to simulate the thermal process of SATIR inspection in order to transfer measurements of DTref_Max on AC samples to HHF units.

Definition of the model: On Figure 5, experimental results obtained on AC samples are plotted and compared with the calculated DTref_Max for 0° and 45° angle positions. The analysis was performed by finite element calculation including a non-linear thermal property behaviour function of space and temperature. The model was validated on HHF tests and it compared satisfactory at various positions with the experiments; thus it could be extended to HHF unit geometry (figure 6).

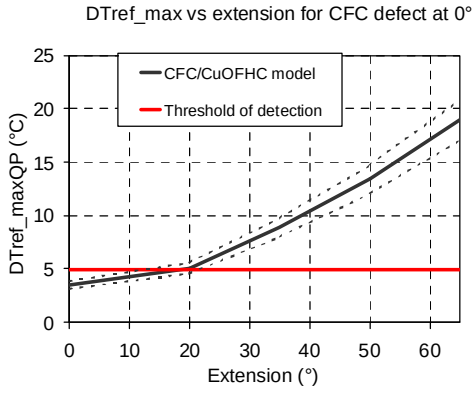

Figure 6: Extended model to ITER PFC geometry

Determination of the position θ and length L:

The position (θ) and an estimation of length (L) of a defect are given by the reversed geometric projection of the defect at the CFC/Copper interface, taking into account the orthotropy ratio of the CFC thermal properties (figure 7). The error margin on the estimation of the defect position is evaluated at ± 5° angle. However the length of defect would be also measurable on the projection but it could not be experimentally validated with defects axially crossing over the block. Nevertheless we estimate its precision to ± 2.5mm.

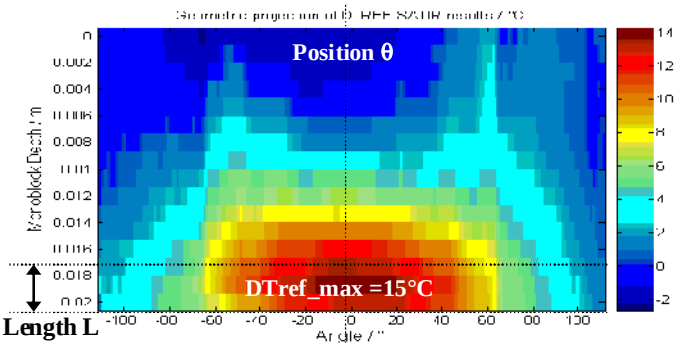

Figure 7: Projection of the 3 DTref_max cartographies of the analysed monoblocks at the CFC/Cu interface to define the defect position θ and length L

Determination of the extension Δθ:

It was to be noted that, in case of AC samples, the implemented artificial defects cross over axially the monoblock, so that in the model, the length of the defect is equal to the length of the monoblock (i.e. 20 mm), this is a bidimensional (2D) situation from a thermal point of view. A method was proposed based on the estimation of an empirical Factor (F) to account for a length lower than the monoblock axial length: F=1 if L > Lmonoblock / 3 and F=Lmonoblock / 3L if L ≤ Lmonoblock / 3. Then, F is applied to Δθ2Dlim to obtain
Δθ3Dlim: Δθ3Dlim = Δθ2Dlim x F.

To estimate the defect extension Δθ3D for a defect shorter than Lmonoblock, a 3D approach is needed. Summarizing, the analysis is carried out in two steps. First a 2D model was used to obtain Δθ2D, starting from a measured DTref_Max, θ and assuming L = Lmonoblock. Then a corrective coefficient "k" was used to obtain
Δθ3D: Δθ3D = Δθ2D / k.

The coefficient k is obtained by a set of 3D calculations of SATIR inspection and given in a form of abacus (figure 8). For instance, for θ = 0° and Δθ2D = 57°, L/Lmonoblock = 1/5 then F= 5/3 and k = 0.3, we obtain a 3D extension of the defect Δθ3D = 190°.

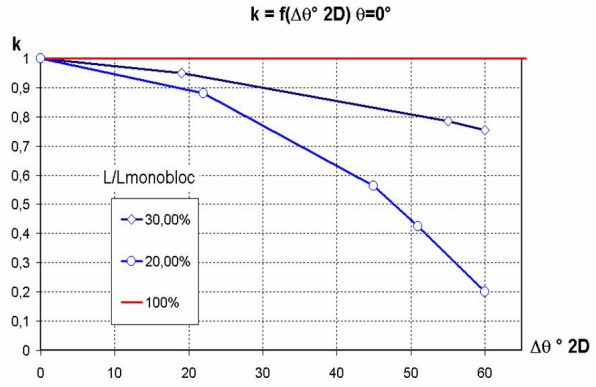

Figure 8: Corrective coefficient "k" vs. Δθ2D for a given θ (here θ = 0°) and L as parameter

EXPERIMENTS RESULTS

Each CFC monoblock was SATIR tested and analysed. Table 2 shows examples of analysed CFC monoblocks with regard to the 2 criteria defined by IO, involving 3 various decisions: questionable, derogated and accepted.

- Criteria 1 (C1): Δθ3D< Δθ3Dlim (more than one of CFC monoblocks per HHF unit)
- Criteria 2 (C2): Δθ3D< 40° x F (more than three of CFC monoblocks per HHF unit)
- "Questionable" decision if the both criteria (C1 and C2) are not verified
- "Derogated" decision if C2 is not verified

Table 2: Examples of SATIR analysis for 3 CFC monoblocks

SATIR inspection results			3D processing				Respect		Decision
DTref_max (°C) ± 1.5	θ (°) ± 5	L ± 2pixels	k	$\Delta\theta_{3D}$ (°) ± 8	F	$\Delta\theta_{3D}^{lim}$ (°)	C1	C2	
15	0	$1/5L_{monoblock}$	0.28	190	5/3	83	No	No	Questionable
11	-30	$1/2L_{monoblock}$	0.95	48	1	50	Yes	No	Derogated
5.7	-45	$L_{monoblock}$	1	32	1	50	Yes	Yes	Accepted

Infrared thermography analysis

All the Cu/CuCrZr joints of HHF units were tested by ultrasonic technique. No significant indications of defect presence at the Cu/CuCrZr joint were reported in the ultrasonic inspection reports from manufacturers. Consequently, 100% of SATIR indications most probably stem from defect located at the interface CFC/Copper (or from the CFC itself). In the case of one monoblock, an unusual delay cooling during the SATIR testing was identified probably due to a misorientation of carbon fibres during the machining of the CFC monoblock. Indeed, direction of maximum of the conductivity seems to be 90° misorientated.

80% of HHF units are declared acceptable by CEA taking into account uncertainties of measurement. In addition 98% of tested CFC monoblocks meet both criteria. This remark highlights the need to set up a repairing procedure in order to accept a maximum of number of HHF units during Divertor procurement.

Thermo mechanical analysis

The analysis demonstrated that 55% of thermal imperfections at the CFC/Copper interface are located at the position 45° angle where the residual shear stresses (σxy), due to the manufacturing, are maximum (figure 9) [5]. The remaining thermal imperfections were distributed on the other positions (θ).

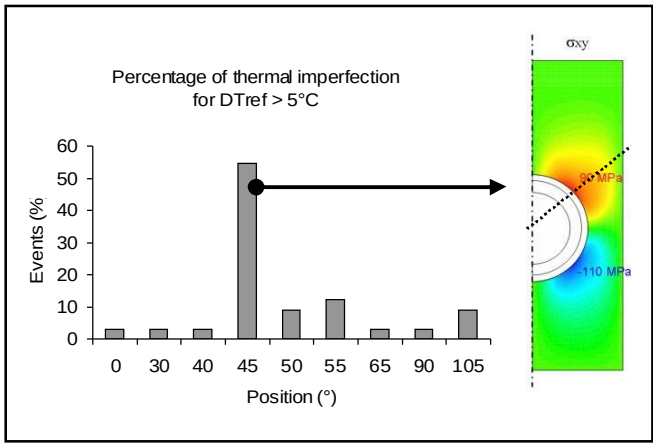

Figure 9: Percentage of rupture occurring according the position θ - Agreement with thermo mechanical calculations σxy

CONCLUSIONS

This paper deals with the SATIR inspections results performed on 165 CFC monoblocks manufactured by EU industry. CEA proposes a preliminary conclusion on the acceptance of the 15 HHF units.

The results highlight the need to set up a repairing procedure in order to accept a maximum of number of HHF units during Divertor procurement. In the frame of the study, several analysis tools complementary to SATIR method, like reversed geometric projection, were set up. Nevertheless this last method needs to be experimentally validated in order to read directly the position and the defect extension Δθ3D. SATIR method gives global information on the cooling capability of the component and allowed in the frame of this work to point out a misorientation of the carbon fibre of 90° angle. The SATIR technique allows to be confident in the capability of commissioning components reaching the required design values of the ITER Divertor PFCs. Nevertheless further discussions already started on modification of the proposed maximum acceptable dimensions and the related acceptance criteria and in particular onto the necessity to introduce a questionable zone. The next step of this qualification work will concern the high heat flux testing of units, which will allow the consolidating of the acceptance criteria defined in the frame of the EU procurement for the Inner Vertical target of the ITER Divertor.

REFERENCES

[1] Merola M. et al.; "EU R&D on ITER Divertor components", p.75-79, Fusion Eng. and Design 325-31(2005)

[2] Durocher A. et al.; "Advanced Qualification Methodology for Actively Cooled High Heat Flux Plasma Facing Components" p.1682-1689, Nucl. Fusion 47 (2007)

[3] Durocher A. et al.; "An operational non-destructive examination technique for ITER Divertor plasma facing components" NUMA43989 10.1016/j.jnucmat.2008.12.274

[4] F. Cismondi et al., "Analysis of SATIR test for the qualification of high heat flux components: defect detection and classification by signal-to-noise ratio maximization", p. 213-217, Physica Scripta T128 (2007)

[5] Chevet G. et al. "Damage of actively cooled plasma facing components of magnetic confinement controlled fusion machines" FUSENGDES-D-08-00343

REPORTS AND PUBLICATIONS

Quality Plan of SATIR test of vertical target qualification prototypes, Internal CEA Report CFP/PCD-2007.006

Visual tests of ITER vertical target qualification prototypes, Internal CEA Report CFP/PCD-2007.004

Control of ITER vertical target qualification prototypes by infrared thermography, Internal CEA Report CFP/PCD-2007.003

Infrared thermography inspection of the ITER vertical target qualification prototypes manufactured by European industry using SATIR, Fusion Eng. Des. (2009), doi:10.1016/j.fusengdes.2008.12.095, A. Durocher, et al.

Evaluation of plasma facing components thermal performance by infrared thermography – InfraMation workshop 2008, Reno -USA A. Durocher, et al.

TASK LEADER

Alain DUROCHER

DSM/IRFM
CEA-Cadarache
F-13108 Saint-Paul-lez-Durance Cedex

Tel: 33 4 42 25 62 24
Fax: 33 4 42 25 43 54

e-mail: alain.durocher@cea.fr

CEFDA06-1411

Task Title: TW6-TVB-ACCTEST: Be/CuCrZr HIP JOINING FOR ITER FW QUALIFICATION TESTS

INTRODUCTION

The ITER blanket-shield concept is a modular configuration mechanically attached to the vessel. It is constituted with Shield modules and First Wall (FW) panels mechanically attached on the shield blocks. Shield modules are made with 316LN stainless steel whereas the First Wall panels are constituted with a 316LN stainless steel backing plate, a CuCrZr copper alloy that acts as a heat sink material and beryllium tiles that act as an armour material against the plasma. 316LN stainless steel, CuCrZr copper alloy and beryllium tiles are joined together by Hot Isostatic Pressing (HIP).

The first objective of this work is to continue the development programme started in the frame of task TW3-TVB-JOINOP to improve the performance of Be/Cu joints under High Heat Flux. The technical solutions developed in this program are tested under relevant ITER operating conditions by manufacturing 96x86mm² small scale mock-ups.
The second objective of this work is to manufacture three qualification mock-ups to validate the technical solutions that will be used to manufacture the FW panels. The qualification mock-ups are 260mm long, 81mm wide, 84mm thick and are constituted by three 80x80x10mm^3 beryllium tiles.

2007-2008 ACTIVITIES

To improve the performance of Be/CuCrZr joint under High Heat Flux tests, several new fabrication parameters have been investigated. These parameters are the beryllium grade (S65C or other grades), the size of the beryllium tiles, the depth of the slits between the beryllium tiles and also new interlayers to avoid or limit the formation of Be-Cu brittle intermetallic compounds.
To study the influence of all these fabrication parameters on the performance of Be/Cu joints, we manufactured six small scale mock-ups with 1, 9 or 16 beryllium tiles. In each case, the thickness of the beryllium tiles is about 10mm. As the same materials and the same processes are used for the fabrication of the qualification mock-ups, we detail their fabrication in a same paragraph.

MATERIALS SPECIFICATIONS FOR THE FABRICATION OF THE MOCK-UPS

The type and the chemical composition of the main materials used for the fabrication of the mock-ups are presented in table 1, table 2 and table 3. 316LN material used to manufacture the mock-ups is a special heat supplied by AREVA whereas CuCrZr alloy is provided by KME Europa.

Table 1: Chemical composition of 316LN stainless steel material

Wt%	C	Ni	Cr	Mo	S	P	Si	Mn	N2
ITER	<0.03	12-12.5	17-18	2.3-2.7	<0.025	<0.035	<0.5	1.6-2	0.06-0.08
316LN	0.027	12.210	17.530	2.455	0.001	0.024	0.305	1.845	0.069

Table 2: Chemical composition of CuCrZr copper alloy

Wt%	Cu	Cr	Zr	$R_{0.2}$ (MPa)	R_m (MPa)	Used for the fabrication of
ITER	Remainder	0.6-0.8	0.07-0.15	250	360	
CuCrZr	99.2	0.65	0.11	247	381	Small scale mock-ups
CuCrZr	99.2	0.63	0.11	365	439	Qualification mock-ups

Table 3: Manufacturer specification for the chemical composition of S65C beryllium grade (from ITER material handbook)

Max (Wt %)	Be	BeO	Al	C	Fe	Mg	Si	Other metal impurities
S65C	99	1.0	0.06	0.1	0.08	0.06	0.03	0.04

FABRICATION PROCESS OF SMALL SCALE AND QUALIFICATION MOCK-UPS

Fabrication of the bi-metallic CuCrZr/316LN support

After the machining operations, all the pieces are controlled accurately to verify if their sizes and their mean roughness are under the machining specifications. Then the pieces are thoroughly cleaned and assembled inside a canister.

The standard HIP cycle used to manufacture the bi-metallic support of the mock-ups is presented in figure 1. The diffusion welding plateau is 2 hours long and is made at 1040°C and 140MPa.

After the HIP cycle, 316LN/CuCrZr supports are submitted to a thermal treatment to restore the CuCrZr mechanical properties. All the mock-ups are treated at 980°C during about one hour and cooled quickly at about 60°C/min to freeze the solid solution of Cr and Zr inside the copper matrix (see figure 2). In the case of mock-ups made for ITER qualification tests, the temperature is measured by three thermocouples placed inside the CuCrZr block. After this heat treatment, the mock-ups are machined to receive the beryllium tiles.

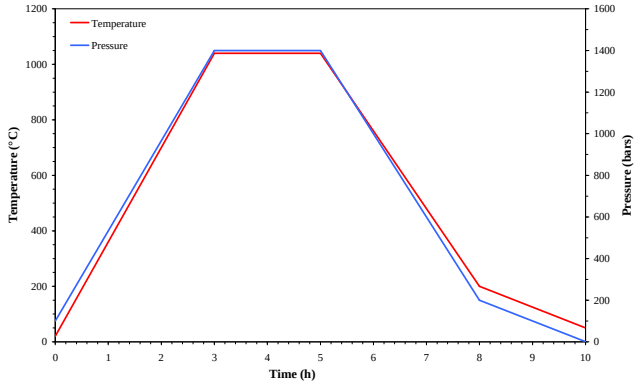

Figure 1: Theoretical HIP cycle to weld by diffusion CuCrZr and 316LN materials

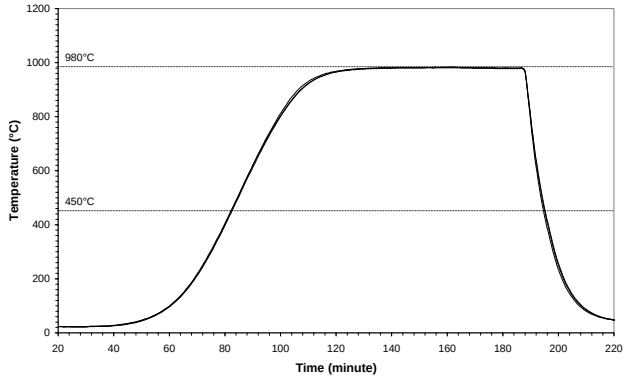

Figure 2: Thermal treatment applied on mock-ups to restore the CuCrZr mechanical properties after a 1040°C HIP cycle

Fabrication of Be/Cu joints

As for the fabrication of CuCrZr/316LN joints, the beryllium tiles and the CuCrZr surfaces are size controlled and thoroughly cleaned before their assembly.

The beryllium tiles and the CuCrZr heat sink alloy are welded by diffusion at 580°C and under 140MPa. These two parameters are kept constant during two hours to obtain a joint with good mechanical properties and also to confer to the CuCrZr alloy mechanical strength that fulfils the ITER requirements [1].

According to the development work programme, six small scale mock-ups have been manufactured. Four of them have been made with beryllium tiles presenting different sizes, grades and with slits having different shapes. The two last mock-ups have been manufactured with a new interlayer that could favour a reduction of the diffusion welding temperature between Be and Cu and thus limit the formation of Be-Cu intermetallic compounds. Photographs of the six mock-ups made during the development programme are presented in figure 3.

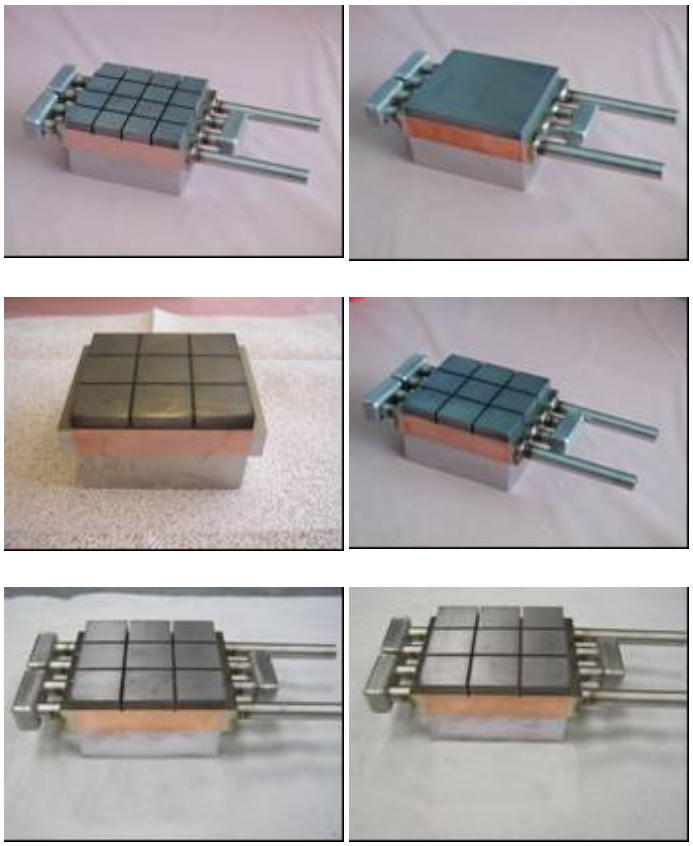

Figure 3: Six small scale FW mock-ups to validate some fabrication parameters

CuCrZr MECHANICAL PROPERTIES

To check the mechanical properties of the CuCrZr heat sink material at the end of the fabrication process, several tensile specimens have been machined from a specific mock-up made together with the ITER qualification mock-ups. It has the same size as the qualification mock-ups presented in figure 4 but it has only two 56x56x10mm^3 beryllium tiles.

Tensile properties (yield strength, ultimate tensile strength and total elongation) of CuCrZr have been measured with a deformation rate equal to 10^{-4} s^{-1} at 20°C and 10^{-3} s^{-1} at 250°C. At 20°C the measurements were done on an Adamel DY36 electro-mechanical machine whereas high temperature measurements were done on an MTS hydraulic machine equipped with a vacuum furnace. The temperature of the samples was measured with two thermocouples in contact with the sample (the accuracy of the temperature measurement is in the range ±5°C). The measurements were done according to standard NF EN 10002-1 and NF EN 10002-5. The tensile specimens present a diameter equal to 6mm and a gauge length equal to 30mm and they are machined along the rolling direction of the CuCrZr plate. Elongation of the tensile specimens at 20°C is measured with an MTS extensometer with a gage length equal to 25mm.

The qualification mock-ups are made with three 80x80x10mm beryllium tiles. A photograph showing one of these mock-ups is presented in figure 4.

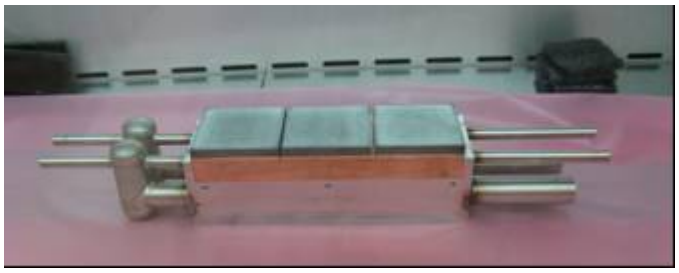

Figure 4: One of the three FW mock-ups for ITER qualification tests

Figure 5 and 6 show the tensile results obtained at 20°C and 250°C. The mechanical tests performed show a sharp reduction of the CuCrZr tensile properties. The yield strength of the CuCrZr batch used to manufacture the ITER qualification mock-ups decreases from 365MPa in the as-received state to about 175MPa. The values just fulfilled the ITER requirements given in [1]. This loss of mechanical properties can be explained by the different thermo-mechanical histories. The material supplier does not want to give information about the main fabrication parameters of the alloy, so it is difficult to point precisely the differences. However, we can infer that, since work hardening is lost during the mock up fabrication process, work hardening plays a role.

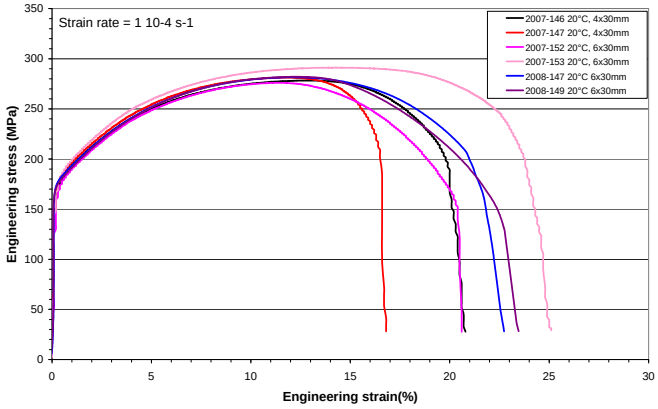

Figure 5: CuCrZr tensile properties measured at 20°C after the fabrication process of ITER qualification mock-ups

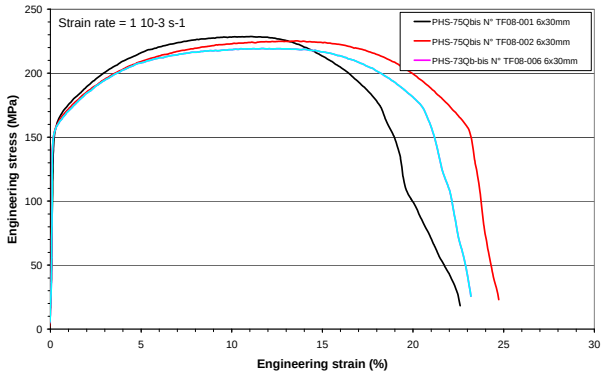

Figure 6: CuCrZr tensile properties measured at 250°C after the fabrication process of ITER qualification mock-ups

Metallographic examinations reveal also a large increase of the CuCrZr grain size as shown in figure 7. The mean size of the CuCrZr grain in the as-received state is about 100µm.

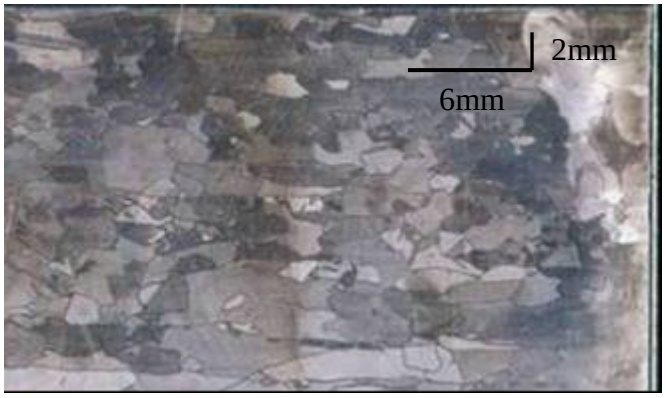

Figure 7: CuCrZr grain size at the end of the fabrication process

As observed in figure 7, the alloy exhibits with very heterogeneous grains after the fabrication process. The rolling direction is clearly identified by the grain shape. The average size of the grains is measured according to the European Standard NF EN ISO 2624 by using the intercept method. The average grain size along the rolling direction varies from 1.7mm to 3.4mm. However, larger grains with length close to 6mm are also observed. Along the transverse direction, the average grain size ranges from 1mm to 1.9mm.
As the mechanical properties of the CuCrZr depends mainly on the Cr and Zr particles put in solid solution inside the copper matrix, we expect that the grain growth has not a strong influence on its tensile properties.

HIGH HEAT FLUX RESULTS

Small scale mock-ups presented in figure 3 were tested under High Heat Flux. The different technical fabrication parameters investigated in the development work programme give approximately the same results. A reduction of the diffusion welding temperature enables to reduce the thickness of the Be-Cu intermetallic layer.

The qualification mock-ups have been tested in the USA and in the Russian Federation according to the qualification work programme. All the mock-ups have passed successfully the tests.

Be/CuCrZr REFERENCE SAMPLES FOR MECHANICAL TESTING

To complete the high heat flux qualification tests, mechanical tests of the different types of joints included in a First Wall (FW) panel are required by ITER Organisation. In order to standardize the procedures for the measurement of the mechanical properties of the joints, to demonstrate that the components meet minimum mechanical requirements and to provide a database for tests during the series production, mechanical tests have to be done on Be/CuCrZr joints. To allow these tests before and after irradiation, several Be/CuCrZr samples were machined in

the qualification mock-ups made with two 56x56mm² beryllium tiles. These samples were machined according to drawings proposed by ITER Organisation [2] but modified according to the testing possibilities of the laboratories. Mechanical tests after irradiation will be performed by SCK-CEN in Belgium whereas unirradiated samples will be tested by IEF2 at Jülich in Germany. In both cases, tests will be conducted under a maximal temperature of 300°C.

CONCLUSIONS

Concerning the first part of the study, six 96x86mm² high heat flux mock-ups were fabricated with several Be/CuCrZr configurations. The several fabrication parameters listed above do not allow to improve significantly the performance of the Be/Cu joints under high heat flux and the mock-ups withstand a load of about 3MW/m².

Concerning the fabrication of ITER qualification mock-ups, our work enabled the fabrication of three mock-ups; Two of them passed successfully the qualification tests in USA and in the Russian Federation. These results indicate that our technology is reliable to manufacture the ITER First Wall panels.

REFERENCES

[1] K. Oki and all. “Six party qualification program of FW fabrication methods for ITER blanket module procurement”, Fusion Engineering and Design, 2007, 82, pp. 1774-1780

[2] V. Barabash and A. Peacock “Preliminary recommendation for standard test methods for the measurements of the strength properties of joints during manufacturing of the ITER first wall” ITER_D_22L725 V1.2

REPORTS AND PUBLICATIONS

P-E. Frayssines, G. Roux, O. Gillia, B. Oresic, J.-M. Leibold, P. Lemoine, A. Montani, «Be/CuCrZr HIP joining optimisation for ITER FW qualification tests», Final report EFDA 06-1411, TW6-TVB-ACCTEST, Technical note DTH/DL/2008/113, dec 2008

TASK LEADER

Pierre-Eric FRAYSSINES

DRT/LITEN/DTH/LTH
CEA-Grenoble
17 rue des Martyrs
F-38054 Grenoble Cedex 9

Tel: 33 4 38 78 28 59
Fax: 33 4 38 78 54 79

e-mail : pierre-eric.frayssines@cea.fr

CEFDA07-1700-1617

Task Title: TW6-TVB-FWPROT2: DESIGN OF CLAMPED POLOIDAL LIMITERS FOR ITER

INTRODUCTION

A layout of a bolted CFC tile concept for ITER inner poloidal limiters allowing heat fluxes up to 1 MW/m² has been performed during 2007-2008 activities based on former NET studies and the design of Tore Supra inner guard limiters [1,2,3]. 2D-thermohydraulic finite element calculations of the tile heat sink structure and elastic tile attachment mechanism have been realised.
Halo and disruption forces, based with however insufficient available data's, have been estimated by hand calculations.
The design has been oriented in order to implement the armour concept on the existing ITER shield blanket geometry with a minimum, as far as possible, of design modifications on the heat sink structure.

2007-2008 ACTIVITIES

DESIGN PRINCIPLE

The proposed design is a "flat tile" concept allowing individual tile front accessibility for the attachment to the blanket panel heat sink without additional cooling tube structures on the back side as used e.g. in clamped "tube in tile" concepts (LHD). Tile and attachment mechanism is a mechanical integral part for manipulation (figure 1) [1].

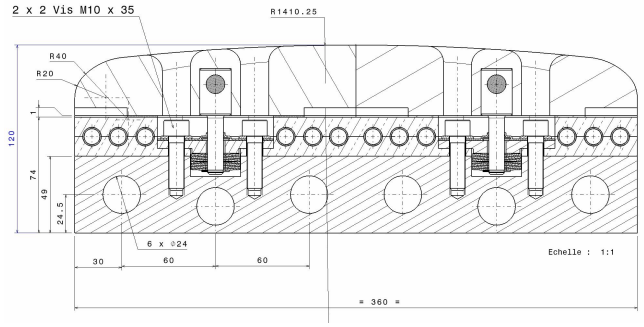

Figure 1: Cross section of two tiles attached on a blanket panel

In order to avoid thermal contact loss of the tile assembly during steady state heat loads and therefore minimizing the tile surface temperature, a sufficient soft and (if possible) conductive compliant layer has to be inserted between tile and heat sink. Indeed, as the tile bends during the incident heat load due to the temperature gradient in the tile thickness, this deformation has to be compensated by an e.g. PAPEX® or Panasonic-PGS® exfoliated compliant layer. The concept is based on a low tile contact pressure (with a reasonable spring mechanism) in the range of 0.3 to 0.5 MPa. Than the global heat transfer coefficient is dominated by the thermal conductivity of the layer taken to be 0.5 mm in thickness.

The tile-bending Δ under heat deposition, which has been simply evaluated for different materials at the given tile geometry (tile th = 40 mm, size 180x180 mm^2) and a heat load of 1 MW/m² led to the following values:

CFC: Δ= 0.04 mm;
Be: Δ= 0.8 mm;
W: Δ= 0.22 mm.

These bending values, **with exception of CFC**, can not be accommodated by the compliant layer even at 0.5 MW/m² [2]. ***Therefore this concept can not be applied to a Be or W tile of equivalent dimensions.***

THERMOHYDRAULIC RESULTS BY FINITE ELEMENT CALCULATIONS

Tile/heat sink
The 2D calculation with CASTEM2000 has been performed (figure 2) with different load cases and recently following parameters given in an executive summary by A. Loarte et al. on 14 September 2007:

Radiated and CX load perpendicular = 0.44 MW/m²,
Plasma load parallel: = 5.3 MW/m², λ_q = 1 cm,
Volumetric neutron heating [ITER G 16 DDD 35 R0.1]:
CFC = 4.8 W/cm^3; CuCrZr = 6.5 (heat sink and sliding piece); stainless steel = 5.8 (this includes the spring washer and fastener).

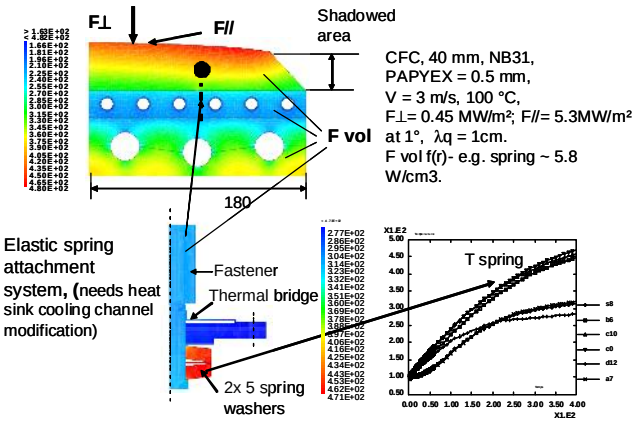

Figure 2: 2D thermohydraulic calculation example of a CFC bolted tile concept for ITER; tile shaping not optimized

The CFC NB 31 high conductivity fibers of the tiles (maximum tile thickness 40 mm) are oriented parallel to the incident heat flux.
The maximum surface temperature is 480°C (figure 2); the CuCrZr heat sink is around 260 °C; the rear side of the cooled stainless steel blanket panel reaches 380°C. Component steady state conditions are reached roughly after 300 s.

For the same calculation case however F⊥= 1MW/m², the CFC surface temperature is 890°C. The temperature gradient in the tile thickness reaches more than ~400°C which should be considered as the limit for tile bending compensation by the compliance layer [2]. These results are obtained with an "ideal" non modified heat sink cooling structure (ITER reference design). In reality, for each tile, two of the 6 "stainless steel tube lined" cooling channels in the CuCrZr heat sink have to be locally deviated in order to allow insertion of the 2 elastic attachment mechanism. If however these two channels would be omitted, the local heat sink temperature would be rise until 480°C for the same heat load which is unacceptable. It should be remembered that the heat sink cooling channels are lined by 1 mm thick stainless steel tubes, which is thermally not an advantage!

Elastic attachment mechanism

The attachment of the tile has to be elastic in order to maintain the contact pressure during differential expansion of components. **The critical point seems to be the temperature evolution (neutron irradiation) in the spring washers.** Even with small soft copper "contact enhancement" washers inserted between the fastener, springs (Inconel 718/750X) and sliding piece (or copper coatings), the heat transfer by conduction to the heat sink is still low and the temperature reaches at least 480°C after 400s (figure 2) and 570°C after 1000s and has not attained steady state conditions. Therefore the final temperature depends on the operation duty cycle.

DEGRADATION OF PHYSICAL PROPERTIES OF MATERIALS UNDER NEUTRON IRRADIATION

A stress relaxation and issued spring force reduction of about 30 % at 1 dpa [2] should be considered as the design limit in order to avoid an excessive contact pressure release on the compliant layer interface (reduced layer deformation) which could lead to local loss of thermal contact between tile and heat sink.

The modification of physical properties of carbon based materials (CFC), especially the thermal conductivity as a function of irradiation temperature, is not included in the thermohydraulic calculations.

The fatigue behaviour of the compliant material in an ITER environment is unknown. However Tore Supra applications with PAPYEX did not reveal any problems. Very little is known about irradiation induced decrease of thermal conductivity and creep. Theoretically the thermal conductivity should be little affected due to the special structure of the material (already low conductivity determined mainly by the contact resistance between the graphite flakes).

HEAT LOAD

The peaking factor is evaluated geometrically by meshing a limiter and calculating its intersection with a 6.5 MA plasma (end of limiter phase, 6 s before X-point formation, typically scenario 2 at 24 s) figure 3, and [3]. The mutual shadow between individual limiter beams is evaluated using field line tracing. This mutual shadow increases further the peaking factor, then at 17. The results are normalized to a surface heat flux of 1 MW/m² which is the design heat flux for a bolted technology.

Surface heat flux	Extracted power	λ_q	Number of inner poloidal limiters	Heat flux on the magnetic surface of the limiter
1 MW/m^2	1.7 MW	17 mm	18	17 MW/m²

In addition to the results mentioned above, the modelling shows that the penetration between limiters is 8 mm, which is an useful input for the optimization of the surface profile: there is few use[1] to have a detailed shaping of the surface beneath a 1 cm depth with respect to the most inner point of the limiter.

NB: Such calculation only uses the magnetic configuration and the λ_q as inputs.

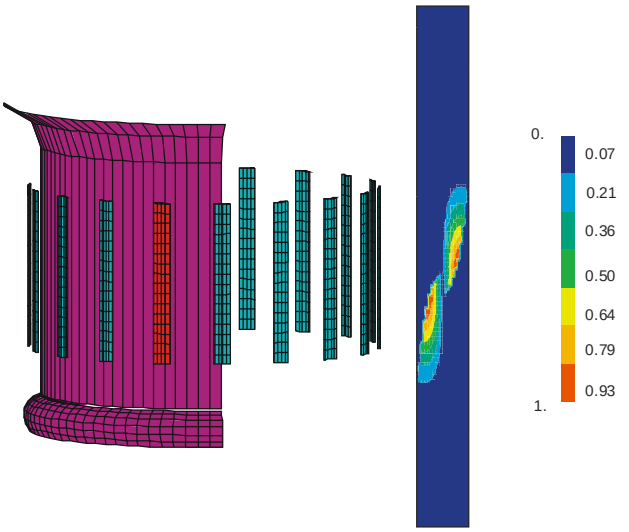

Figure 3: Model for the heat flux modelling on a set of inner limiters and heat flux distribution on the limiter surface (in MW/m², for 1.7 MW of incoming power and a λq of 17 mm)

CONCLUSIONS

Analyses showed that the design of a bolted CFC tile concept for ITER poloidal limiters represents in principle a sound solution for heat loads up to e.g. F⊥= 1.0 MW/m² ; F// =5.3 MW/m², λq=1cm including ITER related volumetric heating rates. However heat evacuation (neutrons) combined with creep strength under load in the elastic spring washers is an issue. Independently, the allowed spring stress relaxation, due to neutron irradiation, would be expected to occur after about 13000 DT full power burns. Remote manipulation possibilities of the relative small components could not be investigated, due to the lack of available informations. A minimum of blanket panel heat sink modifications (cooling channel geometry) are necessary. In order to maximize the tile/component geometry in ITER (reducing tele-manipulation time) the present optimized tile size for CFC cannot be used for a Be or W tile at the same heat flux!

Local heat load estimations for discrete poloidal limiter sections showed quite low extraction power capabilities for a tile design heat flux up to 1 MW/m².

[1] Misalignments may still need to be accounted for.

REFERENCES

[2] Design of an independent water cooled plasma facing armour with mechanically attached conduction cooled tiles for NET first wall, Final Report, Contr. NET/90/239 , M. Lipa, 25/9/1992

[3] Heat exhaust capability of poloidal limiters in ITER, R. Mitteau , CFP/NTT-2007.044

REPORTS AND PUBLICATIONS

[1] M. Lipa, R. Mitteau et al.; Design of clamped tile concept for ITER poloidal limiters, EFDA contract TW6-TVB-FWPROT 3- Subtask2, final report CFP/NTT-2008.001, Jan. 2008

TASK LEADER

Manfred LIPA, Raphael MITTEAU

DSM/IRFM/SIPP
CEA-Cadarache
F-13108 Saint-Paul-Lez-Durance

Tel : 33 4 42 25 46 58
Fax : 33 4 42 25 49 90

e-mail : lipa@drfc.cad.cea.fr

CEFDA07-1700-1622

Task Title: TW6-TVB-HIPJOIN: HIP JOINING DEVELOPMENT AND APPLICATION TO THE FW DESIGN OF NBI MODULES

INTRODUCTION

The ITER Blanket-shield system is the innermost part of the reactor directly exposed to the plasma. Its basic function is to provide the main thermal and nuclear shielding to the vacuum vessel and external reactor components. Its concept is a modular configuration mechanically attached to the vacuum vessel. The Blanket modules consist of a water cooled austenitic stainless steel blocks and separable First Wall (FW) panels mechanically attached to the shield block. The typical dimensions of the FW panels are 1x0.25x0.07m^3. They are constituted of a bi-metallic support structure made from a 20mm thick CuCrZr alloy heat sink material with embedded 10/12mm diameter 316LN-IG stainless steel tubes and bonded to a 40mm thick 316LN stainless steel backing plate with 12mm diameter cooling channels. Joining of these materials is done by HIPing. A thick beryllium layer of about 10mm is used as a protective plasma facing material and is bonded to the CuCrZr alloy heat sink material in the form of tiles by HIPing. The FW panels are designed to sustain a peak surface heat flux of 0.5MW/m², a maximum neutron wall load of 0.8MW/m² and an average neutron fluence of at least 0.3MWa/m² for a nominal number of 30 000 cycles. According to the present ITER Design Requirements, they shall also sustain a limited number of 10 seconds transient events of up to 1.4MW/m².

A research and development programme for the ITER blanket shield has been implemented in Europe to provide input for the design and the manufacture of the full scale production components. In particular, FW mock-ups (small scale and medium scale) and full scale prototypes of FW panels have been fabricated and tested. There is however the need to further increase the performance under high heat flux of the Be/CuCrZr joints of the FW armour to offer comfortable margins against off-normal operations and to consolidate their industrialization.
To achieve these goals we search new interlayers that prevent the formation of brittle intermetallic layers between Be and CuCrZr and also new cleaning media to replace the products used to prepare the surface of the Be tiles before the HIP operation, since they will be prohibited in the future. The investigated and chosen solutions will be validated by manufacturing and testing under High Heat Flux three small scale mock-ups. Furthermore, two other small scale mock-ups will be manufactured to test the influence of the copper thickness between Be and CuCrZr.

Furthermore, before the preparation of the blanket procurement specifications, a critical fabrication review of one FW module located around the Neutral Beam Injector (NBI) openings will be done. Starting from the initial CATIA drawings of the module, we will propose design changes or improvements to make the manufacture of such module cost effective. This review will include also possible critical fabrication issues identified during the design review to manufacture FW mock-ups.

2007-2008 ACTIVITIES

Improvement of Be/CuCrZr joint performance under High Heat Flux by using metallic interlayers

To avoid the formation of brittle intermetallic layers between beryllium and copper during the HIP diffusion welding process, several metallic interlayers were used up to now. These interlayers are Ti, Cr, Si, Al and Ni. Most of these interlayers react with copper or beryllium to form brittle intermetallic phases and reduce the performance of Be/CuCrZr joint under High Heat Flux operations. According to SEM and IBA analyses, Cr is the only metallic interlayer that does not react with Be or Cu.
To increase the performance of Be/CuCrZr joint under High Heat Flux, we are looking for new metallic interlayers which are both metallurgically compatible with Be and Cu. Unfortunately, Be reacts with a lot of metallic elements according to the binary phase diagram handbook of the beryllium alloys[1]. As the experimental data given in [1] do not take into account the kinetics of the chemical reactions, we searched metallic elements metallurgically compatible with copper and verified their compatibility with Be during a standard HIP cycle.
Metallic elements metallurgically compatible with copper are refractory metals. Thus, some of these elements have been chosen and tested during this task. To verify that they are metallurgically compatible with Be, we have coated small beryllium tiles (10x10x4mm^3) with a 1 µm thick layer of refractory metals by physical vapour deposition (PVD). Then, the coated tiles have been heat treated in a vacuum furnace and analysed by X-Ray diffraction (XRD). The temperature of the furnace was regulated to reproduce the temperature variation of a standard HIP cycle with a temperature plateau at 580°C during two hours. To have references, we have heat treated at the same time tiles covered respectively by a thin layer (1µm) of Cr and Cu.

After the heat treatment process, “low” incidence and θ-2θ locked-coupled X-Ray diffraction (XRD) analyses have been performed using the Cu Kα radiation. For low incidence experiments, the incident angle is fixed: it is chosen for each coating nature, so that the X-Ray penetrates through the 1 µm thick coating and reaches the Be/interlayer interface. The depth of analysis stays constant all along the experiment and the diffracted signal related to the Be bulk material is limited in these conditions, in comparison with θ-2θ analysis where the depth of the analysis increases with θ.

Our analyses confirm that Cr does not react with Be whereas Cu reacts to form two intermetallic phases which

are BeCu and Be_2Cu. The refractory metals tested in this task do not react with Be.

Following these observations, several Be/CuCrZr joints were manufactured with the selected refractory metals as interlayers. These samples were manufactured by HIPing coated Be tiles onto CuCrZr at 580°C during two hours. During the diffusion welding plateau the pressure is equal to 140MPa.

After the HIP cycle 25x25x15mm^3 samples have machined from the Be/CuCrZr joints and tested at ambient temperature by applying a rising force on one side of the beryllium tiles whereas the CuCrZr part is fixed inside holding jaws (see figure 1). The mechanical tests are underway. According to the mechanical results and the metallographic observations of the manufactured joints we will choose the best interlayers to manufacture High Heat Flux mock-ups.

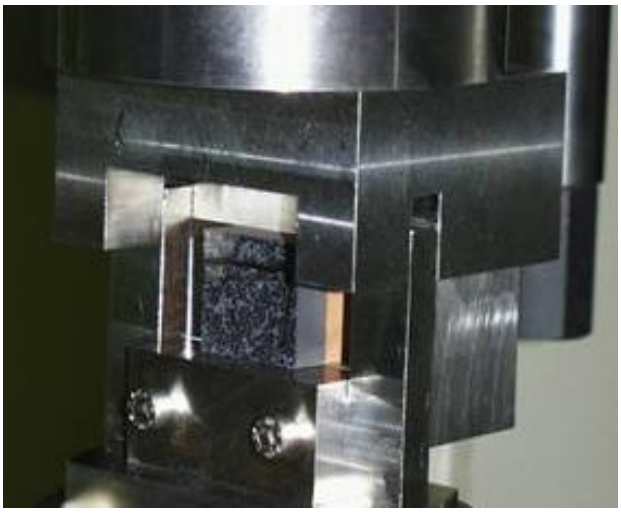

Figure 1: Photograph of a shear test performed on a Be/CuCrZr joint

Consolidation of Be/CuCrZr joint industrialization

To consolidate the industrialization of the Be/CuCrZr joint we are searching for new cleaning products that could replace the present cleaning media. The cleaning of the tiles is proceeded by a degreasing and an etching operation but we address only the degreasing process in this paper. Etching process is studied at the moment and all the results are not yet available.

Concerning the degreasing of the beryllium tiles, we tested two products named A and B for confidential reasons. These products are compared to our reference cleaning product C. The Be tiles are cutted by spark machining, finely milled on one face and then cleaned by the products A, B and C. After the cleaning operations, the tiles are dried by a neutral gas flow and stored immediately under vacuum to protect them during the shipping from the cleaning room up to the XPS apparatus. XPS analyses were performed with a SSI probe and the photoelectrons have been collected with an angle equal to 35°.

Low resolution survey XPS spectra associated to the beryllium tiles cleaned with the products A, B and C are presented in figure 2 to figure 6. Whatever the cleaning product used, XPS spectra are similar. They present a low increase of the signal to noise ratio with increasing binging energy, which is a good indication of the cleanliness of the surface.

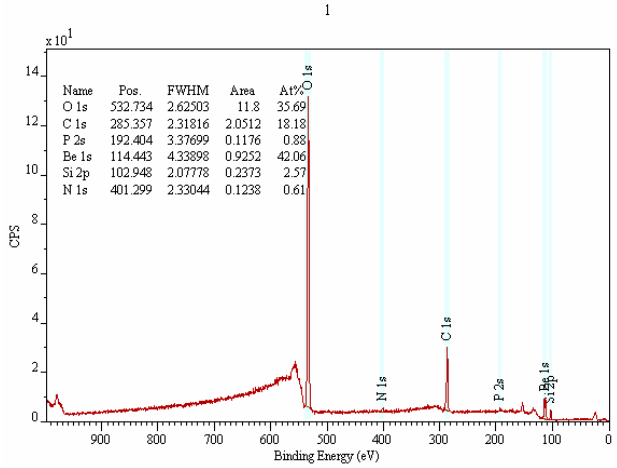

Figure 2: Survey spectrum associated to the beryllium tile cleaned with product A during 10min

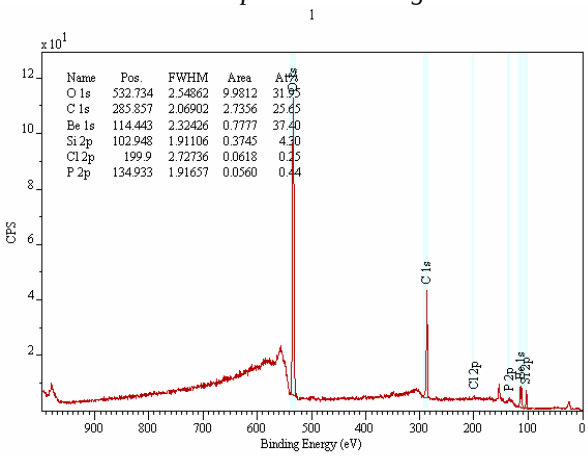

Figure 3: Survey spectrum associated to the beryllium tile cleaned with product A during 30min

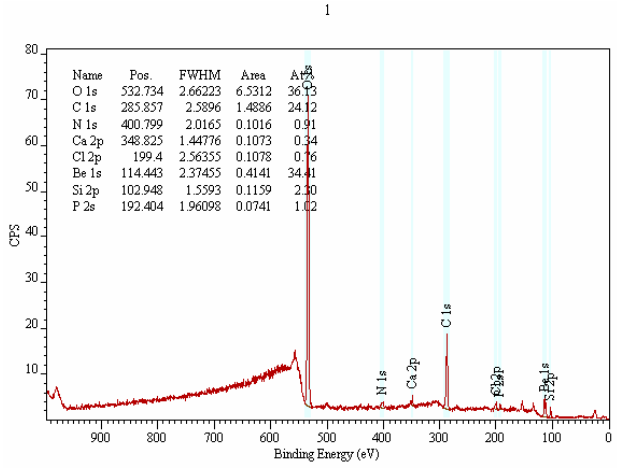

Figure 4: survey spectrum associated to the beryllium tile cleaned with product B during 10min

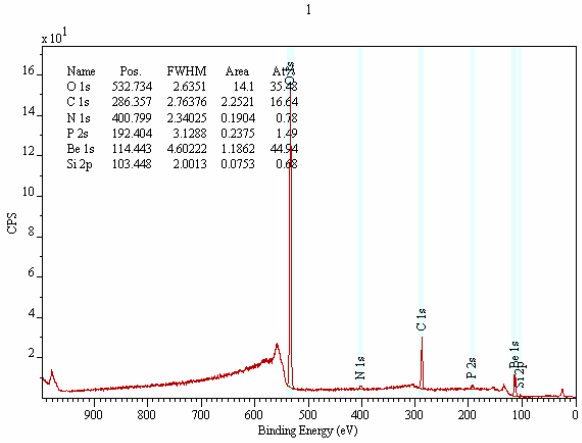

Figure 5: Survey spectrum associated to the beryllium tile cleaned with product B during 30min

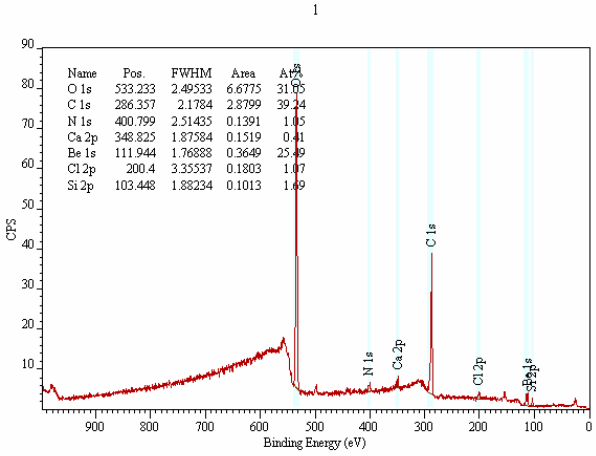

Figure 6: survey spectrum associated to the beryllium tile cleaned with our reference product C

Tables 1 and 2 give the residual pollution measured on the surface of the beryllium tiles. With a residual carbon concentration of about 40 at.%, tile 5 cleaned with our reference product C presents the highest organic pollution. Tiles 1, 2, 3 and 4, cleaned with products A and B during 10min or 30min, have a similar carbon concentration of about 20 at.%. XPS analyses also reveal other polluting elements on the beryllium surface. These elements are Si, P, N, Cl and Ca.

Table 1: Semi-quantitative results in at. % obtained with spectra presented in figure 2 to figure 6

Tile N°	Product	Be	O	C	Si	P	N	Cl	Ca
1	A-10mn	42.06	35.69	18.18	2.57	0.88	0.61	-	-
2	A-30mn	37.40	31.95	25.65	4.3	0.44	-	0.25	-
3	B-10mn	34.41	36.13	24.12	2.3	1.02	0.91	0.76	0.34
4	B-30mn	44.94	35.48	16.64	0.68	1.49	0.78	-	-
5	C	25.49	31.05	39.24	1.69	-	1.05	1.07	0.41

Table 2: Sum of the residual pollution measured on the surface of the beryllium tiles

Tile N°	1	2	3	4	5
Sum (Si+P+N+Cl+Ca)	4.06	4.99	5.33	2.95	4.22
Sum (C+Si+P+N+Cl+Ca)	22.24	30.64	29.45	19.59	43.46

High resolution spectra have been recorded to go further into our conclusions. High resolution Be1s spectra associated to beryllium tiles 1 to 4 are presented in figure 7. These spectra are constituted with two peaks which are related to the beryllium oxide (Be ox) and the beryllium metallic contribution (Be met). Each peak presents approximately the same broadening and the same amplitude indicating that the residual pollution layer on tiles 1 to 4 is very close to each other. Moreover, the detection of the Be metallic peak indicates that the residual pollution layer on the beryllium tiles is about a few nm. Similar results are obtained in tile 5 even if the Be1s peak is more broadened due to the higher residual pollution on the tile. According to data presented in table 1, we assume that the oxide layer that makes the pollution layer is mainly a beryllium oxide because [O]/[Be] ratio varies from 0.8 to1.

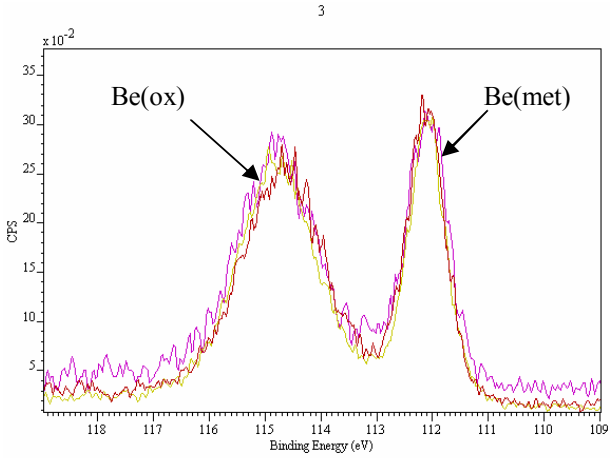

Figure 7: High resolution Be 1s spectra measured on samples 1, 2, 3 and 4

According to the XPS results, some conclusions can be made:

- The low resolution XPS spectra show that the beryllium tiles can be degreased by the new products as well as or better than our reference degreasing product,
- The beryllium tile cleaned with our reference product presents the highest residual pollution. This pollution is mainly due to carbon which may be a residue of the organic product used for the cleaning operation,
- The thickness of the oxide layer is about a few nm and experiments are on the way to find chemical products that could remove it.

Influence of the copper thickness on the performance of Be/CuCrZr joint under High Heat Flux tests

FEM simulations show that the thickness of the copper layer put between Be and CuCrZr influences the stress at Be/Cu interface and thus may have an effect on the behaviour of FW mock-ups under High Heat Flux operations. To verify our numerical results, two small scale mock-ups were manufactured with two different

copper thicknesses. These mock-ups are 96mm long, 86mm wide and 60mm thick. Each one is constituted with nine 30.6x27.3mm² Be tiles. A photograph showing one of these two mock-ups is presented in figure 8.

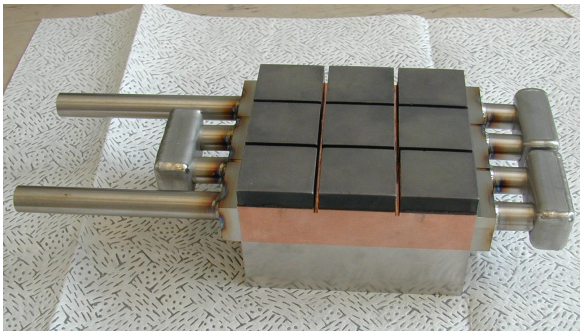

Figure 8: Small scale mock-ups to test the influence of the copper thickness on the performance of Be/CuCrZr joint under high heat flux

Design review of module M15-S3

Before the preparation of the blanket procurement specifications, a critical fabrication review of one FW module located around the Neutral Beam Injector (NBI) openings (see figure 9) has been done. According to the initial CATIA drawings of one of the most complicated module that constitutes the NBI openings (see figure 10), we proposed design changes and improvements to make the manufacture of such module cost effective.

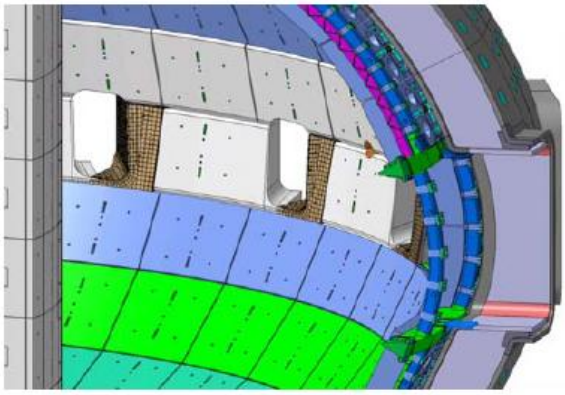

Figure 9: NBI localisation inside ITER reactor

CONCLUSIONS

To increase the strength of Be/CuCrZr joint under high heat flux operations, we searched new interlayers metallurgically compatible with Be and Cu to avoid the formation of brittle metallic compounds at Be/Cu joint. As refractory alloys are compatible with Cu we have chosen and tested the compatibility of several refractory metals with beryllium. These metallic elements were sputtered on small Be tiles and the tiles were heat treated at 580°C during two hours. Low incidence and θ-2θ X-ray diffraction analyses reveal that chosen refractory metals do not form intermetallic compounds with Be. Thus we conclude that these elements are metallurgically compatible with Be and Cu. Following these results small scale Be/CuCrZr samples were manufactured to test mechanical the Be/CuCrZr joints made with these metals. Mechanical tests are underway.

To replace the degreasing product used up to now to clean the beryllium tiles, several new products were tested. XPS results obtained are quite good and confirm that the investigated products can replace the reference product. At the moment, our investigations are still running to find other products that could replace the product used to deoxidize the beryllium tiles after the degreasing operation. The experiments are on the way. Last, we made a critical fabrication review of one FW module located around the Neutral Beam Injector (NBI) openings.

Part to design

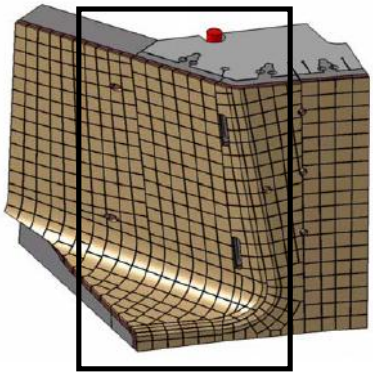

Figure 10: Part of the NBI opening to design

REFERENCES

[1] H. Okamoto and L. Tanner, “Phase diagrams of binary beryllium alloys” ASM international, 1987

REPORTS AND PUBLICATIONS

P-E. Frayssines, G. Roux, F. Vidotto, B. Oresic, J-M. Leibold, C. Chabrol and E. De Vito “HIP joining development and application to the FW design of NBI modules Interim report” EFDA 07-1700/1622, TW6-TVB-HIPJOIN, technical note DTH/DL/2008/103, December 2008

TASK LEADER

Pierre-Eric FRAYSSINES

DRT/LITEN/DTH/LTH
CEA-Grenoble
17 rue des Martyrs
F-38054 Grenoble Cedex 9

Tel: 33 4 38 78 28 59
Fax: 33 4 38 78 54 79

e-mail: pierre-eric.frayssines@cea.fr

Task Title: INVESTIGATION OF THE EFFECT OF CREEP-FATIGUE INTERACTION ON THE MECHANICAL PERFORMANCE AND LIFETIME OF CuCrZr

INTRODUCTION

The aim of this task is to have a better knowledge of the creep-fatigue behaviour of CuCrZr and to check whether a cumulative linear law is adapted or if another law is needed.

This task also presents some LCF experiments initially planned in the TW3-TVM-JOINT. They correspond to fabrication route B1, B3 and B3 done on the CuCrZr batch of the TW3-TVM-JOINT task. For this task, a new batch of CuCrZr was provisioned because there was no more CuCrZr from the JOINT task.

Initially, the program consisted in performing mechanical testing on a CuCrZr heat treated the same way it is heat treated during the manufacturing of PFW panels for ITER.

The heat treatment foreseen (namely route B1) consists in:

- a HIP cycle at 1040°C during 2 hours,
- a solution annealing heat cycle at 980°C with a controlled cooling rate around 60°C/min,
- an ageing heat cycle at 560°C during 2 hours.

Another route was planned to be explored (route B2):

- a HIP cycle at 1040°C during 2 hours,
- a solution annealing heat cycle at 980°C with a controlled cooling rate around 120°C/min,
- an ageing heat cycle at 560°C during 2 hours.

Another route was planned to be explored (route B3):

- a HIP cycle at 1040°C during 2 hours,
- a solution annealing heat cycle at 1040°C with a controlled cooling rate around 60°C/min,
- an ageing heat cycle at 560°C during 2 hours.

To meet the objective, five different tests procedures are necessary:

1) Isothermal strain controlled fatigue R=-1 (CRPP / CEA)
2) Relaxation tests (CRPP)
3) Isothermal Creep-fatigue tests (CRPP / CEA)
4) Constant load creep tests (CEA)
5) Constant stress creep tests (CRPP)

Some tensile tests are also performed to have a basic knowledge on the material behaviour. This experimental campaign is shared with CRPP (Centre de Recherche en Physique des Plasmas, Switzerland), CEA is in charge of some testing conditions, CRPP is doing a complementary program. We only present results from CEA. The samples have been manufactured. The program was then modified because of the discovery of an abnormal grain size on the B1 or B3 heat treated material (in April 2006). A new reduced program has then been constructed to finish the task on a lower grain size material even tough this heat treatment differs from B1 route. Samples have been manufactured after a so-called D3 heat treatment. D3 corresponds to:

- a solution annealing heat cycle at 980°C with a controlled cooling rate around 60°C/min,
- an ageing heat cycle at 580°C during 2 hours.

This report presents all the experimental results obtained at CEA: those done before discovering the grain size problem on route B1 and B3 and those done on samples from route D3.

2007-2008 ACTIVITIES

TENSILE TESTS RESULTS

Generally speaking, all the tensile tests from routes B1, B3, D3 give low properties whatever the CuCrZr heat (figures 1, 2, 3, 4). This is normal if we consider that all materials are in an over-aged state (560°C or 580°C rather than 480°C which is known to be the best ageing temperature), and that over-ageing is considered to be the most softening parameter on the material properties [2]. But there are differences between material batches.

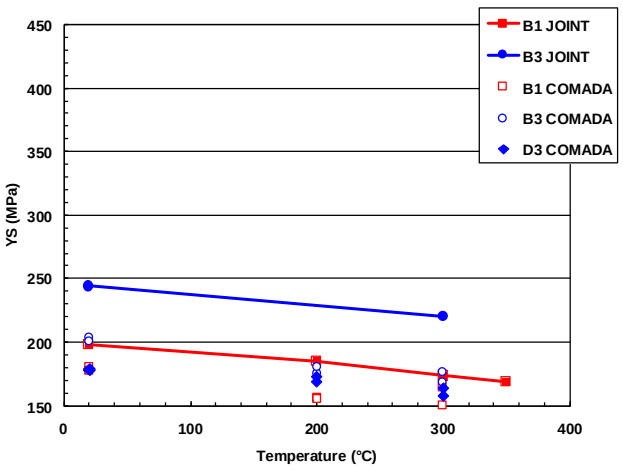

Figure 1: Yield Strength of the studied materials

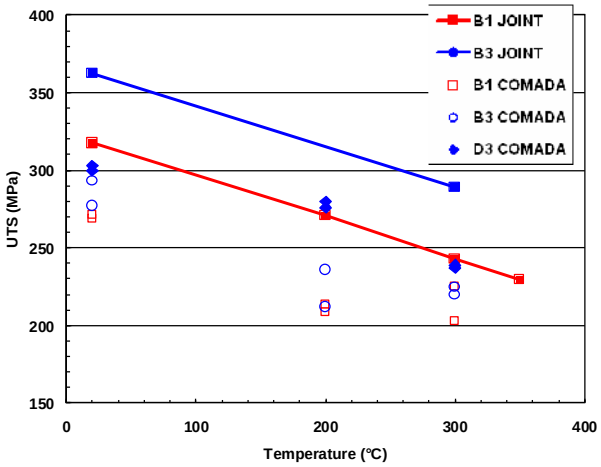

Figure 2: Ultimate Tensile Strength of the studied materials

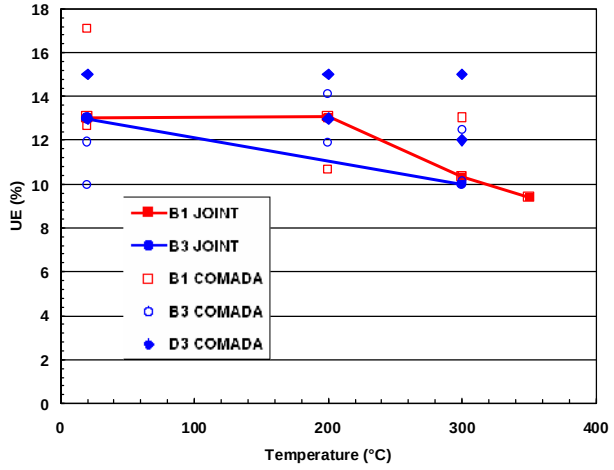

Figure 3: Uniform Elongation of the studied materials

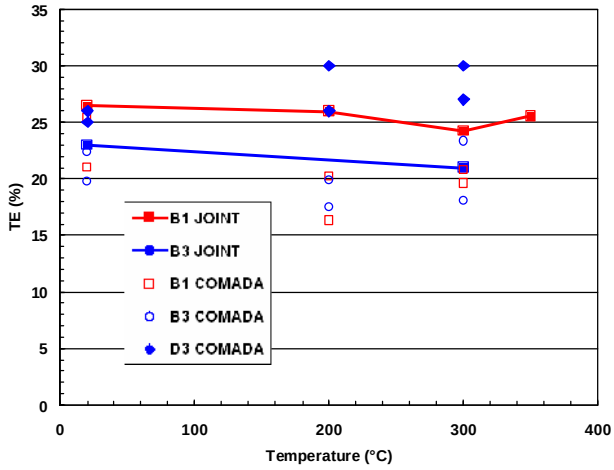

Figure 4: Total Elongation of the studied materials

For the tensile tests that have been performed on samples manufactured with route B1 and route B3, the conclusion is that B1 and B3 heat treatment from the COMADA CuCrZr batch exhibit a significant lower strength, especially concerning UTS. Let recall that the grain size of route B1 and B3 from COMADA is much bigger. In fact, uniform quantities are not much affected by the grain size, whereas the effect is more pronounced on ultimate values. Concerning D3 route, as expected, the tensile properties are quite equivalent to route B1-JOINT. This means that a preliminary HIP and a slightly bigger grain size have no effect. The over-aged state principally governs the properties.

Compared to last specification for ITER [3], the properties of the B1 and B3 COMADA are very near the acceptable values for YS and for TE. They are a bit lower concerning UTS, especially on route B1 COMADA.

PURE FATIGUE RESULTS

Figures 5 and 6 show some results of peak-valley stress amplitude as a function of number of cycles. Some general trends can be observed:
a) the higher the strain amplitude, the higher the stress plateau,
b) the curves exhibit some hardening in the first hundreds of cycles, and then the stress level stabilizes.
There is a peculiar behaviour of the curve for D3-COMADA material at $\Delta\varepsilon=\pm 0.9\%$ strain amplitude. The material is hardening in the first cycles then it is softening quite a lot before rupture.

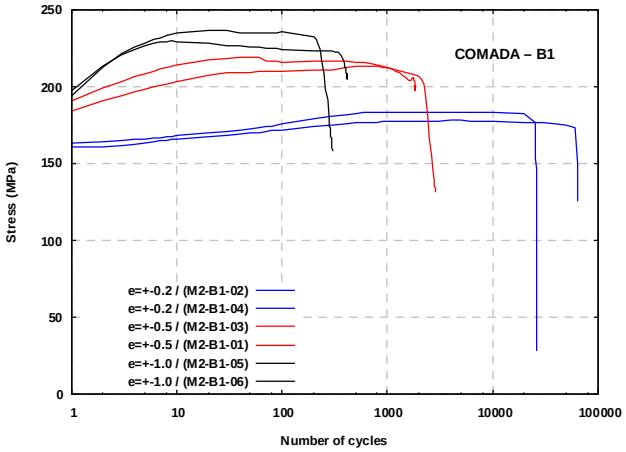

Figure 5: Peak-Valley stress amplitude as a function of number of cycles – route B1 COMADA

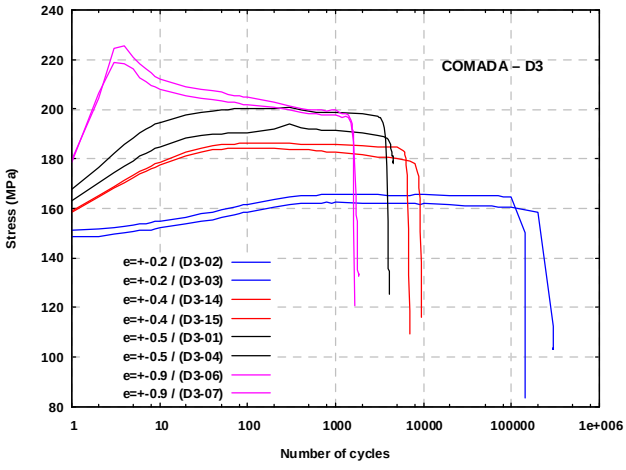

Figure 6: Peak-Valley stress amplitude as a function of number of cycles – route D3 COMADA

The figure 7 gives the Δε-N diagram. When looking at the results in a Δε-N diagram, it clearly appears that D3 route shows the longer lifetime for all strain amplitude conditions. The B1-COMADA route gives the lower values and it is difficult to conclude for B1-JOINT and B2-JOINT conditions. They are in between D3-COMADA and B1-COMADA.

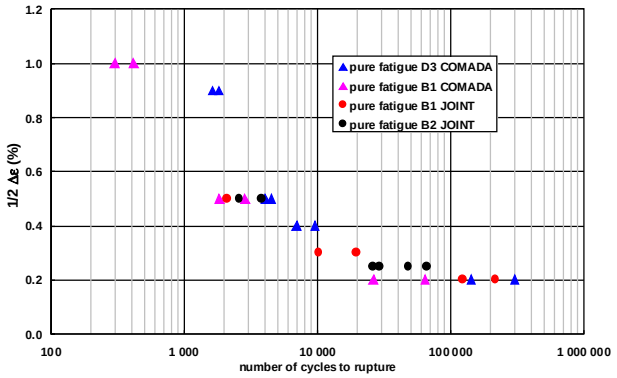

Figure 7: Results on pure fatigue for CuCrZr B1 and D3 heat treated routes

CREEP FATIGUE RESULTS

The tendencies are observable on Δε-N graph presented on figure 8. The presence of relaxation clearly diminishes the number of cycles to rupture. Besides, it is also difficult to conclude on the influence of a 300s relaxation period. At least we can say that it is not worse than 30s holding period.

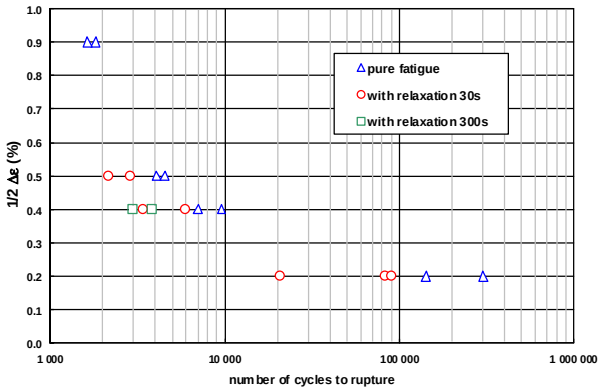

Figure 8: Results on fatigue-relaxation tests for CuCrZr D3 heat treated route

CONCLUSIONS

Due to grain size problem with the particular CuCrZr batch provisioned for the COMADA task, the studied heat treated route has seen its solutionning temperature reduced to the conventional 980°C (instead of 1040°C required for HIP joining CuCrZr to 316SS).

Generally speaking, all the tensile properties from routes B1, B3, D3 are low because of the over-ageing heat treatment. Nevertheless, compared to last specification for ITER [3], the properties are very near the acceptable values for YS and for TE. They are a bit lower concerning UTS.

Concerning LCF, D3 route shows the longer lifetime for all strain amplitude conditions, especially for high strain amplitude.

If some creep (one should say "relaxation") is present during the tensile phase of LCF, the number of cycle to rupture clearly diminishes. Besides, it is difficult to conclude on the influence of a 300s relaxation period. At least we can say that it is not worse than 30s holding period.

To finish, it seems that an important problem about an abnormal grain growth of the CuCrZr has been discovered. Under some conditions and depending on the CuCrZr batch, grains of CuCrZr can reach a size of several millimetres. This problem appeared with the CuCrZr bought for the COMADA task, the grain size of the CuCrZr from the JOINT task was acceptable. In fact all is due to the high temperature involved in the HIP treatment when manufacturing ITER PFW panels; 1040°C is needed to achieve bonding of CuCrZr to 316LN as well as bonding 316LN to 316LN. Although mechanical results on this big grains material are not too bad, a serious and reliable mechanical study of the material properties (especially creep study) is not possible. From the present knowledge we have about the CuCrZr provisioned and heat treated, we cannot conclude on the reason of such an instability concerning the behaviour of the CuCrZr (particularly grain size and properties to a lower extend). A special study should be devoted to understanding the phenomenon linked to grain growth and the relation between Zr and Cr contents and the precipitation and mechanical properties.

REFERENCES

[1] I. Bretherton et al., "The mechanical properties of two copper alloys: final report", AEAT/RJCB/RD01267/R02, Issue 1, June 2001

[2] O. Gillia, I. Chu, P. Lemoine, "TW3-TVM-JOINT – Characterisation of the CuCrZr/316LN junction strength for different blanket manufacturing conditions", Note Technique DTEN/DL/2005/027

[3] K. Ioki et al. "Six-party qualification program of FW fabrication methods for ITER blanket module procurement", Fusion Engineering and Design 82 (2007) 1774–1780

[4] U. Holzwarth, H. Stamm, "The precipitation behaviour of ITER-grade CuCrZr alloy after simulating the thermal cycle of hot isostatic pressing", Journal of nuclear materials, Vol. 279 (2000)

REPORTS AND PUBLICATIONS

O. Gillia, P. Lemoine, "TW5-TVM-COMADA, Investigation of the effect of creep fatigue interaction on the mechanical performance and lifetime of CuCrZr - Final Report", rapport technique DTH/DL/2007/091, dec. 2007

O. Gillia et al., Characterization of CuCrZr and CuCrZr/SS joint strength for different blanket components manufacturing conditions, International Conference on Fusion Reactor Materials, Nice, 2007. To be published in Journal of Nuclear Materials (2009), doi:10.1016/j.jnucmat.2008.12.244

TASK LEADER

Olivier GILLIA

DRT/DTH/LTH
CEA-Grenoble
17 rue des Martyrs
F-38054 Grenoble cedex 09

Tel: 33 1 4 38 78 62 07
Fax: 33 1 4 38 78 58 91

e-mail: olivier.gillia@cea.fr

TW5-TVR-WHMAN

Task Title: DEVELOPMENT OF A LINEAR HYDRAULIC JOINT FOR REMOTE HANDLING APPLICATION

INTRODUCTION

Hydraulic technology can provide powerful actuators in small volumes. For that reason hydraulics becomes an interesting technology to build heavy duty manipulators for maintenance operations in space constrained areas, like Fusion plants.

Due to potential leaks, oil hydraulic can not be used for maintenance operations in ITER. Pure water hydraulics proposes a good alternative to oil and today's developments are focusing on that direction.

Architecture of hydraulic manipulators with force feedback capabilities available on the market are essentially based on rotary joints arranged in a serial manner. On the contrary, traditional Mechanical Master Slave systems with high payload capacities (MT200 La Calhène, CRL Model 8, A100 Wälischmiller) are equipped with a telescopic joint to extend the reach capability in hot cells while in some specific tasks, deployment of a manipulator in a constrained area can not be achieved with a combination of rotations and requires an additional prismatic joint. Designing a hydraulic manipulator with a prismatic joint could therefore propose a heavy duty multi-purpose tool with extended reach capabilities and alternative access to space constrained area.

After problem analysis, addition of a linear joint in serial architecture of hydraulic actuators used in manipulator for Remote Handling proved to be a more complex task than expected. Assessment of the performances required during standard operations showed that creating a "pressure bus" within the manipulator to allow each servovalve to obtain its required fluid flow was the best answer to the problem. Preliminary tests on a functional mock-up are presented and discussed.

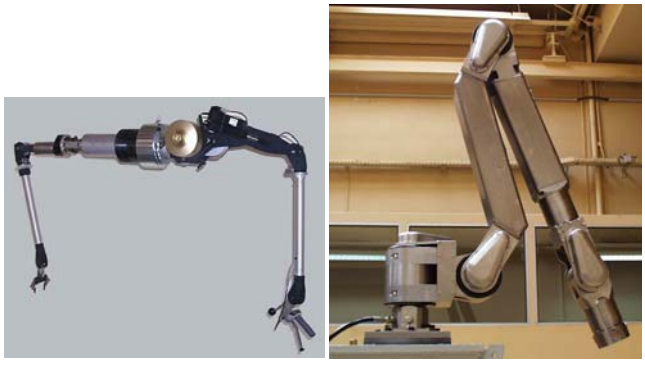

Figure 1: MSM and Manipulator t examples with six rotational joints in series

Figure 2: MT200 TAO telerobotic system

2007-2008 ACTIVITIES

CONCEPTS FOR TELESCOPIC EXTENSIONS

To be used within manipulators the systems need to provide at the same time:

- Fluid transmission through the system during de/reployment phases of the telescopic joint and not only during stops,
- No hydraulic hoses,
- Compact system to limit weight inertia and size of linear joint.

Counteracting forces are balanced within the system to avoid any displacement when the pressure is high.

An answer to these problems is found with designs similar to that of figure 3. In this system the fluid under pressure enters in the left or right side of the jack. During extension phase of this passive element:

- Volume of chamber 1 increases,
- Volume of chamber 2 decreases,

Fluid from chamber 2 is transferred towards chamber 1 through the pathway drilled into the blue piston of the system,

Air enters through the holes in the backside of the outer cylinder.

If diameter of all elements are such as the section S1 and S2 are equivalent, the length of the system is changed without any variations of the fluid volume.

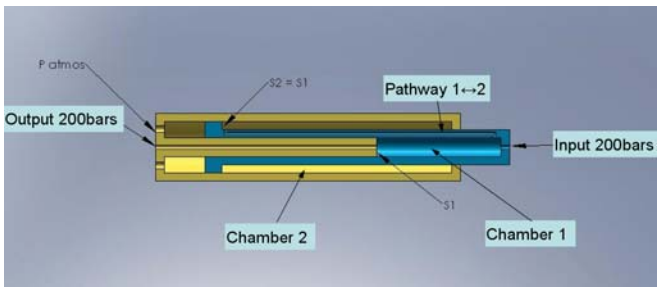

Figure 3: Design principle 1 – Reference design

TEST RIG

The test rig was designed to be modular and adaptable. Attention was paid to test the functions of the components and not to save space and build a fully integrated system.

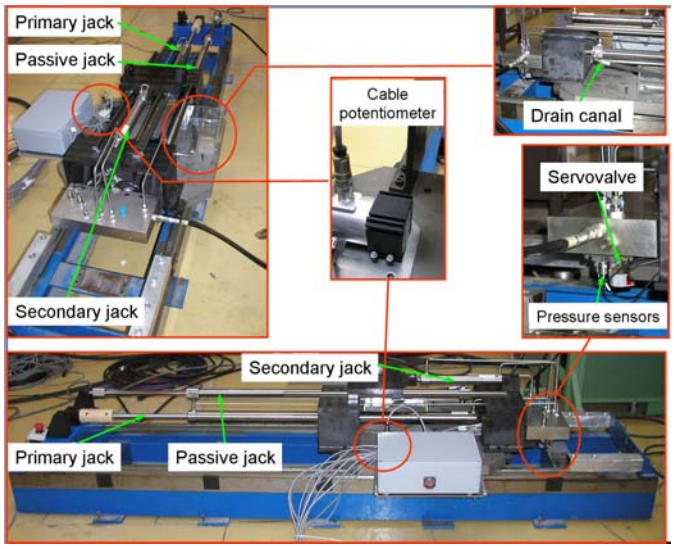

Figure 4: Test rig

Position is measured with an Artus-Kollmorgen resolver. Sensors and pre-actuators used for the test rig are:

- Pressures sensors,
- Cable potentiometers,
- Servovalves.

Characteristics of those equipments are as follows:

- Pressure sensors ENTRAN model EPXM-N22-350b
  - Range 350bars,
  - Resonant frequency = 190kHz,
  - Nominal output 5V.
- Cable potentiometers µ-epsilon WDS-1500-P60-SR-U
  - 1.5m stroke,
  - Nominal output 0-10V.
- Servovalve MOOG model 4633116000
  - Nominal flow ±6l/min,
  - Input ±10mA.

PRELIMINARY TESTS: INFLUENCE OF PASSIVE JACK

In the present design, the passive jack is one of the main components of the actuator. Due to its design and location within the system's kinematics it will act as a damping system. It is therefore interesting to test the performances of the system with and without this component to characterize its influence on the whole behaviour.
Response of the actuator to a step signal is shown on figure 5. Description of the set signal is as follows:

- Shape: step,
- Amplitude: ±150mm,
- Frequency: 0.1Hz.

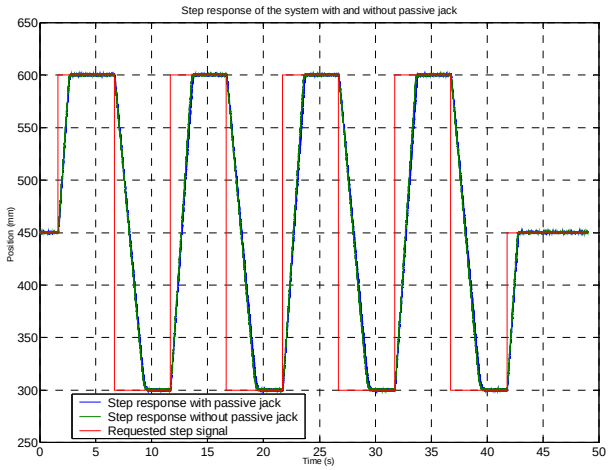

Figure 5: Step response of the mock-up with and without the passive jack

Saturation of the speed is a consequence of the servovalve's saturation. Figure 6 presents the force within the primary jack when operated with and without passive jack. The command signal is the triangular signal previously defined. Reconstruction of the force was made according to the pressure values within the chambers. The results are in agreement with the expectations (higher friction, both dry and viscous with passive jack).

It can be noticed that the friction level is high and close to the load capacity we are focusing on.

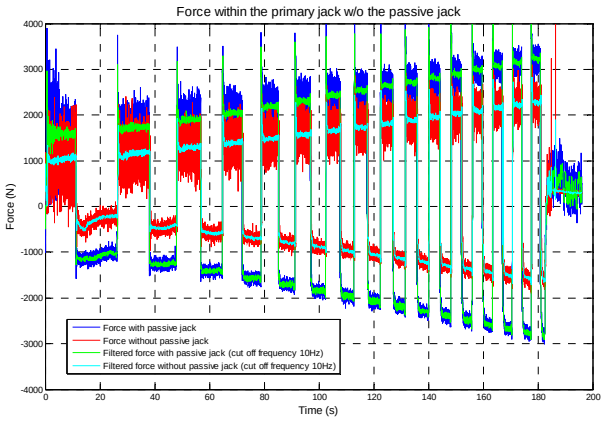

Figure 6: Force measured in the primary jack with and without passive jack

A complete mechanical identification, with and without passive jack shows a rise of dry friction (see also figure 6) and slice modification of viscous friction (20 % more viscosity than without passive jack).

Table 1: Mechanical parameters issued from identification process

Parameter	Test with passive jack	Test without passive jack
Viscous friction N/(m/s)	24600	20600
Dry friction (N)	738	214
Offset (N)	305	-378

CONCLUSIONS

After problem analysis, addition of a linear joint in serial architecture of hydraulic actuators used in manipulator for Remote Handling proved to be a more complex task than expected. Assessment of the performances required during standard operations showed that creating a “pressure bus” within the manipulator to allow each servovalve to obtain its required fluid flow was the best answer to the problem. Due to the lack of systems available in the state of the art, an innovative design and derivations of this design were proposed. Definition and assembly of functional test mock-up is achieved and first performances analysis in position control were proposed. Performances of the position measurement need improvements to overcome limitations in the tuning of the control loop and provide a speed signal compatible with ‘force control’ loop. It is proposed to investigate the possibility to introduce data fusion procedures between two distinct sensors to reach the requested quality level. Next year’s program will focus on the implementation and test of a force control loop after definition of a model of the whole system.

REPORTS AND PUBLICATIONS

DTSI/SRI/LPR/06RT018 Results on qualification of a water-hydraulics joint for force feedback applications, G. Dubus

TASK LEADER

Yvan MEASSON

DRT/DTSI/SRI
CEA-Fontenay-aux-Roses
BP 6
F-92265 Fontenay-aux-Roses Cedex

Tel: 33 1 46 54 97 19
Fax: 33 1 46 54 89 80

e-mail: yvan.measson@cea.fr

CEFDA04-1127

Task Title: TW4-TMSC-SAMAN1: MANUFACTURE OF SUBSIZE SAMPLES

INTRODUCTION

The tests of the ITER TF model coil in 2001-2002 have shown that the performance of the conductor was lower than expected [1]. New high performance strands have been ordered by EFDA to industry.

In the framework of this task, CEA has to explore the sensitivity of these high performance Nb_3Sn strands on stainless steel jacketed subsize samples, regarding the critical properties. This has been done by ordering and manufacturing subsize samples in the industry and then by participating in the tests at FZK (Germany) in the FBI (F force, B field, I current) test facility, and in their interpretation.

In the first stage of the scientific program, using OST strands, subsize cables of different cable layouts (9, 45 and 180 strands) have been produced, the number of pure copper strands, the void fraction or the cabling pattern have been varied. This activity has taken place in 2006 [2]. In the second stage of this task, strands originated from different companies have been tested on two kinds of subsize samples such as to compare the sensitivity of the different strands to the strain. This activity has been carried out in 2007 and is reported here.

2007-2008 ACTIVITIES

The second phase of the task was dedicated to understanding of the specific characteristics of the different strands available in Europe. They were tested during the qualification phase of the European suppliers of Nb_3Sn strands for ITER. This was intended to be done on two kinds of samples with the standard void fraction (32%) and the standard sequence of twist pitches:

- 3x3x5 subsize samples with two superconducting strands and one copper strand in the first triplet,
- 3x3x5x4 subsize samples with one superconducting strand and two copper strand in the first triplet.

For the stretching phase, the main results have been summed up in table 1 showing the specific behaviour of each strand.

The weakest sensitivity to strain is observed on OCSI and OST type 2 samples. For the EAS 3x3x5 sample an abnormal behaviour is observed and the results from the 3x3x5x4 sample have been added as most probably more representative.

Table 1: Difference between predicted and observed current at maximum during stretching for 3x3x5 samples

Type of strand	Critical current at maximum (experiment) I_{maxexp} (A)	Expected maximum current from strand model I_{maxmod} (A)	ratio I_{maxexp}/I_{maxmod}
OST type 1	7230	9200	0.76
OST type 2	6808	7970	0.85
OCSI	5671	6540	0.87
EAS	3042	5800	0.53
EAS 3x3x5x4	8565	11600	0.74
Pori	4802	7250	0.66
Alstom	3425	4650	0.74

Before stretching, it can be seen in figure 1 that the effective strain is depending of the magnetic field revealing sensitivity to the increased Lorentz force. Again the 3x3x5 EAS sample exhibits an abnormal behaviour, which is not confirmed on the 3x3x5x4 EAS sample.

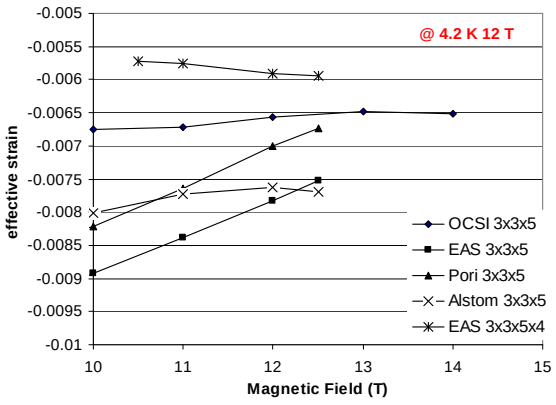

Figure 1: Effective strain of different cables before stretching (second phase)

All details about the technical results are given in the final internal report related to the task [4].

Further activity on FBI

Difficulties have been inevitably met linked to the fabrication of this great variety of samples at a company. Difficulties have been met also in the operation of FBI with a severe damage on one of the split coil during experimentation on lot 2, which has been very rapidly replaced.

Overcoming these difficulties, FBI has proven to be a very useful test facility to observe the influence of different parameters on the sensitivity of ITER conductors to Lorentz force.
Regarding the twist pitch sequence of the first conductor stages, a subject which is much debated, it could be envisaged to test several sequences of twist pitches on FBI to select the best one for ITER and to compare experimental results and models.
Note that the reduced length of the zone with the acceptable field homogeneity is not an obstacle as the self field on these samples can be neglected contrary to the situation in full size samples in the Sultan test facility.
Effect of cycling the current at given field, which leads to cycling of the Lorentz force without stretching, could be studied in FBI using existing spare samples.
Stretching at 14 T the samples could confirm that at weak Lorentz force (due to high field) there is no widening gap.

CONCLUSIONS

In spite of their reduced size, degradation effects are already visible on ITER subsize conductors. It has to be highlighted that experiments on subsize samples in FBI are far less expensive than experiments on full size samples which are certainly also necessary. These degradation effects and the sensitivity to strain are visible by stretching the samples and therefore increasing the Lorentz force per strand. They are also visible before the stretching phase by operating at low field and observing the tendency on the effective strain. Detrimental contribution of short twist pitches (35/65/110 mm vs 45/85/125 mm) and high void fraction (45 %) are confirmed. Note that this effect related to short twist pitches had been already predicted in [3]. Further activity can help to adjust the final parameters of ITER TF conductors.

REFERENCES

[1] A. Ulbricht, D. Ciazynski, J.L. Duchateau, W. Fietz, H. Fillunger, S. Fink, R. Heller, R. Maix, S. Nicollet, S. Raff, M. Ricci, E. Salpietro, G. Zahn, R. Zanino et al. 2005 "The ITER toroidal field model coil project" Fusion Engineering and Design 73 (2005) 189-327

[2] K.P. Weiss, R. Heller, W.H. Fietz, J.L. Duchateau, N. Dolgetta, A. Vostner "Systematic approach to examine the strain effect on Nb3Sn CICC" 2007 IEEE Trans. On Appl. Sup. 17 1469

[3] A. Nijhuis, Y. Ilyin, H.H.J. ten Kate, "Transverse load optimisation in Nb_3Sn CICC design; influence of cabling, void fraction and strand stiffness", Supercond. Sci. Technol. 19 (2006) 945-962

REPORTS AND PUBLICATIONS

[4] N. Dolgetta, J.L. Duchateau "EFDA contract 04-1127 Final report on manufacture of subsize samples" CEA Internal report AIM/NTT-2007.018

TASK LEADER

Jean-Luc DUCHATEAU

DSM/IRFM/STEP
CEA-Cadarache
F-13108 Saint-Paul-lez-Durance Cedex

Tel: 33 4 42 25 49 67
Fax: 33 4 42 25 26 61

e-mail: jean-luc.duchateau@cea.fr

CEFDA04-1170

Task Title: TW4-TMSC-RESDEV: DEVELOPMENT AND TESTING ON NEW RESIN SOLUTION

INTRODUCTION

New advanced cyanate ester-based resin materials have been tested and found to have significantly improved radiation resistance as compared to currently used resins. Because of the risk of an exothermic reaction, it was necessary to test the impregnation process with this new resin in an industrial environment, so the possible problem areas can be addressed and solved prior to the ITER TF coils impregnations.
A mock-up has been built and its dimensions were defined in such a way that about 50 kg of resin could be used. The aim was to:

- Verify the capability of the new resin to be used in an industrial process of the coils manufacture, which requires a vacuum pressure impregnation (VPI) process,
- Validate the conditions of use of this resin and extract samples from the insulation material for electrical, mechanical and thermal tests.

2007-2008 ACTIVITIES

Qualification of the resin system

The Hunstman company developed a resin system (LMB 6653 / LMB 6622; 40 / 60 pbw), which fulfills the initially specified requirements to be used in the industrial process of the TF coils manufacture.
At 60°C, the impregnation temperature, the viscosity of 200mPa.s (value used to define the pot life of the blend) is reached after about 72h. Even at the temperature close to 50°C, the viscosity of the product is below 100mPa.s.
As the required curing temperature (150°C) is lower than the temperatures normally used for curing cyanate esters, tests were carried out by Huntsman to compare the conversion rate of the resin on samples of the new resin system LMB 6653 / LMB 6622 cured at 150°C and on earlier samples tested by ATI and cured at 160°C which presented good results regarding irradiation and mechanical properties. The two samples presented similar "on set" glass transition temperatures, ≈ 150°C, and similar degrees of curing, around 90%, therefore similar mechanical properties can be expected.

Because of stability and safety reasons, the system could not be supplied as a one component system. The following two-component system has been preferred: the first component is LMB 6622 (formulated epoxy resin component containing catalyst) and the second component is the cyanate ester based product called LMB 6653. The stability of the formulated epoxy component LMB 6622 was tested (12 months shelf life at 2 – 40°C).

NB: the name of the products will change when they become commercial (it may change for instance to XB6622 and XB6653).

Realization of the mock-up

After an international call for tender, a contract was signed with the ASG Superconductors Company, located in Genoa, Italy, to perform the realization of the mock-up.

The mock-up was designed to have about the same cross section dimensions as the ITER TF winding pack and a length of one meter.
It has been constructed of 7 couples of stainless steel plates, which simulate the double pancakes (DP) modules constituting the ITER TF winding pack.

After cleaning, 5 of the couples of plates were covered with a de-moulding tape to allow the extraction of insulation samples. The 2 other couples of plates were sand blasted, so the block can be used to assess the bonding between resin and plates. Then each of the 7 couples of plates was wrapped with layers of glass fiber tape and Kapton tape as shown in figure 1 (2 half overlapped layers of S2-glass fiber tape + 5 half overlapped layers of S2-glass/kapton co-wound tape + 1 side by side layer S2-glass fiber tape). The number of layers was adjusted in such a way that the final layout will be similar to the layout of the samples used by ATI, to allow an easier comparison during the tests.
The 7 couples of plates were then stacked and wrapped with several layers of glass fiber tape to form an additional insulation layer.

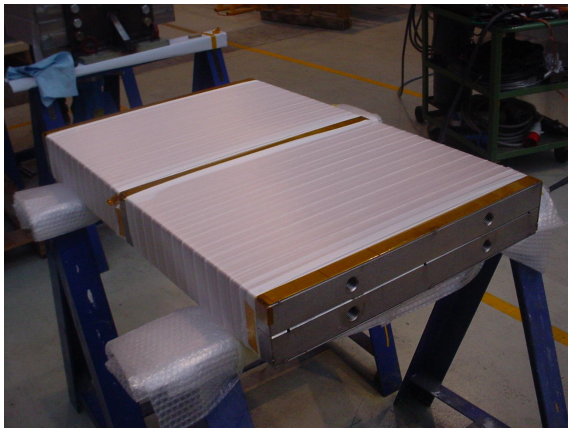

Figure 1: Insulated plate

The pack was inserted into the impregnation mould constituted from a resin tight reservoir, the "impregnation box", and the structure which compresses the box during the following operations (figure 2).

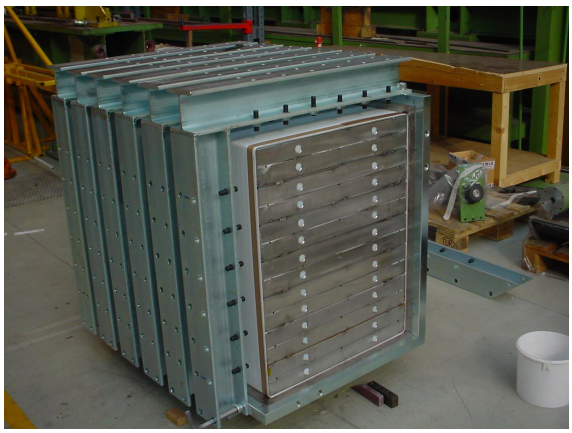

Figure 2: Mock-up in the impregnation mould

The mock-up, as well as the resin inlet / outlet circuits and the cooling circuits were instrumented using temperature sensors which allowed to follow the temperature variations during all the process (9 points inside the mock-up). The mock-up was dried at a temperature of 100°C ± 5°C, at a pressure of about 1mbar during 48 hours.
About 25 litres of resin were injected into the mock-up (excluded the inlet / outlet pipes and the expansion tank reservoir). During the resin filling operation, the temperature of the resin was kept at 50°C and the viscosity of the blend has always been measured below 150mPa.s.
During the impregnation, the temperature of the mould was held at 60°C and the pressure at 5mbar. After the resin filling, were performed a series push-pull by using nitrogen gas (5mbar ÷ 1-2 bar).
Then the curing of the resin was carried out using the following prescriptions:

- ramp from 60°C to 100°C at 2°C/h,
- jellification 100 ± 5°C for 8h,
- ramp from 100 °C to 155°C at 2°C/h,
- curing at 155 ±5°C for 12h,
- natural cooling down to room temperature.

The thermal homogeneity in the mock-up was kept within ± 3°C.

After the curing process, the mock-up was extracted from its impregnation mould. The figure 3 shows the mock-up after the extraction from the VPI mould. As it was shown by the aspect of the different layers, the impregnation was complete and of good quality.

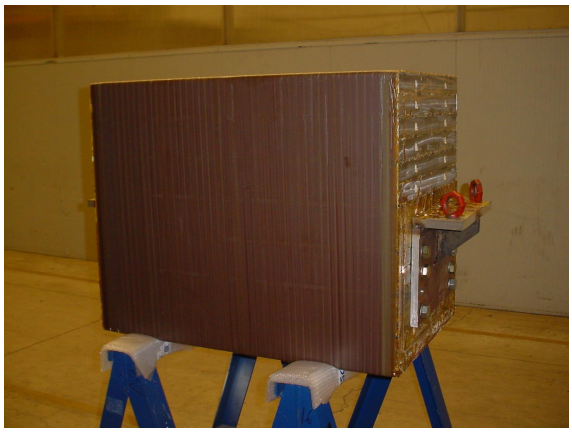

Figure 3: Mock-up extracted from the VPI mould

The samples required for the different characterizations were extracted from the mock-up by cutting and sent to the labs : ATI (inter plate insulation for irradiations tests), CEA–Grenoble (inter plate insulation for tests on thermal conductivity and thermal contraction), FZK (block of 2 plates with insulation for mechanical tests), Huntsman (inter plate insulation to control the curing cycle) and CEA-Saclay (the 4 remaining pieces of inter plate insulation + some pieces of mass insulation for storage for possible future tests).

CONCLUSIONS

The developed resin system LMB 6653 / LMB 6622 fulfills the initially specified requirements to be used in the industrial process of the TF coils manufacture. Its viscosity is suitable and its pot life is about 72 hours, time to 200mPa.s at 60°C (the time to 100mPa.s, which is the definition retained for the pot life in the data sheet, is 50-52 hours at 60°C).
The impregnation of the mock-up with the new resin system is a success. So it has been demonstrated that this resin system can be used for the impregnation of large coils in an industrial context. Especially, the mock-up demonstrates the feasibility of the developed resin system with regard to the DP insulation, the inter DP bonding interface and the WP (winding pack) ground insulation. Regarding the turn insulation, according the design of the DP, the propagation of the resin along all the grooves will have to be checked carefully.

As the exothermicity of the reaction is the critical point, it will be essential to control the temperature and thermal homogeneity of the coils, as well as the temperature of the inlet / outlet resin piping, the resin reservoir and the outlet buffer. Some cooling systems have to be foreseen.

With the mock-up, we were in a favourable configuration from a thermal point of view because of the large amount of stainless steel. Thermal studies have to be done in the pancakes and coils configurations to evaluate the energy dissipation in both cases and to optimise the thermal cycle for the curing according to the response of the complete system (coil + heating system). It will be especially important for the second impregnation, where the electrical insulation of the pancakes will also act as a thermal insulation (no more direct contact with the radial plates).

The final report was issued in December 2008 and accepted [1].

REPORTS AND PUBLICATIONS

[1] Final report to the fusion program contract number FU 06 CT 2004-00158 (EFDA contract number EFDA/04-1170) – CEA internal report RESDEV – T-025-08b – 10/12/2008

TASK LEADER

Françoise RONDEAUX

DSM/IRFU/SACM/LEAS
CEA-Saclay
F-91191 Gif-sur-Yvette Cedex

Tel. : 33 1 69 08 64 49
Fax : 33 1 69 08 69 29

e-mail : francoise.rondeaux@cea.fr

CEFDA05-1370

Task Title: TW6-TMSC-TFPRO: ITER TF FULL SIZE PROTOTYPE CONDUCTOR

INTRODUCTION

In agreement with the ITER Team, EFDA-CSU Garching decided to qualify the manufacturing feasibility of the present ITER TF conductor design. To this purpose, three full size TF conductor lengths were manufactured according to the ITER design, using lower performance Nb_3Sn strand. CEA followed up the whole manufacturing process and procured all required components including the lower performance Nb_3Sn strand.

The work consisted of the following sub-tasks:

- Procurement of Cr plated copper strand and lower performance Nb_3Sn strand,
- Cabling and jacketing of a dummy conductor length using copper strands,
- Cabling and jacketing of three conductor unit lengths according to the ITER TF conductor specification using lower performance Nb_3Sn strands.

After writing of a technical specification and corresponding call for tender, the contract was passed with the NEXANS company which has the equipment needed for production of ITER type cables and corresponding jacketing, and a wide range of cabling machines in different factories.

2007-2008 ACTIVITIES

CABLING AND JACKETING OF CONDUCTOR

After specification and procurement of the main components as central spiral, dummy and superconducting strand and jacket-tubes during year 2006 [1],[2],[3], the cabling was started at NEXANS under CEA suupervision [4],[5]. The first stages were cables at OPTICABLE (B) when the two last stages were cabled at CORTAILLOD (CH). These different factories were chosen because they offer the required equipment to produce future big lengths of conductor foreseen for ITER. In a general way, all the stages were manufactured by cabling then drawing the cable through dedicated dies. To save time for the final cabling, and after EFDA agreement, the dummy and the superconducting cables were linked together. After trials on the dummy cable, the last stage compaction was performed by drawing the cable through three sucessive dies to reach progressively the target cable diameter. One 1160 mm dummy and three 3660, 5000 and 5000 mm cable lengths were producted. These cable lengths were shorter than the required values due to the lack of available strand and the need of extra lengths to achieve correctly the machine parameters. The cables were finally jacketed and compacted by co-drawing at JEUMONT (F) to reach the target void fraction.

CONDUCTOR ANALYSIS

During all the cabling process, the dummy then the superconducting cable twist pitches as well as cable layout and diameter were checked by CEA on picked samples. The final conductor analysis was led on each of the delivered lengths. The first conductor length was not satisfactory because the length was not enough to set correctly the machine parameters. The two last lengths were found to fulfill the specification in term of twist pitches as well as cable void fraction (figure 1).

Figure 1: The ITER TF conductor produced

CONCLUSIONS

This task was mainly devoted to qualify a new conductor manufacturer which is the European company NEXANS. After material procurement, the different stages were cabled in the factories foreseen for these activities using a cabling process proposed by NEXANS with dies for cable compaction. Although the available length was not enough for correct adjustement of the cabling parameters on such big cabling machines, the final cable lengths were successfully produced. After jacketing, the final conductor lengths were analysed and found to be within the specification [6]. By this task, Nexans has proved their capability for such conductor manufacture and is now ready to continue its development with the manufacture of longer prototype for ITER.

REPORTS AND PUBLICATIONS

[1] Spécification technique pour la fabrication de longueurs de spirales type ITER, note AIM/CCH-2006.001, P. Decool, 10/04/2006

[2] Rapport contrôle qualité des tubes inox- Tache TFPRO, note AIM /RCQ.2006-001, J.L. Marechal, 07/06/2006

[3] Manufacturing of full scale ITER TF conductor prototype lengths (English translation of AIM/CCH-2006.003), note AIM/CCH-2006.004, N. Dolgetta, 23/03/2006

[4] Task TFPRO: visit to NEXAN-CORTAILLOD (switzerland) to attend the TFPRO cabling, week 5-9/february/07, note AIM/CRM-2007.001, N. Dolgetta, P. Decool, 27/02/2007

[5] TFPRO Task: visit to NEXAN-JEUMONT to attend the jacketing of TFPRO cables samples, week 26-28/march/2007, note AIM/CRM-2007.002, J.L. Marechal, H. Cloez, 30/03/2007

[6] Contract EFDA 05-1370 : Deliverable 3 - Final report on “Cabling and Jacketing of ITER TF Prototype Conductor”, note AIM/NTT-2007.015, P. Decool, H. Cloez, N. Dolgetta, J.L. Maréchal

TASK LEADER

Patrick DECOOL

DSM/IRFM/STEP
CEA-Cadarache
F-13108 Saint-Paul-lez-Durance Cedex

Tel: 33 4 42 25 43 50
Fax: 33 4 42 25 26 61

e-mail: patrick.decool@cea.fr

CEFDA06-1515

Task Title: TW6-TES-CRYO-03: DESIGN OF THE ITER CRYOPLANT AND CRYODISTRIBUTION SYSTEM

INTRODUCTION

The main objective of this task is to provide cryogenic information to the ITER project for further progress in the design of the machine.

The task was subdivided into the following subtasks:

- Subtask 1: Detailed design of a test loop to study how to mitigate pulsed heat loads associated with advanced plasma scenarios on the LHe system of the ITER cryoplant,
- Subtask 2: Detailed analysis of cryoplant operational modes,
- Subtask 3: Development plan for the ITER Cryogenic System.

2007-2008 ACTIVITIES

DETAILED DESIGN OF A TEST LOOP

Due to the pulsed operation of the ITER tokamak, the refrigerators have to face strongly varying heat loads, which is very demanding for such systems. A load smoothing device has been proposed by the ITER team which needs to be validated. To do this, a scaled-down experiment (similitude) continues to be studied in this subtask of the contract.

The work performed here is based on a previous task named TW5-TES-CRYO1 where a global design of the test loop was done. The goal of the current activities is to perform the details drawings of the scale down (1/60) experiment to validate different methods of load smoothing. Before the execution of the drawings, a revue of the inputs was performed in order to take into account the evolution of the project.

In addition to the detailed drawings, a process and instrumentation diagram was established including, as usually for this kind of document, the instrumentation for the analysis of the experiment. In parallel to the design activity, contacts with industry for critical components (heat exchanger and circulation pump) were taken with an estimation of the cost of these devices.

The figures 1 and 2 present the 3D model of the loop. Figure 1 show the vacuum vessel where the experiment is installed and the second one gives a view of the circuit used for the test of the load smoothing method.

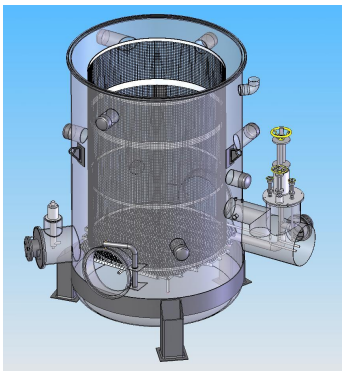

Figure 1: Vaccum vessel for the installation of the test loop (2.0 m in diameter and 3.5 m in height)

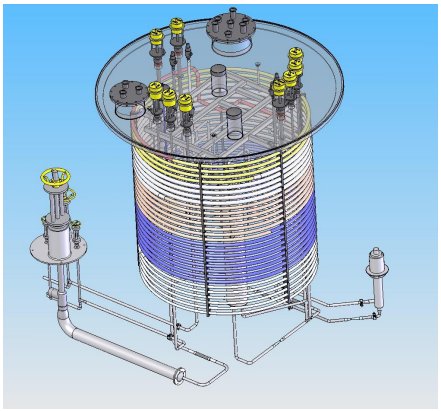

Figure 2: Circuit for the test of the smoothing method

DETAILED ANALYSIS OF THE OPERATIONAL MODES

This study follows the study perform in 2006 (TW6-TES-CRYO1). During this new task a review of the normal operational modes of the ITER cryogenic system was done and an analysis of the abnormal modes for magnet and cryopump distribution was performed. Finally the software used for the process flow diagram (PFD) was changed in order to facilitate the implementation of the modes.

- Based on the last published cryogenic Process Flow Diagram (PFD), a revue of the normal operational modes was done that has also been imposed to take into account the modification of the input data that occurred between CRYO1 and CRYO3. Of course the work was focused on the magnet and cryopump distribution.
- The second part of the work done is the analysis of the abnormal cryogenic mode. Potential problems of the different parts of the system were studied from the production of the cold power in the cryoplant to the final distribution of cryogen in the terminal cold box. A generic difficulty identified during this work is the failure

of all the rotating machines used either to expand the gas for the cool down effect or to compress the gas.

- The software used to implement the PFD and imposed by ITER before this study was not really adapted to the handling of this kind of document; consequently, it was chosen to change the tools always in the frame of the tools accepted by ITER. Of course, some modifications of the PFD were done due to the analysis of the modes (normal or abnormal). After this work, the modes were implemented inside the document for an easy understanding of the operation proposed by CEA.

DEVELOPMENT PLAN OF THE ITER CRYOGENIC SYSTEM

After the decision of the construction of the ITER project, it seemed important to propose a strategy for the construction of the cryogenic system of the machine. It was done during this part of the task.

First of all a rapid review of the reference solution was performed in order to highlight the technical issues than can impact the project. In correlation with that point, a work plan was proposed to take into account these issues. Several points can be mentioned which present risks for the project:

- The wide amount of partners requires an adapted project management with a detailed definition of the function of everybody (technical specification, boundary, interface definition, validation process …).
- In comparison with other large plants, tokamaks have a variable heat load which is a major key point for cryogenics. The investigation of the smoothing methods is consequently important and their validation is mandatory. A scale down experiment was proposed for this purpose.
- The operability and maintainability is also an important question. The cryogenic components required regular maintenance in an environment with limited access and restricted available space. Particular dispositions will be required.
- The installation of the system is complicated and must also be studied in detailed, especially for the "early delivery cryoline" that is installed during the erection of the building.
- The last important issue highlighted is the standardisation of the instrumentation required for components furnished by at least five parties.

Finally an estimation of the resources required during the different phases of the construction was proposed.

CONCLUSIONS

TEST LOOP

A load-smoothing device was proposed by ITER team by using a by-pass valve on the TF structure. The validation method by using a reduced scale experiment was reviewed. Other methods (proposed by CEA) than the reference solution can also be tested. The detailed design of the experiment was performed with a cost estimation of the different part of the system. A particular attention was taken for the specific components (heat exchanger and circulating pump).

CRYOPLANT OPERATIONAL MODES

A review of the normal modes was performed and the abnormal modes were studied. The analysis covers all the part of the machine (cryoplant, cryodistribution for magnets or cryopumps). An update of the PFD was proposed and also a migration of these documents to another software for an easier use. The modes were implemented on this new tool.

DEVELOPMENT PLAN

A strategy for the construction of the cryogenic part of the ITER machine was proposed. The major key points of the system have been pointed out and outlined. The smoothing of heat loads and the operability of the machine seems to be the major difficulties to solve.

REFERENCES

[1] Investigation of a test loop for the cooling system of the ITER TF coil under pulsed heat load – P. Roussel, A. Girard, S. Maze, J.M. Poncet, V. Kalinin, D.Murdoch, M. Sanmarti – CEC 2007 at Chattanooga (USA) – 17-20 / 07 / 07

REPORTS AND PUBLICATIONS

[1] Detailed analysis of the ITER cryoplant normal and abnormal modes – Denis Henry, Pascal Roussel, Pascal Reynaud, Jean Marc Poncet – CEA Report CC3D/CC3D-2008.001

[2] Scale down-loop to simulate the smoothing of ITER heat loads – B. Rousset – CEA Report SBT/CT/08-25

[3] Development plan of the ITER cryogenic system – J.Y. Journeaux, J.M. Poncet – CEA Report CRYO/NTT 2008.008

TASK LEADER

Jean-Marc PONCET

DSM/INAC/SBT
CEA-Grenoble
17 rue des Martyrs
F-38054 Grenoble Cedex 9

Tel: 33 4 38 78 57 46
Fax: 33 4 38 78 50 84

e-mail: jean-marc.poncet@cea.fr

CEFDA06-1521

Task Title: TW6-TMSC-HEAT1: HEAT TREATMENT OPTIMIZATION OF ADVANCED Nb_3Sn STRANDS STUDY OF HEAT TREATMENT EFFECT ON CRITICAL POPERTIES OF INDUSTRIAL ADVANCED Nb_3Sn STRANDS FOR ITER

INTRODUCTION

In the framework of European Nb_3Sn strand procurement actions several new strand types were developed and produced. Due to the different layouts of the strands individual heat treatment (HT) schedules are being used. HT studies are necessary to minimise the duration and reaction temperature without significantly reducing the strand performance. In view of ITER, it is advantageous to have one common heat treatment since it enables the HT of different pancakes at the same time.
For this purpose two batches of strands are extensively characterized after an imposed HT (not optimised for part of them) and their properties are compared with the optimised configuration.

2007-2008 ACTIVITIES

EXPERIMENTAL PROGRAM

Two batches of Nb_3SN strands were heat treated, handled and characterized in CEA test facilities. The characterization included different measurements:

- Critical current (I_C) at T=4.2K and magnetic field between 10T and 14T,
- Hysteresis losses at T=4.2K with B varying between ±3T,
- RRR between T=293K and T=20K,
- Micrographic analyses (strand diameter before and after HT).

The overall experimental program together with strand labels is shown in table1.

Table 1: List of strands with associated tests

Strands labels	Batch #	I_C	hysteresis losses	RRR	micrography
Dipole 9319	1	x	x	x	x
Dipole 9357-2	1	x		x	
Dipole 9358-2	1	x		x	
Dipole 9485	1	x	x	x	x
Pori 8303	1	x		x	
OCSI	1	x		x	
OSTII 7878	1	x	x	x	x
Alstom B5/2660-A1-1	2	x	x	x	x
Alstom B5/2660-A1-2	2	x				
Alstom B5/2660-A1-3	2	x				
Alstom B3/2660-A1-1	2	x	x	x	
Alstom B3/2660-A1-2	2	x				
Alstom B3/2660-A2-1	2	x	x	x	
Alstom B3/2660-A2-2	2	x				
Alstom B10/2660-1	2	x		x	
Alstom B10/2660-2	2	x		x	

RESULTS

Critical current

A total of 16 measurements were foreseen, 15 of which were realized (1 strand broken during handling). A mix of stable and unstable strands was observed, some of them showing systematic premature quench before transition.
Table 2 shows the dipole strand properties (unstable) in terms of quench current I_Q instead of critical current I_C.

Table 2: Dipole strands results

B(T)	I_Q (A)			
	OST 9485 (dipole)	OST 9358-2 (dipole)	OST 9357-2 (dipole)	OST 9319 (dipole)
10	270			*(broken)*
11	250			
12	240	546	514	
13	229			
14	220			

Table 3 shows the batch#1 ITER strand properties (stable).

Table 3: ITER batch#1 strands results

B(T)	IC (A)		
	PORI 8303	OCSI	OST II 7878
10	237	251	282
11	198	212	238
12	164	176	199
13	135	143	165
14	111	115	134

Table 4: ITER batch#2 strands results

	IC(A)							IQ(A)
	Alstom B5/2660-A1-1	Alstom B5/2660-A1-2	Alstom B5/2660-A1-3	Alstom B3/2660-A1-1	Alstom B3/2660-A1-2	Alstom B3/2660-A2-2	Alstom B10/2660-2	Alstom B3/2660-A2-1
10	414	412	414	430	436	421	443	408
11	353	356	354	367	373	361	379	349
12	298	302	300	312	318	308	322	296
13	258	260	255	268	268	262	272	253
14	216	218	214	225	226	221	228	221

Table 4 shows the batch#2 ITER strand properties (stable & unstable).

RRR

The RRR values are close or higher to the specified limit of 100, except for the sample labelled 9357-2 in the first batch, which shows very low value. If not confirmed by another source, this could be explained by poor experimental conditions for this sample (voltage taps soldering, DAS) or by an external pollution during HT.

AC losses

The results found are consistent with the expected values, and a clear discrimination between high J_C strands (dipole) and moderate J_C strands (ITER) is visible.

Table 5: Hysteresis losses results
Units in mJ.cm^{-3}, with reference to strand volume

sample	Batch#	Qhyst (mJ.cm-3)
Dipole 9319	1	1854
Dipole 9485	1	1898
OSTII 7878	1	153
Alstom B5/2660-A1-1	2	250
Alstom B3/2660-A1-1	2	251
Alstom B3/2660-A2-1	2	233

Micrography

An example of a micrographic view is given in figure 1.

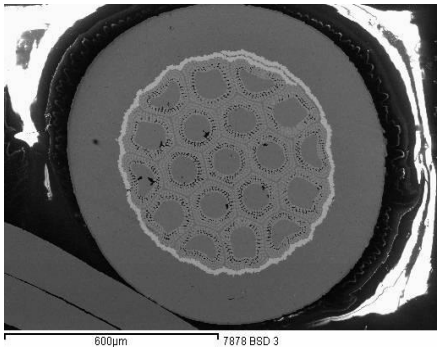

Figure 1: Sample 7878 (reacted) cross-section view

The dimensions found are shown in table 6.

Table 6: Micrography results for the 3 types of strands

sample	Batch #	Diameter ∅ (µm)	Δ∅ (µm)
Dipole 9319 no HT	1	819	± 4
Dipole 9319 with HT	1	830	± 3
Dipole 9485 no HT	1	818	± 3
Dipole 9485 with HT	1	834	± 2
Alstom B3/2660-A1-1 with HT	2	820	-

Dipole samples 9319 and 9485 are both showing a 10-15 µm diametric expansion.
The filament diameters were also found around 65µm in the dipole strands, satisfactorily consistent with the calculation from the hysteresis losses results.
For Alstom sample B3A1, the diameter is evaluated at 0.82mm.

CONCLUSIONS

In this work, the characterization of Nb_3Sn strands was performed, either in critical current, AC losses, micrography or RRR.
Two different batches were tested: one related to the EFDA dipole conductor, another to the ITER TF conductor. The Heat Treatments used were performed respectively following the dipole and ITER procedures.
The highlighting points of the measurements results are:

- Dipole strands (batch#1) showed systematic instabilities at values under the expected critical values. This could be linked to strand properties, as high-J_C strands are often prone to be unstable with respect to low-J_C strands,
- All ITER strand (batch#2) showed consistent J_C values, in the expected order of magnitude. One strand only was found unstable (B3-A2) and could not reach the critical criterion,
- AC losses were found consistent for the two batches to recover the filament diameter values observed by micrography,

- All RRR but one were found within the expected range,
- The micrographic views gave satisfactory results, both on the ITER strand with clear unreacted zones appearing, and on the dipole strands, showing a 10µm strand diameter increase after HT, with a confirmation of the effective filament diameter.

REPORTS AND PUBLICATIONS

Final report: Heat Treatments optimization of advanced Nb_3Sn strands – CEA Report AIM/NTT 2008.020 - L. Zani, M. Tena, M. Nannini, S. Girard, C. Roux, H. Cloez, J.-P. Serries, P. Decool, A. torre

TASK LEADER

Louis ZANI

DSM/IRFM/STEP
CEA-Cadarache
F-13108 Saint-Paul-lez-Durance Cedex

Tel.: 33 4 42 25 29 67
Fax: 33 4 42 25 26 61

e-mail: louis.zani@cea.fr

CEFDA07-1700-1565

Task Title: TW6-TTFD-VP76: CRYOPUMP VALV BOX AND CRYO JUMPER DESIGN STUDY

INTRODUCTION

In ITER, three types of cryopumps are used with different kinds of characteristics:

- 8 pumps for the torus pumping (main gas concerned: hydrogen and its isotopes),
- 2 pumps for the vacuum vessel which contains all the magnets,
- 4 pumps for the neutral beam injection to warm the plasma.

The main objective of this task was to update the available design of the cryopump valve box (CVB) for torus. It exists differences between the boxes and we choose to work on the more complex one (those that includes the supply of the pellet injection system). A lot of input data was required to perform the job, even if a work on that field was performed, finally, a part of the task was dedicated to the study of the scenarios in order to establish some input data.
The regeneration at 100 K or 470 K was studied. Of course, the activities performed had consequences on the architecture and modifications of the process flow diagram (PFD) were done.

2007-2008 ACTIVITIES

STUDY OF SCENARIOS

The first step of the work was the study of all scenarios in order to respect the constraints applied on the pump. The major parameter is the accumulation of hydrogen or its isotopes with some deflagration risks.
A regeneration of the pumps is consequently required to transfer hydrogen accumulated through the tritium plant. Operation modes were updated or proposed to respect these requirements.
This task was performed in major part by ITER-IO but with the participation of the CEA.

MASS FLOW IN STEADY STATE OPERATION

The first task performed for the work was the calculation of mass flows required in steady state or during the pumping phases for all kinds of pumps but also by taking into account the location of the pumps in the circuit which have an impact on the required values.
The loads applied depend also on the plasma; consequently, these calculations were performed for all the scenarios. Several evolutions of the scenarios were done during our task so we updated our calculations.

REGENERATION AT 100 K AND 470 K

As already mentioned, a regular regeneration of the pumps is required; due to hydrogen risks but also to re-obtain the full capacity of the pump (the accumulation of gases saturates progressively the pump so a warm-up of the pump is periodically required). Two kinds of regeneration are used for ITER, the first one at 100 K to remove hydrogen and helium and the second one to remove all the gases. The major difference between these two operations is the time available which is less important for the first one. The second one permits also to verify if no problem exists on the machine by the analysis of the gases released (presence of air, water …).

The allowed time for regenerations is limited, especially for those at 100 K, a detailed study of these operations were consequently done. In this task the work was performed for torus cryopump, the study of the neutral beam one will be examined in a future task. At 100 K, the allowable time depends on the scenario with a minimum value for the 3000 s scenario (600 s). The regeneration at this level of temperature was consequently studied for this case. The calculations of the temperature variation were done for the cryopanels but also for the thermal shield of the pump. Figures 1 and 2 present the regeneration of the cryopanels at 100 K and 470 K.

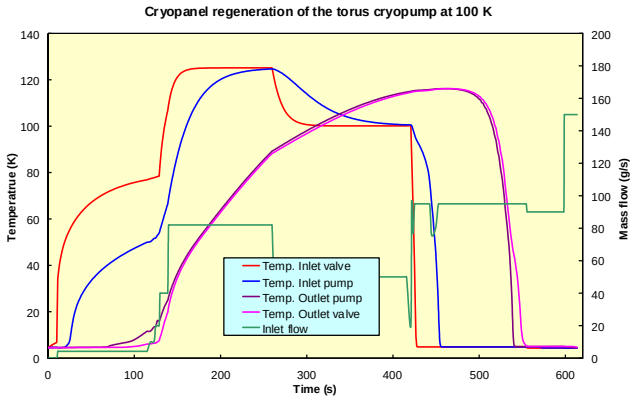

Figure 1: Regeneration of cryopanels at 100 K

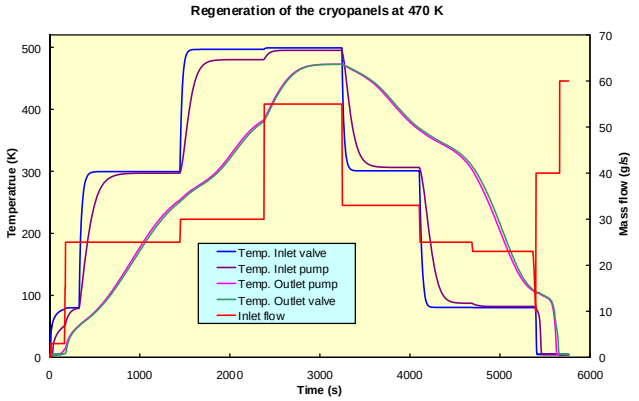

Figure 2: Regeneration of cryopanels at 470 K

This activity permitted to calculate all the mass flows necessary for these operations in relation with the available temperature level. The other interest of the mass flow calculation is the estimation of the Cv of the valves or in other words their size required for the design of the valve box.

OPERATION OF THE PELLET INJECTION SYSTEM

Different strategies and modes were envisaged for the pellet injection system (PIS) by the ITER group with consequences on the architecture of the CVB. Different updates on this part of the CVB have been performed either for the PFD, the operation modes and the design. Finally, CEA proposed a solution for the global management of the PIS that has been accepted by ITER with a simplification of the system inside the CVB.

PROCESS FLOW DIAGRAM AND MODES

As already mentioned, several updates of this document were performed in order to take into account the new proposals for modes depending on plasma scenario or depending on consequences of the different CEA calculation. The process and instrumentation diagram for the CVB designed has also been updated.

DESIGN OF A COLD VALVE BOX

A first study of the more complex cold valve box was studied. The work focussed on the environment constraint due to the low available space and also by taking into account the maintenance requirement. Figure 3 presents the design proposed with all the utilities needed for this cold box (plateform for maintenance, purge panel, electrical cabinet, safety valve pipe collector, cryolines …).

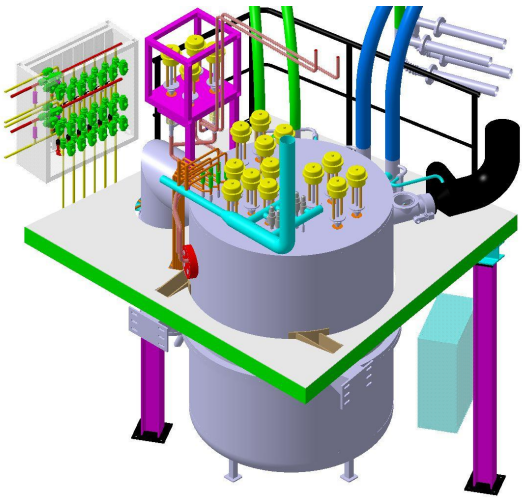

Figure 3

CONCLUSIONS

A complete study of scenario was performed in collaboration with ITER-IO with important modifications on the architecture of the cryopump distribution. This study permitted the calculation of the steady state mass flow used during pumping phase for all kind of pumps. The study of the regeneration at 100 K or 470 K was performed for the torus cryopumps. That has permitted to size the valves used in the cryopump valve box. Finally, a first draft of the design was proposed. In the future these works will be updated in order to take into account new evolutions of the system.

REFERENCES

[1] Status of the Cryogenic Interface of the ITER Cryopumps - Christian Mayaux, Mike Wykes, Robert Pearce, Yong-Hwan Kim, Liam Worth, Lean Louis Bersier, Bastien Boursier, Curt Gliss, Denis Henry, Michel Chalifour, Luigi Serio, Vladimir Kalinin, Jean Marc Poncet, Mathieu Scannapiego, Christian Day, Matthias Dremel, Manel Sanmarti Cardona, Giovanni Piazza, Rainer Laesser. – 25th symposium on Fusion Technology – September 2008 – Rostock – Germany

REPORTS AND PUBLICATIONS

[1] PFD and P&ID of the cryopump cryodistribution and general design of one CVB - First intermediate report of the VP76 task – CEA Report SBT CT 08 – 18 - M. Scannapiego, J.M. Poncet, P. Reynaud

[2] PFD of the cryopump cryodistribution, P&ID and general design of one Cold Valve Box (CVB) - Final report of the VP76 task - CEA Report SBT CT 09 – 8 M. Scannapiego, J.M. Poncet, P. Reynaud

[3] PFD of the cryopump cryodistribution, P&ID and general design of one Cold Valve Box (CVB) - Final report of the VP76 task - Appendix - CEA Report SBT CT 09 – 9 - M. Scannapiego, J.M. Poncet, P. Reynaud

TASK LEADER

Jean-Marc PONCET

DSM/INAC/SBT
CEA-Grenoble
17 rue des Martyrs
F-38054 Grenoble Cedex 9

Tel: 33 4 38 78 57 46
Fax: 33 4 38 78 50 84

e-mail: jean-marc.poncet@cea.fr

CEFDA07-1700-1603

Task Title: TW6-TMSM-CRYOGT: MATERIALS CRYOGENICS TESTING

INTRODUCTION

Following the CRYOLA task [1], this task was mainly dedicated to the transfer of know-how of thermal contraction measurement method using dual extensometers. These sensors are developed by the expert Arman Nyilas, who works as a consultant (CEME) after his retirement from FZK (Germany).

This task started the second semester of 2008 and is on going in 2009 with the preparation of a new bench for thermal contraction measurement at CEA and the training for manufacturing dual extensometers.

Mechanical and thermal tests on ITER materials were also planned in 2008 but because of lack of input data from Europe and / or ITER team, these tests were postponed in 2009 when additional information will be communicated to CEA (definitions of the tests, the material samples). The mechanical tests will be performed by Air Liquide / DTA (Young modulus, tensile tests, compression tests, fatigue tests …) while thermal tests will be carried out by CEA / SBT (thermal expansion, thermal conductivity …).

2007-2008 ACTIVITIES

DUAL EXTENSOMETERS

The sensors are dual extensometers with 50 mm gauge length and are made of Be-bronze, machined by electro discharge. 2 sensors were supplied by CEME:

- 50 mm gauge length,
- 44 mm gauge length (available in June 2009).

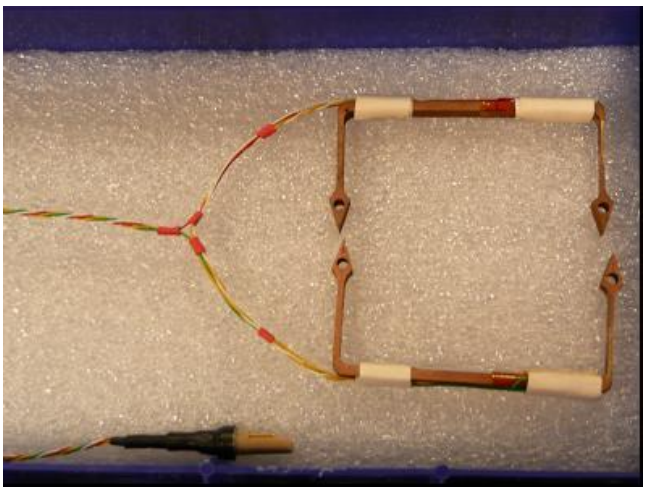

Figure 1: Dual extensometers

PRELIMINARY TESTS AT CEA

The measurement procedures were tested on material samples (Copper and Zerodur) from 77K to 300K. These preliminary tests aimed at validating the measurement procedures:

- Manipulation of the sensor and the samples,
- Calibration of the dual extensometers,
- Data acquisition,
- Post-treatment analysis (dedicated software tools).

These tests were conclusive and highlighted the important steps of the method. A report [3] describes the measurement procedures, analyses the possible improvements and simplifications.
Supplementary tests will be performed to assess the measurement precision, and to compare the data with the ones obtained with the thermal contraction bench at CEA (current reference method with bonded strain gauges on the samples). The dual extensometer used for this comparison is the one with the 44 mm gauge length. Therefore, the same samples can be measured with both methods.

HARDWARE MATERIAL FOR DATA ACQUISITION

Different equipments were purchased and tested for the data acquisition:

- IOTECH Data acquisition board Personal DAQ 54,
- Linear regulated power supply 13.8 V,
- Temperature sensors CERNOX,
- Digital micrometer,
- Connectors.

PREPARATION OF A NEW BENCH FOR THERMAL CONTRACTION MEASUREMENT

A new cryostat was designed for a dedicated thermal bench using these dual extensometers. It will be purchased and supplied in mid 2009.

MANUFACTURING OF DUAL EXTENSOMETERS

Different actions were taken to gather the equipment and tooling necessary for manufacturing of dual extensometers. Different suppliers were contacted for selecting the required equipments:

- Strain gauges,
- Teflon insulated silver plated and stranded cables,
- Soldering unit,
- Bench vise,
- …etc.

Arman Nyilas will train the SBT team to get the skills for manufacturing the dual extensometers (June 2009).

CONCLUSIONS

The contract CRYO-GT has not yet started. A meeting with Europe and ITER shall clarify the needs for thermal and mechanical tests on ITER materials. However, CEA/ SBT started to work on a new thermal contraction measurement method, more flexible and with high precision (+/- 10 μm/m) on the thermal contraction coefficient, using dual extensometers. This transfer of technology from Arman Nyilas to CEA/SBT well progressed and is going on in 2009. Hence, CEA/ SBT will be able to answer the future ITER requests for thermal contraction tests, with well adapted thermal benches.

REFERENCES

[1] Task TW4-TMSC-CRYOLA, Cryogenic tests on ITER magnet structural materials

REPORTS AND PUBLICATIONS

[1] Minutes of meeting Grenoble 13/01/09

[2] Thermal contraction measurement with dual extensometers, January 2009 campaign, to be published

TASK LEADER

Jean-Marc PONCET

DSM/INAC/SBT
CEA-Grenoble
17 rue des Martyrs
F-38054 Grenoble Cedex 9

Tel: 33 4 38 78 57 46
Fax: 33 4 38 78 50 84

e-mail: jean-marc.poncet@cea.fr

CEFDA07-1700-1606

Task Title: TW6-TMST-VINCAN: THERMOHYDRAULIC ANALYSIS FOR THE ITER CRYOGENIC SYSTEM

INTRODUCTION

In the framework of thermohydraulic analysis for the ITER superconducting coils, the objective of this study is to provide assistance to the ITER International Team by performing thermohydraulic analysis of the global ITER magnet system.

The ITER superconducting magnet system has four main subsystems:

- 18 toroidal field coils (TF) for the magnetic field that produces the confining / stabilizing toroidal field,
- One central solenoid (CS), composed of six independently powered modules (CS3L, CS2L, CS1L, CS1U, CS2U, CS3U), for the majority of the magnet flux needed to initiate the plasma, maintain the current during burn time and control the plasma,
- 6 poloidal field coils (PF) for magnetic field that shapes the plasma and controls its position during the various phases of operation,
- 9 correction coils (CC) to correct the field errors.

The magnet system weights, in total, about 9550 tons. Both CS and TF coils operate at high field and use Nb_3Sn superconductor. PF coils and CC use NbTi superconductor. All coils are cooled by supercritical helium at ~ 4.5 K.

Simulations of the PF and the CS cooling loops under the reference scenario conditions have been carried out by ITER IO. The first part of the work deals with the analysis of CS system; the second one describes the most relevant results on PF+CC loop and the third one assesses a global behaviour with the TF system (lTHCoil Task).
The analysis was focused on hydraulic parameters like pressure, temperature and mass flow at various locations of the cooling loops, as well as the heat power inventory.

The scenario under consideration in this analysis, the so-called reference scenario, is an inductive plasma with 500 MW, Q = 10 and 15 MA operation with heating during current ramp-up.

2007-2008 ACTIVITIES

ANALYSIS OF CENTRAL SOLENOID (CS) COOLING LOOP

Simulated cooling loop for the CS winding packs includes a heat exchanger, a liquid helium bath and a circulating pump with feeders and cryolines. The magnet system itself concerns 6 CS modules connected to the cryolines and feeders with a supply/return pipe inside each CS module. .All modeled CS pancakes are wound by one-in-hand CIC conductors and filled by supply and return tubes. The SHe flows in opposite direction for adjacent pancakes.

For the normal operation mode, the initial conditions for the helium cooling circuits and CS modules are as follows:

LHe bath temperature = 4.3 K

Helium circuits temperature = 4.3 K

Temperatures of the CS conductors = 4.3 K
Initial pressure = 0.33 MPa.
Mass flow rate in both circuits = 2 Kg/s

The heat loads taken under consideration are:
1D model:

- AC losses coming from central solenoid modules. They are non-uniformly distributed along the conductors,
- Thermal steady state radiation and conduction on cryolines from / to heat exchanger,
- Transient heat loads coming from the CS joints located at the coil outer diameter (8 joints for each module),
- Any thermal steady state loads are taken into account for feeders connected to the cryolines (to / from CS modules),
- Steady state of power pump.

2D model:

- Eddy current losses deposited in the buffer zone.

The more relevant results are shown on figure 1.

Table 1: Heat distribution on CS system

CS system: heat inventory (average over 1800 s)	Power (W)	%
AC losses	4618	61.1
Eddy currents	527	7
Cryolines	600	7.9
Supply/Return CS module pipes (joints)	47	0.6
Pumping (1.91 Kg/s) Pumping (2.09 Kg/s)	1764 2150	23.3
Total for 1.91 Kg/s Total for 2.09 Kg/s	7556 7942.5	100

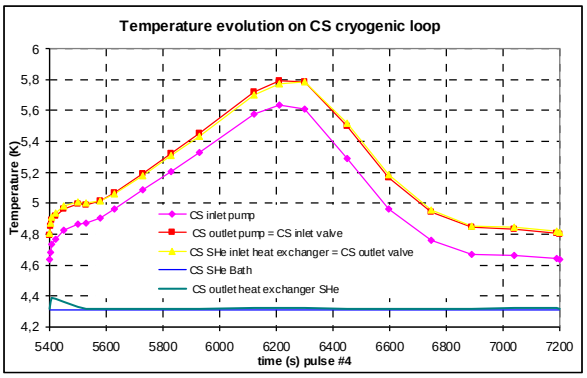

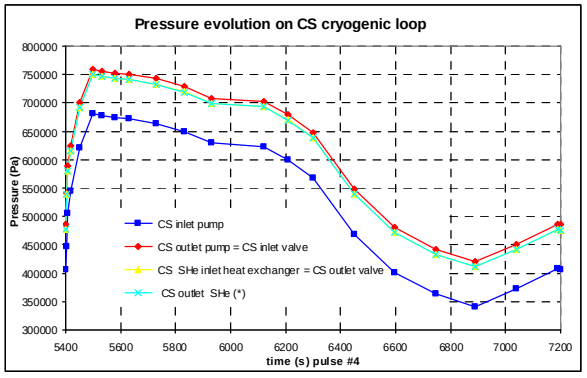

Figure 1: Temperature and Pressure evolution on CS cryogenic loop during one plasma cycle

ANALYSIS OF POLOIDAL AND CORRECTION COILS COOLING LOOP

Cooling loop for the PF and CC Winding packs includes a heat exchanger, a liquid helium bath and a circulating pump with feeders and cryolines. The magnet system itself concerns 6 PF and 9 pair of CC connected to the cryolines and feeders with a supply/return tubes inside the PF modules. All modeled PF pancakes are wound by two-in-hand CIC conductors and are filled by supply and return tubes. The thermal diffusion for 6 PF coils is modelled individually for each PF with a set of cross sectors equispaced.

The initial conditions for the helium cooling circuits on normal operation mode are as follows:

- LHe bath temperature = 4.3 K,
- Helium circuits temperature = 4.3 K,
- Temperatures of the PF&CC conductors = 4.3 K,
- Initial pressure = 0.33 MPa,
- Mass flow rate in both circuits = 1.8 Kg/s.

The heat loads taken into account for the PF+CC simulation are:

- AC losses generating in the PF cables. They are non-uniformly distributed along the conductors on 1D model,
- AC losses coming from three independent sets of correction coils (CCs) distributed along conductors on 1D model. CCs start at t in cc = 72.5 s during the plasma ramp up phase and stop at t out cc = 580 s on plasma ramp down,
- Thermal steady state radiation and conduction in cryolines and feeders,
- Thermal steady state radiation and conduction for supply /return tubes inside PF modules,
- Steady state of power pump,
- Heat load applied to PF coil surfaces (two dimensional thermal diffusion model):
  - Steady state thermal radiation,
  - Nuclear heating,
  - Eddy currents losses in clamps and cover.

The more relevant results are shown on figure 2.

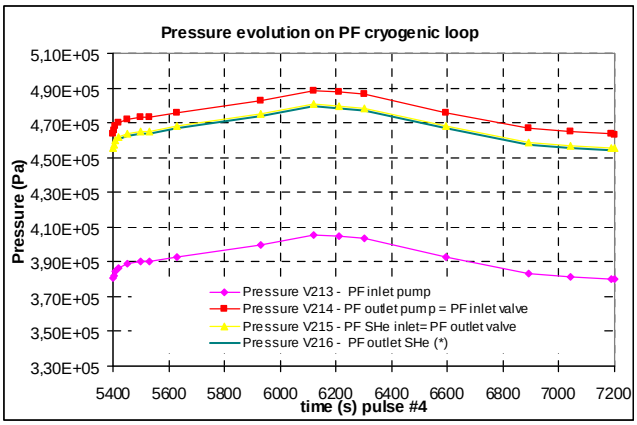

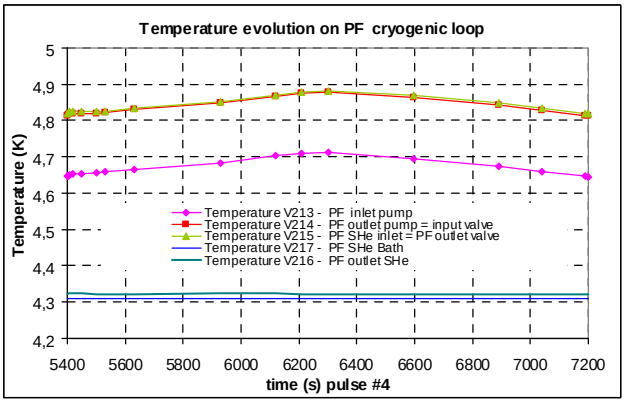

Figure 2: Temperature and Pressure evolution on PF cryogenic loop during one plasma cycle

Table 2: Heat distribution on PF system

PF+ CC system: heat inventory (average over 1800 s)	Power (W)	%
PF AC losses	712.8	19.25
CC AC losses	18.3	0.5
Cryolines and CTB	1170	31.6
Supply/Return PF module tubes	67.51	1.8
Pumping	1733	46.8

CONCLUSIONS

This work describes the thermohydraulic analysis of simulation cryogenic cooling loops for global ITER magnet system. Numerical results were analyzed for the reference scenario.
Energy balances have been performed for CS and PF system.

The Central Solenoid System:

For the CS system two mass flow rates have been analyzed:

- Constant mass flow rate of 1.91 Kg/s giving an input average heat load of 7.5 KW,
- A mass flow rate of 2.09 Kg/s obtained by pump operating curve that gives an input average heat of 7.9 KW.

PF+CC system:

For the PF+CC system, a constant mass flow rate of 1.8 Kg/s gives an average power, including circulating pump, of 4990 W.

The analysis shows a good distribution of mass flow excepted for CS coils during the plasma initialisation. The CS mass flow is about 7.5 g/s for conductor with a maximum helium temperature of 5.8 K at the inlet of heat exchanger. The mass flow of PF conductors is 9.5 g/s with a helium temperature of 4.9 K at inlet heat exchanger.

For PF+CC coils 80 % of heat corresponds to the steady state contribution (radiation, conduction and pumping); only 20 % are released by AC losses on magnets.
For CS system 68 % is due to AC losses and Eddy currents.
For TH coils the transient heat contribution represents 36 %.

REFERENCES

[1] ITER IO PF simulations under reference scenario

[2] ITER IO CS simulations under reference scenario

[3] TFCOIL

[4] VINCENTA Code V.5.9

[5] VINVENTA Code V.6.0

[6] Development of the Base VINCENTA Models for parametric Thermohydraulic Analysis of ITER Magnets by IT Specialits. Part 1. The Base VINCENTA Model for CS Magnet Systems

[7] Development of the Base VINCENTA Models for parametric Thermohydraulic Analysis of ITER Magnets by IT Specialits. Part 2. The Base VINCENTA Model for PF&CC Magnet Systems

[8] Proposal for the Final Design of the ITER Central Solenoid. K. Yoshida et al. IEEE Transactions Applied Superconducting, Vol 14. N°2, June 2004

REPORTS AND PUBLICATIONS

Thermohydraulic analysis for the ITER superconducting coils. R. Vallcorba, Ch. Meuris, B. Rousset, F. Michel, B. Lacroix, S. Nicollet, D. Bessette, H. Rajainmaki (F4E), N. Shatil ICEC22 Conference. Seoul July 21-25 2008

Thermohydraulic Analysis for the ITER Cryogenic System. Final report. January 2009

TASK LEADER

Roser VALLCORBA

DSM/INAC/SBT
CEA-Grenoble
17 rue des Martyrs
F-38054 Grenoble Cedex 9

Tel: 33 4 38 78 97 25
Fax: 33 4 38 78 51 71

e-mail: roser.vallcorba-carbonell@cea.fr

TW1-TMS-PFCITE

Task Title: POLOIDAL FIELD CONDUCTOR INSERT (PFCI)

INTRODUCTION

The PFCI is a single-layer wound solenoid using a 45 m long ITER type NbTi conductor. An intermediate joint connects the main winding to a second piece of the same conductor, which is called the upper bus bar. The conductor is relevant to the ITER PF1&6 coils. The Intermediate Joint (IJ) was fabricated according to the so-called overlap shaking-hand concept as foreseen for the ITER PF coils in the aim to test the behaviour of a joint under relevant ITER PF operating conditions. The PFCI was designed by EFDA and fabricated by Tesla Engineering, UK, under the monitoring of EFDA. The cable (including the NbTi strand) was produced in Russia and jacketed at Ansaldo Superconduttori, Italy. The PFCI is well instrumented as well from the thermal-hydraulic point of view as from the electromagnetic point of view. The coil was positioned for testing in the bore of the ITER Central Solenoid Model Coil (CSMC) facility at JAEA in Naka (Japan). The CSMC provided the background field (6 T nominal) whereas the operating current of (45 kA nominal) added a significant non-uniform contribution across the cable cross section, as in a real coil.

Because of large difficulties encountered during its fabrication, the coil was completed only in summer 2006, delivered in Japan in 2007, and tested in the CS Model Coil (CSMC) at JAEA, Naka, in 2008. Unfortunately, the High Voltage (HV) tests performed at JAEA showed that the PFCI could not withstand the required 10 kV voltage to operate in series with the CSMC with the JT60 power supply for relevant pulsed operations. At the end, because of its HV limitation, the PFCI could only be tested in DC mode under a DC background field provided by the CSMC, or without current and under a pulsed background field. Pulse current tests (under a DC background field) were confined to current cycling operation and were thus very limited in versatility. In addition, several thermometers located on the winding were damaged during the HV test and they require some in-situ recalibration during the experiment since they could not be replaced.

2007-2008 ACTIVITIES

In 2007, our activities were reduced because of the time needed to ship the PFCI to Naka, to perform the reception tests, to repair the coil instrumentation, and last to install the coil in the CSMC facility. In 2008, CEA participated in the preliminary discussions and modelling for the definition of the test program (Test Meeting at Cadarache on March 4th), in the test itself at JAEA during summer, as well as in the analysis of the test results during fall and winter in view of a poster presented at the 22nd IAEA Fusion Energy Conference, Geneva, October 13-18 October. Presentations were also made during our remote participation in the PFCI Test Meeting, Naka, October 28-29.

The work done at CEA concentrated on DC conductor and joint performance with respect to strand properties, ramp rate limitation during pulse current operation, conductor and joint AC losses estimated by calorimetry, joint magnetization under field pulse, conductor stability, and mechanical analysis during cool-down and operation. Only the most significant points are developed in this report.

CONDUCTOR DC PERFORMANCE WITH RESPECT TO STRAND

Estimations of the conductor performance (current sharing temperature T_{CS} at 10μV/m) from strand properties were performed by using the available tool at CEA which allows to compute the average electric field in the cable cross section, taking into account the magnetic field map. In a first step the current distribution among the 1440 superconducting strands of the cable is assumed to be uniform. Also of interest is the T_{CS} of any strand located at peak magnetic field (called T_{CS} (B_{MAX})). Figure 1 shows an example of the computed and measured electric fields vs. temperature whereas table 1 shows the experimental results compared to computation. Note that, for currents above 25 kA, the critical electric field criterion (10μV/m) could not be reached stably and therefore only the quench temperature (T_Q) could be defined. One can see in table 1 that the measured T_{CS} (or T_Q) is generally lower (by 0.05 to 0.1 K) than the computed value whereas T_Q is quite close to T_{CS} (B_{MAX}), which would suggest that the strands located at B_{MAX} are unstable. However, this is not the case for a single strand tested on a barrel under equivalent conditions. Therefore, all these results together rather suggest that the current distribution among the strands was not fully uniform, indeed some simulations using a simple model developed at CEA tend to show that a non-uniformity of ± 45% could explain the experimental results, when assuming the temperature measurement to be perfect.

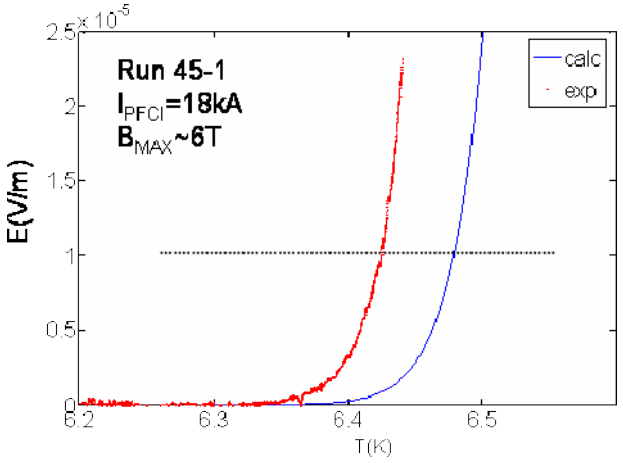

Figure 1: Computed (calc) and measured (exp) electric field vs. temperature in run#45-1

Table 1: Summary of the main experimental results compared to computations

Run #	I_{PFCI} *(kA)*	B_{MAX} *(T)*	T_{CS} exp. (K)	T_Q exp. (K)	T_{CS} calc. (K)	$T_{CS}(B_{MAX})$ (K)
25-1	*44.9*	*5.93*	-	6.27	6.35	6.23
28-1	*51.9*	*6.33*	-	6.03	6.12	5.99
31-1	*49.7*	*3.80*	-	7.21	7.29	7.19
45-1	*18.0*	*5.92*	6.43	6.46	6.48	6.42
53-1	*6.0*	*5.92*	6.47	6.57	6.57	6.55
138-1	*54.3*	*6.86*	-	5.73	5.87	5.73
146-1	*44.0*	*8.38*	-	4.99	5.12	5.00

CONDUCTOR PERFORMANCE WITH PULSED CURRENT (RAMP RATE LIMITATION)

During the whole experiment, there was only one run entirely dedicated to the testing of the PF Insert under pulsed current condition. This ramp-rate test was performed at 300 kA/min (= 5 kA/s) during run 148-01. In addition, another ramp-rate limitation (RRL) was observed during a cyclic test at run 58-01. During both runs, the PF Insert quenched prematurely compared to its DC performance. The transition was identified to start at about 30 kA in both runs although with quite different operating temperatures. The results are reported in table 2, compared to $T_{CS}(B_{MAX})$, which can stand as the DC performance. Also in this table is given run 59-01 for which no quench occurred at 30 kA thanks to a slightly lower background magnetic field.

Table 2: Pulsed and DC properties at 30 kA for runs 148-01, 58-01 and 59-01

Run	**148-01**	**58-01**	**59-01**
Quench	yes	yes	no
B_{MAX} (T)	8.27	8.30	7.91
T_{op} (K)	5.01	4.32	4.42
$T_{CS}(B_{MAX})$	5.34	5.32	5.52
$I_c(B_{MAX})$	53.8	171.3	201.1

CONDUCTOR AC LOSSES

The AC losses of the conductor of the PFCI were measured under a fast magnetic field discharge produced by the CSMC. Each run consisted in a CSMC exponential dump from 4 T, with τ_{dump} ~ 5.7 s and I_{PFCI} = 0 kA. Such a run was performed regularly during the conductor mechanical cycling. The conductor AC losses were estimated by calorimetry but some mismatch between the upstream and downstream temperatures led to apply some re-calibrations which depend on the choice of the reference time and which give different estimations. The results are summed up in figure 2 as "initial" and "final" points. One can see in this figure the increase of the losses with cycling (the runs correspond to cycles # 0, 430, 1700, 2800, 4000, 4002, and 9000), while the sudden decrease correspond to run 119-2 performed after a quench of the conductor.

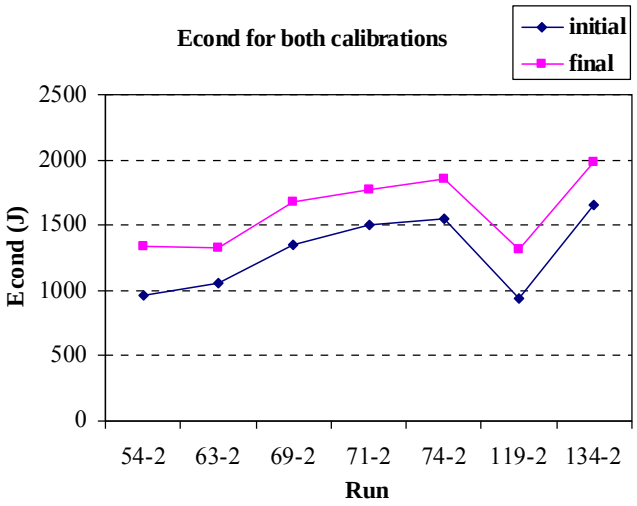

Figure 2: AC losses estimations in PFCI conductor

In order to compute the conductor nτ value (specific of the coupling losses), the CEA model presented in [1] was used. This model has been developed using the THEA code, in which classical formula have been implemented for calculating coupling and hysteretic losses in the conductor. The results are reported in figure 3 where it can be seen that nτ follows the same trend as the total loss energy and reaches a maximum value of about 50 ms after 9000 cycles.

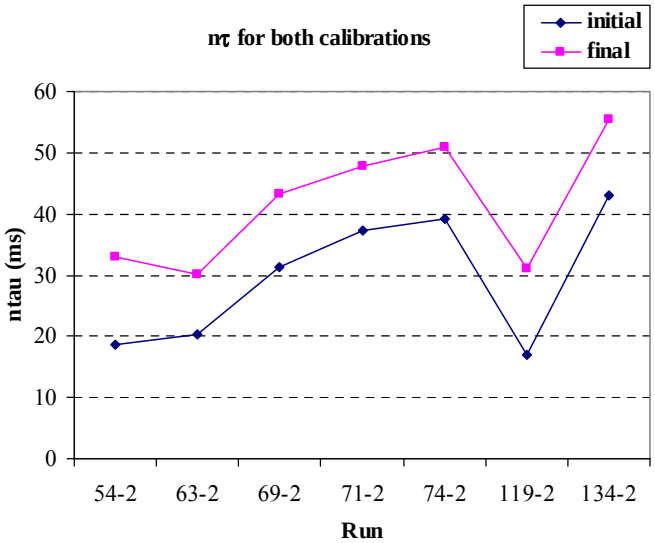

Figure 3: nτ estimations for both calibrations

JOINT DC RESISTANCE AND QUENCH TEMPERATURE

The PFCI Intermediate Joint (IJ) DC resistance was found much lower than expected from preliminary estimations based on the tests of PFI Sultan sample (PFIS) and dedicated mock-ups. Indeed a value of about 2.2 nΩ was measured against 5 nΩ expected. The way this low value (about 1/5 of the PFIS joint) could have been achieved is not yet clear; it is likely related to the use of a large quantity of solder to bond the cable onto the copper sleeves in each half-joint. No significant magneto-resistance effect (i.e. within the error bars) could be measured between 2 and 6 T.
On the other hand, low quench temperatures were measured on the IJ compared to the regular conductor as can be seen in table 3. Note again that $T_{CS}(B_{max})$ stands as conductor performance. Therefore, the loss of T_{CS} is about 1 K in the joint.

Table 3: Joint operating conditions and quench temperature

Run #	I_{PFCI} (kA)	B_{max} (T)	$T_{joint\ bus}$ at quench (K)	$T_{joint\ cond}$ at quench (K)	$T_{CS}(B_{max})$ (K)
142-01	44.9	3.79	6.36	6.38	7.36
143-01	51.9	4.82	5.94	5.82	6.88
149-01	30.1	5.23	5.70	5.69	6.77
156-01	9.31	2.09	7.45	7.43	8.19

JOINT AC LOSSES AND MAGNETIZATION

The AC losses of the PFCI joint under a pulse magnetic field produced by the CSMC were estimated both by calorimetry and by magnetization. The magnetization technique makes use of two pick-up coils oriented along the coil radial and axial directions, each of them is compensated from the main magnetic flux by subtracting the flux of a compensating coil.
The magnetization pick-ups allowed to observe clear "flux jumps" on both axial and radial magnetization loops (figure 4). These flux jumps (i.e. fast relaxation of the magnetization during the cycle) are likely produced by local quenches of overloaded strands carrying high coupling and/or circulating currents.

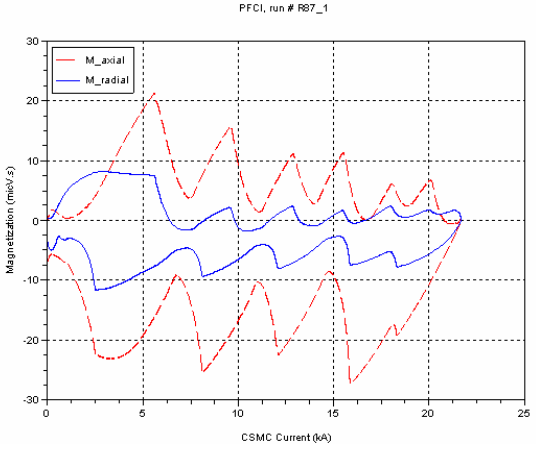

Figure 4: Successive flux jumps on joint magnetization loops (trapezoidal field pulse)

The joint AC losses measured during the reference CSMC exponential dump are presented in table 4. The total loss energy was estimated both by magnetization and calorimetry. Note that magnetization signals allow not only to observe flux jumps but also to separate the contributions from the two field directions. Taking into account the inaccuracies associated with the two estimating methods, the results can be found in good agreement, which gives some weight to this estimation although turns it is quite larger than the preliminary value given by the CEA model (around 750 J).

Table 4: Loss energy in the PFCI joint (fast CSMC dump)

Run #	Magnetization			Calorimetry
	E_{radial} (J)	E_{axial} (J)	E_{tot} (J)	E_{tot} (J)
54-02	134	1663	1797	1506 – 1336
63-02	156	1733	1888	1714 – 1467
71-02	182	1358	1540	1680 – 1465
74-02	166	1115	1282	1698 – 1462
119-02	167	1745	1912	1591 – 1325
134-02	136	1782	1917	1703 – 1424

CONCLUSIONS

The PFCI was tested in the CSMC facility at JAEA, Naka (Japan) in summer 2008. CEA participated in the preliminary discussions and modelling for the test program, in the test at JAEA as well as in the analysis of the test results. The results of the DC tests have been found very promising in terms of current sharing temperature (TCS) or quench temperature (T_{quench}) of the conductor, with a performance close to the performance of the strand at maximum magnetic field in the cable. Although this good result does not exclude some possible uneven current distribution among strands (petals), the final result shows that the performance of such a conductor in a coil is not much affected by the joint quality.
On the other hand, the T_{CS} of the joint was found at a much lower level (about 1 K) than the conductor under equivalent operating conditions, which has not yet been explained.
The few pulse current runs available have also shown some significant ramp rate limitation of T_{CS} at 5 kA/s, compared to the DC performance. This point has however not been fully clarified since the two runs available did exhibit some discrepancy in their performance (about 0.7 K in temperature).
Under the CSMC pulse magnetic field, the conductor showed AC losses at the expected level, increasing with cycling but reinitiated after quench tests.
The joint DC resistance was found much lower than expected from previous estimations and measurements (2.2 nΩ instead of 5 nΩ) but the joint exhibited rather (unexpectedly) high AC losses under pulsed magnetic field, particularly for field variations along the coil axial direction. Clear "flux jumps" (FJ) could be observed on both (radial and axial) field directions thanks to the pick-up coils located in the winding. Since no pulse field tests with current in the PFCI could be performed, the impact of these FJs on the joint (and conductor) stability could not be evaluated.

The pressure drop through the PFCI conductor looks in line with already tested conductors (such as the TFMC one) and with models already developed. The stability test of the conductor showed lower performance than computed for the ITER PF equivalent conductors, but the accuracy on the measurement of the deposited energy is not fully assessed.
Last, the mechanical behaviour of the coil during cool-down and energizing was found consistent with the computation by mechanical models.

REFERENCES

[1] B. Lacroix et al., "Predictive study of the Poloidal Field Coil Insert behaviour under pulsed current tests", 8th European Conference on Applied Superconductivity (EUCAS 2007), Journal of Physics: Conference Series 97 (2008) 012201

TASK LEADER

Daniel CIAZYNSKI

DSM/IRFM/STEP
CEA-Cadarache
F-13108 Saint-Paul-Lez-Durance Cedex

Tel: 33 4 42 25 42 18
Fax: 33 4 42 25 26 61

e-mail: daniel.ciazynski@cea.fr

Task Title: HTS MATERIALS FOR FUSION MAGNETS

INTRODUCTION

This report summarizes the work undertaken at CEA-Saclay and CEA-Cadarache on high temperature superconducting materials. It is focussed on Bi2212 material developments and the measurement of superconducting ribbons. CEA initiated R&D activities on round HTS superconducting wires.

During the scope of this work Bi2212 appeared as being the most suitable HTS material for high field applications. Recent progress on Bi2212 developments led in the US at the National High Magnetic Field Laboratory and Los Alamos laboratory have showed impressive critical current density values up to 45 T.

2007-2008 ACTIVITIES

SUPERCONDUCTING MATERIALS

Two types of conductors were tested, a ribbon and a round wire, as shown on figures 1 and 2. The parameters of these two superconductors are given on table 1.

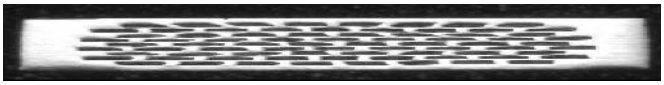

Figure 1: Bi2212 ribbon cross section

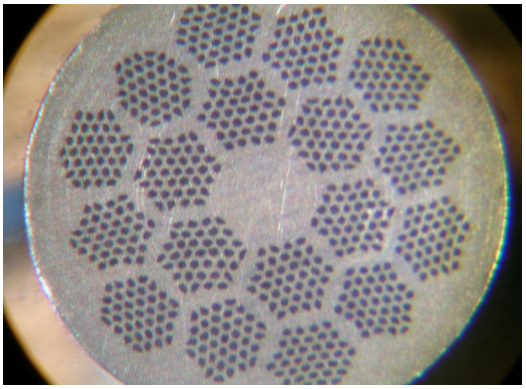

Figure 2: Cross section of the superconducting wire

Table 1: Ribbon and round wire data

	Unit	Ribbon	Round wire
Width	mm	4	
Thickness	mm	0.21	
Diameter	mm		0.8
Cross section	mm²	0.84	0.5
Number of filaments		76	666
Number of sub elements			18
SC cross section	mm²	0.21	0.053
SC / Non SC ratio	%	25 %	10.5 %

RIBBON MEASUREMENTS

Critical current measurement as a function of the magnetic field is shown on figure 3. Critical current measured on samples coming from the same batch allowed to estimate the scatter within this production batch as 11%, 10%, 15% and 30% for measurements done respectively at 4.2 K, 10 K, 20 K and 30 K.
Assuming the behavior in the 5 to 15 T areas is linear enables to extrapolate the critical field value for each temperature. These are 35.6 T, 35.5 T, 28.2 T and 19.8 T respectively for 4.2 K, 10 K, 20 K and 30 K as plotted on figure 6.
Plotting the values of critical current from figure 3 as a function of temperature gives figure 4. Approximating the curves of figure 4 with lines allows determining the slopes which varies from 4.7 A/K @ 0 T to 3.5 A/K @ 15 T.

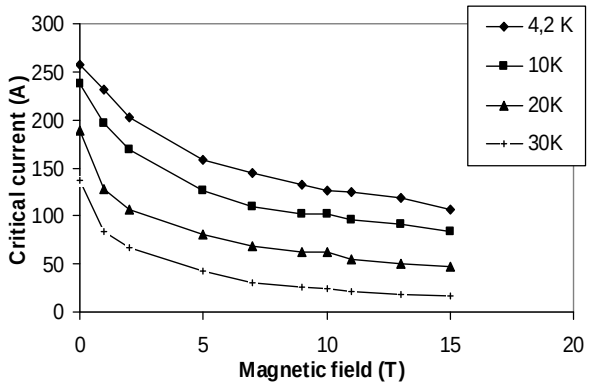

Figure 3: Mean values of the critical current measured on ribbons at T = 4.2, 10, 20 and 30 K

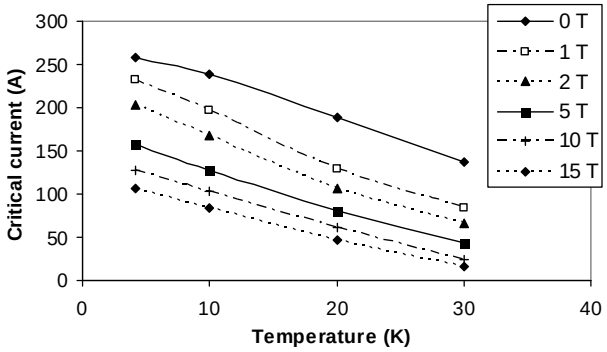

Figure 4: Critical current as function of temperature for different magnetic fields

ROUND WIRE MEASUREMENTS

Similar measurements were undertaken on the round wire (figure 5). It appears that this wire does not withstand magnetic field as efficiently as the ribbon. Nevertheless its critical current density without magnetic field is substantially higher than the one of the ribbon.

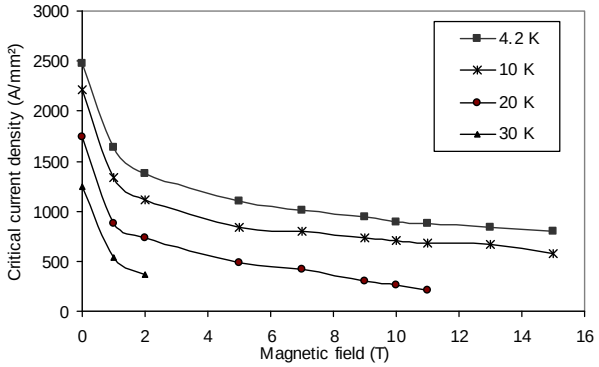

Figure 5: Critical current as a function of magnetic field for the round wire samples

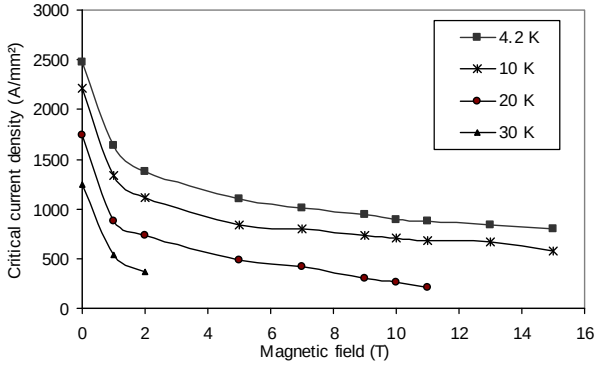

Figure 6: Critical current density for the round wire sample tested

MODEL DEVELOPMENT

Magnet designers always dream of having simple laws to estimate superconducting properties of their conductors based on a reduced number of simple experimental measurements.
In order to predict critical current values a model has been developed based on the knowledge of critical current without field. As the effective cross section of superconducting material is uneasy to estimate after heat treatment reaction the use of critical current density does not seems to be appropriate. Plotting the critical current without magnetic field normalized to its value at 4.2 K versus temperature shows a linear behavior. The points on figure 7 come from different samples ribbons and round wire and follow the same following fit:

$$I_c(T, B = 0T) = -0.0189\ T + 1.0894$$

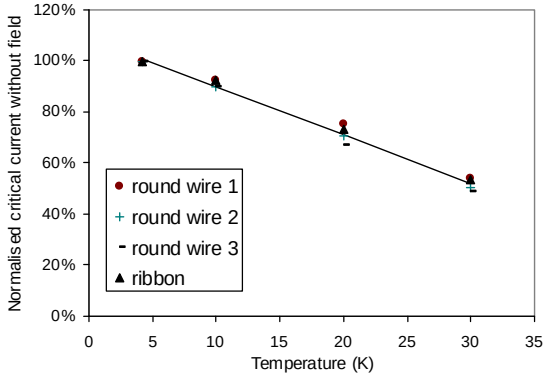

Figure 7: Critical current without magnetic field normalized to the critical current at 4.2 K without field plotted versus temperature

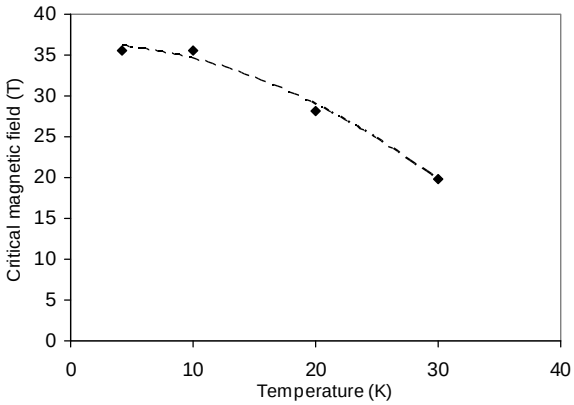

Figure 8: Critical magnetic field versus temperature

This equation represents an intrinsic parameter (not shape dependant) of the superconducting material, like the critical field plotted on figure 8 using the data extrapolated from figure 3. The critical field approximation follows the fit:

$$B_c(T) = -0.0188\ T^2 + 0.0033\ T + 36.392$$

The type of formula chosen for the critical current model comes from diffusion process. The following formula proved to be effective with the set of parameters given in table 2.

$$I_c = I_c(T, B = 0T)\ \exp(-KA^n C^m)$$

With: $A = B/(B_c(T) - B)$

$C = T/(T_c - T)$

Table 2: Parameters used in the model

Symbol	Ribbon	Round wire
K	2	2.5
n	0.45	0.3
m	0.25	0.27

Figure 9 gives the calculated values obtained with the model on dashed lines to be compared with the dots representing the experimental values in the case of the ribbon. Similar results have been found for the round wire.

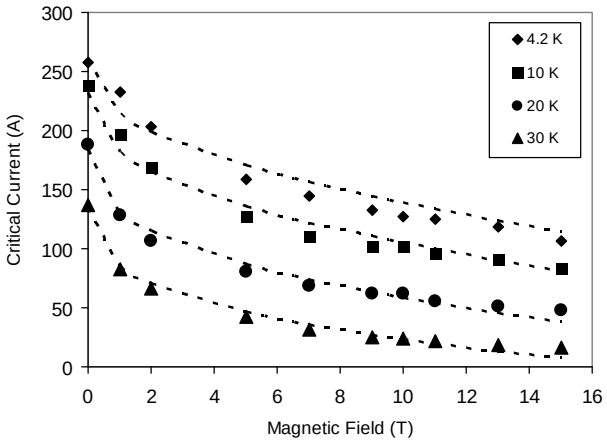

Figure 9: Critical current lines at various temperature obtained from model calculation compared with experimental points measured on ribbon as a function of magnetic field

LOSSES MEASUREMENTS

Induction losses have been measured on the SPEEDY test station from Cadarache. Part of the round wire has been twisted prior to heat treatment to look at the losses reduction. Comparative results between the ribbon and the untwisted round wire are shown on figure 10. Results are proportional to the transverse conductor section crossed by the induction field as expected.

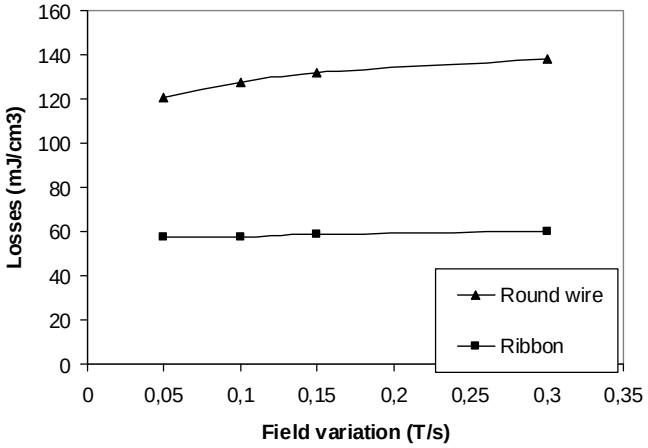

Figure 10: Comparison of losses measured on ribbon and an untwisted round wire as a function of magnetic field variation

The speed of field variation has an influence on the level of losses but this effect is lower than the pitch contribution itself (figures 10 and 11).Nevertheless and despite the fact that heat treatment had been done after twisting the critical current is reduced for short twist pitches as shown on figure 12.

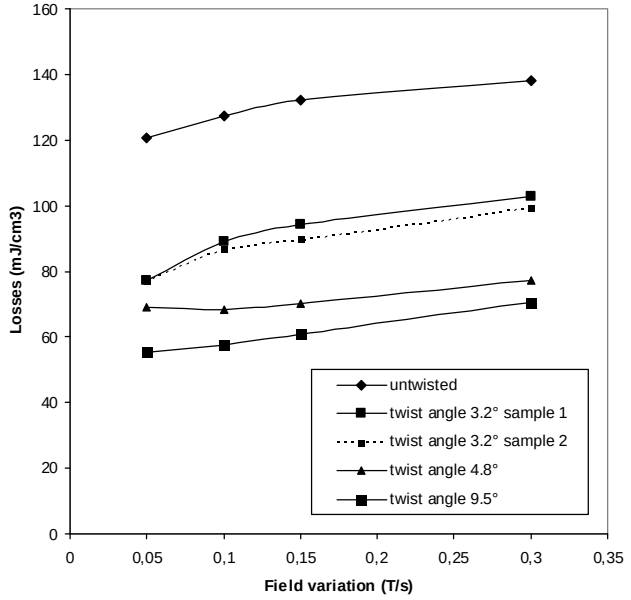

Figure 11: Losses measured on the round wires having different twist pitches expressed a function of the field variation

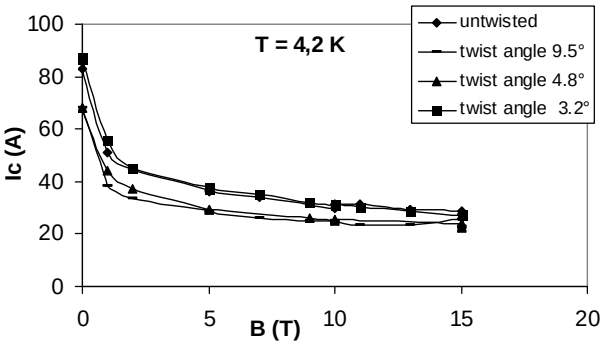

Figure 12: Critical current at 4.2 K on a round wire as a function of twist pitch

CONCLUSIONS

A new Bi2212 round wire was produced, tested and compared to existing Bi2212 ribbon. Its critical current density at low field is higher than the one of the ribbon. At medium to high induction the critical current density are equivalent. Normalized critical current for round wire and ribbon are different. This difference is attributed to conductor shape and its influence on superconducting crystal orientation. For both conductors the overall properties reflects the behavior of the location having the lowest superconductor cross section or the largest local defect.

An empirical model was developed to calculate the critical current as a function of temperature and magnetic field using 3 parameters and 2 experimental fits for the critical magnetic field and the critical current without field. These two equations reflect intrinsic properties of the Bi2212 superconductor and we suppose the 3 parameters are shape and process dependant.

Losses have been measured on Bi2212 ribbon and a newly developed round wire. Results have been compared to losses of low Tc superconductors. Losses on the round wire are of the same level as NbTi wire. The Bi2212 ribbon showing lower losses despite large untransposed filaments.

Twisting effect of the Bi2212 round wire reduces the losses but a degradation of the critical current appears also for short twist pitches. From this last statement cabling degradation have to be expected.

REFERENCES

[1] P. Tixador, M. Deleglise, A. Badel, K. Berger B. Bellin, J. C. Vallier, A. Allais, and C. E. Bruzek "First Tests of a 800 kJ HTS SMES", Applied Superconductivity, IEEE Transactions on, Vol. 18, No. 2, June 2008, pp. 774-778

[2] Hanping Miao; Marken K.R.; Meinesz M.; Czabaj B.; Seung Hong; Twin A.; Noonan P.; Trociewitz U.P.; Schwartz J.; "High Field Insert Coils From Bi-2212/Ag Round Wires" Applied

Superconductivity, IEEE Transactions on, Volume 17, Issue 2, Part 2, June 2007 Page(s):2262 – 2265

[3] Hanping Miao; Marken K.R.; Meinesz M.; Czabaj B.; Seung Hong; "Development of round multifilament Bi-2212/Ag wires for high field magnet applications" Applied Superconductivity, IEEE Transactions on, Volume 15, Issue 2, Part 3, June 2005 Page(s):2554 – 2557

[4] Marken K.R., Jr.; Miao H.; Meinesz M.; Czabaj B.; Hong S.; "Progress in Bi-2212 Wires for High Magnetic Field Applications" Applied Superconductivity, IEEE Transactions on, Volume 16, Issue 2, June 2006 Page(s):992 – 995

[5] Ha D.-W.; Kim S.-C.; Han I.-Y.; Oh J.-G.; Lee J.-H.; Oh S.-S.; Ha H.-S.; Song K.-J.; Sohn M.-H.; Ko R.-K.; Kim H.-S.; Kim T.-K.; "Study on Bi-2212 Rutherford Cabling Process for SMES" Applied Superconductivity, IEEE Transactions on Volume 18, Issue 2, June 2008 Page(s):1192 – 1195

[6] Dong-Woo Ha; Sang-Cheol Kim; Jae-Gun Oh; Hong-Soo Ha Nam-Jin Lee; Kyu-Jeong Song; Tae-Hyung Kim; Rock-Kil Ko; Ho-Sup Kim; Seong-Kuk Park; Sang-Kil Lee; Yu-Mi Roh; Sang-Soo Oh; "Influence of Filament Number on Workability and Critical Current Density of Bi-2212/Ag Superconducting Wires" Applied Superconductivity, IEEE Transactions on, Volume 17, Issue 2, Part 3, June 2007 Page(s):3099 – 3102

REPORTS AND PUBLICATIONS

[7] Jean-Michel Rey, Arnaud Allais, Jean-Luc Duchateau, Philippe Fazilleau, Jean-Marc Gheller, Ronan Le Bouter, Olivier Louchard, Lionel Quettier, Daniel Tordera, "Critical current measurement in HTc Bi2212 ribbons and round wires", Presented at ASC 2008 Chicago

[8] Jean-Michel Rey, Lionel Quettier, Arnaud Allais, Hervé Cloez, Jean-Luc Duchateau, Jean-Louis Marechal, Louis Zani, Sylvain Girard, "Losses measurement in HTc Bi2212 ribbons and round wires", Presented at ASC 2008 Chicago

[9] EFDA Task: TW5-TMS-HTSPER, HTS Materials on Fusion Magnets, Final Report, Deliverable 2, April 2008

TASK LEADER

Jean-Michel REY

DSM/IRFU/SACM/LEAS
CEA-Saclay
F-91191 Gif-sur-Yvette Cedex

Tel: 33 1 69 08 66 85
Fax: 33 1 69 08 69 29

e-mail: j-m.rey@cea.fr

TW6-TMSC-FSTEST

Task Title: PARTICIPATION TO CONDUCTOR TESTS AND EVALUATION OF TEST RESULTS

INTRODUCTION

In the framework of the EFDA Technology Work programme, additional full-size conductor samples are being manufactured and tested in order to assess the gain in performance by using advanced Nb_3Sn strand. The scope of this work can be summarised as follows:

- Preparation of the test programme and review of the instrumentation,
- Predictive DC performance analyses and the basis of the strand data,
- Participation in the testing campaigns for TF/PF conductors,
- Evaluation of the test results,
- Preparation of the Final Report describing the main results and conclusions extrapolated from the testing campaigns.

In 2005-2006, the EU PT tested in the SULTAN facility four full-size conductors based on the TFMC conductor design but using qualified 'advanced' Nb_3Sn strands coming from four European companies: OST, EAS, OKSC (Luvata Pori), and OCSI (Luvata Italy). In 2007, the TFAS1 (EAS-OST) sample was retested after filling with solder all its joints and four new conductors based on the actual ITER TF conductor design (layout #1) and using again the EAS and OST advanced strands were tested. However, these new conductors already anticipated some variations of the original ITER design such as a lower cable void fraction or/and longer cabling twist pitches in order to improve the conductor performance after the poor test results of the TFMC-type conductors. Two new samples TFPRO1 (EAS strand) and TFPRO2 (OST strands) were thus fabricated by CRPP from conductors manufactured by Luvata Italy under the monitoring of ENEA.

2007-2008 ACTIVITIES

After its first analysis presented in 2006 [1], CEA launched in 2007 a reassessment of the performance of the old TFAS1 and TFAS2 conductors (TFMC design) with respect to the ITER TF conductor, including the 4th TFAS1 test campaign performed end of 2006. CEA also participated in 2007 in the retest of TFAS1 with soldered joints (5th test campaign) as well as in the tests of TFPRO1 and TFPRO2. The tests were performed in the SULTAN facility at CRPP Villigen (Switzerland). CEA also contributed to the reduction of the experimental data, to the extensive analysis of the DC test results with regard to the properties of the strand composing the tested conductors, and to the analysis of the conductors AC losses. CEA participated in the ITER Conductor meeting held at CRPP Villigen on July 2-3, 2007. CEA presented the test results at the EUCAS'07 Conference held in Brussels on Sept. 16-20, 2007 [2] and contributed to a presentation of the test results at the MT20 Conference, held in Philadelphia (USA) on Aug. 27-31, 2007 [3]. The final report of the task was delivered to EFDA on Aug. 31, 2007 [4]. The present report focuses on the main milestones of the task in 2007.

Reassessment of TFAS1 and TFAS2 extrapolations to ITER TF conductor

The old extrapolation method was based either on linear extrapolations or interpolations from the experimental points. Then, corrections for the self field and for the IxB effects were applied through models to recover the proper ITER operating conditions. This method which aimed to minimize the effect of the model on the final results was finally too much sensitive to single point inaccuracy, particularly with extrapolations. The new method is simpler and sounder as it is based on the use of models to fit (adjusting the free parameters) a series of experimental points (e.g. 1st points of 1st campaign, last points of 3rd campaign, etc.), and then to apply the model to the ITER TF operating conditions. Obviously, it requires that the test were performed up to a relevant IxB operation (i.e. 758 kN/m) and that enough data points are available in a series to establish a reliable fit.
The results are plotted in figure 1, including the points of the 4th test campaign of TFAS1 (before soldering the joints). THE ITER TF specification lies at T_{CS} = 5.7 K. Note that the ITER-type Nb_3Sn conductor performances are generally assessed with respect to strand performance using smeared models. In model m1, a fully reversible degradation can be modeled by adding an extra strain ε_{extra} (proportional to the total Lorentz force IxB on the cable) to the thermal strain ε_{th} of the Nb_3Sn filaments, whereas in model m2, a fully irreversible degradation of the strand current capability can be modeled by applying a coefficient α_{eff} (< 1) to the conductor critical current computed (from strand properties) with only the thermal strain.
There are no big changes compared to the results presented in [1] except the EAS performance is know better and ends closer to the ITER line with an apparent improvement during the 4th campaign.

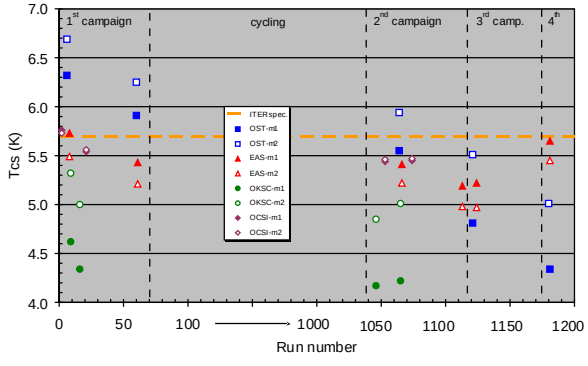

Figure 1: Reassessment of TFAS1 and TFAS2 extrapolations to ITER TF conductor

Short description of TFPR01 and TFPRO2

TFPRO1 and TFPRO2, as all the big SULTAN samples, are composed of two straight conductor legs connected together at one end through an electrical joint and having each at the other end a terminal joint to connect the sample to the facility transformer. The four conductor legs are based on the ITER TF layout #1 conductor design (figure 2) but each of them has its own peculiar features. The common cabling pattern is:
((2s/c+1Cu)x3x5x5+core)x6, with a core made of 3x4 pure Cu strands. The diameter of all the strands is 0.815±0.005 mm. Except for the s/c strand, the differences between the conductors lie in the cable void fraction and the cabling twist pitches (table 1); the closest to the ITER TF layout #1 design is TFPRO1-EAS1. Whereas the TFPRO1 conductors make use of the same EAS strand, the TFPRO2 made use of slightly different OST strands (OST2 being the same as in TFAS1).

Figure 2: Cross-section of TFPRO1-EAS1 (Courtesy of ENEA)

Table1: Main features of TFPRO1 and TFPRO2 cables

Conductor	Strand	Twist pitches sequence (mm)	Cable void fraction (%)
TFPRO1-EAS1	EAS	45-87-126-245-460	34
TFPRO1-EAS2	EAS	45-87-126-245-460	29
TFPRO2-OST1	OST1	45-87-126-245-470	29
TFPRO2-OST2	OST2	116-182-245-415-440	28

Test results for TFPRO1 and TFPRO2

Compared to the TFAS samples, the tests of TFPRO1 and TFPRO2 were reduced to a kind of minimum, within the philosophy of a qualification test. Almost all the tests were performed at a single level of magnetic field. The operating conditions were defined by the ITER Team to be relevant as much as possible to the ITER TF conductor operating conditions. The SULTAN field was then fixed at 10.78 T in order to get in the sample the same effective field as in the ITER TF conductor. After a few calibration runs, the operation could then be seen as a cycling test (ramping current up and down between 0 and 68 kA, under 10.78 T) with a T_{CS} measurement at particular cycle numbers. These numbers were: 1, 3, 10, 200, 400, 600, 800, and 1000. After the thousandth cycle, T_{cs} was measured under slightly different currents and field in order to adjust modelling parameters.
As for the TFAS samples, the voltage drops measured on TFPRO1 and TFPRO2 were not free of the so-called linear offset (i.e. a voltage offset varying linearly with the sample current). Although these offsets were reduced in the 450 mm-tap voltage drops, they were quite significant in the 350 mm-tap voltage drops. This result which can be explained by the fact that the distance of 450 mm between taps corresponds roughly to one cable twist pitch length, shows that the main subcables (petals) of the cable are not equipotential. For consistency with the previous (TFAS) analyses, the linear offsets were removed from all the voltage drops for the conductor performance assessments. The evolution of T_{CS} at 10 µV/m from the different voltage drops is plotted in figures 3 and 4 for TFPRO1 and TFPRO2, respectively (the historical order corresponds to the T_{CS} series given above). Considering the 450 mm voltage drops to be more accurate and reliable, on can conclude that the TCS of the two EAS conductors lie above 6.0 K, with a bonus of about 0.1 K for the more compacted cable (EAS2), and with little variations with cycling. The TCS of the OST1 conductor does show some degradation with cycling, with a final value of 6.0 K and the T_{CS} of the OST2 conductor does not show any degradation with cycling and lies at the very high value of 7.3 K. Note that calorimetric measurements (through helium enthalpy variation due to Joule heating) could be performed on TFPRO2 and confirmed the T_{CS} values obtained by the 450 mm voltage drops.

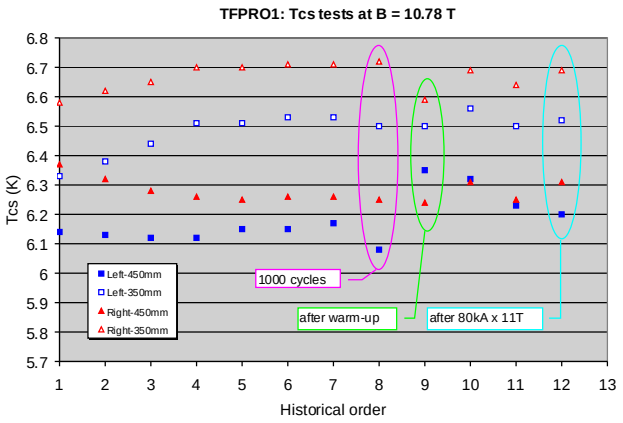

Figure 3: T_{cs} at Bs = 10.78 T and I = 68 kA for EAS1 (left) leg and EAS2 (right) leg

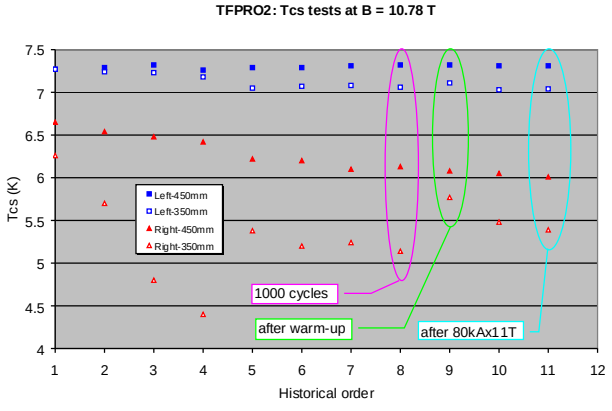

Figure 4: T_{cs} at Bs = 10.78 T and I = 68 kA for OST2 (left) leg and OST1 (right) leg

The n index characterizes the way the electric field is varying with current (i.e. as an n power law); it can be used as a quality index for both strands and cables and must be as high as possible. Table 2 gives the measured values of n on both conductors and associated strands. It can be seen in this table that the cable n index are significantly lower that the corresponding strand n index (except for OST2) which is a clear sign of a degradation of the strands in these cables.

Table 2: Measured n index on conductors and strands

Conductor	N (cable)	N (strand)
TFPRO1-EAS1	7-8	30
TFPRO1-EAS2	7-8	30
TFPRO2-OST1	7-8	21
TFPRO2-OST2	18	18

The AC losses of the conductors were measured using sine pulses of applied magnetic field in SULTAN. The $n\tau$ value is a constant used to characterize the AC losses from coupling currents at low frequency (i.e. when the energy loss per cycle is linear vs. pulse frequency). Table 3 gives the measured $n\tau$ in virgin state (before any Lorentz force was applied) as well as after full cycling (1000 cycles). The specification for the ITER TF conductor is about 130 ms, but this value is not critical. One can see first the drastic decrease of $n\tau$ with cycling, which is quite classical, and second that a higher cable compaction and higher twit pitches tend to increase the AC losses.

Table 3: Coupling loss time constant $n\tau$ (strand volume) for TFPRO1 and TFPRO2 conductors

Conductor	$n\tau$ (ms) virgin	$n\tau$ (ms) cycled
TFPRO1-EAS1	131	7.6
TFPRO1-EAS2	214	n.a.
TFPRO2-OST1	285	16
TFPRO2-OST2	305	73

The ITER-type Nb_3Sn conductor performances are generally assessed with respect to strand performance using smeared models. A fully reversible degradation can be modeled (m1) by adding an extra strain ε_{extra} (proportional to the total Lorentz force on the conductor) to the thermal strain ε_{th} of the Nb_3Sn filaments, whereas a fully irreversible degradation of the strand current capability can be modeled (m2) by applying a coefficient α_{eff} (< 1) to the conductor critical current computed (from strand properties) with only the thermal strain. In order to estimate reliably and accurately the values of these parameters, on needs to measure the conductor T_{CS} over a wide enough range of operating conditions around the nominal TF operation (figure 5). Only cycled (i.e. stable) values should be used in this exercise. The values of the best fit parameters used in models m1 and m2 are given in table 4. One can see in this table the good consistency of the results for the EAS conductors, with a low sensitivity to the Lorentz force (i.e. $\gamma < 10^{-4}$ %.kA^{-1}T^{-1}), the rather high sensitivity of the OST1 conductor. The OST2 (long twist pitches) conductor appears not only free of any degradation, but also with a low thermal strain $|\varepsilon_{th}|$, which explains its exceptionally high T_{CS} value at about 7.3 K.

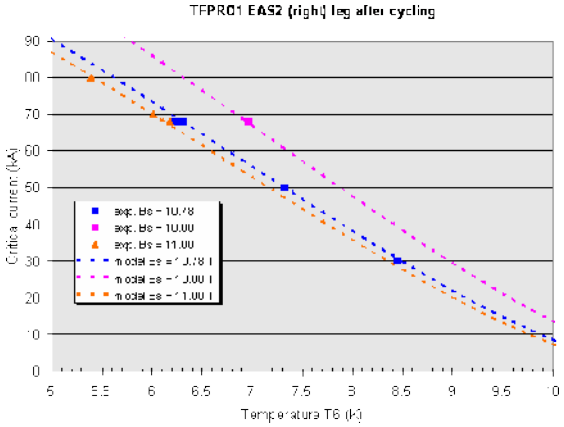

Figure 5: Comparisons of best fit (model m1) T_{cs} with experiment on EAS2 leg

Table 4: TFPRO1 and TFPRO2 best fit values of model parameters after cycling

Conductor	Model m1		Model m2	
	ε_{th} (%)	γ (%.kA^{-1}T^{-1})	ε_{th} (%)	α_{eff}
EAS1	-0.585	0.000095	-0.550	0.80
EAS2	-0.585	0.000075	-0.560	0.84
OST1	-0.530	0.000310	-0.450	0.48
OST2	-0.473	0	-0.473	1

CONCLUSIONS

In 2007, CEA performed a reassessment the TFAS1 and TFAS2 extrapolations to the ITER TF conductor and participated in the tests and the test analysis of the new ITER-type EU conductor samples TFPRO1 and TFRO2.

The new four European TF conductors for ITER tested in 2007 have shown much better performance than the previous conductors tested in 2005-2006, particularly with a current sharing temperature T_{CS} above the ITER specification. Since the same Nb_3Sn strands were used in the old (TFAS1 and TFAS2) and the new conductors, this improvement of performance has to be related only to the change in the cable structure. However, for all but one conductors the reasons for this improvement have not been clearly identified and could lie in the sum of slight improvements leading to a better mechanical support of the strands inside the cable, such as better shaped subcables, smaller spiral, longer last cabling twist pitches. For one conductor, the improvement can be associated with the increase of the first cabling twist pitches, as predicted by the TEMLOP code developed at the University of Twente. However, even for this conductor, the exceptionally high

measured T_{CS} cannot be explained without considering a low thermal strain in the Nb_3Sn filaments which a priori cannot be related to the change of the cable structure.

REPORTS AND PUBLICATIONS

[1] D. Ciazynski, "Review of Nb_3Sn Conductors for ITER", Fusion Eng. and Design 82 (2007) 488–497

[2] D. Ciazynski et al. "Influence of Cable Layout on the Performance of ITER-type Nb_3Sn Conductors", presented at the 8th EUCAS, Brussels, 16-20 Sept. 2007. Published in Journal of Physics: Conference Series (2008)

[3] P. Bruzzone et al., "Test Results of Two European ITER TF Conductor Samples in SULTAN", presented at 2006 Applied Superconductivity Conference (Seattle, 29 Aug. – 1st Sep. 2006), published in IEEE Trans. on Appl. Supercond. (2008)

[4] D. Ciazynski, S. Nicollet, N. Pauty, "EFDA Task TW6-TMSC-FSTEST: Final Report" CEA Internal Note AIM/NTT-2007.020, August 30, 2007

TASK LEADER

Daniel CIAZYNSKI

CEA/DSM/IRFM/STEP
CEA-Cadarache
F-13108 Saint-Paul-Lez-Durance Cedex

Tel: 33 4 42 25 42 18
Fax: 33 4 42 25 26 61

e-mail: daniel.ciazynski@cea.fr

CEFDA07-1700-1573

Task Title: TW6-TTB-COMON: TECHNICAL MONITORING AND ASSESSMENT OF THE KNT/ASSYSTEM CONTRACT ESC06-002

INTRODUCTION

In order to position the current situation of European Test Blanket Modules (TBM) boxes design and manufacturing with regard to the available rules insuring to fulfil the requirements previously described, a dedicated study was launched by EFDA 0]. This contract aimed at identifying missing information (design rules, categories of welds, material properties, etc) in the present SDC-IC or in existing industrial codes (RCC-MR Ed. 2002) or EU standards (EN), with the following expected outcome:

- Identification of missing design analyses (structural, thermo-mechanical) obtained after a systematic review (to be used in future work program for completion of the design activities),
- Identification of missing structural material and joints properties (limited to the expected operating conditions of TBMs in ITER, e.g. fluence < 1 dpa in Eurofer) (to be used in future work program for completion of material characterization),
- Identification of missing rules for qualification of fabrication & NDE procedures and for procurement (to be used as basis for official demand to ITER Organization, Codes Editors and/or preparation of complementary R&D program on fabrication – "code cases").

This task consisted in the follow-up of the ESC-06-002 contract: The purpose was to prepare, check and present all input technical contract: The purpose was to prepare, check and present all input technical information, to perform the technical monitoring including participation to the progress meetings, analysis of progresss reports, orientation of technical activities with regard to HCLL and HCPB Project needs, and to assess the intermediate and final technical reports.

2007-2008 ACTIVITIES

This work consisted in:

- Preparing, compiling and transmitting to KNT/ASSYSTEM all the reference technical information and documentation, related to the HCPB and HCLL TBM projects, necessary for the good realisation of the ESC06-002 contract,
- Monitoring the ESC06-002 contract, by following up the technical realisation and conclusions of the work, by checking its consistency with its technical specifications, and by reporting results, difficulties, issues for the TBM, activities to launch, to EFDA CSU Garching. This monitoring included the preparation, organisation, and reporting of intermediate and kick-off meetings.

It was decomposed into:

- Preparation and transmission of reference technical information to KNT/ASSYSTEM
- Organisation of meetings:
  - progress meetings linked to KNT/ASSYSTEM progress reports, according to the needs, to be defined in collaboration with KNT/ASSYSTEM,
  - kick-off meetings assessing the closure of a deliverable and launching the activities for the following deliverable.
- Redaction of the minutes of the meetings; the minutes of the kick-off meetings will be included in a kick-off report, which will also give a list of the transmitted information and documentation, as well as a the main conclusions, difficulties, and organisation corresponding to this kick-off phase.
- Redaction of technical follow-up documents:
  - monitoring memos, based on the intermediate progress reports produced by KNT/ASSYSTEM, in which the main results, the possible difficulties and solutions are highlighted;
  - deliverable assessment report, based on the deliverable reports produced by KNT/ASSYSTEM, synthesising the main results and key issues for the TBM project.

4 documents were produced in the frame of this Task:

- an assessment report [R1] of the ESC06-002 deliverable 1 [2], consisting in a review of the structural material properties and a review of the performed design analyses, which are intended to help future choices on needs for characterisation of Eurofer according to design rules, and to give designers some guidance in the design analyses process;
- an assessment report [R2] of the ESC06-002 deliverable 2 [3], consisting in the establishment of a comprehensive list of data in preamble to welded joints assessment with regard to code & standards, and checking the agreement of the current design of TBMs welds with the required/recommended rules of codes & standards;
- an assessment report [R3] of the ESC06-002 deliverables 3&4 [4], providing a synthetic detailed overview of the available standards entering in the field of the qualification of welding procedures and associated techniques for the European Test Blanket Modules (TBM) manufacturing, and assessing the situation with regard to regulation and design code RCC-MR;
- a synthesis report [R4] highlighting the conclusions resulting of the follow-up of the studies performed

under the ESC06-002 contract; the main issues of regulation, requirements, codes & standards in the TBM context have also been recalled in order to get a wider overview, as well as the main expectations and specifications of the ESC06-002 contract. The author, as project contributor in the design field, completed these conclusions with additional ones considered of importance for the TBM project, and with comments or notes expressed during meetings or discussions with experts.

CONCLUSIONS

The technical monitoring and assessment of the KNT/ASSYSTEM contract ESC06-002 consisted in:

- the preparation, checking and presentation of all input technical data foreseen in contract,
- the technical monitoring of the contract, including participation to progress meeting, analysis of progress reports, orientation of technical activities with regard to the HCLL/HCPB TBM project needs,
- the assessment of the intermediate and final technical reports (Deliverables 1 to 4).

REFERENCES

[1] EFDA Close Support Unit – Garching, Task Agreement ESC06-002 “First review of the EU Test Blanket Modules (TBMs) design and manufacturing with respect to ITER Code & Standards”, Annex A: technical specification

[2] M. Daichendt, R. Pascal, “First review of the EU Test Blanket Modules (TBMs) design and manufacturing with respect to ITER code & standards”, Kraftanlagen/Assystem report, Doc-No: ESC06-002/Del001/Rev3, July 2008

[3] R. Pascal, B. Calcagno, “First review of the EU Test Blanket Modules (TBMs) design and manufacturing with respect to ITER code & standards”, Kraftanlagen/Assystem report, Doc-No: ESC06-002/Del2/Rev2, July 2008

[4] R. Pascal, “First review of the EU Test Blanket Modules (TBMs) design and manufacturing with respect to ITER code & standards”, Kraftanlagen/Assystem report, Doc-No: ESC06-002/Del3&4/Rev1, July 2008

REPORTS AND PUBLICATIONS

[R1] G. Rampal, “Assessment report of ESC06-002/Del. 1”, CEA report SEMT/BCCR/RT/07-066/A, September 2008

[R2] G. Rampal, “Assessment report of ESC06-002/Del. 2”, CEA report SEMT/BCCR/RT/08-008/A, September 2008

[R3] G. Rampal, “Assessment report of ESC06-002/Del. 3&4”, CEA report SEMT/BCCR/RT/08-018/A, September 2008

[R4] G. Rampal, “Synthesis on the follow-up of the ESC06-002 contract”, CEA report SEMT/BCCR/RT/08-025/A, September 2008

TASK LEADER

Gilles RAMPAL

DEN/DM2S/SEMT
CEA-Saclay
F-91191 Gif-sur-Yvette Cedex

Tel: 33 1 69 08 41 44
Fax: 33 1 69 08 94 26

e-mail: gilles.rampal@cea.fr

TW2-TTBC-002-D02

Task Title: BLANKET MANUFACTURING TECHNOLOGIES MANUFACTURING AND TESTING OF MOCK-UPS QUALIFICATION SAMPLES FOR HCLL AND HCPB TBM

INTRODUCTION

This task is dedicated to joining developments for the realization and manufacturing of a demonstration mock-up of a TBM demonstrator. This report gives the status of the work performed in establishing manufacturing choices and welding procedures, NDT controllable. The conclusions drawn remain valid, despite the fact that the TBM definitions used in this work had been fixed 2 years ago for an older design. Several metallurgical and technological breakthroughs have been made that limit distortions, in association with NDT testing and advanced welding processes, combined with complex welding tools. It is shown that the results obtained can be easily transferred to new designs, by widening the assembly and welding possibilities, which were not the case before the start of this task. A new operating field for new joining processes, such as High Power Nd:YAG continuous Laser and Hybrid processes, has been opened compared with the standard available processes, such as GTAW and Electron Beam processes

2007-2008 ACTIVITIES

ITER Test Blanket Modules (TBM) are complex sub-assemblies and difficult to manufacture (figures 1 and 2 respectively for HCLL and HCPB concepts).

For both concepts, manufacturing requirements are the same for First Wall / Cap / Stiffening Grid (Vertical and Horizontal) joining. The work to be done under this task was defined by the TBM design team in 2006.

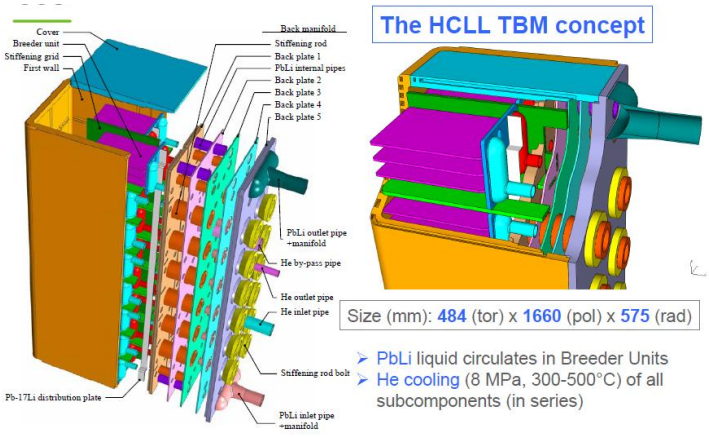

Figure 1: HCLL TBM design

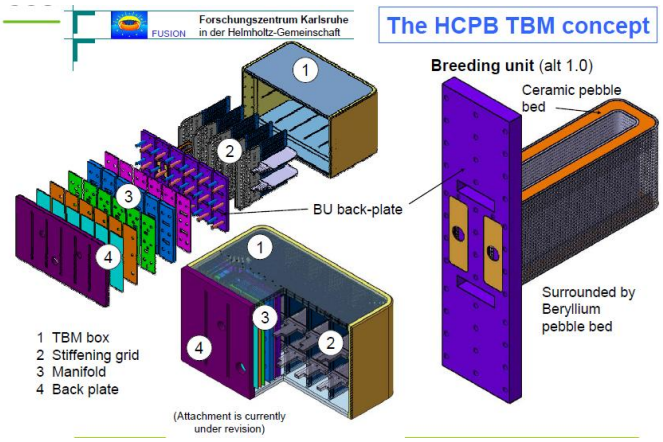

Figure 2: Exploded view of the HCPB-TBM in its horizontal arrangement

Manufacturing of both modules would lead to important distortions due to welding residual stresses. The main objective of this work is hence to reduce these distortions, with high relevant joint performances, including in creep behaviour. Pressure vessel rules and procedures must be applied to this complex structure.
Figure 3 shows areas to be welded. In this figure, Stiffening Grid (SG) is in green and First Wall (FW) in brown. For both welding situations: stiffening grid joining and stiffening grid joining to the first wall, welding developments to conduct are exactly the same: joint geometry, thickness, low access requirement, weld thermo field…

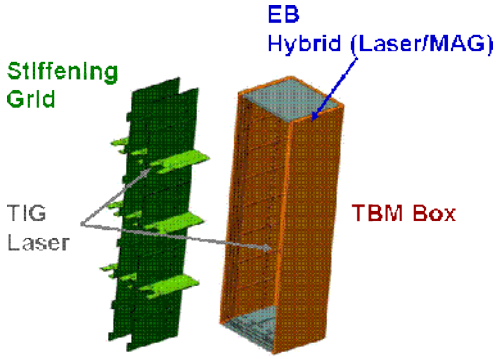

Figure 3: Welds to perform

Welding process developments under this task and under TW5-TTMS-004 tasks, have conducted to the following selections:

- Stiffening grid joining: laser instead of TIG (GTAW results in high distortions levels),
- Stiffening grid joining to the first wall: TIG (GTAW results in high distortions levels). It was demonstrated that the same welding as the stiffening grid joining can be applied,

- Cap / first wall joining: Hybrid process that combines MAG and Laser processes. Electron Beam process was discarded because of hot cracking effect, δ ferrite formation, high pores with size around 0.1 to 0.7mm diameter.

Stiffening Grid welds

For performing these joints (figure 4), laser welding was selected. The joining difficulty is the very low joint position to the vertical stiffening plate or first wall: 8 mm. To achieve such relevant welds, dedicated welding tools must be developed with enhance laser process. A severe difficulty due to design changing on the stiffening thickness from 8 to 11 mm required huge welding developments.

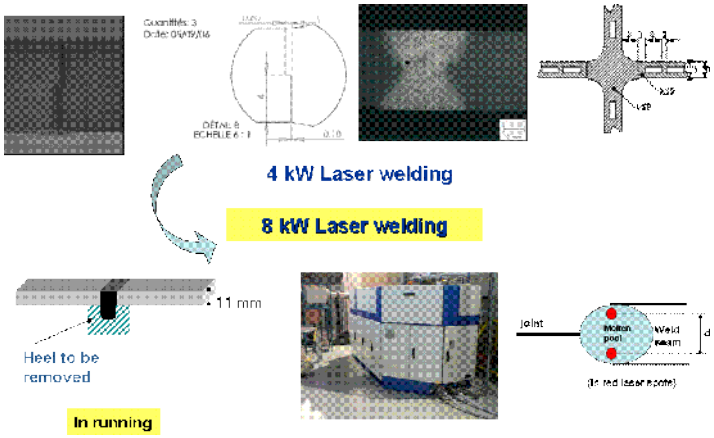

Figure 4: New design requirements

By developing a new enhanced laser welding process, Eurofer 11mm thickness was successfully welded with 8 and 10 kW laser (figure 5).

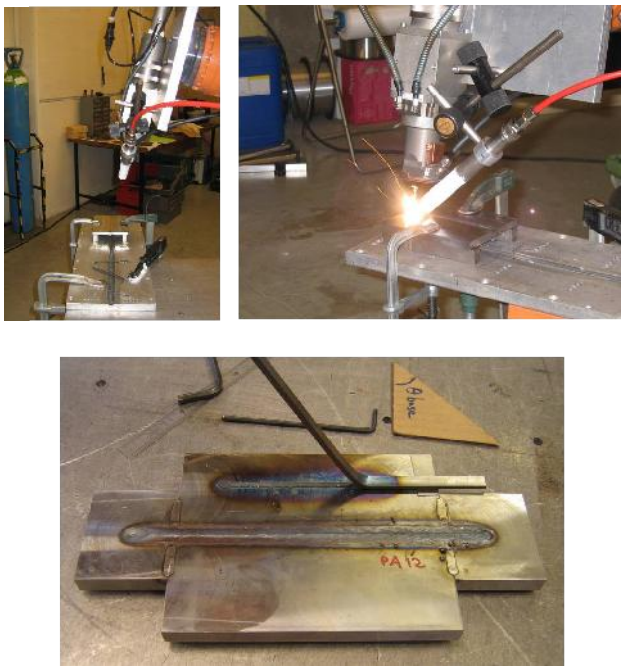

Figure 5: Eurofer 11mm thickness samples welding

The welding tricks are to use a Eurofer back plate of low thickness (around 3mm) for playing the rules of:

- Liquid molten pool support,
- Reflector of the laser energy passing through the keyhole (around 15 % the input laser energy) with low absorption effect,
- Thermal radiator to heat the weld root for helping the root bead in avoiding undercut,
- Out-gazing effect due to a gap of 0.5mm, managed for decreasing pores rate inside the fusion zone,
- Absorption of laser welding fluctuation due to molten pool movements, increasing thus strongly welding stability.

A new welding configuration was tested with a very low focusing sot size, in the range of 200 µm, instead of 500-800 µm in the case of twin spot configuration for the former standards laser welding parameters. At the rear position, output of the keyhole, the remaining laser beam is defocused and cannot play a role of welding actor. Thus, the back plate can be easily removed.

TBM Box assembly: Hybrid welding

The MIG/laser hybrid process technology was developed in several different ITER Vessel-In Vessel tasks. Hybrid process consists in combining Nd: YAG continuous laser and MIG processes. The two processes interact in the same molten pool. In first approximation, laser and MIG welding energy are roughly in the same level, around 4 kW. For getting an enough sidewall welding penetration on the chamfer groove, the laser beam is divided in two spots, which bring thus more welding energy close to chamfer walls (figure 6). Side wall penetration thickness in the range of 1mm is thus obtained, in the same range than NGTIG process.

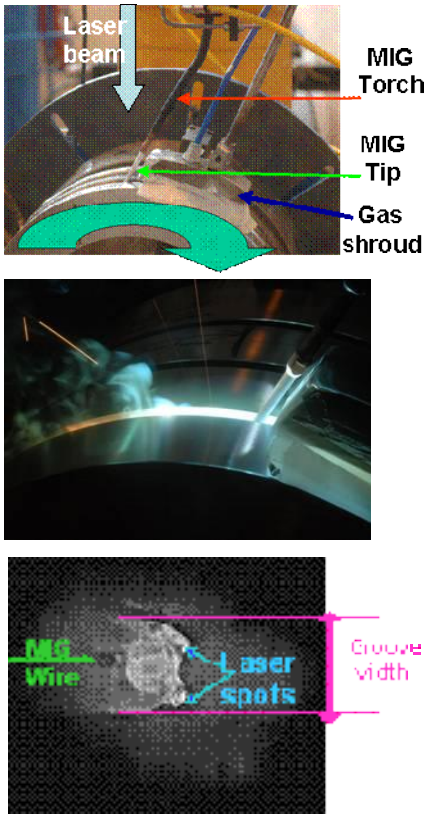

Figure 6: Hybrid process

CEA promotes, for distortion reducing, MIG/laser hybrid process. The technology was fully applied on Eurofer 25mm thickness plates, the only Eurofer thickness available for performing this task.
Hybrid process is a high speed multi-pass welding process, procuring a travel speed of 1.3 m/min, compared to the reference one Narrow Gap TIG welding (NGTIG: 0.1 m/min), with a quite reduced top groove width: 8mm (NGTIG: 14mm) presented in figure 7. Each welding pass performs 2.5mm penetration depth thickness (1.2mm in NGTIG). Deposited mass rate is 10 times higher in hybrid process, and distortions are thus obviously strongly reduced. Joining experience on the hybrid technology is referred in application upon 316 LN (ITER Grade) and 9% Chromium steel plates. For filling the joint groove, 14 filling passes were realized, with the chamfer design of figure 7.

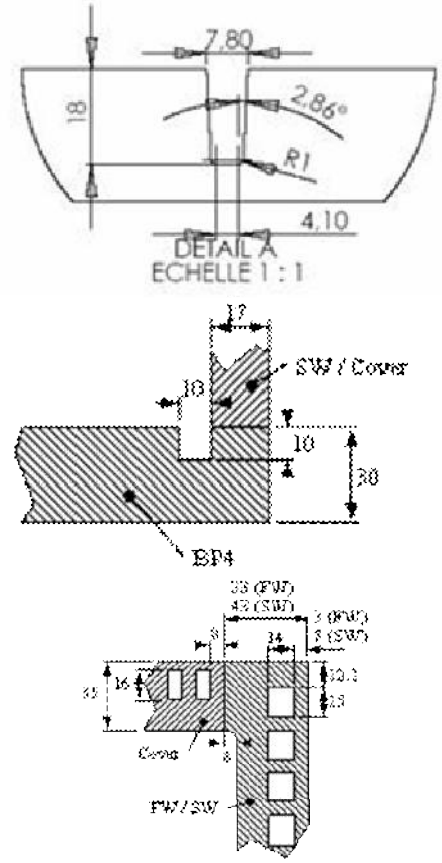

Figure 7: Hybrid chamfer and application examples in TBM design

Welds obtained for each welding pass have good external aspect without any oxidation. Hybrid welds looks homogeneous and its borderlines quite nearly parallel. It is observed no defect such sidewall sticking, and only few pores (0.3mm diameter).

Figure 8 shows weld geometry, with a side wall penetration depth in the range of 0.5 to 1mm. Hybrid welds show coarse grain formation in the fusion zone. Equiaxe grains with 20 µm grain size of martensite laths are fully produced in all welds, which is twice the base material grain size (12 µm). No δ ferrite and carbides have been seen in FZ. In figure 8, coarse grain zone can be observed in the area where the layer of the former welding pass is heat affected by following one.

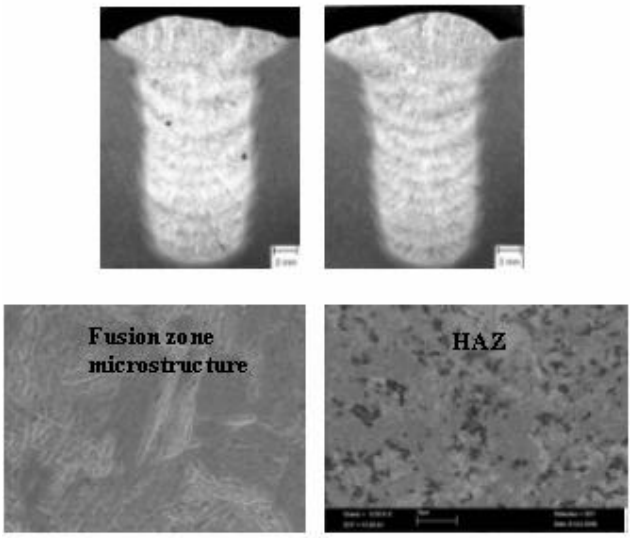

Figure 8: Hybrid transverse macrographs and microstructure

PWHT process
Ferritic-martensitic steels like Eurofer suffer from hardening and embrittlement due to uncontrolled martensite formation in the weld and softening effect in Heat Affected Zone. Welding behaviour is summarized in figure 9.

Weld Penetration depth (mm)	Process	Grain Size (µm)		δ ferr.	Fusion Zone		HAZ	
		Fusion Zone	HAZ		Width (mm)	Hardness Level (HV1)	Width (mm)	Hardness Level (HV1)
Base Material	/	12 to 15	12 to 15	No	No	220 - 230	No	230
40	EB	30	15 to 20	Yes	3	420 - 460	1,5 to 2	200 - 210
20	Hybrid	20	8	No	9	410 - 490	1,5 to 2	210 - 220
8	TIG	40 to 100	8	No	7.6	400 - 460	2 to 3	200 - 210
8	Laser	10 to 20	10 to 15	No	6.8	430 - 480	0.8	210 - 220

Figure 9: Welds microstructures

To restore good weld properties, Post Weld Heat Treatment (PWHT) are necessary, with or without Pre and Post Heating Treatment (PPTT) during the welding phase. On the different process welded samples, the same welding behaviour is observed, with attenuation or enhanced effects, depending on cooling rates and weld penetration. Strong hardness increasing in FZ and smoothing effects in HAZ are observed for each welding configuration. The Fusion Zones are composed of martensite laths, with low grain size. In HAZ, martensite grains are observed with $M_{23}C_6$ carbide precipitation. δ–ferrite was observed only in Electron Beam welds, due to very high cooling rates in solidification phase, related to strong enhanced weld shape.

From these results, Post Welding Heat Treatment was applied for reducing the coarse grain region of fusion zone, and carbides precipitation in the HAZ and smoothing these negative effects. A high temperature PWHT was tested for restoring a uniformly distributed fine grains in a full two-step heat treatment (austenitization plus tempering).

A second one step PWHT (simple tempering), with sufficient reduced temperature, was also investigated. PWHT definition is a real breakthrough to overcome. However, distortions of the TBM structure will be increased by high temperature multi or single treatments, and by consequence the complexity of the clamping tool, if this one is maintained in position inside the TBM during the PWHT sequence. If it is switched off before PWHT, the risk of strong distortions increasing is quite high.
Two PWHT processes have been defined and tested (figure 10).

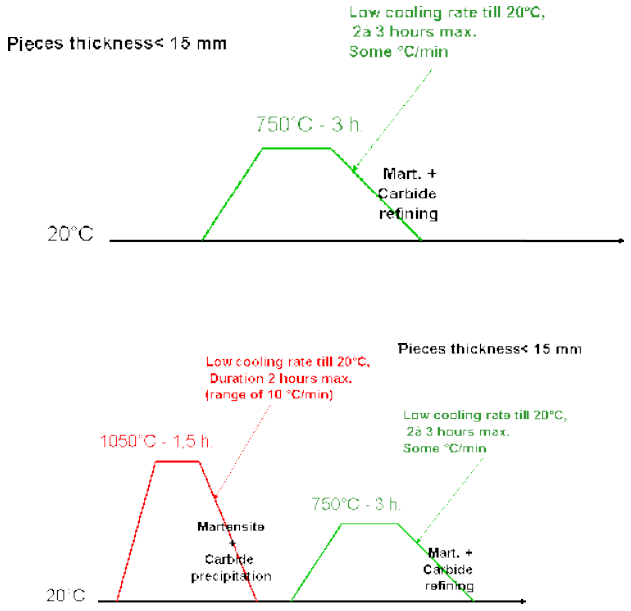

Figure 10: Definition of the 2 PWHT processes

Samples microstructures

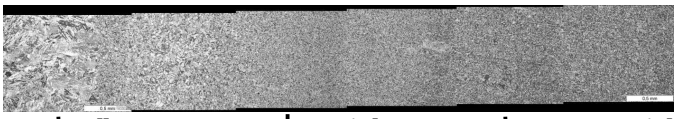

Figure 11: Microstructure evolution

Samples with one step 750°C PWHT

These samples were tempered at 750°C, after welding. FZ structure is fully tempered martensitic, which is confirmed by hardness profiles, with fine carbide precipitation. In HAZ, a progressive increasing of the granular structure size is observed. The precipitation type and morphology is not at all the same inside the weld. Base material supported 2 tempered processes: before and after welding (over tempering). Pure martensitic area, after welding, supported only one tempering. This explains the differences of hardness observed.

Samples with two steps 1050°C PWHT

PWHT provided a full re- austenitization, eliminating fully the structure gradients induced by welding thermal cycles. The structure is fully tempered martensite, which explains a homogeneous hardness profile all along the joint. However, 1050°C austenitization did not allow providing a homogenous granular structure in the whole joint. In FZ, the grain size of former austenite grains is higher than in other joint areas.

Hardness profiles show:

- 750°C PWHT procured a FZ and HAZ softening, where hardness level is in the range of 240 HV_1,
- Austenitization 1050°C PWHT, followed by a 750°C tempering gives a homogenous hardness level of 210 HV1, same value as the one of the Base Material.

In conclusion, it is not necessary to perform an austenitization PWHT. A standard tempering PWHT (3 hours at 750°C +/- 10°C / cooling till 20°C in 3 to 5 hours) is sufficient to restore joints performances, in quite the same range than the Base Material. It is a good point for final TBM distortions mastering.

First One Cell mock-up welding

Mock-up description is given in figure 12.

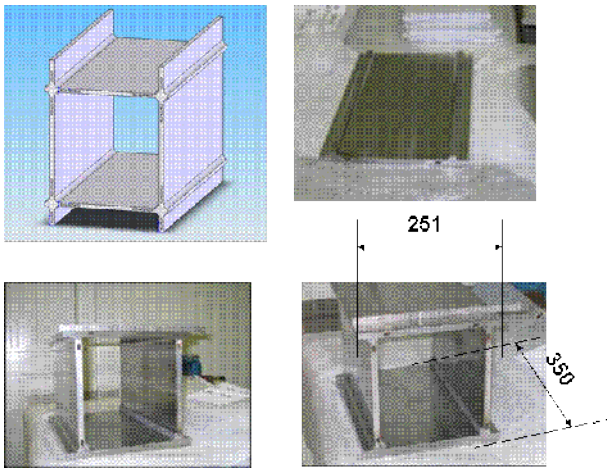

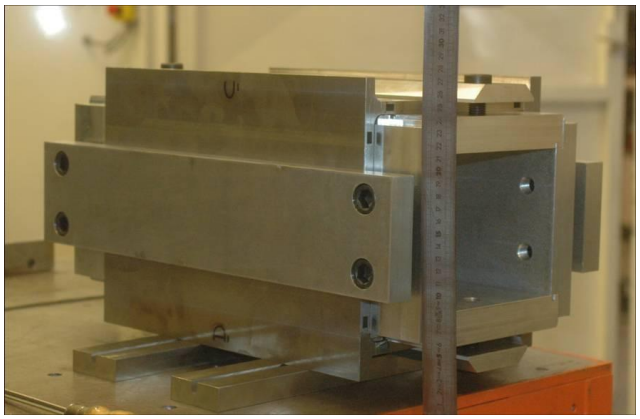

Figure 12: One Cell Mock-up description

A complex clamping device was manufactured. The principle is to build an indeformable hyper static structure, which does not move during welding phase procuring high heat and residual stresses (4 weld lengths of 320mm to

perform). This structure is put in position inside the One Cell elementary parts. Complex machining permitted these functions. The clamping tool maintains obviously in position the elementary parts of the mock-up in front the welding laser beam. There is thus no need of seam tracking system for the robot or gantry during the welding phase. External clamping plates, screwed on the internal clamping tool, maintained the mock-up in a strong clamping fixture. Precision machining was managed to let in position each thin Eurofer back plate, for the welding phases.

The different welds were performed in cross operation, to equilibrate the welding stresses from each weld (figure 13): the mock-up fixed inside the clamping tool was half turned, after each joint processing, for welding in Horizontal Position.

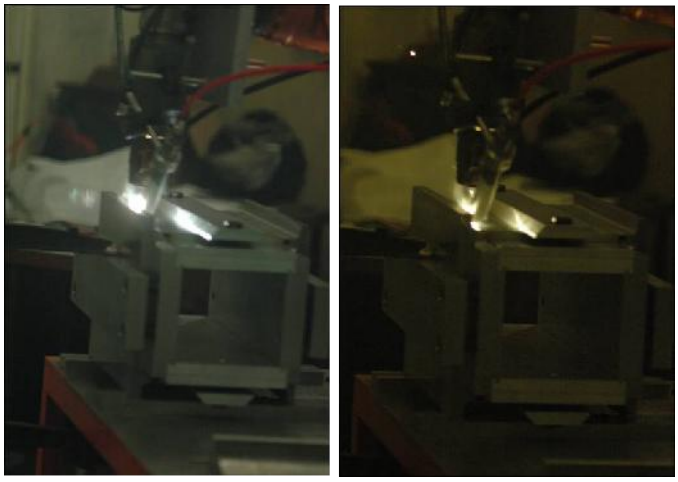

Figure 13: One Cell Mock-up welding

Second One Cell welding

Taking in account the first One Cell Mock-up experience, the clamping tool was modified to obtain stronger clamping forces. Bigger steel screws and external fixing plates were provided. Laser welding occurred, with the following welding parameters:

- 1 pass welding at 10 kW YAG
- Gas shield: argon
- Laser spot size: 300 µm
- Laser welding tool tilt: 5°
- Welding travel speed: 1.9 m/min.

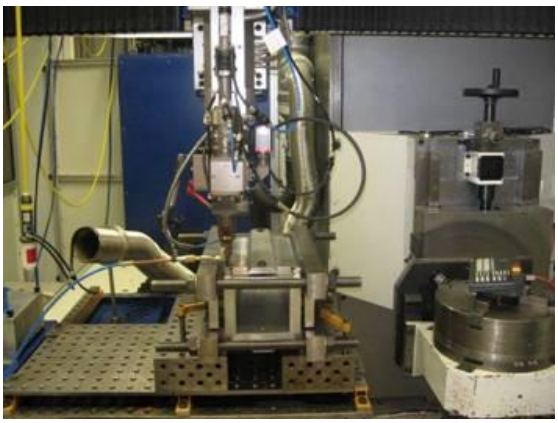

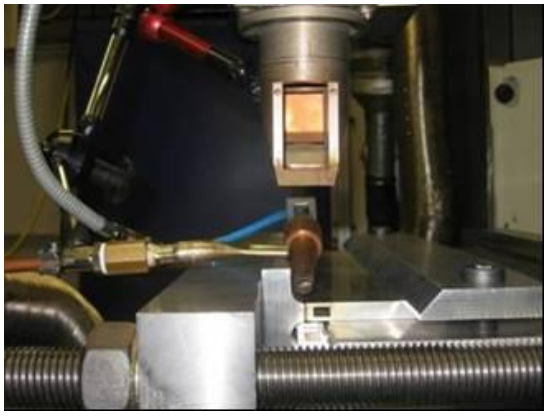

Figure 14: Second One Cell Mock-up 10 kW laser welding

Photographs of the second One Cell Mock-up are presented in figures 14 and 15, with internal clamping tool. The black inscriptions on the mock-up are the control points to be 3D measured.
This welding test showed clearly, even with a reinforced clamping tool, the necessity of performing tack welding, before applying the nominal laser welding parameters. This tack welding must have a penetration depth of half the Stiffening Grid thickness, i.e. 5mm. This new phase in the welding sequence will be applied for the third One Cell Mock-up.
The clamping tool was removed with no trouble, by simply disassembling.

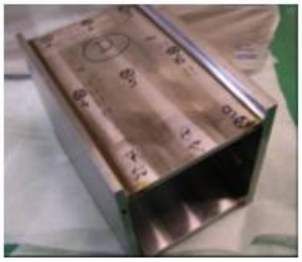

Figure 15: Second One Cell Mock-up photographs

In first stage, the second cell mock-up was geometrically controlled on a 3D control machine with a precision +/- 1 µm. On the same control points, same controller, same control procedure and same 3D control unit the second mock-up was controlled, after switching off the internal clamping tool.
It can be clearly concluded that before withdrawing the internal clamping tool, a maximum of 90 µm of distortions is observed for the whole mock-up. After switching off the internal clamping tool, an increasing distortion of 40 µm is measured.
On maximum residual distortions on a pseudo hyper static structure, a maximum rate of 120 µm (+/- 60 µm) was measured. This value is quite low and very encouraging for the full TBM distortions management, if laser solution is taken into account.

CONCLUSIONS

The main objective was to develop welding procedures for a process, which will be certified in the following F4E tasks. These welding processes must reduce residual distortions in the modules, major TBM manufacturing trouble.
This task was dedicated to manufacturing demonstration. Several breakthroughs were made and key trends were achieved, including PWHT definition to obtain high Eurofer joint strength, with acceptable distortions.

For performing Stiffening Grid assembly and Stiffening Grid / TBM Box joining, 2 joining processes were carried out: NGTIG and Continuous Nd: YAG laser. The design change of Stiffening Grid thickness from 8 to 11mm, decided in mid 2006, intensively modified the task management. It implied a huge welding breakthrough by single pass welding using a high power enhanced laser. It has required an important welding breakthrough by single pass welding using a high power enhanced laser. This difficulty resulting from a late decision nevertheless permitted to solve in one shot the major difficulty of TBM assembly. Very high travel speeds were used for welding the mock-up with a 10 kW Nd:YAG laser: around 2 m/min, which is a breakthrough in welding domain. This point places definitively laser welding as the manufacturing process to take into account.

It can be estimated that there is no more distortions trouble for such complex structure. The newly developed high power laser welding process allowed to perform two “One Cell Mock-Up” with a distortion rate below 200 µm for the full One Cell Mock-Up, pseudo hyper static structure. On the last mock-up, a maximum rate of 120 µm (+/- 60 µm) was measured. This value is quite low and very encouraging for the full TBM distortions management, if laser solution is taken into account.
Subsequent residual welding stress relaxation adds a distortion level on the order of 40 µm when switching off the clamping tool from the welded mock-up, which is quite low and very encouraging for the future.

Cap / First Wall joining was evaluated, in particular the two welding processes procuring minimum distortions such as Electron Beam and Hybrid MIG / Laser processes. Electron Beam process is not well adapted for this application, in respect of high level of welds requirements. Processing troubles has been demonstrated (pores, very narrow FZ, δ ferrite). Very interesting results have been obtained using the MIG/laser hybrid technique developed by CEA. Joints mechanical performances are very high, with a joint coefficient of 1. Hybrid process is a high speed multi-pass welding process, procuring a travel speed in the range of 1.3 m/min, compared to the reference one Narrow Gap TIG welding (NGTIG: 0.1 m/min), with a quite reduced top groove width: 8mm (NGTIG: 14mm). Each welding pass performs 2.5mm penetration depth thickness (1.2mm in NGTIG). Deposited mass rate is 10 times higher in hybrid process, and distortions are thus obviously strongly reduced.

It is shown that the interesting results obtained can be easily transferred to new designs, by widening the assembly and welding possibilities, which were not the case before the start of this task. A new operating field for new joining processes has been opened compared with the standard available processes, such as GTAW or NGTIG.

It is not necessary to perform an austenitization PWHT. A standard tempering PWHT (3 hours at 750°C +/- 10°C / cooling till 20°C in 3 to 5 hours) is sufficient to restore joints performances, in quite the same range as the Base Material. It is a good point for final TBM distortions mastering.

Important breakthroughs and key trends were achieved, including PWHT definition to obtain high Eurofer joint strength, with acceptable limited distortions. The results of this task would, therefore, pave the way for future TBM manufacturing works.

The only conclusion to keep in mind is that TBM manufacturing is possible. Costs and efforts must not be wasted, that is the only challenge.

REPORTS AND PUBLICATIONS

TBM Manufacturing – Final Report, Philippe Aubert, CEA Report DEN/DM2S/DIR/RT/08-0009/A, December 2008

TASK LEADER

Philippe AUBERT

DEN/DM2S
CEA-Saclay
F-91191 Gif-sur-Yvette Cedex

Tel: 33 1 69 08 37 99
Fax: 33 1 69 08 66 42

e-mail: philippe.aubert@cea.fr

TW5-TTBC-001-D05

Task Title: TBM DESIGN, INTEGRATION AND ANALYSIS FINALIZATION OF THE HCCL TBM PROTOTYPICAL MOCK-UP INCLUDING INTERNAL HEATING SYSTEM

INTRODUCTION

The production of functional mock-ups is a necessary step in the development of breeding blankets test modules (TBM – Test Blanket Modules), because they belong to the experimental qualification process of this complex component and of its associated systems. Several studies of such a type of mock-ups (PMU – Prototypical Mock-Up) were carried out in the framework of EFDA tasks.

The present task consisted in particular in the establishment of a detailed design of a PMU for the Helium Cooled Lithium Lead blankets line, for a test campaign in the European Breeding Blanket Testing Facility (EBBTF, located in ENEA Brasimone, Italy). This detailed design, based on the preliminary conceptual design developed within the task TW5-TTBC-001-D02 0, could not be carried out up to now, for the main following reasons: i) the strong similarity between the proposed conceptual PMU and the corresponding TBM results in similar difficulties for manufacturing, making the PMU possibly too complex as a mock-up; ii) the evolving TBM design does not allow to rely on a stable basis to get into the details of a relevant mock-up.

As a consequence, it was proposed during the last "HCLL/HCPB breeding blanket monitoring meeting" in F4E/Barcelona (February 20-22, 2008) to replace the proposal for a detailed design as it was initially defined by reconsidering the strategy for operational test mock-ups and proposing technical solutions for achieving redefined objectives. Thus, a report was issued with the purpose of establishing a stronger basis for the development of PMUs, by: i) contributing to a clarification of the objectives of a PMU; ii) defining clear specifications; iii) providing main parameters and characteristics, iv) proposing technical solutions in concordance with the specifications, v) synthesising the previous preliminary studies (reported in particular in [1], [2] and [3]).

2007-2008 ACTIVITIES

The final report [4] addresses several points establishing the basis for the development of PMUs for the contribution to the out-of-pile qualification of the HCLL TBMs before their operation in ITER.

CONTRIBUTION TO A CLARIFICATION OF THE OBJECTIVES OF A PMU

EBBTF main features and specifications

The EBBTF facility consists of a liquid PbLi loop coupled to a He loop which is an upgrade of HeFus3 facility (originally aimed at testing thermal-mechanics and thermal-hydraulics in normal and off-normal conditions in support to HCPB design). These two loops can be operated separately, but are fully interfaced for their control (unique control system and control panel).

This facility is intended at the testing of European breeding blanket components for their qualification in support to the licensing requested before operation in reactor. It goes from small mock-ups up to full scale components. In the framework of the HCLL TBM development activities, the facility will be used to test Prototypical Mock-Ups (PMU), up to a full scale TBM prototype. The PMU extent is defined in terms of breeding cells (reduced number), keeping other geometrical parameters as much identical as the TBM ones.

A set of assumptions defining the general test objectives

In order to define and orient the design of a PMU, and taking into account the qualification needs for the TBM and the characteristics of the EBBTF, the following assumptions were retained for the test objectives:

- **GO1** → Contribution to the qualification of the thermo-mechanical behaviour of the TBM,
- **GO2** → Relevancy of the manufacturing processes,
- **GO3** → Contribution to the qualification of ancillary systems,
- **GO4** → Feedback on the design, test programme, and operation.

In order to cope with the general objectives, a list of functional tests was established

This list is presented in table 1.

Several items of the general objectives cannot be filled directly by functional test, but should provide useful feedback to support R&D activities. This is the case for example for the general objective GO2, related to the manufacturing abilities, through which confidence should be gained for the validation of manufacturing techniques; this is also the case for implementation and operation of instrumentation. A list of those items that cannot be quantified but from which feedback is expected was proposed.

At last, several TBM features which are excluded of the test matrix, either due to their unavailability in the test facility or to avoid redundancy with other test programmes, were listed.

Table 1: Proposition of functional tests to be performed with PMU

Field	Functional test	Objectives	GO
Thermal-hydraulics	Heat removal	• To test heat removal from First Wall and Breeding Zone. • To verify the correlations used to determine the exchange coefficient with coolant. • To verify predictability of structure temperatures	GO4
Thermal-hydraulics	Coolant flow control	To control flow parameters (evaluation of global pressure drops, regulation with by-pass)	GO4
Liquid metal technology	Breeder flow control	• To test filling and draining procedures. • To test controllability of operating parameters (flow and temperature). • To test corrosion effects.	GO3
Thermo-mechanics	Mechanical endurance and cycling	To test mechanical withstanding under nominal conditions (under monotonic and cyclic loadings)	GO1
Thermo-mechanics	Mechanical endurance	To test thermo-mechanical withstanding under accidental conditions (by simulating LOCA and LOFA)	GO1
Tritium control	H control (simulation of T) in the module	• To test permeation towards the coolant. • To test measurement of H concentration in the circuit. • To test controllability of H partial pressure and PbLi purity.	GO4
Tritium control	H control (simulation of T) in the ancillary systems	• To test and validate Coolant Purification System. • To test and validate Tritium Extraction System. • To evaluate the parasitic losses, their probable sources, and the possible measurements.	GO3

DEFINITION OF SPECIFICATIONS

Main issues for the PMU design

- A TBM-relevant PMU fabrication should lead to non-negligible development time before final manufacturing,
- The quantity of investigated fields and objectives has a negative impact on the design,
- Although a dismountable design for internal access (maintenance and repair, instrumentation modifications, limited risk in manufacturing) would be suitable, no solution could be envisaged up to now.

Reconsidered specifications and design strategy proposals

It was proposed to have 2 PMU for the progressive achievement of the test programme:

- A first one (Model 1) for assessing "local" effects for which only relevant portions of the TBM structure are represented,
- A second one (Model 2) for which complementary "local" effects and "global" effects could be assessed.

As a consequence, solutions for the issues identified up to now could be envisaged:

- less dependency of development time for manufacturing techniques,
- reduction of the quantity of tests to be performed on one mock-up,
- more flexibility to propose a dismountable design for the first mock-up,
- possible "recycling" of some fabrication "partial" mock-ups for Model 1.

An assignment of the functional tests to each mock-up has been preliminarily proposed.

Basic design features for Model 1

- The PMU model 1 front structure is a reduction of the TBM front structure, covering 2 breeding cells width and two breeding cells height, addressing the following points:
  - Usage of "4 cell mock-ups" manufactured in the framework of the development of manufacturing techniques, and aiming at demonstrating the ability to assemble a First Wall mock-up with a Stiffening Grid mock-up and 2 Caps Mock-ups,
  - Reduced heating devices power accordingly with testing facility specification,
  - Main dimensional parameters kept similar to the TBM, at the exception of global height of First Wall, Caps and vertical Stiffening Plate. Cooling channels should be similar. A strong relevancy of the manufacturing techniques should be insured. A good relevancy of mechanical solicitation should be reached in local areas,
  - The 2 breeding cells height provides the ability to circulate liquid metal in a similar way as the TBM (1 internal circulation loop).
- The Breeder Unit, such as defined for the TBM, can be limited to a single Cooling Plate for assessing its performance. A relevant heat deposition can be achieved through heater elements, dedicated to creating heating conditions at the CP boundary surfaces. It addresses the following points:
  - More free space is available in a breeding cell for the insertion of heaters for the simulation of power deposition,
  - Less complex manifold system for a single CP.
- The PMU model 1 has no He back manifold in the sense of the TBM. The collecting and distribution of He is performed by local manifolds linked with pipes, externally to the main box structure. It addresses the following points:
  - Removes the additional complexity of the Back Plates mounting sequence along with the associated manufacturing risks. However, this will have to be balanced with the complexity of the envisaged manifold system,
  - Offers the ability to close the breeding cells volume with a dismountable Back Plate, for which tightness will have to be insured for liquid metal only, and not He; a mechanical tightening can be envisaged,
  - The removable Back Plate is used as support structure for Cooling Plates and electrical heaters, providing full access to the box internals when removed. Thus, the breeder units, as defined for the TBM, are not present in the PMU model 1 design.

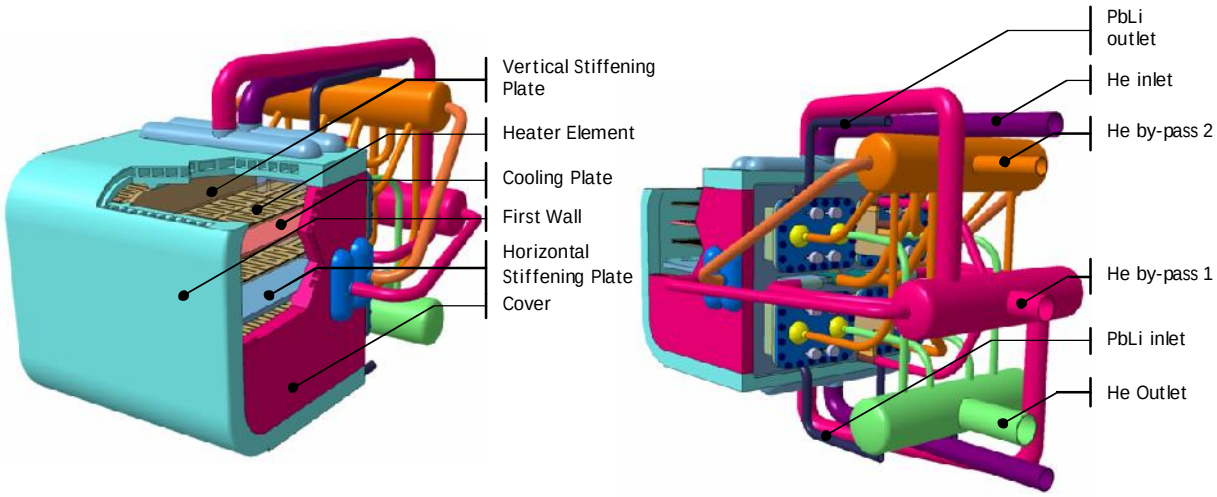

Figure 1: Overview of the proposed design for PMU Model 1

Basic design features for Model 2

- The basic layout is very similar to a simple reduction of the number of breeding cells of the reference TBM. It should insure a fabrication and assembly sequence very near of the TBM one. The principle of 4 breeding cells used in the PMU Model 1 is kept.
- The design makes reference to the PMU Model 1 for the cooled sub-components and for the simulation of heat deposition; the Back Manifold of the Model 1 is replaced by a multi-stages Back Manifold based on the TBM one.
- The Breeder Units keep the principle of Model 1, with 1 Cooling Plate and 2 heaters, but are no more extractible; the electrical connection of heaters is an additional issue as a crossing of the Back Plates is required.

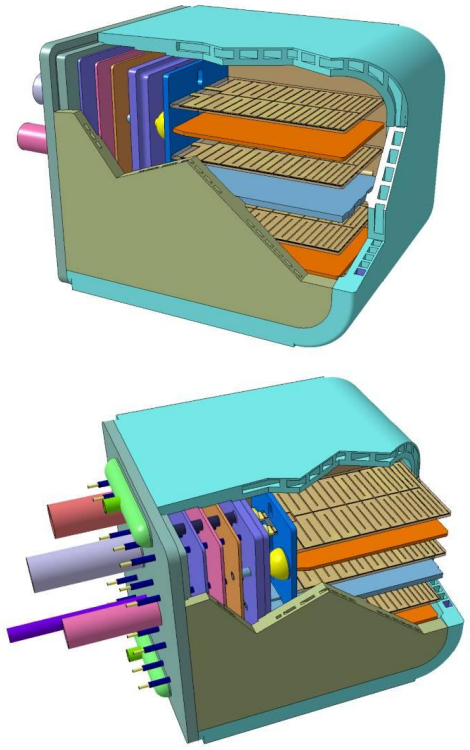

Figure 2: Overview of the proposed design for PMU model 2

Identification of main parameters and characteristics

The design options and preliminary parameters for Model 1 were assessed in order to determine the heating and cooling schemes allowing reaching the suitable relevant conditions. Because the preliminary design proposals are based on the on-going evolutions of the TBM design, mainly the vertical cooling of the First Wall, issues were raised in the reduction of the TBM geometry to the PMU one: the respective First Wall heating / cooling schemes cannot be similar.

Thus, several sets of assumptions were explored and compared; basically:

- AS1: Determination of suitable FW heating power for TBM-like cooling scheme and parameters,
- AS2: Modified FW cooling scheme,
- AS3: Modified FW inlet temperature.

The calculation of the resulting cooling schemes parameters were performed by considering analogies between the power deposition / extraction in the TBM (current on-going design) and in the PMU; keeping similar temperature increases and coolant velocities.

The main design options were discussed:

- 2 by-passes are necessary in order to keep relevant temperatures and velocities in the Cooling Plates,
- the control of the regulation with by-passes will have to be further assessed,
- no set of assumptions on design parameters could be selected because:
  - each one has drawbacks,
  - an optimal compromise has to be found between higher FW heat flux, FW channels passes, and FW inlet temperature,
  - only deep thermal and mechanical analyses will allow assessing precisely the achievable relevancy; additionally, analyses will be used to determine the exact distribution of extracted power and the suitable position of heaters in the Breeding Units,
  - other sets of assumptions can be proposed.

Examples of input data for the test facility according to the various assumptions have been proposed.

Next steps for the HCLL PMU design

The next steps for the development of the HCLL PMU design were proposed:

- the establishment of a detailed tests matrix,
- the identification of measurement types and points, number and type of instrumentation signals, technical solutions for instrumentation implementation,
- the continuous verification of the compliance between the test facility specifications and the PMU requirements,
- the performing of accurate thermal and mechanical analyses of the structure in order to determine the design parameters (geometry, heat loads, cooling scheme),
- the proposal of a technical solution for the regulation and control of the He flow scheme with the help of by-passes,
- the validation of technical solutions for the external and internal heaters,
- the update of the supporting structure.

CONCLUSIONS

In the framework of experimental qualification of the Test Blanket Modules to be installed in ITER, the production of functional mock-ups is a necessary step. Several studies of such a type of mock-ups (PMU – Prototypical Mock-Up) were carried out in the framework of EFDA tasks, in particular for the Helium Cooled Lithium Lead breeding blankets line.
The finalisation of this task consisted in the production of a report intended to be an input point in the future development of PMU for the HCLL TBM; it gathers in a single document as much as possible information available on the inputs and strategy to follow. In addition to a synthetic overview of past studies, it proposes:

- a clarification of the objectives of a PMU,
- the definition of clear specifications for the design process,
- the provision of main parameters and characteristics,
- a discussion on the issues linked to the PMU specificities, and on the optional choices that will have to be decided to fix the final design,
- technical solutions in concordance with the specifications, through preliminary CAD models,
- an overview of the further work to be performed.

REFERENCES

[1] G. Rampal, “Finalization of the conceptual design of the prototypical HCLL TBM mock-up”, CEA report SEMT/BCCR/RT/06-037/A, May 2007

[2] L. Cachon, “Internal heater plates for TBM mock up - Task TW5-TTBC-001-D02”, CEA report DEN/DTN/STPA/LTCG 05-039, October 2005

[3] L. Cachon, “External heater for TBM mock up - Task TW5-TTBC-001-D05”, CEA report DEN/DTN/STPA/LTCG/2006/022, June 2006

REPORTS AND PUBLICATIONS

[4] G. Rampal, A. Morin, “Assessments on a Prototypical Mock-up as HCLL TBM qualification test”, CEA report SEMT/BCCR/RT/08-036/A

TASK LEADER

Gilles RAMPAL

CEA-Saclay
DEN/DM2S/SEMT
F-91191 Gif-sur-Yvette Cedex

Tel: 33 1 69 08 41 44
Fax: 33 1 69 08 94 26

e-mail: gilles.rampal@cea.fr

TW5-TTBC-001-D07

Task Title: TBM DESIGN, INTEGRATION AND ANALYSIS DETAILED TBM DEVELOPMENT WORPLAN UP TO EM-TBM INSTALLATION IN ITER

INTRODUCTION

In order to be able to install a HCLL Test Blanket Module (TBM) in day 1 of ITER operation, as envisaged up to now in the testing strategy for EU concepts of breeding blankets, it is necessary to establish both a detailed HCLL TBM development workplan up to EM-TBM fabrication and installation in ITER and a Project technical specification document. These documents will be a basis to identify the activities (on R&D, analyses, needs of out of pile test, supplies and fabrication,…) to be launched, and will help to follow the project taking care of the critical path. The objectives of the task were: i) to produce a detailed HCLL TBM development workplan (MS-Project), and ii) to produce a first version of a Project technical specification document.

2007-2008 ACTIVITIES

First part of the task concerning the workplan being achieved in 2006, the activities have concerned the second objective on Project specifications description.
Important part of activity performed in the framework of this subtask has again been devoted to the technical follow-up of the main progresses realised in the project, leading to the publication of 2 papers in international conferences [1, 2]. In parallel of the technical changes, definition of the ITER, of international relationship and of EU organisations with concern to the TBM projects has been progressively defined, leading to a moving scheme of the project management requirement. Moreover, the maturity of specifications in each topic of the project is at different level so that it was impossible to have a coherent and complete definition of the HCLL-TBM project specifications. Nevertheless, the list of project topics with some considerations on main specifications/requirements/interfaces that can be envisaged at the moment has been established and described.

Products to be delivered and requirements

The list of products that will have to be delivered in the HCLL-TBM overall project is the following:

- HCLL EM-TBM including materials and diagnostics for monitoring and testing experiments
- HCLL NT-TBM including materials and diagnostics for monitoring and testing experiments
- HCLL TT-TBM including materials and diagnostics for monitoring and testing experiments
- HCLL IN-TBM including materials and diagnostics for monitoring and testing experiments
- HCLL TBMs back shield (one for each TBM, same design if possible)
- HCLL dummy TBM with same characteristics in terms of shielding capacity and FM Steel content (number to be defined)
- HCLL feasibility, qualification and testing small scale mock-ups
- HCLL feasibility, qualification and testing medium scale mock-ups
- HCLL qualification/testing TBM full scale mock-up (prototype)
- HCLL Helium Coolant System (HCS)
- HCLL Coolant Purification System (CPS)
- HCLL PbLi ancillary system including Tritium extractor for PbLi
- HCLL Tritium Recovery from Purge gas System (TRPS)
- HCLL Port Cell ancillary equipments including AEU and RH tools
- HCLL Hot Cell ancillary equipments including RH tools
- HCLL Post Irradiation Examinations (PIE) ancillary equipments including shipping transfer cask
- HCLL data and tools for experiments specifications/follow-up/analyses/extrapolation
- HCLL system Control and Monitoring equipments

Each product to be delivered in the frame of the HCLL TBM project will answer to technical specifications that will contain requirements of different natures. Some considerations have been given for:

- Operator (ITER Organisation, IO) requirements,
- French Nuclear Safety Authorities (NSA) requirements,
- Project requirements.

List of Project activities, preliminary specifications

In order to deliver the different products present in the scope of the project, an extensive list of activities has to be performed. These activities will need to take into account both the technical and organisational requirements listed before. Some of the specifications for these activities are quite well known, some can be well guessed, and to

produce some of them will require a consistent work. List of these activities tentatively gathered in groups and outline the main overall specifications for each of them have been identified, summarizing in each case the main expected outputs.

They have been detailed for:
Design activities:
- CAD Drawings
- Analyses
- Qualification tests
- Tools for monitoring and control

Material activities,
Manufacturing activities,
System integration activities,
Experimental testing program in ITER activities,
Project management activities.

CONCLUSIONS

The initial ambit of the remaining deliverable for the task TW5-TTBC-001-D07, which was to produce a draft version of the HCLL-TBM project technical specifications for each activity of the workplan established before, appeared to be difficult for several reasons: moving context both in IO specifications and project organisation, lack in precise definition of the project scope, large discrepancy in the maturity of each field, available expertise…

Moreover, it is quite obvious that even in a well defined scheme; in most cases the writing of the specifications will necessitate a huge amount of work. Nevertheless, a tentative list of key information necessary to develop these project specifications has been identified. It describes the products to be delivered, the main activities to be performed and some identification of the main specifications and outputs of these activities.

The final report [3] delivery was initially envisaged for mid-2006. Even if large part of the work has been produced in time for integration in the various scheduled organisational discussions (TBM ad-hoc group, publications, call for tenders …), the issue of the final report has been delayed to try to follow the various changes in technical and organisational features of the project. It describes in a first part the HCLL development workplan and its integration in the EU project (part of the subtask closed end 2006) and in a second part lists the information that will be necessary for the establishment of the detailed project technical specifications.

REPORTS AND PUBLICATIONS

[1] J.-F. Salavy, G. Aiello, O. David, F. Gabriel, L. Giancarli, C. Girard, N. Jonquères, G. Laffont, S. Madeleine, Y. Poitevin, G. Rampal, I. Ricapito and K. Splichal, "The HCLL Test Blanket Module System: Present reference design, System Integration in ITER and R&D Needs", Oral presentation to ISFNT-8, Heidelberg, 2007, Engineering and Design 83 (2008) 1157–1162

[2] J.-F. Salavy, G. Aiello, P. Aubert, L.V. Boccaccini, M. Daichendt, G. De Dinechin, E. Diegele, L. M. Giancarli, R. Lässer, H. Neuberger, Y. Poitevin, Y. Stephan, G. Rampal and E. Rigal, "Ferritic-Martensitic Steel Test Blanket Modules: status and future needs for design criteria requirements and fabrication validation", Invited presentation to ICFRM-13, Nice, 2007, tbp in J. Nucl. Mater., 10.1016/j.jnucmat.2008.12.239

[3] J.-F. Salavy, Detailed TBM development workplan up to EM-TBM installation in ITER, CEA report SERMA/RT/06-3816/A, issued March 2008

TASK LEADER

Jean-François SALAVY

DEN/DM2S/SERMA
CEA-Saclay
F-91191 Gif-sur-Yvette Cedex

Tel : 33 1 69 08 71 79
Fax : 33 1 69 08 99 35

e-mail : jfsalavy@cea.fr

TW5-TTBC-002-D02

Task Title: BLANKET MANUFACTURING TECHNOLOGIES FEASIBILITY OF THE TUBE FORMING + HIP FABRICATION PROCESS FOR THE BENT PART OF THE FW OF HCLL AND HCPB TBMs

INTRODUCTION

Hot Isostatic Pressing – Diffusion Welding is a preferred process for the fabrication of fusion blanket sub-components, in particular the First Wall [1]. The use of round tubes inserted between grooved plates is a promising solution [1]. Since the channels are square or rectangular, the behaviour of the tubes during expansion is of particular relevance. Depending on the expansion conditions tube cracking can be observed [2], [3].

The objective of the work is to model the tube expansion process in order to define achievable channel geometries. Previous work has shown that expansion during HIP is a risky route. In this work, expansion of the tubes before HIP is considered.

In a first step, the mechanical properties of soft annealed Eurofer have been measured as well as its behaviour upon stress relieving. The mechanical properties have been used to fit the mechanical behaviour used for finite element calculations. Finally, experiments have been made in order to validate the model.

2007-2008 ACTIVITIES

EXPANSION EXPERIMENTS

The tubes used for the experiments are soft annealed Eurofer 97-1 [a].

Expansion of straight tubes
The expansion tools are mainly made of tool steel. Plugs allowing a smooth transition from the round shape to the square or rectangular shape are inserted in the ends. The tube is fitted inside the cavity, and welded on the ends. One bulk stainless steel plug is welded on one end while a high pressure fitting is welded on the hydraulic pump side. The tube is filled with oil and the pressure is increased. The pressure is measured by a manometer.

Expansion of bent tubes
The same experiments have been made on bent tubes using appropriate expansion tools. Three bending radii have been chosen: 30mm, 38.5mm (HCLL dimension) and 58mm. All the tubes have been bent with an angle of 90°.

Table 1: Summary of expansion tests results

	Case	trial	Applied pressure	Rupture	Rupture pressure	Estimated full expansion pressure*
Straight tubes	Case 1 14.2/16 tubes in 16x16 cavity		180MPa	No		140MPa
	Case 2 14.2/16 tubes in 16x20 cavity	A	until rupture	yes	58MPa	
		B	until rupture	yes	90MPa	
		C	until rupture	yes	59MPa	
		D	53MPa	no		
	Case 3 14.2/16.85 tubes in 17x17 cavity		200MPa	no		130MPa
	Case 4 14.2/16.85 tubes in 17x20 cavity	A	until rupture	yes	82MPa	
		B	160MPa	no		120MPa
Bent tubes	Case 1 : bent radius R = 58mm		180MPa	No		170MPa
	Case 2 : bent radius R = 30mm		180MPa	No		170MPa
	Case 3 : bent radius R = 38.5mm	A	180MPa	No		170MPa
		B	100MPa	No		

*First fixed value of pressure (during the expansion step, after each pumping step, the tube volume variation makes the pressure decrease).

CALCULATION CONDITIONS AND RESULTS

Calculation conditions

Isoparametric quadratic elements (QUA8 Type) are used. The tube is systematically positioned in the centre of the cavity. The calculations are realised in large displacement, and a "following pressure" is imposed inside the tube. Contact conditions are imposed between the tube and the cavity with a Coulomb type friction ($\tan\Phi = 0.3$).
Finally, the plane strains hypothesis is chosen to be representative of the middle of the tube. For bent tubes, an elliptical shape is considered which is more representative of the bent tube ovalization.

Shapes comparisons

With the mechanical behaviour identified on tensile tests and a friction coefficient of 0.3, the simulations fit very well the experimental tubes shape, for both straight and bent tubes, if no rupture occurs. After rupture, the large crack opening (that is not simulated) modifies the shape too much to allow the comparison.

Case 3: Tube 14.2/16.85mm, cavity 17x17mm

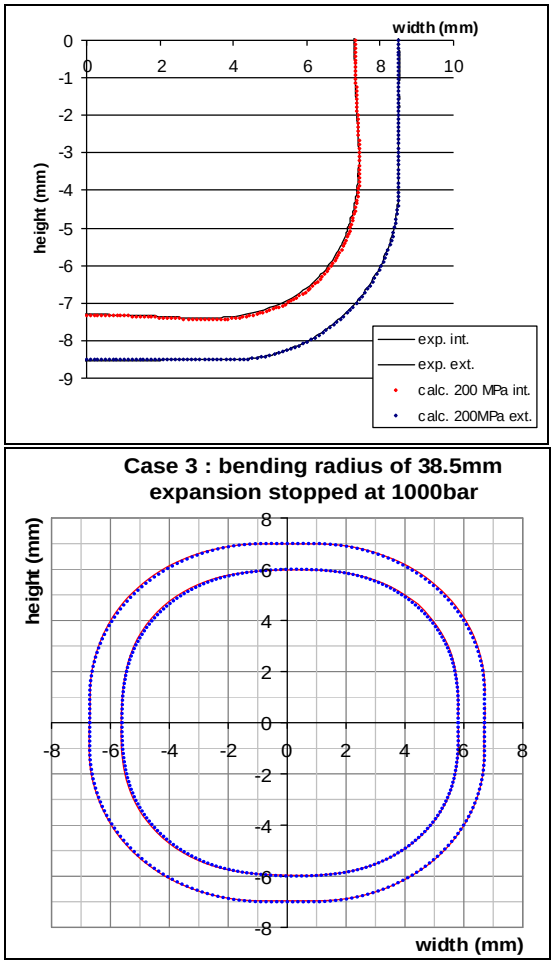

Figure 1: Examples of comparison between calculated shapes and experimental ones

Local mechanical fields

The aim of this part is to understand the tube mechanical behaviour in the cavity all along the loading path, as well as the rupture that may occur. For each case, the mechanical fields are studied in the section on the tube. The plastic strain, the Von Mises stress, the maximum principal stress and the triaxiality are analysed.

Straight tubes

The location of the maximum loading depends on the cavity shape but also on the pressure level. These maxima are located along the inner surface of the tube. The stresses and strains reach a maximum at the beginning of the contact zone, which corresponds to all the crack location observed experimentally. However for some cases, we do not obtain the maximum of the mechanical fields near the experimental rupture zone, and the study of these fields can not explain the rupture observed for case 4A compared to the absence of rupture for case 4B.

Bent tubes

For the bent tubes the maximum loading corresponds to the thinner thickness area, near the tube extrados. The smaller the bending radius, the higher the mechanical fields.

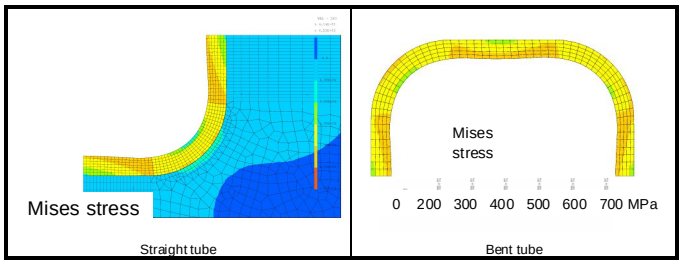

Figure 2: Examples of Von Mises fields for straight and bent tubes

Mechanical fields in the tube thickness

In order to present the results as detailed as possible, the plastic strain, the Von Mises stress, the maximum principal stress and the triaxiality have been studied for each case, through the tube thickness for several orthoradial positions. No obvious conclusion can be stressed, except that the ruptured tubes present the higher triaxiality.

Effect of a coaxiality defect on straight tubes expansion

To understand the experimental results and more especially the experimental dispersion, calculations have been made to simulate the effect of a 0.1 mm coaxiality defect. At high pressure (90MPa), the coaxiality defect modifies completely the strain localisation, which is then more consistent with the experimental observations. This shows that one source of the experimental dispersion can be due to the orthoradial tube position in the cavity.

Rupture Criterion

We propose to use a rupture criterion based on the triaxiality such as the Rice and Tracey one [4].

$$D = A\int_0^{\varepsilon p_f} \exp(\frac{2}{3}\chi).d\varepsilon_p$$

The evolutions of the damage through the thickness for several orthoradial positions and for each case are analysed. For straight tubes, it is confirmed that the expansion in a square cavity is less damaging. A coaxiality defect or a material problem can be responsible for the dispersed ruptures for rectangular cavities. For bent tubes, it is confirmed that a small radius is more damaging. Moreover,

the order of magnitude of the damage calculated for each case is comparable with the straight tubes in square cavities and consistent with the fact that no rupture occurs.

CONCLUSIONS

The main results are as follows:

- The application of a soft annealing heat treatment allows increasing the ductility of Eurofer and decreasing its strength. As a result, the hydraulic expansion of tubes at room temperature is facilitated.

- Experimental and numerical work showed the following features:
  - Square channels can be achieved rather easily, but ruptures are encountered for rectangular channels with an aspect ratio equal to 1.25.
  - A FEM model has been developed that predicts accurately the shape of the tube after expansion.
  - A rupture criterion based on a combination of plastic strain and stress triaxiality has been proposed, however a precise prediction of the rupture is not possible in all cases because of experimental dispersion.
  - Experimental dispersion is thought to come from the tube/tool contact and from the tube dimensions inaccuracy. In particular, the effect of a coaxiality defect has been demonstrated.
  - The First Walls of the two European blanket concepts are feasible.

Since a good confidence can be put in the feasibility of the process, further development of this process would benefit from collaboration with a partner specialised in hydraulic forming. Specifications for tube procurement deserve particular attention. Last, cost reduction is also an issue.

REFERENCES

[1] E. Rigal, F Vidotto, JM Leibold, B Riccetti "Fabrication processes for HCLL and HCPB TBMs, EFDA task TW2-TTBC-002 Blanket manufacturing technologies, deliverable 1, final report", rapport technique DTEN/DL/2005/041, 27 oct. 2005

[2] E Rigal, C Grandjacques "Development and qualification of key fabrication methods: HIP forming of bent structures, task WPB3.1.2, final report" report NT DEM 107/2000, 8 dec. 2000

[3] E Rigal, C Grandjacques, F Bruchon "Second bent HCPB first wall mock up manufactured by improved HIP forming technique, sub task TW0-TTBB2.3 - Blanket manufacturing technologies" report NT DTEN 61/2001, 27 june 2001

[4] J.R Rice and D.M Tracey, On the ductile enlargement of voids in triaxial stress fields, J. Mech. Phys. Solids, 17, 201 (1969)

REPORTS AND PUBLICATIONS

M. Reytier, M. Elie, E. Rigal, F. Vidotto, B. Riccetti, « Feasibility of the tube forming + HIP fabrication process for the bent part of the FW of HCLL and HCPB TBMs », EFDA task TW5-TTBC-002 Blanket manufacturing technologies, Deliverable 2, final report, report RT DTH DL 2007/69, dec. 2007

TASK LEADER

Emmanuel RIGAL

DRT/LITEN/DTH/LTH
CEA-Grenoble
17 rue des Martyrs
F-38054 Grenoble Cedex 9

Tel: 33 4 38 78 97 22
Fax: 33 4 38 78 54 79

e-mail: emmanuel.rigal@cea.fr

Task Title: PROCESS AND AUXILIARY COMPONENTS MODELLING OF TRITIUM PERMEATION AND BEHAVIOUR WITH EXPERIMENTAL DETERMINATION OF KEY MODELLING PARAMETERS

INTRODUCTION

The objective of this deliverable is to study the sensitivity of Pb-Li velocity profile on the estimation of the Tritium mass flow rate towards the He-coolant under DEMO and ITER TBM conditions for a Breeder Unit.

2007-2008 ACTIVITIES

2007 and 2008 activity related to this task was to complete the work initiated in 2006, publish it [1] and issue the final report [2]. The local finite element modelling of the tritium permeation through the HCLL breeder unit cooling plates has been finalised. The tritium concentration in the helium and in the lithium lead have been evaluated by solving partial differential equations governing the tritium balance, the thermal field and the lithium-lead velocity field in a simplified 2D-geometrical representation of the breeder unit at the mid-equatorial plan. Using a factorial design at two levels as numerical experiments it has been shown that the magnetic field and the natural convection are not relevant for the estimation of the permeation.
Moreover, numerical analyses showed a developed concentration boundary layer acting as a mass transfer resistance which is equivalent to a PRF of 30.

PERMEATION MODELLING

The T concentration in the helium circuit and remaining in the lithium-lead circuit are evaluated by solving partial differential equations governing the T concentration balance, the thermal field and the lithium lead velocity field. The geometrical model simplified for simulations is shown on figure 1.

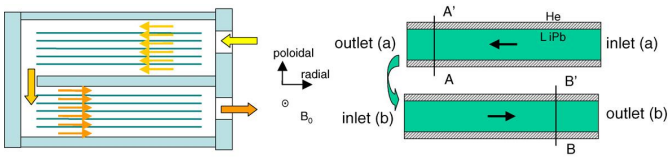

Figure 1: Geometrical model for the simulation

MAIN RESULTS

Taking into account the relevant governing equations solved using the CEA FEM code CAST3M and several boundary conditions; the sensitivity of the velocity profile on the three interesting outputs allowing specifying the processing elements of the circuits has been evaluated.

Figures 2 and 3 present temperature and concentration fields for the NE 1 at 10 T. The temperature field is higher near the FW and looks like a pure diffusion field. Near the outlet b, the temperature field is almost constant and follows the prescribed wall temperature. Tritium concentration gets enriched as it flows toward the FW. One can see the development of concentration boundary layer near the wall where the T concentration is lower than in the bulk.

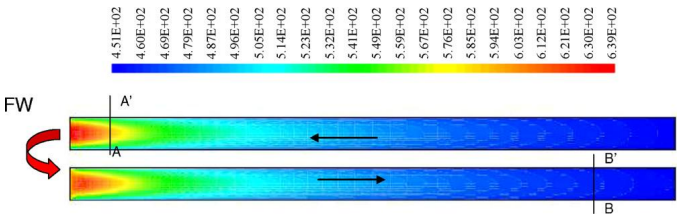

Figure 2: Temperature distribution for NE 1–10 T

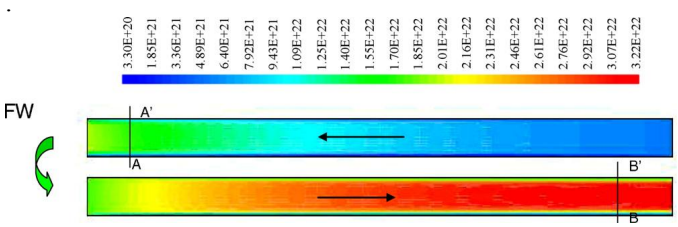

Figure 3: Tritium concentration field for NE 1–10 T

Velocity profiles and concentration profiles for the NE 2 and 4 are shown in figures 4 and 5. The velocity profiles, present in figure 4b have a Mshape profile due to the magnetic field (the lower channel is almost isothermal). By opposition, buoyancy effect can readily be observed (figure 4a) although this effect is damped for higher magnetic field value. However, if velocity profiles are different, the concentration profiles are almost unchanged (figure 5).

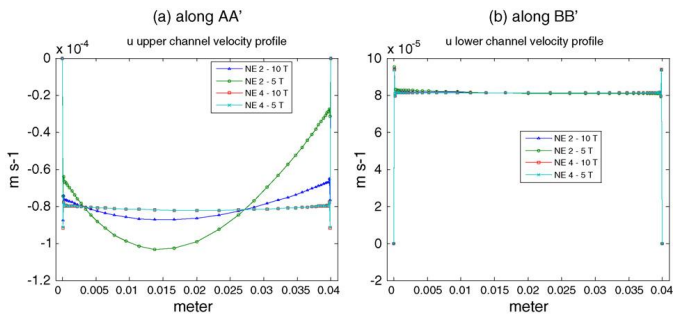

Figure 4: Radial velocity profiles along the poloidal direction

Table 1: Parameters of the response surfaces

	a_0	a_1/a_0	a_2/a_0	a_3/a_0
Φ_3 (g/m^2 day), 5 T	2.93×10^{-3}	−0.08%	−0.66%	−0.10%
$\bar{C}_f$ (mol m^{-3}), 5 T	0.0454	−0.10%	0.26%	−0.08%
Φ_3/Φ_1 (%), 5 T	21.16	−0.08%	−0.66%	−0.10%
Φ_3 (g/m^2 day), 10 T	2.94×10^{-3}	0.015%	−0.21%	−0.005%
$\bar{C}_f$ (mol m^{-3}), 10 T	0.0453	−0.023%	0.066%	−0.013%
Φ_3/Φ_1 (%), 10 T	21.25	0.014%	−0.21%	−0.005%

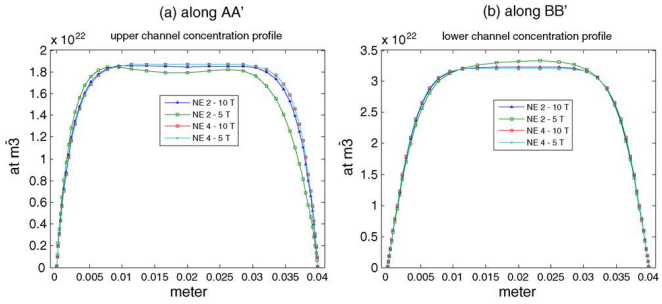

Figure 5: Concentration profiles along the poloidal direction

The sensitivity of the outlet velocity boundary condition and the effect of the natural convection are evaluated (thank to the realization of two factorial designs analysis at two levels) by estimating the parameters of the following response surfaces:

$$y(X_{CL}, X_{CN}) = a_0 \left(1 + \frac{a_1}{a_0} X_{CL} + \frac{a_2}{a_0} X_{CN} + \frac{a_3}{a_0} X_{CL} X_{CN}\right)$$

where y is any of the three considered outputs (Φ_3, $\bar{C}_f$ and Φ_3/Φ_1). It must be noted that a0 is the mean value of the numerical outputs, a1 expresses the effect of the velocity boundary conditions, a2 expresses the effect of the natural convection and a3 expresses the effect of the interaction between the boundary conditions and the natural convection. Table 1 gives the estimated values of these parameters. The Φ3 quantity is divided by our wetted Pb–15.7Li surface (110m^2) in order to be useful for other studies. It appears that the outlet velocity boundary limit and the natural convection have no effect on the observed outputs. Indeed, the highest value is around 0.66% and is to be compared to 1. This may be not the case for modules where gravity is parallel to the prescribed flow (top and bottom of the reactor). Moreover, mean values show that the observed outputs are not sensitive to the value of the magnetic field. This is valuable information as permeation experiments have to be performed.

CONCLUSIONS

In this study, a local finite element modelling of the tritium permeation rate through the HCLL breeder unit cooling plates is presented.

The permeation rate through the helium circuit and remaining in the lithium lead circuit are evaluated by solving partial differential equations governing the tritium concentration balance, the thermal field and the lithium lead velocity field for a simplified 2D-geometrical representation of the breeder units. It is shown, for the mid-equatorial HCLL modules with the retained assumptions, that the permeation through the helium circuit, the mean outlet tritium concentration in Pb–15.7Li and the ratio between the permeation through the helium circuit and the production rate are insensitive to the magnetic field and the buoyancy effects. However, due to the flow, a concentration boundary layer exists and is to be regarded as an equivalent permeation reduction factor of 30. Considering the difficulty encountered in the past years to obtain stable and reproducible high PRF with Al-based coating on Eurofer, an equivalent PRF of 30 is of great importance for the tritium inventory in the HCLL blanket and should relaxed the coolant purification system requirements.

REPORTS AND PUBLICATIONS

[1] F. Gabriel, Y. Escuriol, F. Dabbene, O. Gastaldi J.F. Salavy, L. Giancarli, "A 2D finite element modelling of tritium permeation for the HCLL DEMO blanket module", Fusion Engineering and Design 82 (2007) 2204–2211

[2] F. Gabriel, "Simulation of tritium permeation - Task TW5-TTBC-005-D05-final report", CEA internal report SERMA/LPEC/RT/08-/4451/A, May 2008

TASK LEADER

Franck GABRIEL

DEN/DM2S/SERMA
CEA-Saclay
F-91191 Gif-sur-Yvette Cedex

Tel: 33 1 69 08 79 76
Fax: 33 1 69 08 99 35

e-mail: franck.gabriel@cea.fr

TW6-TTBC-001-D03

Task Title: HCCL TBM DESIGN AND INTEGRATION ANALYSES

INTRODUCTION

In the frame of the EFDA Programme, the detailed engineering design of the HCLL Test Blanket Modules (in particular the IN-TBM and EM-TBM) and associated systems was further developed in particular with focus on integration of diagnostic and monitoring instrumentation, integration of fabrication R&D issues, ITER environmental and schedule constraints and performances optimization.

The objectives of the present task were:

- the further development of the TBM design, and in particular the update of the TBM dimensions according the constraints of the last frame design update, the improvement and optimisation of the He flow scheme according to the last DEMO studies, and the instrumentation integration,
- the evaluation of design margins regarding the design criteria, as they impact the manufacturing choices,
- the assessment of the maintenance sequence of the TBM (installation, replacement, dismounting),
- the analysis and improvement of the Helium Cooling System of the TBM.

2007-2008 ACTIVITIES

DESIGN ANALYSES AND TBM DRAWINGS UPDATE ACCORDING TO LAST FRAME DESIGN UPDATE

In 2006, the ITER Port Plug Frame design was revised leading to the reduction of the dimensions of the internal space available for the TBM. The existing TBM design 0] could not fit into this space. The strong impact on the TBM design due to the necessary reduction of its poloidal and toroidal dimensions implied, based on this previous design:

- to re-define the number of breeding cells, taking into account the new TBM overall dimensions, without loosing the DEMO relevancy,
- to re-define consequently the First Wall design (channels section and pitch, thickness, number of sweeps,…) with the following steps: analytical thermal-hydraulics optimisation, mechanical behaviour validation, thermal-hydraulics computation for final validation,
- to reconsider the back plates stiffening and the attachments system.

In addition, further improvements of the design were made:

- according to the TW5-TTBC-001-D06 work on the reference He flow scheme for DEMO, the He flow scheme for the TBM has been updated; the new scheme being serial, a forth stage had to be added in the back collector, and the cooling channels of the Stiffening Plates, Covers, and Cooling Plates had to be adapted, and the corresponding pressure drops assessed,
- the positions of the Covers feeding and by-pass pipe had to be consequently re-defined,
- the Covers cooling has been assessed and optimised (circulation path, front channel in the First Wall).

Several additional improvements were brought to this new design, in particular:

- the PbLi flow path and distribution was revised (bottom to top circulation, new internal distribution, modification of the number of Cooling plates…),
- the back manifold design was revised to optimize the Back Plates thicknesses and the organisation of stages for a better mechanical behaviour under thermal loads, and to improve the definition of the stiffening rods by separating their tightness and mechanical functions,
- some issues linked with the box manufacturing have been solved.

These updates were performed on the In-TBM, which is the basis of design for the other TBMs.

The updated design is shown in figure 1 and figure 2.

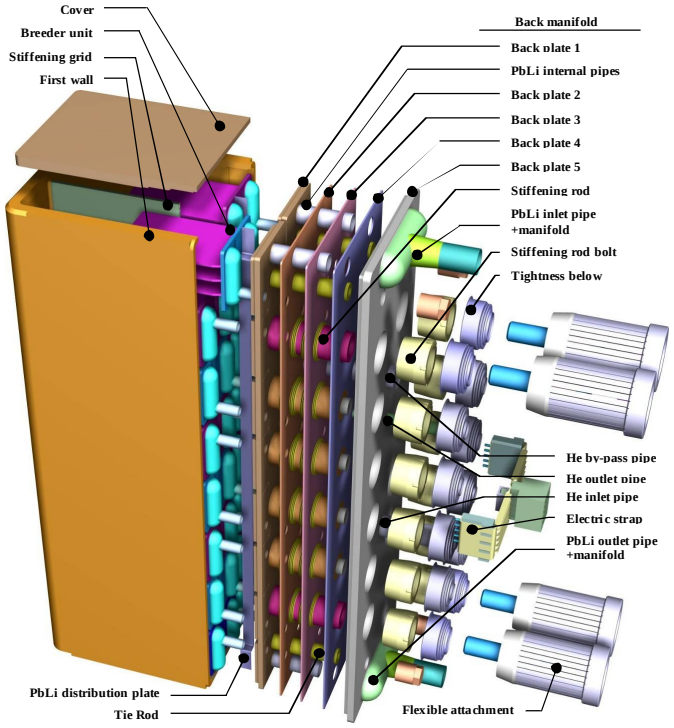

Figure 1: Exploded view of the HCLL TBM

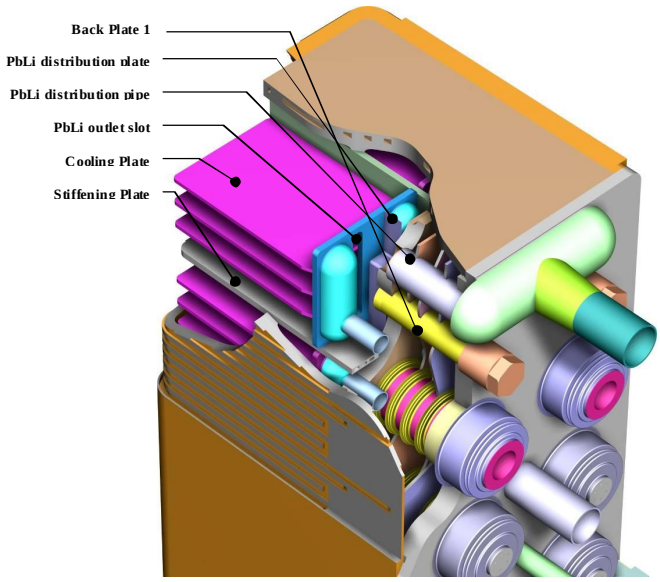

Figure 2: Scorched view for details on Back Manifold and PbLi distribution

The new He cooling path was designed under the following requirements and assumptions:

- In-series scheme, similar to DEMO,
- Channels cross-sections near the DEMO ones for each cooled sub-component,
- Minimisation of the pressure drop (assumed allowable value of 0.2 MPa for FW),
- Minimisation of the global He mass flow (assumed allowable global value of 1.5 Kg.s^{-1}),
- Maximum temperature of 550°C in the structure,
- Mechanical withstanding to the 8 MPa pressure,
- Minimisation of the recovering effect between components (limitation of temperature gradients between neighbouring components),
- For the FW/SW: round number of channels legs / breeding cell + nearly square channels cross-sections,
- For the SP: channels cross-section similar to DEMO + minimal distance between stiffening grid joints and nearest channel wall of 5 mm.

The main He flow scheme parameters are shown in figure 3.

The Back Manifold design update consisted in:

- the optimisation of the Back Plates thicknesses and Stiffening Rods,
- a new collecting stages organisation: configuration to get better behaviour under thermal expansion with, as additional advantage less crossings (less constraints on manufacturing) an as drawback an outlet temperature of the module below 500°C,
- for the Stiffening Rods design, a separation of mechanical and tightening functions including the principle of a tight path for instrumentation.

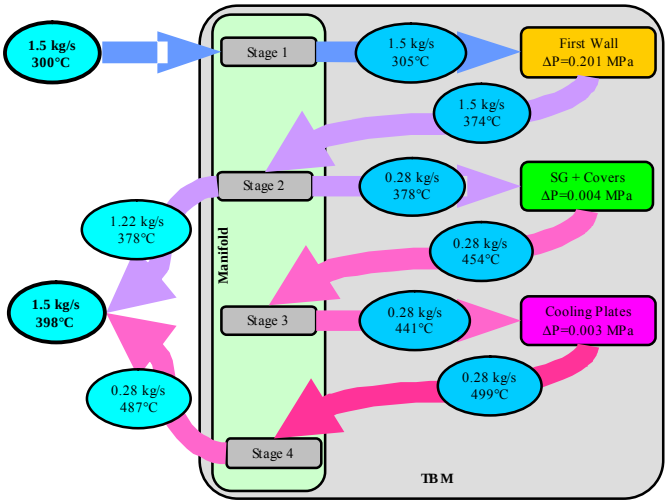

Figure 3: Temperatures, He mass flow and pressure drops in the cooling system of the TBM

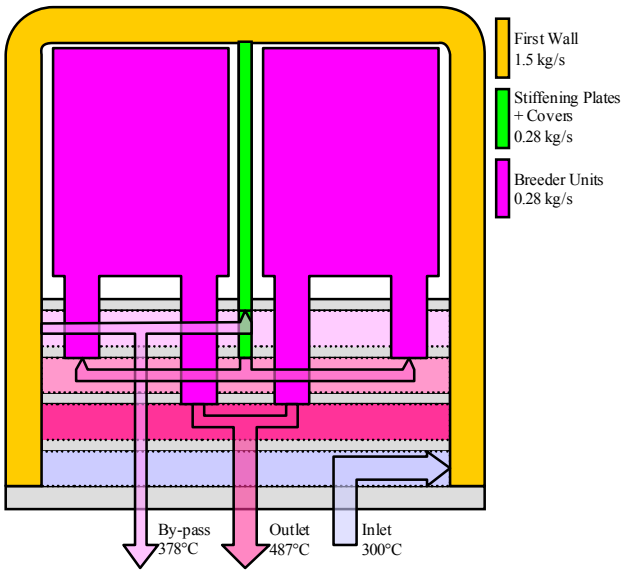

Figure 4: Scheme of the organisation of He stages in the Back Manifold

In order to support this update, new analysis models were developed and used to optimize the thermo-hydraulics and mechanical behaviour.

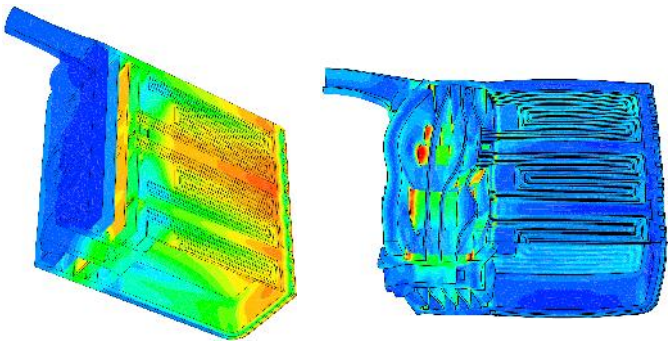

Figure 5: Temperature field and ratio to mechanical criteria for primary stresses under nominal conditions

The final report [3] is the reference design report for the 2007 update of the Helium Cooled Lithium Lead Test Blanket Module for ITER.

DEFINITION OF A DESIGN SPECIFICATION PACKAGE FOR FABRICATION R&D

The final report [4] of this sub-deliverable presents a general methodology to assess the impact of manufacturing defects on the design of the HCLL-TBM FW. The study was focused on the maximum allowable temperature in the steel structures but the effects on mechanical resistance criteria could also be analysed by using the same methodology.

Two criteria were defined: the first one, representing the maximum allowable deviations from the nominal dimensions can be used in the selection of the manufacturing process. The second one, using the complete expression of the response surface with the parameters defined by an equation, is to be used to check if the manufactured part will satisfy the thermal criterion.

This methodology can be extended by the inclusion of additional parameters and/or additional design criteria. It can also be adapted to different TBM sub-components (CPs, SPs …).

MECHANICAL INTEGRATION OF POSSIBLE INSTRUMENTATION INTO TBM

The updated design proposes a preliminary design for the integration of instrumentation in the TBM, through the Stiffening Rods of the Back Manifold. A sleeve, welded on the Stiffening Rod for tightness, is used as a guide through which are brazed thermocouples sheath. This principle is illustrated in figure 6.

Complementary studies were reported in [5]. Alternative solutions are proposed, based on a similar principle, with additional detail on barrels insuring both tightness through brazed junctions and guiding (see figure 7). Feedback is reported to be good. The need for the development of PbLi-resistant thermocouple sheath is highlighted, as well as the availability of the DIADEMO facility for testing purposes.

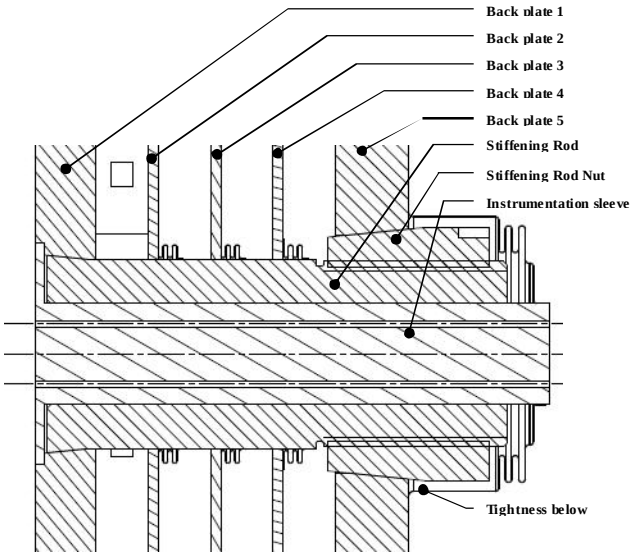

Figure 6: Detail of the Stiffening Rod design

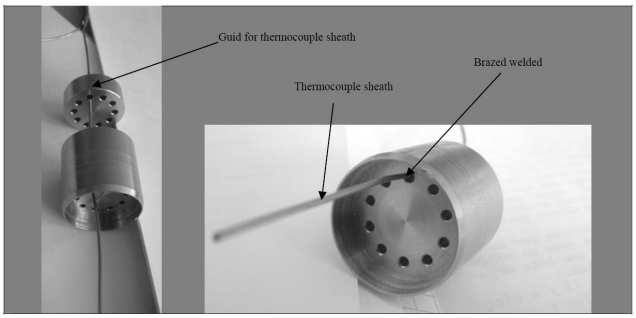

Figure 7: Principle of barrel-based tight path for instrumentation

FURTHER DETAILED ANALYSIS OF THE MAINTENANCE SEQUENCE TAKING INTO ACCOUNT ITER SPACE REQUIREMENT / INTERFACES AND ORE PRELIMINARY ISSUES

The objective of this sub-deliverable was to produce further detailed analysis of the HCLL TBM system maintenance sequence taking into-account ITER space requirement / interfaces and ORE preliminary issues with a focus on Remote Handling considerations.

The final report [4] highlights the following conclusions:

- A short summary of ITER safety rules was presented. Although the dose level at interface 2 is still under limits for human intervention, TBM replacement counts for a non negligible part in the cumulated collective dose target for all workers during one shutdown. For that reason, due to ALARA concerns, an assessment of the potential gain on the collective dose if the work is performed using RH techniques becomes a safety request,
- Resistance of RH system to radiations is related to its components design and materials. Solutions leaving a RH system at interface 2 during operations will need assessment with the expected dose rate during operations. To help TBM designers, a summary or the effects of radiations on RH system was provided,
- Design recommendations and operational feedback were also briefly described for information. It is now well established that reliability of RH operations is improved and duration of tasks is minimised when RH engineers are part of the design process since its inception. Recent developments in simulation and modelling greatly improved the preparatory and feasibility work. However final validation on a representative physical mock-up with representative tools and tasks is always needed before real operations. A scale 1 mock-up of the representative part of the TBM will therefore be requested,
- Starting from the work done on CAD models for the HCPB maintenance, real examples of similar situations in the nuclear industry using RH equipment were presented. An overview of tooling and process feasibility were briefly given. Anyway the particular case of the HCLL TBM will require further investigations in that direction,
- Although no RH system is today available to carry out such operations and some difficulties are raised by the

TBM environment, developments to overcome such difficulties should find answers in the next few years. Attention should be paid to the fact that developing an RH system is a matter of years and usually takes 6 to 8 years between the first design of prototypes to the industrial version. In that particular case, technologies and concepts could be re-used from other systems and minimise the development time. Anyway, to be ready for ITER operation, preliminary studies and development of a complete system should start in the following years. If RH maintenance of the TBM is necessary, installation time for the tools are rapidly needed for making the choice between hands-on or remote activity.

CONCLUSIONS

This work establishes a new reference design of the Helium Cooled Lithium Lead Test Blanket Module for ITER, for which the main guidelines were:

- to conform to updated dimensions of the ITER Port Frame,
- to implement a new cooling scheme consistent with the reference DEMO one.

Several additional modifications were brought to the design in order to improve its functional features. New analysis models were developed and used to optimize the thermo-hydraulics and mechanical behaviour.
In addition, various considerations such as design margins for fabrication, instrumentation integration, manufacturing sequence, remote handling aspects…were addressed.

Several issues still present on the updated design were raised which need future work. Two major ones, linked to the Back Manifold can be highlighted: the consequence of the re-arrangement of the collecting stages implying a temperature at the outlet of the module inferior to the specified 500°C, and the overload of the Back Plate 3 under thermal expansion. An important revision of some principles of the Back Manifold should be envisaged.

Further work will have to focus on the consistency with possible specifications update, on the Back-Manifold design, thermo-hydraulics and thermo-mechanics, on the improvement of the analysis models to get full assessment on fully-relevant geometries, on the instrumentation integration, and on the attachment system and electrical strap design.

An important quantity of design-related information can be found in the issued report which can be used as reference for future updates.

REFERENCES

[1] G. Rampal, “Design and analyses of the HCLL TBM including design of supporting system and instrumentation integration”, final report of the EFDA task TW5-TTBC-001-D01, CEA report SEMT/BCCR/RT/06-004/A, September 2006

REPORTS AND PUBLICATIONS

[2] G. Rampal, G. Aiello, “HCLL TBM design and analyses - EFDA task TW6-TTBC-001-D03, del. 3a, 3c & 3e”, CEA report SEMT/BCCR/RT/07-056/A, February 2008

[3] G. Aiello, F. Gabriel, “Preliminary Assessment of Manufacturing Margins for the HCLL-TBM First Wall”, CEA report SERMA/LPEC/RT/07-4625/A, November 2007

[4] O. David, “Preliminary analysis of TBM maintenance procedures from a RH point of view”, CEA report DTSI/SRI/08.321, August 2008

[5] L. Ayrault, “Helium-Cooled Lithium-Lead: TBM Design, integration and analysis”, CEA report DEN/DTN/STPA/LTCG/2007-031
November 2007

TASK LEADER

Gilles RAMPAL

DEN/DM2S/SEMT
CEA-Saclay
F-91191 Gif-sur-Yvette Cedex

Tel: 33 1 69 08 41 44
Fax: 33 1 69 08 94 26

e-mail: gilles.rampal@cea.fr

TW6-TTBC-002-D01

Task Title: BLANKET MANUFACTURING TECHNOLOGIES IMPROVEMENT OF THE 2-STEP HIP DIFFUSION WELDING PROCESS FOR THE MANUFACTURING OF TBMs SUBCOMPONENTS

INTRODUCTION

The aim of this study is the improvement of the 2-step HIP process in the frame of the development of manufacturing processes for test blanket modules (TBMs) subcomponents. The previous study [1] concerning this process showed that very good dimensional accuracy can be achieved but unsatisfactory results are obtained in terms of joint impact toughness. The objective is to improve the joint impact toughness by working on the samples preparation. The outgassing of Eurofer is studied and a series of joining experiments is made to evaluate the influence of the chosen preparation processes.

2007-2008 ACTIVITIES

DESCRIPTION OF THE CONTEXT AND ACTIONS PLAN

The 2-step HIP process is based on the diffusion welding of grooved plates. A first HIP cycle at low pressure is used to bond tightly the plates without significant deformation of the channels. Then, the channels are opened and a second high pressure HIP cycle is applied to achieve expectedly high joint mechanical properties [2]. Previous investigations on the 2-step HIP process on Eurofer showed that very low channel deformation could be achieved but joint mechanical properties were not satisfactory [1].
Different hypothesis were proposed [1]:

- The encapsulation technique used for past experiments may damage the interface,
- The outgassing of entrapped channels during the first HIP cycle may be an issue and cause the inclusions formation.

Actions plan for the improvement of the 2-step process:

OUTGASSING INVESTIGATIONS

During the first HIP cycle of the 2-step HIP process, the interfaces are not fully closed and are submitted to high temperature (1000°C), which may favour reactions between the interfaces and residual atmosphere. Therefore investigations on the outgassing of Eurofer have been made.

COMPARATIVE STUDY ON THE INFLUENCE OF THE PREPARATION AND DEGASSING STEPS

Following the outgassing experiments, a series of tests has been chosen to try different ways to improve the two-step HIP process. The two main improvements concern the encapsulation method and the outgassing procedure.

OUTGASSING EXPERIMENTS

A device has been settled to analyse the outgassing behaviour of Eurofer. It is composed of an air furnace with an opening in the door that allows connecting the outgassing tube (quartz) to a secondary vacuum pump equipped with an Inficon Transpector gas mass spectrometer. Chips of the studied material are inserted into the tube. All the tubes, connections and valves are dried thanks to heating tapes.

DESCRIPTION OF THE TESTS AND STUDIED MATERIALS

The outgassing temperature has been fixed at 1000°C. A low heating rate has been chosen.

- empty tube,
- 2g of Eurofer chips,
- 2g of Eurofer chips and 1,5g of getter material chips.

RESULTS AND ANALYSES

For each test, temperature, pressure and mass spectra were recorded (figure 1).

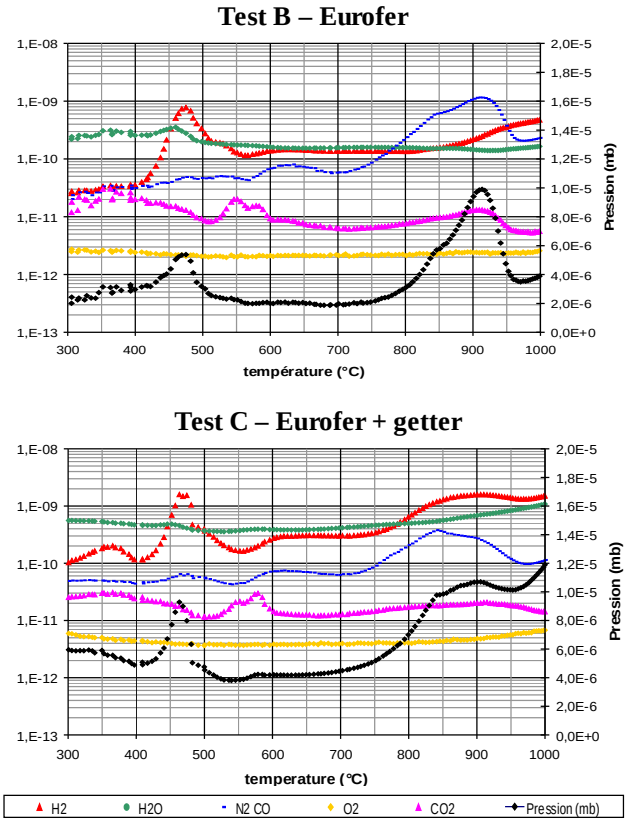

Figure 1: Graphs showing the evolution of the outgassed species and pressure as a function of temperature

NOTA
The CO_2, H_2O and O_2 spectra are due to the system outgassing.

Analysis of Test B : Eurofer
Two pressure peaks are observed at 475 and 915°C. The first peak corresponds mainly to the degassing of H_2 molecules probably from the bulk material. The second peak at 915°C is due to the outgassing of CO molecules which also presents a lower peak between 500°C and 700°C.
We assume that the first CO peak can be attributed to the removal of chemisorbed layers, while the second one is probably due to the reduction of iron and chromium surface oxides by carbon diffusing from the bulk. The CO intensity presents a shoulder at 840°C and decreases sharply at 915°C. These temperatures correspond roughly to the austenite start and finish temperatures (820 and 880°C respectively, [4]).

Analysis of Test C: Eurofer + getter
Two main effects on the spectrum are observed:
- a significant reduction of the CO intensity above 700 °C
- an increase of H_2 degassing, which is due to the diminution of hydrogen solubility in the getter at high temperature.

Conclusion
To improve the 2-step HIP outgassing process, getters could be used to reduce the presence of CO molecules between the interfaces after the first HIP cycle, during which interfaces are not fully bonded.

2-STEP HIP PROCESS EXPERIMENTS

DESCRIPTION OF THE ASSEMBLING TESTS CONFIGURATIONS AND DEGASSING PROCESSES

All the tests are composed of two Eurofer disks (Eurofer 97-2 bar, heat 993 378) assembled with an improved encapsulation technique:
- TEST 1: Reference test: joining of two Eurofer plain samples,
- TEST 2: influence of channels: joining of two Eurofer grooved samples,
- TEST 3: influence of a getter inserted in a ceramic cartridge placed in the channels, with a moderate outgassing temperature,
- TEST 4: influence of a getter inserted in a ceramic cartridge placed in the channels, with a high outgassing temperature,
- TEST 5: influence of getter material as deposits: The insertion of getters inside channels would be hardly realisable for very small channels or bent channels. In this test, the getter is deposited on a steel foil that is wrapped around the Eurofer specimens,
- TEST 6: influence of getters material wrapped in a foil. The aim of this test is to test the efficiency of getters in channels when they are wrapped in a metallic foil instead of a ceramic cartridge.

All the experiments are made following these steps:

- Outgassing:
  Tests 1 and 2: the outgassing step is the same as the same as for past experiments,
  Tests 3, 4, 5 and 6: the outgassing step has been improved.

- First HIP cycle: 1000°C, 40 bar,
- Channels opening ,
- Second HIP cycle: 1100°C, 1200 bar,
- Heat treatment (normalization at 980°C, 2h, air quench and tempering at 750°C, 2h).

RESULTS

The properties of tests 3 and 4 are not reported here since the junction failed: Ta/V carbides have been found at the interface, which may be due to the presence of carbon rich gas molecules in the residual atmosphere, probably due to the cartridge.

Dimensional measurements
No significant deformation of the channels is noticed.

Mechanical properties
Full size U-notch Charpy specimens (KU, 10x10x55 mm^3) and reduced V-notch specimens (KLST, 3x4x27 mm^3) have been machined to test the joint (table 1) at room temperature.
The properties are compared to past experiments:
- Past experiment no. 1 : Joining of Eurofer plain disks using a single high pressure HIP cycle [3]
- Past experiment no. 2: Joining of Eurofer grooved plates using the 2-step HIP process [1].

Table 1: Impact toughness energy of Eurofer joints (mean values)

	KU specimens		KLST specimens		
	Energy absorbed (J)	fully broken specimens	Energy absorbed (J)	% of base material	fully broken specimens
TEST 1	102±3	none	8.3 ± 0.4	79%	none
TEST 2	107±5	none	8.5 ± 0.6	81%	none
TEST 5	97.5±3	none	8.3 ± 0.3	79%	none
TEST 6	107±7	none	7.8 ± 0.5	74%	none
Base material [(1)]	N/A[(3)]	N/A[(3)]	10.5 ± 0.3	N/A(3)	N/A(3)
Past exp. no. 1 [(2)]	N/A[(3)]	N/A[(3)]	9.1 ± 0.4	87%	none
Past exp. no. 2 [1]	N/A[(3)]	N/A[(3)]	4.2 ± 0.9	40%	1 over 3

(1) The base material impact toughness has been measured on KLST machined from Test 1 with the notch far from the joint line.
(2) New measurements have been made for past experiment no. 1.
(3) N/A: Non Available

- Effect of the grooves:
The impact tests showed similar impact toughness for the plain and grooved samples (~80% that of base material). Therefore the grooves do not seem to have an influence on the joint toughness, which means that they do not affect the outgassing process.

- Effect of the encapsulation technique:
The good joint impact toughness obtained for tests 1 and 2 (with the same outgassing step as past experiments) show that the influence of the encapsulation technique is fundamental and very probably the cause of the poor mechanical properties of past experiment no. 2. The light difference between test 1 and past experiment no. 1 is probably due to the fact that the surface preparation and the Eurofer heat were not exactly the same.

- Influence of getters:
Tests 5 and 6 give similar joint impact toughness to tests 1 and 2. This means that the use of getter materials does not help improving joint impact toughness in this specific configuration.

CONCLUSIONS

Conclusions regarding the outgassing experiments
The most problematic characteristic of Eurofer outgassing is the release of CO molecules at high temperature. The use of a getter material can reduce significantly the amount of CO molecules thanks to its absorbing properties.

Conclusions regarding the joining experiments
The results show that the encapsulation technique improvement leads to very good joint impact toughness for both plain and grooved samples, and with or without getter materials. This means that the outgassing of entrapped channels has no impact on the joint quality, and that getters cannot help improve it. A hypothesis of the slight decrease in joint impact toughness when the 2-step process is used (from ~90% to ~80%) is probably due to another parameter, namely the surface condition. Therefore the 2-step HIP process does not intrinsically result in impact toughness lower than other kinds of HIP joints.

REFERENCES

[1] E. Rigal et al. “Fabrication processes for HCLL and HCPB TBMs – EFDA task TW2-TTBC002 Blanket manufacturing technologies, deliverable 1, final report”, rapport technique DTEN/DL/2005/041

[2] E. Rigal et al. “Fabrication processes for HCLL and HCPB TBMs – EFDA task TW2-TTBC002 Blanket manufacturing technologies, deliverable 1, second interim report”, rapport technique DTEN/DL/2005/006

[3] E. Rigal, F Bruchon “Solid HIP process qualification, application to complex shapes, subtask TW1-TTMS-004-D06 (qualification of fabrication processes)”, Note technique DTEN 2002/22

[4] A. Danon, A. Alamo “Behavior of Eurofer97 reduced activation martensitic steel upon heating and continuous cooling”, Journal of Nuclear Materials 307–311 (2002) 479–483

REPORTS AND PUBLICATIONS

M. Elie, E. Rigal, F. Vidotto, J.-M. Leibold, Improvement of the 2-step HIP diffusion welding process for the manufacturing of TBMs subcomponents, EFDA task TW6-TTBC-002 Blanket manufacturing technologies, Deliverable 1, final report, RT DTH DL 2007/66, nov. 2007

TASK LEADER

Emmanuel RIGAL

DRT/LITEN/DTH/LTH
CEA-Grenoble
17 rue des Martyrs
F-38054 Grenoble Cedex 9

Tel: 33 4 38 78 97 22
Fax: 33 4 38 78 54 79

e-mail: emmanuel.rigal@cea.fr

CEFDA06-1470

Task Title: TW6-TTMS-MODUNI2: DD SIMULATION OF THE INTERACTION AND He CAVITIES IN Fe-ALPHA

INTRODUCTION

The objective of this task is to study the interaction of dislocations and cavities in BCC Fe using dislocation dynamics (DD).
This task involves the development of a new DD code dedicated to BCC structures and coupled to the Finite Element Method. Firstly, the image forces induced by the cavity are analysed as a function of the distance to the cavity and the position of the dislocation slip plane in a static configuration. Then dynamic simulations give access to local rules depicting the interaction of dislocations and a single cavity. The objective of the local rules is to perform large scale simulations of dislocation activity within a volume containing a large number of cavities.

2007-2008 ACTIVITIES

COUPLING DD AND FEM

BCC version of the DD code

A Discrete Dislocation Dynamics (DDD) code dedicated to Bulk Centred Cubic (BCC) structures (Fe-α) was developed within the Ph.D. work of Julien Chaussidon [1]. The code is derived from the edge-screw model TRIDIS initially developed for FCC crystals [2]. It was modified using a multiscale procedure involving molecular dynamics (MD) simulations at the atomic level [3]. Using an Embedded Atom Method potential [4], static simulations demonstrate that the stress needed to move a screw dislocation from one Peielrs valley to the next one does not obey the Schmid law. This feature is found to be related to the core structure of the screw dislocations in BCC.
Depending on the sign of the shear stress, one can observe an easy glide (in the so-called twin direction) and a difficult glide in the anti-twin direction. At the DD scale, this implies that the screw motion strongly depends whether the maximum resolved shear stress plane is comprised within two twin $\{110\}_T$ plane or within a twin $\{110\}_T$ and an anti-twin $\{110\}_{AT}$ plane. In the first case the dislocation glide will be a combination of glides in the two planes whereas in the latter the dislocation motion is confined to the $\{110)_T$ plane. This twin anti-twin asymmetry was introduced using a probability law (residence time algorithm) for the selection of the glide planes which depends on the stresses on the considered {110} planes. Since the dislocation mobility computed by MD was only valid for large stresses, in the DDD code, the mobility for the screw segments is introduced in a classical manner using classical thermal activation theories. Parameters of the activation energy (Kock's law) have been determined experimentally by strain and temperature jump performed on bainitic stainless steels [1].

Finally, the time integration algorithm of the DD code was modified to account for the large difference between the edge mobility ($v = \tau b / B$) and the screw mobility (eq. 1). Practically, the edge are moved over several time steps (typically 100 steps at $\delta t=10^{-9}$s) before the position of the screw segments is actualized. Such time integration means that the edge mobility is infinitely higher than the screw mobility so that the real simulation time is imposed by the time step of the screw segments.

Coupling with FEM

In a DDD simulation, the effective stress field at each dislocation segment is computed as the summation of the applied stress field and the internal stress field generated by all the dislocation segments contained within the simulation volume. When the applied stress field is not homogeneous as in the presence of a cavity, one needs to couple the DDD code to a finite element method (FEM) or boundary element method. Note that a full coupling of the two codes is needed so that the dislocation position is always computed accordingly to the FEM solution and inversely.
In this study, the BCC version of the DD code was coupled to the finite element code Cast3M-v07 [5]. The cavity can be introduced by means of an elastic inclusion with null elastic constants.

DISLOCATION-CAVITY INTERACTION

Static case

The objective is to compare DDD simulations with atomic simulations. Thus, a cavity of radius 1 nanometer is located within a cylindrical volume of radius 12.5 nanometers and height 10 nanometers. The cylinder axis is $(1\,\bar{1}\,0)$ corresponding to a possible glide plane of the dislocation. The cavity is meshed into 3168 20-nodes elements (12605 nodes) as represented in figure 1. The matrix is meshed into 23450 elements (24870 nodes).

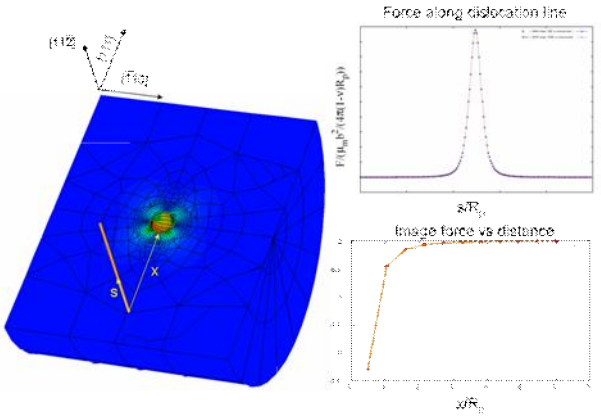

Figure 1: FEM mesh used to simulate the dislocation – cavity interaction and typical image forces computed along the dislocation line (coord. s) and evolution of the maximum shear stress as a function of the distance between the dislocation and the cavity (coord. x)

First, static simulations are performed in order to validate the DD-FEM coupling. Image forces induced by the presence of the cavity are computed on a long edge dislocation located at a distance x from the cavity center taken along (111) and at an altitude y measured along (-110). Results are shown in figure 2. Each point corresponds to one specific DD-FEM computation. As depicted in figure 2, the image force is the highest for an edge dislocation located in the sphere mid plane (y=0).

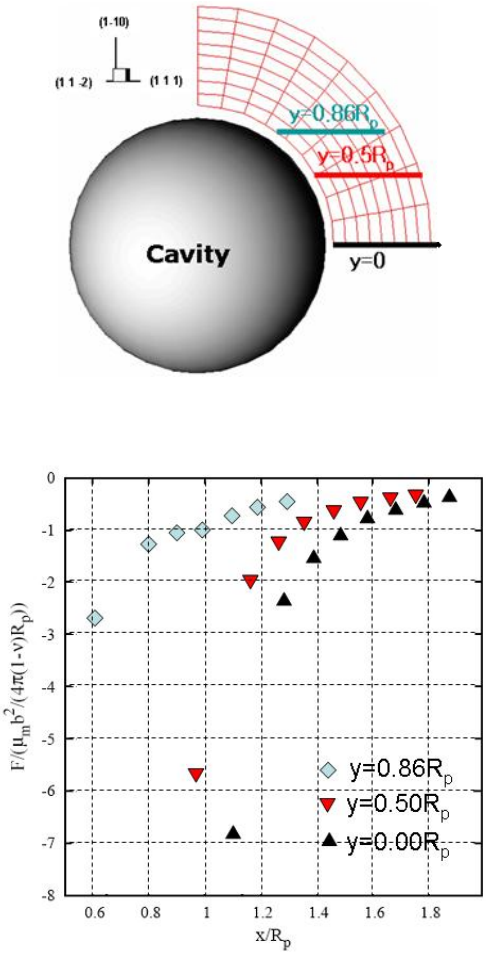

Figure 2: Image forces (normalized) induced on an edge dislocation located at x/Rp from the cavity center and within a plane located at a distance y from the medium plane

Dynamic case

Dynamic simulations are now performed in order to check the reaction between the dislocation and the sheared cavity. Figure 3 shows the shear stresses resolved on the primary slip system containing the dislocation and also on the deviate slip systems D_1 and D_2 when the dislocation is in contact with the cavity.

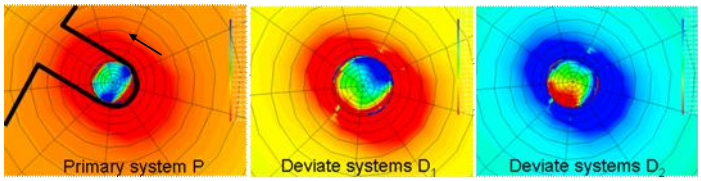

Figure 3: Shear stresses resolved on the three possible glide plane of the dislocation. The Burgers vector and the dislocation line are indicated in the first graph

From these plots one can derive a probable scenario for dislocation motion that may explain the formation of jogs as observed in MD. Indeed, one can notice that the stress fields have the same sign on the two opposed sides of the cavity. Then, the two screw components of the dislocation line will feel a stress in the deviate planes that will make cross slip favourable. The two screw components will feel a force with an out of plane component in the two opposite glide directions as imposed by the line direction of the dislocation. Then the two arms may try to move and annihilate inside the cavity. As a result the leaving dislocation will have a double jog, one down and the other one up. This may explain the jog evidenced by the MD simulations.

Facet approximation

FEM can not be used to treat the case of multiple cavities. Indeed, such a simulation would require a too much complicated mesh as well as a huge calculation time. Thus, it is useful to replace the action of the image forces by local rules. In practice, the spherical cavity is meshed into quadrangular facets. Each facet is given a critical strength required for a segment to shear this obstacle.

The DD simulation is then adapted to treat the case of a nanometric cavity similar to Haghigat et al. [6]. Periodic boundary conditions are applied along the dislocation line direction. The inter-cavity distance is fixed to L=12nm. The void size is changed in the range visited by the authors i.e. it varies between 1 and 5 nm. Thus the volume size is changed from D=13 to D=17nm. An edge dislocation of length L+D is introduced in the simulation box. The objective is now to find the optimized facet strength τ_{facet} that will lead to the closest results to the MD simulations. Results are reported in figure 4.

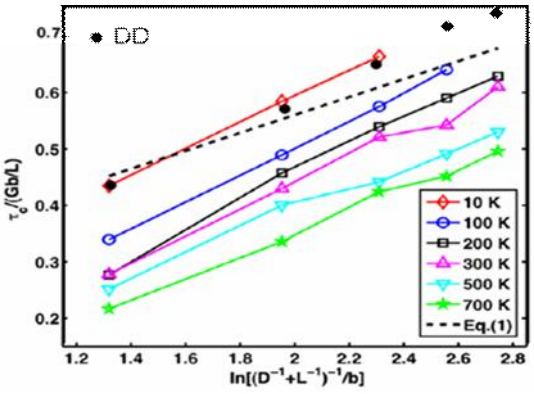

Figure 4: DD simulation of dislocation-cavity interactions obtained with τ_{facet} =1525MPa and comparison with MD simulations

CONCLUSIONS

It can be concluded from this simulation campaign that DD can reproduce the MD results obtained at T=10K with the Dudarev-Derlet potential if the cavity is represented by facets with a strength τ_{facet} =1525MPa. This local rule can now be used in large scale DD simulations.

REFERENCES

[1] Julien Chaussidon, Etude multiéchelle de la plasticité à basse température du Fer-α - Application au clivage, INPG thesis report, labo SIMaP-GPM2, 30 octobre 2007

[2] M. Verdier, M. Fivel and I. Groma, Mesoscopic scale simulation of dislocation dynamic in fcc metals: Principle and applications, Modelling and Simulation in Materials Science and Engineering, 6 (6), (1998)

[3] J. Chaussidon, M.C. Fivel and D. Rodney, The Glide of Screw Dislocations in BCC Fe: Atomistic Static and Dynamic simulations, Acta Materialia, 54, (2006)

[4] M. Mendelev, S. Han, D. Srolovitz and G. Ackland, Development of new interatomic potentials appropriate for crystalline and liquid iron, Philos. Mag. 83, (2003)

[5] CAST3M, Finite Element Software developed by CEA/DM2S/SEMT/LM2S

[6] S.M. Hafez Haghighat, M. Fivel, J. Fikar and R. Schäublin Dislocation–void interaction in Fe: A comparison between molecular dynamics and dislocation dynamics, to appear in Journal of Nuclear Materials (2009)

REPORTS AND PUBLICATIONS

Coupling DD code (BCC version) and FEM and application to dislocation-cavity interaction (static case)

Dislocation-cavity interaction (dynamic case) and comparison with MD simulations – (Final Report)

TASK LEADER

Marc FIVEL

Laboratoire SIMaP, Grenoble INP, CNRS
1130 rue de la Piscine – BP 76
F-38402 Saint Martin d'Hères Cedex

Tel: 33 4 76 82 64 63
Fax: 33 4 76 82 63 82

e-mail: marc.fivel@simap.grenoble-inp.fr

TW4-TTMS-007-D02

Task Title: MODELISATION OF IRRADIATION EFFECTS AB-INITION STUDY OF THE INTERACTION OF Cr ATOM AND PRECIPITATES WITH He AND He-V CLUSTERS IN α-Fe, AND TEM EXAMINATION OF SINGLE BEAM IRRADIATED Fe AND Fe-Cr MODEL ALLOY

INTRODUCTION

FeCr alloys are foreseen as strong candidates for future fusion applications, mostly as structural materials for the reactor vessel and tritium breeding blanket. As it is very well known experimentally, irradiation modifies the response of such an alloy reducing considerably its working lifetime. During irradiation with fast neutrons He and H are produced by transmutation. How He atoms interact with this base material is not well understood. In this report we investigate the influence of dilute Cr on the formation of HenVm complexes and how interstitial He diffuses close to such an atom.

2007-2008 ACTIVITIES

Method of calculation

Present calculations have been performed within the Density Functional Theory (DFT) as implemented in the SIESTA code [1]. The calculations are spin polarized and use GGA approximation. Core electrons are replaced by nonlocal norm-conserving pseudo-potentials. Valence electrons are described by linear combinations of numerical pseudo-atomic orbitals. The pseudopotential and the basis set for Fe atoms are described in ref. [2] where it was shown that this approach captures successfully the properties of self-defects in α-Fe. He-He interaction is described in reference [3] where the properties obtained using this methodology were satisfactory compared to those given by the DFT-PWscf code using plane waves and other more accurate calculations as configuration interaction calculations (CI) and quantum Monte Carlo (QMC) reaching the conclusion that the approach used is accurate enough for the type of calculations to perform. The maximum cutoff radius for the pseudo-potential of Cr is set to 1.26 Å, and its basis set consists in two and three localized functions for the 4s and 4p states respectively, and five for the 3d states.
The cut-off radii are 3.8 Å, 5.1 Å and 2.5 Å respectively. Supercell calculations were carried out to study the properties of several defects and defect complexes. Except for cases specified, all the following data have been obtained with a 128-atom supercell, using a 3x3x3 k-point grid and the Methfessel-Paxton broadening scheme with a 0.3 eV width.
The calculations were performed at constant pressure, therefore relaxing both, the atomic positions and the shape and volume of the supercell.
The diffusing paths were calculated using the drag method: the atomic positions relative to the center of mass are constrained to relax in the hyperplane perpendicular to the vector that connects the initial and the final states. Hereafter, the definition for the binding energy used is as the energy difference between the situation where the defects are infinitely separated from the complex and where it is added to the complex.

Cr and He in α-Fe and their interaction

Firstly, we studied various properties of Cr and He atoms in a α-Fe matrix and we compared our results with those from the literature. A summary of all these results is shown in table 1. We clearly see that our approach overestimates the magnetic moment of Cr, which is thought to lead to an increase in magnitude of its solution energy. Even though we are well aware of that, it is also true that the qualitative behaviour for those relevant values is in any case the same. Moreover, when calculating Cr-Cr or Cr-vacancy interactions, meaning basically the binding energy, the values as given by SIESTA and by more accurate Projector Augmented Wave (PAW) approaches as shown in table 1, get closer.

Table 1: Comparison of Cr behaviour in α-Fe between different approaches, plane waves (VASP) [4, 5] and norm-conserving pseudopotentials (SIESTA)

	Cr in Fe μ_B	*E_{sol} (eV) Cr in Fe*	*V-Cr exchange barrier in Fe (eV)*	*Cr-V 1nn (eV)*	*Cr-V 2nn (eV)*	*Cr-Cr 1nn (eV)*	*Cr-Cr 2nn (eV)*
PAW (VASP)	1.6-1.8	-0.12	0.54	0.06	0.01	-0.24	-0.12
NC (SIESTA)	2.55	-0.47	0.57	0.06	0.00	-0.36	-0.19

The binding energies between Cr and a substitutional He (He_{subs}) or a vacancy (V) and between two Cr atoms interaction are shown in figure 1. We choose that positive binding energies mean attraction. We show that the interaction values for Cr-V and Cr-He_{sub} are indeed negligible. The values for Cr-He_{Sub} and Cr-V and some for Cr-Cr are close to the precision of the approach (±0.05 eV). We can see as well, that the Cr-Cr interaction is strongly repulsive for first nearest neighbors (1nn), at least partly due to magnetic frustration. Only partly because second nearest neighbours interaction is also repulsive but there is no frustration in this case. This calculation has been stretched up to the 10th shell to check for a possible change in sign, as reported in [6]. In agreement with those results we also found that the binding energy becomes positive.

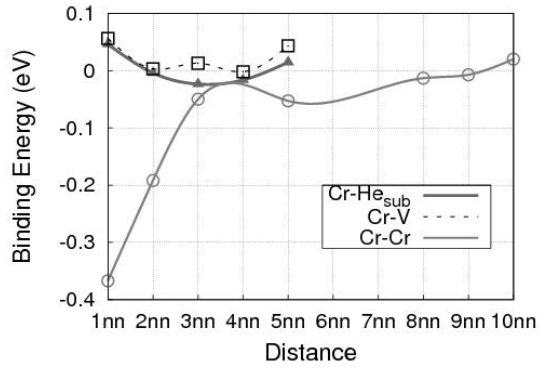

Figure 1: Binding energy between a Cr atom diluted into an α-Fe matrix and another Cr, or He_{Sub} atom or a V as indicated in the legend

However, image effects have to be ruled out through performing larger cell calculations in order to become conclusive.

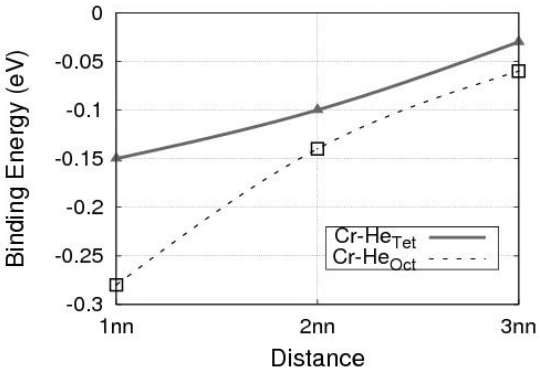

Figure 2: Binding Energies for $CrHe_{tet}$ and $CrHe_{oct}$

The binding energies between interstitial He, either tetrahedral or octahedral, and a Cr atom in a α-Fe matrix have also been analysed. Taking as reference the energy of a pure Fe system with a tetrahedral He in both cases, the obtained values are shown in figure 2.
We can see that the Cr-He_{tet} and Cr-He_{oct} interactions are always repulsive up to the third nearest neighbour configuration. For all considered structures, it follows from the plot that a tetrahedral site near a Cr atom is always more energetically favourable than an octahedral one. This repulsion suggests that in equilibrium, the concentration of He around an isolated Cr atom in a Fe matrix will be lower than the average He concentration in the matrix.
Analysing the diffusion path of a He interstitial atom between a tetrahedral and an octahedral site nearest neighbours as shown in figure 3, we may conclude that the octahedral site is in this case unstable as there is no energetic barrier between both sites. This means that close to a Cr atom, interstitial He sits always in a tetrahedral site. This behaviour is different from that in a pure Fe matrix where the octahedral site is metastable.

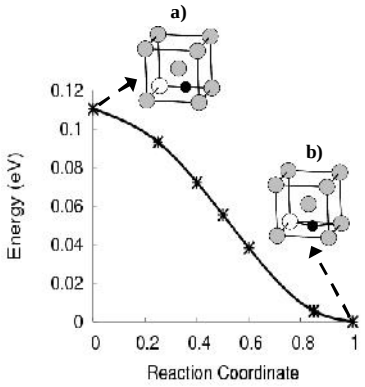

Figure 3: Diffusing path of interstitial He between an octahedral site 1nn of Cr (a) and tetrahedral site 1nn of Cr (b) (He:solid cicle, Cr: Open circle, Fe :Grey circle)

Cr effects on the formation of He_nV_m clusters.

We started studying the limiting cases: clusters containing either only vacancies (n = 0) or only interstitial He atoms (m = 0). We calculated the binding energies for the most stable configurations and compared the results for the same structures in pure Fe, as given in [3]. These lowest energy structures in the case of a Cr atom close to a pure He or vacancy cluster and their binding energies corresponding to reactions $Cr + He_n \rightarrow CrHe_n$ and $Cr + V_m \rightarrow CrV_m$ are shown in figures 4a) and 4b) respectively.

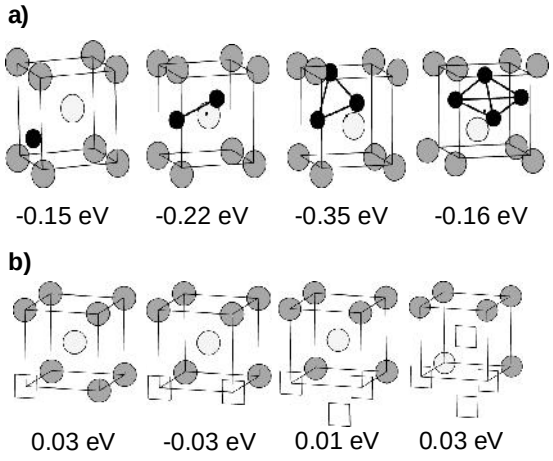

Figure 4: Lowest energy configurations for:
a) $CrHe_n$ complexes and binding energies of the reaction $Cr + He_n \rightarrow CrHe_n$
b) CrV_m complexes and binding energies of the reaction $Cr + V_m \rightarrow CrV_m$ (Negative values for repulsive interactions)

As we mentioned above, the binding energy of a tetrahedral He and a substitutional Cr is repulsive and equal to E^b=-0.15 eV. In general, the interaction between any He_n cluster and Cr is also repulsive, showing a maximum at n=3. We see as well that the interaction between a Cr atom and a vacancy cluster is very weak.
In figures 5a) and 5b) the binding energies for the reactions $CrHe_{n-1} + He \rightarrow CrHe_n$ and $CrV_{m-1} + V \rightarrow CrV_m$ are shown and compared with the corresponding reactions without Cr (Hen-1 + He → Hen and Vm-1 + V → Vm). In the former case (figure 5a), the energy that we gain adding a He to a He_{n-1} cluster is lower with a neighboring Cr than without it for n<4. However, this gain becomes higher for n = 4. For the case of vacancy clusters (figure 5b), the values are closer one from another. In both cases the gain of energy is always positive.

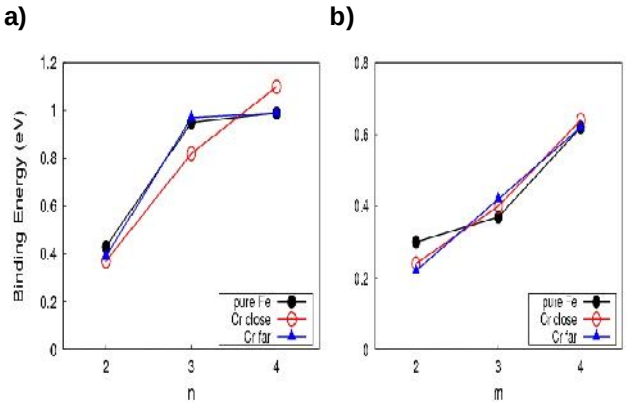

Figure 5: a) Binding energy for the reaction $CrHe_{n-1} + He \rightarrow CrHe_n$
b) Binding energy for the reaction $CrV_{m-1} + V \rightarrow CrV_m$

Tetrahedral He diffusion in dilute FeCr alloys

When He atoms are created by transmutation upon fast neutron irradiation, they occupy initially the most stable interstitial sites, i.e. the tetrahedral ones. In figure 6 the energy landscape for He diffusion between various tetrahedral sites is shown. We observe that the energy barrier for a He to move from second nearest neighbours of a Cr to first nearest neighbours is double ($\Delta E^{mig}_{Cr1nn}[He] \approx 0.12$ eV) the one in pure Fe ($\Delta E^{mig}_{Fe}[He] \approx 0.06$ eV) (see [3]).

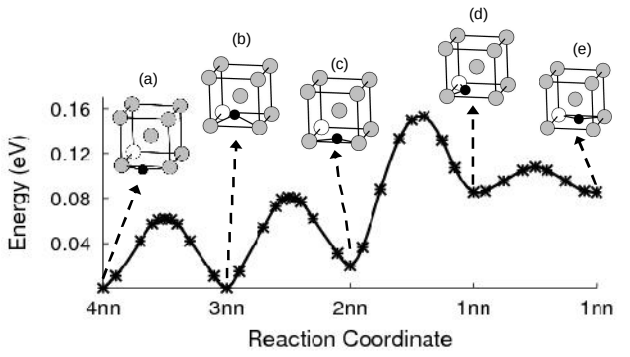

Figure 6: Energy landscape for a diffusing tetrahedral He in a dilute FeCr alloy. In black is represented the He atom, in white the Cr atom and in grey the Fe atom

This large difference in energy barrier implies that at a steady state, the concentration of He atoms around a Cr in an Fe matrix would be depleted from the concentration in the matrix. Moreover, the most probable path for the He diffusion is the one the furthest from the Cr atom. This means that the percolating effects induced in the He atom by the presence of Cr might be important at the time of the formation of bubbles. If that would be the case, in a dilute alloy, the formation of these bubbles would take place in the matrix, far from the Cr atoms. This possibility would be investigated by performing several kinetic Monte Carlo simulations including the tetrahedral sites.

TEM examination of single beam irradiated Fe and Fe-Cr model alloy

The experimental work done in 2008 consists in the sample preparation and microstructural TEM characterisation of the Fe-5wt.%Cr model alloy irradiated under mono-beam conditions within JANNUS at CEA-Saclay.

Materials and irradiation conditions

The materials studied were a high purity iron, with a carbon content of 3 wt. ppm and FeCr model alloys with the same amount of C and 5, 10 and 14 wt. % Cr. They were elaborated within the EFDA project at the Ecole des Mines de Saint-Etienne (F) by induction melting from high-purity metals. The C content was measured by oxidation melting after elaboration.
The resulted ingots were cold worked after a hot forging from 1000 to 1150°C. To release the stresses and get a well recrystallised material, final heat treatments were performed from 700 to 850°C under argon atmosphere for one hour followed by an air cooling. The grain size obtained is about 100 µm in all the materials.

The materials were irradiated under bulk shape (samples of 3 mm in diameter and 100 µm in thickness) with 10 MeV Fe ion within JANNUS with the Pelletron accelerator "Epiméthée". The irradiation temperature was 500°C. The Fe – 5 wt. % Cr studied by TEM was exposed to an ion flux of $7.66 \cdot 10^{11}$ ions.cm^{-2}.s^{-1} during around 21 hours. The damage generated is given in the figure 7. No degrader was used because the damage is quite homogeneous before the Bragg peak.

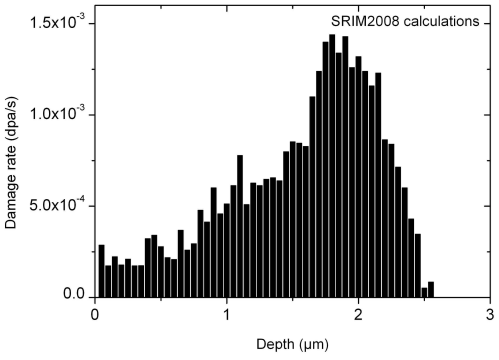

Figure 7: Profile of the damage rate induced by 10 MeV Fe ion in an iron target (SRIM2008 calculation [7]). An energy threshold of 40 eV for the iron atom displacement was chosen

The TEM characterisation was performed at the Department of Materials at Oxford University (UK) using a Philips CM20. Standard diffraction contrast methods were used to image point defect clusters [8]. Chemical analyses were performed using an Oxford Instruments INCA energy dispersive X-ray system (EDS).

Preparation of samples

The surface is a sink for the free migrating point defects (PD) and PD clusters. To reproduce in-service conditions of fusion plant materials, it is necessary to avoid the surface effect. That's why we need to irradiate bulk materials and to remove the surface to quantify the radiation-damage in the volume. Furthermore, since the damage generated by ions is strongly depth-dependant, it is necessary to know precisely the amount of material removed. It has to be high enough for the elimination of PD on the surface to be negligible compared with the other sinks (grain boundaries or dislocation lines). Starting from the 100µm-thick slices, a fixed thickness has to be removed from the irradiated side. To control this step, we combined electropolishing with indentations on the surface. The depth of the indents increased from 50 nm to 1250 nm by step of 50 nm. The thickness of material removed is controlled by noticing the disappearing of indents during the electropolishing. The electrolyte is composed of 10 % perchloric acid and 20 % butoxyethanol-2 in methanol at 40°C. The optimized voltage is 28 V. It corresponds to a current of about 0.8 A. A polishing rate of about 100 nm/s was obtained. The issue is that this value corresponds only to the first seconds of polishing. For longer time, indents are polished at the same time as the matrix so the control is not possible any more. Tests are actually ongoing using a profilometer. The thin foil is then prepared by the well-known back-thinning method.

Microstructural TEM characterisation of the ion irradiated Fe-5wt.%Cr model alloy

The Fe-5 wt. % Cr was electropolished after irradiation during 6 seconds. Assuming a polishing rate of 100 nm/s, a thickness of 600 nm from the surface, was removed. The damage rate in the area observed by TEM was thus $2\text{-}3\cdot10^{-4}$ dpa/s (figure 7) and the dose reached was 18-30 dpa. After irradiation, no dislocation loops are visible by TEM. However, a huge density of precipitates is present (figure 8). They have a length of around 1 µm and a thickness of around 100 nm. Furthermore, their mean Cr content is 46 ± 16 at. % Cr (figure 9b). In the matrix, the Cr depletion is quite low. The Cr content is equal to 4.6 ± 0.3 at. % Cr after irradiation (figure 9a) while a value of 5.2 at. % was measured before irradiation by chemical analyses.

The TEM analyses were not conducted on the other materials because it is likely that the samples were heated during irradiation. It is worth noticing that the irradiation temperature of 500°C refers to the temperature of the specimen holder. Since the thermal contact between the specimen holder and the specimen is not perfect, calculation of the sample heating is not possible. Measurements are ongoing with an optical pyrometer to quantify the heating.

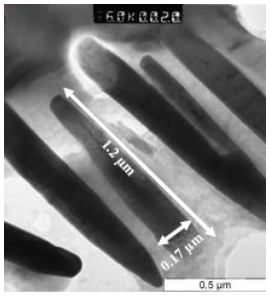

Figure 8: BFTEM image of the ion irradiated Fe-5 wt. % Cr

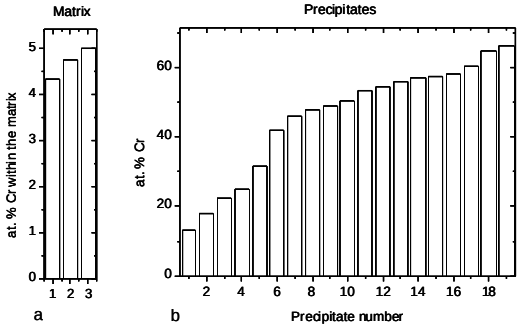

Figure 9: EDS analyses performed in the irradiated Fe – 5 wt. % Cr within the matrix (a) and on the precipitates (b)

CONCLUSIONS

On the modeling side, study of the interaction between a He atom and a Cr and Fe atom in a dilute FeCr alloy was carried out by ab-initio calculations. Although He is a closed shell atom, and both Fe-He and Cr-He interaction can be mainly described by simple pairwise repulsive interactions, unexpectedly, we noted a weak electronic interaction between He and either Fe in pure Fe or Cr in the dilute FeCr, The binding energies between either a substitutional He and a Cr atom in Fe or a vacancy and a Cr atom have been found to be negligible. On the other hand, the interaction between a Cr atom and an interstitial He is stronger and always repulsive. Moreover, the octahedral position first nearest neighbour of a Cr atom is unstable, and always decays to a tetrahedral position. From the study of the behaviour of He_nV_m clusters around a Cr atom we may conclude that the interaction He-Cr is rather strong which leads to increasing the dissociation energy of a vacancy from the cluster.

Diffusion of a tetrahedral He was studied as well and its diffusing landscape was depicted, showing that, because of the He_{int}-Cr repulsive interaction, there is an energy barrier for a He to get close to Cr in dilute alloys which might lead to percolation at low temperatures and the formation of bubbles the furthest from the Cr atoms.
On the experimental side, we report the preliminary results of the microstructural characterisation of the damage induced by ion irradiation in FeCr model alloys. The first step is the sample preparation. Tests are ongoing to define a well-controlled method allowing the removal of a known thickness at the surface of an irradiated specimen.

In addition, tests are ongoing to quantify the heating generated during irradiation at high ion flux within JANNUS (CEA-Saclay).

REFERENCES

[1] J.-M. Soler, J. Phys. Cond. Mat. 14 (2002)

[2] C.C. Fu, F. Willaime and P. Ordejon, Phys. Rev. Lett. 92, 175503 2004; C. C. Fu, J. Dalla Torre, F. Willaime, J.-L. Bocquet and A. Barbu. Nat. Mater. 4, 68 2005

[3] C. C. Fu, F. Willaime. Phys. Rev. B 72, 064117 (2005)

[4] T.P. C. Klaver, R. Drautz and M.W. Finnis, Phys. Rev. B 74, 094435 (2006)

[5] P. Olsson, C. Domain and J. Wallenius, Phys. Rev. B 75, 014110 (2007)

[6] P. Erhart, B. Sadigh and A. Caro, Appl. Phys. Let. 92,141904 (2008)

[7] J.-F. Ziegler, J.-P. Biersack, and U. Littmark. Stopping and Range of Ions in Matter., New York, (1985)

[8] M.-L. Jenkins, M.-A. Kirk, Characterisation of Radiation Damage by Transmission Electron Microscopy, Institute of Physics Series in Microscopy in Materials Science, (2001)

REPORTS AND PUBLICATIONS

[P1] C. C. Fu and E. Meslin,: ‘ab-initio study of the interaction of Cr atoms & precipitates with He and He-V clusters in α-Fe, and TEM examination of single beam irradiated Fe and Fe-Cr model alloy’, EFDA subtask 2008 report

TASK LEADER

Chu Chun FU

DEN/DMN/SRMP
CEA-Saclay
F-91191 Gif-sur-Yvette Cedex

Tel: 33 1 69 08 29 32
Fax: 33 1 69 08 68 67

e-mail: chuchun.fu@cea.fr

Task Title: IRRADIATION PERFORMANCE POST IRRADIATION EXPERIMENTS OF THE ARBOR2 IRRADIATION IN BOR-60 REACTOR

INTRODUCTION

Previous irradiation experiments showed that Reduced Activation Ferritic/Martensitic (RAFM) steels, which are candidate materials for the structures of future fusion devices, exhibit hardening and embrittlement (shift of the Ductile-to-Brittle Transition Temperature and decrease of fracture toughness) when irradiated at temperatures below approximately 400°C. However there is hardly any data on the mechanical behaviour of these steels for irradiation doses approaching the values to be reached at end of life in first wall materials.

Therefore, several RAFM steels were irradiated at 325°C to high doses in BOR-60 fast reactor as part of two successive experiments. The Post Irradiation Experiments of the materials irradiated up to a maximum dose of about 40 dpa in the first irradiation phase (ALTAIR experiment) have already been carried out [1, 2].

In a second phase (ARBOR-2 experiments), specimens previously irradiated as part of ALTAIR were re-irradiated up to 37 dpa together with new specimens. The purpose of the present task was to perform post-irradiation experiments (tensile and impact tests), whose main outcomes are summarized here after.

2007-2008 ACTIVITIES

The following materials were irradiated in the ARBOR2 experiment:

- Eurofer 97 (9Cr1WTaV), 9Cr2WTaV, 9Cr2WTaVB RAFM steels already irradiated in the ALTAIR experiment,
- Eurofer HIP joints and TIG welds and JLF1 (Japanese RAFM steel, 9Cr2WVTa).

These materials were produced as plates in the Normalized and Tempered metallurgical conditions and irradiated as tensile and subsize Charpy (KLST) specimens. After irradiation the specimens were shipped to CEA-Saclay hot laboratories where mechanical tests and fractographic examinations were carried out.

Tensile properties

The irradiated tensile specimens were tested in air at room and irradiation temperature. RAFM steels have retained significant ductility after irradiation up to the highest dose (78 dpa) as shown by the results of tensile tests (figure 1) as well as by Scanning Electron Microscopy (SEM) examinations of fracture surfaces. It must be emphasized that this behaviour is in contrast to that of conventional 9Cr steels, 9Cr1Mo (EM10) and 9Cr1MoVNb (T91) irradiated up to 42 dpa and which displayed much higher irradiation-induced hardening than RAFM steels together with a brittle failure mode (figure 1 and [2]). In this experiment, 9Cr2WB also displayed high hardening and a brittle behaviour when tested at room temperature. This may be an effect of the helium produced by boron transmutation during irradiation. Furthermore the marked difference of the tensile properties after irradiation of Eurofer TIG weld and HIP joints must be noted. HIP joints exhibited a tensile behaviour very similar to that of Eurofer irradiated to the same dose, while the TIG weld specimens displayed higher hardening and broke in a brittle manner during testing at room temperature.

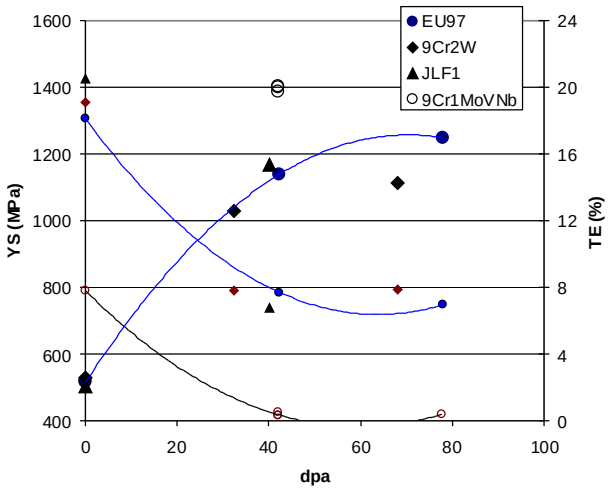

Figure 1: Evolution of the tensile properties (Yield Stress depicted by large symbols and Total Elongation, smaller symbols) measured at room temperature as a function of dose. Results obtained as part of the Altair experiment are indicated as well [1, 2]

Impact properties

Impact properties were measured following irradiation in ARBOR-2 of 9Cr2W (78 dpa) and JLF1 (40 dpa) subsize KLST specimens. Impact properties of Eurofer TIG welds and HIP joints (irradiated to 38 dpa) were determined as well. The obtained data are plotted in figure 2. As expected for tempered 9Cr martensitic steels irradiated at low temperature to high doses, irradiation induced a significant increase of the DBTT as well as a decrease of the Upper Shelf Energy (USE). However, the following points can be emphasized:

- the impact properties of 9Cr2W irradiated to 78 dpa have deteriorated only slightly compared to the properties measured following 32.5 dpa of exposure [2]. This is in agreement with the moderate increase of irradiation-induced hardening measured in the case of 9Cr2W. Furthermore it must be underlined that the impact behaviour of 9Cr2W irradiated to 78 dpa is much superior to that of conventional 9Cr-1Mo steels (EM10 and T91) irradiated to 40 dpa [2],

- As in the case of tensile properties, the impact behaviour of Eurofer HIP joints is better than that of TIG welds, in particular as regards the USE values.

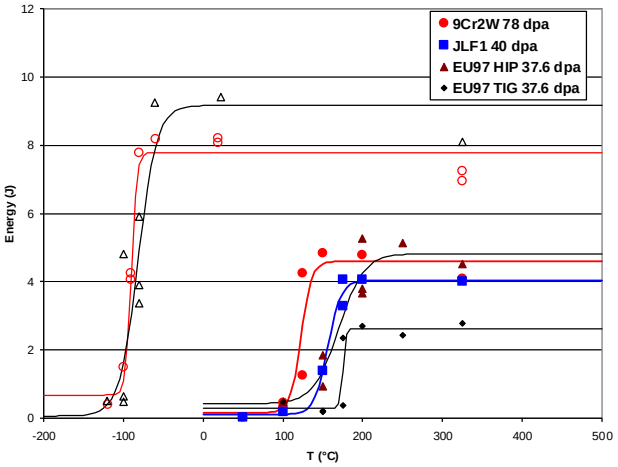

Figure 2: Impact properties of 9Cr2W, JLF1, Eurofer HIP joints and Eurofer TIG welds irradiated in BOR-60 reactor at 325°C to doses ranging from 38 up to 78 dpa. Empty symbols correspond to impact curves of unirradiated control specimens

CONCLUSIONS

The tensile and impact properties of RAFM steels (Eurofer 97, 9Cr2W, JLF1), Eurofer TIG welds and HIP joints were measured after irradiation in BOR-60 at 325°C to doses which ranged from 38 up to 78 dpa. The results can be summarized as follows:

- The irradiation induced hardening for Eurofer and 9Cr2W steels after 68-78 dpa of exposure is significantly less than the values measured in the case of conventional 9Cr-1Mo steels (EM10, T91) irradiated to 42 dpa [2]. The present results also show that 9Cr2W and Eurofer 97 retained significant ductility (Total Elongation values above 6% at room and irradiation temperature) up to 78 dpa, while 9Cr-1Mo steels displayed a fully brittle behaviour when tested at room temperature [2].
- Likewise, the impact properties of 9Cr2W irradiated to 78 dpa are much superior to those of 9Cr-1Mo steels irradiated to 40 dpa.
- Eurofer HIP joints irradiated to about 40 dpa displayed a better tensile and impact behaviour compared to TIG welds irradiated to the same dose.

Detailed microstructural examinations at the nanoscale (using techniques such as Transmission Electron Microscopy, Small Angle Neutron Scattering and possibly Tomographic Atom Probe) are now needed to understand the reasons for the significantly better mechanical behaviour of RAFM steels after low temperature irradiation compared to that of conventional 9Cr FM steels.

REFERENCES

[1] A. Alamo and J.L. Bertin, Post-irradiation examinations (PIE) of materials irradiated in BOR-60 at 325°C up to 42 dpa – Final Report TW2-TTMS-001-D02, CEA report NT SRMA 2005-2767, 2005

[2] A. Alamo, J.L. Bertin, V.K. Shamardin, P. Wident, Mechanical properties of 9Cr martensitic steels and ODS-FeCr alloys after neutron irradiation at 325 °C up to 42 dpa, Journal of Nuclear Materials, Volumes 367-370, 2007

REPORTS AND PUBLICATIONS

J. Henry, X. Averty, A. Alamo, Mechanical properties of Reduced Activation steels irradiated in BOR-60 at 325°C up to 78 dpa. Final Report – TW5-TTMS-001-D03, CEA report NT SRMA 2009-3004/A, 2009

TASK LEADER

Jean HENRY

DEN/DMN/SRMA/LA2M
CEA-Saclay
F-91191 Gif-sur-Yvette Cedex

Tel: 33 1 69 08 71 79
Fax: 33 1 69 08 99 35

e-mail: jean.henry@cea.fr

Task Title: QUALIFICATION FABRICATION PROCESSES CHARACTERIZATION OF WELDING DISTORSION OF SIMPLIFIED WELDED MOCK-UPS

INTRODUCTION

This work is part of developments aiming to process high quality welds according to Helium-Cooled Lithium-Lead (HCLL) DEMO Blanket Module design. Several parts of the test blanket module are planned to be joined by welding process.
This task follows the development of task TW2-TTMS-004-D02 and is in close link with the task TW2-TTBC-002-D02 (mock-up fabrication by CEA) and TW5-TTMS-004-D03 (residual stress characterization by ENEA).
The main task objective is to produce simplified mock-up of the TBM's stiffening grid assembly in order to characterize the residual stress and the distortion induced by the welding process. The experimental trials will be compared to numerical simulations carried out with the finite element code SYSWELD®.

2007-2008 ACTIVITIES

Two representative mock-ups of the cooling plates of the TBM welded by the YAG laser dual beam process have been realized and simulated considering a complete thermal metallurgical mechanical modeling. Comparison between calculation and neutron measurement (performed by ENEA) of the residual stresses has been carried out.

Weld pool modeling of the laser dual beam process

The mock-up consists in assembling two plates in EUROFER 97 by the laser dual beam process (figure 1). The laser dual beam process consists in two spots (both sides of the weld line) focalized on the top surface of the piece. The dimension of each plate is 100x45x8 mm^3 and it contains 2 channels (8x3 mm^2).

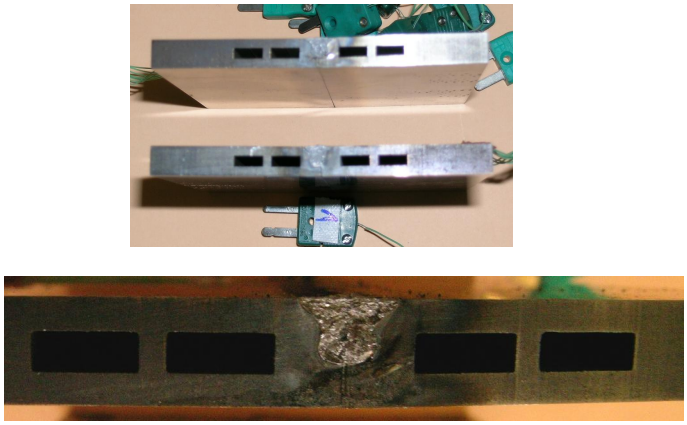

Figure 1: Cooling plates mock-up after welding

The mock-up was instrumented with thermocouples. By solving the inverse heat conduction problem the parameters of the heat input model of the laser dual beam process can be determined. The simulations carried out with this calibrated heat input model lead to very good agreement between simulation and experiment for the bead shape (figure 2) and thermal temporal evolution near the bead (figure 3).

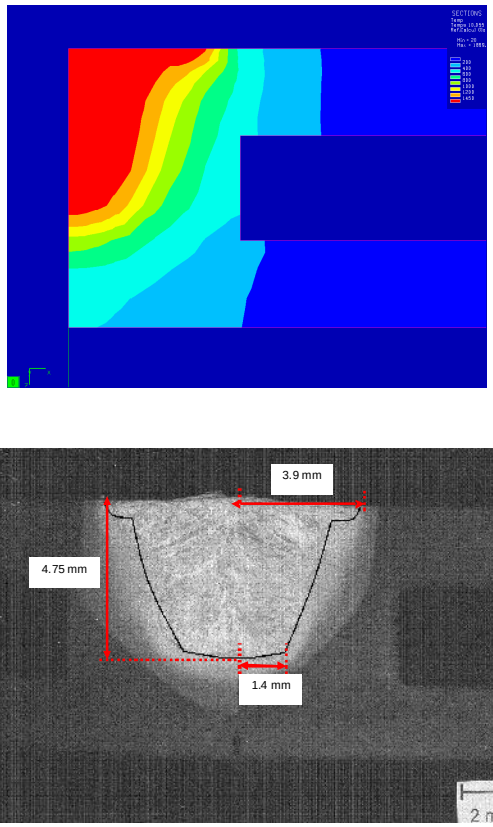

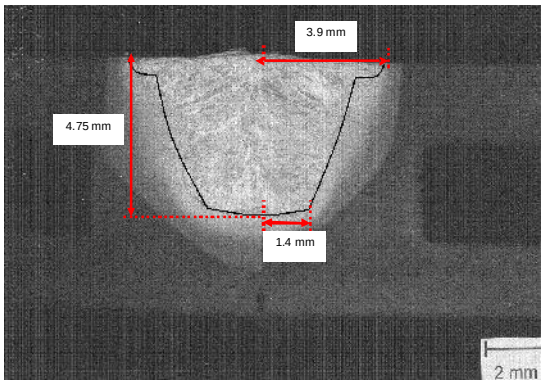

Figure 2: Simulation of the weld pool and comparison with macrographic cross section of the bead

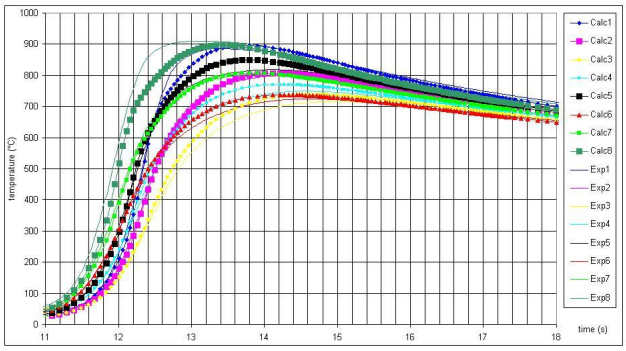

Figure 3: Comparisons between experimental and calculated temperatures

Calculation of residual stress distribution in the mock-up after welding and comparison with neutron measurement

The residual stress distribution is calculated (figure 4) according to the heat input model and the thermal metallurgical mechanical welding model designed for EUROFER 97. The maximum tensile stresses (750 MPa at the maximum) are in the longitudinal direction and are located in the welding line in the bulk of the piece. The maximum transverse tensile residual stresses are located mainly near the heat affected zone on the top surface of the pieces and are about 700 MPa at the maximum. High tensile residual stresses (530 MPa) are found on the internal face of the two channels.

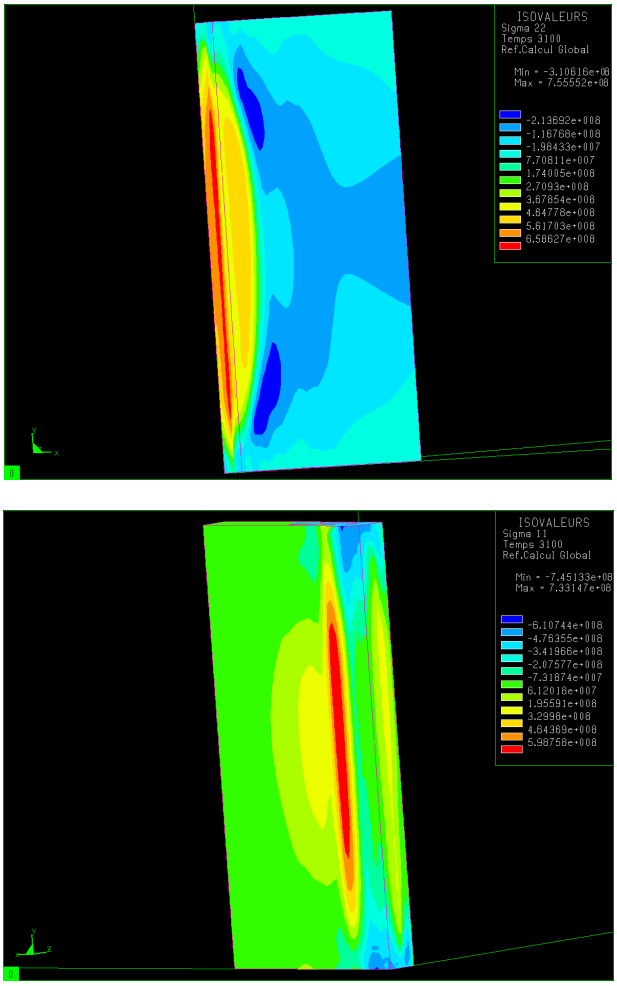

Figure 4: Longitudinal and transverse residual stresses distribution

Neutron diffraction measurements have been carried out (by ENEA in the frame of task TW5-TTMS-004-D03) at a depth of 1.25 mm from the top surface and at different distances from the weld line. The gauge volume is about 1.5 mm^3 and the stress free lattice has been measured remote from the weld (40 mm from the weld line) at a location where it could be assumed that the residual stress was close to zero. Results are presented in figure 5 with the corresponding predicted values by the finite element simulation.

Out of the bead a good agreement is found between predicted and measured residual stresses. Longitudinal stresses values are the most important and are quite well predicted but further neutron measurement are needed to complete the last performed.

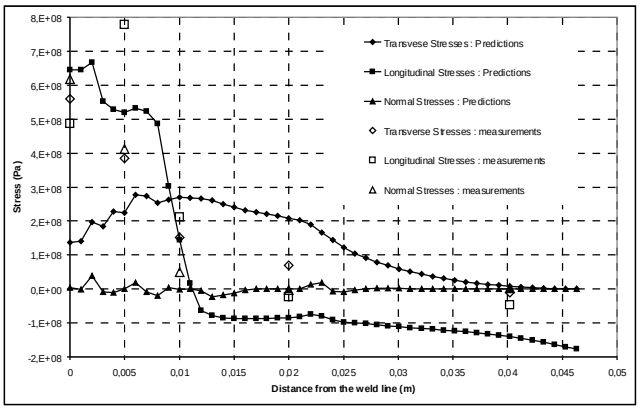

Figure 5: Comparisons between residual stress predictions and measurements

REPORTS AND PUBLICATIONS

A. Monnier - O. Asserin : "Thermomechanical FEA of a representative TBM welded mock-up: comparison with experimental measurements."
DM2S/SEMT/LTA/RT/08-004/A, Final report

TASK LEADER

Olivier ASSERIN

DEN/DM2S/SEMT/LTA
CEA-Saclay
F-91191 Gif-sur-Yvette Cedex

Tel: 33 1 69 08 37 21
Fax: 33 1 69 08 90 23

e-mail: olivier.asserin@cea.fr

Task Title: QUALIFICATION FABRICATION PROCESSES OPTIMISATION OF FILLER WIRE CHEMISTRY FOR EUROFER WELDS

INTRODUCTION

This task was launched to mitigate hot cracking problems, observed in some Eurofer welds (EB and Laser processes) and to reach a relevant stiffness level for Eurofer welds in the frame of ITER TBM Manufacturing. Selection of appropriate filler wire composition and welding technique are methods usually employed to solve hot cracking in the fusion zone. In this work wire chemical composition was optimised through metallurgical considerations, experience in Eurofer welding and 9Cr welding experience (same welding behaviour as Eurofer steel). Filler wire welding technique is applied with 4 available standard filler wires. GTAW (or TIG) were carried out to determine the trends of the filler wire chemical composition.

2007-2008 ACTIVITIES

SELECTION OF 4 FILLER WIRES

Coming from the upper conclusions, have been met. Resulting a round with several filler wire providers, it was decided the following procurement (table 1).

Ref.	Designation	Diameter (mm)	Target	Applications
1	SUPERCORE F92 FCW (Metrode Company)	1.2	Bringing more weld creep strength, and lower hardening level inside the fusion zone	9Cr steel flux cored wire for P92 alloy for operating at temp. up to 625°C and high temp. Rupture strengths up to 30% greater than for P91.
2	Thermanit MTS 616 (Böhler Welding group)	1.2	Considered as a prototype reference for the optimized filler wire performing same low activation work	P92 Filler Wire procuring high joint strength and creep strength, with good welding characteristics according to ASTM A 355.
3	Thermanit MTS 4 SI (Böhler Welding group)	1.2	Different chemical compositions compared to Supercore F92 FCW (Metrode) for matching the joining effect of some specific compounds on hot cracking effects.	P92 Filler Wire mainly dedicated to 12 Cr steels welding, good welding characteristics and high creep strength.
4	Eurofer	1	Same composition as base material	Eurofer welding

Table 1: Filler wires chemical composition

Filler Wire Chemical Composition					
Weight %	Eurofer Base Material	Ref. 1 Supercore F92 FCW	Ref. 2 Thermanit MTS 616	Ref. 3 Thermanit MTS 4 Si	Ref. 4 Eurofer Filler Wire
C	0,105	0,110	0,110	0,180	0,105
Mn	0,550	0,800	0,630	0,600	0,550
P	0,003	0,017			0,003
S	0,001	0,010			0,001
Si	0,030	0,300	0,220	0,300	0,030
Cu	0,005	0,050			0,005
Ni	0,030	0,500	0,690	0,600	0,030
Cr	8,950	9,000	8,800	11,000	8,950
Mo	0,005	0,450	0,530	1,000	0,005
Al	0,006	0,010			0,006
Nb	0,004	0,040	0,050		0,004
V	0,202	0,200	0,190	0,300	0,202
N2	0,038	0,040	0,050		0,038
O2	0,001				0,001
W	1,040	1,700	1,520	0,500	1,040
Ti	0,001		0,007		0,001
Co	0,009				0,009
B	0,001	0,003			0,001
Ta	0,140				0,140

Modelling metallurgical knowledge is not sufficient to predict weld phases, in different processes. Small differences in filler wire could affect modelling prediction, where the precise effect of each element is not available yet. Even ThermoCalcTM software must be coupled to other welding models. The much more advanced methods, Sysweld, is not precise enough for good predictions in terms of inter or intra granular composition. The modelling scale is too rustic to take into account the influence of some ppm differences of different compounds of the filler wire on the micro segregation inside the grains of the fusion zone. For determining the optimized filler wire chemical composition, several rules can be applied. Schaeffler diagram is commonly used, but errors produced lead to take into account another diagram: Lippold diagram dedicated to martensite/ferrite area. Cr and Ni equivalent formulae are the following:

$$Ni_{equivalent} = \%Ni + 35\times\%C + 20\times\%N$$
$$Cr_{équivalent} = \%Cr + 2\times\%Mo + 10\times(\%Al+\%Ti)$$

Iso-ferrite lines and austenite + martensite + ferrite / martensite + ferrite limit are shown in Delong diagram (figure 1).

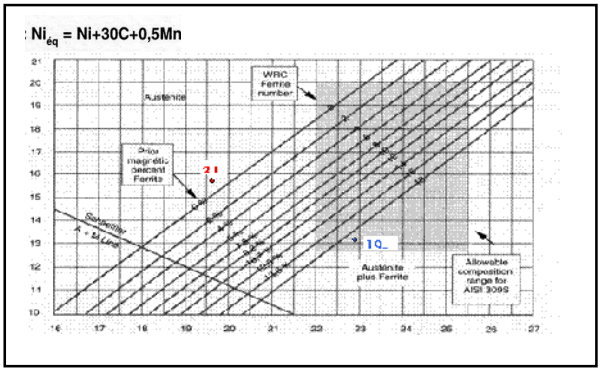

Figure 1: Delong diagram

Kaltenhauser factor (FF) allows the approximate prediction of delta ferrite apparition in martensite.

FF= %Cr + 6x%Si + 8x%Ti + 4x%Mo + 2x%Al+ 4x%Nb – 2x%Mn – 4x%Ni – 40x%C- 40x%N

For a FF value below 6, no δ ferrite appears. For a value above 11, δ ferrite appears. Between these two values, variable amounts of δ ferrite appear.

A second criterion can be used, called Chromium equivalent:

$Cr_{equivalent}$ = %Cr + 6x%Si + 4x%Mo + 1.5x%W + 11x%V + 5x%Nb + 12x%Al + 8x%Ti – 40x%C - 2x%Mn – 4x% Ni – 2x%Co - 30x%N - %Cu

A full martensitic structure at values below 8, δ ferrite can appear.

Those criteria produce partial conclusions with a high uncertainly level. In fact, if one takes into account only two criteria such as Cr eq. and Ni eq., it can be easily observed the low possibilities of acting on some compounds to respect the former criteria.

Welding trials

Welding trials were carried out using the GTAW (Gas Tungsten Arc Welding) process, in applying dedicated welding-tests in order to evaluate the tendency to hot-cracking vs. filler wire chemistry. Eurofer 97 plates were cut in coupons with dimensions 80 x 50 x 2 mm^3, for these experiments. The welding experiments were performed on an automatic gas tungsten arc welding machine Manager Plasma TIG. The welding equipment is composed of:

- Power source: NERTAMIC 300 TR,
- Welding torch: SAT TIG MEC 4,
- Welding torch nozzle diameter: 18 mm,
- Welding electrode: a 3.2 mm diameter tungsten electrode,
- Shielded gas: Arcal 1 (100% argon),
- Root shielded gas: Arcal 1 (100% argon).

Coupons were butt welded with a gap of 1 mm, with the following welding parameters (table 2).

Table 2: Welding parameters

Sample reference	Welding wire	Voltage (V)	Current (A)	Travel speed (cm/min)	Gas Type EN439	Gaz flow rate (l/min)
1A	Supercore F92 FCW	10,7	90	8	I1	20
2B	Thermanit MTS 616	10,2	90	12	I1	20
3A	Thermanit MTS 4 Si	10,6	90	12	I1	20
4A	Eurofer	10,2	95	15	I1	20

Visual aspect of the weld joint

Surface and root aspects of the weld joint are shown in figure 2. Excepted with the flux cored wire (Super core F92 FCW) much more difficult to process rather than full massive round wires, weld joints present a smooth and regular aspect. All welded joints exhibit a good penetration. Coupon welded with the flux cored wire reveal some slag residues.

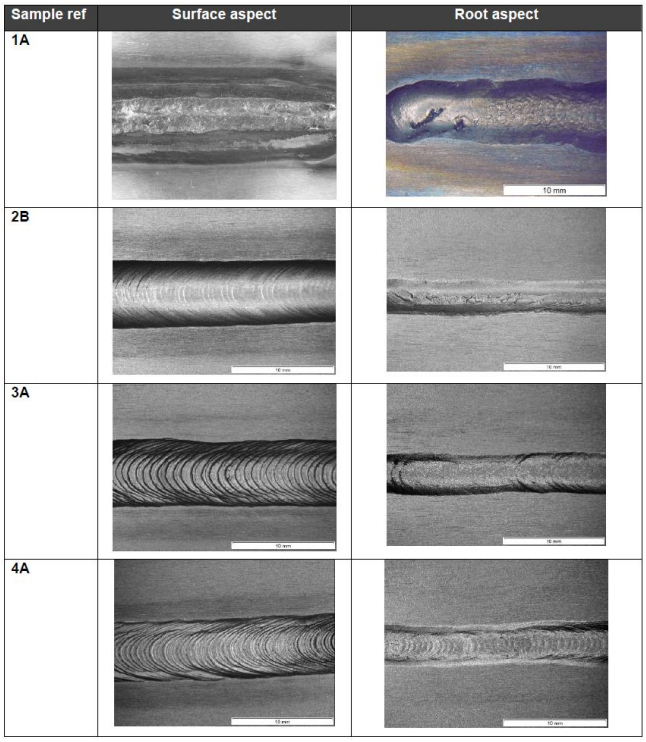

Figure 2: Surface and root aspects of the weld joints

Macrographic cross sections

All joints present a good compacity.
Indeed, no internal defects such as porosity or hot cracks are observed. However, slag inclusions are observed for sample reference 1A.

Micro hardness measurements

Vickers micro hardness measurements (HV1) were performed on cross sections of the weld joint. For each sample, 2 filiations were carried out: one at a 0.5 mm depth and the other at 1.5 mm depth from the top surface (figure 3).

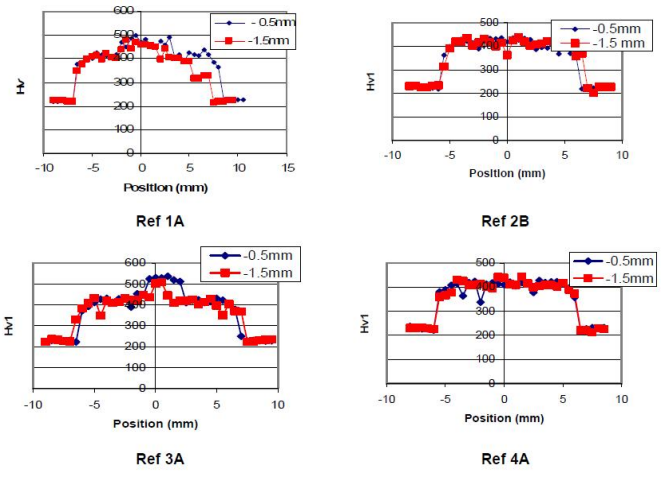

Figure 3: Micro hardness test results

The base material is characterised by a hardness of 210 HV1. In HAZ (Heat Affected Zone), an increase in hardness is observed. Indeed, close to the base material, the temperature reached is just above the critical temperature AC1. A partial austenisation is produced during heating and then the austenite formed is transformed to martensite during cooling. Close to the fusion zone, the temperature reached increases hence the volume fraction of martensite formed is higher. The hardness progressively increases. Above AC3, the material is fully transformed to a martensitic structure and the hardness reaches about 400 HV1. With the Supercore F92 FCW and Thermanit MTS 4 Si filler metal, the fusion zone hardness reaches in average 500 HV1 whereas with Thermanit MTS 616 and Eurofer Filler metal, the hardness reaches in average 400 HV1.

Micrographic analysis

Figure 4 shows the evolution of microstructure from the base material to the fusion zone of the sample ref 1 A.

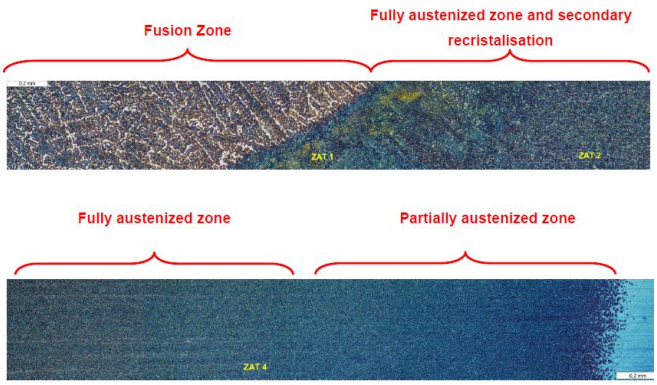

Figure 4: Microstructure evolution in the welded joint ref A1

The base material is composed of a tempered martensitic matrix. In the HAZ, close to the base material, due to a partial austenisation during heating, the microstructure is composed of tempered martensite and fresh martensite. A partial grain refining is observed. Closer to the fusion zone, the microstructure becomes fully martensitic due to a total austenisation. Close to the fusion zone, the grains grow due to a secondary recristalization (Grain coarsening region).This microstructure evolution in the HAZ is similar whatever the filler metal.

With the flux cored wire, some inclusions were observed in the fusion zone. No other internal defects such as porosity or cracks were revealed. The hardness measurements show differences in fusion zone. These hardness's are comprised between 400 HV1 and 500 HV1 according to the filler metal. This difference depends on the composition of the welding consumables which implies differences in chemical composition of the fusion zone. In the fusion zone, the structure is fully martensitic whatever the filler metal. In the HAZ, close to the base material, the microstructure is composed of tempered martensite and transformed martensite. Closer to the fusion zone, the microstructure becomes fully martensitic. Close to the fusion zone, the grains grow due to a secondary recristalization.

One key conclusion can be expressed:
Whatever the filler Wire chemical composition, even for wires out the standard selection window for 9 Cr families, no hot and cold cracks are observed. No defects and very good compacity were processed.

With the flux cored wire, some inclusions were observed in the fusion zone. No other internal defects such as porosity or cracks were revealed. The hardness measurements show differences in fusion zone. These hardness levels are comprised between 400 HV1 and 500 HV1 according to the filler metal. This difference depends on the composition of the welding consumables which implies differences in chemical composition of the fusion zone. It was clearly shown [6] the benefit of an optimized PWHT which decrease strongly to a rate of 300 HV1 in fusion zone by applying by example 750°C – 2 or 3 hours.

The only way to discriminate filler wires is mechanical tests:

- Tensile,
- Bending,
- DBDT, shear,
- Creep,
- …

This shows the huge mechanical and metallurgical efforts to follow, due to the nowadays lack of real predictive behaviour modelling.

CONCLUSIONS

Eurofer weldability can be concluded as not critical for the TBM development. Whatever the filler Wire chemical composition, even for wires out the standard selection window for 9 Cr families (12 Cr steels), no hot and cold cracks are observed in Eurofer welds. Defect free welds and in fact very good compacity have been achieved. Even at micro structural levels, no internal defects such as porosity or cracks were observed. The hardness measurements show differences in fusion zone, comprised between 400 HV1 and 500 HV1 according to the filler metal. This difference depends on the composition of the welding consumables which implies differences in chemical composition of the fusion zone. The benefit of an optimized PWHT, such as 2-3 hours at 750°C, that can reduce the hardness to about 330 HV1 in the fusion, is demonstrated.

TBM welds can be classified in thin section wall category: below 40 mm, with typical thicknesses of 5 – 11 – 25 – 40mm. The thickness of 40 mm is quite thin in the field of nuclear or chemical components, where sections of 100mm are common. Section thicknesses in TBMs can be compared with those of pipelines. So the rules and guidelines of thin thickness welding must be used, rather than those recommended for 100mm thickness. For example, δ ferrite problems that exist in large thickness welding are not present in thin section welding. The important work, quite well published, developed by standard industry, can provide basic guidelines for the future Eurofer welding developments without the need for extensive theoretical considerations.

Modelling of metallurgical knowledge is not sufficient to predict welds phases in different welding processes. Prediction of small differences in filler wire compositions would need a high modelling precision that is not available yet. Therefore, more considerations should be given to the experience of welding laboratories and metallurgist experts in Institutes or martensitic steel producers and filler wire manufacturing companies.

It is concluded that Eurofer weldability is not a critical problem during TBM manufacturing. A wide chemical composition window can be investigated, that in turn would allow developers to focus on low activation elements and compositions with improved creep strength. This conclusion is indeed good news for the TBM development and can allow significant savings in TBM budget.

REPORTS AND PUBLICATIONS

EFDA TW6-TTMS-004 - Filler Wire Task, Final Report, Philippe AUBERT, CEA/DEN/DM2S/DIR/RT/08-0008/A, December 2008

TASK LEADER

Philippe AUBERT

DEN/DM2S
CEA-Saclay
F-91191 Gif-sur-Yvette Cedex

Tel: 33 1 69 08 37 99
Fax: 33 1 69 08 66 42

e-mail: philippe.aubert@cea.fr

Task Title: MATERIAL MODELLING IMPROVED FATIGUE LIFE PREDICTIONS AT LOW STRAINS

INTRODUCTION

This task can be divided in two parts that correspond to the two main topics studied:

- modelling of the fatigue behavior of 316L stainless steel polycrystals,
- modeling of the influence of microstructure on the development of the plasticity at the crack tip of microstructurally short fatigue cracks and the possible effect on crack propagation (acceleration / arrest depending on the local microstructure).

First topic is required for proposing and adjusting constitutive laws at the grain scale.

2007-2008 ACTIVITIES

Simulation of the cyclic response of 316L single crystals and polycrystal using three dimensional elastic-plastic crystalline finite element computations

In this section, we present FE element calculations performed using UMAT's subroutine implemented in the finite element code Cast3m in order to simulate the fatigue behavior of 316L single crystals and polycrystals. Generally, to determine the hardening law that will govern the stress strain response of each grain of a polycrystals, inverse identification is used (the law is chosen such that it reproduces the behavior of the polycrystal).
However, the originality of the work presented here stems from the fact that, no inverse identification is made, and the hardening law is identified at the scale of the "grain" using experimental data on single crystals.

The main results obtained are summarized in the publication written for MSMF5 Conference held in BRNO in june 2007.
The same approach is used to model the fatigue response of other FCC alloys.

In the work presented here an elastic-plastic crystalline finite element method is used to simulate the cyclic behavior of 316L austenitic stainless steel single crystals and polycrystal. The evolution of the back stress on each slip system is described using a non linear kinematics hardening law to account for the hardening induced by long range dislocation interactions. As the contribution of short range interactions is assumed to be negligible, the value of the friction stress is kept constant. Three dimensional finite element calculations are performed to simulate the cyclic stress strain curves in the case of a single crystal oriented for multiple slips, as well as for the case of the polycrystal. Simulations are compared to experimental data. They seem to be satisfactory for low strain values ($\Delta\varepsilon_p\backslash 2 < 10^{-3}$) whereas, for $\Delta\varepsilon_p\backslash 2 > 10^{-3}$, they underestimate the hardening observed experimentally.

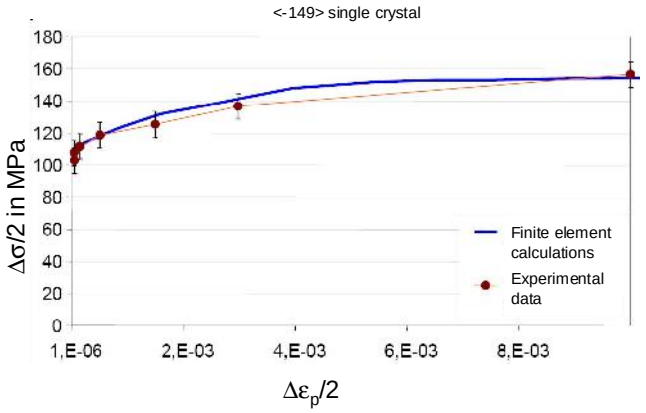

Figure 1: Cyclic stress strain curve obtained by finite element calculations for an austenitic stainless steel single crystal <-149> oriented for single slip. The experimental values obtained by Gorlier et al. are also represented for comparison

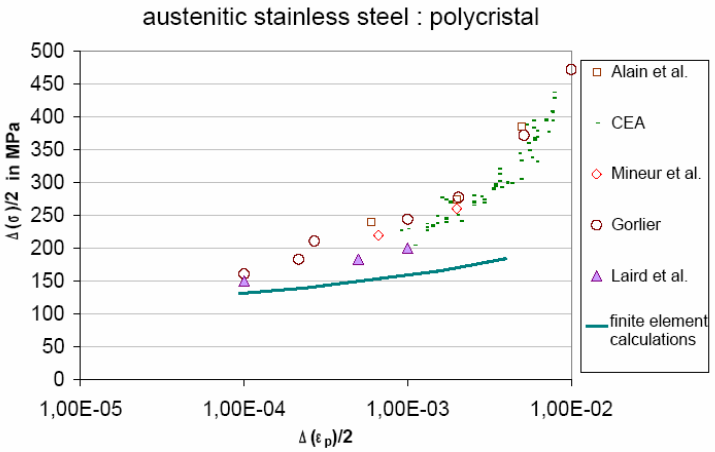

Figure.2: The curve represented by a plain line corresponds to the cyclic stress strain curve obtained by finite element calculations for a polycrystal composed of 216 grains. The different symbols correspond to experimental values obtained by different authors for 316L stainless steel

Study of the influence of microstructure on fatigue crack propagation in the high cycle fatigue regime in 316L steel

In this part, we study the influence of the microstructure i.e. crystallographic orientation of the grains, on the propagation of microstructurally short fatigue cracks. These cracks are said to be short because their size is comparable to the grain size. As these cracks are small, the plasticity at the crack tip is not confined. Therefore, linear elastic fracture mechanics concept, such as stress intensity factor

and fatigue crack propagation law, that are used to predict the fatigue life of large structure cannot be used.
To be able to determine the total fatigue life of real structure, it is important to understand the contribution of the microstructure on crack propagation.
A bibliographical study also showed that, among the different factors that can be responsible for the scatter in the number of cycles to failure observed in the high cycle fatigue regime, the microstructure is a non negligible one. Its contribution to scatter in lifetime being very difficult quantifies; some modeling would help to do so.
To study the influence of the microstructure on crack propagation, we will concentrate on the very first stages of fatigue crack propagation just after initiation. The crystallographic configuration studied, as well as the main results obtained is summarized in the publication written for the ICFRM13 conference.
In this study, three dimensional finite element calculations taking into account cubic elasticity and crystalline plasticity are performed in order to quantify the influence of the crystallographic orientation on the development of the plasticity at the crack tip of microstructurally short cracks in 316L stainless steel.
The case of a transgranular stage I crack that "propagates" towards a grain oriented for multiple slip is considered. The values of the crack tip opening/sliding displacements are calculated for the crack located at different distances of the multiple slip grain. Two multiple slip orientations are considered for this adjacent grain: a <111> orientation and a <1-10> orientation. Calculations show that the opening/sliding displacement at the crack tip is higher (up to a factor 1,7) if the crack propagates towards a <1-10> grain than towards a <111> grain. This could imply that propagation towards a <111> grain is more difficult than towards a <1-10> grain.

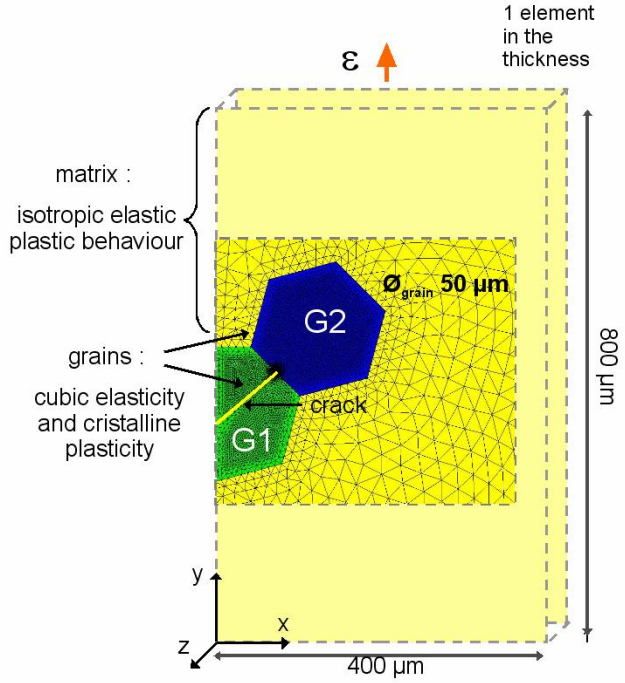

Figure 4: Finite element mesh representing grain G1 containing the stage I crack, the adjacent grain G2 and the surrounding polycrystalline matrix. The displacement is applied on the upper surface along the z axis

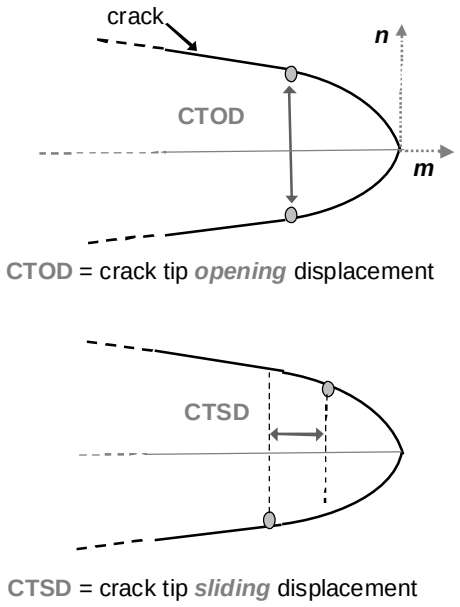

*Figure 5: Schematic representation of the crack tip opening displacement and crack tip sliding displacement. The vector **m** is the slip direction and **n** is the normal to the slip plane*

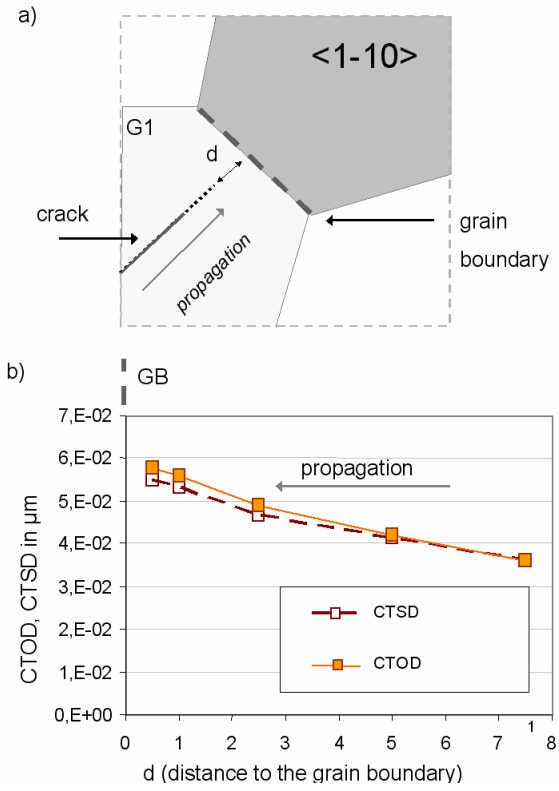

Figure 6: (a): Schematic representation of the crack located at a distance d to the grain boundary between G1 and the <1-10> grain (4 slip systems with a Schmid factor of 0,408)
(b) Evolution of the CTOD and CTSD with the distance (d) between the crack tip and the grain boundary along the [1-10] direction ; decreasing values of d correspond to the propagation towards grain <1-10>

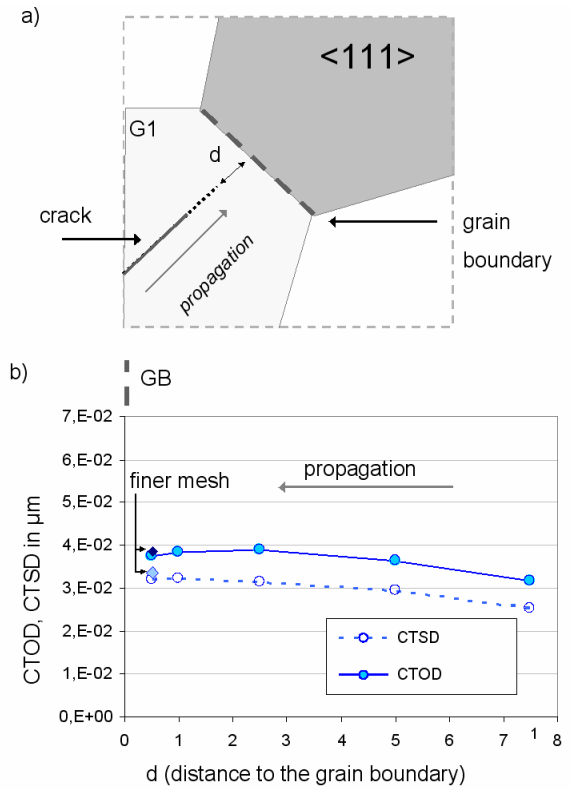

Figure 7: (a): Schematic representation of the crack located at a distance d to the grain boundary between G1 and a <111> grain (6 slip systems with a Schmid factor of 0.27).
(b) Evolution of the CTOD and CTSD with the distance (d) between the crack tip and the grain boundary along the [1-10] direction ; decreasing values of d correspond to the propagation towards grain <111>.

CONCLUSIONS

Concerning First topic, the modeling of FCC polycrystals and more particularly for 316L, it will be necessary to improve the hardening law used to better mimic the behavior or each grain, and more particularly the number of activated systems, and also, to consider the fact that grain that exhibit multiple slip behave in a different way than single slip and could hence be modeled by a different law.

Concerning Second topic, it will be interest to consider more realistic microstructures (experimental data given by Patrick Villechaise (ESMA – Poitiers – France) will be used) and also other misorientations (effect of tilt or twist angles with respect to the crack plane in the first grain). If a large number of random microstructures could be considered and the corresponding crack evolution numerically evaluated then, this modeling could help to evaluate the scatter in lifetime induce by the random character of the polycrystalline microstructure.

TASK LEADER

Maxime SAUZAY and E. FERRIE

DMN/SRMA
CEA-Saclay
F-91191 Gif-sur-Yvette Cedex

Tel: 33 1 69 08 35 67
Fax: 33 1 69 08 71 67

e-mail: maxime.sauzay@cea.fr

TW6-TTMS-007-D02

Task Title: MODELISATION OF IRRADIATION EFFECTS COMPREHENSIVE AB-INITIO STUDY OF GRAIN BOUNDARIES IN α– Fe, EQUILIBRIUM CONFIGURATIONS AND MIGRATION PATHWAY OF He IN GRAIN BOUNDARIES

INTRODUCTION

Ferritic steels play an important role as structural materials for future fusion reactors. One of the principal sources of their mechanical property degradation is the inter-granular embrittlement caused by segregation of solutes at grain boundaries (GBs). In particular, fusion reactors create 14 MeV neutrons that interact with the structural material, which cause nuclear transmutations and create significant amount of helium. The formation of helium bubbles at GBs is known to lead to high temperature embrittlement. First principle calculations provide quantitative descriptions of the interaction of He atoms with grain boundaries at atomic scale, which is not directly accessible through experiments.
In 2006, ab-initio and empirical potential (EP) calculations were performed to study properties of representative symmetric tilt grain boundaries in α-iron. Density Functional Theory within the Generalised Gradient Approximation is used to study the structural, energetic and magnetic properties of two representative Σ3 GBs in bicrystals containing a few hundred atoms. The interactions of He and these GBs are indeed attractive. We found that, unexpectedly, the lowest energy sites for isolated He atoms are substitutional at the rather compressed sub-interface layer rather than interstitial at the interface. Also, He atoms prefer to be in GBs with large excess volume and high formation energy. We noted that even isolated He atoms contribute to decrease the inter-granular cohesion up to 3 eV/He, which is of the same order of magnitude as the cohesive energy of bcc iron.
These ab-initio data are compared to EP results using similar and much larger systems, which allow to validate the existing Fe-Fe and Fe-He empirical potentials and to suggest hints to fit new, improved ones. The present study is a first promising step towards a predictive description of the segregation of He at GBs in the steels.

2007-2008 ACTIVITIES

Method of calculation

We considered two symmetric tilt grain boundaries with the (110) tilt axis: Σ3 {112} and Σ3 {111} with respectively small and large excess volume [1]. Supercells containing two identical GBs are used, and periodic boundary conditions are applied in all the three directions, either parallel or perpendicular to the GB plane. Ab-initio calculations were performed using Density Functional Theory (DFT) within the Generalised Gradient Approximation as implemented in SIESTA code [2], while empirical potential calculations were carried out using a FS [3] potential for Fe-Fe, and a new pairwise potential [4] for Fe-He interaction. It is worth mentioning that this Fe-He pair potential, recently developed by Juslin et al. has been fitted on DFT results and therefore describe satisfactorily the relative stability of interstitial and substitutional sites for He in iron. All the following *ab-initio* results correspond to 192 atom cell simulations with 24 atomic layers parallel to the GB plane and 8 atoms per layer.

Migration of He at grain boundaries

Ab-initio and complementary molecular statics and dynamics simulations were carried out using empirical potentials. Migration properties of an interstitial He, and of a substitutional He by dissociation mechanism near the grain boundary Σ3 {112} (110) are discussed below, and compared with the migration of He in the bulk.

First, we studied the migration of an interstitial He parallel to the GB plane. Finite temperature molecular dynamics simulations (MD) were used to extensively explore the low energy migration paths of an interstitial He parallel to Σ3 {112} (110) GBs (figure 1). Then accurate DFT calculation was performed to calculate the corresponding energy barrier. The obtained DFT value at 0K is 0.13 eV which is rather smaller but of the same order of magnitude than the EP results (table 1). All these migration barriers are indeed much higher than the corresponding energies in the bulk (0.06 eV). Therefore, our results predict that interstitial He migration along the GB may be unexpectedly slower than in the bulk.

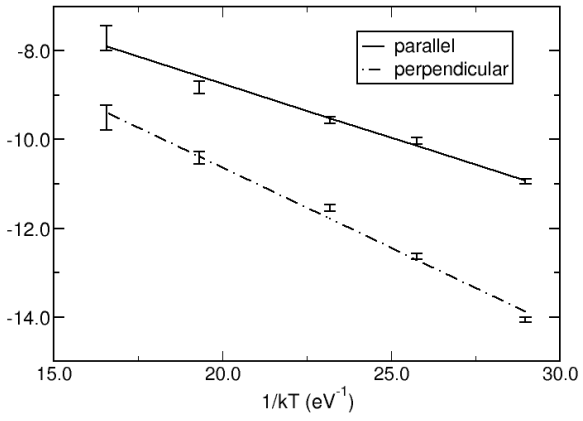

Figure 1: Arrhenius plots of interstitial He migration parallel to a Σ3 {112} grain boundary and from the GB to the bulk. The results come from 400–700K molecular dynamics simulations using empirical potentials, where the statistical error bars are shown.The activation energies (pre-exponential factors) of the parallel and perpendicular migrations are 0.24 eV ($1.8x10^{13}$ Hz) and 0.36 eV ($3.3x10^{13}$ Hz) respectively

Concerning the diffusion of substitutional He parallel to the grain boundary plane, we investigated in detail the dissociation mechanism which is the dominant He diffusion mechanism in the bulk when thermal vacancies prevail [5]. The corresponding effective diffusion energy can be written as the sum of two terms as shown in Table 1: the difference in formation energy of interstitial and substitutional He nears a GB, and the migration energy of an interstitial He parallel to the GB. The first term was found to be 0.29 eV and the second 0.13 eV for Σ3 {112} (110) according to our DFT results. As a consequence of the slow migration of interstitial He near this grain boundary, the diffusion of substitutional He by dissociation is also slower along the GB than in the bulk. However, this result is expected to be reversed for GBs with larger free volume, where interstitial He will have lower formation and migration energies.

Table 1: Differences between formation energies of an interstitial and a substitutional He ($E^f(He_{int}) - E^f(He_{sub})$), migration energy of an interstitial He ($E^m(He_{int})$) and a substitutional He by dissociation mechanism ($E^m_{dis}(He_{sub})$) are calculated for He in the bulk and near a Σ3{112} grain boundary.Migration energies resulting from both static 0K and finite temperature molecular dynamics simulations are shown

	Bulk		Σ3 {112}		
	DFT (0K)	EP (0K)	DFT (0K)	EP (0K)	EP (400K-700K)
$E^f(He_{int}) - E^f(He_{sub})$ (eV)	0.17	0.31	0.29	0.18	0.18
$E^m(He_{int})$ (eV)	0.06	0.06	0.13	0.32	0.24
$E^m_{dis}(He_{sub})$ (eV)	0.23	0.37	0.42	0.50	0.42

Dissociation barrier of interstitial He to escape from the Σ3{112}(110) GB was also evaluated by performing finite temperature MD simulations, the obtained value is 0.36 eV according to this Fe-He pair potential, which is indeed larger than the He migration barrier along this GB according to the same potential (0.24 eV). He atoms are therefore expected to preferentially diffuse along grain boundaries rather than going to the bulk. This ratio between the parallel diffusion and dissociation rates are expected to be even larger for grain boundaries with higher excess volume due to the increase of He-GB binding energy as function of excess volume.

Small He-vacancy clusters near grain boundaries

In order to understand the behaviour of He-vacancy clusters near GBs, we started investigating the lowest energy configuration of small He_nV_m complex (n, m = 1, 2) near a Σ3{112} or a Σ3{111} grain boundary by DFT calculations. Then we calculated their binding energies with these two grain boundaries, and we evaluated the stabilities of these He_nV_m complexes by measuring respective He-complex and vacancy-complex binding energies.
The following results are interesting to be pointed out:

- All these small complexes (HeV, HeV_2, He_2V, He_2V_2) are attracted by these grain boundaries as well as the single defects (V, and He_{int}), their binding energies depend mainly on the characteristics of the GB i.e. the binding are systematically stronger for GBs with larger excess volume (figure 2).

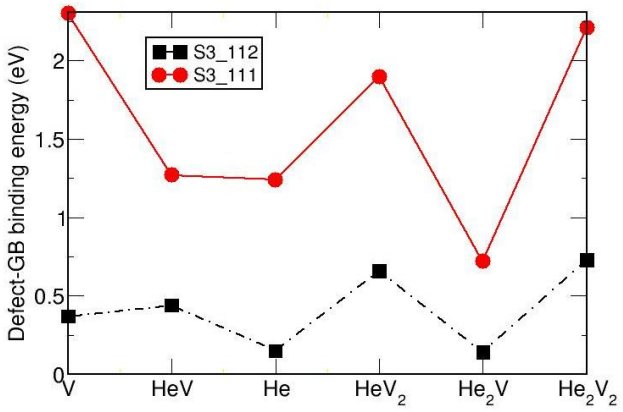

Figure 2: Binding energies between He_nV_m complexes (n, m = 1.2) and a Σ3 {112} or a Σ3 {111} grain boundary

- Vacancy-rich complexes (V, HeV_2, He_2V_2) have systematically larger binding energies with a given grain boundary (figure 2).

- Mainly due to the competition between vacancy-helium, and vacancy-GB attraction, the small He_nV_m complexes are less stable near GBs than in the bulk (figure 3). In particular, their stabilities significantly decrease when located near GBs with larger excess volume. Small vacancy-helium clusters are expected to hardly survive in large free volume GBs at moderate and high temperatures. These results suggest that the formation mechanism of bubble/voids near GBs observed at high temperatures may be very different from the one in the bulk.

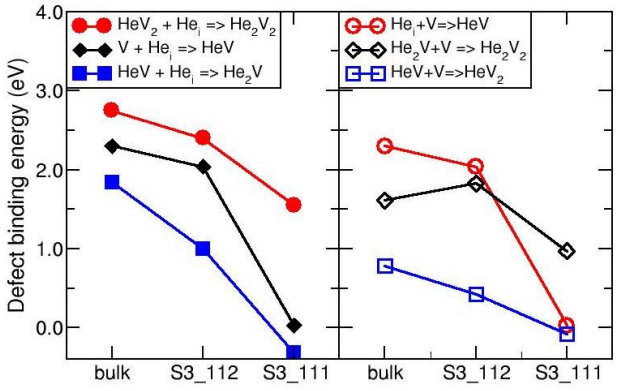

Figure 3: Binding energies of He_nV_m complexes (n, m = 1, 2) in the bulk, and near a Σ3{112} or a Σ3{111} grai

CONCLUSIONS

Density functional theory and empirical potential calculations were carried out to study the migration of interstitial and substitutional He near a Σ3 {112} GB.
We showed that parallel migrations to a small free volume GB e.g. the Σ3 {112} may be significantly slower than the

corresponding He migration in the bulk when thermal vacancies dominate.

The present study also reveals that the interaction between small He_nV_m (n, m = 1, 2) clusters and both Σ3 grain boundaries are indeed attractive. These attractions are shown to be stronger for the GB with larger excess volume, i.e. Σ3 {111}, whereas the stability of these small helium-vacancy clusters has a reversal trend. Also, these clusters are generally less stable near a GB than in the bulk.

REFERENCES

[1] R.J. Kurtz and H.L. Heinisch, J. Nucl. Mater, 329-333, 1199, (2004)

[2] J.M. Soler, E. Artacho, J.D. Gale, A. Garcia, J. Junquera, P.Ordejon and D. Sanchez Portal, J. Phys. Cond. Matter 14, 2745 (2002)

[3] G. J. Ackland, D. J. Bacon, A. F: Calder, and T. Harry, Phil. Mag A 75, 713 (1997)

[4] N. Juslin and K. Nordlund, to be published

[5] C.C. Fu and F. Willaime Phys, Rev. B, 72, 064117 (2005)

REPORTS AND PUBLICATIONS

[P1] C. C. Fu, Ab-initio study of He in grain boundaries in α-Fe, EFDA subtask 2007 report

[P2] C. C. Fu, Ab-initio study of He in grain boundaries in α-Fe, EFDA subtask 2008 report

[P3] N. Gao, C.C. Fu, S. Samaras, R. Schaublin, M. Victoria and W. Hoffeiner, J. Nucl. Mater. 385, 262 (2009)

TASK LEADER

Chu Chun FU

DEN/DMN/SRMP
CEA-Saclay
F-91191 Gif-sur-Yvette Cedex

Tel: 33 1 69 08 29 32
Fax: 33 1 69 08 68 67

e-mail: chuchun.fu@cea.fr

TW6-TTMS-007-D08

Task Title: MATERIAL MODELLING AB-INITIO INVESTIGATION OF SCREW DISLOCATIONS IN Fe

INTRODUCTION

The objective of this work is to provide a quantitative description, from first-principles – or *ab-initio* – electronic structure calculations, of the properties of the line defects governing the plastic behavior of iron base materials, namely the [111] screw dislocations. These properties include: the dislocation core structure, the glide mechanism, and in the longer term, their interaction with solutes (C, Cr), transmutation products (He, H) or radiation defects (vacancies, interstitials). Besides the information that can be directly retrieved from such calculations, such as the glide plane of the dislocation, these results are essential for the validation or fit of empirical potentials, which can in turn be used for larger scale simulations.

2007-2008 ACTIVITIES

METHODOLOGY

The present *ab-initio* calculations were performed in the framework of the Density Functional Theory (DFT), using the SIESTA code [1], which was chosen for its efficiency stemming the use of strictly localized basis sets. This approach was validated by performing numerous comparisons on test quantities with plane wave-pseudopotential results. Three representative empirical potentials for iron are benchmarked against the obtained *ab-initio* results: the Finnis-Sinclair potential proposed by Ackland *et al.* in 1997 [2], the improved EAM potential obtained by Mendelev *et al.* by including *ab-initio* properties in the fit [3] or more precisely the updated version by Ackland *et al.* [4], and finally the magnetic potential developed by Dudarev and Derlet [5]. In the following these potentials are denoted respectively: A97, M03, AM04 and D05.

GENERALIZED STACKING FAULT ENERGY SURFACES IN α-Fe

The generalized stacking fault energies, or γ-surfaces, represent the excess energies obtained by cutting a perfect crystal and displacing the two parts relative to each other in a direction parallel to the cut plane, while allowing atomic relaxations in the perpendicular direction. They have received considerable attention in the context of dislocation studies due to their close relation to the core structure. The [111] screw dislocations in the body centered cubic (bcc) structure, can adopt basically two types of structures: either a degenerate or non-degenerate core, depending on whether it is spread asymmetrically or symmetrically in the three {110} planes. The following simple criterion was proposed by Vitek and Duesbery for having a degenerate core:

$$\gamma_{\{110\}}(b/3) < 2\gamma_{\{110\}}(b/6),$$

where $\gamma_{\{110\}}(b/3)$ and $\gamma_{\{110\}}(b/6)$ are the fault energies at b/3 et b/6 respectively, for the {110} γ-line in the [111] direction [6].

We performed a comparison between LDA and GGA functionals and the validation of SIESTA with plane wave codes (present work using the PWSCF code and Ref. [7]). The {110} γ-lines obtained within DFT and with the AM04 potential suggest a non-degenerate core structure according to the Duesbery-Vitek criterion while a degenerate core structure is expected for the D05 potential. These predictions are indeed confirmed by a direct calculation of the core structure (see below and [7,8]). On the other hand, the {110} γ-lines obtained with the A97 potential suggest a non-degenerate core structure, at variance with the direct calculation of the core structure: the Ackland potential is therefore an exception to the Duesbery-Vitek rule.

CELL ARRANGEMENTS AND BOUNDARY CONDITIONS FOR DISLOCATION CORE CALCULATIONS

For the calculations on dislocations, we compared the two cell geometries proposed in the literature: the cluster approach [9] and the periodic array of dislocation dipoles [10]. Within the cluster model, a single dislocation is placed at the center of a "cylinder" and the surface atoms are fixed to the positions predicted by the anisotropic elasticity theory, while the inner ones are relaxed. For Peierls stress calculations, flexible boundary conditions are used [9]. In the dipole approach, we compared two arrangements: a triangular and a square-like periodic array of dislocation dipoles. In the triangular geometry, the dislocations are positioned on a honeycomb lattice, that preserves the three-fold symmetry of the bcc lattice in the [111] direction. The square-like lattice corresponds to a quadrupolar arrangement. We have optimized the cell geometry by adding tilt components to the cell vectors in order to accommodate the plastic strain introduced by the dislocation dipole. These tilt components are deduced from elasticity calculations; the atomistic calculations confirm that they indeed yield vanishing shear stress components.

CORE STRUCTURE OF [111] SCREW DISLOCATION

Two high symmetry configurations have been reported in the literature for the [111] screw dislocation. They are both

positioned at the center of three nearest neighbor [111] rows and they are related to each other either with (i) a common geometrical center and opposite Burgers vectors or with (ii) a common Burgers vector and geometrical centers displaced from a triangle to an opposite triangle. In the hard core structure, the three central atoms are in the same (111) plane, whereas in the easy core structure they are shifted by b/3 with respect to each other (but with an opposite sign compared to what they are without dislocation). DFT results show that the relaxed structure of the easy configuration of [111] screw dislocation does not lead to any broken symmetry about the <110> axes or any spreading along the <211> directions, so that the easy core structure exhibits a non-degenerate core configuration in agreement with previous calculations [7, 8] and as expected from the γ-line calculations. The degenerate easy core structure is found to be unstable. The hard core corresponds to an unstable extremum of the potential energy surface with an excess energy with respect to the easy configuration of about 50 meV/b. These relaxed core structures are found to be close to elasticity theory. The small deviation from the prediction of elasticity can be illustrated by subtracting the anisotropic elastic displacement field and represents the screw component. The AM04 potential also exhibits a non-degenerate core structure – as expected from the Duesbery-Vitek criterion – but with an opposite deviation to elasticity for the screw components. As expected from the γ-line calculations, the D05 potential reveals a degenerate core structure at variance with DFT results.

The deviation from elasticity can also be seen on the edge component maps, i.e., the displacement field in the (111) plane. The edge component obtained with DFT reveals the existence of a dilatation elastic field exerted by the dislocation core that corresponds to a formation volume of about 0.5 Ω_0/b, where Ω_0 is the atomic volume. We successfully coupled anisotropic elasticity and atomistic simulation to describe this formation volume. The edge component of the DFT displacement field is also dominated by elasticity – provided that the dilatation term is taken into account – even close to the core. The results obtained with the AM04 potential do not lead to such a core dilatation. The magnetic moment of the three core atoms is increased by 0.2 μ_B from its bulk value (2.3 μ_B) for both the easy and hard cores. The cluster and dipole approaches are in very good quantitative agreement with each other.

PEIERLS POTENTIAL

The Peierls potential is the two dimensional energy landscape seen by a straight dislocation as it moves perpendicular to the Burgers vector. We have successfully calculated two cross sections of this energy surface using the SIESTA code and the AM04 potential: the path going from an easy core position to the adjacent hard core configuration along the <211> direction and the path going from an easy core position to the next easy core configuration along the <211> direction, i.e. the Peierls barrier. The hard core energy is found to be overestimated with the AM04 potential (figure 1a). The effect of the exchange-correlation functional within DFT appears to be significant. The Peierls barrier displayed by the AM04 potential yields a camel hump shape and at the halfway position, the core spreads between two easy core positions while within DFT it exhibits a single hump barrier with a height of ~ 25 meV/b, where b is the Burgers vector, and a nearly hard core structure at halfway position (figure 1b). Therefore, DFT yields no metastable split configuration at halfway position, and is an exception to the Takeuchi rule, that establishes a correlation between the existence of a metastable core configuration and the non-degenerate core structure [11]. The energy landscape between hard and saddle-point is very flat with DFT. The results obtained using the square-like periodic arrangement of dislocation quadruples are in excellent agreement with the cluster approach results.

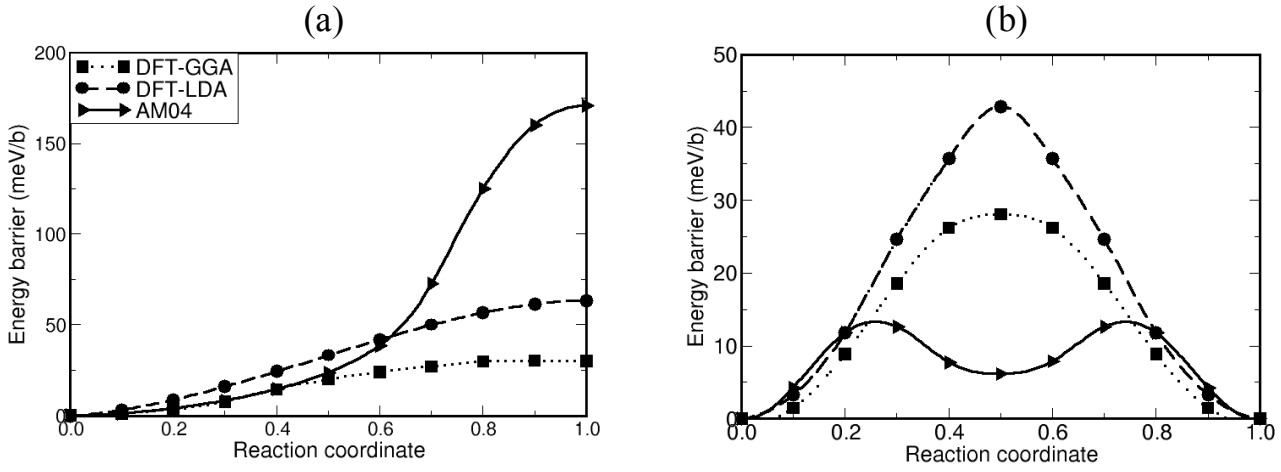

Figure 1: (a) Energy variation when moving from an easy core structure to an adjacent hard core structure along the <211> direction within the cluster approach (252 atoms/b): comparison between SIESTA using the two exchange-correlation functionals, LDA and GGA, and the AM04 potential. (b) Peierls barrier calculated within the cluster approach (261 atoms/b)

OPTIMIZATION OF CELLS FOR KINK FORMATION ENERGY CALCULATION

We successfully set up fully periodic simulation cells to perform accurate calculations on [111] kinked screw dislocations in bcc iron using the quadrupolar distribution of dislocation dipoles, for the two types of kinks, namely, the interstitial-type and the vacancy-type. We developed the procedure for introducing a single kink while satisfying the periodicity along the dislocation line, i.e. by removing/adding a slab of atoms of thickness b/3 and adding components to the cell vector along the dislocation line. This methodology was applied using the AM04 potential for iron. The two types of kinks are found to have the same width, namely w=20 b. This value is in very good agreement with the value of 19b proposed from an analysis of flow stress dependence on temperature and strain rates in high purity α-iron, below 250K [12].

The convergence of the formation energy with cell size along the dislocation line has been studied in the range from 4b to 100b. From a representation as function of the inverse of the cell size, two regimes are identified: above 40b, the formation energy of the single kink has a constant value, and below 20b, it has a perfect linear dependence as a function of the inverse of the distance between the kink and its periodic image along the dislocation line. The slope is the same for the two types of kinks. Below ~40b, the kink has not reached its equilibrium width. In this regime of "overlapping kinks", it can be shown that the change in line length (compared to the perfect dislocation) is proportional to the inverse of the cell size. In a line tension model, the energy will therefore also vary as the inverse of cell size, as observed here. However the intercept has a finite value – at least for the interstitial-type – such that a core contribution to the energy should be added to the line tension. For cell sizes of 40b or more, the kink has reached its equilibrium width, which can be seen as the value minimizing the sum of the line tension energy and the Peierls contribution. We also tested the convergence of the formation energies with the distance between the dislocations, i.e. with the number of atoms per {111} plane. The change in formation energy when using cells containing from 135 to 1215 atoms/b, is found to be small. It is proportional to $\sqrt{\ln N}$, where N is the number of atoms per unit length, as a result of the dependence of the dislocation line tension with $\ln N$ [13]. Thus the formation energy diverges with distance between dislocations but the divergence remains slow, as other quantities within dislocation theory. As a result, the values obtained for the formation energies of the vacancy and interstitial types of kinks are respectively 0.08 eV and 0.57 eV. Therefore the two types of kinks have quite different formation energies. Their sum gives the double-kink formation energy. The calculated value, 0.65 eV, is in very good agreement with the value deduced from flow stress measurements, i.e. 0.6 eV [12].

Finally, we computed the Peierls potential for the side motion of the single kink along the dislocation line, i.e. the Peierls potential of the second kind for the two types of kinks, using the drag method. The energy barriers are found to be very small, less than 0.1 meV, suggesting that both types of kink will propagate athermally along the dislocation line.

METHODOLOGY FOR PEIERLS STRESS CALCULATIONS

The method which appears to be the most appropriate to calculate the Peierls stress within the cluster approach is that of the flexible boundary conditions proposed by Woodward *et al.* [9]. This method has been successfully implemented and applied for the calculation of the Peierls stress of screw dislocations in the past in various bcc transition metals, using either empirical potentials, the Bond Order Potential or DFT calculations within VASP. It has not been used to date for DFT calculations in Fe. Our goal was first to implement the flexible boundary conditions in the SIESTA code, and in our empirical potential code – the NDM code – and then to validate the tri-periodic boundary condition method within the dipole approach on the reference flexible boundary condition method.

The Peierls stress has been computed by applying strain increments, until the dislocation moves. An excellent agreement is obtained between flexible and tri-periodic boundary conditions on the value of the Peierls stress and its variation with crystal orientation, characteristic to bcc metals. Using the M03 potential, we obtained that the dislocation moves in the {110} plane above 1.3 GPa, in agreement with previous results [14] and that the Peierls stress varies asymmetrically with the angle between the glide plane and the shear plane, deviating strongly from the Schmid law.

CONCLUSIONS

The DFT results obtained on screw dislocation in iron allow discriminating between the various empirical potentials available for iron. The shape of γ-surfaces is not well reproduced by the Dudarev-Derlet potential, which yields a degenerate core structure. The Ackland potential yields a better shape for γ-surfaces, but again a degenerate core structure. Only the Mendelev potentials are able to reproduce the correct shape for the γ-surfaces and the correct core structure. Table 1 summarizes the results of the comparison between the present DFT calculations and the Mendelev potential for iron on the core structure, Peierls potential, Peierls stress, and kink formation.

Table 1: Properties of core structure, Peierls potential, Peierls stress, and kink formation of [111] screw dislocation in Fe: comparison between DFT results and empirical potential calculations using the M04 potential (except for the Peierls stress

		DFT	Empirical potential
Core	Screw component	Non-degenerate Opposite deviations from elasticity	
	Edge component	$V_f^{\perp} \sim 0.5\Omega_0/b$	0
Peierls potential	$E_{max} - E_{min}$	30 meV/b	Too high
	$E_{Peierls}$	25 meV/b	Too low
	Peierls barrier	Single	Double
Peierls stress		In progress	M03 ≠ AM04 M03: {110} glide, 1300 MPa Non-Schmid behavior
Kink formation	Width	In progress	$w_I \sim w_V \sim 20$ b
	E_f		$E_f^{I} \sim 0.6$ eV ; $E_f^{V} \sim 0.1$ eV

REFERENCES

[1] J. M. Soler *et al.*, J. Phys. Cond. Mat. 14, 2745 (2002)

[2] G.J. Ackland *et al.*, Philos. Mag., A 75, 713 (1997)

[3] M. I. Mendelev *et al.*, Philos. Mag. 83, 3977 (2003)

[4] G. J. Ackland *et al.*, J. Phys.: Condens. Matter 16, S2629 (2004)

[5] S. L. Dudarev and P. M. Derlet, J. Phys.: Condens. Matter 17, 7097 (2005)

[6] M. S. Duesbery and V. Vitek, Acta. Mater.46, 1481 (1998)

[7] S. L. Frederiksen and K. W. Jacobsen, Philos. Mag. 83, 365 (2003)

[8] C. Domain and G. Monnet, Phys. Rev. Lett. 95, 215506 (2005)

[9] C. Woodward and S. I. Rao, Phys. Rev. Lett. 88, 216402 (2002)

[10] W. Cai *et al.*, Philos. Mag. 83, 539 (2003)

[11] S. Takeuchi, Philos. Mag. A 39, 661 (1979)

[12] D. Brunner and J. Diehl, Phys. Stat. Sol. (a) 124, 455 (1991)

[13] J. D. Eshelby, Proc. Roy. Soc. London A 266, 222 (1962)

[14] J. Chaussidon, M. Fivel and D. Rodney, Acta Mater. 54, 3407 (2006)

REPORTS AND PUBLICATIONS

L. Ventelon and F. Willaime, J. Computer-Aided Mater. Des. 14, 85 (2007)

E. Clouet, L. Ventelon and F. Willaime, Phys. Rev. Lett. 102, 055502 (2009)

L. Ventelon, F. Willaime and P. Leyronnas, J. Nucl. Mater. (in press)

Ab-initio investigations of a screw dislocation in Fe, Final report for the TW6-TTMS-007-D08 task, 8 june 2007. L. Ventelon, F. Willaime

TASK LEADER

François WILLAIME

DEN/DMN/SRMP
CEA-Saclay
F-91191 Gif-sur-Yvette Cedex

Tel: 33 1 69 08 28 10
Fax: 33 1 68 08 68 67

e-mail: francois.willaime@cea.fr

TW3-TTMA-001-D04
TW3-TTMA-002-D04

Task Title: EFFECTS OF IRRADIATION ON ADVANCED MATERIALS IRRADIATION OF ADVANCED SiC/SiC COMPOSITES FURIOSO EXPERIMENT

SUMMARY

This report concludes the work engaged under the EFDA tasks TW3-TTMA-001 and -002 with the same deliverable number of D04. A complementary note will cover, at a later date, the remaining issues: experiment's dosimeters evaluations, packaging of specimens for picking up by partners from CEA-Saclay and eventually the agreement for testing some of the specimens at CEA.

Under the above tasks, diffusivity, bend, tension and impact specimens from various SiC_fSiC composites (2D and 3D) and tungsten alloys, supplied by partners from Europe, Japan and USA have been irradiated in the OSIRIS reactor to a target dose of 5dpa (iron). The experiment was code named "Furioso" and used a rig divided into two sections, one operating at 600°C and another at 1000°C. An insulator layer separated the two sections.

The temperature inside the rig was adjusted through the flow of an inert gas (mixture of He-Neon), the parameters of which were monitored by a control box positioned outside the reactor. The rig was divided in 12 levels and specimens at each level were placed inside specimen holders that were in turn placed inside metallic baskets, along with temperature and dose detectors.

Apart from a few minor glitches, the experiment has been successfully terminated and diffusivity, impact, bend and tension specimens have achieved their irradiation goals and are ready for post-irradiation examinations.

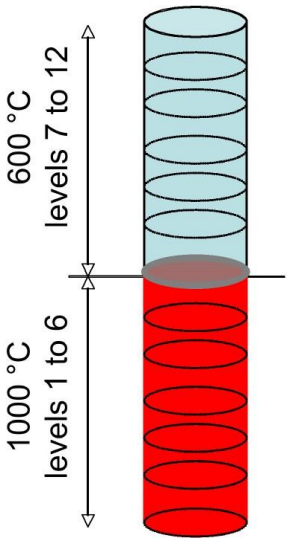

Figure 1: Schematic presentation of the Furioso Irradiation capsule

INTRODUCTION

The main objective of this work was to determine the effects of high temperature neutron irradiation on physical and mechanical properties of SiC_f/SiC ceramic composites and tungsten alloys.

SiC_f/SiC composites are low activation materials and have good mechanical properties at temperatures up to about 1000°C. R&D work on these materials for application in advanced fusion devices has been going for more than 2 decades. Recently, industrial scale productions have been achieved: in 2004 (2D material) and in 2005 (3D material).

Presently, SiC_f/SiC composites are considered, in the short term, as inserts in one of the EU TBM concepts and, in the long term, as structural materials for power reactors. However, the main problems of these composites for the latter application are low thermal conductivity and low fracture toughness that are further degraded under neutron irradiation.

Tungsten alloys are envisaged as functional materials in the high heat flux regions of ITER divertor, and as structural materials in the future high temperature power reactors. The key issues for these alloys are low fracture toughness, sensitivity to production history and limited knowledge on the effects of irradiation on their mechanical properties.

The Furioso experiment undertaken here targets the above issues for these materials.

2007-2008 ACTIVITIES

MATERIALS

Specimens used in the Furioso experiment come from several European associations, as well as, the Japanese and the American partners. Details of the materials and specimens used are given in the full report.

SiC_f/SiC composites
Materials used are:

- Different nuances of SiC_f/SiC ceramic composites (2D and 3D), supplied by EFDA and manufactured in Europe by MAN Technology (Germany).
- A 2D-NITE SiC_f/SiC composite supplied by Japan.
- Four types of composites (TySA-CVI-Ti / HNLS-CVI-Ti / Hybrid-CVI / Reference), 3 supplied by ORNL (U.S.) and 1 (called ref.) by PNNL (USA).

Specimens cut from the above materials and used in the present work are: diffusivity, bend and tension types.

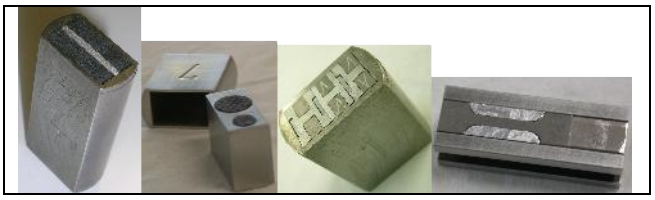

Figure 2: Specimen loading after thermal calculations

Tungsten alloys

Two types of tungsten alloys are used: one containing lanthanum oxide (W-1%La_2O_3) and another with potassium addition (W-K). The specimens taken from these materials are: plate tensile and Charpy-V sub-size (KLST) specimens (for bend tests).

In all 142 specimens have been irradiated in the Furioso experiment, out of which:

- - 108 are SiCf/SiC composites and
- - 34 are W alloys

98 specimens are kept in reserve, out of which 28 are tungsten alloys.

Figure 3: Specimen markings, on left traces of felt pen marking on diffusivity specimens, on right laser marking

PREPARATION

All specimens were carefully examined upon reception before irradiation.
A few SiC_f/SiC diffusivity discs had traces of felt pen marking. Despite repeated cleaning according to the recommended procedures some showed still ghost markings. Most of these were replaced with new ones from the reserve, except 5 diffusivity specimens. Other specimens had laser markings.
A rig with 12 levels, divided into 2 sections separated by an insulator layer was designed for irradiation at temperatures 600 and 1000°C. Prior to the actual irradiation, results of the rig mockup fabrication, thermal calculations and plan of loading of specimens were presented to all partners. Small modifications in the initial loading plan, at levels 6 and 7, for better temperature distribution were also signaled.

A powerful furnace (Phaeton) was designed and manufactured for operation of rig at high temperatures. A control box was procured and installed next to the reactor.

The temperature inside the rig was regulated via the box, using a flowing mixture of inert gas (helium-neon), inside and outside the sample holder.
In parallel with the above preparations safety documents were prepared and sent to relevant safety authorities. Modifications requested by the authorities were carried out and the authorization for experiment was obtained, initially for 6 days and then for full period.

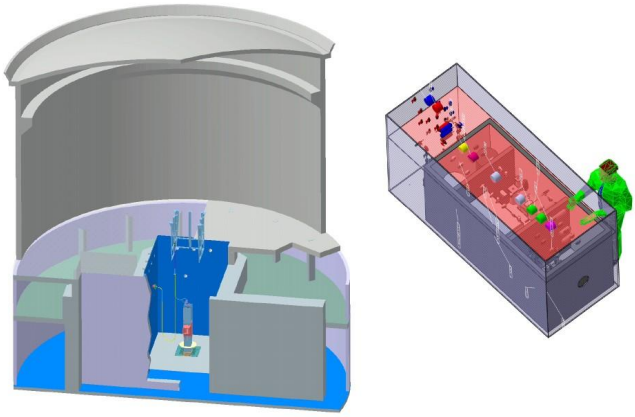

Figure 4: Schematic presentation of the control box procured and installed in 2006 next to the reactor. This box regulates the irradiation temperature inside the rig through flow of heated gases

VALIDATION TESTS, REACTOR CYCLE 219

Furioso experiment started with a short campaign (6 days in the position 64 SO of OSIRIS core, cycle 219, July 2007). The results of this short campaign were used to verify the mockup calculations and obtain extension of authorization to full period.

- 16 thermocouples were placed at different rig levels to monitor the temperatures.
- 14 dosimeters, one at each level, except at levels 1 and 12 that had 2 each, were placed in the rig to record the irradiation doses.

The experiment was conducted in a manner that the upper temperature at each part would not exceed +50°C of the target temperature. The results obtained were satisfactory and allowed continuation of the experiment.

FURIOSO EXPERIMENT

The rig was put back in the reactor at cycle 220 (September 2007) till the end of the experiment at cycle 230 (December 8, 2008), when the estimated dose of 5dpa (iron)[1] was achieved.

During the experiment two minor anomalies were observed. One was a reading from a detector signalling accumulation of small amounts of oxygen with time. The reading persisted even after the exchange of detector and was probably due to a leak in the detector box or release of

[1] Displacement per atom dose is calculated for iron and not for SiC composites or tungsten at this stage.

oxygen from the detector itself, in both cases outside the internal gas circuit. Nevertheless, as a precautionary measure, it was decided to replace the helium and neon gas cylinders more frequently so that even if this minor leak enters the gas circuit it would not seriously affect the gas purity.

Another difficulty observed was also in parts not affecting the actual experiment. It resulted in stopping the experiment for one cycle for repair.

CONCLUSIONS

Furioso experiment has successfully terminated. Specimens of SiC_f/SiC composites and tungsten alloys irradiated in OSIRIS reactor at temperatures 600°C and 1000°C have reached their target dose of 5dpa.
Irradiated specimens will be sorted and packaged after cooling down for pickup by partners. Negotiations are in progress with those partners who wish the PIE to be done at CEA.

REPORTS AND PUBLICATIONS

1 F. Tavassoli, et al, "Irradiation of SiC/SiC composites and W alloys, Furioso Experiment", 7th IEA workshop on SiC/SiC materials, NRG, Petten, The Netherlands, Sept. 18-20, 2007

2 F. Tavassoli, "SiC_f/SiC composite irradiation programme at CEA", EFDA Monitoring meeting, Barcelona, July 26, 2007

TASK LEADER

Farhad TAVASSOLI

DEN/DMN
CEA-Saclay
F-91191 Gif-sur-Yvette Cedex

Tel. : 33 1 69 08 60 21
Fax : 33 1 69 08 80 70

e-mail : tavassoli@cea.fr

CEFDA05-1359

Task Title: TW5-TTMI-004a: PRELIMINARY RH HANDBOOK FOR IFMIF

INTRODUCTION

The International Fusion Material Irradiating Facility (IFMIF) is a large facility whose primary mission will be to generate a materials irradiation database for the purpose of construction, design, licensing and safe operation of a fusion demonstration reactor.
Safety objectives in experimental facilities like IFMIF must be part of a general reflection process started at the early beginning of the project. Because such facilities are unique and intensively promote the use of new techniques, schemes based on the application of well defined standard safety procedures for production facilities often do not cover the wide range of situations encountered.
Whether it will be for highly radioactive materials or for tritiated samples, handling of samples, test rigs, connectors or fluids in IFMIF will often be completely impossible with human hands. Therefore, Remote Handling (RH) means are already identified as a necessity for the facility.
Although the frontier is not always very clear, the choice between RH or hands-on operations is a matter of safety and ALARA reflections. We chose to follow the maintenance classification principles defined in ITER as primary guidelines for the definition of RH equipment. Design recommendations to build RH systems were made according to available dose rate estimations, existing design of the facility and requirements defined for the accelerator building and conventional facilities. Sections related to the test and target facilities should be included in an equivalent study to be issued by ENEA.

2007-2008 ACTIVITIES

Robot activities summary

The period was dedicated to establish a RH analysis and design guidelines for IFMIF. As IFMIF will be an accelerator and a nuclear plant, we chose to start the analysis with radiation effect presentation, and the limits and effect on maintenance operation, as long as it becomes necessary to remotely operate. A chapter dedicated to design guidelines introduces manipulator classification and present existing systems in use in various accelerators such as SNS (ORNL, US), SINQ (PSI, Switzerland), ISOLDE (CERN, Switzerland) and at last Myrrha (SCK-CEN, Belgium).Operational experience in JET is also introduced to propose an assessment of components to be maintained, and classify them, establish requirements for a RH system and the different options one can take for RH operations.

Limits for hands-on work vs radiation exposure

An analysis made on the International Commission on Radiological Protection (ICRP) recommendation and guidelines taken by ITER and IFMIF shows immediately that RH is an absolute necessity in all areas where dose rate exceeds 1mSv/hr. Between 10 µSv/hr and 1 mSv/h, it will be the result of ALARA considerations.

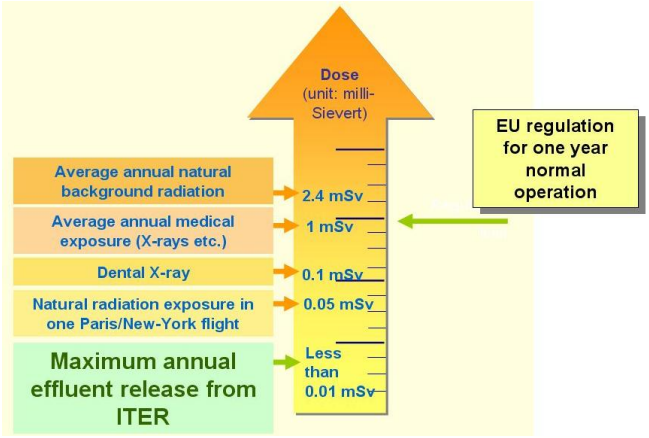

Figure 1: Dose chart issued from ITER safety and licensing presentation from J-PH Girard, SOFT 2006

The effect of radiation on telerobotics systems is not to be underestimated. A special attention will be paid to electronics components which are the most fragile elements in those systems. ITER provides for design purpose a database of components and their estimated dose rate to be taken into account while designing a teleorobotics system. Architecture choice is also very important and the choice of an appropriate architecture can lead to considerably reduce complexity and also rise up gamma-dose limits of the complete system.

Design guidelines: manipulators

Many mechanical master/slave manipulators (MSM) are used in nuclear facilities. Next figures show most common systems used for hot cell maintenance.

Figure 2: Example of articulated manipulator (MA11 La Calhène, A200 Wälischmiller)

Figure 3: Manipulator with telescopic arm (CRL Model 8 A100 Wälischmiller, MT200 La Calhène)

Main drawbacks of those systems are their poor level of assistance (non perfect gravity compensation) and the fact that there is no force ratio between master and slave, so that manipulation is limited by operator capacity. Furthermore, as shown in figure 4, dexterity decreases while payload increases.

One can find heavy load manipulators but they are not force reflective systems and then their dexterity (and then complexity of the task to be achieved) is low.
Telerobotics systems, like servo-manipulators, are not to be considered as industrial systems but present many advantages, especially when they are equipped with computer aided teleoperation controllers:

- use of different arm morphologies and technologies for the master and the slave,
- work in the Cartesian coordinates,
- compensation of the weight of the tool,
- adjustable force and speed ratios,
- virtual mechanisms,
- ...

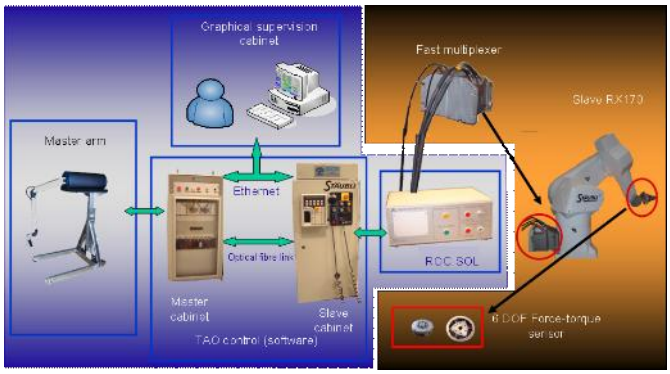

Figure 5: Complete telerobotic system

Telerobotics systems no longer have mechanical links between master and slave and address control of the slave with high level orders. While not always required to reduce the size of the umbilical passing through the shield of the hot zone, rad hardened multiplexing systems or embedded low level controller are now available to cumulated does up to 10kGy.

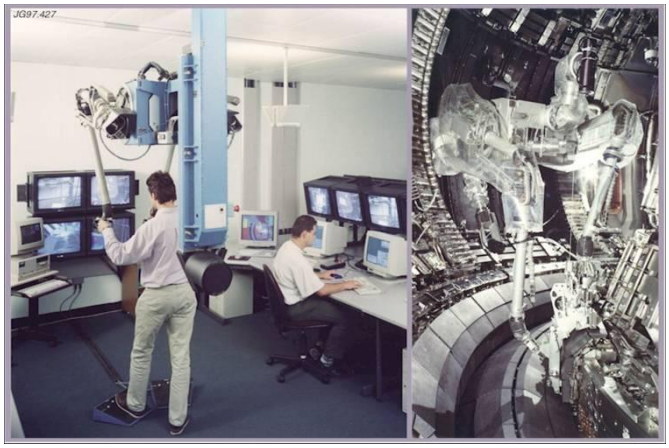

Figure 6: Remote Handling at JET with 'Mascot' servomanipulators

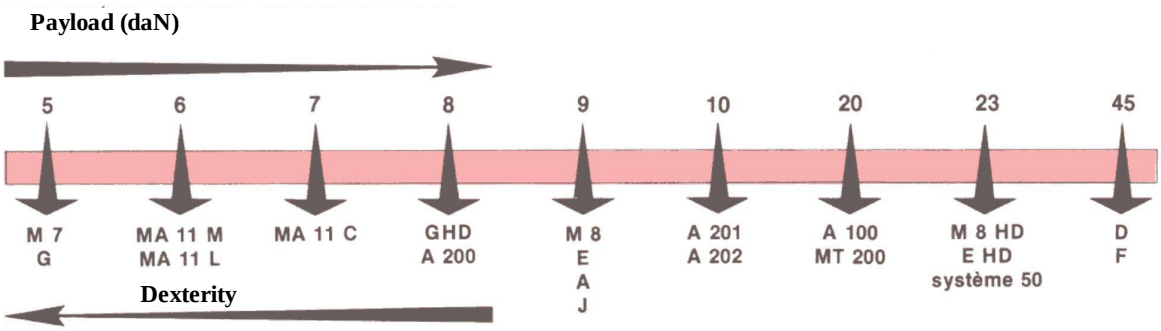

Figure 4: Payload of MSM models

Existing RH means in accelerators

Accelerator facilities already make use of RH telemanipulators and deployers for those systems.
Figures 7, 8 and 9 show some examples of those systems.

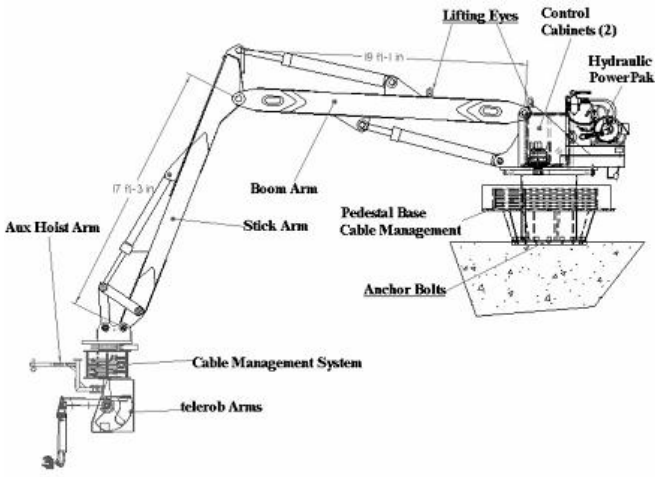

Figure 7: Pedestal mounted boom system for operations above the shielding monolith

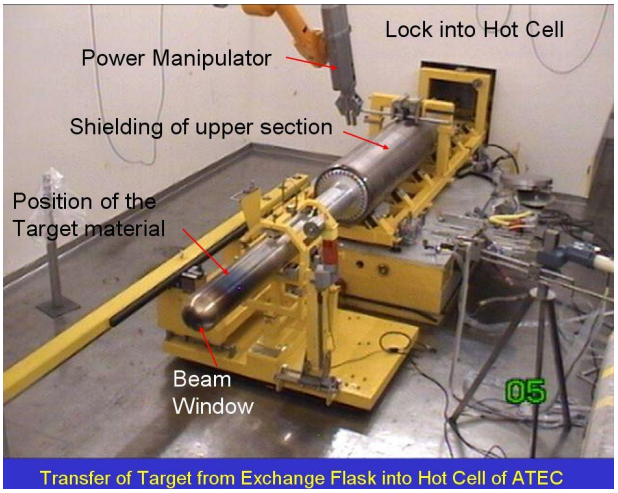

Figure 8: Operations in hot cell on SINQ target

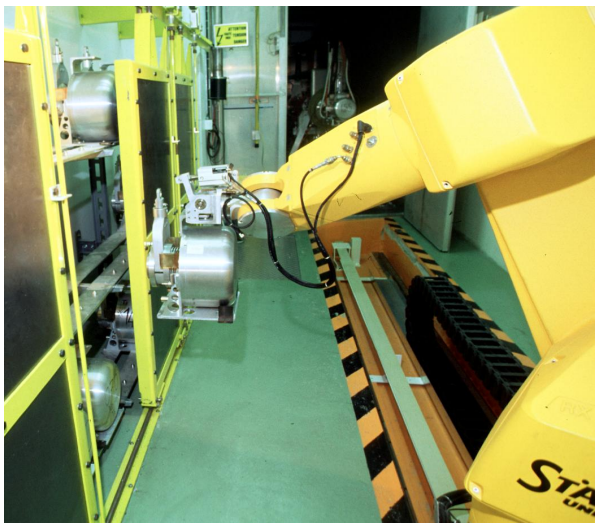

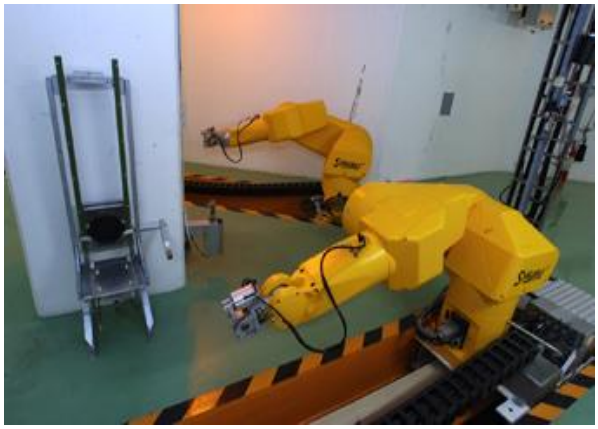

Figure 9: Stäubli RX robots used at the Isolde facility

Maintenance classification

Starting from the results of the Reliability and Maintainability analyses (RAM analyses) established in the CDA, a first attempt to build a list of elements needing maintenance and their classification was made. These rules are as follow:

- RH class 1= requiring regular planned replacement,
- RH class 2 = components that are likely to require repair or replacement,
- RH class 3 = components that are not expected to require maintenance or replacement during the lifetime of facility but would need to be replaced remotely should they fail,
- RH class 4 = components that do not require remote handling.

Hands-on or RH maintenance were defined according to discussions with people in charge of the design of the accelerator. In fact, except for the HEBT (Beam dump still needs definition) all maintenance is supposed to be carried out manually as a design requirement.

Table 1: Examples of RH Maintenance in the IFMIF accelerator facility

Zone	Element	Maintenance type	Maintenance classification
HEBT		RH or limited hands-on access	
	Quadrupole chain (cooling, power-supply,coil)		III
	Dipole chain (cooling, power-supply,coil)		III
	Octupole chain (cooling, power-supply,coil)		III
	Buncher cavity chain		III
	Ion pump chain for beam tube vacuum systems		
	Scraper		II
	Diagnostics (BPM like)		II
	9 degree achromatic lens		
	Neutron shield		
	Drift tube		
Beam Monitoring Station	Dump, diagnostics	TBD RH or limited hands-on	

Requirements for a RH system:

Although lots of studies were performed to demonstrate feasibility of the IFMIF accelerator, designs of all the accelerator facility at the beginning of this study were at very preliminary level. It was therefore decided to propose to designer concepts or simple rules that are usually followed by Remote Handling designers to make an equipment RH compatible.

It was assumed that within the same area, all maintenance operations will be carried out with RH means. Therefore, no installation or removal of any shielding element was taken into account. Such operations would need to be added in the maintenance scheme if shielded equipment were likely to appear.

Although RH solutions are often based on the same architecture, performances and size of the equipment has to be adapted to the facility. For that reason, the solution proposed hereafter shouldn't be taken as the real one but only as a tentative option to:

- Propose a concept,
- Identify RH operations,
- Start to define interfaces,
- Point out areas where definition of standards could improve reliability and confidence in the equipment,
- Identify limits of the RH operations.

For the accelerator facility, the best system could be composed of:

- A heavy duty crane bridge with XY motions,
- Two six degrees of freedom servomanipulators mounted on a second but lighter crane bridge,
- RH carrier bridge system should provide XY motion and being equipped with a Z axis to lower the dual arm system and give access to all part of the facility,
- RH equipment should be provided with an auxiliary hoist to handle components whose weight is out of the manipulator's capacity or to ensure a higher level of safety for all handling operations,
- A vision system covering the whole facility area. Usually composed of cameras equipped with pan and tilt motions and zooming capabilities,
- A second vision system embedded in the servomanipulator bridge to provide close view of the operation area. Usually a set of three cameras with pan-tilt motion and zooming capabilities,
- A real time supervision system with anti-collision capabilities based on virtual reality tools to enhance operational safety and propose robotic trajectories to reach the working area.

But a more simple option could be composed of:

- A heavy duty crane bridge with XY motions,
- 1 six degrees of freedom servomanipulator mounted on a platform lifted by the heavy duty crane bridge. Positioning of the platform in ensured by means of inserts in the concrete floor. The platform self clamps to the floor once in position,
- A vision system covering the whole facility area. Usually composed of cameras equipped with pan and tilt motions and zooming capabilities,
- A second vision system embedded in the servomanipulator platform to provide close view of the operation area. Usually a set of three cameras with pan-tilt motion and zooming capabilities,

- A real time supervision system with anti-collision capabilities based on virtual reality tools to enhance operational safety and propose robotic trajectories to reach the working area.

CONCLUSIONS

The choice between RH and Hands-on operations is always a balance between safety rules and application of ALARA considerations. The boundary between the two operation modes is therefore something that highly depends on the context.

Proposals were made to use for the IFMIF facility the maintenance classification scheme followed in ITER and sort all elements needing RH maintenance or repair according to their replacement frequency. The main advantage of such classification is to define priorities between the tasks and the associated reliability, availability and complexity level for the RH equipment.

A preliminary classification for the maintenance of accelerator components was issued from available data. Update of this classification will be required following the forthcoming design of the accelerator. No components requiring scheduled and frequent replacement were identified in this section of the facility. Unless final design of the accelerator makes fundamental changes in the design of the CDR, maintenance in the accelerator building will therefore be limited to elements that are likely to fail during the lifetime of the facility, meaning that the RH system will have to be transportable, and adaptable.

Since the design of the accelerator is only starting now, a definition of the complete RH system is difficult. Two preliminary concepts were proposed but the main analysis concentrated on giving accelerators designers simple design recommendations that would make RH operations easier and more reliable.

Although operations carried out in these conventional facilities can be considered as routine work in the fission industry, the level of radiations expected for some components makes the task more complex than expected and as explained in the previous sections, will limit the choice in the available equipment and technology for operating in these zones.

REPORTS AND PUBLICATIONS

O. David et al., Overview of the preliminary remote handling handbook for IFMIF, Fusion Eng. Des. (2009), doi:10.1016/j.fusengdes.2009.01.089

TASK LEADER

Olivier DAVID

DRT/DTSI/SRI
CEA-Fontenay
BP 6
F-92265 Fontenay-aux-Roses Cedex

Tel: 33 1 46 54 78 78
Fax: 33 1 46 54 89 80

e-mail: odavid@cea.fr

CEFDA06-1414

Task Title: TW6-TSL-002: SAFETY ASSESSMENT OF EU-TEST BLANKET MODULES TO SUPPORT ITER LICENSING PROCESS

INTRODUCTION

During operation, the neutron flux within ITER activates the structure elements. Among those elements, the TBMs are located within a steel allow frame subject to activation. Moreover, maintenance of the TBM may require access by an operator from behind the bio shield and the frame.
The present task aims at giving:

- Estimated dose rates for two tritium-breeding blanket systems – HCLL and HCPB – which may be used as test blanket modules (TBM) in ITER. The first system is a helium-cooled lithium/lead tritium-breeding system while the second (HCPB) is a helium-cooled lithium/beryllium tritium-breeding system,
- Estimated dose rates originating from the frame of TBM systems and the integrated dose during maintenance operation.

2007-2008 ACTIVITIES

DOSE RATE FROM TBM

The dose rates for each system were calculated using the MCNP4C2 calculation code. The most conservative source terms were selected when calculating the dose rates.

The two tritium-breeding systems, HCPB and HCLL, are modelled using the following assumptions:

- An identical uniform metal housing for both systems,
- The metal matrix is covered with an identical beryllium layer in both systems,
- A uniform internal matrix is composed of PbLi for HCLL and BeLi for HCPB,
- The most conservative front wall source term is used for each uniform housing matrix,
- Dose rates are calculated under pseudo-contact conditions (5 cm), 10 cm, 30 cm, and 1 m from the housing matrix.

For HCPB:
- Average activity is calculated.

FRAME MAINTENANCE DOSIMETRY

The aim of this section is to explain the methodology used to obtain the dose rates from the TBM frame and the integrated dose during maintenance.
The dose rate was calculated using the MCNP4C2 calculation code. The major source terms were obtained by activation calculation of the frame with a defined geometry.

The calculations were conducted in the following conditions:

- A simplified geometry,
- A uniform metal housing,
- The conservative source term consists in a homogeneous distribution in the back wall of the frame,
- Dose rates are calculated under pseudo-contact conditions (5 cm), 10 cm, 30 cm, and 1 m from the frame, by Monte Carlos method and 5 and 100 cm behind the bioshield by deterministic method (attenuation of 60Co),
- The TBM modules themselves were not included into the geometry. Their activation is comparable to the frame, but their contribution to the dose rate behind the frame can be considered negligible (because attenuated by the 30cm back frame) compared to the contribution of the frame activation (section 10),
- Two source estimates of the activation of the TBM have been considered, corresponding to the activation at the front and back wall of the TBM.

The different step of the removal and reinstallation of TBMs are then associated with positions of calculated dose rates. Dose rates and work effort allow the estimation of integrated dose for the TBM maintenance operation.

For consideration of hypothetical attenuation and/or re-evaluation of the activation, attenuation factors have been considered. The work effort has been recalculated considering attenuations of 1/10, 1/100 and 1/1000 of the source term.

SUMMARY OF TBM DOSE RATES

Dose rates obtained using the MCNP4C2 calculation code were performed for various time-periods after irradiation and for a range of distances (under pseudo-contact conditions, at 10cm, 30cm and 1m), with the TBM considered to be a rectangular volume composed of a first beryllium layer, eurofer housing and a matrix made of BeLiFe (in HCPB) or PbLi (in HCLL).
A cross-check was performed consisting of calculating the dose rates using Microshield and MCNP for two radioelements, ^{54}Mn and ^{60}Co. The two methods were found to converge.

HCPB

The dose rate results under pseudo-contact conditions range from $4.21 \cdot 10^{3}$ to $6.31 \cdot 10^{-1}$ Sv/h.

It can be seen that the beryllium layer influences neither the dose rates (0.1%) nor the activity (2.56%). It was also observed that 4 days after reactor shutdown, 60% of the initial activity is due to the source matrix, but that 80% of the associated dose rate results from the gamma radioelements of the housing matrix (i.e. ^{56}Mn, ^{187}W , ^{52}V and ^{182}Ta). Beyond this time (> 4 days), the induced dose rate and activity result from the housing matrix.

HCLL

The percentage of the activity and the dose rate for each matrix (housing matrix, source matrix and beryllium layer) of the HCLL was calculated.
As the beryllium layer was not taken into consideration in the basic data, it was decided to use the values for the HCPB where the times after irradiation were similar. It can be seen that the beryllium layer influences neither the dose rates (0.01%) nor the activity (0.24%). The same findings were established for the HCPB TBM.

It was also found that:

- Upon reactor shutdown, 98% of the activity came from the LiPb matrix. The induced dose rate therefore comes from the dosing lead radioelements, i.e. ^{207m}Pb, ^{203m}Pb, ^{20}F, and ^{208}Tl,
- 4 days after reactor shutdown, approximately 70% of the initial activity was due to the source matrix, but that more than 99% of the associated dose rate came from the gamma radioelements of the housing matrix (i.e. ^{56}Mn, ^{187}W , ^{52}V and ^{54}Mn),
- Beyond this time (> 4 days), the induced dose rate and activity come from the housing matrix.

The dose rate (in Sv/h) as a function of time (in days) was estimated for:

- a TBM that has not been drained of LiPb,
- a TBM that has been drained.

At reactor shutdown, it can be seen that 50% of the total dose is due to PbLi radiocontaminants. As these radioelements have a short half-life (^{207m}Pb: 0.8s, ^{203m}Pb: 6.3s, ^{20}F: 11 s, ^{208}Tl: 3 min), the dose rate decreases very rapidly, contributing to less than 1% of the total dose after 4 days. Beyond 4 days, the dose rate comes mainly from the metal housing. During TBM handling, the storage of PbLi should not raise any problems in terms of dosimetry.

The HCLL TBM will be handled empty, i.e. once the PbLi has been drained. The dose-rate results for the drained HCLL under pseudo-contact conditions are ranging from $3.77 \cdot 10^{3}$ to $1.24 \cdot 10^{-3}$ Sv/h.

Although it is not one of the majority elements accounting for 90% of activity, ^{210}Po appears on the list of radionuclides given by activation calculations. However, as this element is an alpha emitter, it poses no problem in terms of radiation protection (dose rate).

SUMMARY OF DOSE ESTIMATION FOR MAINTENANCE OPERATION

Estimations of dose rate from the frame at 5 (pseudo contact), 10, 30 and 100 cm are conducted using a simplified modelled method. The dose rate calculation behind the bioshield at 5 (pseudo contact) and 100 cm is estimated using a deterministic calculation code Microshield.

A summary of the dose rates results are provided in the table 1.

For dose estimation during maintenance operation, the following steps for the removal and reinstallation of TBMs as well as the associated work effort are taking into account (table 2).

Table 1: Dose rates results

Source hypothesis	Time	Activity Bq	Frame				Bioshield	
			Dose rate Sv/h 5 cm	Dose rate Sv/h 10 cm	Dose rate Sv/h 30 cm	Dose rate Sv/h 1 m	Dose rate Sv/h 5 cm	Dose rate Sv/h 1 m
3.15 cm	1 s	9.51E+16	5.46E+03	5.22E+03	4.23E+03	1.85E+03	6.01E-07	4.71E-07
	4 days	1.12E+16	4.62E+02	4.42E+02	3.59E+02	1.58E+02	5.14E-08	4.02E-08
	12 days	1.07E+16	4.43E+02	4.24E+02	3.45E+02	1.52E+02	4.94E-08	3.87E-08
	1 year	4.80E+15	1.60E+02	1.52E+02	1.24E+02	5.43E+01	1.77E-08	1.38E-08
41.85 cm	1 s	4.80E+15	1.60E+02	1.52E+02	1.24E+02	5.43E+01	1.77E-08	1.38E-08
	4 days	2.99E+14	1.26E+01	1.21E+01	9.84E+00	4.32E+00	1.40E-09	1.10E-09
	12 days	2.83E+14	1.21E+01	1.16E+01	9.41E+00	4.13E+00	1.34E-09	1.05E-09
	1 year	7.02E+13	4.24E+00	4.05E+00	3.29E+00	1.44E+00	4.68E-10	3.67E-10

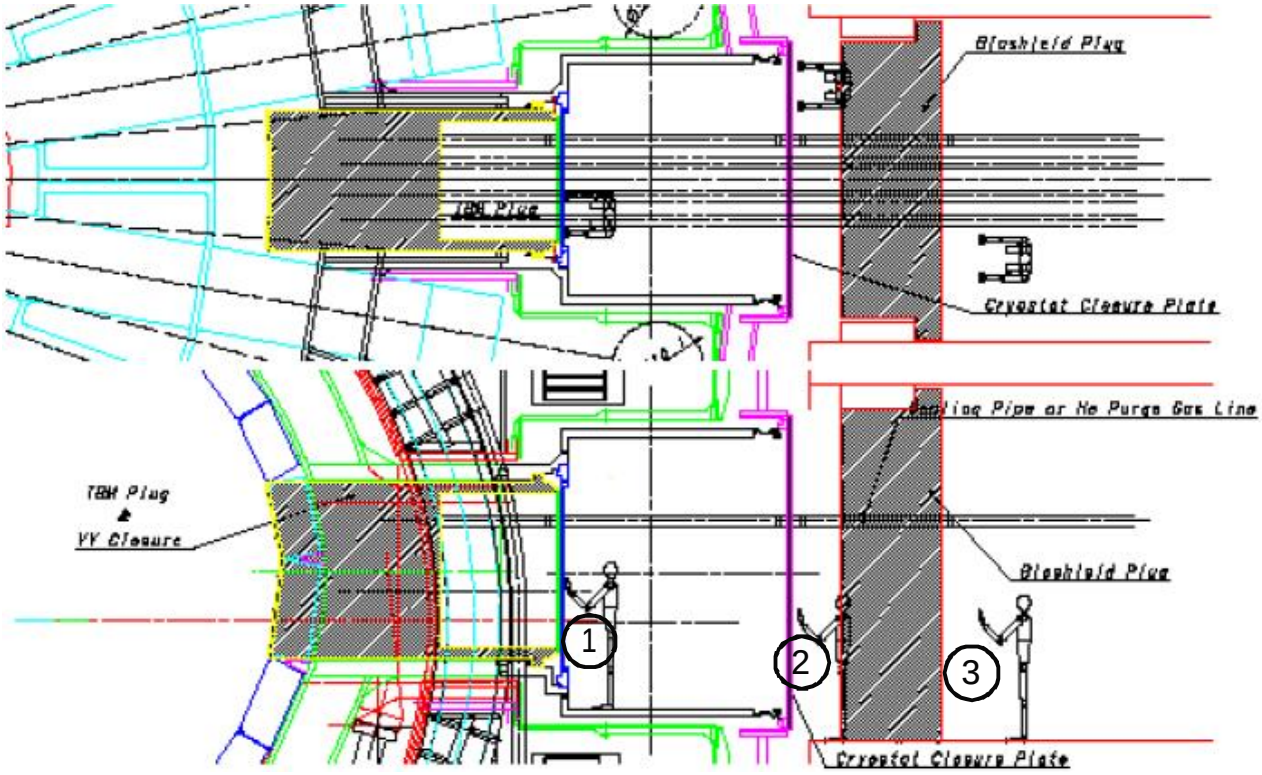

Figure 1

Table 2: Steps for removal and reinstallation of TBMs

Operating Step	Description	Work Effort (h)
1	Clear Port Cell for RH Cask Access	201.95
2	Remove Bio-Shield Block	57.20
3	Clear Port Interspace for RH Cask Access	178.25
4	Prepare port flange for RH cask docking	12.25
5	TBM Removal & Replacement	0.00
6	Rework Port Flange	13.50
7	Reinstall Port-Interspace Piping	182.90
8	Reinstall Bioshield Block	41.15
9	Reinstall Port-Cell Piping	206.80
TOTAL		894.00

According to the steps of the removal and reinstallation of TBMs and from the dose rate calculation, the following three positions are retained for the dose calculation (figure 1):

- Position 1: dose rate calculated 1m behind the TBM frame,
- Position 2: dose rate calculated 3 m behind the TBM frame,
- Position 3: dose rate calculated 5 cm (pseudo-contact) behind the bioshield.

In order to keep a conservative approach, the dose rates have been assigned to each step as shown in table 3.

Table 3

Operating Step	Dose rate position	Note
1	3	conducted behind the bioshield
2	3	conducted behind the bioshield
3	1	includes handling of pipes from the TBM
4	2	conducted in the port–interspace at a certain distance from the TBM
5	X	Remotely controlled
6	2	conducted in the port–interspace at a certain distance from the TBM
7	1	includes handling of pipes from the TBM
8	3	conducted behind the bioshield
9	3	conducted behind the bioshield

The work conducted behind the bioshield seems in accordance with the international radioprotection recommendation. A more detailed study is necessary in order to optimize, with an ALARA approach, the work conducted behind the bioshield.

The present approximation was to set conservatively the entire activation within the back frame. A more detailed activation calculation would provide an a priori lower estimate. In particular, the elements located in the space remaining between the TBM and the back frame could provide a form of neutron shielding susceptible to reduce the activation of the back frame.

The work conducted within the port interspace will need remote control. According to the dose rate results it will not be possible to send workers in this zone.

REPORTS AND PUBLICATIONS

Nuclear Dosimetry of HCLL and HCPB TBMs, CEA internal report
DTN/STPA/LPC/2007/41, October 22/2007 – G. Manon, O. Gastaldi, C. Lacressonniere

TASK LEADER

Christelle LACRESSONNIERE and Karine LIGER

DEN/DTN/STPA/LPC
CEA-Cadarache
F-13108 Saint-Paul-lez-Durance Cedex

Tel: 33 4 42 25 35 50
Fax: 33 4 42 25 24 10

e-mail: christelle.lacressonniere@cea.fr

CEFDA06-1513

Task Title: TW6-TTFD-TR66-2: DESIGN STUDY ON ITER HVAC/LAC, DEPRESSION SYSTEMS, ADS/VDS AND SAFETY TRITIUM MONITORING

INTRODUCTION

This work constitutes a synthesis of design requirements and fundamental safety demonstration of ITER nuclear ventilation and detritiation systems.
It describes since general and regulatory requirements, the development of functions and design requirements held for ITER.
This work would be the starting point of the detail design of nuclear ventilation and detritiation systems.
NB: The ventilation of the control room of the nuclear complex would need specific devices to protect the operator during any accidental events. These devices and functions have not been developed in this study.
In a first part, all the main regulatory reference documents are presented, from decrees to ISO standards and so on. In a second phase the methodology for dimensioning safety functions of ventilation. Then comes a detailed description of the safety functions linked to ventilation and the regulatory and standards requirement are presented for each function. A proposal of transposition is done to comply with ITER specificities. The consequences on ITER design are then analysed. And then a basic configuration is proposed to ITER designers.

2007-2008 ACTIVITIES

METHODOLOGY FOR DIMENSIONING SAFETY FUNCTIONS OF VENTILATION

The safety design of ventilation systems is mainly based on the analysis of dissemination risk. It gives a containment-area classification of rooms according to the level of contamination, which could be reached (cf ISO17873 §8.1.1) in the different situations.
It can be highlighted that for the safety analysis on dissemination risk, it is needed to overestimate the internal exposition level based on the simple inhalation of integrated doses due to transfer through the skin.
From the confinement class of each area, the usual values of the main parameters of design and sizing of ventilation system for each area can be determined.
The situations to analyse for the ventilation systems design are:

- Normal situations of operation:
  - Nominal situation of ventilation functioning:
    All functions are maintained at nominal level
  - Situations with lower functions or reduced functioning of ventilation:
    The confinement function is preserved (direction of the air flow) and compensatory devices are taken as exploitation restriction permitting to limit risks of dissemination incident or level of consequences
  - Exceptional operating conditions:
    The functions of the ventilation system are stopped in a volunteer manner to insure exceptional maintenance operations or modifications of the facility. The operations are prepared in advance and the facility is put in safe state
- Incidental situations of dissemination
  Safety functions of the ventilation must be provided at their nominal performances
- Accidental situations taken into account in the design of ventilation systems
  The ventilation limits consequences of the accident
- Accidental situations not taken into account in the design of ventilation systems

The limitation of accidental consequences is based on a set of containment barriers (static confinement) which is safer in these cases than dynamic confinement *[The safety relies on a set of static barriers of confinement and not only on the primary confinement]*.

The analysis of devices adapted to confine and to treat aerosol contamination and tritium contamination needs to differentiate risks from aerosol radioactive contamination, risks from toxic chemical aerosol (Beryllium) and risks from tritium contained in gaseous compounds.
Classification in radiological area concerns the addition of internal and external radiological exposure for normal operation situations. Though the containment classification for the ventilation could be different and specific care shall be taken to avoid compatibility between the two classifications (cf: ISO17873 §8.1.2).
The analysis and evaluation of each risk of internal or external aggression leads to reinforce or to complete the arrangement of dynamic confinement system in order to be able to guarantee the upholding of the performances needed to manage the aggression scenarios.

DESCRIPTION OF THE FUNCTIONS AND CONSTRAINTS OF VENTILATION SYSTEMS

After a brief recall of the main parameters of design for ventilation systems, a description of the functions and constraints of ventilation systems is given.
This part of the work allows identifying how can be taken into account in ITER design the functions and the constraints induced by regulations and standards used in France for the conception of nuclear ventilation systems.
The classical functions of nuclear ventilation systems are described on the basis of the definitions given in ISO 17873 standard.

The complementary functions and the ITER specific functions (not precised in the standard) are defined on the basis of the experience of nuclear ventilation experts.
The nuclear specificity of ventilation systems does not exclude the need to insure conventional functions (such as heating and air conditioning) of ventilation systems.
In the following chapter, an example is given on the way to proceed with each safety function. The example concerns cleaning function. Cleaning is a classical safety function of ISO17873 Standard:
"Cleaning: the ventilation system renews the volume of air within a room in order to minimize the risks associated to the corresponding atmosphere".

ANALYSIS OF EACH REQUIREMENT AND CONSEQUENCES ON DESIGN

In all the following tables, the values which are proposed only answer to the requirements in the first column of the table, without doing any synthesis of other requirements. Then the designers must take care choosing the most stringent values in order to define and size the systems and equipments.
The same example than previously is develop fed (cleaning function).

Regulatory and standard requirements:	ITER requirements held for the design
1. To supply fresh air for workers as near as possible of their work station	1. To supply fresh air for workers as near as possible of their work station
2. To renew air of areas to dilute and discharge the toxic or dangerous compounds present in the atmosphere in normal operation conditions and to come back quickly to a normal level after an incident/accident in order to limit the exposure of workers	2. To renew air of rooms, enclosures or plenum tank atmosphere to reduce the pollution level in normal operation conditions and to come back as quickly as possible to a normal level after an incident
3. To do extraction as near as possible from origins of pollution to evacuate pollutant	3. To do extraction as near as possible from the origin of pollution to evacuate pollutant
4. To mix the atmosphere of room to reduce risk of accumulation in dead zone	4. To mix the atmosphere of room to reduce dead zone
5. To take into account internal hazards and specifically fire, explosion and anoxia risks	5.1 To participate to the getting rid of the smoke without being obliged to size the systems to get rid of the smoke in the rooms.
	5.2 To limit explosion risks by limitation (as far as possible) of the concentrations at values lower than explosivity limits
	5.3 To limit anoxia risk by limiting as far as possible the concentrations at values lower than anoxia limits.
	5.4 To check other internal hazards have no consequences on the cleaning
6. To take into account external hazards and specifically seismic consequences	6.1 To limit damages induced by a seism on the systems allowing the cleaning
	6.2 To check other external hazards have no consequences on the cleaning

ITER requirements held for the design	Point of design mainly concerned	Proposed values or devices [justification of configuration proposed]	Safety and technical fundamental elements ITER has to demonstrate for this design
1. To supply fresh air for workers as near as possible of their work station	**HVAC:** Flowrate	**25m^3/h to 60m^3/h per person according to physical efforts of the work** [work code Article R232.5] [NB: These values are not sizing criteria for nuclear ventilation systems]	
2. To renew air of rooms, enclosures or plenum tank atmosphere to reduce the pollution level in normal operation conditions and to come back as quickly as possible to a normal level after an incident	**HVAC:** Extraction flowrate Threshold of switching from HVAC to VDS	• Room containment class C2 normally non active with no specific hazard: renewal rate =1/h • Room containment class C2 with medium potential hazard: renewal rate =2/h • Room containment class C3 with high potential hazard: renewal rate =3/h **[ISO17873 §8.2.5]**	Prove renewal rate is sufficient to maintain in normal situation residual tritium concentration in rooms < 1 DAC. Prove renewal rate is sufficient to limit the worker exposure in incidental situation. Prove renewal rate permit to limit the explosion risk.
	Room VDS: Extraction flowrate Threshold of switching from HVAC to VDS	• Rooms containment class C3 in incidental situation: renewal rate > 25%/h ***"[to limit the increase of the contamination < 4000DAC for a switch threshold of 300DAC]"*** • Rooms containment class C3-C4 for normal operation : renewal rate = 20%/h	Prove renewal rate is sufficient to limit the tritium concentration in the threshold of the containment class of room (C3 < 4000 DAC) after a switch from HVAC to Room VDS. Prove renewal rate permit to limit the explosion risk.

ITER requirements held for the design	Point of design mainly concerned	Proposed values or devices [justification of configuration proposed]	Safety and technical fundamental elements ITER has to demonstrate for this design
2. To renew air of rooms, enclosures or plenum tank atmosphere to reduce the pollution level in normal operation conditions and to come back as quickly as possible to a normal level after an incident	**Enclosure VDS:** Extraction flowrate Threshold of switching from HVAC to VDS	• Glove box containment class C4 : renewal rate = 0.25 Vol/h	To check renewal rate is sufficient to control neutral atmosphere of glove box Prove renewal rate is sufficient to control the tritium concentration in case of failure of GDS
	GDS: Extraction flowrate Threshold of switching from HVAC to VDS	• Glove box containment class C4 for normal operation: renewal rate = 5 Vol/h • Glove box containment class C4 in incidental operation: renewal rate = 15 Vol/h	Prove normal renewal rate is sufficient to maintain in normal situation tritium concentration < 5500DAC [Valduc value] Prove incidental renewal rate is able to catch 99% of tritium after 1 hour [Valduc value]
3. To do extraction as near as possible from the origin of pollution to evacuate pollutant	**HVAC and Room VDS:** Piping **Building:** Room arrangement	**Extraction points in room are laid out to be near the risk**	
4. To mix the atmosphere of room to reduce dead zone	**HVAC and Room VDS: Blowing rate**	**HVAC:** **The blowing network deserves all points of the room** **The air jet range reaches all points of the room.** **Room VDS:** ***"Many dead zone without blowing system" [the self diffusion of gas is not very fast and could lead to stratification, then the quality of mixing remains important]***	Prove dead zone are few many because of the design Check by test that instrumentation (contamination, fire …) will be detected. .
5.1 To participate to the getting rid of the smoke without being obliged to size the systems to get rid of the smoke in the rooms	**HVAC, Room VDS, Enclosure VDS, GDS:** Pilotage	**To isolate the HVAC of room in case of fire detection, no more cleaning in the room during the fire** **Start a cleaning operation by Room VDS recycling after the extinction of the fire in case of tritium release in the room** ***[Taking into account the low renewal rate allowed by detrititation systems, recycling remains one of the only way to lower the level of fumes and contamination of areas after incident or maintenance operations]***	
	HVAC Protected area	**Participate to evacuation of fumes**	
5.2 To limit explosion risks by limitation (as far as possible) of the concentrations at values lower than explosivity limits	**HVAC**	**Sufficient renewal rate compared to hydrogen source** **Redundancy of active equipments of HVAC**	Check that renewal rate of rooms are sufficient to limit the risk
5.3 To limit anoxia risk by limiting as far as possible the concentrations at values lower than anoxia limits.	**HVAC**	**Sufficient renewal rate compared to anoxia source**	Check that renewal rate of rooms are sufficient to limit the risk
5.4 To check other internal hazards have no consequences on the cleaning	**HVAC, Room VDS, Enclosure VDS, GDS:**		Prove other internal hazards have no consequences on HVAC and VDS
6.1 To limit damages induced by a seism on the systems allowing the cleaning	**HVAC**	**Limit degradation for a SL0/SL1 seism to help the post accidental management**	
	Room VDS, GDS:	**Limit degradation for a SL0/SL1 seism to help the post accidental management**	
	Enclosure VDS	**Working after a SL1/SL2 seism**	
6.2 To check other external hazards have no consequences on the cleaning	**HVAC, Room VDS, Enclosure VDS, GDS:**		Prove other external hazards have no consequences on HVAC and VDS system

CONCLUSIONS

This work is a first in order to precise what could the specific requirements on ITER ventilation towards an analysis of regulatory documents and ventilation experts feedback in the particular case of tritium.
This work is iterative with the design and the safety analysis and strategy in order to be completely in coherence with the definitive retained design.
A large part of demonstration is needed to show that the retained design is in coherence with the requirements.

REFERENCES

Main regulation texts about confinement and ventilation:

- Decree 63.1228
  - Nuclear safety in France
- Order of December 31st,1999 modified on January 31st ,2006
  - Protection of the environment
- Decree Mai 4th, 1995
  - Liquid and gas release
- Order of November 26th ,1999
  - Limits and technical requirements for normal releases
- Order of October 7th ,1977
  - Periodicity for checking parts of ventilation system and purification devices
- Regulation about protection from radiation (order concerning radioprotection zoning, order concerning internal exposure of workers, count of expositions doses)
  - Workers protection against radiation
- Work code article R.232-5
  - Workers protection
- Decree 2003-296
  - Workers protection
- Decree 2002-460
  - People protection

Main safety documents linked to confinement and defining objectives to reach for ITER:

- Safety options files (DOS, GSSR, …)
  - Safety Objectives
- Specific needs coming from DAC, RPrS (from safety analysis)

Main Safety Rules:

- RFS II.2 (1991)
  - Requirements about design and operation of ventilation system
- RR1 (1986)
  - Requirements for Research Reactor about purification devices and efficiency
- Guide for application of the order of December 31st 1999: fire topic of 01/04/2006
  - Integration of the requirements on the arrangements concerning fire

International and French Standards:

- Standard ISO17873 (2004) = NF/ISO17873(2006)
  - Criteria for the design and operation of ventilation system for nuclear installations
- Standard NF/ISO11933-4 (2001)
  - Ventilation system for containment enclosures
- Standard ISO10648-1 and 2
  - Tightness test of enclosures
- Standard NFX44.01
  - Test to check the filter efficiency
- And standards about containment box, security enclosures, aeraulic machines, ventilation duct, climatic conditions for comfort, method of test …

French guides:

- "Guide de ventilation des installations nucléaires" from CEA/CETREVE (1987)
  - Rules of design for nuclear ventilation system
- CEA/PMDS guides about containment enclosures and their ventilation
  - Recommendations to choose the tightness of a glovebox
- IRSN functional specifications (CTHEN documents n° 93.030 et 93.031)
  - Specifications for equipment to have the homologation as nuclear equipment

REPORTS AND PUBLICATIONS

Technical document CEA/DTN/CAD/DTAP/STL/GFDV DO 300
ITER – HVAC- Ventilation and Detritiation System-Requirements
Synthesis of design requirements of ITER ventilation and detritiation systems

TASK LEADER

Olivier GASTALDI

DEN/DTN/STPA/LTTS
CEA-Cadarache
F-13108 Saint-Paul-lez-Durance Cedex

Tel: 33 4 42 25 37 87
Fax: 33 4 42 25 79 49

e-mail: olivier.gastaldi@cea.fr

CEFDA06-1518
CEFDA07-1700-1591

Task Title: TW6-TSS-SEA4.5: FEASIBILITY STUDY OF POSSIBLE PREVENTION OF HYDROGEN EXPLOSION IN ITER BY INJECTION OF NEUTRAL GAS – EXPERIMENTS AND CALCULATIONS FOR DEMONSTRATION OF INERT GAS INJECTION FEASIBILITY

INTRODUCTION

The feasibility study of possible prevention of hydrogen explosion in ITER by injection of inert gas has been investigated in the case of the so-called wet-bypass scenario accident in the frame of this task by three associations: Studsvik (Sweden), FZK (Germany) and CEA.

Analyses are based on the scenario definition and data described in [1] and are performed with different numerical tools based on different models and numerical methods. Due to the complexity of the phenomena encountered, a large number of parametric studies were performed to evaluate the sensitivity of the results to unknown or not well known parameters.

The pressure build-up in the vacuum vessel (VV) and in the suppression tank (ST) is predicted and the risk of hydrogen explosion is evaluated. The analyse shows a strong reduction of the hydrogen explosion risk when mitigation is done by nitrogen injection, however this mitigation is not enough to circumvent totally the risk.

2007-2008 ACTIVITIES

Our activity during this period was of twofold, first we performed a full analysis of the wet by-pass scenario and the efficiency of mitigation, second, during this period, we were in charge of coordinating the action of the three partners involved (Studsvik, FZK and CEA) and prepared a synthesis note.

SCENARIO STUDIED

The studies of interest here concern the so-called wet bypass scenario characterized by the following sequence:

- Break of the first wall cooling loop inducing a water leak in the vacuum vessel (VV), the break size corresponds to the area of the five first wall cooling tube.
- The maximum flowrate is estimated to be 40 kg/s of water from a previous MELCOR calculation (figure 1) extracted from [1]. The break is assumed to be located at one of the equatorial port (EP) of the vacuum vessel.
- Simultaneously, break of one window of a penetration, with an area of 0.01 m² inducing ingress of air from the atmosphere. Previous MELCOR calculation gave an estimate of this flowrate (figure 2 extracted from [1]). The break is assumed to be located at one of the equatorial port (EP) of the vacuum vessel.

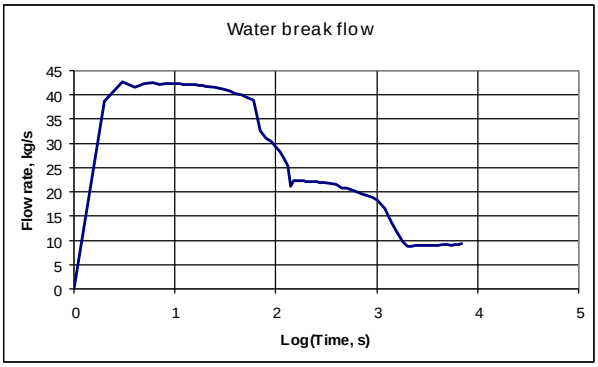

Figure 1 : Water break flow in the VV at "wet bypass" event (without gas injection)

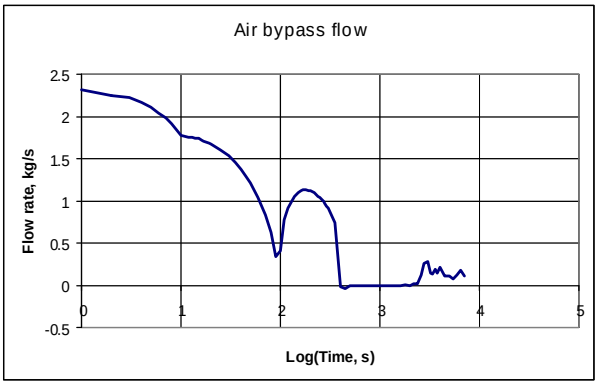

Figure 2 : Air bypass flow in the VV at "wet bypass" event (without gas injection)

- Beryllium-steam reaction occurs and produces 20 kg of hydrogen during the first 10 seconds of the transient.
- A few seconds after leaks detection, nitrogen injection is started at a maximum flowrate of 6.4 kg/s, the exact time and location of nitrogen injection is not strictly defined and will be investigated through parametric studies.
- The low pressure at the beginning of the transient (4.2 kPa) in the vacuum vessel (VV) will increase due to the steam and air ingress and further increased when nitrogen injection is started. When the pressure difference in the relief pipes increases 90 kPa, the valves will open.

When pressure difference increases further to 150 kPa, the first rupture disk will open and the second rupture disk will open for pressure difference between of 20 kPa.

RESULTS

The analysis performed by Studvik [2] with INTRA model is a lumped parameter integral model of the facility, including VV and VVSS represented as 0D volumes and connected by flow junctions.

The analysis performed by FZK [3] with GASFLOW is composed of two baseline simulations; mitigated and unmitigated and a set of 32 sensitivity calculations.

The CAST3M model used by CEA is a 3D-fluid dynamics code based on finite-element techniques for solving the compressible Navier-Stokes equations under the assumption of Low Mach Number flows. The time discretization uses an implicit projection method allowing relatively large time steps. The meshing is 3 dimensional and uses an unstructured grid to account for complex geometries. Turbulence is modeled by an algebraic mixing length model.

The model proposed is limited to the vacuum vessel (VV), the vacuum vessel pressure suppression system (VVPSS) is not modeled so the transient stops at the time the relief valves open that is when pressure raises to 90 kPa.

Beryllium-Steam reaction is not modelled, the transient begins assuming an initial homogeneous distribution of 20 kg of hydrogen.

Wall temperature evolutions are imposed from the MELCOR model [4].

In order to be conservative, the total water mass flow rate is not taken from the MELCOR results. Instead, a constant steam mass flowrate is fixed at 5 kg/s (average value of steam mass flow rate given by the MELCOR model [4]. The air ingress mass flowrate is calculated via a critical flow model using a discharge coefficient of 1 and taken constant equal to 4.5 kg/s. The nitrogen mass flowrate is taken constant equal to 5 kg/s, several injection times and injection locations are tested.

This model allows the prediction of the spatial distribution and velocities of steam and non-condensable gases and uses relatively coarse meshing.

The concentration distribution is then used to calculate the risk of hydrogen explosion using a detonation index derived from the upper limit of the hydrogen-steam-air flammability curve [4].

The analysis performed by CEA with CAST3M is composed of a set of four sensitivity analysis to analyse the influence of steam and air mass flow rate location.

INFLUENCE OF STEAM AND AIR MASS FLOWRATE

Four calculations were performed. In order to have a conservative assumption by limiting the oxygen dilution by steam it was assumed that the air and steam inlets are located opposite on sides of the VV. The inlets are located at the equatorial port 1 (EP1) for the steam and EP10 for the air. The steam mass flowrate is taken equal to 5 kg/s (1 kg/s for parametric study) and the air flow rate is 2.5 kg/s (4.5 kg/s for parametric study). For nitrogen, a constant value of 5 kg/s was considered distributed over the 9 lower ports (LP). In the main case, the pressure of 0.9 bar corresponding to the opening of the relief valve is reached after 50 seconds.

As soon as the air enters the VV, a flammable cloud is created around the air inlet because of the quasi pure hydrogen existing at the beginning of the transient and the distance existing between the air and the inerting gases (nitrogen and steam) inlets. The mass enclosed in this flammable cloud varies from 1.5 kg to 17.5 kg depending on the assumptions made for the air and steam flowrates.

This analysis points out that the initial homogeneous hydrogen concentration hypothesis is very severe but could be removed only if more confidence were gained in the modelling of steam and beryllium dust distribution and chemical reaction. Another important parameter is the steam to air flowrate ratio which should be as large as possible to promote the premix of air. This parameter could be kept high by a careful design of the penetration line. Burning the hydrogen as soon as it is created is also mentioned as a possibility.

INFLUENCE OF STEAM AND AIR INLET LOCATIONS

Twenty calculations were performed. The steam mass flow rate is 5 kg/s and several locations of the inlet are successively used at EP and LP. The air mass flow rate is 2.5 kg/s located successively at EP6 or EP15. For nitrogen, a constant value of 5 kg/s was considered distributed over the 9 LP.

The steam inlet elevation proves to have little influence on the flammable cloud volume although the EP location is slightly safer. The location of the air inlet with respect to the steam inlet is of prime importance and can change the flammable cloud volume up to a factor of seven from 0.3 kg to 21 kg. When the steam inlet is close to the air inlet, the flammable cloud is smaller due to oxygen dilution by steam.

INFLUENCE OF NITROGEN INERTING

Inerting with nitrogen injection leads to a faster pressurization of the VV (50 seconds, to be compared with 80 when no injection is performed) and a faster opening of the bleed line. Nitrogen injection has a positive effect on the flammable cloud development, but it does not eliminate the risk of detonable cloud formation, especially close to and below the air injection location.

INFLUENCE OF NITROGEN SOURCE ELEVATION

Two calculations were compared, one with the nitrogen injections located at the EP, the other one with nitrogen injections located at the LP. Nitrogen injections located at the EP lead to a smaller flammable cloud because of the better mixing with air (air inlet is located at the EP).

CONCLUSIONS

The feasibility study of possible prevention of hydrogen explosion in ITER by injection of inert gas was investigated in the case of the so-called wet-bypass scenario accident in

the frame of this task by three organizations: Studsvik (Sweden), FZK and CEA. Analyses are based on the same data than those described in [1] and are performed with different numerical tools based on different models and numerical methods. Due to the complexity of the phenomena encountered a large number of parametric studies were performed to evaluate the sensitivity of the results to unknown or not well known parameters.
The three models developed describe the pressure build-up in the vacuum vessel (VV). The time for rupture disks opening is estimated to be 50 s for the CAST3M model, 60 s for the INTRA model and 100 s for the GASFLOW model. It should be noted that this time depends strongly on the steam generation from water release at the break, impinging jet on the hot wall and sump boiling and that these phenomena are not taken into account accurately in the models used. The pressure build-up in the suppression tank (ST) after the rupture disk opening is also driven by the amount of non condensable gases entrained in the ST. The higher the nitrogen injection is the more important will be the pressure build-up. The entrainment on non-condensable gases to the suppression tank depends on the local concentration in the VV and the HNBI modules and is not modelled accurately.

Investigation performed with GASFLOW and CAST3M propose an evaluation of the hydrogen explosion risk based on the space and time evolution of hydrogen, steam, air and nitrogen concentrations. The hypothesis used are very different: GASFLOW models the chemical reaction leading to a local hydrogen production during 35 seconds whereas CAST3M considers an homogeneous initial concentration of hydrogen; the air and nitrogen flow rates are time dependant for GASFLOW whereas they are constant for CAST3M and finally, the explosion risk is characterized by flame acceleration and deflagration to detonation criteria in the case of GASFLOW and by a detonation index in the case of CAST3M. Nevertheless both analyses show a strong reduction of the hydrogen risk when nitrogen mitigation is used but still explosion risk cannot be excluded. Both analyses showed that local concentration of explosive mixture can exist (which could not be identified with the previous lumped parameter analyses performed). Both analyses found a detonable cloud close to the air inlet.

Based on these analyses, two directions of improvement are proposed: the first one is based on the current knowledge and proposes to review the design to reduce the hydrogen risk; the second highlights areas where a research effort could allow a better understanding of physical processes to allow relaxing conservative assumptions. It is suggested that both improvement should be investigated.

First, a significant reduction or removal of the oxygen or hydrogen source should be obtained by design; this could be obtained by limiting the penetration section to 0.005 m², by using a more effective flame suppressant than nitrogen or by removing hydrogen and oxygen by early deliberate ignition. A combination of these three actions should be studied.

Second, these studies relied on conservative hypothesis due to a lack of knowledge of actual processes that could take place during the accident. This knowledge should be improved by specific research actions, including both experimental and modeling effort in three directions:

- Better understanding of the dust mobilization processes and dust-steam reaction kinetic,
- Better understanding of the distribution and mixture of light and heavy gases processes (hydrogen, nitrogen, air and steam) at the specific thermodynamic conditions and geometry encountered in the ITER reactor (including local effects at the vicinity of the heating neutral beam injector (HNBI),
- Better understanding of the steam formation at the break as steam will have a negative effect on pressure build up but a positive effect on the flammability of the mixture. The quantity of steam produced by direct vaporization, hot surfaces impingement and pool boiling should be assessed.

REFERENCES

[1] L.Topilski, Main parameters and assumptions that should be taking into account in the model of inert gas injection system for hydrogen explosion suppression, Technical report ANNEX 2 TO TA G 81 TD 29 FE, 2006

[2] Zemichael Yitbarek, 2007, INTRA simulation results: Hydrogen explosion prevention during wet bypass accident, EFDA-04-1193/D3, Studsvik report N-07/157

[3] J. Xiao, J.R. Travis, W. Breitung, T. Jordan, Feasibility study of possible prevention of hydrogen combustion in ITER by injection of inert gas, Forschungszentrum Karlsruhe, EFDA 06-1517, IKET, February 2008

REPORTS AND PUBLICATIONS

[4] F. Dabbene, 2008, Feasibility study of possible prevention of hydrogen combustion in ITER by injection of neutral gas, EDFA Task TW6-TSS-SEA4.5 D1, D2 CEA Report DM2S/SFME/LTMF/RT07-059/A

TASK LEADER

Alain BENGAOUER

DEN/DM2S/SFME/LTMF
CEA-Saclay
F-91191 Gif-sur-Yvette Cedex

Tel: 33 1 69 08 59 36
Fax: 33 1 69 08 82 29

e-mail: alain.bengaouer@cea.fr

CEFDA07-1700-1549

Task Title: TW6-TSS-SEA5.6b: VALIDATION OF THE PACTITER COMPUTER CODE AND RELATED FUSION SPECIFIC EXPERIMENTS IN CORELE LOOP

INTRODUCTION

The Activated Corrosion Products (ACP) in the ITER Primary Heat Transfer Systems (PHTS) or Tokamak Water Cooling Systems (TCWS) can be a major concern as contributor to the source term of potential released activity to the environment in case of accident and to the Occupational Radiological Exposure (ORE) during the normal operation of ITER. By consequences, the precise determination of ACP inventories and the estimation of the resulting doses to personnel is thus an important safety issue.
The PACTITER code was used for the calculation of generation and transport of ACP in the various PHTS or TCWS. The CORELE test facility, devoted to the measurement of the release of industrial tube section, provides data for the PACTITER code.

2007-2008 ACTIVITIES

2007-2008 activities were dedicated to the PACTITER V3.3 code release and to the experimental characterization of the release from two stainless steels (SS316L and SS304/B4) under ITER representative conditions.

STAINLESS STEEL RELEASE RATE EVALUATION IN THE CORELE TEST FACILITY

Principle and description of CORELE

The principle of the measurement of release rates in the CORELE loop consists in continuously trapping the cationic metals released from two test sections on mixed bed ion exchange resins (see figure 1) and the particles of oxide on 0.45µm Millipore filters.

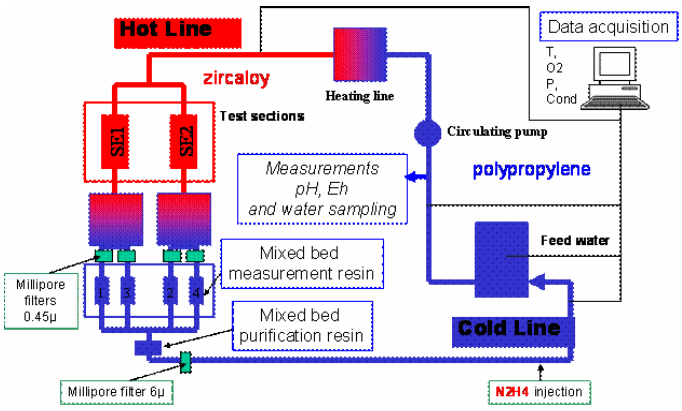

Figure 1: Schematic view of the CORELE loop

After sufficient release test duration, the resins and the 0.45 µm Millipore filters are disconnected from the circuit and the trapped quantity of the studied element is measured by chemical method, and the net release rate R (mg/dm²/month) is given by:

$$R = \frac{W}{At}$$

where:

- W: mass of metal in measurement resin or in filters (mg),
- A: exchange surface area between test specimen and water (dm²),
- t: time during which the resins and the filters are trapping the released products in the loop (month).

Acidic elution of the mixed ion exchange resins bed enables the release of the metallic ions. Each solution is analysed by ICP-AES spectroscopy. The metals trapped in the filters are dissolved by an acidic solution, the content of metallic elements being analyzed by ICP-AES spectroscopy.

Test SS08-1 on SS316L(N)-IG samples

This experimental phase on 316L(N)-IG test specimen was performed in 3 phases :

- T1: 100°C (574 hours)
- T2: 150°C (164 hours)
- T3: 125°C (130 hours)

The chemical composition of the CORELE water is deionised, deoxygenated (by N_2 bubbling) and with a very low water conductivity ensuring a neutral pH.
The measured values during this first experimental campaign (SS08-1) were the followings:

- pH: 6.75 – 7.19
- Conductivity: from 0.058 µS/cm to 0.073 µS/cm
- O2: between 80 ppb and 100 ppb
- Eh: between +175 and +280 mV (vs. Ag/AgCl).

Test SS08-2 on SS304/B4 and SS316L(N)-IG samples

The tests were performed at 100°C with a total duration of 934 hours.
The chemical composition of the water is deionised, deoxygenated (by N_2 bubbling) and with a very low water conductivity ensuring a neutral pH during a first experimental phase of a 736 hour duration.

The measured values during this second experimental campaign (SS08-2) were the followings:

- pH: 6.50 – 7.02,
- Conductivity: from 0.058 µS/cm 0.073 µS/cm,
- O2: between 48 ppb and 99 ppb,
- Eh: between +240 and +440 mV (vs. Ag/AgCl).

A second 198 hour experimental phase aimed to establish and control N_2H_4 content in the CORELE water. The pH was close to 7.5 and the conditions were clearly reducing.

Results on SS08-1 experiment on SS316L(N)-IG
One may note the following points:

- A low initial release rate with a fast decrease vs. time. Both release rates of Fe and Ni are under the detection limit (# 0.1 mg/dm²/month) after 17 days,
- No effect of flow velocity was detected,
- No significant amount of Fe or Ni was observed on filters.

The total release rate evolution during the SS08-1 experiment is shown figure 1, estimated by the sum of the release rates of iron and nickel.

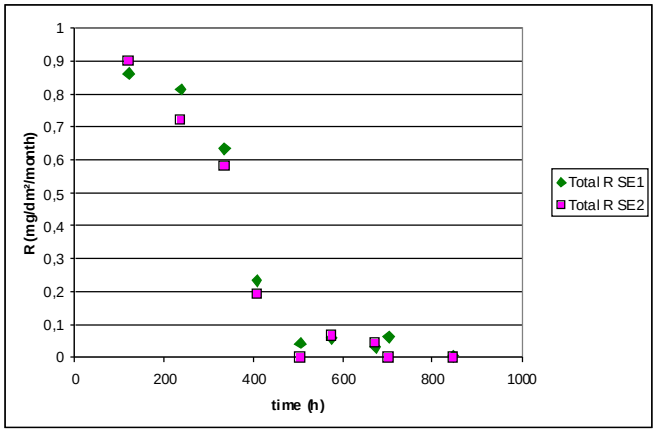

Figure 1: Total release during the SS08-1 experiment with pure water on SS136L (N)-IG test specimen

Results on SS08-2 experiment on SS304/B4 and SS316L (N)-IG
This SS08-2 experiment in the CORELE loop on SS304/B4 and SS316L (N)-IG provided some consistent data between nickel and iron:

- A low release rate, decreasing under the detection limit (# 0.05 mg/dm²/month),
- No significant amount of Fe or Ni was observed on filters,
- SS304/B4 and SS316L have the same kind of behaviour,
- The effect of reducing conditions is significant on SS304/B4 and SS316L.

The SS316L (N)-IG specimen display a lower release rate during the SS08-2 than during the SS08-1. This is consistent with the assumption of a progressive passivation of the metal.
In the considered period the three reports related to the operation experience of the Toroidal Field magnets (D01), the PFC cooling system including the analysis of the in-vessel water leak (D02) and the cryoplant (D03) were produced and accepted by EFDA.

PACTITER DEVELOPMENT

The PACTOLE code, developed by CEA in collaboration with EDF and AREVA, was designed to simulate the transfer of corrosion products in the primary system of a PWR. It determines the space-time distribution of masses and/or activity levels of corrosion products and activation products in both solid and liquid phases in the primary system.
On the same physical basis as the PACTOLE code, the PACTITER (Prediction of Activated Corrosion product Transfer for ITER) code was derived for a consistent application to the evaluation of ITER source terms. The last version of the PACTITER code is version 3.3.
There is no validation experiment of the PACTITER V3.3 code in a test loop representative of an ITER PHTS; the experiments performed in the CORELE loop provide input data for the PACTITER V3.3 code. On the other hand, the experimental feedback on PWR contamination by ACP is very large [1].
In order to provide elements of validation of the PACTITER V3.3 code, the modelling of the PACTITER V3.3 code is described in [1]. Then, a typical PWR operation is simulated with the PACTOLE V3.3 code and the results are compared to the contamination range of the French nuclear plants. Finally, the Divertor/Limiter cooling loop of the ITER TCWS is simulated with the PACTITER V3.3 code (see figure 2).

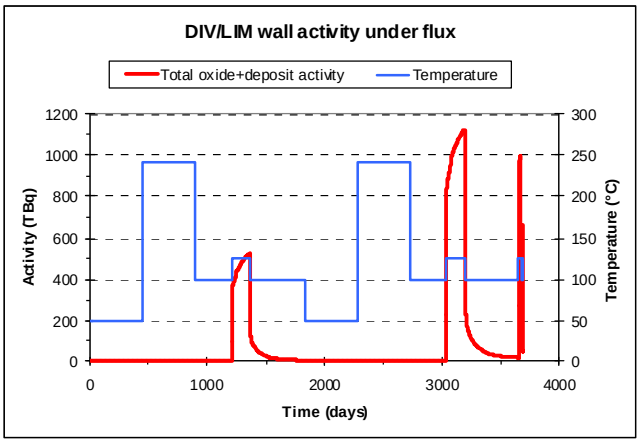

Figure 2: PACTITER V3.3 – Divertor under-flux wall activity (oxide + deposit)

CONCLUSIONS

Two test campaigns aimed to quantify the release of two stainless steels (SS316L(N)-IG and SS304/B4) were performed in the CORELE test loop. In pure water with slightly oxidizing conditions, the release rates of SS316L(N)-IG and SS304/B4 tend to decrease in 500 hours

to become negligible. We didn't point out any effect of flow velocity or temperature on the total release. On another hand, the effect of reducing conditions obtained by the injection of hydrazine (N2H4) on the release of SS316L(N)-IG and SS304/B4 test specimen appears to be significant.

The PACTOLE V3.3 code is validated for the transfer of the corrosion products in ionic form: the surface and volume activities of the two major radionuclides, ^{58}Co and ^{60}Co, calculated with the PACTOLE V3.3 code are similar to the on-site measurements. On the other hand, some ACPs are mainly transported in particle form and some nuclear auxiliary systems are mainly contaminated by the deposit of activated particles.
The simulation of the Divertor/Limiter cooling loop showed that the surface activities calculated with the PACTITER V3.3 code are of the same order of magnitude as those calculated with the PACTITER V2.1 code [2] . In addition, the PACTITER V3.3 code showed that the low purification flowrate could not assure the respect of specifications on element concentrations and on pH (conductivity in fact) during all the different operating phases.
The ways of improvement of the PACTITER code would be to better simulate the transfer of ACPs in particle form, to improve the copper behaviour and, above all, to perform an integral validation test in a test loop representative of an ITER PHTS.

REFERENCES

[1] F. Dacquait, C. Andrieu, L. Guinard, J.L. Bretelle, F. Bardet, A. Rocher, C. Brun, « Status of primary system contamination in French PWRs », Proceedings of the International conference on Water chemistry in nuclear reactors systems, 2004, San Francisco (USA), Session 2 Paper 4

[2] L. Di Pace, « Activated Corrosion products evaluation for the ITER TCWS DIV/LIM loop using PACTITER V2.1", ENEA FUS-TN-SA-SE-R-079, October 2003

REPORTS AND PUBLICATIONS

L. Di Pace, F. Dacquait, P. Schindler, V. Blet, F. Nguyen, Y. Philibert and B. Larat, "Development of the PACTITER code and its application to safety analyses of ITER Primary Cooling Water System", Fusion Engineering and Design, April 2007, Volume 82, Issue 3, Pages 237-247

F. Dacquait, "Status of the PACTITER code development", CEA Technical Report DTN/SMTM/LMTR/2007-003, February 2007

E. Tevissen and Y. Philibert, "CuCrZr release rate evaluation in ITER operating conditions"
CEA Technical Report DTN/SMTM/LMTR/2007-027, February 2007

E. Tevissen and F. Dacquait, "Quality Plan Task Objectives and detailed test matrix", CEA Technical report DEN/DTN/SMTM/LMTR/2008-015, May 2008

E. Tevissen and Y. Philibert, "Measurement of stainless steels release in CORELE loop", CEA Technical report DEN/DTN/SMTM/LMTR/2008 – 045, December 2008

F. Dacquait, F. Herbelet and M. Monin-Baroille, « Elements of validation of the PACTITER V3.3 code », CEA Technical report DEN/DTN/SMTM/LMTR/2008-46, December 2008

TASK LEADER

Frederic DACQUAIT

DEN/DTN/SMTM/LMTR
CEA-Cadarache
F-13108 Saint-Paul-lez-Durance Cedex

Tel: 33 4 42 25 61 62
Fax: 33 4 42 25 49 90

e-mail:frederic.dacquait@cea.fr

TW6-TSL-004

Task Title: COLLECTION OF DATA RELATED TO TORE SUPRA OPERATION EXPERIENCE ON COMPONENTS FAILURE

INTRODUCTION

The overall objective of this task was to enrich a fusion specific data collection (e.g. component failure rate database or more generally function failure) with data coming from Tore Supra operating experience. It referred to the systems of Tore Supra that are relevant to ITER and not present in other tokamaks:

- Cryo-plant, including Magnets, safety system (quench detection, energy dumping, …), leak detection/localization,
-
- PFC cooling system (including auxiliaries, e.g. power supply, compressed air, leak detection/localization…).

2007-2008 ACTIVITIES

In the considered period the three reports related to the operation experience of the Toroidal Field magnets (D01), the PFC cooling system including the analysis of the in-vessel water leak (D02) and the cryoplant (D03) were produced and accepted by EFDA.

The deliverable D1 addresses the analysis of the safety system associated with the superconducting Toroidal Field magnet of Tore Supra and the analysis of the causes and consequences of the Fast Safety Discharges (FSD). A special attention has been brought to the analysis of the operation of the safety system of the Toroidal Field system and on the consequences of malfunctions, which could lead to the triggering of a FSD. Since 1989 the operation of the superconducting magnet of Tore Supra has been found especially safe, stable and reliable. This system is currently operated since 19 years at 89% of its maximum operational capability (1400 A).

The constant improvements made on the systems to reduce as much as possible the occurrence of FSD are reported (figure 1).

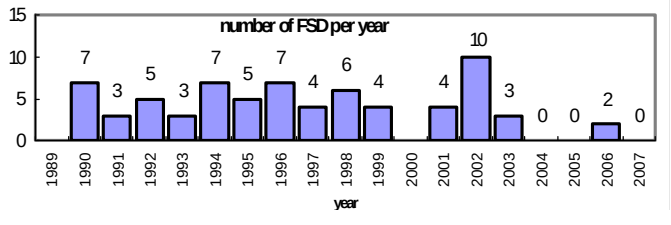

Figure 1: Time distribution of the FSD from 1989 to July 2007

The failures that occurred on the components of the Toroidal Field system were analyzed. The number of failures is so low that statistical analysis is not relevant. These failures concern the lost of 4 safety sensors (3 temperature sensors and one pressure gauge) among the 114 imbedded in the cryostat and in the coils, the 14 failures of the electronics boards and integrated circuits recorded between 1996 and 2007 and the 5 failures associated to the Toroidal Field power supply. The specific problem of the ageing of the DC current breakers was also analyzed.

In the Deliverable D02-1, a functional analysis of the Plasma Facing Components (PFC) cooling water loop, as well as a categorisation and compilation of maintenance/failure rate statistics under the perspective of the ITER design requirements were performed.

An original method based on the automatically stored data from the command-control system and using especially-developed tools for data processing is used to provide accurate estimates of the relevant statistical parameters. This method is used for the analysis of both the PFCs cooling system (deliverable D02-1) and the Cryo-plant (deliverable D03). These data allow the reconstruction of the operation conditions of the system (figure 2) as well as the failures encountered by the components.

The aim of this method is to provide, whenever possible, the information required by the task, which are the: number of individualized failure, number of components, number of damaged components, number of failure/component, mean working time/component (h), global working time (h), global number of demands, real global time of component unavailability (h), real mean time of component unavailability (h), real mean time of system unavailability (h), test interval (h), first date of failures and last date of failures. Given the very small number of failures encountered on the Plasma Facing Components cooling loop, the standard errors are important, even equalling the failures rates when only 1 failure has been confirmed.

A statistical analysis of such a small number of failures may be of dubious value in itself, so that's why it was decided, in addition to the results required by the task, to detail the maintenance performed on the components to obtain the availability measured for the PFCs cooling system, thus giving a more pertinent information.

Typically on the four last years analyzed (2003 to 2006) the average failure rate is one per year and per component (25 components are considered for the PFC cooling water loop). The average downtime per failure is 2h30min, for a typical working time of 6800h/year leading to an average availability of 97% during the operation period (taking into account the average time spent in the test mode). The details are given table 1.

Table 1: PFC cooling water loop availability from 2003 to 2006

		2003	2004	2005	2006
operation modes	Baking	5014 h	4735 h	4924 h	6036 h
	Plasma Preparation	114 h	115 h	159 h	210 h
	Plasma Operation	468 h	535 h	573 h	837 h
	Bypass	395 h	1276 h	430 h	329 h
	Test	109 h	28 h	515 h	73 h
Down time	Downtime on purpose	2614 h	2078 h	2035 h	1247 h
	Downtime on failure	3 h	1 h	85 h	6 h
	Transition or acquisition error	43 h	16 h	39 h	22 h
	Total number of hours	8760 h	8784 h	8760 h	8760 h
Availability relatively to the whole year (Baking+Plasma Prep+Plasma Op+Bypass)/Total		68,4%	75,8%	69,5%	84,6%
Availability relatively to the B30 exploitation (Baking+Plasma Prep+Plasma Op+Bypass)/(Total-Downtime on purpose)		97,5%	99,3%	90,5%	98,7%
Availability relatively to the plasma operation results obtained from analysis of the other sources of data		97,5%	99,2%	98,7%	99,5%

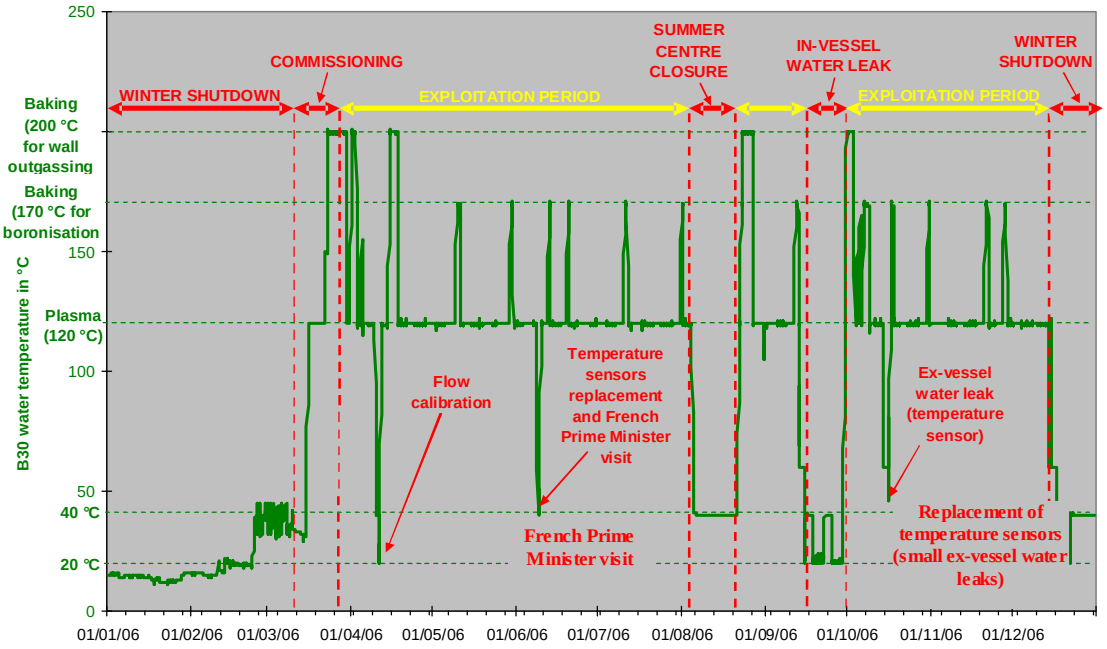

Figure 2: Tore Supra operation in 2006, reconstructed from the PFC cooling water temperature

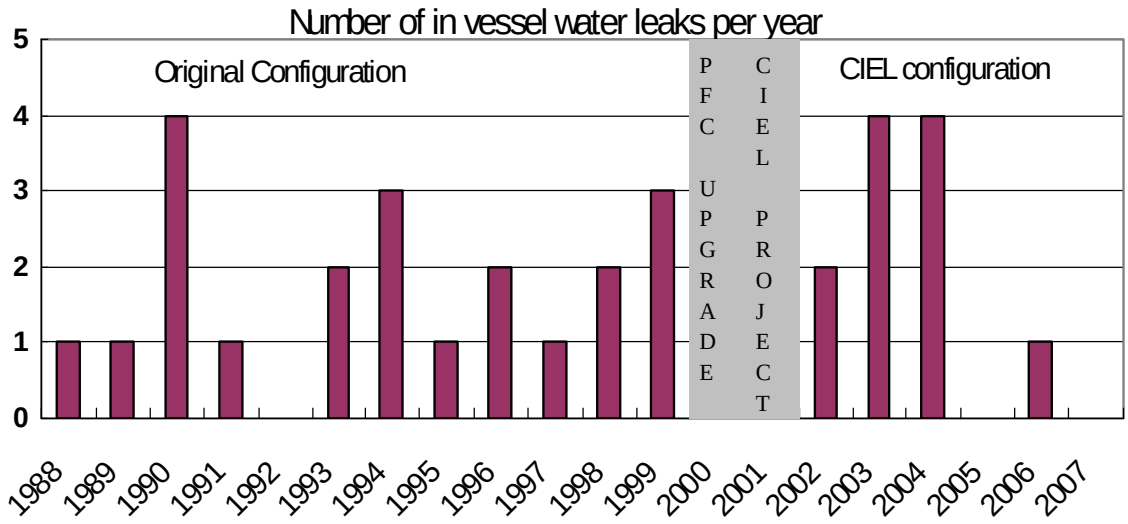

Figure 3: Time Distribution of the in-vessel water leaks in Tore Supra

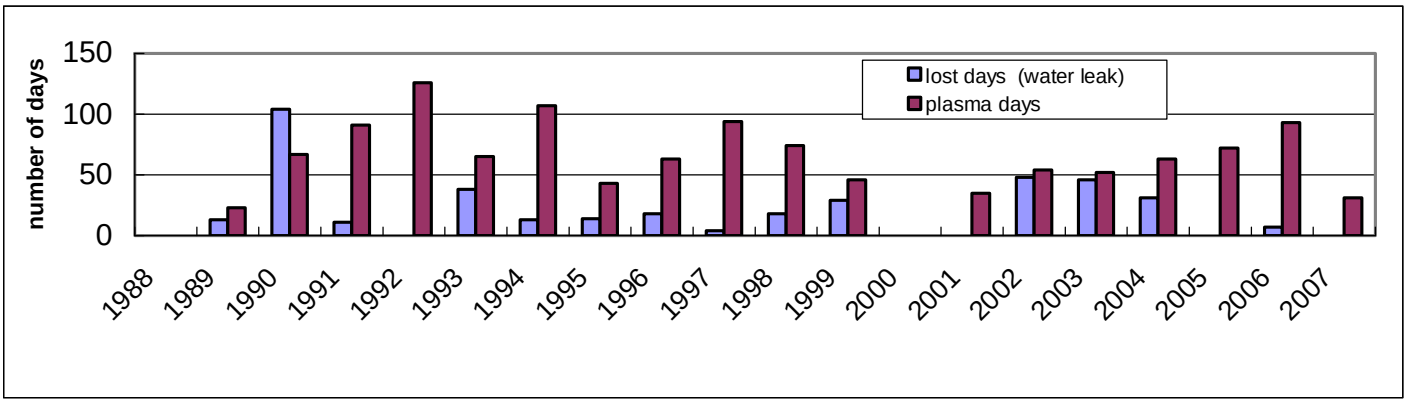

Figure 4: Plasma and lost operation days per year

Additionally, the preventive maintenance programme is presented, thus allowing an estimation of the Occupational Radiation Exposure that the maintenance teams would face during similar interventions on an ITER-like installation.

The overall objective of Deliverable D02-2 is to analysis the causes of the 32 in-vessel water leaks that occurred in Tore Supra from the beginning of operation (spring 1988) to the end of 2007 (figure 3).

The operation conditions of the actively cooled plasma facing components were briefly recalled. The consequences of the In-vessel water leaks expressed in terms of lost operational days were given figure 4.

The lessons learnt at Tore Supra concerning the design, the test and the operation of the actively cooled plasma facing components are presented. The solutions developed at Tore Supra to minimize the occurrence of the In-vessel Water leaks are mainly based on the use of a Quality Assurance policy taking into account the following points: the modelling and design capability of the ACPFC, the development of specific studies, the improvement of the weld testing procedure, the design testing of the Actively Cooled PFC, the acceptance tests of the components, the systematic use of Mock-up for design control and fatigue tests, the feedback on all experience gained, the definition of the plasma operation procedures, the real time survey of the most critical components. For simplicity of the presentation, the water leaks on the plasma facing components were sorted in four categories: leaks resulting from design choices (13), leaks resulting from defects associated to the welding techniques (9), leaks resulting from insufficient knowledge of the tokamak physics (6), leaks resulting from a lack of interlock circuits or of diagnostics (4).

The deliverable D03 concerns the operation experience of the cryogenic system of Tore Supra, it contains a full description of the cryoplant components including brand, type and references. It also includes a functional description of the cryoplant, as well as schematics of the entire cryogenic system. The operation modes, using reading charts of the cryogenic system output temperature (figure 5) and correlating them with the incidents recorded by the operators in the Tore Supra database (table 2) allowed to recreate the rhythm of operation of the cryoplant, while extracting several key variables automatically recorded by the command-control and data acquisition system and processing them with the help of specifically-designed computing allowed calculating estimates of the quantitative requirements of the task regarding components reliability figures.

This analysis also shows the high level of availability achieved by this system (from 76.2 % to 100 % relatively to the experimental campaigns excluding the planned maintenance shutdowns) by applying the preventive maintenance programme detailed with the main active components.

It has also highlighted the operating conditions and the failures encountered during the 4 years considered by the main active components of the cryogenic system: 6 compressors, 17 pumps, 3 turbines and the wet reciprocating expander, along with some of the main passive components.

As for the deliverable D02-1 the statistical data were obtained from the command-control and checked with the log books, the manual entries in the Tore Supra database and active participation of the systems operators and managers. The results are compiled in 7 tables concerning the 4 years considered (2004 to 2007).

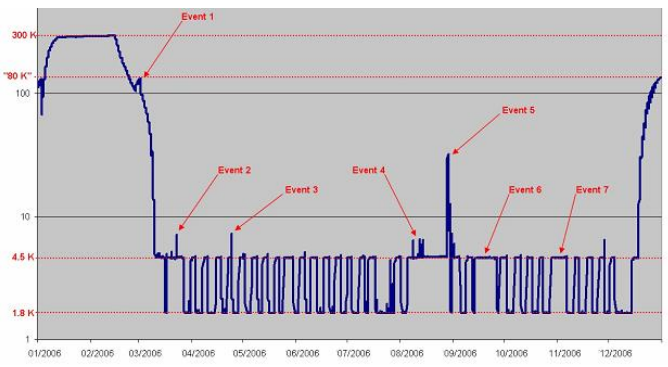

Figure 5: Toroidal magnet temperature throughout 2006

Table 2: Notable events in 2006

	Dates	What happened?	Number of days lost
Event 1	3rd week of February	1st liquefaction at 80 K	NOT A FAILURE
Event 2	2nd half of March	Cooldown and toroidal field test at 1.8 K then 1 week at 4.5 K for baking of the vacuum vessel.	NOT A FAILURE
Event 3	24/04/2006	Cold pumps stop (Compressed air supply failure).	Not related to the cryogenic system.
Event 4	2nd week of August.	Shutdown due to storms and Cadarache 1-week closure for summer holidays.	Not related to the cryogenic system.
Event 5	Last week of August	Test of the rescue cold box, then general power supply failure on Cadarache.	Not related to the cryogenic system.
Event 6	2nd & 3rd week of Sept.	Water leak on water cooling system.	Not related to the cryogenic system.
Event 7	Last week of October.	Legal holidays.	NOT A FAILURE

Some reported events were not taken into account in this analysis, because they were not really due to a true mechanical failure of a component, but were rather induced by the operating conditions. The most striking examples were furnished by the T1, T2 & T3 turbines, which are really vulnerable to the pressure instabilities that can occur in the process. Their cost means that they are protected by very sensitive sensors that tend to overreact to slight pressure variations, thus shutting down the process without any real failure.

It appears that once the operating conditions, transient failures, false alarms and human errors are eliminated, there are only 47 remaining failures for the main components on the studied period. When the failures related to the sensors or the command-control system are left out to consider only the real mechanical failures of the components, this number drops to 18.

A statistical analysis of such a small number of failures may be of dubious value in itself, so that's why it was decided, in addition to the results initially required by the task, to detail the maintenance performed on the active components to obtain the availability measured for the cryogenic system, thus giving more pertinent information to EFDA.

The failure rates obtained in the course of this analysis, considering only the confirmed failures of the components themselves, range from the low 10^{-5} to the mid-10^{-4}. These are good results, and show how the cryogenic team, even with ageing components, can manage to provide the Tore Supra facilities with the means to operate the first superconducting tokamak with a steady increase in performances and availability, 20 years after its commissioning. The results are compiled in 7 tables concerning the 4 years considered (2004 to 2007).

This quasi-industrial operation of the cryoplant is made possible by the slow rhythm of operation of the system, due to its inherent thermal inertia, but also by a combination of factors that must be kept in mind when preparing the operation of future installations:

- Performing daily inspections of the critical components, with controls of the oil and water consumption, vibrations and noise, supplemented by redundant sensors, in order to detect the imminent failures of those components whose life expectancy may vary,
- Keeping a human presence (even of only a few people) on site at any time, every day, in order to be able to quickly react to an alarm, assess the situation, discriminate between false alarms and real failures, and if needed override the automatic command-control system to limit the impact of any problem,
- Implementing maintenance contracts with companies that are able to respond to emergency in a short notice, 1 or 2 days,
- Investing in a stock of spares that are either kept on site, or by the maintenance companies that will remove, inspect, repair and install them on the machine,
- Keeping in contact with the suppliers, manufacturers or other customers or users of the technologies used on the facility, in order to multiply the sources for spares when obsolescence or lack of market applications makes them hard to find and expensive.

This report also includes an analysis of the helium leak detection procedures that was developed. It is also shown how significantly the operation cost is impacted by the helium losses that results of the leaks of helium gas circuits and storages.

CONCLUSIONS

The experience of this analysis can also be used to make some suggestions for the design of the ITER command-control and data acquisition system. It was not planned to use the data continuously and automatically collected and stored by the command-control system, but the retrieval and processing of these data appeared to be the only way to estimate accurately enough the numerical results required by this analysis.

So, in order to make this data even more useful in the next generation of machines, this collection and storage of command-control data should be taken into account and organized from the beginning.

It would especially be useful to:

- collect and stock the command-control data: those are the most important regarding the operating conditions of the systems and their components.
- organize the collected data: regroup the variables on several layers, when they are acquired and recorded, in order to facilitate the filtering and analysis of variables related to specific use, such as human safety, magnetic fields operating time, physical conditions in the PFCs cooling system, and so on. It would be easier to retrieve groups of variables related to a particular use, perhaps linked by key words in a database, than to search amongst thousands of individual variables.
- implement an automatic control of the values acquired and stored for the variables: the data acquisition system could check the values by using comparison between related variables, in order to eliminate, or at least highlight aberrant values.
- keep track of what happens inside the command-control system as it evolves: what do the variables represent? As time passes, the people who designed the command-control system will be replaced by others, who will need to understand how the data acquisition system works "behind the computers screens" of the control room.
- ask for a periodic analysis of the recorded data: the command-control data can be really useful to understand and recreate what precisely happens within the systems. However, if this analysis is made too late, it can be really time-consuming to process the huge amount of data collected. An analysis performed more often will have to deal with less data, and so will be easier, in addition to being able to give more rapidly to the operators an insight on the way their process have been running.

Another important aspect of this study refers to the human factor: along the progress of the task, it was discovered that a lot of useful information existed in the form of "personal log books" kept by the managers and operators on their own, relative to the actions they had performed or taken a part in.

It should be taken into account, in any future project, that these bits of information may be useful to check and correct the data automatically collected by the command-control. It is thus recommended that a procedure should be defined to allow for:

- a standardized way of recording events and especially maintenance intervention, thus permitting to keep a database of the works performed,
- a fast validation process, by the appropriate hierarchy, of the reports feeding the database in order to facilitate and to promote its use by the operators.

As this kind of experience feedback study was not planned at the start of Tore Supra, no unique source of information was defined, and the only way to obtain what was required by the task was by comparing several incomplete sources.

However, as this kind of analysis will undoubtedly be performed in the future on ITER and other installations, it is of the utmost importance that a coherent, complete and precise way of recording and storing components and systems operating conditions should be defined, and that such a system should be based on a shared database.

REPORTS AND PUBLICATIONS

D01: Final report on toroïdal field magnet
CEA report CETS/NTT-2007.002
(Sent July 2007 to EFDA, accepted September 2007)

D02: Final report on PFC cooling system, including the in-vessel water leaks analysis
D02-1: CEA report CETS/NTT-2007.004
D02-2: CEA report CETS/NTT-2007.003
(Sent January 2008 to EFDA, accepted February 2008)

D03: Final report on Cryo-plant
CEA report CRYO/NTT-2008.006
(Sent June 2008 to EFDA, accepted august 2008)

D04: Support to the implementation of the statistical data into the “FCFR database” developed and maintained by ENEA

TASK LEADER

Jean-Claude VALLET

DSM/IRFM/STEP/DIRSTEP
CEA-Cadarache
F-13108 Saint-Paul-lez-Durance

Tel. : 33 4 42 25 61 62
Fax : 33 4 42 25 49 90

e-mail : jean-claude.vallet@cea.fr

TW6-TSS-SEA3.5C

Task Title: IN VESSEL SAFETY: SMALL AND MEDIUM SCALE EXPERIMENTS ON COMBINED HYDROGEN/DUST EXPLOSIONS AND MITIGATION FOR MODEL DEVELOPMENT

INTRODUCTION

An approach to control hydrogen and dust in ITER may be based on oxygen limitation inside the Vacuum Vessel (VV) instead of limitation of dust. Inert gas injection in the VV, with N_2, was considered in a previous task as a possible strategy for fusion application to prevent hydrogen explosion. In order to justify and assess the feasibility of the strategy, large scale experiments and related calculations by using the MISTRA facility were decided in order to qualify the impact of the injection flow rate and location on mitigation effects.

The hypothetic accident scenarios have complex flow pattern [1] and the definition of the matrix of tests was not immediate, due also to scale differences between ITER and MISTRA facility.

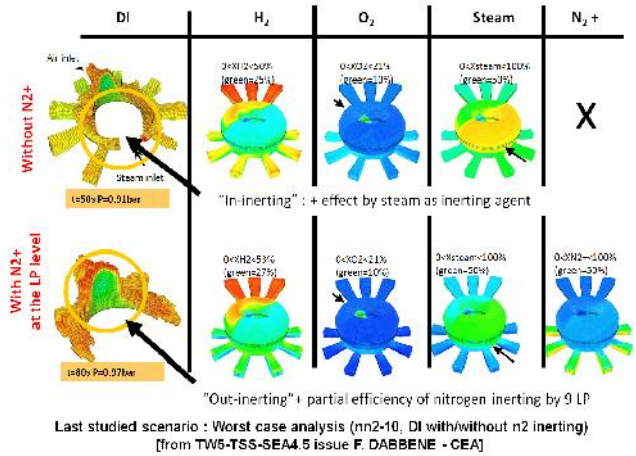

Figure 1: Illustration of gas species molar concentration in the vacuum vessel in case of simultaneous air and steam ingress for a so-called wet-bypass accident scenario [2]

Pre-test computation was done to define the test matrix in relation with the previous task TW6-TSS-SEA4.5 (figure 1, [2]) and the following task TW6-TSS-SEA4.5a [3]. Based on these results we proposed to divide the experimental campaign in two steps. The "MISTRA 2007" campaign is devoted to flow structure studies associated with ten minutes lateral air helium flow ingress at ambient temperature within the air filled MISTRA facility. It will provide initial conditions for the next step where inerting efficiency will be studied in 2009. The "MISTRA 2007" campaign was postponed to 2008 due to difficulties with the man-power in 2007 in MISTRA team [3].
The present report gives an overview of the so-called "MISTRA 2007" test series performed in the MISTRA facility during 2008.

2007-2008 ACTIVITIES

MISTRA FACILITY

The MISTRA facility is a large stainless steel containment of 97.6 m^3 (figure 2). The containment internal diameter of 4.25m and the height of 7.38m were chosen to correspond to a linear length scale ratio of 0.1 with a typical French PWR containment. It comprises two shells, a flat cap and a bottom, which are fixed together with twin flanges.

The vessel itself is not temperature-regulated but thermally insulated with 20 cm of rock wool. Three condensers are inserted inside the containment, close to the vessel walls. Each condenser has its own regulation circuit, providing a more stable and uniform temperature (wall temperature differences less than 1°C are achieved). Until 2004, the test series were based on a free gaseous volume configuration.

Figure 2: Views of MISTRA facility (general and internal with the compartment)

The facility was then modified to accommodate compartments consisting of an inner cylinder and a ring plate (figure 2).

This new configuration allows several possibilities of injection, two vertical in the lower area (centred and off-centred), one vertical at the level of the ring plate (off-centred) and radial injection with different locations. The later was specially created for this programme.
The injection locations were localised at height 4341mm in the confined area above the compartment floor (figures 2 and 3). The injection configuration allows impinging jet on the cylinder wall.

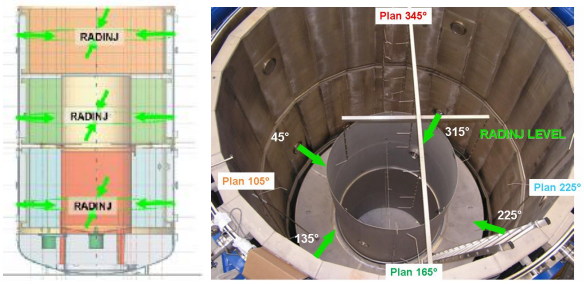

Figure 3: Sketch and view of the lateral injection

With the compartment MISTRA was selected through its pseudo-toroidal configuration with several lateral injection possibilities. The similarity of injection conditions with considering the MISTRA facility possibilities, allow a volumic scaling reduction of 45. The time scales of the transient event are not the same, very fast for ITER, 100-300 sec, slower for MISTRA to allow concentration measurement. Thus, MISTRA is not fully representative of the ITER geometry but allows simulating the same type of flow necessary to validate the CFD models used on the actual configuration of ITER.

The measurement of the first test series is mainly based on temperature and concentration of gaseous species by katharometry and quadripolar mass spectrometry. The katharometry was specially introduced to follow with a fine time resolution the evolution of concentration gradient in the confine volume above the compartment floor and in the free volume of the top (area where the helium stratification occurs). D3 deliverable gives a complete description of MISTRA facility and associated instrumentation.

RESULTS

Seven tests are performed at ambient temperature and pressure. So the condensers are kept at room temperature. A mixture of air and helium is injected at ambient temperature for 600s by one of the four median lateral lines at level 4341 mm (figure 4).

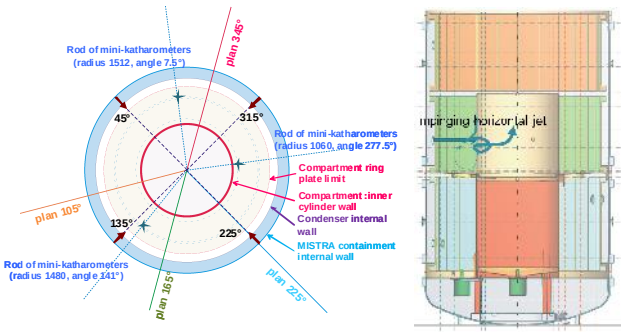

Figure 4: Test configuration at 4341mm height

The mass flow rates are the result of a compromise between three factors:

- A large enough helium concentration to perform measurement,
- Impingement flow on the inner compartment wall,
- Flow rates and injection duration are calculated to limit pressure increase inside the facility.

The Froude number is closed to 300 and corresponds to the upper hypothetic range in ITER. The test matrix is given in table 1.

Table 1: Test matrix

Test reference	Injection location at	Flow rates (g/s)		Duration of gas injection (s)
	Angle (°)	Helium	Air	
ITER_1.1_05-11-2008	315	2	15	600
ITER_1.1_13-11-2008	315	2	15	600
ITER_1.2_18-11-2008	135	2	15	600
ITER_1.3_24-11-2008	225	2	15	600
ITER_1.4_28-11-2008	45	2	15	600
ITER_1.1_02-12-2008	315	2	15	600
ITER_2.1_16-12-2008	315	2	10	600

The implementation of the katharometer allows a fine measurement in time and in space of the helium concentration as flow marker. All the tests are reproducible and the data post-processing is ongoing.
The figure 5 gives an example of the vertical helium molar fraction repartition closed to the injection at angle 277.5° and radius 1060mm for katharometer mast (test ITER_1.1_05-11-2008). The D4 deliverable gives the experimental results [5].

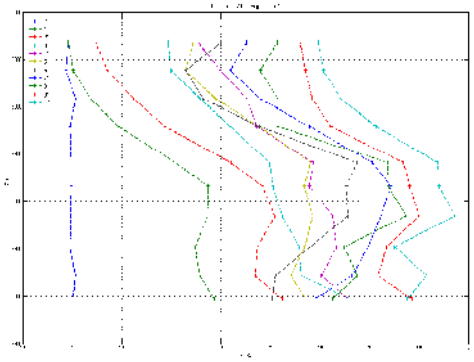

Figure 5: Illustration of concentration measurements by katharometer

CONCLUSIONS

The "MISTRA 2007" campaign is rich in results on the flow pattern in this pseudo-toroidal configuration. A detailed comprehensive analysis of distribution and mixing is actually ongoing in task EFDA/06-1518, TW6-TSS-SEA4.5a. The second step will be the study of the inerting efficiency based on nitrogen injection. This step will be planned for the end of 2009.

REFERENCES

[1] L.TOPILSKI, 2006 "Main parameters and assumptions that should be taking into account in the model of inert gas injection system for hydrogen explosion suppression", Technical report annex 2 TO TA G 81 TD 29 FE

[2] F. DABBENE, 2008 "Feasibility study of possible prevention of hydrogen combustion in ITER by injection of neutral gas" EDFA Task TW6-TSS-SEA4.5 D1, D2 CEA Report DM2S/SFME/LTMF/RT07-059/A

[3] Minutes of the kick-off meeting on "Experiments and calculation for demonstration of inert gas injection feasibility" - Karlsruhe January 2008 - ref. C81TD34FE /TA-DRWG2-EU-01

REPORTS AND PUBLICATIONS

[4] J.BRINSTER et al., "Description of MISTRA facility" EDFA Task TW6-TSS-SEA3.5C, D3 CEA Report RT DM2S/SFME/LTMF/RT07-081/B

[5] D.ABDO et al., "MISTRA experimental results for ITER 2007 test series" EDFA Task TW6-TSS-SEA3.5C, D4 CEA Report DM2S/SFME/LEEF/RT09-004/A

AKNOWLEDMENTS

The task leaders whish to thank the MISTRA team D. ABDO, M. CAZANOU, R. TOMASSIAN, JL.WIDLOECHER for their contribution and F. DABBENE for tests follow-up and fruitful discussions on ITER and hydrogen risk

TASK LEADER

Isabelle TKATSCHENKO and Jérôme BRINSTER

DEN/DM2S/SFME/LEEF
CEA-Saclay
F-91191 Gif-sur-Yvette Cedex

Tel: 33 1 69 08 35 21 / 33 1 69 08 27 21
Fax: 33 1 69 08 82 29

e-mail: isabelle.tkatschenko@cea.fr
jerome.brinster@cea.fr

TW6-TSS-SEA5.1

Task Title: IN VACUUM VESSEL DUST MEASUREMENT AND REMOVAL TECHNIQUES

INTRODUCTION

During ITER lifetime, dusts will be produced due to the interaction of all types of plasmas (including conditioning procedures) with the Plasma Facing Components (PFCs). These dusts will be activated, tritiated and potentially chemically toxic (presence of beryllium). ITER fixed a set of safety limits to manage the potential hazards which might be caused by these dusts. The aim of this task is to assess techniques that could be used during ITER lifetime to control dust inventories within the vacuum vessel and to be able to recover the dusts when the safety limits are reached.

An interim report [1] has been issued in December 2006 to:

- Summarise the work already performed by G. Counsell et al. within the EU Task DV7A-T438 and by the Japanese home team,
- List some other potential techniques,
- Propose future work to be performed within the task to explore selected approaches more in details.

2007-2008 ACTIVITIES

DUST PRODUCTION PROCESSES

Different dust formation processes occur in a tokamak. They can take place in steady state phase (normal operation), off-normal operation modes or during maintenance.

During the steady state phase, the dust formation is closely linked to erosion of PFC materials. The eroded materials tend to re-deposit in layers in cold areas. These layers are made of stratified mixed materials (Be, W, C and metallic impurities) coming from the plasma facing components during the different operating modes. Due to weak adherence of these layers and important mechanical and thermal stresses inside the layers, they can flake once they have reached a certain thickness. Then they can produce dusts of different sizes depending on the stress levels and local deposit structure (typically from some 10 μm to few mm).

The growth of small particles in the edge of fusion plasmas (with low Te (<5 eV), low ne (~ $10^{17}m^{-3}$) and high neutral density) from atomic or molecular precursors which are released by physical or chemical erosion can also lead to dust creation. The particles have a so-called cauliflower shape. This mechanism starts with particle size of about 10-50 nm and may nucleate and grow up to quasi spherical species with diameters exceeding 1 μm.

Off-normal plasma events such as Edge Localised Modes (ELMs), Vertical Displacement Events (VDEs) or disruptions produce high heat load and since the thermal conduction into the layer of the PFC is insufficient, the surface temperature can reach the boiling or sublimation point of the material. Dust particles are then created by either condensation and growth of the vaporized material, or pressure-driven ejection of melt layer material or explosive brittle destruction by heating of gas bubbles. In this case, significant amounts of small dust particles (< 1 μm) are produced and can agglomerate into larger structures.

Unipolar arcs can also produce large particles and droplets of molten metals. In this case, a large amount of energy is deposited at the metal surface leading to melting and vaporization of the material. The dust particles are comparatively large, spherical and composed of a single material.

The wall conditioning procedures involving dc-glow discharge in He or in reactive gases (carbonization, boronization, siliconization) purposefully generates surface films, which are subject to the same degradation as the a-C:H films and are thus potential source of dust particles.

At last, during maintenance activities, large particles can arise from mechanical abrasion during component replacement.

The whole dusts are mainly foreseen on or under the divertor, at the bottom of the vacuum vessel, behind the PFCs, in tile gaps/castellations or between tiles and at the horizontal ports.

ITER CONSTRAINTS

For ITER safety, inventory guidelines were set:

- To limit the mobile activation product inventory inside the vacuum vessel: the mobilisable dust limit inside the vacuum vessel has been set to 100 kg of W, 100 kg of Be and 200 kg of C,
- To ensure that chemical reactivity is adequately controlled: dusts on the “hot” surfaces of the divertor must be limited to 6 kg of Be, 6 kg of W and 6 kg of C in order to produce less than 2.5 kg of H_2,
- To avoid the hazard of dust explosions (not yet explicitly considered).

Calculations have been made in order to determine when these limits could be reached. The administrative guideline

of 100 kg for tungsten dust could be reached in about 500 plasma pulses. This reveals that the administrative guideline is reached before the assumed replacement of the divertor. Dust diagnostics and removal methods are thus highly required.
Based on the data currently available, the techniques to be developed for dust monitoring and removal should be able to deal with the following conditions:

- Dust size between 10 nm and 100 µm with various shapes,
- Composition: Be, C, W and metallic impurities,
- Localisation: bottom of the machine but also in shadowed areas (behind tiles or in gaps/castellations),
- Tokamak conditions: vacuum environment with magnetic and radiation fields and at temperatures up to 240°C,
- In order to limit the impact on operation, preference will be given to non-intrusive techniques.

ASSESSMENT OF DIAGNOSTICS FOR DUST MONITORING

Introduction

For the general limits inside the vacuum vessel, one can set the total amount of eroded material as an envelop value for dust creation assuming 100% conversion of the eroded material to dust. This value could be used for the safety approach to demonstrate that the general limits inside the vacuum vessel are fulfilled. However, this value could be too conservative and could constrain too much the operation time requiring dust removal more frequently than necessary.

In order to reduce the margins, the quantity of deposited materials could also be assessed. In this case margins are reduced compared to erosion quantity and are maybe not so much conservative since some authors noticed that even if these layers are still adhering when they are under vacuum, they may peel off due to external shocks applied by changes of environments and/or ambience (tokamak venting or water leaks).

Finally and ideally, we should be able to monitor dust which could be mobilisable in case of an accident. But in this case, mobilization can be different depending on the conditions which are considered, from mobilization by loss of vacuum up to mobilization by explosion. Even in the case of the “loss of vacuum” event, pressurization rates and positions of leaks may be very different. It would be thus quite difficult to assess the quantity of dust that can be mobilisable from a local measurement in given conditions.

Review of techniques that could be used

Three categories of diagnostics have been considered:
- Optical systems: spectroscopic, laser or imaging techniques,
- Sampling systems: sample extraction for external analysis,
- Gravimetric systems: measure the weight of accumulating materials.

The following diagnostics have been assessed:

Optical systems:
- Detection of the dust motion (movement and oscillations) with high speed, high resolution CCD cameras or speckle interferometry at the interface of the plasma and the surrounding walls (plasma sheath),
- Implantation of trace impurity species (figure 1) with a clear spectroscopic signature at different depths throughout sample plasma facing components for monitoring local erosion phenomena,

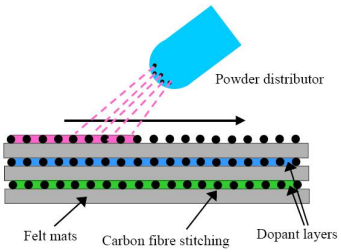

Figure 1: PFC dopant principle

- LADAR (Laser Distance and Ranging): distances are measured via time-of-flight measurements for the reflection of ultra-short laser pulses from a surface,
- Laser Induced Breakdown Spectroscopy (LIBS): the plasma generated by the material ablation is analysed.

Sampling:
- Use of the general pumping system in the divertor region to collect airborne dust and analyse them out-vessel,
- Dust sampling using a highly flexible, remote manipulation and sampling system, similar to a medical endoscope. For collection, a local blast of inert gas is used to dislodge the dust, which is then collected by means of a suction tube.

Gravimetric systems:
- Capacitance Diaphragm Microbalance (figure 2): the cumulative weight of dust, flakes or film growth on the surface of a diaphragm is measured by determining the change in capacitance caused by its deflection relative to a fixed plate,

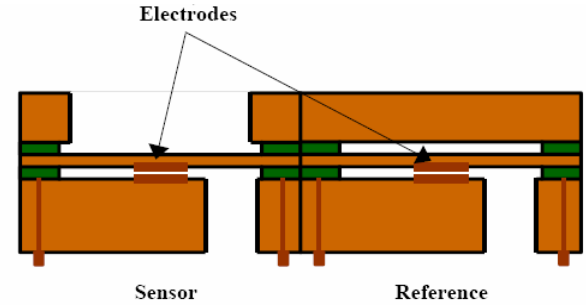

Figure 2: Capacitance Diaphragm Microbalance

- Electrostatic detector: when conductive particles land on the energized grid, a transient short circuit occurs and this current pulse can be easily measured.

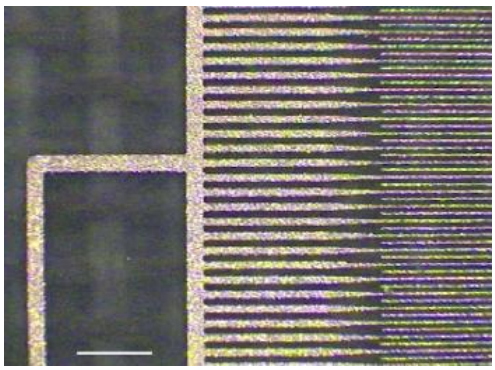

Figure 3: Electrostatic detector

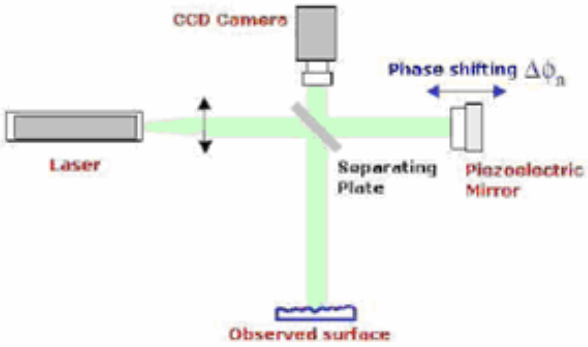

Figure 4: Speckle Interferometry principle

Other techniques assessed
Hereafter, techniques that give access to erosion of tiles as speckle interferometry or deposited layer evolution are also presented. These techniques allow the evaluation of the envelope of the dust in vessel quantity (erosion measurements) or the conversion of layer into dust via layers evolution.
At last, dust in suspension measurements are described.

Near-infrared spectroscopy
It is proposed to use the IR thermography to obtain a mapping of the deposits in the ITER divertor region. IR thermography measurements in a Tokamak give the plasma facing component temperature during fusion plasma. Infra Red thermography used in Tore Supra and JET to measure the surface temperature distribution and evolution on different parts of the machines (divertor, antenna support, limiter) in order to estimate the ageing of the tile during operation. In this case the incident flux is provided by the plasma itself. A classical model was developed to describe the surface temperature evolution during the pulse duration. The interpretation of these measurements was made difficult due to the presence of surface layers that have a low thermal conductivity and low adherence. A specific model was thus developed considering the thermal conductivity of the layer and the heat exchange coefficient between the layer and the bulk material as adjustable parameters to fit with the experimental data. This model reproduces very well the amplitude and the time constant of the experimental temperature curves recorded during the pulse duration. The evolution of the IR signal recorded at different periods of the campaign can be used for our application as a way to highlight the build up of deposits and characterise dust and flakes as well.

Speckle Interferometry
Speckle interferometry can be used to provide quantitative measurements on eroded and redeposited materials providing that there is a reference level. It is based on a Michelson interferometer to improve the sensitivity in the z direction. The laser beam reflected from the observed surface interferes with the reference beam on a CCD camera. A temporal phase shifting is obtained by using a mirror mounted on a piezoelectric component in order to introduce a well known phase shifting between the 2 beams. Erosion and redeposition lead to a variation of the optical phase and measurement before and after a plasma discharge enable to characterize what happened during the discharge. The depth erosion resolution is 10µm.

This technique is proposed for ITER inner and outer divertor targets using respectively the equatorial and the upper port plugs (the maximum sensibility being in the normal direction).

Laser extinction for dust in suspension measurements
The light extinction method is sometimes known as the "turbidimetry technique". This technique is used to infer the particles number concentration in a gas. The basic idea is firstly to light the particles to be analysed by a collimated and polychromatic beam of light; secondly to measure the spectral transmission of this beam after passing through the particulate medium, see figure 5. Under a single scattering assumption, the mean extinction cross section depends on the particles composition, the wavelength λn and the particle size distribution $f(r)$. The determination of $f(r)$ requires to solve an ill-pose problem, a first kind Fredholm integral. Here, one additional difficulty is that extinction measurements require to prior know the dispersion equation of the particles material (e.g. composition). Nevertheless, with light extinction, there is no theoretical limit for the measurement distance range (except the optical thickness of the medium). It is one of the main reasons why this technique is though to be more suitable for tokamaks applications.

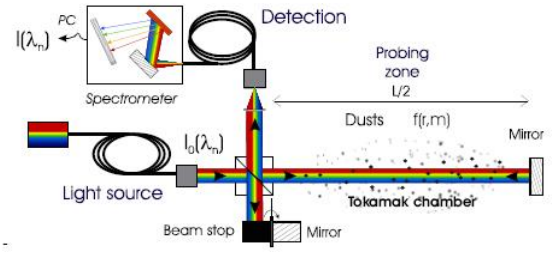

Figure 5: Schematic of laser extinction measurements

Possible strategy for global dust in vessel measurements
Concerning the **global in-vessel inventory**, the strategy is based on the monitoring of the erosion in the vacuum vessel in order to determine the quantity of materials that could potentially lead to dust creation (see diagram 1). In a first approximation, we could consider that 100% of the eroded materials could lead to dust. This approximation

will be reduced using the experience feedback from the H-phase and/or more local measurements. Spectroscopic measurements during the plasma pulses would be the favoured techniques, although R&D is still needed, to determine and separate the erosion sources of Be, C and W. Speckle interferometry in chosen areas of the vacuum vessel could also be used to determine the erosion areas. Other techniques could be used during or in-between pulses (capacitive microbalance and electrostatic detector), during short shutdown (local gas puffing followed by laser extinction measurements or other optical measurements and use of an endoscope for "visual" inspection. It has to be emphasised that the correlation between local measurements and the total mobilizable inventory inside the vacuum vessel fixed by ITER remains as an issue.

Diagram 1

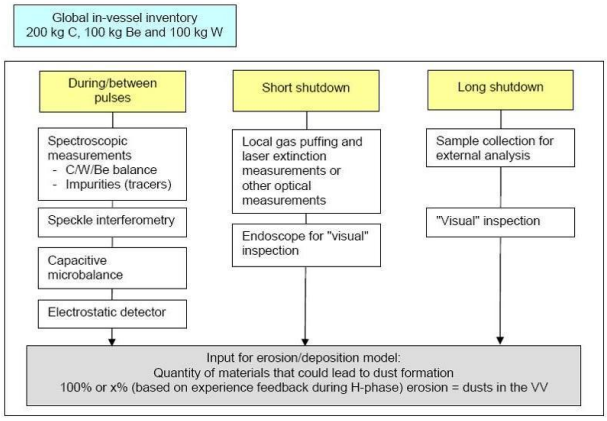

Possible strategy for measurements of dust on hot surfaces

Concerning the **limit on the hot surfaces of the divertor**, the strategy is based on a measurement of the dusts and the co-deposited layer together. From the safety point of view, it is very difficult to determine whether layers remain stable or contribute as origin of dust through flaking.
The strategy is based on (see diagram 2):

- Mapping of a sector of the divertor region (chosen to be representative of the whole divertor region using symmetry) to determine deposition and erosion areas. Up to now, thermography methods are favoured,
- "Calibration" of the deposition areas with local thickness and composition measurements. There are various potential techniques but for the moment, LIBS is favoured,
- Calculation to determine the mass balance of the deposited materials.

Speckle interferometry can be used independently to characterise deposition areas. It would enable to determine the erosion areas and thus contributes to the determination of the carbon erosion source for the global in-vessel inventory.

These techniques need to be experimentally validated on ITER-relevant mock up and/or Tokamak to take into account ITER environment and in particular the divertor design.

Diagram 2

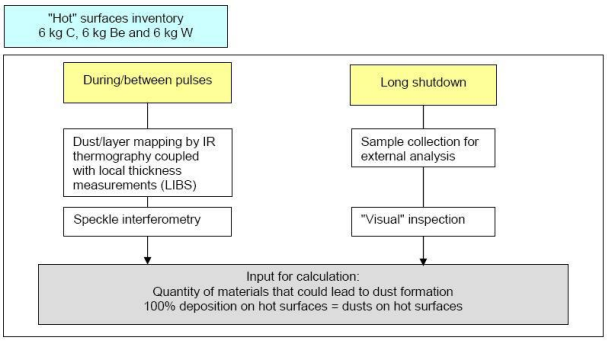

ASSESSMENT OF REMOVAL TECHNIQUES

Introduction

Dust removal may need to be done on a regular basis, perhaps monthly or quarterly, in particular if the diagnostic tools have been proven to be not enough accurate to ensure that the safety limits are respected.
Removal of dust, flakes and deposited films from the vessel is a three stage process:
- Material mobilization: material must be detached from the surface on which it is attached, via inert gas puffing or more abrasive forces,
- Collection of the mobilised material and transport within the vessel,
- Transport outside the vessel.

Possible methods

Vibrating conveyor

This technique, proposed by G. Counsell et al. within the EU Task DV7A-T438, relies on vibration to assist the movement of the material, under gravity, down a slight incline (figure 6). The vibrating conveyor can operate under high magnetic field and under vacuum.

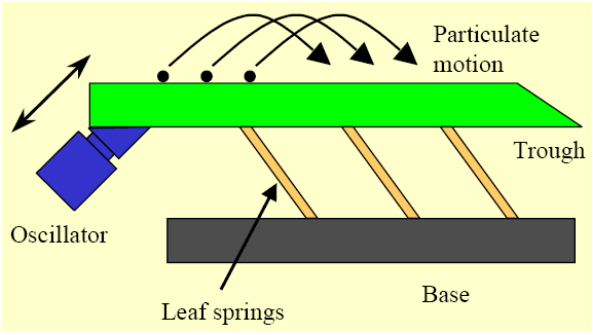

Figure 6: Vibrating conveyor

The installation of such a conveyor was proposed in the divertor region for continuous operation.
The preliminary design (figure 7) foresees a toroidal conveyor with a poloidal shape similar to the vacuum vessel, and that could extend up the inner and outer vessel walls to locations at which the local vessel wall slope is greater than the friction angle of the particulate to be collected and transported.

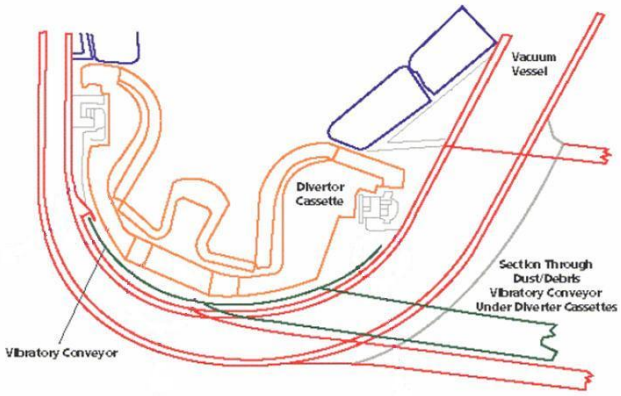

Figure 7: Poloidal cross section showing location of toroidal vibratory conveyor

Electrostatic conveyor

This technique, proposed by the Japanese ITER Home Team, is based on the fact that a particle, which is initially grounded to the floor of the vacuum vessel, can be inductively negatively charged by the application of an electric field by a collection electrode. As a matter of fact, when an electric field is applied, the particle is dielectrically polarized. Since the particle is grounded to the floor the positive charge of the ground surface is neutralised so the particle get negatively charged. This particle is then floated by the Coulomb force due to the electric field between the charge and the electric field.
When a non spatially uniform electric field is applied, a gradient force is produced and the particle can travel according to the non-uniform travelling wave, so called "electric curtain" (figure 8).
Tests have been performed on particules from 10 to 100 µm.

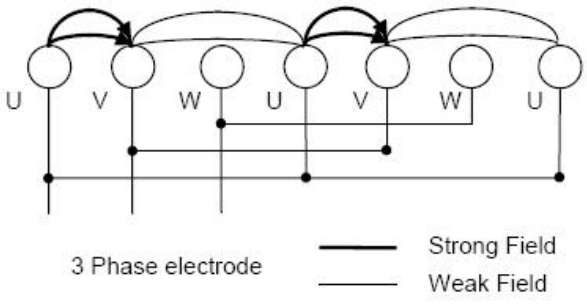

Figure 8: Principle of electric dust conveyer transportation

Based on these properties, two types of devices have been proposed:

- A so-called "dust floatation and transport device", which is developed to act like a vacuum cleaner but able to work in a vacuum ambience. Put on a remote handling arm, it can locally remove dusts from the surfaces of the divertor or from horizontal ports (figure 9).

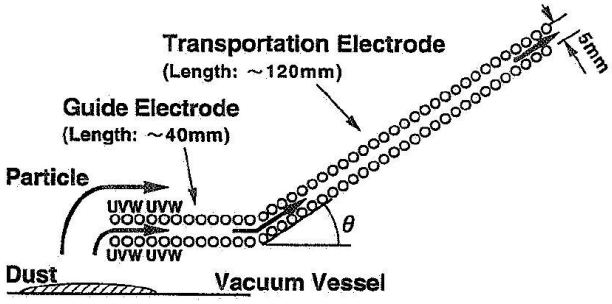

Figure 9: Example of 2-stage linear-type electrode with a guide electrode for the dust transportation test

- A continual dust removal device that could be installed under the divertor to allow a continuous operation (figure 10).

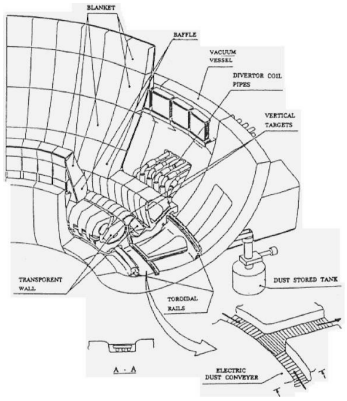

Figure 10: Concept of continual dust removal system

"Dishwasher"

This integrated technique (allowing material mobilization, collection and transport) is based on the injection of liquid through high pressure jets (strategically placed and allowing to be reciprocated into the vessel during cleaning periods), to remove the dusts from the rear of the PFCs. This proposal seems very surprising but is supported by the fact that this technique is able to reach the rear of the PFCs.
Nevertheless, the application of the technique leads to loose the conditioning so the selection of the "ideal" solution is essential.
Many solutions were assessed and fluids developed for the replacement of chlorofluorocarbons (CFCs) and chlorinated solvents could be suitable candidates.

Other techniques

- Gas blasting: localised puff of inert gas to mobilise loose materials from the surface,
- Pellet blasting: frozen pellets of CO_2 are fired at the surface, the ice sublimes and the resulting rapid gas expansion carrying away material,
- Water hammer: regular oscillations of pressure in the coolant circuit supplying each PFC will detach by vibration loose dust and flakes,

- Excimer laser, Xenon light or flash lamp: detachment of the films by selective heating. Molecular bonds in hydrocarbon film deposits are broken by the strong source of UV light,
- Suction,
- Pumping with filter: use of the general pumping system to collect airborne dusts,
- Pumping with electrostatic precipitator: same principle as above except that an electrode is used to stick the dust,
- Wiping out with cloth or swabbing,
- Adhesive tape.

Dust mobilisation by laser interaction

This technique, usually named Dry Laser Cleaning (DLC), consists in the direct irradiation of the particle contaminated surface with a laser beam. As it is shown on the figure 11, few laser shots can lead to the particle ejection from the surface.

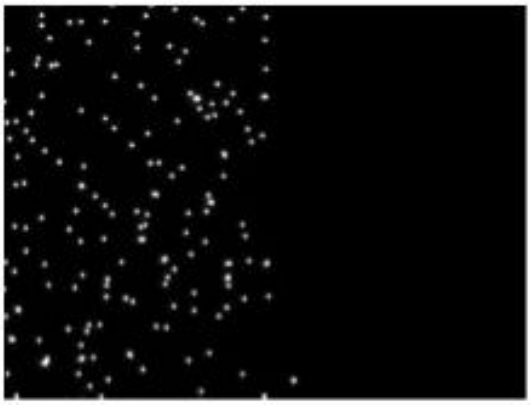

Figure 11: Removal of 385nm PS particle by XeCl laser irradiation. The left part was irradiated with 10 laser shots at 450mJ/cm²

Some ITER related experiments demonstrated the ability of DLC process for dust removal. A KrF laser, with a fluence of 400mJ/cm², was used to clean CFC tiles from Tore Supra on which carbon particles (1-25µm samples kindly provided by Toyo Tanso) were deposited (see figure 12). The first shot induced the ejection of all the particles in the irradiated area, and almost all of them in the surrounding zone. This is due to the shock wave generated during the laser ablation which blow the dust located around the laser spot area.

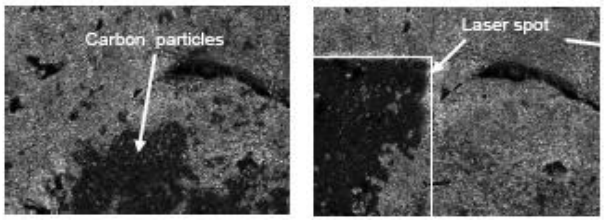

Figure 12: Carbon particles are deposited on CFC tiles (a). A KrF laser (248nm, 27ns, 400mJ/cm²) irradiated the bottom left part of the sample. Almost all the particles and part of the co-deposited layer are removed by one shot

This shock wave efficiency was also used to clean surfaces under atmosphere as illustrated in figure 13. This technique was applied successfully to clean tokamak castellations filled up with carbon Toyo Tanso particles.

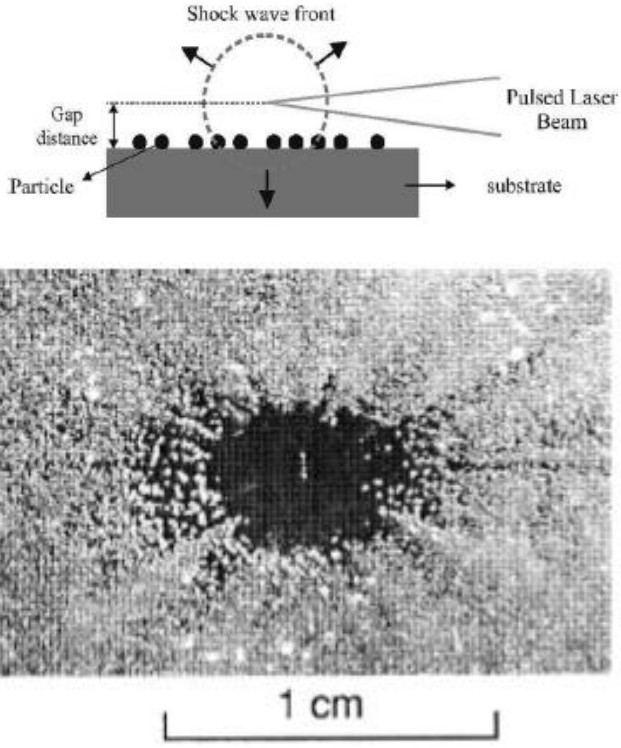

Figure 13: Scheme of the laser induced shockwave cleaning technique. Silicon surface with dust particles (Al_2O_3, 1-10mm) after exposure to 50 laser pulses

Possible strategy for dust removal:

Concerning **removal**, various techniques can be applied at various stages of the machine operation (between pulses or during shutdown) with various objectives (see diagram 3).

Between pulses, the objective is to limit the increase of the dust inventory inside the Vacuum Vessel without loosing the conditioning. For this, the use of continuous conveyor (vibrating or electrostatic) seems the most promising technique but requires space allocation in the divertor region. If modelling shows that dust removal needs are not so frequent, the impact of removal on operation time will not be important. In these conditions, the removal operations can be foreseen without vacuum using a vacuum cleaner for example. If frequent removals are needed, the design will have to be reviewed to allow the implantation of dedicated dust removal systems. Laser could be used in addition to create shock waves in order to push the particles from recessed areas to the divertor bottom (if necessary). This conveyor technique will probably act only on the larger particles but would enable to limit the increase of dust inventory inside the Vacuum Vessel. Another technique would lead to use a laser to mobilise dusts, then to use glow discharge to charge the particles negatively and finally to use electrostatic removal via a charged electrode (long range recovery system).

Diagram 3

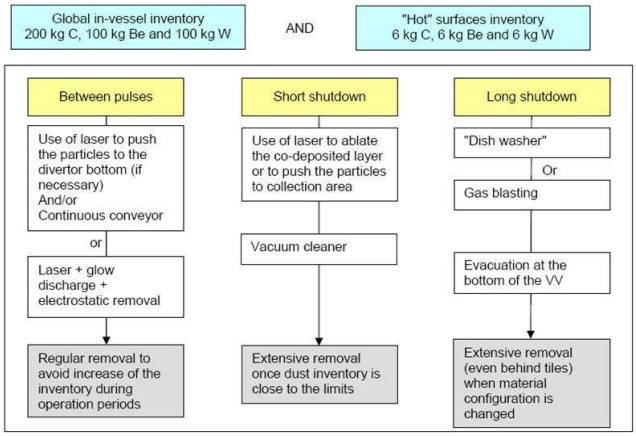

Once the dust inventory is close to the limits, an extensive removal will be required. Then short shutdown will be needed with risk of loosing the conditioning for more efficiency. Laser could be used to ablate the codeposited layers or to push the particles from recessed and hot areas, such as castellations, to the divertor bottom. Vacuum cleaner could then be used to remove the large quantities of dusts. It thus requires the use of remote handling tools.

During longer shutdown, when the material configuration is changed for example, an extensive removal (even behind the tiles) will be needed. Techniques such as the "dishwasher" or the gas blasting can be foreseen. In this case the ITER design must provide a possible evacuation of all the by-products at the bottom of the Vacuum Vessel.

REPORTS AND PUBLICATIONS

[1] 'Interim Report on in-vessel dust measurement and removal techniques', S. Rosanvallon, 22nd Dec 2006

[2] Assessment of in-vessel dust measurement and removal techniques for ITER TW6-TSS-SEA5.1 Delivrable 5 - Final Report, CFP/NTT-2007.030 (2007), S. Rosanvallon

[3] Dusts in ITER: Diagnostics and Removal Techniques Journal of Nuclear Materials, (2009), doi:10.1016 (2009) S. Rosanvallon, C. Grisolia, P. Delaporte, F. Onofri, S. Hong, G. Counsell, J. Winter

TASK LEADER

Sandrine ROSANVALLON and Christian GRISOLIA

DSM/IRFM
CEA-Cadarache
F-13108 Saint-Paul-lez-Durance Cedex

Tel: 33 4 42 25 43 78
Fax: 33 4 42 25 44 90

e-mail: christian.grisolia@cea.fr

TW6-TSS-SEA5.5C

Task Title: CRYOGENIC EXPERIMENTS ON THE CEA EVITA FACILITY

INTRODUCTION

The computer codes which are used for the analysis of the accidental sequences in ITER should have good quality assurance level. The EVITA facility (figure 1) has been designed for the simulation of the physical phenomena occurring during coolant ingress into the cryostat of a fusion reactor, which is one of the identified accidental sequence in the reactor safety report.
Studied physical phenomena are namely ice formation on a cryogenic structure, heat transfer coefficient between walls and fluid, flashing, two-phase critical flow. The comparison between calculations and experiments allows the ability of the computer codes to treat the relevant physical phenomena to be assessed.

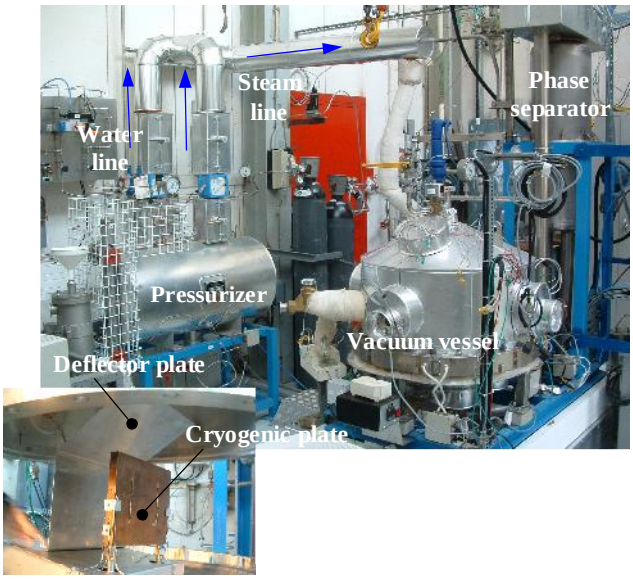

Figure 1: View of the EVITA facility

2007-2008 ACTIVITIES

EXPERIMENTS

Since the beginning of the EVITA program more than fifty tests have been performed on the facility with different operating conditions such as injection of water w/o cryogenic surface, injection of steam w/o cryogenic surface and injection of steam or water w/o gas (N_2).
Some results of the EVITA experiments are still difficult to understand and to interpret. Therefore the 2007 task consisted, in collaboration with the ENEA, in the analysis of in-depth results of the last set of experiments, trying to identify the origin of the discrepancies between similar tests.

MAIN RESULTS

The analysis of the different tests performed on the EVITA facility shows that the steam and water injection quality was not reproducible. Considering the series denoted 6.xx and 5.xx, there is probably a better quality (less droplets of cold water) steam/water flow at the beginning of these injections. The behaviour of the tests with steam injection is easier to explain. The tests 7.xx show that there is probably more liquid water in the steam flow than in the test 5.5x. The video records of the tests confirm this hypothesis. The lower rate of droplets in the steam flow makes the heat impact too important compared to the heat exchange capacity of the plate (see 5.5x, lower rate of droplets). In the case 7.xx (lower enthalpy and high rate of droplets), the plate is more efficient and can evacuate the heat impact and trap the most part of the steam flow.

This analysis does not allow us to explain clearly the test with water injection. The study of the sensitivity of phenomena observed in tests with steam injection should be tested with the CONSEN code developed by ENEA in the frame of this task. Thus it must be possible to better understand the test with pressurized water injection. Concerning more precisely the ice formation on cryogenic surfaces in the case of water injection, the tests performed on the EVITA facility does not allow to have a good accuracy on the measured values because of the discrepancies in the flow injection. In case of a good quality of steam injection, the heat exchange with plate is limited and all the steam cannot be trapped by the plate (ice formation underestimated); in case of an injection with lot of cold water droplets, ice formation is also underestimated.
To improve the quality of the tests, it is necessary to enhance the facility in order to avoid cold points on the injection lines by adding heaters and temperature measurements to control the steam line temperatures more accurately.
Concerning the cryogenic loop, expert analysis has proposed to add a phase separator at the inlet of the cryogenic plate in order to eliminate the nitrogen gas due to facility. That will allow to obtain the same cryoplate heat exchange conditions from one test to another.
This analysis has been completed by some codes calculations of the ENEA in the frame of this task [3].

CONCLUSIONS

The analysis of non-repeatable tests has been done and the discussion with the cryogenic CEA experts has helped in the detection of the reasons of the unexpected trends. After the analysis, new simulations with the CONSEN code [3] have been performed to check the influence of the identified parameters responsible of the discrepancies.
The experimental program on the EVITA facility was achieved in 2007.

REPORTS AND PUBLICATIONS

[1] EFDA Technology Work programme 2003 - 2006 FIELD SAFETY & ENVIRONMENT, STATUS REPORTS, 2007 (Rev. 0, status 24 July 2007)

[2] L. AYRAULT, "Evita, in depth analysis of the experiment and facility", CEA Technical note, DTN/STPA/LTCG NT 2007-013, 09/2007

[3] M. T. Porfiri, "Definition of the complementary CONSEN calculations for EVITA cryogenic tests type 5, 6 and 7", EFDA Task TW6-TSS-SEA5.5c, Deliverables 2 and 3, ENEA/FUS-TN-SA-SE-R-184, December 2007

TASK LEADER

Laurent AYRAULT

DEN/DTN/STPA/LTCG
CEA-Cadarache
F-13108 Saint-Paul-Lez-Durance

Tel : 33 4 42 25 44 72
Fax : 33 4 42 25 66 38

e-mail : laurent.ayrault@cea.fr

TW6-TSW-003-D02

Task Title: STUDY ON EXISTING DETRITIATION PROCESSES AND CHARACTERIZATION OF TRITIATED MATERIALS, FOR APPLICATION TO ITER AND DEMO

INTRODUCTION

In ITER and future fusion reactors, high heat flux (plasma facing) components (PFC) will need to be replaced at regular intervals. Owing to the proximity of the plasma (high temperature) and the presence of tritium, the transfer of material will occur from the plasma to the PFC. Before being stored in hot cells or sent to final disposal, these components or parts of them must thus be detritiated to recover the large quantities of tritium contained in the matrix (recycling tritium as fuel) and facilitate the waste acceptance in storage. This study aims at evaluating the capability of a detritiation process to match the ITER requirements.
In a first part, detritiation processes are evaluated in order to select a reference one which potentially could be relevant. In a second part, due to the lack of data concerning experimental tritium profiles in PFC, we describe a pragmatic approach in order to evaluate them. Then these calculated profiles are used as initial conditions for the detritiation process evaluation.

2007-2008 ACTIVITIES

REVIEW OF THE POTENTIAL METHODS FOR METAL DETRITIATION

Several methods are available for the detritiation of metallic waste, based on chemical or physical methods. Among all the methods, the most promising solutions are:

- **Thermal treatment with or without melting**. This can be done in a conventional furnace and produce good results on stainless steel [1]. A detritiation factor of about 30 can be reached by a simple treatment at 600°C for 20 h. Some improvements can be achieved by successive treatments and oxide layer removal. However, such layers could play a positive role in term of degassing due to the permeation limitation. For melting, an induction furnace could be used which would make it possible to accelerate tritium release from the metal. The CEA already used such techniques successfully [2]. However, the method could be optimised to obtain higher detritiation factor (DF) this potentially leading to the downgrading of certain types of wastes. Such process still needs to be optimised, including technical and economical studies to confirm the feasibility of this solution with large waste fluxes.

- **Chemical treatment,** which can be divided into two sub-categories: the use of liquid or gases as chemical reactants. Tritium extraction is based on several phenomena: extraction of tritiated species in gaseous form by a carrier gas, oxidation reaction with decontamination medium, and isotopic exchange (the recovery of tritium by an isotopic swap with protium atoms from the molecules of the decontamination medium). Some experiments have been performed either at laboratory or pilot scale. The preliminary results are encouraging and the best methods will have to be validated for bulky metallic pieces.

Tritium fraction removed (α) in % and the Detritiation factor (DF) are defined by:

$$\alpha = 1 - \frac{C_F}{C_0} x100 \qquad DF = \frac{C_0}{C_F} = \frac{100}{(100 - \alpha)}$$

α	In %
C_F	Tritium concentration after treatment
C_0	Tritium concentration before treatment
DF	Without dimension

As an illustration, the table 1 gives some detritiation factors for different metals obtained using isotopic exchange [3].

Table 1: Comparative efficiency of detritiation experiments by isotopic exchange for different metals [3]

	Metal	*α (%)*	*DF*
Isotopic exchange with gaseous hydrogen (770K)	Stainless steel	86	7
	Inconel®	66	3
	Copper	97	33
	Alu. bronze	88	8
	Beryllium	92	12.5

EVALUATION OF TRITIUM LOADING IN PLASMA FACING COMPONENTS

The ITER machine will not operate permanently. The phenomena encountered may be represented by Heaviside functions. The operating conditions differ, depending on the precise moment during the pulse, dwell time or baking (treatment performed to desorb in situ part of the tritium in the materials composing the plasma-facing components).
Simulation of the tritium loading in the Plasma Facing Components (PFC) parts must take into account the different phases of the machine's life. Integration of this pulsed scheme into parameters such as the diffusivity constants or partial pressures makes it possible to reproduce the phenomena occurring with more precision.

Simulations of the loads in the parts are based on data from [4] which describes the sequential operation of the facility. The burn times are those of short pulses (400 s) and the related dwell times are 1400 s.
The two main types of databases for this study are the masses of the waste and their specific activity in tritium. [4, 5, 6, 7]. These simulations constitute the boundary conditions at the plasma surface of the PFC of the following modelling.
The tritium loading in the PFC is assumed to be based on Fickian diffusion in an isotropic material:

$$\frac{\partial c}{\partial t} = D\left(\frac{\partial^2 c}{\partial x^2}\right)$$

Where c is the tritium concentration in the PFC (mol/m^3), D the apparent coefficient of diffusion of tritium in PFC (m^2/s), and x the dimension of the PFC (m).
This modelling is performed in a multi layer material describing the real arrangement of the components. The thicknesses of the different materials are: 39 mm for tungsten, 1.5 mm for cooper alloy (CuCrZr) and 35.5 mm for stainless Steel.
Some assumptions have been made in order to simplify this modelling without losing the physical relevance (not detailed in this summary).
As an illustration, figure 1 gives the tritium concentration profile after the loading sequence in an Inner Vertical Target (IVT) top part.

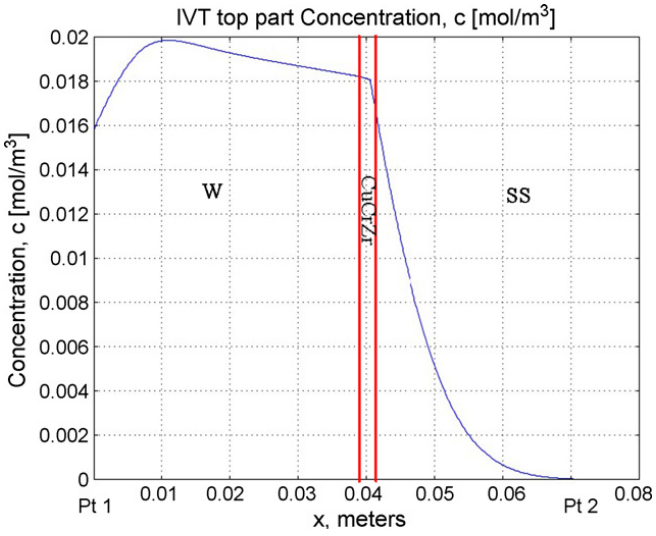

Figure 1: Tritium concentration profile in an Inner Vertical Target top part after loading

DETRITIATION RESULTS

For the evaluation of the thermal detritiation process, desorption calculations, have been performed using the"reverse" modelling described above and taking into account ideal conditions or "real conditions" as boundary conditions for both surfaces of the PFC.

IDEAL CONDITIONS

These conditions have been established to maximize the flux of outgassing tritium (and then the DF) by "numerically pumping" the tritium at the surface of the PFC. These conditions enable to quickly verify whether a thermal treatment is interesting for ITER objectives and give a rough estimate of its sensitivity to operational conditions like temperature. Two working temperatures have been chosen (800 and 1000°C). Results are summarized in table 2 and are coherent with the literature, especially with the fact that a temperature of 1000°C greatly favours the outgassing.

Table 2: Detritiation results in ideal conditions (263h)

Pieces	*Temperature*	*Detritiation factor*	
		800°C	**1000°C**
Inner Vertical Target	top part	130	42000
	bottom part	180	99000
Outer Vertical Target	top part	50	4500
	bottom part	140	52000
Dome		13	94

"REAL CONDITIONS"

Real conditions are obtained by considering the whole process of detritiation which could be used in the Tritium Recovery system located in the ITER Hot Cells.
The gas issued from the thermal desorption equipment is composed of tritium and a gas vector (argon) and must be oxidised into tritiated water. The heating power of this equipment is around 225 kW and the working temperature about 1000 °C. Oxidation can be done through a copper oxide bed (the bed must be regenerated by circulation of an oxygen flow) or a catalytic reactor (with platinum), or by adding oxygen to the gas flow. The gas phase must be pre-cooled before the oxidation step.
The tritiated water is condensed in a condenser; the water flows out to buffer tanks, before being sent to the Water Detritiation System (WDS) in the tritium plant. Incondensable gases are extracted from the condenser with an exhaust fan, and treated through a molecular sieve to trap tritiated water vapour from exhaust gases. The concentration of hydrogen in the thermal detritiation equipment is 5% in volume.
The material balance is based on the limits and efficiencies of the various steps. The limits of the characteristics of the tritiated water are:

- Maximal activity: 500 Ci.L^{-1},
- Production flow rate: almost 1.5 kg.h^{-1} our maximum (fixed in comparison of the design of the Water Detritiation System).

In a first approach, the mass balance in the thermal treatment equipment can be modelled as:

$$V.\frac{dC_{oven}}{dt} = \Phi - Q_s.C_{oven}$$

Where V denotes the oven volume (m^3), Φ the degassing flux (mol.s^{-1}), C_{oven}, the tritium concentration in the oven

(mol.m^{-3}) and Q_S, the volumetric flow rate of the gas phase (m3.s^{-1}).

This simple modelling assumes that:

- Globally the tritium flow in the oven is one-dimensional, i.e that no redistribution of flow occur (dead volumes, recirculations...) due for instance to thermal gradients in the facility. The gas flow rate is then assumed to be a constant.

- The outgassing flux is not influenced by the flow of the gas phase, i.e the renewal of the PFC surface is assumed to be perfect so that this flux is maximized.

These assumptions lead to a conservative modelling of the detritiation process; if the DF is too small for ITER needs then an other detritiation process will be required. On the other hand if the DF is relevant, more precise calculations will be needed to assess the technical interest of such process.
Basically the difference between the two boundary conditions relies in the fact that the real "one" considers the dilution of the tritium in the oven while the ideal one consider that all the produced tritium is immediately extracted from the oven.

In the design of the industrial process (based on the principal recalled by figure 2), several parameters could be used to optimise the detritiation treatment conditions:

- The temperature of treatment; in some case, an optimal temperature can be found due to the combination of several effects (Sievert's constant value and diffusion coefficients varying both with temperature),
- The renewal rate in the oven atmosphere that can improve the DF but produce larger amounts of water,
- An initial removal of Be (or not); Be is the limiting material in terms of diffusion,
- Impact of the duration of the thermal treatment.

Example of impact of renewal rate of the oven atmosphere is given in the following chapter.

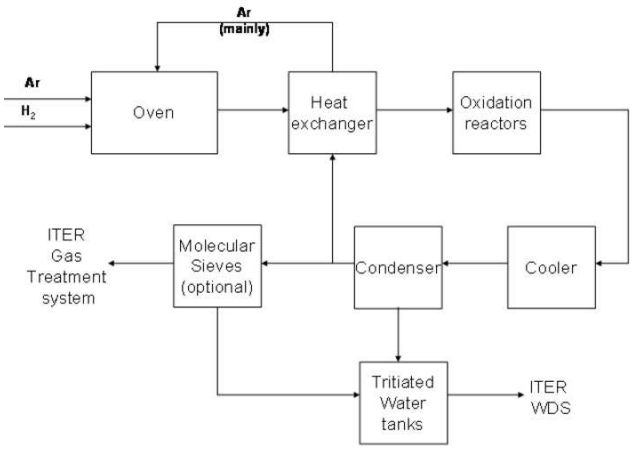

Figure 2: Overall scheme of detritiation process

IMPACT OF THE RENEWAL RATE OF THE OVEN ATMOSPHERE

Different calculations were performed using either ideal or real conditions and different Q_s. The results are summarized in table 3, the renewal rate ($1/\tau$) being defined as the ratio of the volume of the oven by the gas flowrate (V/Q_s). The treatment duration is defined according to the refurbishment planning, the volume of the oven is adapted to the baskets filled with the PFCs and the gas flowrate is chosen to allow a sufficient renewal rate.

Table 3: Effect of renewal rate on DF and production of tritiated water for an 8 m^3 oven at 1000°C (example on IVT top part)

Argon flow Nm^3.h^{-1}	Flow (T=1273 K) m^3.s^{-1}	τ s	Renewal rate. h^{-1}	DF	Tritiated water kg.h^{-1}	C_{HTO} Ci.L^{-1}
20	2.59E-02	309	12	1563	0.68	476.7
26	3.37E-02	238	15	1937	0.88	366.7
34	4.40E-02	182	20	2415	1.15	280.4
50	6.48E-02	124	29	3312	1.69	190.7
100	1.30E-01	62	58	5786	3.39	95.3
150	1.94E-01	41	87	7955	5.08	63.6
200	2.59E-01	31	117	9911	6.77	47.7

Not surprisingly figure 3 points out that the DF is largely overestimated when the ideal case is considered instead of real conditions.
As an example, the detritiation factor for IVT top part at 1000°C is 42000 in ideal conditions and drop down to 1563 in real conditions (V=8 m^3 and $1/\tau$=12 h^{-1}), i.e. divided by a factor of 27.

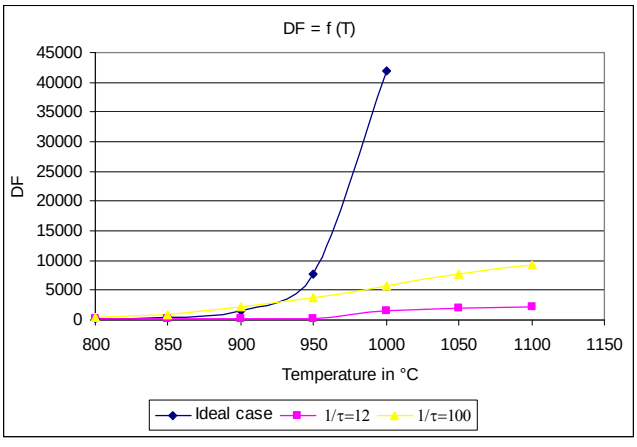

Figure 3: DF versus temperature in the case of IVT, duration 263h, V= 8 m^3 with different values of $1/\tau$

For "real" conditions, two different renewal rates have been tested ($1/\tau$=12h^{-1} et $1/\tau$=100h^{-1}), showing that the gain in terms of the DF due to temperature is low above 1000°C for 12 renewals per hour, in comparison with the one obtained when the temperature is increased from 950°C to 1000°C.

When a renewal rate of 100 per hour is considered, this effect is not so pronounced.
It is important to highlight that the DF obtained at 900°C and $1/\tau = 100h^{-1}$ (around 2000) is equivalent to the DF obtained at 1050°C and $1/\tau = 12h^{-1}$. Considering the consequences of a strong increase in the renewal rate on the volume of tritiated water produced, the temperature increase could be preferable, as shown in the figure 2. Indeed, for an $8m^3$ oven and 1000°C temperature, the tritiated water flow is over $1.5kg.h^{-1}$ if the renewal rate is higher than $30h^{-1}$.

CONCLUSIONS

The experimental results of the literature were obtained on small samples without studying the impact of real thick geometries on the efficiency of detritiation and under quite limited temperatures compared to what could be technically achieved. In order to evaluate the potentiality of heat treatments as detritiation techniques for ITER conditions, modelling of loading and de-loading of PFC were performed from an engineer point-of view. Since only average value of tritium concentration in the different materials is available in the ITER documentation, the initial tritium profile was numerically estimated.
This work enables to check the interest of such detritiation technique in terms of potential Detritiation Factor due to the fact that the loading an de-loading tritium flux have been maximized. This first approach has now to be improved by a large experimental and modelling program studying tritium loading and deloading of multilayer metallic pieces representative of ITER plasma facing components but also thermal-hydraulics in the oven. Only such a program will guarantee a precise design of the process.
If the level of efficiency to reach by such treatment was higher than the objectives defined in this paper, the process should be reviewed and mainly the detritiation technique. Another process like metal melting after Beryllium removal could probably be used.

REFERENCES

[1] O. Gastaldi, J. Chêne, P. Trabuc, Report on stainless steel detritiation by thermal treatment, EFDA Task TW1-TSW-002

[2] S. Rosanvallon, G. Marbach, J.P. Daclin, A-M. Brass, J. Chêne, Fusion Eng. And Design, 51- 52 (2000) 605-609

[3] A. N. Perevezentsev, Experimental trials of methods for metal detritiation for JET, Fusion Science and Technology, Vol 52, July 2007

[4] Generic Site Safety Report, Volume V, G 84 RI 4 R 0.2

[5] J. How, Project Integration Document, ITER doc, 2007, V 3.0, (www.iter.org/bl)

[6] Design Description Document, Blanket, ITER doc, (www.iter.org/bl)

[7] Design Description Document, Divertor, ITER doc, (www.iter.org/bl)

REPORTS AND PUBLICATIONS

Technical document DTN/STPA/LPC/2007/064, 12/2007
Study on existing detritiation processes and characterisation of tritiated materials for application in ITER and DEMO, Final Report, N. Ghirelli, O. Gastaldi

TASK LEADER

Olivier GASTALDI

DEN/DTN/STPA/LTTS
CEA-Cadarache
F-13108 Saint-Paul-lez-Durance Cedex

Tel: 33 4 42 25 37 87
Fax: 33 4 42 25 79 49

e-mail: olivier.gastaldi@cea.fr

CEFDA05-1285

Task Title: TW5-TRP-003: DEMO BLANKET SEGMENTATION AND MAINTENANCE

INTRODUCTION

The next generation of fusion reactor after ITER is studied through DEMO project. This reactor should demonstrate the productivity in industrial context. To prove the efficiency of DEMO, the availability is an important factor.
The components facing the plasma are exposed to very high thermal loads, so it's necessary to replace them at given periods.
Due to the radiation level, it is necessary to make the operations fully by Remote Handling. This critical maintenance needs to be done in acceptable times in regard to the reactor availability. This task focuses on the aspects concerning the Remote Handling of the blanket elements during maintenance phases.
As it is impossible to refurbish the worn blanket inside the torus, it will be necessary to carry it entirely to the hot cells. This operation implies that the first wall is segmented in smaller parts called blanket modules, or segments. Each module needs to be connected to the coolant circuit, and to a tritium extraction and circulation system.

2007-2008 ACTIVITIES

CONFINEMENT PROBLEM

The inside of the vessel being tritium contaminated, it is indispensable to respect high safety instructions inspired from the actual fission reactors. Each step of the maintenance scenario shall preserve a high tightness:

- Always keep one barrier intact,
- All the cutting tasks inside the vessel,
- No pipe through the access doors,
- Opening/closure doors by "double door" system,
- Control tightness for every cutting/welding operation.

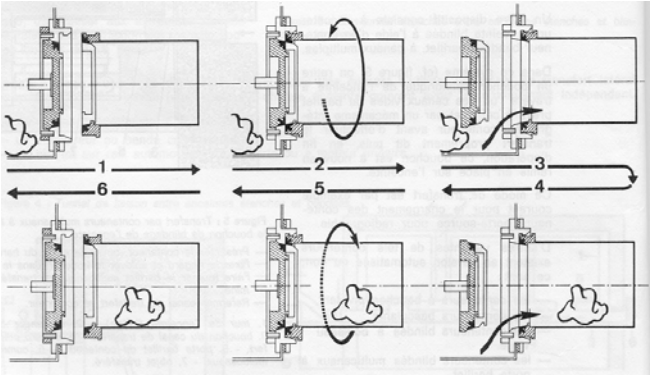

Figure 1: Double door System

TRANSFER SYSTEM

The transfer to the hot cells can be performed by several means. The table 1 resumes the properties of each solution.

Table 1: Properties of each solution for the transfer

Solutions	Advantages	Inconvenient
Corridor linking directly the hot cells to the vessel	few connection/disconnection tasks	huge corridor to control
Mobile cask travelling from the vessel to the hot cells	one universal cask	several connection/disconnection tasks
One fixed cask connected to the vessel + One mobile cask travelling to the hot cells	tasks parallelisation	several connection/disconnection tasks

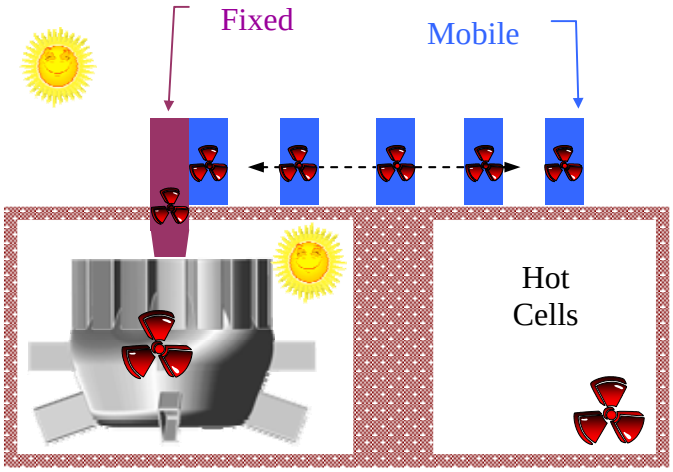

Figure 2: Maintenance scheme of the fixed and mobile cask

BLANKET TRAJECTORIES

The conceptual design of the reactor (the shape, the fastening systems, free space…) imposes to the segments complex trajectories. The maintenance should be done without shocking the segments in any area. In the case, the modules will be broken and we will need to throw away the segment and to clean the vacuum vessel from every pieces of dust. The grasping areas of the segment are also very limited because we can not grasp the modules. The only grasping area is the manifold and on the manifold one side is blocked by the neighbouring segment. The trajectories are a combination of several simple movements (figure 3).

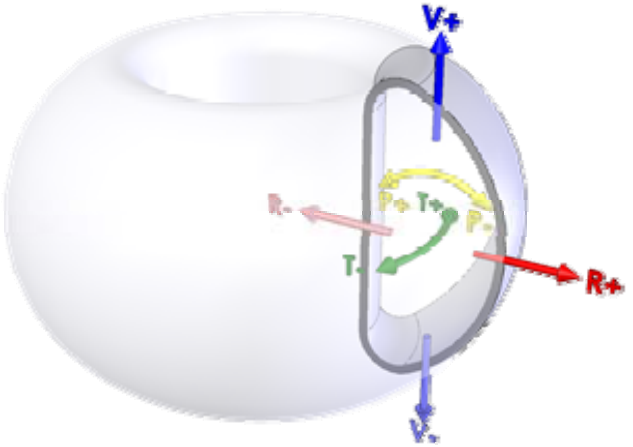

Figure 3: Main Movements in the Torus

- **Inboard Segment Trajectories**:

  - ✓ Escape the wall : R+, P+, V-
  - ✓ Go to the Maintenance Port : T+
  - ✓ Position in front of the Maintenance
  - ✓ Port : R+
  - ✓ vertical extraction : V+

- **Outboard Segment Trajectories:**

  - ✓ Escape from the onside segment : T+
  - ✓ Escape the wall : R-, P-, V-
  - ✓ Put right the segment : R+, P+
  - ✓ Go to the Maintenance Port : T+
  - ✓ Position in front of the Maintenance
  - ✓ Port : R+, V+, P+, P-
  - ✓ Vertical Extraction : V+

The maintenance machine must be able to impose adequate stresses to perform the trajectory.

The first difficulty is the introduction of such a machine into the vacuum vessel. The maintenance ports are the upper ports and the divertor port. The maintenance inside machine will be able to move on the divertor rail (components located at the bottom of the torus and preliminary removed) for the toroidal movement.

The results we present here consider an introduction by the divertor port only. The strategy for the introduction is to compact the maintenance machine in a kind of divertor cassette smaller and lighter. Once the maintenance cassette introduced, the maintenance machine will deploy inside the vacuum vessel. The type of maintenance machine studied is similar to the system called “Moving table, Jack and Vertical Mover”.

The latest DEMO studies in EU started in 2005, after the completion of the EU Power Plant Conceptual Study (PPCS).

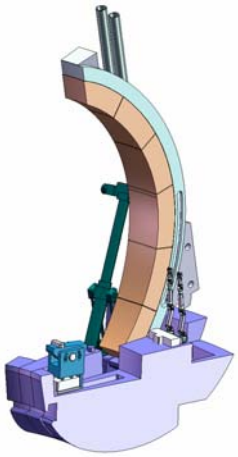

Figure 4: Toroidal Mover

The machine is composed of 3 maintenance cassettes. On the first hand, there is a mobile jack, on the second one, an outboard moving table and industrial maintenance robots (MAESTRO), and one the last one, the inboard moving table and industrial maintenance robots (MAESTRO).

CONCLUSIONS

This report addresses several issues related to maintenance in plasma fusion reactor undertaken within the European EFDA-DEMO studies. The design driver for the maintenance scheme that affects both design of the DEMO machine design and the Remote Handling system is the safety related issue of confinement i.e. to maintain the tightness of the system all along the process. This safety issue related to confinement induces to consider in priority proven design option, as the one already in use in the Fission facilities. Along each step of maintenance operation, the RH systems shall meet these safety requirements. Machine availability is a high DEMO priority considering the operation requirement; therefore, maintenance duration is a very high design driver for the remote handling systems and the In-Vessel component (number, size shape, connection…). The idea to parallelize tasks is very welcome and should be assessed further considering flow issue. The study provides first set of maintenance system design options for the DEMO reactor. Further studies have to be done to confirm their feasibility.

REPORTS AND PUBLICATIONS

DTSI/SRI/LRM/06RT027 Remote Handling Issues, J.-P. Martins, C. Dechelle

DTSI/SRI/LRM/07RT041 Selection of Reference Maintenance Concept, J. Bonnemaison, Y. Perrot, J.-P. Friconneau

J. Bonnemaison, et al., Contribution to DEMO reactor RH maintenance assessment, Fusion Eng. Des. (2009)

TASK LEADER

Jean-Pierre FRICONNEAU

DRT/DTSI/SRI
CEN-FAR Fontenay
BP 6
F-92265 Fontenay-aux-Roses Cedex

Tel: 33 1 46 54 89 66
Fax: 33 1 46 54 89 80

e-mail: jean-pierre.friconneau@cea.fr

CEFDA06-1452

Task Title: TW6-TRP-003: DEMO MULTI MODULES BLANKET ATTACHMENT CONCEPTUAL DESIGN

INTRODUCTION

The latest DEMO studies in EU started in 2005, after the completion of the EU Power Plant Conceptual Study (PPCS).
Following the establishment of a DEMO physics basis and a number of scoping studies, the design activity associated with the main in-vessel components led to the definition of a consistent set of DEMO parameters made with the PROCESS code whose main parameters are an electrical power output of 1000 MWe and a major radius of 7.5 m.

2007-2008 ACTIVITIES

This present activity is focussing on design and integration aspects. Work carried out concerns the following scopes, like design of internal components (HCLL, HCPB and DCLL blanket), maintenance, neutronic analysis, magnet system, balance of Plant, design integration.
The final CEA deliverable of this task, recovering the year 2007-2008, aggregates the contributions on:

- The design of internal HCLL components and their attachments,
- The maintenance,
- The ex-vessel integration.

DEMO MULTI MODULES BLANKET ATTACHMENT CONCEPTUAL DESIGN

The present study assumes that the Helium Cooled Lithium-Lead (HCLL) blanket is the reference DEMO blanket. The HCLL blanket concept derived from the PPCS/Model AB studies based on the large modules concept. The lifetime of the blanket is supposed to be 5 years. It implies several blanket replacements during the DEMO reactor lifetime (assumed to be about 40 years). Therefore, the “large modules” replacement capability is one of the main critical issues since it requires to perform several cutting/rewelding works in a region where the neutron fluence is relatively high. The PPCS/Model AB studies ended with the suggestion of attaching each column of modules on a common back-plate and removing them as a single piece from a top port which would allow to locate all cutting/rewelding works to a top well protected area. This suggestion leads to the Multi-Module Segment (MMS) concept that is the basis of the present study.

In this concept, each module consists of a He-cooled Eurofer-steel box reinforced with toroidal and poloidal He-cooled Eurofer stiffeners. He-pressure is 8 MPa and inlet/outlet temperatures are 300°C/500°C.

The Pb-15.7Li slowly flows within the grid in radial direction and is cooled by He flowing in radial-toroidal steel cooling plates immersed in the Pb-15.7Li. In the rear side, the module box is closed by several steel plates acting as distributing/collecting chambers for the He-coolant and the Pb-Li. There are 16 toroidal coils that define 16 vacuum vessel sectors. Each sector is made of 2 inboard and 3 outboard banana-shaped MMS. Each MMS has 6 to 8 modules which are sharing the last two He-collecting chambers whose walls act as a strong back-plate structure for each banana-like MMS.

The main topics assessed in this report are: attachments, feeding pipes layout, thermohydraulic and thermomechanic studies in the set “segment + module”, poloidal adaptation of the basic module design, manufacturing issue.
Besides the description of the blanket design and the performances corresponding to the latest DEMO specifications, this report focuses on the integration aspect of HCLL MMS blanket including the corresponding vertical maintenance scheme and a detailed study of the blanket attachment which has to comply with thermal expansion between vacuum vessel and the blanket segments.

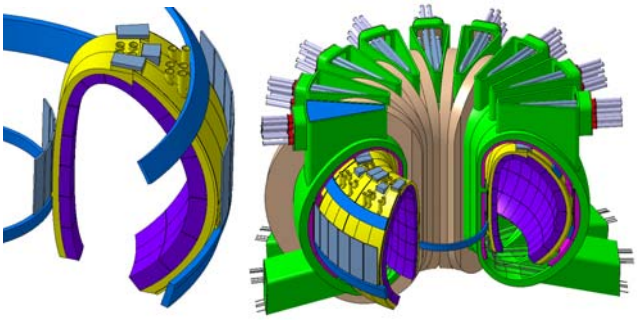

Figure 1: MMS fixation option, with an additional ring

The main idea of this attachment concept is to hang up the torus shaped rigid whole made of the assembly of all the segments by means of flexible bars sets, linking the vacuum vessel to two rings, on which MMS are fixed, located on internal and external sides of lower part of the MMS structure. This kind of design can withstand the electromagnetic loads by reducing stress level in flexible attachments.
The results have shown that the design of an acceptable breeding blanket isn't an easy task when considering all integration requirements. Moreover, additional work should be required to upgrade the design by taking into account updated input data coming from EM loads and neutronic calculations. As a result, the conceptual design of MMS flexible attachments introduced in this document is well suited to the DEMO's available requirements.

BLANKET SEGMENTATION AND MAINTENANCE

SELECTION OF REFERENCE MAINTENANCE CONCEPT

In this study, we focused on the possible maintenance schemes for DEMO. The replacement time of the first wall has a significant impact for the availability of DEMO facility. All in-vessel maintenance operations should meet the safety requirements of the installation. This could affect the possible maintenance schemes.
Safety imposes strong requirements on the confinement. Because of use of tritium, this implies to preserve a high tightness during all the cycle of life of such a reactor. During in service conditions, three physical barriers isolate the Vacuum Vessel volume from non-restricted volumes. During the maintenance, we consider only the first barrier to remain always closed. Therefore, to cross this first barrier without breaking the confinement, the opening/closure access door should be based on a system similar to the double door system used for glove boxes in nuclear facilities. Removal of first wall component requires cut of cooling pipes. To meet the confinement requirements, this must be done inside the Vacuum vessel. The space in the access ports should be totally cleared from equipment to allow the necessary clearance required during segment extraction. It is also necessary to provide enough gap between cut pipe and segments to allow safe movement during segment extraction. When considering no permanent confined corridor between Tokamak and hot cells, it is required to use tightened transfer cask systems to allow transfer of tritiated component of RH Equipment from vacuum vessel to hot cells.

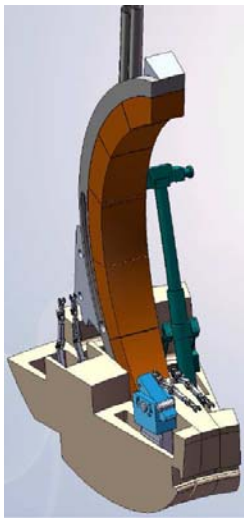

Figure 2: Maintenance Machine

The number of access dedicated for maintenance are set to a maximum of four because the option presents more credibility compared with the use of all ports (16 ports). Nevertheless, the access to the 16 ports appears necessary to perform the cut of pipes. Taken into account the limited number of maintenance ports, the sequences of removal of segments is not free and impose a strong limitation. Several design options (corridor, mobile cask, fixed cask) were assessed relative to the transfer of equipment between the hot cells and the vacuum vessel. The one that we recommend is the one composed of a fixed cask on the vacuum vessel and a transfer cask because of its benefit when considering the confinement and simplification of the interface to the buildings. Instead of connecting several times the cask and adjusting the misalignment, we split this task to limit the number of risky operations and maintaining the set of simple elementary tasks. To minimize the spent time, we can also parallelize the maintenance operations. Indeed, the segment extraction inside the reactor should be made simultaneously with the transfer to the hot cells task. The availability of the reactor being an important criterion, it is necessary that the maintenance time be as less as possible. The frequent operations should be optimised and simplified. The fixed cask option is better in this context.
The handling tools should be able to perform the orientations and the trajectories to the segments required for their replacement. The maintenance handling device is composed of several tools such as, tools to tilt the segment, tools for the toroidal movement and tools for the cutting/welding of pipes. The good accuracy of positioning is also required due to the limited gap between segments: space of 20 mm. Installation is time consuming and requires minimization and design of RH equipment should take care of this requirement with high priority. We assessed various design options for the RH devices and proposed, at conceptual design level, tentative design options and recommendations to meet the very high level set of requirements for DEMO first wall replacement.

EX-VESSEL INTEGRATION

The DEMO ex-vessel integration activity, where HCLL blanket has been chosen as the reference blanket, outlines components and systems related to the following topics:

- Heating and Current drive systems,
- Diagnostics,
- Magnet system and in particular benefits of HTS,
- Balance of Plant.

Neutral beam ion and electron cyclotron heating and current drive system are recommended for a DEMO reactor, considering that 75 % of power is produced by neutral beam.
A list of diagnostics to control the plasma was proposed. It is proposed to locate these diagnostics in four equatorial equidistant ports. The tritium production ratio is only weakly affected by heating system and diagnostics. However, these considerations do not take into account radiation effects on materials, the required shielding could increase the required space. The preliminary design of the magnet was assessed. It appears that the density current chosen in this design is too high. A more realistic value of 44 A/mm² is proposed (instead of 100 A/mm²) by increasing the major radius. A magnet system, using Bi2212 and YBCO high temperature superconductors was designed. It appears that, if there are no real benefit in terms of recycled power consumption to use these conductors, they could increase the temperature margin and then simplify the conception of the machine.
For the balance of plant, a pre-conceptual design and sizing of the main equipment and pipe work of the primary heat transport system was proposed.

The divertor and blanket heat transport system is divided into eight identical helium cooling loops of 100 bars even if blanket module were designed for 80 bars. The Pb15.7Li circuit has no reason to be very different from the one proposed in the WCLL circuit or in the PPCS.

The possibility to adjust in line the enrichment in Li6 allows to control the tritium production rate. With the new SOLE [5] tritium solubility and taking into account a mass transfer coefficient due to Pb-15.7Li flow, tritium permeation is not a major issue, less than two percent of the tritium production rate should permeate through the helium coolant system.

DEMO provisional parameters were set to obtain a net electrical power to the grid of 1000 MWe. However, the calculated net electrical power in this study is around 700 MWe. The net efficiency of the DEMO is around 23.3%. Around 47 % of the gross electrical power is recycled in order to operate the tokamak. 94 % of the recycled power is due to the He pumping power and the heating and current drive system. Substantial gain could be obtained by investigation in these two topics.

CONCLUSIONS

All this work permitted to identify the difficulties of designing an acceptable breeding blanket when all integration requirements are taken into account. Despite some further optimization is still necessary, this study allows to conclude the Helium-Cooled Lithium-Lead blanket is a very promising candidate for being the breeding blanket for the future DEMO reactor.

REFERENCES

[1] Determination of hydrogen solubility in lead-lithium using SOLE device
A. Aiello, A. Ciampichetti and G. Benamati
Fusion Engineering & Design, V81, Issues 1-7, p 639 (ISFNT-7)

REPORTS AND PUBLICATIONS

[2] L. Cachon, "Helium Cooled DEMO design activities - Final deliverable of the contract EFDA/06-1452", CEA Technical Report NT DTN/STPA/LTCG-2008-030

[3] L. Cachon et al., "DEMO Multi modules blanket attachment conceptual design – TW6-TRP-003-D01", CEA Technical Report DTN/STPA/LTCG/2007-028

[4] J. Bonnemaison, "TW5-TRP-004B – Fusion DEMO - Blanket segmentation and maintenance", DTSI/SRI/LRM/07RT.041

[5] F. Gabriel , " DEMO 2006 – Ex-Vessel Integration - Task TW6-TRP-003-D03", Rapport DM2S SERMA/LPEC/RT/08-4343/ind1

TASK LEADER

Lionel CACHON

DTN/STPA/LTCG
CEA-Cadarache
F-13108 Saint-Paul-lez-Durance Cedex

Tel: 33 4 42 25 74 25
Fax: 33 4 42 25 66 38

e-mail: lionel.cachon@cea.fr

TW5-TRP-002-D03a
TW6-TRP-002-D02

Task Title: ANALYSIS OF CURRENT PROFILE CONTROL IN TOKAMAK REACTOR SCENARIOS USING REALISTIC TREATMENT OF CURRENT DRIVE EFFICIENCIES

INTRODUCTION

On the path to the development of the first commercial fusion reactor, DEMO will be the next step after ITER, with the aim of testing the main technology options at a somewhat reduced electrical power with respect to the commercial reactor (1 GW vs 1.5 GW). The DEMO reactor should work in steady-state, therefore, one of the main physics challenges will be the establishement and the control of a non-inductively driven current density profile. This task, continuing earlier preliminary studies, consists in the analysis of this problem by means of the integrated modelling code CRONOS. CRONOS [1] is a suite of numerical codes for the predictive/interpretative simulation of a full tokamak discharge. It integrates, in a modular structure, a 1-D transport solver with general 2-D magnetic equilibria, several heat, particle and impurities transport models, as well as heat, particle, current and momentum sources. This task has provided a set of CRONOS simulations of DEMO discharges, in which the various current sources combine to yield a stable current density profile. It should be stressed that the existence of such a scenario is not a priori guaranteed. Therefore, the 1-D modelling is an essential step for the first design phase of DEMO and of course also of the following commercial reactor.

2007-2008 ACTIVITIES

SIMULATION RESULTS

The DEMO scenarios considered in this paper are inspired by the Model-C scenario in [2], which is based on advanced physical assumptions, i.e. it is characterised by a high β and high confinement, MHD stabilisation by strong plasma shaping, a high bootstrap current fraction and low Zeff (≈2.2).

In order to clarify such scenarios, two different regimes have been studied in this work: one with the aim of maximizing the fusion gain and minimizing the number of external heating systems, just by using Neutral Beam Injection (NBI) (scenario1), the second one with the aim of obtaining a full non-inductive current steady-state scenario by adding a ECH/ECCD system to the previous one (scenario2). The global characteristics of the operation scenarios considered are the following: major radius R = 7.5 m, minor radius a = 2.5 m, elongation / triangularity = 1.9 / 0.47, magnetic field B = 6 T, plasma current Ip = 19 MA, central density 1.1 10^{20} m^{-3} (Greenwald fraction ~1.2).
The transport model used is GLF23 [3]. Additional details on these simulations can be found in [4].

Scenario1: pulsed DEMO

The plasma density, the electron and ion temperature profiles as well as the current density profiles obtained for scenario1 at t=3000s are shown in figure 1.
Electron and ion temperature profiles are quite similar, with $T_{i,0}$=32.5 keV, $T_{e,0}$=31.7 keV and T_{ped}≈7.8 keV. The current density profile structure is dominated by the 2 MeV off-axis NBI driven current at normalised radius ρ ≈ 0.3 due to the high peak obtained. On the other hand, the bootstrap current completely determines the current profile at the edge, and in fact, a large amount of the total bootstrap current, I_{boot}=10.0 MA, comes from the plasma edge. Owing to its high CD efficiency, the NBI current is also very high, i.e., I_{nbi}=6.8 MA for an injected power of 98 MW.
Therefore, in this scenario the total non-inductive current is large, I_{ni}=16.8 MA, and represents a high fraction over the total current, f_{NI}=88%, with a bootstrap current fraction f_{boot}=52.6%, as shown in figure 2.
Although a high pedestal has been considered, the bootstrap current fraction is still somewhat smaller than in [2], where f_{boot}=63%.

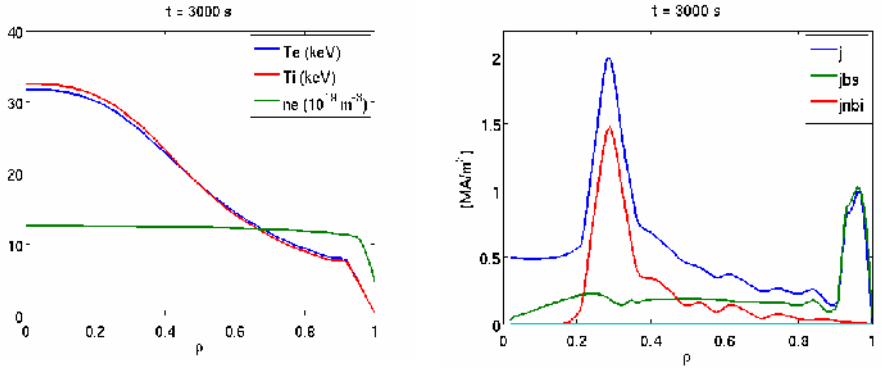

Figure 1: Electron and ion temperature profiles for DEMO scenario1 obtained with CRONOS when t=3000s (left) Current density profiles for DEMO scenario1 when t=3000s (right)

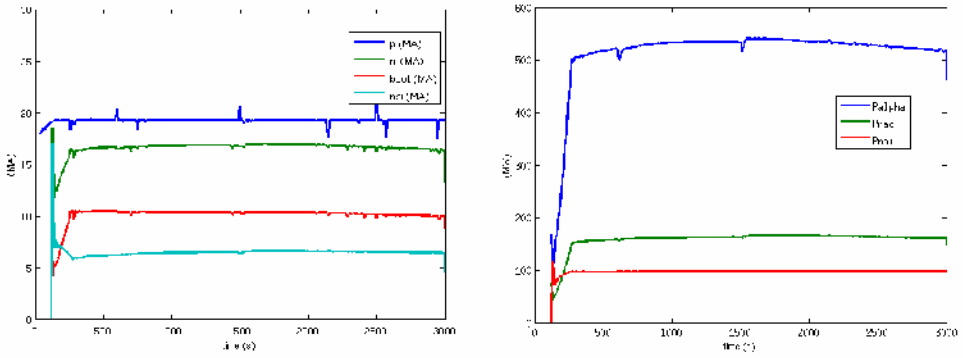

Figure 2: Evolution of the total current (Ip), total non-inductive current (Ini), bootstrap current (Iboot) and NBI current drive (Inbi) (left). Alpha (Palpha), radiated (Prad) abd NBI (Pnbi) power evolution (right)

In figure 2 the time evolutions of the alpha power, NBI power and radiated power are given. The fusion power obtained is 2.6 GW, which means roughly 1 GW net electrical power (assuming a conversion efficiency ≈ 40 % as in [2]. Therefore, the analysis presented here downscales the electrical power from the 1.45 GW obtained in the 0-D analysis carried out in [2]. The main reason is that we have considered a conservative value on the Greenwald fraction, 1.2, compared to that used in [2], 1.5, with the aim of avoiding too optimistic results on the fusion power. In this scenario, the long pulse operation is made possible by a low amount of injected power (= 98 MW), which implies a rather high Q = 26.5, which is one of the main goals of the DEMO design. In spite of using a 2 MeV system for the NBI, the current drive efficiency is still far from the one considered in [2] for all the H&CD systems, i.e. 0.7 $AW^{-1}10^{20}m^{-2}$.

Scenario 2: steady-state DEMO

With the aim of analysing a regime with no inductive current, close to the so-called "steady-state" regimes of ITER, a scenario with the characteristics of scenario1 but with the addition of off-axis current drive (CD) has been considered. 66 MW of Electron Cyclotron CD have been added to the previous simulation at t=1500s. Two wave beams have been used for different purposes: 23 MW are mainly used to control the evolution of q_0 with the aim of obtaining a reversed shear (deposition at ρ ≈ 0.2), whereas 43 MW are used to drive as much current as possible and to broaden the current profile at ρ ≈ 0.3-0.4 by increasing the toroidal angle. The frequency is 200 GHz at the first harmonic, ordinary mode polarisation. Note that further optimisation of this scenario might be obtained by using a multi-frequency wave system, however, it seems hard to reach the current efficiency considered in [2] since the one obtained in this paper for the ECH/ECCD system, γ_{CD}=0.2 AW^{-1} $10^{20}m^{-2}$, is much smaller.
The electron and ion temperature profiles as well as the current density profiles obtained for this regime when t=3000s are shown in figure 3. As expected, both ion and electron central temperatures are higher than in the previous case, $T_{i,0}$=34.3 keV and $T_{e,0}$=34.5 keV.
The q profile is now highly stabilized and reversed during the period 2000-3000s in the region 0.05<ρ<0.2.

The time evolution of the currents is shown in figure 4. In this scenario, a non-inductive current close to 100% is obtained due to the increased bootstrap current and the current from ECCD (=1.6 MA). Since the temperatures are higher, the alpha power is also increased up to 564 MW, however this is not enough to compensate for the increased input power, and finally the fusion gain drops to Q=17.2.

Therefore, although the fusion power is high enough in this scenario to have 1GW of net electrical power, it seems a problem to obtain without an ITB a Q>20, which will be a strong requirement for the future commercial reactor.

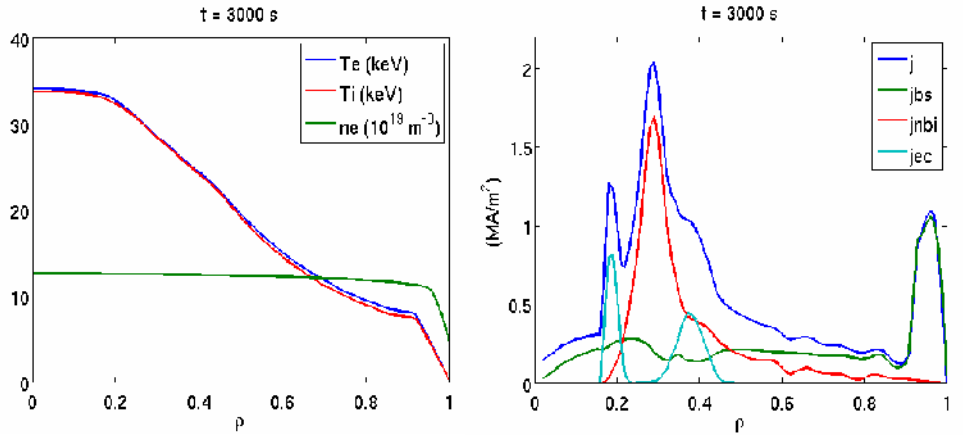

Figure 3: Electron and ion temperature profiles for DEMO scenario2 obtained with CRONOS when t=3000s (left). Current density profiles for DEMO scenario2 when t=3000s (right)

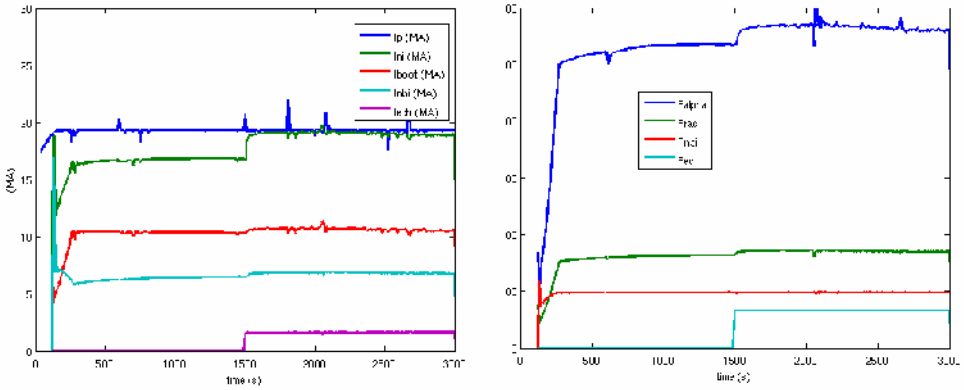

Figure 4: Evolution of the total current (Ip), total non-inductive current (Ini), bootstrap current (Iboot), NBI current drive (Inbi) and ECCD current drive (Iech) (left). Alpha (Palpha), radiated (Prad), NBI (Pnbi) and ECH (Pec) power evolution (right)

CONCLUSIONS

The CRONOS suite of codes has been used to simulate and analyze the DEMO design in two different scenarios: pulsed and aiming at steady-state, respectively. A large Q=26.5 is obtained in the pulsed scenario, which is possible due to the low injected power considered (=98 MW) and a high pedestal temperature, 7.8 keV, leading to a hybrid-like q profile with q_0>1. The non-inductive current fraction is rather high, 88%, with a high amount of bootstrap current, 10.0 MA mainly coming form the pedestal, and 6.8 MA of NBI current drive, which is possible due to the 2 MeV launcher system considered. It has been shown that, due to the large density considered for these scenarios, a 1 MeV NBI system could not be enough to drive sufficient current, as well as the redistributed current inside the plasma could be a handicap to control the q profile.
Although q is above 1 in the previous scenario, its evolution is not completely stable and slowly falls to the q<1 region. In order to fix this issue, a system of 66MW of ECH has been considered in the second scenario. In this new scenario, a 100% non-inductive current is obtained due to the additional current drive form the ECH system and the increased bootstrap current due to the reversed q profile which is also controlled by means of this system. However, the reversed q is not enough to create an ITB and therefore the increased alpha power cannot compensate the large amount of ECH input power, which finally leads to a scenario with Q=17.2. This may not be sufficient for DEMO, however, more studies are needed (probably with other transport models) to properly account for the ITB formation in DEMO with reversed q profile.

REFERENCES

[1] Basiuk V. et al., Nucl. Fusion 43 822 (2003)

[2] Maisonnier D. et al., Nucl. Fusion 47 1524 (2007)

[3] Kinsey J.E. et al., Phys. Plasmas 12 052503 (2005)

[4] Garcia J. et al., Nucl. Fusion 48 075007 (2008)

REPORTS AND PUBLICATIONS

Analysis of current profile control in tokamak reactor scenarios using realistic treatment of current drive efficiencies

CEA internal report October 2007
J. Garcia, J.-F Artaud, V. Basiuk, F. Imbeaux, J. Johner, M. Schneider

TASK LEADER

Gerardo GIRUZZI

DSM/IRFM/SCCP
CEA-Cadarache
F-13108 Saint-Paul-Lez-Durance

Tel: 33 4 42 25 73 44
Fax: 33 4 42 25 62 33

e-mail: gerardo.giruzzi@cea.fr

Task Title: DELIVERY OF THE MAGNET SYSTEM OUTLINE FOR A DEMO REACTOR

INTRODUCTION

In the framework of DEMO conceptual studies, the TF magnet system has to be integrated at an early stage in the overall design development.
As a matter of fact, located at the very heart of the tokamak, the TF system interacts with many aspects of the machine. In 2006 CEA presented which tools will be used to perform this integrated analysis, In particular ESCORT.
2007 activities have been mainly dedicated to analyse the DEMO TF inner leg as it is presented in the preliminary design of the machine [1].

2007-2008 ACTIVITIES

ANALYSIS OF THE DEMO TF INNER LEG

Non copper section

The non copper current density J_{noncu} is a decreasing function of the magnetic field. The estimation presented in the following figure 1, is based on the recent developments regarding Nb_3Sn strands for ITER TF system [2, 3, 4]. The performance of five types of strands fitting to the ITER specifications (J_{noncu}=800 A/mm^2 at 12 T, 4.2 K and -0.1 %) are presented in a representative condition of strain.
The performances are presented as a function of the magnetic field for a temperature of 5.7 K which includes a margin for stability and operation of 0.7 K and a typical strain of -0.77 %, such as presently considered for ITER.
J_{noncu} for ITER is in the range of 270 A/mm^2, but due to the increased magnetic field in DEMO TF system, J_{noncu} for DEMO is presently estimated under 150 A/mm^2. The magnetic field value to consider is the effective field value (around 13.5 T) lower than B_{tmax}.

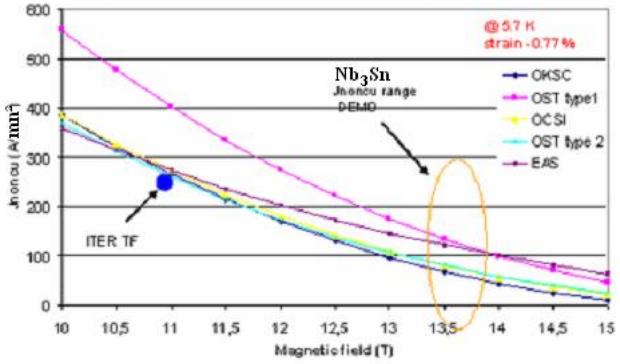

Figure 1: Performance from different European Nb_3Sn strands as a function of magnetic field [2, 3 and 4]

For the present study, a value of 150 A/mm^2 for J_{noncu} will be taken into account for the TF system based on possible improvement of Nb_3Sn strands.

Other options were investigated and in particular the use of HTS materials instead of Nb_3Sn with an operation of the TF system at higher temperature. This can contribute to decrease the recirculating power of the Tokamak by 10 MW and improve the temperature margin of the superconducting material [5]. It is shown that there is no interest to aim at operating the TF system at a temperature higher than 20 K, a temperature achievable with Bi2212 strands which are already produced in kilometric unit length. The main interest is in the increase of the temperature margin for a better reliability of the machine because the gain in efficiency will be low. A substantial R&D has to be carried out to develop high current HTS conductors.

Copper section

The copper section in the CICC plays a leading part in case of quench detection and associated fast safety discharge. The copper section can be calculated using the so-called hot spot criterion.

The amount of copper has to be such as to maintain the temperature at the end of the fast safety discharge less then 250 K (hot spot criterion). The time constant of the discharge τ is linked to the acceptable maximum voltage to the ground V_{maxg} at the beginning of the discharge. This voltage is a function of the magnetic stored energy W_{mag} of the system, of the number of groups of coils N_c of the TF system and of the conductor current I_{op}. Each group is in series between two banks of discharge resistors. N_c cannot be larger than the number of coils in the TF system.
The following formula (1) can be given, if the discharge is supposed to be exponential, L being the inductance of the TF system. The real time constant taking is τ' which is shorter considering a non exponential discharge thanks to Ni resistor.

$$W_{mag} = 0.5\ L\ I_{op}^2$$
$$V_{maxg} = L\ I_{op}/(2\ N_c \tau) \qquad (1)$$
$$\tau = W_{mag}/(I_{op}\ N_c\ V_{maxg})$$

In table 1, both situations in DEMO and in ITER are compared. The copper section is calculated such as not to exceed locally adiabatically the allowable voltage of 4 kV and the maximum temperature. Due to the larger stored energy in DEMO than in ITER, even by increasing the number of groups of coils (in comparison with ITER) and increasing slightly the voltage to the ground, τ is nearly twice the time constant of ITER which means that the copper section has to be large.

Table 1: Fast discharge parameters in ITER and DEMO

	ITER	DEMO
W_{mag}	40 GJ	120 GJ
I_{op}	68 kA	57.3 kA
N_c	9	16
V_{maxg}	3.5 kV	4 kV
τ	18.7s	32.2 s
τ'	11 s	20 s

Overall current density in the inner TF leg J_{cond}

From the non copper section and the copper section, it is possible to deduce the current density in the superconducting cable in conduit. A realistic value can be estimated around 40 A/mm^2 taking into account also the helium section, while the preliminary value of DEMO is 100 A/mm^2 which is far too large and certainly underestimates the amount of the copper section in the conductor
Using the results of the previous sections and the analytical structural analysis presented in [6], it is possible to further estimate the overall current density J_{cond} in the TF inner leg including the steel section which is dominating. It can be seen that a realistic value of J_{cond} is around 10 A/mm^2 and not 15 A/mm^2 as taken in the preliminary design of DEMO.

CONCLUSIONS

The solution for superconducting materials in the TF system of DEMO has to be selected in tight relation with the cryogenic refrigeration concept of the magnet. Whatever the solution, it is observed that the overall current density in the present preliminary design of the DEMO TF system is too large. The reason for this is linked to the selection of a too high value of the cable current density around 100 A/mm^2 while a more realistic value is around 50 A/mm^2. To relax the overall current density it is suggested to increase the major plasma radius of the DEMO system in the range of 8.5 m while decreasing the toroidal magnetic field around 5.5 T, such as to keep constant the thermonuclear fusion power.

REFERENCES

[1] Hayward J. Presentation at Garching DEMO EFDA meeting (26 June 2007)

[2] EFDA Internal note 2007 Qualification of industrial suppliers of Nb_3Sn strands with increased values of J_c N11 TD 91 FE ITA 11-02-EU

[3] Taylor D. M. J. and Hampshire D. P., 2005 Supercond. Sci. Technol. 18 241

[4] Ilyin Y., Nijhuis A. and Krooshoop E. 2007 Supercond. Sci. Technol. 20 186

[5] Duchateau J.-L., Journeaux J.-Y. and Millet F. Nucl. Fusion 46 94

[6] Duchateau J.-L, Hertout P. and Johner J., 2007 IEEE Trans. Appl. Supercond 17 1342

REPORTS AND PUBLICATIONS

J.-L. Duchateau, P. Hertout, "Which superconducting material for the toroidal field system of the fusion DEMO reactor?" 2008 J. Phys.: Conf. Ser. 97 012038

J.-L. Duchateau, P. Hertout "EFDA contract TW6–TRP-006 Final report" CEA Internal report AIM/NTT-2007.019

TASK LEADER

Jean-Luc DUCHATEAU

DSM/IRFM/STEP
CEA-Cadarache
F-13108 Saint-Paul-lez-Durance Cedex

Tel : 33 4 42 25 49 67
Fax : 33 4 42 25 26 61

e-mail : jean-luc.duchateau@cea.fr

CEFDA06-1483

Task Title: TW6-TDS-QA1: SUPPORT IN THE DEVELOPMENT OF THE QA SYSTEM FOR THE ITER EU DOMESTIC AGENCY AND IMPLEMENTATION OF A QUALITY ASSURANCE PROGRAMME IN THE EUROPEAN FUSION ASSOCIATIONS FOR ITER-RELEVANT ACTIVITIES

INTRODUCTION

EFDA developed under the former task (TW5-TDS-QA) a draft Quality Management System in order to comply with:

- the IAEA standard (IAEA50-C/SG-Q),
- its transcription into the French law (Decree of August 10th,1984),
- ITER Quality Programme.

The present task is to prepare, from the documents of the former task, a proposal for a draft QMS for F4E in order to comply with the ITER Quality Programme and taking into account some changes such as the IAEA safety standards (IAEA-GS-R-3). The first steps of the necessary culture change are also implemented, in order to help the different associations.

2007-2008 ACTIVITIES

During the period, CEA submitted to EFDA, a Quality Management System applied to all activities performed by 'Fusion for Energy', including activities performed by subcontracting qualified laboratories and industries as well as activities performed using internal resources.

The main objective of the Quality Management System is to allow 'Fusion for Energy' (F4E) to act as an ITER Organization (IO) supplier with respect to French Nuclear Regulation (Decree of August 10 th, 1984). The Quality Management System is coherent with ISO 9001:2000 and with IAEA Safety standards (IAEA Safety Requirements N° GS-R-3 (excluding quality assurance for site selection, commissioning, operation and decommissioning).

In order to comply with F4E customers' needs and to meet their requirements, the main process implemented by F4E is "*project management*". The objective of this process is to implement and to control activities that allow F4E to reduce the risks associated to the procurement (technical risks, organizational risks, safety risks…). Each project is divided into one or more work packages that are then contracted. Both the project and its related work packages are managed by F4E following project management practices.

Whatever the nature of the project, it is divided in three sequential phases:

- Preparation phase,
- Execution phase,
- Closure phase.

The detailed activities and contents of these phases must be adapted to the nature of the project (R&D, design, manufacturing, tests and acceptance, construction, etc...).

In order to commensurate the QMS to the F4E objectives, the CEA showed:

a) how such QMS was applied with a similar project and,
b) how we can implement it with on-going tasks - at the EFDA level and with their suppliers from European Laboratories.

This last activity was shared with IST. One exercise on a "Port Plug design", performed by CIEMAT, was led by CEA, the second one on a "TBM design", performed by FZK, was led by IST.

The Quality System has been correctly accepted and well understood by both associations and EFDA Responsible Officers. They found the QA principles are efficient to improve the relationship between them and EFDA in the framework of the contract.

According the results of this exercise and in order to implement in good conditions the QMS developed for F4E, we recommend for improvement of the QA practice:

- Within European laboratories

- to provide EFDA support to the laboratory to define and develop Quality Plan,
- to provide EFDA support to the laboratory to assess actual implementation of the quality provisions in order to improve them,
- to provide support to development of Quality Tools, in close collaboration with F4E.

The implementation of these provisions have to be controlled, inspected or audited by F4E in the course of the project. This assessment can be performed by the F4E responsible officer or by a F4E QA officer.

- Within F4E

- the very high importance to formalize and document the arrangement with ITER organization,
- to establish a development plan for each procurement package that will define coherent work packages in order to facilitate their quality classification (quality requirements grading),
- performance, scheduling and cost control,
- to ensure a proper preparation phase before awarding contract (careful establishment of the procurement documents),
- to develop QA competences in order to provide QA support for the F4E responsible officers to ensure coherence of the QA provisions implemented among the different projects,
- to organize QA and project management training for the F4E responsible officers,
- to formalize the know-how in QA matters to improve the system,
- to perform inspections and audits of the actual implementation of the QA principles to guaranty the compliance with the terms of the contract.

CONCLUSIONS

Conclusions of the exercise for CIEMAT and FZK

The quality requirements established by EFDA for the task have been correctly accepted and understood by both associations. The quality provisions planned and described in the quality plan are clear, simple and properly commensurate to the activities. The associations took the occasion to develop QA procedures (documentation, changes and non-conformances management) that can be used as well for this task as for future work for EFDA or F4E.

The actual challenge of QA for the European research laboratory is not only to write a Quality Plan, but it is the proper implementation of the quality provisions all along the project. The quality of the product is achieved by the technical officer with the support of the QA officer. All the stakeholders of the task have to be strongly involved in the implementation of the quality provisions.

Conclusions of the exercise for EFDA

The exercise was favourably accepted by the EFDA responsible officers. The principles and the advantages of a proper definition of quality requirements were well understood, but also that QA will not solve all the actual difficulties: input data have to be defined, quality classification has to be defined with the associated requirements, interfaces and configuration have to be closely controlled…

The major difficulty was to get reliable information from ITER organization to perform the work. The design was launched without clear and reliable input data from ITER organization. It implies that the EFDA responsible officers are very often by-passed by the associations contacting directly the ITER organization to get information without assurance of their reliability. The control of these relations is one of the major activities to be performed by EFDA responsible officers.

No knowledge of the meaning of the quality qualification provided by ITER organization and of the associated quality requirements grading.

These tasks were preliminary specified with a lot of others tasks regarding the same item. Several European associations are involved in this set of tasks with a lot of interferences. This involves that the various associations share information by-passing the EFDA responsible officer with, as a consequence, that some of them are working with no valid nor controlled data.

No assessment of the consequences of the quality classification for the quality requirements to be applied to the activity.

It is clear from the exercise that many of the quality provisions to be implemented by the Associations, (namely those related to documentation review and approval by F4E and ITER and Configuration Management) will need a strong involvement of the F4E responsible officer and organization to be efficient.

Comments and recommendations

Recommendations for improvement of QA practices within the European laboratories:

- Provide EFDA support to the laboratory to define and develop Quality Plan,
- Provide EFDA support to the laboratory to assess actual implementation of the quality provisions in order to improve them,
- Provide support to development of Quality Tools, in collaboration with F4E.

The implementation of these provisions have to be controlled, inspected or audited by F4E in the course of the project. This assessment can be performed by the F4E responsible officer or by an F4E QA officer.

Recommendations for QA within F4E

- Very high importance to formalize and document the arrangement with ITER organization,
- Establish development plan for each procurement package that will define coherent work packages in order to facilitate their quality classification (quality requirements grading), scheduling and cost control,
- Ensure a proper preparation phase before awarding contract (careful establishment of the procurement documents),
- Develop QA competences in order to provide QA support for the F4E responsible officers to ensure coherence of the QA provisions implemented among the different projects,

- Organize QA and project management training for the F4E responsible officers,
- Formalize the know-how in QA matters to improve the system,
- Perform inspections and audits of the actual implementation of the QA principles to guarantee the compliance with the terms of the contract.

REPORTS AND PUBLICATIONS

L. Jourd'Heuil, Marc Peyrot, Support in the Development of the QA System for the ITER EU Domestic Agency and Implementation of a Quality Assurance Programme in the European Fusion Associations for ITER-relevant Activities. Contract EFDA 06-1483, IRFM Report, ref QUAL/NTT-2007.003 # 01

TASK LEADER

Laurent JOURD'HEUIL

DSM/IRFM/SIPP/CTIQ
CEA-Cadarache
F-13108 Saint-Paul-lez-Durance Cedex

Tel: 33 4 42 25 79 11
Fax: 33 4 42 25 49 90

e-mail: laurent.jourdheuil@cea.fr

CEFDA07-1700-1600

Task Title: TW6-TDS-RAMSUP: CONTRIBUTIONS TO THE DEVELOPMENT OF RELIABILITY, AVAILABILITY AND MAINTAINABILITY (RAM) AND FAILURE MODE, EFFECTS AND ANALYSIS (FMEA) FOR ITER

INTRODUCTION

The main objectives of RAMSUP task are the following: collect data related to ITER-like systems reliability and availability, organize and analyse suitable data to feed a RAM engineering programme, propose computational tools to be used and procedures to follow in evaluating and keep updated the analysis, perform a top down analysis of some major subsystems and allocate reliability/availability 'budgets' in order to guide the on-going design at the earliest stage: Magnets, Cryogenics, Water cooling.
The expected schedule presented at the task kick-off meeting held at Cadarache in September 2007 was roughly respected with draft of final deliverable3 reports issued by the end of July and the task closure meeting by the end of September 2008. One can note that the RAMI analysis was approved by the ITER RAMI officer and that the results obtained were discussed and validated by the ITER plant systems and tokamak systems Responsible Officers (excepted for the Magnet breakdown analysis).One can also note that the formal and quantitative RAMI analysis has been performed with the software package selected by ITER-IO: RELIASOFT (Blocksim+Xfmea+Visio).
The issued deliverables are listed in this report. A CD including Visio files for functional breakdown analysis, BlockSim files for reliability analysis, and reports of Xmfea for each one of the three plant systems was also produced.

2007-2008 ACTIVITIES

METHODOLOGY

The methodology implemented for RAMSUP task completion includes three main steps:
Input data collection for functional breakdown analysis:

- Inventory the hardware interfaces of the system with other ITER systems, and with utilities,
- Inventory the functions performed by the system,
- Inventory the safety functions performed by the system,
- Inventory the missing data (if any) related to the previous points.

Functional breakdown analysis:

- For each system, split it in a “horizontal way” in order to consider operation consistent modules, proceed thereafter to a vertical split to define the major system functions,
- Within each major function repeat the method until the definition of major system components,
- Optimise the breakdown to minimize the links between internal functions or components,
- Translate this function breakdown, through IDef0 formalism, into BLOCKSIM toolkit.

RAMI analysis:

- Perform a bottom-up Reliability analysis by using the Plant Breakdown Structure of each system,
- For each function failure mode, assess the criticality figures,
- Fill the Function Failure Mode Identification Card,
- Proceed to the Criticality evaluation for each Failure Mode, and determine unacceptable risks,
- Propose system design modifications, tests and a maintenance plan to lower the risk level.

MAIN RESULTS

Cryogenics

After identification and RAMI ranking of each failure mode, the critical functions were identified using the occurrence/severity matrix and associated high priority failure modes. The availability of the cryogenic system was estimated by the product of the reliability figures of these critical functions. Table 1 gives these critical functions, initial availability and revised availability after action completion.
The initial availability figure of 91.5 % for the system availability is consistent with that would be performed on the Tore Supra cryogenic system without similar actions excepted redundancies, while the figure of ~98 % seems in line with what is performed on recent cryogenic plant with redundancies and a strong maintenance policy.

Table 1: Availability figures for the critical functions, and result on cryogenic system

Function	Initial availability %	Revised availability %
Water cooling	99.5	99.9
Compressed air	99.5	99.9
Power supply	99.0	99.0
Vacuum pumping	99.5	99.9
Warm compression (4 units)	98.0	99.5
Measuring and actuating	98.0	99.5
Cryodistribution (2 units)	98.0	99.9
System only availability	**96.0**	**98.9**
Total system availability including utilities	**91.5**	**97.6**

Details of proposed actions are given thereafter; they are sorted by design, maintenance and operation type:

Design type actions:

Function / failure	Proposal	Cost and availability assessment
Warm compression functions		
Compressor and motor bearings degradation due to vibration during operation or excessive strain during start up.	Vibration diagnostic implementation associated to alarms checked by the local control to enable a preventive and anticipated maintenance.	Efficiency: moderate, cost estimate: 10 k€ / compressor.
	Introduce an electronic device for progressive starting up.	Efficiency to be assessed, cost : 20 k€ / compressor.
Sensors and actuators functions		
Sensors: breakdown, loss of data transmission, degradation of signal quality, error of measurement. Actuators: breakdown, loss of data transmission, error of actuating (valve), loss of He leak tightness.	Full redundancy of critical sensors (critical sensors to be assessed).	Efficiency: moderate, cost estimate: 200 * 5k€ = 1 M€.
	Perform a specific study for sensor and actuator maintenance scenario, include the recommendations into the system design.	Efficiency: moderate, investment cost: depending on the recommendations.
	Perform a specific study to assess the reliability of sensors and actuators in close tokamak environment, include the recommendations into the system design.	Efficiency: moderate, investment cost: depending on the recommendations.

Function / failure	Proposal	Cost and availability assessment
Cryodistribution (magnet and cryopumps) function		
Over load of 4.5 K power refrigerating units or ACBs by heat loads from magnets and cryopumps during plasma operation, in spite of mitigation capability by thermal storage in the magnet structures.	Reduce the potential effect on power refrigerating unit by enlarge the power margin or a specific design of the last cooling stage, ratio to be assessed.	Efficiency: high, investment cost: to be estimated by supplier.
	Increase the thermal buffer capacity of the ACB LHe bath and SHe cooling loop by enlarging their volumes.	Efficiency: high, investment cost: require a specific study.
Vacuum		
Loss of the cryogenic vessel vacuum pumping systems, air leak ingress, or gaseous O2/N2 release during warm up.	Overcapacity of rough pumping or redundancy.	Efficiency: high, cost: to be assessed.
	Policy of minimizing the vacuum seals and bellows.	Efficiency: high, cost: to be assessed.
	Capacity to assess the air leak in the cryogenic vessels.	Efficiency: high, cost estimate: 100k€.
Utilities		
Water cooling		
Any failure on the WCS with impact on inlet temperature (high value) or flow (low value).	Full redundancy on every cryogenic subsystem: warm compressing, main cooling, vacuum pumping mainly.	Efficiency: high, investment cost: high (regarding function cost).
Compressed air		
Any failure on the compressed air system with impact on pressure, and flow (low value) or moisture (high value).	Full redundancy of air compressors and dryers associated to buffer tanks spread out over the cryogenic system for the actuators of every function.	Efficiency: high, investment cost: high (regarding function cost).
Power supply (main and auxiliaries)		
Any failure on main power supply system with impact on voltage or current availability.	Full redundancy of main power supply for TS cooling, rough vacuum pumping and UPS for instrumentation and control (I&C) for every function of the cryogenic system.	Efficiency: prevent any damage on thermal shields and magnets during a long time breakdown , investment cost: moderate.

Maintenance type actions:

Function / failure	Proposal	Cost and availability assessment
Warm compression functions		
Compressor and motor bearings degradation due to vibration during operation or excessive strain during start up.	Spare on site and fast intervention logistics (specific contract). A list of proposed spare parts in given in annexes to that document.	Efficiency: moderate, investment and operation cost: 50 k€ / compressor.
Sensors and actuators functions		
Sensors: breakdown, loss of data transmission, degradation of signal quality, error of measurement. Actuators: breakdown, loss of data transmission, error of actuating (valve), loss of He leak tightness.	Spare on site and specific contract for sensors/actuators maintenance and calibration. A list of proposed spare parts in given in annexes to that document.	Efficiency: moderate, investment and operation cost estimate: 10 % of 5000 at 3 k€ = 1.5 M€.

Magnets

Table 2 gives the system availability for the system itself (white rows) and for the system with every required utility. It must be noticed that some figures have to be confirmed by relevant FMECA (vacuum and power supplies) or estimates (quench detection, coil structures, electrical insulating.

These results highlight the large impact of all the utilities on availability, while the other operation issues are quench detection and instrumentation. Mechanical and insulating issues are impacting the availability of the system at nominal performance.

Table 2: Availability figures for the critical functions, and result on magnets system

Function	Initial availability %	Revised availability %
Cryogenic cooling	92.5	98.0
Water cooling	99.5	99.9
Compressed air	99.5	99.9
Power supply (AC/DC+FDU)	99.5	99.9
Vacuum pumping	99.5	99.9
Measuring and actuating	99.0	99.5
Quench detection	99.0	99.9
Coil mechanical structures	99.9	99.99
Electrical insulating and grounding	99.9	99.99
System only availability	**97.8**	**99.4**
Total system availability including services	**89.6**	**98.0**

Details of proposed actions are given thereafter; they are sorted by design, maintenance and operation type:

Design type actions:

Function / failure	Proposal	Cost and availability assessment
Insulating and magnetic field generating functions		
Defect on electrical insulation or joint resistance during fabrication.	Lower fast discharge voltage (specific study required).	Efficiency: high, investment cost: low.
Coil structures and supporting functions		
Cracks initiated by local stress due to excessive thermal gradients or abnormal displacement (TF magnet gravity supports).	Strain gauges and motion sensors to analyse the mechanical behaviour of the magnets structures along cool down and warm up operation. Redundancy on temperature slope control for the cryogenic cooling and associated warnings.	Efficiency (detectability only): high, investment cost: 200 k€.
Quench detection and associated sensors function		
Electromagnetic (initiated by RF heating) or ground reference (initiated by NBI: electric breakdown) noise on the quench detection sensors.	Electromagnetic noise rejection: Low level signal sensors (cryogenic temperature) have to be moved in a protected area. Pressure measurements have to be magnetic field shielded. Voltage measurements based triggers have to be delayed. Ground reference perturbations rejection: Sensors and signal conditioning ground have to be insulated from the tokamak ground.	Efficiency: high, investment cost: low but to be further estimated.

Sensors and actuators functions		
Sensors: breakdown, loss of data transmission, degradation of signal quality, error of measurement. Actuators: breakdown, loss of data transmission.	Full redundancy of critical sensors. (critical sensors to be assessed).	Efficiency: moderate, investment cost: low.
	Perform a specific study for sensor and actuator maintenance scenario, include the recommendations into the system design (access, capability to be replaced, …).	Efficiency: moderate, investment cost: depending on the recommendations.
	Perform a specific study to assess the reliability of sensors and actuators in close tokamak environment, include the recommendations into the system design.	Efficiency: moderate, investment cost: depending on the recommendations.
Auxiliaries		
Cryogenics		
Loss of cryogenic cooling: loss of SHe flow or GHe S only), or increase of inlet temperature.	See cryogenic system FMECA.	See cryogenic system FMECA.
Vacuum		
Loss of the cryostat vessel vacuum pumping system, air leak ingress, or gaseous O2/N2 release during warm up.	Overcapacity of rough pumping or redundancy.	See the vacuum system FMECA.
	Capacity to analyse gaseous exhaust from rough pumping during warm up for air detection to assess the air leak in the cryogenic vacuum vessels.	Efficiency: high (air detection only), investment cost: low.
Coil power supply		

Loss of the AC/DC converters of the magnets power supplies.	See the power supplies system FMECA.	See the power supplies system FMECA.
Loss of the FDU (CCU, pyro circuit breakers, controls, dump resistors).		
Utilities		
Water cooling		
Any failure on the water cooling system with impact on inlet temperature (high value) or flow (low value).	Full redundancy of normal conducting busbars power supplies, FDU at least to enable a slow discharge of magnets, and cryogenic cooling at least for STM operation mode.	Efficiency: high, investment cost: moderate.
Compressed air		
Any failure on the compressed air system with impact on pressure, and flow (low value) or moisture (high value).	Full redundancy of air compressors and dryers associated to buffer tanks spread out over the magnet system for the actuators of cryogenic cooling and FDU.	Efficiency: high, investment cost: low.
Main power supply		
Any failure on main power supply with impact on voltage or current availability.	UPS for instrumentation, control (I&C), quench detection and FDU, AC/DC converters control.	Efficiency: high, investment cost: moderate.

Tests type actions:

Function / failure	Proposal	Cost and availability assessment
Insulating and magnetic field generating functions		
Defect on electrical ground insulation or joint resistance during fabrication.	Insulating test during fabrication and final acceptance cold test for coils, busbar and current leads.	Efficiency: high, investment cost: moderate.
Coil structures and supporting functions		
Cracks leading to He leak at cryogenic temperature under local stress by thermal contraction.	Cold tests of each coil, busbar and current lead to check Hetight at cryogenic temperature (<= 80 K).	Efficiency (detectability only): high, investment cost: moderate.

Maintenance type actions:

Function / failure	Proposal	Cost and availability assessment
Insulating and magnetic field generating functions		
Defect on electrical ground insulation or joint resistance during fabrication.	Spare of one TF coil. Spare of PF and CS conductor for rewinding a full coil or module.Spare of a couple of current leads and busbar for each magnet.	Efficiency: high, investment cost: moderate (regarding system cost).
Sensors and actuators function		
Sensors: breakdown, loss of data transmission, degradation of signal quality, error of measurement. Actuators: breakdown, loss of data transmission.	Spare on site and specific contract for sensors/actuators maintenance and calibration: see cryogenic proposal for spare part list.	Efficiency: moderate, investment and operation cost: low.
Quench detection and associated sensors function		
Failure of quench detection system.	Spare and skill for maintenance on site: one full system for each TF, PF and CS magnet, and associated sensors and signal conditioners.	Efficiency: high, investment cost: low.

Operation type actions:

Function / failure	Proposal	Cost and availability assessment
Quench detection and associated sensors function		
Electromagnetic (due to RF heating) or ground reference (due to NBI: electric breakdown) noise on the quench detection sensors.	Fast discharge prevention: Implementation of a quench detec-tion analysis system coupled to the Plasma Control System for RF or NBI power reduction (electromagnetic noise mitigation).	Efficiency: high, investment cost: low.

Water cooling

Most of the sub-systems of the Cooling Water System are conventional. For critical ones, if redundancy principle is applied as well as a convenient maintenance strategy, their availability can be over 99%. The quality of water is an important parameter for the HRS/TCS and HRS/WCS. Risks of corrosion, scaling and fouling may appear if raw water is used. Therefore, we propose to design pumps with 50% flow capacity for the loops (WCS 1A 2A (PHTS HX cooling), 100% flow capacity for the WCS 3A (CVCS Letdown HX cooling), 4A (cryoplant cooling), 5A (PHTS main pumps cooling). For the other loops (CCWS, CHWS), we propose to adopt the same principle. It has a cost. If it is not applied, the different users must be organized in hierarchy in case of defect on one pump.

The TCWS loops are more specific of a fusion power plant. The nuclear environment, the presence of activated products, and the paramount risk of leak on plasma facing components will probably reduce drastically the availability of the PHTS. A realistic and possibly optimistic value for each PHTS may be derived from the data of the plasma facing components cooling loop of Tore supra (B30), which is the only large system presently used on the Tokamak. Table 3 gives an availability of 99% of the PHTS over 4 years of operation (2003-2006).

The RAMI analysis on the PHTS identified the most critical functions:

- Radioactive products confinements related to leak on components,
- Loss of flow related to pumps or valves defects or malfunctions,
- Power Supplying,
- Loss of pressure control due to N2 supply loss for the VV and NBI PHTS,
- Loss of valve control due to compressed air supply loss.

Note that a shut-down on the CVCS loops has an important effect on the related PHTS (volume control, pressure control, flow control, coolant chemistry control).

Table 3: Availability figures for the critical functions, and result on Tokamak Cooling Water System

Function	Initial availability %	Revised availability %
Compressed air	99.5	99.9
Power supply	99.0	99.0
N2 supply	99.5	99.9
Tokamak Components Cooling (6 units)	99.0	99.5
Measuring and actuating	99.0	99.5
Heat Rejection and water circulation		99.9
PHTS System only availability	**94.1**	**97.0**
Total system availability including utilities	**92.2**	**95.8**

Even with an individual availability of 99% for each of the PHTS (3x FW/BLK, Div/Lim, VV, NBI), the availability of the TCS can be assessed at 94% without taking into account the availability of the HRS.

The greatest uncertainty is due to the time required to repair if a leak occurs on a plasma facing component (leak localization, circuits drain-out and drying, removal of component, repair, conditionning).

In the FMECA of the PHTS performed, we have not taken into account the event of a failure on a in vessel-component. This failure mode will have a severity of 4, and an occurrence of 4 and is not acceptable. Operation procedures must be produced to operate the Tokamak in a safe way. But as ITER is still a research machine, we cannot exclude that leaks on the plasma facing components occur. A convenient and effective leak detection procedure is absolutely required to mitigate promptly the leaky component.

Note that the operation plan must take into account the mandatory visits and tests which are imposed by the regulation for the vessels under pressure. The capacities and components of the PHTS are concerned with these rules.

Design type actions:

Function / failure	Proposal	Cost and availability assessment
FW/BLK PHTS, Div_Lim PHTS, NBI PHTS and VV PHTS functions		
Leak on a PHTS component.	Convenient secondary coolant quality to avoid corrosion, scaling and fouling.	Efficiency: notable, investment cost moderate to notable.
FW/BLK PHTS, Div_Lim PHTS, NBI PHTS and VV PHTS functions		
Main Pump defect.	Design speed controller to reduce stress on the shaft and sealing.	Efficiency: notable, investment cost notable.
Heat Rejection System function		
Cooling Tower fan or motor failure.	Design speed controller to reduce stress on the shaft and sealing.	Efficiency: notable, investment cost notable.

Maintenance type actions:

Function / failure	Proposal	Cost and availability assessment
FW/BLK PHTS, Div_Lim PHTS, NBI PHTS and VV PHTS functions		
Leak on a PHTS component.	Perform preventive maintenance on valves and other equipments every two years	Efficiency: moderate, investment cost moderate.
	Inspection of HX each year	Efficiency: moderate, operation cost moderate.
FW/BLK PHTS, Div_Lim PHTS, NBI PHTS and VV PHTS functions		
Main Pump defect.	Perform preventive maintenance on pumps each year (Vibration monitoring).	Efficiency: moderate, operation cost moderate
Loss of main pump cooling.	Perform preventive maintenance on CVCS each year.	Efficiency: moderate, operation cost moderate.
	Perform preventive maintenance on CCWS each year.	Efficiency: moderate, operation cost moderate.
Heat Rejection System function		
Cooling Tower fan or motor failure.	Perform preventive maintenance on CVCS each year.	Efficiency: moderate, operation cost moderate.

CONCLUSIONS

The RAMSUP task provides first FMECA analyses of the cryogenic, magnets and water cooling ITER plant and tokamak systems. Unfortunately, these analyses have been only partially validated by the ITER responsible officers. They are however to be considered as good basis for further discussions on reliability improvement of these three systems. In order to go ahead in this objective and above the validation issue, it appears that these analyses have to:

- Be kept updated and further detailed along the progress of the detailed design in particular for every function of the cryogenic and water cooling plant systems, and for the most critical functions of the magnets: electrical insulating, structures, quench detection and sensors which are still under design.
- Integer the recommendations of exploitability analysis and close tokamak environment compliance studies which are still missing and seem necessary to be undertaken.
- Be completed by the cost estimates which are still missing in this present analysis due to a lack of recent industrial references for such components.

REPORTS AND PUBLICATIONS

Data

The following data files are delivered for each system on a single CD ROM.
- Visio description (source).
- BlockSim description (source).
- Copy of Xfmea database for each system.
- Pdf copy of the deliverables.

TW6-TDS-RAMSUP task Quality plan
IRFM/QUAL/NTT-2007.005 (2007)

Partial report TW6-TDS-RAMSUP-D1 IRFM/ SUR/NTT-2008.001
J.-Y. Journeaux, F. Sagot

Partial report TW6-TDS-RAMSUP- D2.1 on cryogenics IRFM/ SUR/NTT-2008.001
J.-Y. Journeaux, F. Sagot

Partial report TW6-TDS-RAMSUP- D2.2 on magnets IRFM/ SUR/NTT-2008.002
J.-Y. Journeaux, F. Sagot

Partial report TW6-TDS-RAMSUP- D2.3 on CWS IRFM/ SUR/NTT-2008.006
M. Chantant, F. Sagot

Partial report TW6-TDS-RAMSUP- D3.1 on Cryogenics IRFM/ SUR/NTT-2008.003
J.-Y. Journeaux, F. Sagot

Partial report TW6-TDS-RAMSUP- D3.2 on magnets IRFM/ SUR/NTT-2008.004
J.-Y. Journeaux, F. Sagot

Partial report TW6-TDS-RAMSUP- D3.3 on CWS IRFM/ SUR/NTT-2008.007
M. Chantant, F. Sagot

TASK LEADER

Jean-Yves JOURNEAUX / Jean-Claude VALLET

DSM/IRFM/STEP
CEA-Cadarache
F-13108 Saint-Paul-Lez-Durance

Tel. : 33 4 42 25 61 62
Fax : 33 4 42 25 49 90

e-mail : jean-claude.vallet@cea.fr

CEFDA06-1386

Task Title: JW6-EP-ICRH-CEA: CEA CONTRIBUTION TO RFAD FOR THE JET ICRH ITER-LIKE ANTENNA

INTRODUCTION

In the framework of the JET-EP ITER-Like Antenna (ILA), two new arc detection systems were designed in order to complete the traditional VSWR protection systems and to increase the antenna safety. SMAD: Scattering Matrix Arc Detection was developed by ERM (Belgium) and SHAD: Sub-Harmonic Arc Detection developed by the CEA. Three SHAD systems have been used on three Tore Supra antennae since 2005. The same system has also been used on the TS ITER-like Antenna with good efficiency on the 2007 campaign.

2007-2008 ACTIVITIES

We developed in 2006 with industrial support two SHAD systems on the principle developed for Tore Supra. These systems were delivered in time to EFDA-JET in January 2007. One system was installed on the test bed in order to qualify it with the first commissioning procedure, but it had some technical problems during the antenna commissioning. The antenna is divided in four identical parts; one part did not held the commissioning voltage level and the antenna had to be equipped with a new capacitor. Due to this delay, the first system was not fully commissioning because there was not enough time to have some signals during the last strap tests. The different commissioning phases: vacuum, multipactor, L mode and H mode were described in a new commissioning procedure and planned on the 2008 plasma tests of the ILA.

In 2008, the installation in the generator hall J1H was carried-out in spring with all first checking tests without RF power. The 2 systems commissioning was performed in summer during the different commissioning phases of the ILA on JET plasmas.
The antenna commissioning took more time than expected due to the coupling complexity with the plasma and we had to wait some significant RF power on the 2 parts upper and lower of the antenna in order to have some signals above the noise level. Extensive measurements of the RF field in the transmission lines were carried out in autumn using 2 fast sampling oscilloscopes. The signals recorded by the fast oscilloscopes and the CODAS acquisition system allowed to compute by FFT the harmonic spectrum after each plasma shot and to compare them with the other RF signals.
See figures 1, 2 and 3, example of the SHAD signals analysis on pulse JET 75348.

The operation of SHAD, and its ability to detect arcs during ILA operation on JET (in particular during ELMy H modes), were studied and we obtained highlight conditions where good correspondence of SHAD events with other arc detection systems (VSWR and Scattering Matrix Arc Detection (SMAD) is found or not found. Spectrum analysis of the RF field was performed in different conditions:

- Arc is detected simultaneously by SHAD and other systems,
- Sub-harmonics are detected by SHAD but no arc detected by other systems,
- Arc detected by other systems, but no sub-harmonics detected by SHAD.

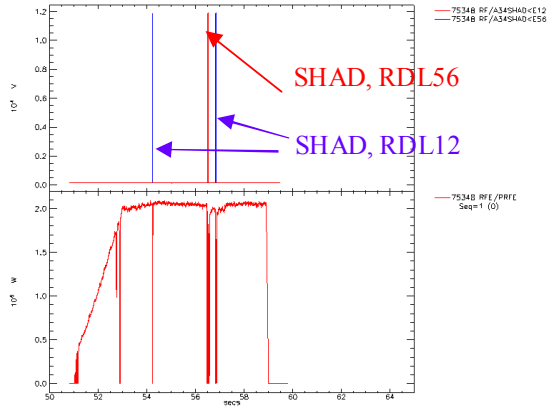

Figure 1: Pulse 75348. Only the top row was used with 2 MW launched. SHAD events corresponding to trips are recorded at 54.2 sec, 56.5 sec, and 56.8sec. The oscilloscopes were triggered at 54.2, allowing analysing rf signal when a SHAD event is detected in RDL12

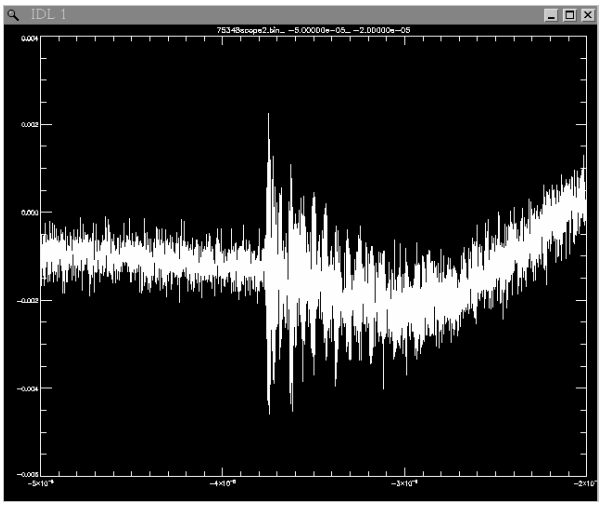

Figure 2: Time trace of the RF signal (filtered) from APTL-Reflected RDL12, right before the trip of the generators at 54.2 sec. The signal in the SHAD detection band increases at -38 µs, the generator trips at -10 µs

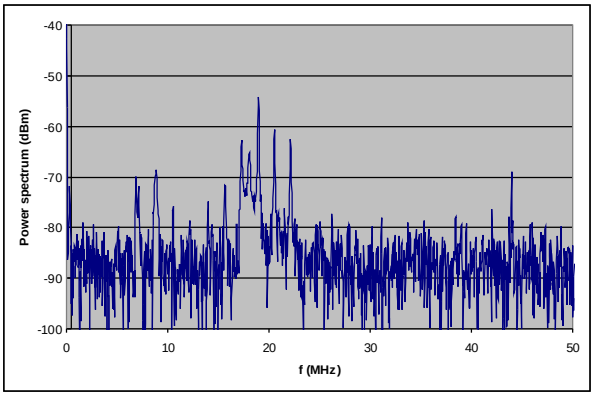

Figure 3: Spectral analysis on the RF signal (filtered) from APTL-Reflected RDL12, right before the trip of the generators at 54.2 sec

CONCLUSIONS

The JET SHAD system was tested and validated during the 2008 campaigns of plasma tests of the ILA. These tests will end during the beginning of 2009 on C26 and C27.

REFERENCES

Cahier des charges du projet SHAD pour l'antenne JET ITER-like (SHAD= Sub Harmonic Arc Detection) CH/CCH-2007.001 (2007) G. Berger-By

SHAD (Sub Harmonic Arc Detection) project advancement and the 2008 Commissioning at JET CH/PPT-2007.001 (2007) G. Berger-By

REPORTS AND PUBLICATIONS

Progress in Arc Safety System Based on Harmonics Detection for ICRH Antennae 17th Topical Conference on Radio Frequency Power in Plasmas (2007) G. Berger-By, B. Beaumont, G. Lombard, L. Millon, P. Mollard, D. Volpe

Final report on EFDA Task JW6-OEP-CEA-38A, CEA Report CH/NTT-2008.002#01 (2008) G. Berger-By

TASK LEADER

Gilles BERGER-BY

DSM/IRFM/SCCP/GCHF
CEA-Cadarache
F-13108 Saint-Paul-lez-Durance Cedex

Tel: 33 4 42 25 61 20
Fax: 33 4 42 25 62 33

e-mail: gilles.berger-by@cea.fr

CEFDA06-1422

Task Title: JW6-PS-EP2-BET-01: ITER-LIKE FW EXPERIMENT PROJECT: TILE SHAPING CHECKING

INTRODUCTION

For the ITER-Like Wall that will be installed on JET, there will be no carbon facing the plasma. This will be achieved by making the majority of the protection tiles out of Beryllium. The tiles are generally made as an assembly of Be blocks attached to an Inconel carrier.

The Be plasma facing surfaces are properly shaped in order to optimise the power deposition (minimum exposure of edges). Castellation of the Be surface is made to reduce the thermal stresses in the material. Protection of castellation edges has also to be addressed. The scope of this task is the checking of the Be Tile shaping in terms of shadowing of the edges for a number of plasma configurations.

When a complete shadowing is not performed, the lateral face of a block is wetted by the plasma. In that case, the penetration depth is calculated and the maximum power density at the face is determined. The different wetted areas are compared using a simple thermal computation, giving a temperature representative of the heat flux deposition on a single place.

The work is carried out as follows:

- The JET CATIA cad models are modified according to the needs of the calculation,
- Meshes are generated within CATIA cad system and exported to CAST3M/CFPFLUX code,
- Heat flux or shadowing calculation are then performed and post-processed.

2007-2008 ACTIVITIES

During the years 2007-2008, most of the main chamber Be components have been analysed for five magnetic configurations. Synthesises results for all studied limiters are shown on table 1. The most heated areas are front faces, and in case of penetration (tile to tile groove or castellation), the temperature increase is still dominated by the power deposition on the front (more than 80%). The supplementary temperature increase caused by the castellation is marginal.

Table 1: Synthesis results – Heat flux

Limiter & tile	Case	Type of deposition	Front Flux (MW/m^2)
IWGL T13	3610004	Front face	24
IWGL T13	3610004	Castellation	20
IWGL T14	3610003	Front face	21
IWGL T14	3610007	Front face	21
UO saddle coil	3610005	Front face	20.4
UI saddle coil	3610005	Front face	19.6
IWGL T13	3610004	Tile to tile groove	15
PL Vri T03	3610003	Front face	18.7
PL Vri T03	3610003	Tile to tile groove	17
NPL T23	3610006	Front face	18
IWGL T9	3610003	Tile to tile groove	14
UO saddle coil	3610007	Front face	17.6
IWGL T9	361003	Castellation	20
NPL T10	3610003	Front face	16
IWGL T8	3610004	Tile to tile groove	12

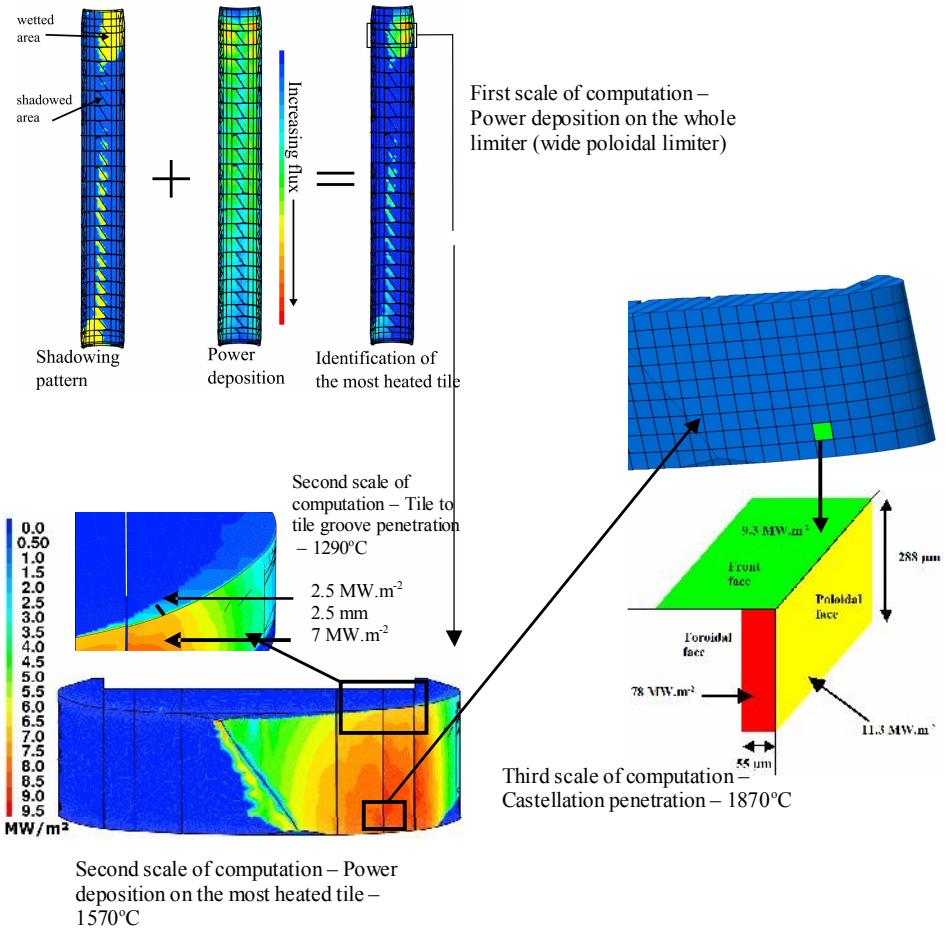

Figure 1: Iterative process to define the most heated area – Wide Poloidal Limiter

CONCLUSIONS

The analysis done in the frame of this task allow to predict the heat load on the JET ITER-Like wall beryllium tiles with a high level of details for several plasma configurations. The methodology is both accurate and efficient at computing power deposition and shadowing on crucial tiles. The additional heating caused by the penetrating tubes is small (generally less than 20%) compared to the main face heat flux.
This means that operation will be primarily limited by front heat flux. Considering the heat exhaust capacity provided by the overall shaping, it confirms that the design is similar essence from the previous one with carbon tile. The tile surface heat flux will have to be controlled by passive and/or active monitoring to avoid overheating.

REPORTS AND PUBLICATIONS

Tile shape checking of the beryllium tiles for the JET ITER-like wall 25th Symposium on Fusion Technology (2008) to be published in Fusion Engineering and Design - R. Mitteau, M. Firdaouss, E. Villedieu, V. Riccardo, P. Lomas, Z. Vizvary, C. Portafaix, P. Thomas, I. Nunes, P. De vries, Y. Stephan

PEFC/NTT-2009.003#01 - C. Portafaix
ITER like wall project – Tile shaping checking

PEFC/NTT-2008.035 - C. Portafaix
ITER like wall project – Tile shaping checking divertor mode configuration

CFP/NTT-2008.041 - C. Portafaix
ITER like wall project – Tile shaping checking ICRH poloidal limiters

CFP/NTT-2008.022 - R. Mitteau
JET ITER like wall – Tile shaping checking final report for the task JW6-BEP-CEA-39

CFP/NTT-2008.023 - R. Mitteau
JET ITER like wall – Tile shaping checking phase 1 report of JOI revision contract

CFP/NTT-2008.021 - R. Mitteau
ITER like wall project – Tile shaping checking heat flux modelling on the dump plates in near null configuration

CFP/NTT-2008.004#01 - R. Mitteau

ITER like wall project – Tile shaping checking LHCD limiter

CFP/NTT-2008.004 - R. Mitteau
ITER like wall project – Tile shaping checking LHCD limiter

CFP/NTT-2008.002 - R. Mitteau
ITER like wall project – Tile shaping checking evidences of high fluxes on the bottom horizontal LHCD short tile

CFP/NTT-2007.081 - R. Mitteau
ITER like wall project – Tile shaping checking A2 protection limiters

CFP/NTT-2007.035#02 - R. Mitteau
ITER like wall project – Tile shaping checking ICRH side limiters

CFP/NTT-2007.077 - R. Mitteau
JET ITER like wall – Tile shaping checking second intermediate report

CFP/NTT-2007.070 - R. Mitteau
ITER like wall project– Tile shaping checking ICRH private limiter cross beam and septum

CFP/NTT-2007.014#02 - R. Mitteau
JET ITER like wall – Tile shaping checking first report for the inner wall guard limiter

CFP/NTT-2007.059 - R. Mitteau
ITER like wall project– Tile shaping checking saddle cils and tile carriers

CFP/NTT-2007.036#01 - R. Mitteau
ITER like wall project – Tile shaping checking narrow poloidal limiter

CFP/NTT-2007.035#01 - R. Mitteau
ITER like wall project – Tile shaping checking ICRH side limiters

CFP/NTT-2007.041 - R. Mitteau
ITER like wall project– Tile shaping checking dump plates

CFP/NTT-2007.014#01 - R. Mitteau
JET ITER like wall – Tile shaping checking first report for the inner wall guard limiter

CFP/NTT-2007.036 - R. Mitteau
ITER like wall project – Tile shaping checking narrow poloidal limiter

CFP/NTT-2007.035 - R. Mitteau
ITER like wall project – Tile shaping checking ICRH side limiters

CFP/NTT-2007.016 - R. Mitteau
ITER like wall project – Tile shaping checking Wide poloidal limiter misalignment cases (tolerance assessment)

CFP/NTT-2007.014 - R. Mitteau
JET ITER like wall – Tile shaping checking first report for the inner wall guard limiter

CFP/NTT-2007.010 - R. Mitteau
JET ITER like wall – Tile shaping checking intermediate report

TASK LEADER

Christophe PORTAFAIX

DSM/IRFM/SIPP/GIPM
CEA-Cadarache
F-13108 Saint-Paul-lez-Durance Cedex

Tel: 33 4 42 25 46 09
Fax: 33 4 42 25 49 90

e-mail: christophe.portafaix@cea.fr

JW5-FT-5.25

Task Title: HUMAN FACTORS EXPERIENCE FEEDBACK ON JET

INTRODUCTION

The objective of the "Human Factors approach" in the ITER design is to define provisions as regard human factor means, technical means and organizational means to optimize performance of experiments conducted in the context of the fusion research program while respecting safety and security requirements.
One of the methodological principles to take into account Human Factors in a future facility is to collect and to analyze data relative to human factors experience feedback in existing facilities.
Feedbacks from human factors experience have been gathered for two tritium laboratories: one at CEA/Valduc centre in France, the other at the Karlsruhe research centre in Germany. The analysis based on experience feedback has allowed questions to be raised that will be examined in the more general context of ITER project.
Questions raised concern on the one hand, generic human factor provisions likely to contribute to ITER safety in an overall manner (management of skills, organization) and on the other hand, specific human factor provisions to be implemented to ensure the safety of sensitive activities.

The same methodology can be applied to the JET facility in particular on the three following topics: the operation of the tritium handling facility (Active Gas Handling System) for completing the Tritium related analysis; the Tokamak operation in order to set the basis for ITER tokamak operation and its overall management; finally, the remote handling operations, involved in particular for the JET maintenance, and which will be applied in ITER prospect.

2007-2008 ACTIVITIES

The task JW5-FT5.25 has been carried out in 2006-2007 to be ended in June 2007, with the final report "Human Factors Experience Feedback on JET".
The part of the task achieved in 2006 concerned the AGHS operation and the plasma operations.
In 2007, another period of stay was organized on JET (first quarter in 2007) to collect data in relation to the last topic on remote handling operations. The objective was to study in particular the human/machine interaction in the remote handling operations, and more generally the conditions of field operations during the preparation of the shutdown of the facility.

Quantitative features of the JET Human Factors study carried out in 2006-2007

The analysis of the HF experience feedback has been carried out by two Human Factor specialists and a plant operation expert. It required three periods of stay at the JET site:

- The first one (Feb. 2006) has consisted in establishing the first contact with the facility and it's organisation and in setting the practical organisation of the study [1],
- The second one (March 2006) lasted 4 days and was dedicated to the operation of the tritium handling facility (AGHS) and of several other "ancillary" systems involved in the ITER operation (ex: waste management facility),
- The third one (June 2006), also lasting 4 days, concerned essentially the torus operation,
- The fourth one (March 2007), lasted 2 days and concerned the Remote Handling (RH) operation, in support of the shutdown period.

About twenty interviews have been carried out with a panel of personnel representing relevant activities on the various parts of the facility, either directly involved in the operation or at a more managerial position. In the case of the tritium handling facility, a day-long observation of routine activities in the AGHS control room has also been performed. Concerning the torus operation, the systematic and direct observation of plasma operation activities has not been possible but several opportunities of "indirect" observation of pulse operation phases were offered during the interviews times. Concerning the Remote Handling operation the interviews carried out during the preparation of the shutdown, have been completed with commented visits in the dedicated RH control room and in the RH installations located in the assembly hall (mock-up, maintenance area).

Main qualitative results

The main results on the HF experience feedback data collected at the JET facility are presented according to the four "conventional" fields of the human factors approach : the work organization, the work force and competencies management, the technical systems design including workplaces design and the working environment characteristics. Thus, the report is structured in 4 chapters related to the **organization** of the operation activities, the **jobs and competencies** of the personnel involved in the operation, the **technical systems** in interaction with the human activities and **the working environment characteristics.**

- ***The organisation of the operation activities***: the objective is to identify what are the characteristics of this organisation that may impact the safety and efficiency of the operation, positively or negatively. In this domain, the aspects concerning the clarity of roles, the modes of coordination of the activities at the local and global level, and the management of experience feedback are studied.
Concerning the plasma operation, the global organisation to manage a pulse, the role and interfaces of the main actors are studied, in particular the people holding key positions in the organisation of the pulse schedule, such as: the Session Leader, the Engineer in Charge, the Diagnostic

Coordinator, the Scientific Coordinator and the operation shift. Their dedicated roles, before, during and after the pulse are described and also the tools used to manage their activities. One conclusion concerns the importance of the teamwork to manage effectively the pulse: the operation team acts as a real team sharing common objectives, and not an aggregation of individuals with their own preoccupations. Beyond the sharing of common objectives, close communication is a good way for avoiding too rigid a partition between the "scientific" and "operational" worlds, either during the preparation of the sessions, or during the sessions. One must be aware of the communication difficulties inherent to such internationally run facilities that are not only due to language problems: cultural differences might also be an obstacle to an efficient communication as well as the distance between local and remote team members.

Concerning the AGHS operation, the composition of the shifts and the organisation of the operation, according to the operational levels of the facility are presented. The case of the tritium loop operation with the tritium transfer operations and measurements follow-up are described with attention because of their safety significant tasks component.

Concerning the remote handling operation, the general organisation and the more "local" RH team who controls the RH from the dedicated control room (adjacent to the assembly hall) are described. Then the role of equipments and tools to manage the RH operation are presented, such as the mock-up to prepare the shutdown operations and the procedures in the preparation and the follow-up of the RH operation.

- ***The jobs and competencies of the personnel*** involved in the operation are analysed with a particular emphasis on the mode of acquisition and of maintenance of these competencies and their adequacy with the job exigencies. The competencies of the engineer in charge and of the session leader, are particularly developed in relation to the these two following questions : balance between scientific and operational knowledge, full time or part time job and the enhancement of the professionalism (full time) in the case of a fully licensed plant. Concerning the AGHS competencies, the necessary combination of knowledge to be effective are presented : technical knowledge of the equipments and system and "working" knowledge of operation procedure, based on coaching and "on-the-job" training. Concerning the RH competencies, as RH operators have to be effective during the shutdown, the means to prepare and train them were particularly underlined.

- The technical systems in interaction with the human activities: this concerns of course the characteristics of the human system interface (HSI) and of the workplace layout, but also the various tools helping the workers in the performing of their tasks, like for example operation guidance documents (procedures, alarm sheets, etc…) or various software tools supporting diagnostics or calculations. In some cases it may also include some particular characteristics of the machine itself, which may be the source of excessive operational burden on the operation teams. Finally, this domain concerns also the study of the interaction of humans with the automatic functions performed by I&C systems, with the objective to keeping the humans in the control loop.

Concerning the workplaces to operate, the characteristics of the different control rooms are presented: main control room to operate the pulse, the AGHS control room (a separated one) and the Remote Handling operation. Two issues are particularly discussed in relation to the control room layout:

- the necessary cooperation to operate both the torus operation and the AGHS in particular during tritium loop operation and the question of separated or integrated control room,
- even though a close cooperation between the scientific personnel and the operational one is required to ensure optimal operation there is the need to avoiding that the control room becomes a forum for scientific discussions between scientists not directly involved in the operation, which will disturb the operation. The design of separate experimental follow-up rooms (on site and, possibly, remote) is a solution worth being considered, in order both to ensure optimal serenity in the activity of the operating team and to provide enhanced on-line follow-up possibilities for "external" scientists.

The question of automatic control of technical systems is then presented in relation to AGHS and remote handling operation. Even a high level of automation is foreseen, the automation choice must not prevent the human operators to play an active role in the control of these activities, as this human intervention is the only way to provide sufficient flexibility to face unexpected situations or changes in the operation planning.

Then, different software tools that provide to the operators to support them in carrying out of their own tasks are presented. It concerns in particular:

- the Pulse Schedule Editor, as an example of tool supporting the synergetic work of several persons to prepare, optimise and validate the conditions of the pulse and to prepare the machine configuration,
- the tritium transfers and balances calculations that need accurate calculation and data logging system,
- the data and knowledge management tools and the necessity to provide on-line access to the information concerning the machine operation for operation teams as well as for "external" people,
- the Remote Handling tools data base : as the large amount of tools used for RH operations, the management of the tooling is made with help of a database, using barcodes put on the bags and in the storage areas to help people know where the tools are located,
- Visualisation and Virtual reality to support Remote handling operation: the use of virtual models at JET (particularly displaying of the virtual model on the large wall screen) has proven to be an efficient tool for complementing the visual feedback during operation (particularly for the monitoring of the movements of the boom) and also for preparing the activities in addition to mock-up testing (see previously: preparation of shutdowns).

Some “hardware” tools, also used to support the operators’ activities, are presented. This term concerns essentially the various operating guides and procedures used for guiding the operation team in their activity (operation procedures in case of torus operation, of the AGHS, of the RH activity), and the various logbooks enabling to keep track of the operations that have been carried out. Most of them are under the form of paper documents (“hardware”), although a few ones are now managed under the software form (ex: alarm sheets).

- ***The working environment characteristics***: this concerns the identification of the physical characteristics and hazards (noise, heat, irradiation /contamination, accessibility, etc…) of the operation layout that may impact the work conditions and subsequently the risk for safety but also for personnel security.

CONCLUSIONS

This HF experience feedback survey at JET has permitted to collect valuable elements about the conditions for the efficient and sure operation of a TOKAMAK facility, at the organisational level as well as at the facility design one. Some preliminary recommendations have been presented in case of findings with obvious generic implications. This “macroscopic” approach of the global operation layout, even though useful it may be, need to be completed later on with a deeper (“microscopic”) approach of the human activities, particularly in the case of safety-relevant ones, in order to analyse the design and organisational features which are suitable to minimize the human failures which may occur during these activities. This will be done when the activities profiles of the future ITER personnel are known in more details.

REPORTS AND PUBLICATIONS

Human Factors Experience Feedback on JET-Final Report (CEA internal report)
B. Papin, V. Paulus, M. Tosello (2007).

TASK LEADER

Michele TOSELLO

DEN/DPIE/SA2S/GAS
CEA-Cadarache
F-13108 Saint-Paul-Lez-Durance

Tel. : 33 4 42 25 28 31
Fax : 33 4 42 25 25 99

e-mail : michele.tosello@cea.fr

JW6-FT-1.11

Task Title: THERMAL DESORPTION OF FLAKES

INTRODUCTION

Thermal conductivity, diffusivity and sputtering properties must be known in detail for the different materials used in vacuum vessel, first wall in particular.
The aim of this work is to characterise the chemical and radiochemical composition of the flakes and to study the efficiency of thermal desorption of trapped tritium and effect of oxidation on the flakes at relatively high temperature (800°C).

To reach the goal, the X-ray diffraction permits a qualitative chemical compound determination before and after thermal detritiation.
The study of thermal desorption is done in two ways:

- Without oxidation and under Hytec gas (5% vol. hydrogen, 95% vol. argon) up to 800°C
- With oxidation, up to 800°C, under different oxidizing atmosphere
  - 2% vol. oxygen in nitrogen or argon
  - 5% vol. oxygen in nitrogen or argon
  - 10% vol. oxygen in nitrogen or argon

In both cases (without oxidation and in the best case of oxidation conditions), it is foreseen to study the kinetic of tritium desorption at a fixed temperature.

The Mark IIa divertor consists of an Inconel® 600 support structure containing arrangement of large carbon-carbon fibre composite tiles. The compositions of the flakes sampled with the cyclone vacuum cleaner are representative of the different peaces of the divertor. A major of carbon, some metallic element providing from inconel or other metallic peaces and beryllium traces are characteristic of the samples.
The tritium activities of different samples are very high, between $5.97 \cdot 10^9$ and $2.27 \cdot 10^{10}$ Bq/g of flakes.

2007-2008 ACTIVITIES

Samples [5]

- Cyclone pot 6: Vacuum cleaning MK2GB carriers in-situ on the 11th June 1999,

- Cyclone pot 7: Vacuum cleaning and inspection of the structure at 12BN, on the 28th June 1999,

- Cyclone pot 8: Vacuum cleaning the divertor carriers, from 11th August 2001 to 9th November 2001,

- Cyclone pot 9: Vacuum cleaning under the divertor structure (sample flakes from below divertor), on the 10th October 2001, prepared for sampling.

Mineralization

The aim is to know the total tritium activity of the flakes and the chemical composition. The study of full mineralization procedure leads to the following operating mode:
In a tight reactor connected to different traps for tritium measurement,

- A volume of sulfuric and perchloric acid is used at 100°C for the dissolution of the flakes,
- Some drops of hydrogen peroxide are added to fully mineralize the sample,
- Some drops of hydrogen peroxide are added to fully mineralize the sample.

The wiring diagram (figure 1) shows the procedure scheme.

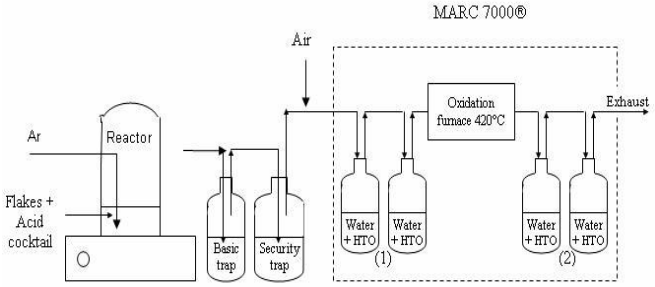

Figure 1: Wiring diagram for the mineralization of flakes sample

The principle of this method is to measure the tritium contained in the flakes, released as vapor (HT and HTO) and the tritium contained in the acidic solution of the reactor. The HTO form is trapped in a first set of bubblers filled with water (1). Then, the gas containing reduced form of tritium (HT) is oxidized in a furnace at 420°C to HTO and trapped in the other set of bubblers (2).
Upstream the furnace, a basic trap neutralizes the acid vapors. The security trap may collect liquid solution that could get into the furnace.
Acidic and basic solutions are distilled prior to tritium measurement. Tritium content of each bubbler is measured by liquid scintillation technique.

Total tritium activity measurement

The tritium is measured in the different traps (MARC 7000® traps, basic traps) and in the reactor. The extracted activity in the traps is a volatile form tritium.
Table 1 presents the obtained results.

Table 1: Tritium activity in the samples

Samples pot	**9**	**6**	**7**	**8**
Dates	12/03/08	21/03/08	02/04/08	22/04/08
mass sample (g)	0.130	0.175	0.051	0.256
Tritium Activity (GBq/g flakes)	**22.7**	**8.9**	**16.1**	**6.0**

The tritium activities are very different for the different pots. Pot 9 was measured by UKAEA on December 2006 and the measured activity of tritium was 16 GBq/g (5). We found 22.7 GBq/g in April 2008, it's a little bit more but the samples are probably heterogeneous.

Chemical characterization

After the tritium distillation, the mineralized samples are measured by ICPOES apparatus. Table 2 presents the obtained results.

Table 2: Chemical concentration of the different pots

ICPOES Results	6 mg/g	7 mg/g	8 mg/g	9 mg/g
Al	16.7	162	51.7	30.4
Ba	<0.1	<0.2	<0.1	<0.1
Be	13.5	10.6	10.3	8.6
Ca	3.2	14.5	3.1	3.4
Cd	<0.1	<0.2	<0.1	<0.1
Co	<0.2	<0.7	<0.3	<0.2
Cr	4.2	7.8	6.6	22.3
Cu	7.7	4.3	4.8	3.2
Fe	5.6	16.1	11.0	10.1
K	<0.6	<1.9	<0.8	<0.8
Mg	0.4	2.2	0.9	1.3
Mn	<0.05	<0.12	<0.05	<0.05
Mo	<1.6	<5	<2.2	<2.2
Ni	18.1	27.8	23.8	90.6
Sr	<0.02	<0.04	<0.02	<0.02
Ti	0.5	<0.4	<0.2	<0.2
V	<0.2	<0.8	<0.3	<0.3
Zn	<0.1	<0.4	<0.2	<0.2

The chemical concentrations of the samples are very different. They are sampled in different places. Furthermore they are inhomogeneous.

Aluminium, and iron are the main components. For sample 7, Ca and Fe concentrations are little higher than in other sample. Nevertheless, they are still low. For sample 9, Cr concentration is higher than in other samples. Beryllium concentration is low too (between 8.6 and 13.5 mg/g).
A lot of chemical elements are under the lower limit detection because of the very small quantity of the mineralized samples. The lab can only handle a tritium activity of $1.2 \cdot 10^{10}$ Bq/sample. So because of the tritium activity, the quantity of the samples was limited.
The X-ray diffraction of the pot 6 confirms that Be is only present in few quantitiy and not more.
The rest of the non measured compound of the samples can be considered as carbon. Then the concentration can be estimated as it is shown in table 3.

Table 3: Carbon concentration

	6	7	8	9
C %	~92	~74.5	~88	~82.5

The nickel in the samples may have been the result of localised splat of Inconel®. The compositions of the samples from the Mark IIa divertor are close to the flakes compositions measured at JET [1] and measured by X-ray micro-analysis at FZK [2].

THERMAL DESORPTION

Reductive gas

The reductive gas used is a mixed of 5% vol. hydrogen, and 95% vol. argon (Hytec) and the thermal desorption is done up to 800°C.
The heating program for the detritiation step is between 340°C up to 800°C. Figure 2 gives the scheme of the termal program.

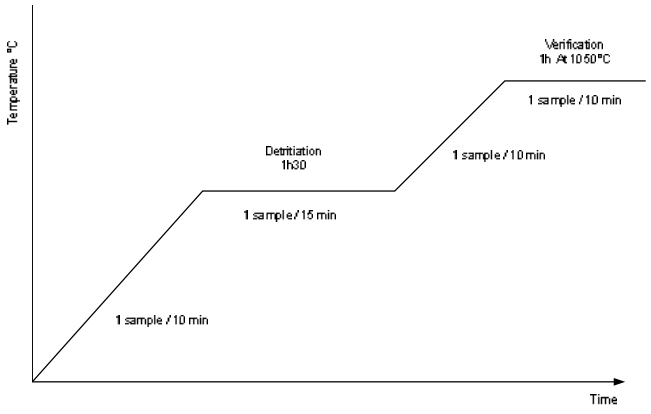

Figure 2: Steps of heating and sampling

The best results obtained are with the sample 8 at 800°C. With these conditions, 35.2% of the tritium is extracted from the sample. It's the only case where a maximum peak can be observed (figure 4) and a decrease of activity during the step. With the other samples under lower temperature, the efficiency of the tritium desorption is very low.

Between 700 and 800°C seem to be a good compromise to detritiate sample.

If thermal detritiation under reductive gas is a good process with metallic samples (the major part of tritium is on the first micron of the surface of materials), with flakes (major of carbon, beryllium carbide), the process is not very efficient. The tritium bounded in the basal plan of graphite and trapped in different carbides of the sample is very difficult to extract.

With 5% of hydrogen in argon, it seems to be complicated to have a good detritiation factor in a short time. An approach with oxidant gas is necessary.

Oxidant gas

The oxidant gas used is a mixed of 2% vol. oxygen, and 98% vol. argon and the thermal desorption is done at 750°C. Figure 3 presents the different steps of the thermal desorption under Hytec.

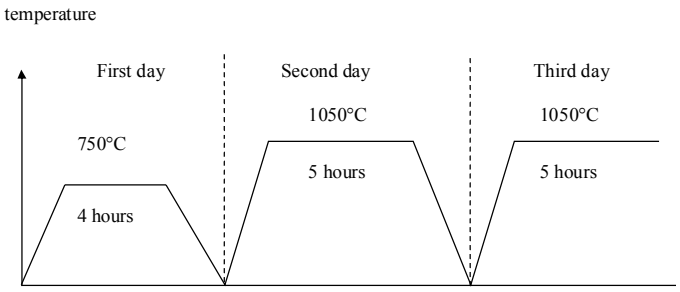

Figure 3: Measured activity after each sampling

The sample 9 was treated with this procedure with a mass of 0.0609g.
Figure 4 shows the obtained results after the different sampling each 10 minutes.

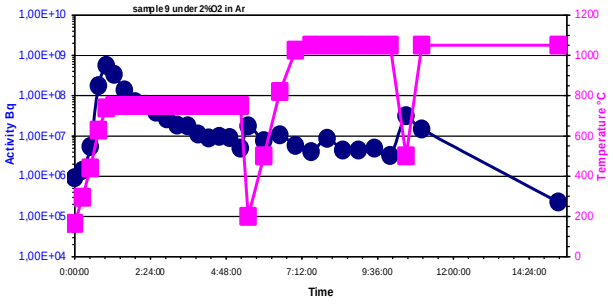

Figure 4: Measured activity after each sampling

Because of the oxidant gas, all the tritium is under HTO form. The results obtained with samples 9 are presented on table 4.

A maximum of activity can be seen after half an hour at the step 750°C.
At the beginning of each heating step, a maximum of released tritium is observed on the curve.
The mass of the sample after the detritiation is 0.0356 g so the mass loss is 41.5%.

Table 4: Activity of sample 9

Activity	HTO (Bq)	Removed relative fraction (%)
From the beginning to 750°C after a during step of 1 hour	$1.34 \cdot 10^9$	83.2
after a during step of 3 hours more	$0.15 \cdot 10^9$	9.3
1050°C (second day)	$7.0 \cdot 10^7$	4.3
1050°C (third day)	$5.0 \cdot 10^7$	3.1
Total	$1.61 \cdot 10^9$	

The total tritium activity measured by chemical dissolution of sample 9 is $22.7 \cdot 10^9$ Bq/g and the tritium activity with thermal desorption under oxidant gas until the step at 750°C is $1.21 \cdot 10^9$ Bq, that is to say 75.6% of the tritium removed

Due to the high activity of the tritium and the number of dilution of the sample to be able to do the tritium measurement with liquid scintillation, the efficiency of the detritiation (alpha factor: C_0/C_f x100) is about 100.

To know exactly and to confirm the rest of the tritium in the sample 9, the solubilisation of the thermal treated sample is necessary.

The figure 5 shows the removed relative fraction % extracted function of the temperature.

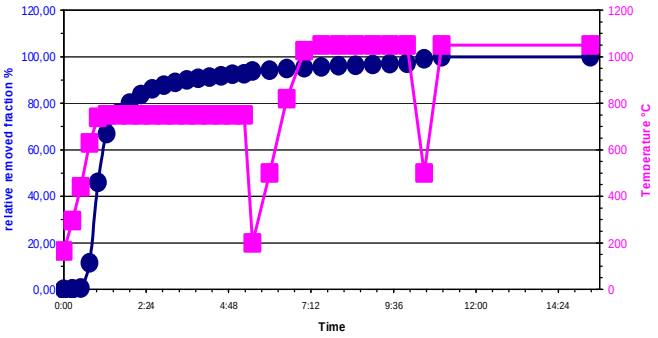

Figure 5: Relative removed fraction %

After 4 hours, 92.5% of the sample is detritiated.

With a step of one hour and reductive gases, the most important detritiation rate obtained is 35.2% at 800°C. It seems to be complicated to find any solution to detritiate correctly under reductive gas whereas with oxidant gases (2% of oxygen), at 750°C and the same during step, the detritiation rate is 83.2%. The sample is not fully oxidised.

S. Grünhagen [6] observed a loss of mass above 650°C under O2/Ar (50%/50%) and a fully oxidisation at 850°C when the metal content (Be,…) is less than 10%. The obtained results are in the same way as S. Grünhagen because the samples contain a few quantity of metallic component (Be,…).

5 % and 10% of oxygen are planed to observe the evolution of detritiation factor, alpha factor, samples mineralisation and optimisation of the detritiation time.

An experiment problem prevents us to follow the study. The study will begin again after the obtaining of authorisation by the safety authorities.

CHARACTERIZATION OF THE SAMPLE BEFORE AND AFTER THERMAL TREATMENT

The X-ray diffraction permits to evaluate the chemical form of the samples before and after the thermal detritiation.
The major component of all the samples is graphite with hexagonal structure. Aluminium is present in all the samples excepted number 9 under reductive gas (due to the heterogeneity of the sample). Some impurities like beryllium, iron and cupper are present too. Table 5 presents the obtained results on the different samples.

Table 5: Chemical form of the samples
Av: before thermal detritiation, Ap: after detritiation

Experiment	Major species	Minor species
Be 6 av	C(1), C(2), C(3), Al	BeO
Be 6 ap (Reductive gas 340°C)	C(1), C(2), C(3),	Al, BeO, Be_2C, Al_2O_3
Be 7 av	C(1), Al, Al_2O_3	C(4) , BeO, Be_2C, Cu, $Al_{13}Fe_4$
Be 7 ap (reductive gas 650°C)	C(1), Al, Al_2O_3	Fe, C(3), BeO, Fe_3C
Be 8 av	C(1), Al	Al_2O_3, Cu, C(2), C(3), BeO, Fe, $AlFe_2O_4$
Be 8 ap (reductive gas 800°C)	C(1), Al	Al_2O_3, Cu, C(2),C(3), BeO, Fe,
Be 9 ap (reductive gas 500°C)	C(1), Fe_2O_3 magnetite Fe_2O_3 hematite	BeO
Be 9 av	C(4), B_4C, Be, Cu	BeO, Al, C(1), Be_2C
Be 9 ap (oxidant gas 750°C)	B_4C, C(1), Fe_2O_3 hematite	Fe, Cu, BeO, C(4),

CONCLUSIONS

The use of reductive gas at different temperature for the detritiation leads to an optimal temperature of 750-800°C.

If thermal detritiation under reductive gas is a good process with metallic samples (the major part of tritium is on the first micron of the surface of materials), with flakes (major of carbon, beryllium carbide), the process is not very efficient. The tritium bounded in the basal plan of graphite and trapped in different carbides of the sample is very difficult to extract.

The used of oxidant gases at 750°C is much better. The detritiation efficiency is practically 100%.

Only one experiment with 2% of oxygen in argon is not sufficient to have definitive conclusion. So the experiment with 5 and 10% are necessary to optimise the process (time of the steps, duration of the process,…).

Due to the high activity of the samples, solubilisation of the rest of the detritiated sample is also necessary to calculate exactly the detritiation factor and the alpha factor.

Then it will be possible to conclude if the materials are allowed disposal as Low Level Waste (between 0.4 Bq/g and $1.2 \cdot 10^4$ Bq/g) or as Intermediate level waste ($> 1.2 \cdot 10^4$ Bq/g).

REFERENCES

[1] Dust and flakes in the JET MKIIa divertor, analysis and results A.T. Peacock, P. Andrew, P. cetier, J.P. coad, G. federici, F.Hurd, M.A. Pick and C. H. Wu - Journal of nuclear materials, vol 266-269, March 1999

[2] Chemical analysis of flakes from the Joint European torus H. Kleykamp, Journal of nuclear materials, vol 301, March 2002

[3] First wall material issues and related activities at JET F. Scaffidi-Argentina, S. Ciattaglia, P. Coad, R.-D Penzhorn, V. philipps - Journal of nuclear materials, vol 307-311, Dec 2002

[4] Tritium off-gassing trials on dust and flakes from the JET MKII divertor S.J. Knipe, A.C. Bell, P.D. Brennan, J.P. Coad, C.J. Manning, A.N. Perenvezentsev - Fusion engineering and Design vol 58-59 (2001)

[6] Techniques for tritium Recovery from Flakes and dust at the JET Active Gas handling system S. Griinhagen, A, Perevezentsev, P.D. Brennan, P. Camp, S. Knipe, A. Miller, J. Yorkshades and JET EFDA contributors, EFDA6jet-PR507°49

REPORTS AND PUBLICATIONS

[5] Thermal desorption and characterisation of flakes (monitoring meeting fusion technology JW6-FT-1.11) S. Knipe, (11/06/2007 JET)

TASK LEADER

Pierre TRABUC

DEN/DTN/STPA/LPC
CEA-Cadarache
F-13108 Saint-Paul-lez-Durance Cedex

Tel: 33 4 42 25 43 05
Fax: 33 4 42 25 72 87

e-mail: pierre.trabuc@cea.fr

JW6-FT-2.28

Task Title: ASSESSMENT OF INDUSTRIAL PROCESS OF WASTE TREATMENT

INTRODUCTION

For different reasons, tritiated waste management of fusion facility could need some detritiation techniques. In the case of ITER for example, specifications on tritiated waste concern, on one hand specific activity and on the other hand package degassing. Then it is a major issue to be able to prove that tritium content could be reduced if needed and potential partially correlated degassing limited. For JET, same approach is needed: optimisation of the decontamination factor and reduction of induced secondary waste.
Laboratory studies have been done on detritiation of different waste (stainless steel, plastics, oil, scintillation cocktails, molecular sieve beds, concrete, etc.) and on tritium desorption kinetics. Most of the treatments tested are producing tritiated water.
The objective of the 2006 activity was to determine among all techniques tested the most appropriate one for each type of waste and then to study the process feasibility at an industrial scale. This work is a joint collaboration between CEA, which is in charge of detritiation of soft housekeeping and SCK/CEN in charge of detritiation of oils and scintillating cocktails. Work on detritiation of metals was delayed in 2007.

2007-2008 ACTIVITIES

During the last years, several detritiation techniques for soft housekeeping waste were studied at laboratory scale in order to determine promising processes. The difficulty is to find a compromise between several criteria:

- High detritiation factor,
- Decategorisation of the final waste,
- Acceptable volume of produced effluents.

Processes below were tested by CEA, SCK/CEN or UKAEA and are described in the following section:

- Leaching with hot water,
- Leaching with acidic solution,
- Leaching with basic solution,
- Full mineralization in a digester or combustion,
- Thermal treatment under vacuum conditions.

LEACHING WITH HOT WATER

Leaching consists in a waste immersion in a solution. Labile tritium is transferred to the solution till an equilibrium is reached. In this case, hot water (100°C) was used for the extraction of tritium.

The time duration of leaching was defined experimentally by analyses of sampling of the leaching water. It was estimated that an equilibrium is reached after 6.5 hours for a sample of 3.4g of soft housekeeping. No testing were performed to check if the time duration depends on the mass of the sample and on the volume of the water used.
For this process, the extraction rate measured is about 75%. Note that due to the high temperature of the test, part of the activity is contained in the gaseous phase (nearly 7% of the extracted activity).

LEACHING WITH ACIDIC SOLUTION

In this case, the solution used to extract activity was composed of hot nitric acid solution (2M, 100°C).
The extraction rate measured is about 72% and is in the same order of magnitude than the one obtained with hot water leaching.
Due to the high temperature of the experiments, nearly 8% of the extracted activity is recovered in the gaseous phase.

LEACHING WITH HOT SODIUM HYDROXIDE (1M, 100°C)

The solvent used to extract tritium is sodium hydroxide 1M at 100°C. The extraction rate measured is about 70%. Evaporation due to the hot temperature of the experiment leads to nearly 8% of the tritium activity that is recovered in the gaseous phase.

FULL MINERALISATION IN A DIGESTER OR COMPLETE COMBUSTION

Two types of experimental conditions were tested for the combustion of soft housekeeping:

- Batch combustion under pure oxygen at around 20 bars,
- Batch and continuous combustion under pure oxygen at atmospheric pressure.

Both methods lead to complete destruction of the waste and recovering of 95% of tritium under HTO form (mostly in the gas phase).
The main drawbacks of the first method is the high pressure of pure oxygen and the two pressure peaks up to 100 bars which can be observed.

THERMAL TREATMENT UNDER VACUUM CONDITIONS

One last batch treatment tested consists in placing small pieces of waste (a preliminary cutting operation is needed) in an oven at 60°C under vacuum conditions (primary vacuum). The duration of the treatment is about one night (optimisation of this parameter was not done but seems possible).
After the thermal treatment, one last step consists in compacting the waste and then placing them in non degassing canisters.

It seems that mainly HTO is produced (90% of the tritium activity is under HTO form), which is recovered through a cryogenic trap and then a molecular sieve bed.
This process is used industrially but leads to solid and liquid secondary waste.

CONCLUSION

Among all the processes tested, it appears that the most promising one in term of efficiency and industrial feasibility is continuous combustion under pure oxygen at atmospheric pressure. Preliminary design and safety analysis are detailed in the next section.

PRELIMINARY DESIGN OF THE MOST PROMISING METHOD

INPUT DATA

The general objectives of the process are to:

- Fully oxidise the soft housekeeping,
- Recover the produced HTO,
- Treat the incondensable gases before release to the stack.

The average composition of soft housekeeping was fixed according to literature and is listed below:

- PVC: 30% (weight),
- Polyethylene: 30% (weight),
- Polyurethane: 30% (weight),
- Cellulose: 10% (weight),
- Neglected amount of stainless steel, copper and aluminium.

The initial activity of tritium in the waste is about 7 GBq/kg and 39 tons of soft housekeeping need to be treated over a 2 year period (for the design, it was supposed that the whole amount of the waste was disposed in 780 drums).
The activity released to the stack is limited to 2 GBq/day.
Concerning the operating conditions of the process, the flow rate of waste treated is 100 kg/day, considering that:

- 12 weeks per year are dedicated to maintenance,
- operating phase lasts 5 days/week with 2 day-shifts.

DESCRIPTION OF THE INDUSTRIAL PROCESS

The complete process consists in several steps listed below:
- drum discharging and control of the waste,
- cutting,
- combustion,
- gas treatment.

All these operations are performed in glove boxes, some of which operating under inert atmosphere to prevent from fire.
The general view of the process is given below:

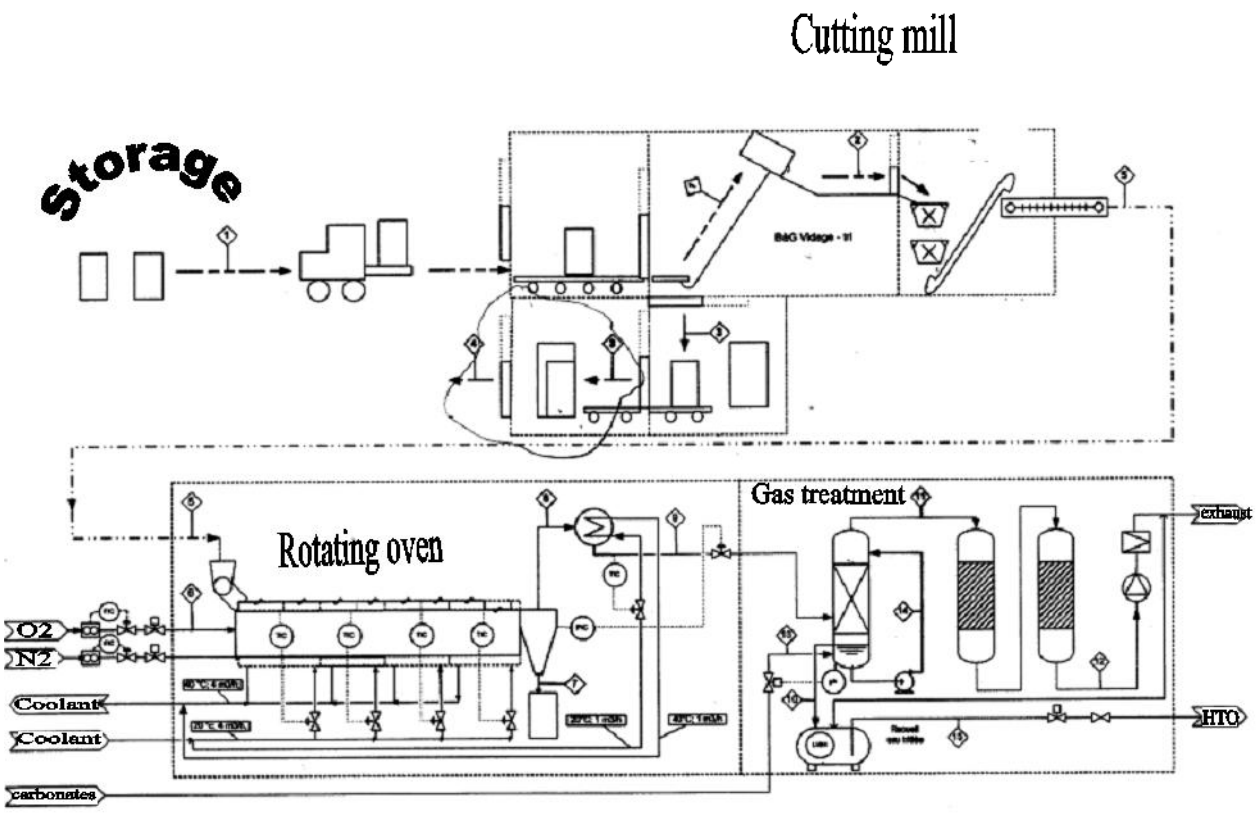

Figure 1: Process design

The drum entering the first glove box is emptied and a first control of the waste is done. Eventually, metallic waste can be separated. Then, the soft housekeeping are sent to a cutting mill to obtain small pieces of waste (about 1 cm^3) before their introduction in a rotating oven. This oven operates with pure oxygen under 1 bar. Temperature reached is about 750°C in the combustion chamber and about 700°C in the post combustion chamber. The combustion produces only few solid residues which are collected after their separation from the gas in a cyclone.
The major secondary waste of the process is composed of CO_2, O_2, H_2O, N_2, NO_x , HCl and is under gaseous form. The gases leaving the oven are cooled and sent to a scrub column, which objectives are:

- condensation of HTO (operating temperature : 4°C),
- neutralization,
- purification (especially for CO_2, as this species is present in large amount and could lead to prematurely saturation of the molecular sieve column).

The aqueous solution used contains KOH (50% weight). HCl, CO_2 and a great part of HTO are then recovered under liquid form.
Finally, the residual HTO, CO_2 and NO_x are adsorbed on molecular sieve column.

SAFETY ANALYSIS

The major risks identified for this process are: nuclear risk due to presence of tritium (transport of radioactive pollutants, exposure to radiation, interaction with materials), non nuclear risk (fire, explosion, chemical, anoxia, thermal, loss of utilities, material handling). Seismic risks were not taken into account for this study.
Classical dispositions were proposed:

- confinement (process equipments, glove boxes with filtration of exhaust, control of tritium activity in the process),
- separation of the main parts of the process (to avoid fire spreading),
- container and retention tank for chemical product,
- protection of hot surface,
- …

Considering soft housekeeping ability to burn, specific dispositions were also taken for some parts of the process:

- the amount of waste introduced in the process is limited,
- inert atmosphere is used in the glove boxes where heat can be produced or hot temperature reached (cutting phase and combustion step),
- Oxygen pressure and pressure in the oven are strictly controlled.

CONCLUSIONS

A global process was proposed to treat the whole amount of soft housekeeping waste of JET. All this process is confined in glove boxes (static or dynamic) and is relatively simple for an industrial scale. It permits also to treat the whole amount of soft housekeeping in the duration time proposed by JET (39 tons in 2 years).

REPORTS AND PUBLICATIONS

Detritriation process for JET waste: Soft housekeeping and metals
Final Report – CEA Internal Report DTN/STPA/LPC/2007-013

TASK LEADER

Karine LIGER

DEN/DTN/STPA/LPC
CEA-Cadarache
F-13108 Saint-Paul-lez-Durance Cedex

Tel: 33 4 42 25 49 08
Fax: 33 4 42 25 24 10

e-mail : karine.liger@cea.fr

JW6-FT-3.30

Task Title: LASER DETRITIATION SYSTEM TESTS IN THE BERYLLIUM HANDLING FACILITY AND JET ENVIRONMENT

INTRODUCTION

Detritiation methods based on laser ablation of deposited layers and H/D thermal desorption by laser have been under study (LILM laboratory, CEA-Saclay) since 2002. Laser system was developed (CEA-Saclay) and successfully applied for tile deposited layers cleaning on BeHF (JET, Culham) [1]. Laser beam/target surface interaction results in the release of a high amount of ablated contaminated matter (microparticles) and gases. To collect the ablated matter, the appropriate aspiration device should be considered, thus requiring to determine the particles physical characterisation (number, size distribution, morphology, mass).
Microparticles resulting from the surface cleaning were under study. The particle size dispersion and number should be regarded essential in choosing the optimal aspiration system to collect the ablated matter by filters. The feasibility of the laser cleaning of complex and shadow zones on the JET divertor mock-up by the developed laser system was also under study.

2007-2008 ACTIVITIES

CARBON MICROPARTICLES CHARACTERISATION [3]

To determine the particle size dispersion and number, TEXTOR and TORE SUPRA graphite tiles with and without deposited layers were under investigations. The developed laser system (CEA-Saclay) based on the Ytterbium fiber laser (IPG model YLP-1/120/20, 1 mJ pulse energy at 1.063 μm wavelength, 20 kHz repetition rate, 120 ns pulse duration) and a galvano-plate X-Y laser beam scanning head was applied for the sample ablation. 12 J/cm^2 fluence at the center of 140 μm laser beam diameter with 1 m/s horizontal scanning speed was applied. The scanning regime was similar to the one applied for the JET tiles detritiation on the BeHF [1-2].

The following measuring devices were applied: Condensation Particle Counter (CPC) – to measure the particles number, Engine Exhaust Particle Sizer (EEPS) and AEROSIZER - to measure the particle size in (5.6 - 560) nm and (0.5 -100) μm range, respectively. The three measuring devices are very sensitive. Only one laser shot on a surface is required to measure the aerosols. The data on the particles are obtained in a quasi real time. To determine the morphology and mass of the resulted particles, a filtration system or an impactor can be applied to collect the particles on the appropriate supports either for Transmission Electronic Microscopy analyses or weight measurements.

Each set of measurements on the graphite samples was made on a new (not ablated) surface. The CPC was applied to determine the number of particles resulted from one laser shot on the tile. For the TEXTOR tile with the deposited layer and for the TORE SUPRA tile with the deposited layer, the particle number was ≈ 5×10^7 particles/shot and ≈ 9×10^7 particles/shot, respectively. For the TEXTOR and TORE SUPRA substrates, the number of the produced particles was 1.5 and 3 times lower, respectively.

Both on the layer and the substrate, the aerosols resulted from a laser shot were composed of a large number of nanoparticles and some submicronic particles. For the two tiles, the EEPS measurements demonstrated the maximum distribution of the particles ≈70-80 nm for the layer and ≈10-35 nm for the substrate (figure 1). For all the tiles, both for the layer and substrate, the AEROSIZER measurements determined the maximal particle size distribution ≈700-800 nm. Assuming each particle as being spherical, these size distributions can be transformed into volume distributions.
For the layers and substrates of the two tiles, the particle volume is constituent mainly from the particles of ≈100 nm diameter. For the layer, the particle volume is 10-100 times more important than the one determined on the substrate.

STUDIES ON THE HIDDEN SURFACE ABLATION

The feasibility of the laser cleaning of the surfaces with a complex shape or hidden (shadow) construction elements (JET divertor tiles, for example) was under experimental study. For the laboratory laser cleaning, the part of the JET divertor was duplicated to reproduce the zones with the thickest deposited layers.

The divertor mock-up (figure 2) was made of Al covered with a black paint (50±10μm thickness). The mock-up was installed on the assembly to provide its inclination with the reference to the horizontal laser beam. Thus, it was possible to study the laser cleaning efficiency of the shadow zones with the inclined laser beam in respect to the surface.
The zones on the front side (figure 2) were the most easily accessible for the laser cleaning.

For the shadow zones, the laser cleaning with a strongly inclined laser beam was required (figure 3). Under these conditions, the ablation efficiency may be affected by the laser fluence on the surface under cleaning (due to the inclined laser beam) and the changes in the laser spot dimensions with x-y scanning on the surface (due to the laser beam divergence angle in the focusing zone).
The laser cleaning of the convex surface on the vertical tile was performed with 7.5 W and 20 W laser beams (figure 2). Each cleaning session was applied practically to the total width of the convex surface (155 mm × 20mm) on the tile. The set of the laser beam waist positions (z_r+6 mm, z_r+ 16 mm, and z_r+ 26 mm) with respect to the reference plane ($z = z_r$) of the tile surface was applied (see figure 2).
Different numbers of scans were applied to clean each tile zone (indicated in figure 2 under the zone for cleaning).

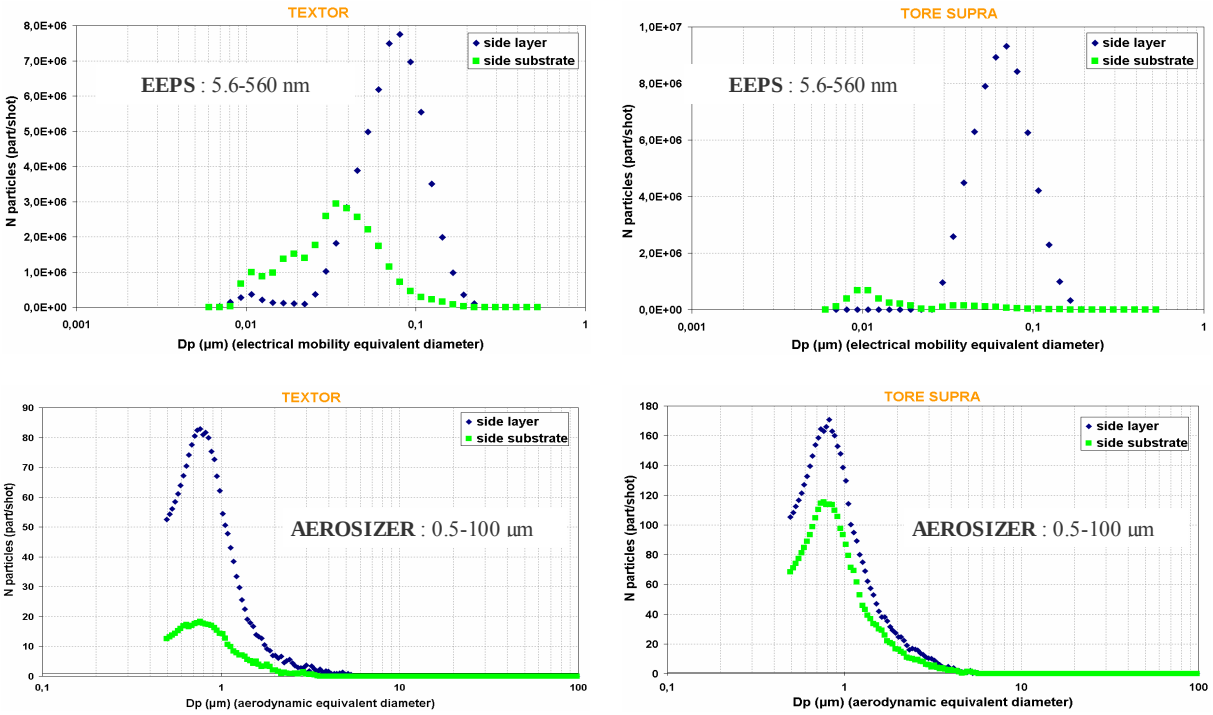

Figure 1: EEPS and AEROSIZER results on particle size distribution

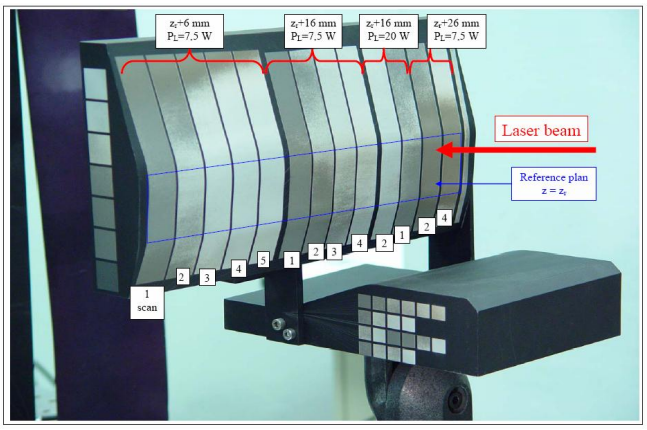

Figure 2: Cleaned zones (155cm×2cm) on the front side of the mock-up vertical tile

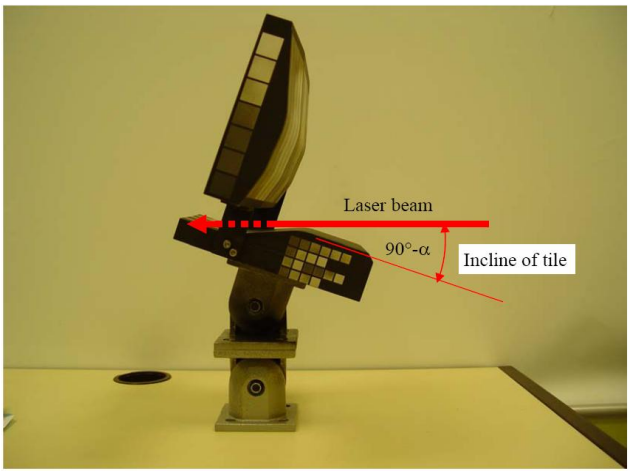

Figure 3: Cleaning of the divertor mock-up shadow zones by a very inclined laser beam

With the laser beam position at $z = z_r+16$ mm, the tile zone (155 mm x 20 mm) was completely cleaned from the paint with four laser scans with the power P=7.5W during ≈ 65 sec. With P = 20W, two scans were required to clean the zone of the same dimensions during ≈ 30 sec.
To check the feasibility of cleaning the shadow zones of the horizontal tile, the JET divertor mock-up was inclined at (90°-α) angle with the reference to the horizontal laser beam (figure 3). At (90°- α = 20°) angle, it was possible to clean only the extreme zones (a - f) of the horizontal tile (figure 4).

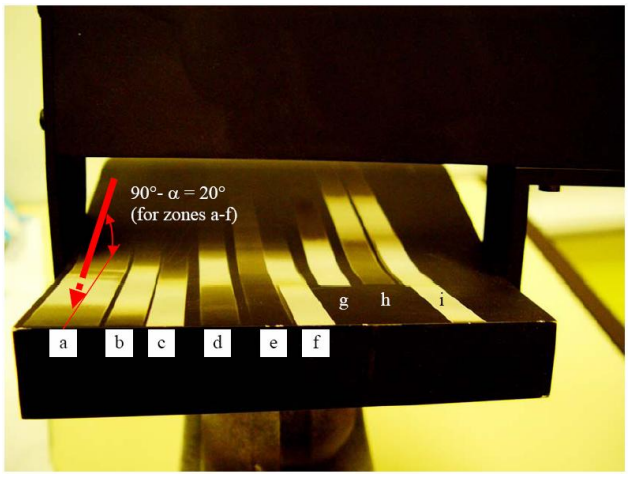

Figure 4: The rear view of the horizontal tile with the cleaned zones (a-i) for the (α) and (z_0) different incline and position of the laser beam with respect to the JET divertor mock-up horizontal tile

To clean the shadow zones (g, h, and i) just behind the tile step (figure 5), the divertor model was inclined at

(90° - α = 35°) angle. To clean zone (i), three different positions (590 mm, 625 mm, and 650 mm) of the divertor horizontal tile with the reference to a certain laser system surface were applied.

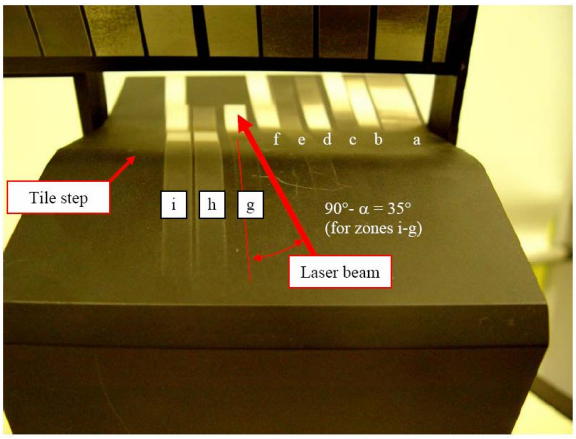

Figure 5: The front view of the horizontal tile with the cleaned zones (a-i) for the (α) and (z_0) different incline and position of the laser beam with respect to the JET divertor mock-up horizontal tile

CONCLUSIONS

Different methods for physical characterization of the particles resulted from laser ablation of the tokamak tiles were investigated. Based on the obtained results, the appropriate aspiration system to collect the contaminated ablated matter was considered.
The granulometry of the laser ablated particles does not seem to depend significantly on the matter. This assumption should be verified for ITER-like deposited layers.

The experiments on the laser cleaning of complex and shadow surfaces of the JET divertor have demonstrated that a complete cleaning of the deposited layer is possible with the appropriate choice of the laser waist position and the laser beam inclination angle. In this case, the efficient laser fluence F_{eff} = E (Joule)/S(z, α) should be higher than the ablation threshold fluence F_{th} for the deposited layer. This condition may be satisfied by IPG-fiber laser applied in the laser system developed in CEA-Saclay for surface cleaning [1-2].

REPORTS AND PUBLICATIONS

[1] A. Semerok, D. Farcage, P. Dewalle, S. Fomichev, P-Y. Thro, C. Grisolia, P. Coad, A. Widdowson, “Laser detritiation system tests in the Beryllium Handling Facility and JET environment”, Report CEA, NT DPC / SCP 08-292-A, December 2008

[2] P. Dewalle, C. Sortais, S. Pontreau, J. Vendel, J.-M. Weulersse, A. Semerok, “Characterization of aerosols produced by laser-matter interaction”, Oral presentation on 1_{st} Workshop on the «Dust in Fusion Plasmas», Warsaw, July 8-10, 2007

TASK LEADER

Alexandre SEMEROK

DEN/DPC/SCP/LILM
CEA-Saclay
F-91191 Gif-sur-Yvette Cedex

Tel: 33 1 69 08 65 57
Fax: 33 1 69 08 78 84

e-mail: alexandre.semerok@cea.fr

JW6-FT-3.33

Task Title: IN-SITU LASER BREAKDOWN SPECTROSCOPY OF JET DEPOSITED LAYERS

INTRODUCTION

The studies on the deposited layer characterisation by LIBS method were started in LILM (CEA Saclay, France) in 2002 [1-5]. To continue our investigations, LIBS feasibility for in-situ analysis of the deposited layers with the JET EDGE LIDAR laser system was under study. Based on the results obtained with the previous two experimental series with the EDGE LIDAR under the JET environment, the optical scheme of the EDGE LIDAR system was modified. To determine the optimal regime of the LIBS measurements within the JET constraints, the laboratory studies (optical spectrometer features, ICCD-camera and detection regime, analytical wavelengths, and spectral line intensities in vacuum) with the TEXTOR and TORE Supra tiles with the deposited layers were made. Low pressure (10^{-8} bar) in the zone of the analysis and a long distance (5 meters) from the laser plasma to the JET optical window were the distinguishing features of the in-situ LIBS measurements on the JET installation. With the EDGE LIDAR optical scheme, the Ruby laser beam (3 Joules, 690 nm wavelength, 300 ps pulse duration) was focused onto the centre of the JET D-T plasma column. Based on the software optical calculations, an additional divergent lens was used to fix the laser beam focal point on the divertor tile surface, thus resulting in the laser intensity increase up to 80 GW/cm^2. Such an intensity is sufficient to ablate the deposited layer and to create the bright laser plasma.

2007-2008 ACTIVITIES

EXPERIMENTAL RESULTS

In the JET experiments made with the optimized LIBS system features (optical collection system, spectrometer, ICCD-detector), a number of strong analytical spectral lines of the laser produced plasma in (665 nm - 340 nm) spectral range were observed. The spectral lines of H, C+, Cr, and Be+ were identified (figure 1). Figure 1 presents the most interesting LIBS spectra with the well resolved and intense spectral lines. The number of the observed spectrum lines was quite limited if compared to the spectra from the other tokomaks (TEXTOR and TORE SUPRA). In contrast to our laboratory experiments [6], strong ionic lines, due to vacuum conditions and a short (300 ps) laser pulse duration, were observed.

The LIBS signal evolution during laser ablation may be applied to the in-depth analysis of the deposited layer. The H_α spectral line in-depth evolution is presented in figure 2. Pulse-to-pulse H_α spectral line in-depth evolution was not regular. After the first laser shot, a very strong H_α spectral line intensity (shot 22) was observed. Then, the H_α spectral line intensity has decreased as a factor of 5 (shot 23) and was followed by the intensity increase (shots 24 and 25). The C+ spectral line intensity was regular with the intensity pulse-to-pulse increase. Thus, the detection of the H_α spectral line in-depth profile can allow to measure the deposited layer thickness and the hydrogen content.

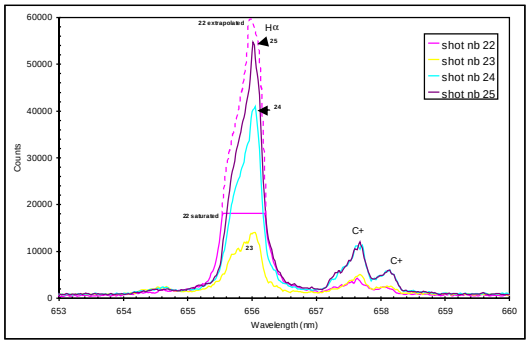

Figure 2: H_α and C+ spectral lines in-depth evolution for JET tile deposited layer. Laser pulse energy – 2.9 J (shot 22), 3.0 J (shot 23), 3.5 J (shot 24), 3.8 J (shot 25), spectrometer slit width = 200 µm, ICCD camera delay = 180 ns, gate width = 2 µs, vacuum

For a zone with a deposited layer on a W-strip, the Cr-, C-, H-, Be-, and W-lines were detected simultaneously.

Figure 3 (shot 46) presents the spectrum obtained with the first laser shot on the divertor tile surface with the deposited layer on W-stripe. For the first shot, only C-, Be-, Cr-, and H-lines were visible. With the increase of the number of the laser shots applied on the same divertor surface (without the laser beam displacement), the H-line intensity was decreasing with the appearance of the tungsten (WI) spectral lines (figure 3**,** shot 56). Thus, with the analysis of the spectral line behavior versus the applied laser shots, it is possible to make in-depth analysis of the deposited layers with the available JET EDGE LIDAR System.

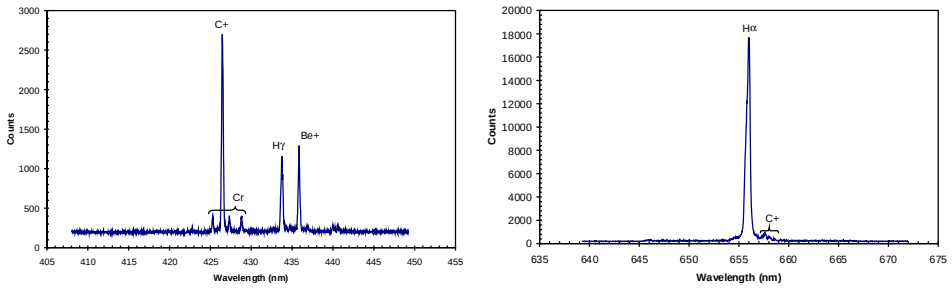

Figure 1: LIBS spectra with observed Cr, C+, Hγ, Be+ and Hα spectral lines

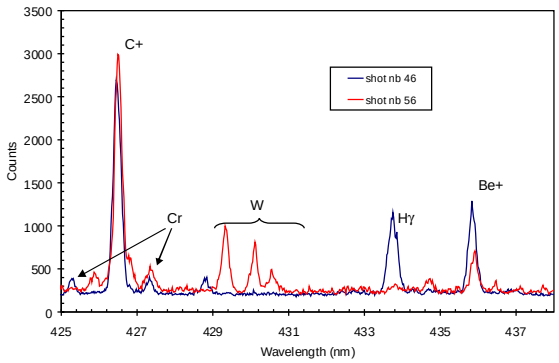

Figure 3: LIBS spectrum after the first (shot 46) and 11th laser shot (shot 56) on the W-stripe zone with the deposited layer. Laser pulse energy ≈ 3.0 J, spectrometer slit width = 200 µm, ICCD camera delay = 180 ns, gate width = 2 µs, vacuum

CONCLUSIONS

The detection system features (optical collection system, spectrometer, ICCD-detector) for the in-situ JET deposited layer diagnostics by LIBS were designed and optimised. An additional divergent lens was applied to move the laser beam focal point to the divertor tile surface, resulting in the laser intensity increase up to 80 GW/cm^2. Such the intensity is sufficient to ablate the deposited layer and to create the bright laser plasma. In the 340-665 nm spectral range, a number of analytical spectral lines (H_α, C+, Cr, Be, W) of the laser produced plasma were observed during our JET experiments. Based on the results obtained, it was concluded that LIBS is suitable for in-situ real-time analysis of the JET divertor deposited layers with the available JET EDGE LIDAR system.

REFERENCES

[1] F. Le Guern, C. Hubert, S. Mousset, E. Gauthier, C. Blanc, P. Wodling and J.M. Weulersse, Laser ablation tests performed on TORE-SUPRA graphite samples. Journal of Nuclear Materials 335 (2004)

[2] A. Semerok, J.-M. Weulersse, P.Fichet, Evaluation of laser ablation optical emission spectroscopy method for graphite co-deposited layer characterization. Task TW3-TPP-ERDIAG, CEA Saclay report, NT DPC/SCP/05-124-A, February, 2005

[3] F. Le Guern, F. Brygo, P. Fichet, E. Gauthier, C. Hubert, C. Lascoutouna, D. Menut, S. Mousset, A. Semerok, M. Tabarant et J. M. Weulersse, Co-deposited layer caracterisation and removal control by optical emission spectroscopy coupled to nano-second laser ablation, Fusion Engineering and Design 81 (2006) 1503-1509

[4] F. Le Guern, J. M. Weulersse, P. Coad, C. Grisolia, M. Kempenaars, J. L. Lacour, D. L'Hermite, A. Murari, V. Philipps, S. Rosanvallon, M. Stamp, M. Walsh, A. Widdowson and JET-EFDA contributors, *First results with Laser Induced Break-down Spectroscopy for co-deposited layer studies at JET"*, 24th Symposium of Fusion Technology, Warsaw SOFT, 11-15 September 2006

[6] J.-B. Sirven, J.-M. Weulersse, A. Semerok and C. Grisolia, Analysis of the Deposited Layer of a TEXTOR Tile by Remote Laser-Induced Breakdown Spectroscopy at low Pressure, Task JW8-FT-3.44, CEA report NT DPC/SCP 08-268 INDICE A, 30 July, 2008

REPORTS AND PUBLICATIONS

[7] J.-M. Weulersse, D. L'Hermite, J.L. Lacour, F. Le Guern, G. Cheymol, P.-Y. Thro, A.°Semerok, C. Grisolia, M. Kempenaars, M. Stamp, N. Bekris, In situ laser breakdown spectroscopy of JET deposited layers, CEA report, NT DPC/SCP/08-293-A, December 2008

TASK LEADER

Alexandre SEMEROK

DEN/DPC/SCP/LILM
CEA-Saclay
F-91191 Gif-sur-Yvette Cedex

Tel: 33 1 69 08 65 57
Fax: 33 1 69 08 78 84

e-mail: alexandre.semerok@cea.fr

JW6-FT-3.36

Task Title: MULTI-COLOUR PYROREFLECTOMETER FOR JET

INTRODUCTION

The surface temperature of Plasma Facing Components (PFCs) in tokamaks is usually measured using infrared cameras. This method requires a precise knowledge of the emissivity of the material. For carbon, the emissivity is known to be high and nearly constant over the range of detection wavelengths and the temperatures encountered in tokamaks. The emissivity of materials like beryllium and tungsten however, is lower and varies with surface condition and temperature. JET will face this question of the unknown emissivity with the ITER-like wall experiment. In the running up to this experiment measurement methods should be developed that can deal with it for JET and thus be relevant for ITER as well. One of the projects pursued in this context is the exploration of the possibility to install a multi colour pyroreflectometer at JET. This is undertaken in the form of a collaboration between the CEA-Cadarache and the CNRS-PROMES, in continuation of previous work on the same subject [1]. The method uses lasers at two or more wavelengths to illuminate the target. The reflected light and the thermal emission at these wavelengths are measured separately. From the reflected light, one can deduce the emissivity und thus determine the true temperature from the thermal emission measurement. This has been successfully demonstrated on Tungsten targets [2] by using near infrared lasers of about 0.1 Watt to measure temperatures above 700°C over a distance of a few meters.
The first objective of the task with JET was to identify potential installation positions of such a device at JET.

The second objective was to estimate the perturbations by reflexions and plasma emission in these positions.The third objective was to select the most promising position for this study. The fourth objective was the preparation of a setup that could work at the selected position at JET. The fifth and final objective was to study a system for operation in the wavelength range of 3-5 µm. The task started with a kick-off meeting the 31 January 2007 and ended with the submission of the final report [4] and the associated reporting 4 December 2008.

2007-2008 ACTIVITIES

Two potential positions for the installation of a multicolour pyroreflectometer have been identified. Both are at octant 5. The first one is the upper triangular viewing port position (meanwhile occupied by the new IR system KL9) with a window diameter of 60 mm. It views the divertor target from a distance of 5 m (figure 1). Next to this port is a larger port with 120 mm diameter, which is also very interesting, but presently not available for putting a pyroreflectometer head on it. The second port considered corresponds to one window of the 6 in the equatorial port used by the edge LIDAR system KE9.
The latter possibility was finally discarded because the window material is BK7 glass which is not ideal for the Near-Infrared range of interest (1.3-1.6 µm) of the present pyroreflectometry system [1]. Furthermore it was considered that the port sharing would have caused significant hindrance to the edge-LIDAR operation. Therefore only the KL9 port was retained for the study.

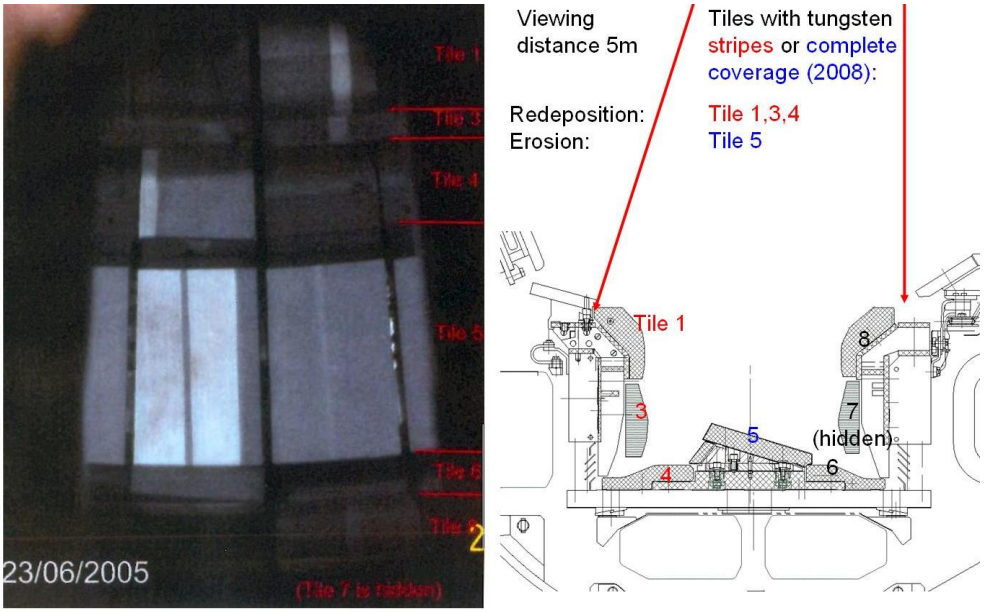

a) b)

Figure 1: a) Divertor target with tungsten surface as seen from KL9 position
b) Schematic of target with indication of width of viewing angle (red arrows) limited by port flange

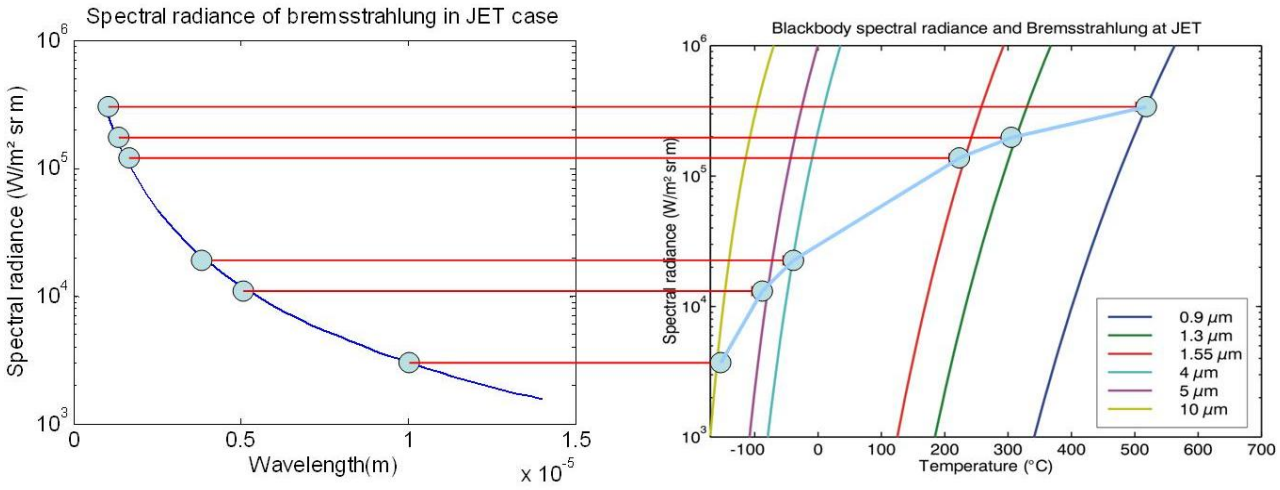

Fig. 2: a) Estimated bremsstrahlung and b) corresponding blackbody temperatures at various wavelengths of interest

The estimation of the perturbations was concerned with bremsstrahlung, diffuse and specular reflections. Bremsstrahlung was estimated using density data measured by the LIDAR systems at JET. According to these data bremsstrahlung in JET will not be a problem for the application of the pyroreflectometry method except if one should want to work at wavelengths shorter than about 1.3 µm (figure 2) where the equivalent blackbody temperature starts to exceed 300°C. Diffuse reflections were estimated using an integrating sphere approach [3]. Assuming (conservatively) a total reflectivity of 0.8 of the ITER-like wall in JET and a inner wall temperature of 300°C it was calculated how much extra temperature would be registered when looking at the inner wall when adding thermal stray radiation from a divertor at 1900°C.

The findings looked tolerable (+10K at 10 µm, +20K at 5 µm and + 35K at 4 µm). More precise predictions will require to use a Monte-Carlo raytracing approach for modelling the reflections and a detailed model of the interior of the tokamak and better data for the reflectivity.
The latter would ideally be obtained from measurements (probably in-situ) of the bi-directional reflection distribution function of the real surface material. The diffuse stray-radiation will only mildly affect one colour measurement methods such as those used for standard mono-colour thermography but a little more importantly ratio methods, to which belongs the two colour pyroreflectometry: e.g. the temperature obtained from the ratio of the spectral radiances at 5 µm and 10 µm would be overestimated by 50K and the ratio using 4 µm and 5 µm would be overestimated by 100°C under the described conditions. Specular reflections which are more localized than diffuse ones can perturb measurements significantly.
For the KL9 position an estimation was made which areas of the target are potentially affected and which ones are likely not to be affected. It seems that about half of the surface of the target of the divertor should be usable for application of the multi-colour pyroreflectometry method without worrying about specular reflections (figure 3).

The other half would require more detailed investigations with Monte-Carlo raytracing methods.

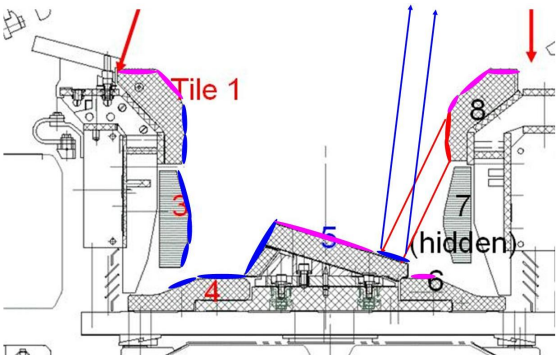

Figure 3: Zones likely to be riddled with specular reflections (blue) from hot zones (e.g. the zone in red) and zones likely not have this problem (magenta).

The CNRS studied the system that one might put on the KL9 port and which performance it would have (figure 4). In the course of this preparation it turned out that with the present illumination power available the signal to noise ratio achievable using the 60 mm wide KL9 port would not be sufficient. Using the port next to it with 120 mm diameter would change this statement - as well as a significant upgrade of the power of the lasers used in the system (which is in fact planned).

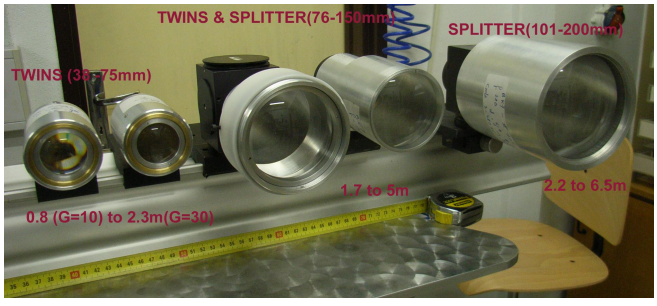

Figure 4: Measurement heads built by the CNRS-PROMES to simulate tokamak measurement conditions

The realisation of a head for JET was not undertaken due to this negative perspective, however all preparations have been made to test a system at ASDEX Upgrade in 2009 where the situation is more promising (figure 5).

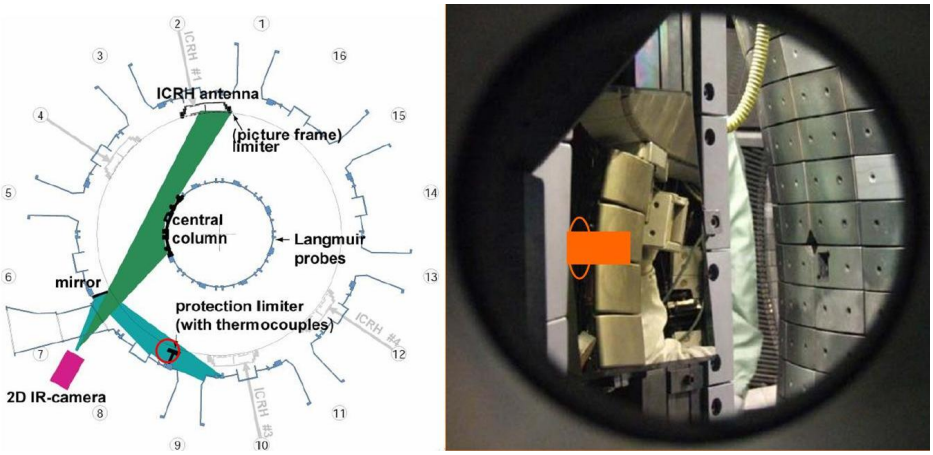

a) b)

Figure 5: a) Location for installation of a pyroreflectometer at ASDEX-Upgrade, next to 2D IR camera, with viewing lines onto a reciprocation probe (red circle) with tungsten surface
b) view of pyroreflectometer onto reciprocating probe (orange rectangle)

With regards to the study of a system that might work in the 3-5 µm range, it was considered interesting to envisage 2D 2 colour IR cameras as detectors which are becoming available commercially (e.g. from SOFRADIR). When looking at laser (or laser-like) sources the situation is more difficult but not without options: HeNe laser at 3.39 µm, CO laser at 5.42 µm. or CEA-EMIR sources initially developed to become IR lasers but finally turned into IR sources that can be customised for emission of narrow light bands (e.g. at 3.3 µm) within the 2-6 µm range. With the present knowledge a meaningful prototype assessment project could be lanced integrating the use of 2 colour IR cameras and IR laser (like) sources.

CONCLUSIONS

The original aim of the task, to give a blueprint for an installation at JET could not be achieved for the small diameter of the chosen port. A port with a two time larger diameter would have been sufficient however. The perturbations turned out not to be hindrance for the application of the method at JET except for a small part of the surface prone to strong reflections. Prototype tests are being prepared for 2009 in ASDEX-Upgrade where the geometry is more accommodating.
A project for using a 2D 2-Colour IR camera on JET and at term at ITER [5, 6] has in our view a high priority. It would certainly also be useful at Tore Supra, where it could be developed. The combination of this project with a proof of principle demonstration for a true IR bicolour pyroreflectometer using IR laser (like) sources would be in our opinion a project with plenty of synergy with such a

REFERENCES

[1] 'Experimental developments towards an ITER thermography diagnostic', Journal of Nuclear Materials, vol. 363-365, (2007) p. 1466-1471, R. Reichle, B. Brichard, F. Escourbiac, J.-L. Gardarein, D. Hernandez, C. Le Niliot, F. Rigollet, J. Serra

[2] 'Development of two colour Pyroreflectometry technique for temperature monitoring of tungsten plasma facing components' D. Hernandez, J.-M. Badie, F. Escourbiac, R. Reichle, Fusion Eng. and Design 83 (2008) 672

[3] D. Guilhem, R.Reichle, H.Roche, QUIRT, 3,2 (2006) 155

REPORTS AND PUBLICATIONS

[4] 'Report on JET Fusion Technology Task JW6-FT-3.36 Multicolour Pyroreflectometry for JET', R. Reichle, D; Hernandez, A. Netchaieff, DIAG/NTT-2008.033

[5] 'Concept and development of instruments for ITER thermography', R. Reichle et al., in 'Burning Plasma Diagnostics', ed. F.P. Orsitto et al. AIP, New York 2008

[6] 'Concept and development of ITER divertor thermography diagnostic', R. Reichle, Ph. Andrew, B. Brichard, S. Carpentier, Y. Corre, M. Davi, R. Daviot, C. Desgranges, J.-L. Gardarein, E. Gauthier, D. Guilhem, S. Gicquel, A. Herrmann, D. Hernandez, M. Jouve, Ch. Le Niliot, Th. Loarer, A. Martin, J.-P. Martins, J.-B. Migozzi, J.-C. Patterlini, C. Pocheau, F. Rigollet, H. Roche, J.-M. Travere, 18th PSI conf. Toldeo, Espagne, 26-30 May 2008, to be published. In Journ. Nucl. Mater. 2009

TASK LEADER

Roger REICHLE

DSM/IRFM/SIPP
CEA-Cadarache
F-13108 Saint-Paul-lez-Durance Cedex

Tel: 33 4 42 25 63 76
Fax: 33 4 42 25 49 90

e-mail: roger.reichle@cea.fr

JW6-FT-3.37

Task Title: ACTIVE IR THERMOGRAPHY BY PULSED-THERMAL METHOD

INTRODUCTION

Infrared thermography is widely applied for the temperature measurements. However, the method suffers certain disadvantages. The measurements are perturbed by the surrounding thermal radiations (reflected by the surface), and the measured temperatures depend on the surface emissivity. To obtain the reliable temperature measurements, the reflected thermal radiation should be avoided, and the surface emissivity should also be known. To overcome these thermography disadvantages, a new method [1] was under our experimental investigations. Two pyrometers at close, but different wavelengths were applied for the temperature measurements. Our investigations were aimed to realise the experimental set-up and to test its efficiency under laboratory conditions.

2007-2008 ACTIVITIES

EXPERIMENTAL STUDIES AND RESULTS

To ensure the surface temperature measurements with two pyrometers of a close, but different wavelengths, it is necessary to induce a low thermal perturbation on the surface under measurements. A signal modulation resulting from the induced perturbation is registered by each pyrometer (figures 1 and 2). The experimental set-up was developed with the following components: an infrared Nd:YAG laser (1064nm), two pyrometers (300÷2300°C and 200÷1000°C temperature ranges, respectively), and two interferential filters (2090nm and 1668nm mean wavelengths, respectively). The laser was applied both to ensure the sample heating up to high temperatures (representative of those expected on the tokamak wall) and to induce the required low thermal perturbation on the surface. A carbon fiber composite (CFC) sample (30mm×30mm, 10mm thickness) was under a few series of measurements.

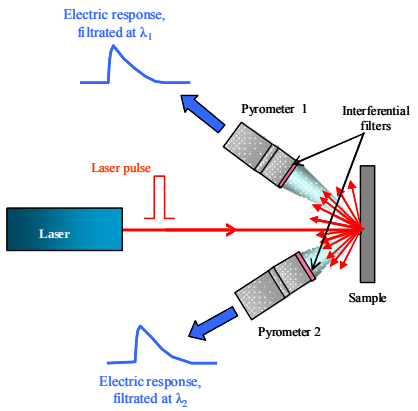

Figure 1: Scheme of the experimental set-up for laser surface heating

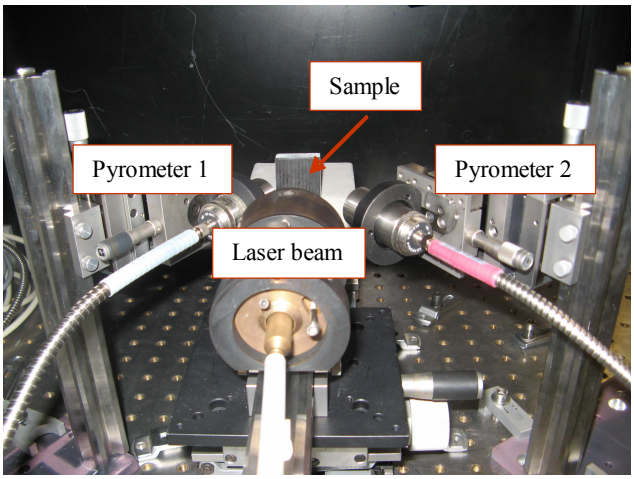

Figure 2: Photo of the experimental set-up with two pyrometers

The ratio of the two signal modulations (ΔR_1 and ΔR_2) is associated with the surface temperature. The signals modulations versus the temperature may be plotted as the "ratio curve":

$$f(T)=\frac{\Delta R_1}{\Delta R_2}=\frac{S\times\Omega_1\times r_1\times\varepsilon_{\lambda 1}\times D_{\lambda 1}\times\tau_{\lambda 1}\times\Delta\lambda_1\times\frac{\partial L^0_{\lambda 1}}{\partial T}\times\Delta T}{S\times\Omega_2\times r_2\times\varepsilon_{\lambda 2}\times D_{\lambda 2}\times\tau_{\lambda 2}\times\Delta\lambda_2\times\frac{\partial L^0_{\lambda 2}}{\partial T}\times\Delta T},$$

where S - surface zone; Ω_i - pyrometer solid angle; r_i - pyrometer electrical resistance; $\varepsilon_{\lambda i}$ – surface emissivity at wavelength λ_i ; $D_{\lambda i}$ - pyrometer detector sensitivity; $\tau_{\lambda i}$ - pyrometer optical scheme transmisivity at wavelength λ_i ; $\Delta\lambda_i$, – pyrometer spectral bandwidth; $L^0_{T,\lambda i}$ - a black-body spectral radiance at wavelength λ_i, and temperature T, K; ΔT – amplitude of the temperature modulation. The ratio curve may be obtained either with the geometrical, electrical and optical parameters of the experimental set-up or else with the pyrometers calibration equations. As some electrical and optical parameters of our experimental set-up were not available, the ratio curve (figure 3) was calculated with the pyrometer calibration equations.

The two-pyrometer method accuracy was verified by comparison of the predicted temperatures with those measured by the direct pyrometer measurements (figure 4). The predicted temperatures were obtained with ≈10% error in 600°C – 900°C range. Thus, the two-pyrometer measurements with different wavelengths may be considered suitable for the temperature measurements in tokamak.

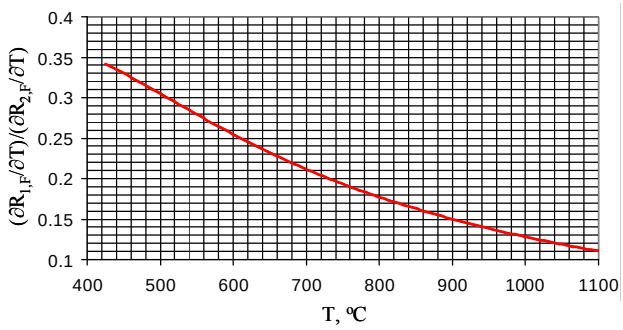

Figure 3: Ratio Curve

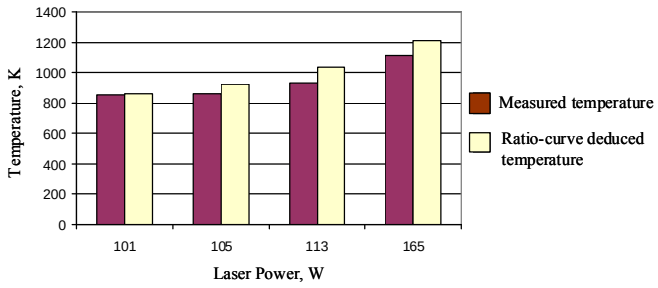

Figure 4: Comparison between the measured temperatures and those deduced by the ratio curve

CONCLUSIONS

The experimental set-up was developed and realised to verify the feasibility of a new method for temperature measurement with two pyrometers. This method is not affected either by the reflected photons flux or the surface emissivity. It was demonstrated that the ratio curve *f(T)* may be determined with the pyrometers calibration curves if geometrical, optical and/or electrical data of experimental set-up are not available. The error of the temperature measurements by two pyrometers ratio curve method was (<10%). The method was proved to be suitable for the temperature measurements in tokamak. The developed conceptual design of an active infrared thermography diagnostics was also proved to be suitable for in-situ measurements on the JET.

REFERENCES

[1] Th. Loarer et al., *Surface Temperature Measurements by Means of Pulsed Photothermal Effects in Fusion Devices,* JNM, 363-365 (2007) 1450-1456

REPORTS AND PUBLICATIONS

[1] A. Semerok, V. Grigorova, D. Farcage, J.-M. Weulersse, P.-Y. Thro, E. Gauthier, H. Roche, Th. Loarer, Ch. Grisolia, *Active IR Thermography by Means of Pulsed Photo-Thermal Method,* CEA report, NT DPC/SCP 07-245-A, December 2007

TASK LEADER

Alexandre SEMEROK

DEN/DPC/SCP/LILM
CEA-Saclay
F-91191 Gif-sur-Yvette Cedex

Tel: 33 1 69 08 65 57
Fax: 33 1 69 08 78 84

e-mail: alexandre.semerok@cea.fr

JW6-FT-4.9

Task Title: GLOW DISCHARGE IMPROVEMENTS FOR JET

INTRODUCTION

In tokamaks, machine dedicated to the study of thermonuclear fusion by magnetic confinement, the conditioning of the vacuum chamber is a key factor [1] and it is used regularly for three main reasons:

- To limit the flux of impurities coming from the walls. This allows plasma initiation and guaranties an acceptable level of contamination of the plasma during the pulse,
- To control the desorption of hydrogen and hydrogen isotopes (H,D,T) and hence the isotopic ratio in the plasma (H/D in today's tokamaks, the fusion power in ITER),
- To minimise tritium inventory in surface layers of plasma facing components, one of the major issues for operation of carbon inner wall based tokamaks.

Various types of plasma discharges are used to clean in-situ contaminated surfaces in today's facilities [1]. Among them, direct current (DC) glow discharges (low temperature plasmas, neon type) in a flow of H_2 (or isotope), He are routinely used for the above reasons. Glow discharges in D_2 or in O_2 have been proved to be efficient in particular for detritiation treatment [2]. In DC glow discharge conditioning, one or more anodes inside the vacuum chamber are biased positively with respect to the vessel walls. Thus the latter act as cathodes and are exposed to a flux of energetic ions. Typical D_2 and He pressures are ranging from 0.3 to 0.5 Pa, while the voltage between anode and cathode is of the order of 500 Volts. Hence typical ion flux densities achieved with present systems are in the range 50-100 mA/m^2. In JET, the He glow current density is a relatively uniform and is about 60 mA/m^2 [3].

However, the attractiveness of such technique is reduced by 1) the relatively high energy of the ions on the plasma facing components, which can lead to damage of the surface, and 2) the difficulty to extend the glow discharge plasma in remote area, e.g. where amorphous carbon layers containing T seem to accumulate. These disadvantages could be overcome by establishing the conditioning glow discharge between heated cathode (-s) and anode (-s) both isolated from the wall which is grounded. Cathode and anodes can be placed in the ports which need to be treated by the ions. This leads to several possible improvements:

- The discharge can be sustained at a much lower pressure than that of the glow discharge which is of interest for impurities pumping out and moreover for ITER where the out-vessel flow has to be treated in an active gas handling system (AGHS),
- Plasma glow potential is determined by the potentials of the cathode and anode. Varying the potentials of the anode and the cathode allows changing the plasma glow potential with respect to the machine wall which is grounded, and therefore the energy of the plasma ions striking the wall.

2007-2008 ACTIVITIES

EXPERIMENTAL ARRANGEMENTS

Vacuum chamber

An existing test reactor was modified in order to reproduce the main geometrical features of a small divertor, with a small port including a set of Langmuir probes. It is shown on figure 1.

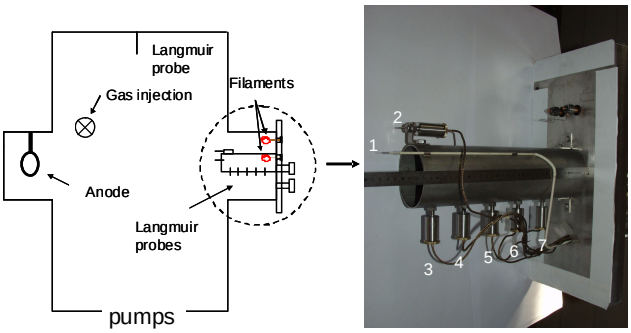

Figure1: Left: test tank with different components, right: duct with Langmuir probes and heated cathodes

The vacuum vessel has approximately a volume of ~ 0.8m^3, for an inner wall surface of about 5 m^2. Its walls can be temperature-controlled and heated-up to 150°C. The power supply was upgraded to supply a 3kV – 1.5A DC power to the anode, the aim being to reach a similar level of current density onto the surface with respect to glow discharges current densities. A DC current from 10A to 40A is applied to a heated cathode (a tungsten filament), located inside the duct, which emits electrons by thermionic effect. The discharge is operated either in He or in H_2. Two pumps (primary pump and turbomolecular pump) allow a working pressure ranging from a few 10^{-5} Pa up to 10 Pa. The pressure, measured by means of a Baratron capacitance gauge, located at the top of the chamber, is feedback controlled by the variation of the gas flow.

Cylinder with heated cathode and Langmuir probes

In order to simulate the inaccessible remote areas of the vacuum vessel, a new flange has been manufactured. A narrow cylindrical duct (10 cm diameter, 32 cm long) is fixed on it, in such a way that it reproduces the remote area which can not be reached by the usual glow discharge. This duct has to be conditioned with the help of the heated cathode. The duct is equipped with 7 cylindrical Langmuir probes (2.0 mm diameter, 10.0 mm long tungsten wires).
Five of them are distributed along its length (probes #3 to #7), as it is shown in figure 1. An eighth Langmuir probe is located at the top of the test tank. Probes #1 and #2, as well as #8, measure the plasma parameters in the bulk of the glow discharge.
The electrical signals from the probes and from the pressure gauge are recorded with an ADC acquisition board (Texas

Instruments SCB68). A Graphical User Interface was built (Labview program)
A heated cathode (heated filament emitting electrons) is placed inside the duct, while a view port allows the observation of the Langmuir probes.

EXPERIMENTAL RESULTS AND DISCUSSION

Langmuir Probe Diagnostics

The Langmuir probe diagnostic consists of placing a conducting wire into the plasma and measuring the current to it at various applied voltages [4]. Under the discharge operation parameters, the sheath is non-collisional and the mean free paths are much larger than the probe dimensions.
A typical current-voltage (I - V) characteristic measured in the test tank in He is shown in figure 2. The measurement was done with the probe # 1 in a He glow discharge at a pressure of 3 Pa. The glow discharge current was set to 1A.
Three main regions can be distinguished on the Langmuir characteristics on figure 2:

- The region where $V_{probe}<<0$, for which all the electrons are repelled by the negative potential and all the positive ions are attracted, so that the current collected by the probe corresponds to the ion current: $I_{probe}=-I_{ions}$.
- Symmetrically opposed, the region where $V_{probe}>>0$ for which the sole electrons are collected and therefore I_{probe} corresponds to the electron current: $I_{probe}=I_e$.
- An intermediate region where $V_{probe}\sim 0$ for which both type of charged particles can reach the wire. In particular, the floating potential is the probe potential for which $|I_e|=|I_{ions}|$.

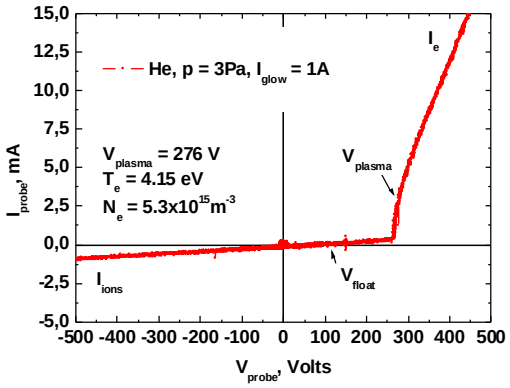

Figure 2: Typical (I–V) curve measured with Probe #1 in a He glow discharge (3Pa , 1A)

While increasing the probe potential in the intermediate region in figure 2, the ion current to the probe decreases down to 0. At this point, the probe potential equals the plasma potential V_{plasma}, i.e. the potential as it exists on average in the plasma volume between charged particles. In cylindrical geometry, where the electron current continues to grow for $V_{probe}>>0$, a practical method to determine the plasma potential is to plot the derivative of the (I–V) curve, since its slope passes through a maximum at V_{plasma}.

Whatever the probe geometry, the electron current for $V_{probe}\leq V_{plasma}$ is given by [5]:

$$I_{probe} \approx |I_e| = 0.4\, A n_0 \sqrt{\frac{k_B T_e}{m_e}} \exp\left(\frac{eV_{probe}}{k_B T_e}\right) \quad (1)$$

where A is the probe area, n_0 is the charged particles density, k_B the Boltzmann constant, Te the electron temperature and $e=1.6\cdot10^{-19}$C Hence the electron temperature Te is inversely proportional to the slope p of $\ln(|I_e|)$ at $V_{probe}\leq V_{plasma}$:

$$T_e(eV) \propto 1/p \quad (2)$$

Knowing T_e and the probe geometry, n_0 can be easily determined. Hence, in the example given in figure 2, the plasma potential measured with Probe #1 is 276 Volts, T_e=4.15 eV and $n_0=5.3\text{x}10^{15}$ m^{-3}.

First observations on the penetration of the glow discharge into the duct

On figure 3 are shown the currents and voltages measured on each probe in the duct with a digital multimeter.
The discharge was operated in helium for three different sets of glow discharge parameters. The dashed and dotted lines were obtained without having switched on the heated cathode. The discharge current was set to 1A. At 1Pa (dashed line), which is a typical gas pressure for glow discharge conditioning, there are more than 3 orders of magnitude between the currents and the voltages measured with probe #1 and those measured with the deepest probe in the cylinder (#7).

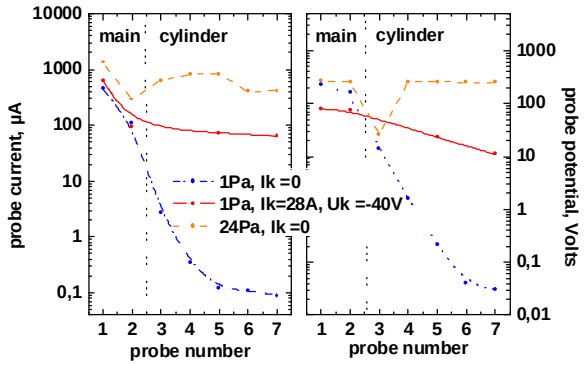

Figure 3: Current (left) and voltages (right) measured at the probes for three different conditions

The glow discharge burns into the main volume of the reactor and does not penetrate into the cylindrical tube, as indicate the low values of both current and voltages measured. There is practically no coverage of the duct by the glow discharge under "standard" conditions. The dotted curve represents the values obtained at 24 Pa. As it can be seen, similar values of current and voltage are measured in the two volume values. If the heated cathode is used (solid line), with the cathode operating parameters given on figure 3, the glow discharge penetrates into the tube, even at 1Pa.

Effect of the gas pressure on the penetration of the glow discharge

In figure 4 are shown the voltages and currents on the probes as a function of the helium pressure.
The pressure was first increased from 1 to 25 Pa (symbolized by a dashed line on figure 4), then decreased down to 8 Pa. At 1 Pa, the currents and the voltages between probe #1 and 7 differ by more than 3 orders of magnitude as found previously. As the pressure increases,

the glow discharge penetrates into the tube above a pressure threshold which is found to be 22 Pa under the present conditions (discharge current 1A). Around this value, close values of voltages and currents are measured at both ends of the tube. As the pressure further increases, the glow discharge tends to escape from the tube.

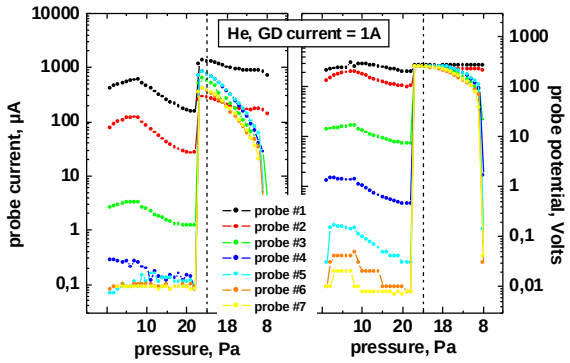

Figure 4: Current (left) and voltages (right) as a function of the gas pressure (He, glow discharge current = 1A)

At 22 Pa, the mean free path of electrons $\lambda_{e-n} = 1/N\sigma_{e-n}$ (where N is the gas particle density, and σ_{e-n} is the total ionization cross section) is of the order of the diameter of the cylindrical duct.
Indeed, taking $\sigma_{e-n} \sim 10^{-17}$ cm^2 [6], one has $\lambda_e \sim 10$ cm. Hence, below 22 Pa, the average distance between two collisions is larger than the tube dimensions, thus avoiding ionization.
On inspection of figure 4, a hysteresis can be observed. Actually, once the discharge is burning into the tube, it can be kept inside while reducing the pressure below the threshold value.

Characterization of the glow discharge in the tube with heated cathode

Influence of the heated cathode current

In this section, results are presented when the heated cathode is used. The behavior of the glow discharge and its dependency on the cathode current I_k are illustrated in figure 5, where are shown the currents and voltages measured in a 1Pa and 0.6A helium for a helium glow discharge as a function of the filament current. In that case, the cathode is biased negatively at -40 Volts with respect to the grounded walls. Clearly, the penetration of the glow discharge into the cylindrical duct occurs for operating values of the cathode current around ~23A, and under the investigated conditions, it is neither depending on the discharge pressure nor on the discharge current.
The current density to the wall in this case is much larger than in the case where the heated cathode is not used. The increase depends on different factors such as the probe location, the pressure and the discharge current. Yet, the current and voltage measured at the different locations show a maximum for some values of the cathode current I_k. For instance, a current and a voltage of about 0.2 mA and 25 V respectively are measured on probe #7 (in the tube) with the digital multimeter at 1Pa (figure 5) for an operating cathode current of 25A, whereas it is null if I_k=0.

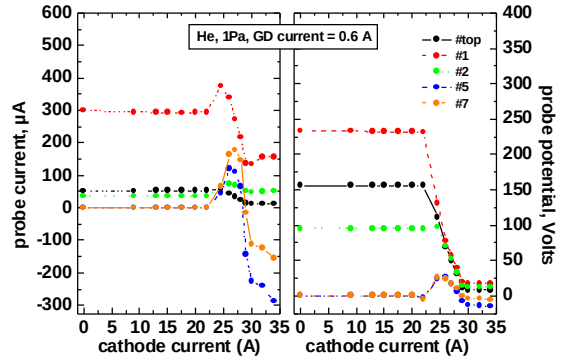

Figure 5: Current (left) and voltage (right) measured on the probes vs. filament current (He, 1Pa, 0.6A)

In the main volume, the current and voltage measured on the top of test tank (top probe) decrease when values of the heated cathode current are above ~23A.
While further increasing the cathode current above the peak value, a strong negative space charge develops in the tube and all current and voltage measured drop down. At 1 Pa, negative currents were even measured (probes #6 and # 7 in figure 5).

Plasma density and parameters

The influence of the heated cathode current on the plasma parameters is shown in figures 6 and 7.

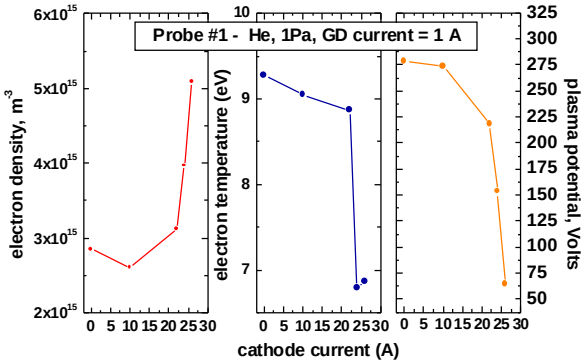

Figure 6: In the main volume: electron density (left) electron temperature (middle) and plasma potential (right) at probes # 1 (He, 1Pa, 1A)

As it is shown in figure 6, both the plasma potential and the mean electron temperature decrease with the cathode current in the main chamber, while the electron density remains almost constant when $I_k < 25$A.
At this value of the operating cathode current, the density rises abruptly from $3 \cdot 10^{15}$ m^{-3} to $5 \cdot 10^{15}$ m^{-3}, while the plasma potential and the mean electron temperature drop down (they are minimum for $I_k \sim 28$A and above). As a consequence of operating the heated cathode at such a current, the energy of the impinging ions is reduced due to the potential drop between the glow discharge and the wall.
In the cylindrical duct (figure 7), the maximum values of the mean electron temperature and of the plasma potential could be measured for $I_k \sim 25$A. As for T_e and V_{plasma} in the main volume, they decrease above this value. Note that for values of the cathode current below $I_k \sim 24$A, the currents collected by the probe are too low to be used for the determination of plasma parameters. The electron density is

maximum ($2.6 \cdot 10^{16}$ m^{-3}) at I_k ~28A and remains above 10^{16} m^{-3} as the plasma potential drops down.

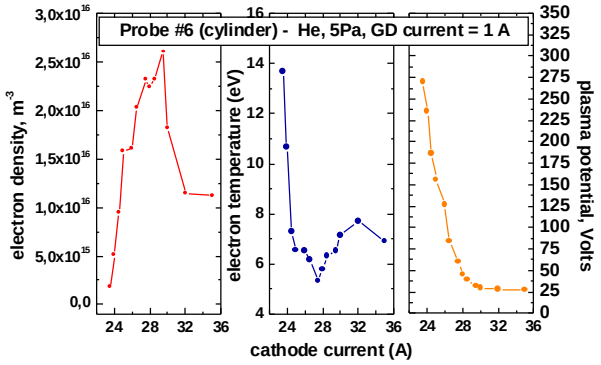

Figure 7: In the tube: electron density (left) electron temperature (middle) and plasma potential (right) at probes # 6 (He, 5Pa, 1A)

CONCLUSIONS

Conventional DC glow discharge conditioning has drawbacks such as relatively high ion energies on the plasma facing components and the difficulty to extend the glow discharge plasma in remote areas. We present some possible improvements of the glow discharge conditioning of remote areas in fusion devices.

The tests were performed in a dedicated reactor in a He-glow discharge. The tests were done at relevant pressure and current regimes. The influence of the gas pressure on the coverage of a cylindrical duct featuring a remote area was first studied. It was shown that if the glow discharge is operated under usual conditions, it can hardly penetrate into remote areas except above gas pressure thresholds for which the mean free path for electron neutral collisions is of the order of the typical dimensions of the remote area. A hysteresis is reported, and generally the glow can be kept inside the tube at a lower pressure than the thresholds.

On the other hand, if an additional cathode, located at the end of the small cylindrical duct, is used, the glow penetrates into the remote area, even at low pressures (~1Pa). Even, a small increase of the pressure leads directly to an increase of the current and voltages measured at the probes in that case. The plasma parameters (density, temperature and potential) as well as the current and voltages were obtained from a set of Langmuir probes distributed over the length of the cylindrical duct and in the main chamber. Moreover, using the heated cathode, it is possible to extend the glow to the remote area. Significant values for the electron density have been measured, whereas it has been null otherwise. In particular, the current in the cathode could be operated in such a way that the density exhibits a maximum. Simultaneously, the plasma potential is reduced, and thus the energy of the ions striking the walls.

REFERENCES

[1] J. Winter, Plasma Phys. Control. Fusion 38 (1996) 1503–1542

[2] Federici et al, J. Nuclear Materials, 266-269 (1999)

[3] P. Andrew, G. Bosia, R. Claesen, L. Grobusch, J. Harling, J. How and H.S. Jensen. The JET Glow Discharge Cleaning System, Fusion Technology 1994, Elsevier (1995)

[4] Francis F. Chen, "Lecture Notes on Langmuir Probe Diagnostics", in Mini-Course on Plasma Diagnostics, IEEE-ICOPS meeting, Jeju, Korea, June 5, 2003

[5] L. Schott, "Electrical Probes" in Plasma Diagnostics, edited by W. Lochte-Holtgreven, North-Holland Publishing Company, Amsterdam, 1968

[6] Y.-K. Kim and M.E. Rudd, Phys. Rev. A 50, 3954 (1994)

REPORTS AND PUBLICATIONS

Glow discharge improvement for JET
Final Report
CEA Report PHY/NTT-2007.003, March 2008

TASK LEADER

David DOUAI

DSM/IRFM/STEP/GPAS
CEA-Cadarache
F-13108 Saint-Paul-lez-Durance Cedex

Tel: 33 4 42 25 62 78
Fax: 33 4 42 25 62 61

e-mail: david.douai@cea.fr

UNDERLYING TECHNOLOGY PROGRAMME

Task Title: OPTIMIZATION OF HYBRID WELDING FOR VV MANUFACTURING

INTRODUCTION

Hybrid welding is expected to be a especially suitable process for manufacturing the vacuum vessel of the next reactor ITER. The hybrid process consists in combining both the MAG process and the laser process (LWP) with potentially high quality of welds at high productivity. Due to this combination, the hybrid process deals with several major operating parameters corresponding to the respective processes (power, welding speed, wire speed, focus) plus the location of each source relatively. In particular, the quality of the weld is highly sensitive to 8 of these parameters.

Today the state of the art upon operational weldability needs suitable models to assess the influence of the various operating parameters with a view to optimise the process.
The main objective of the task is to model the heat input due to the hybrid process as a function of the operating parameters.

2007-2008 ACTIVITIES

During fusion welding, the thermal cycles produced by the moving heat sources (figure 1) cause physical state changes and transient thermal stress and metal movement.

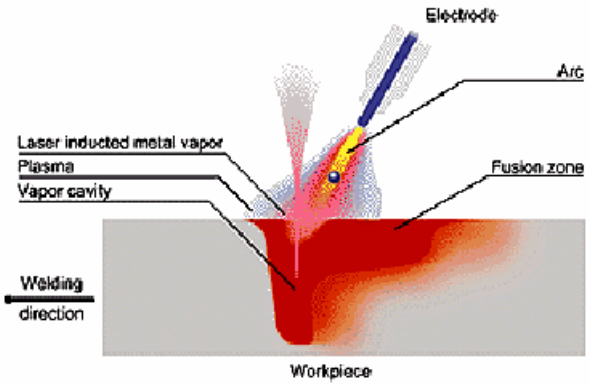

Figure 1: Hybrid process

Laser process (figure 2) and Arc process (figure 3) were modelled in a eulerian approach for heat transfer.

The mathematical expression of the cylindrical-involution-normal heat source model in a frame tied to the laser source is:

$$Qc(x,y,z) = \frac{k\,Kz\,Q_L}{\pi\,(1-e^{-Kz\,S})}\, e^{-k(x^2+y^2)\,-Kz\,Z}\,[\,1-u(z-s)]$$

Where QL is the laser energy of the laser process
K is a factor designating the heat source concentration (m^{-2})
Kz is the involution factor of the heat source (m^{-1})
S is the heat source penetration (m)
u(z-s) is the Heaviside function

Figure 2: CIN distribution for laser process (Cylindrical Involution Normal distribution)

The heat input is distributed with a gaussian distribution in each direction of two semi-ellipsoïd, taking into account the deposit difference between the rear and the front of the source due to advective an Marangoni transport. In a frame tied to the GMAW source, the power density distributions in the front quadrant have the following form:

Front :

$$Q_{Gf}(x_s,y_s,z_s) = \frac{6\sqrt{3}\,Q_G}{a_f\,bc\,\pi^{3/2}}\, e^{-3(xs/af)^2}\, e^{-3(ys/af)^2}\, e^{-3(zs/af)}$$

Rear:

$$Q_{Gfr}(x_s,y_s,z_s) = \frac{\sqrt{3}\,Q_G}{ar\,bc\,\pi^{3/2}}\, e^{-3(xs/ar)^2}\, e^{-3(ys/ar)^2}\, e^{-3(zs/ar)}$$

Figure 3: Goldak distribution for Arc process

Results of simulation

Thermal simulations of each process were analysed. In order to estimate the influence of the distance on the weld pool dimensions, a parametric study of distance between the arc and laser has been performed. Numerical simulations are computed with the CEA Finite Elements Code CAST3M (http://www-cast3m.cea.fr).
The welding parameters are the following:

- Travel speed of the torchs : 1 meter per minute
- Laser heat input : 4 kW
- GMAW heat input : 5.2 kW
- Deposited metal by pass : 2mm

The finite element mesh consists of 74 480 hexadron linear elements and 80 770 nodes. The mesh density is increased in the vicinity of the heat sources (figure 4).

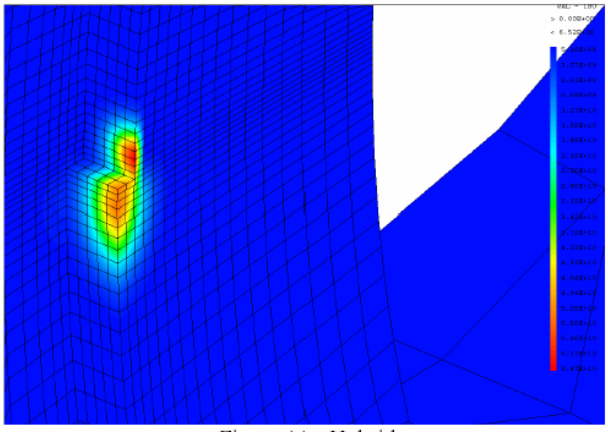

Figure 4: Hybrid source

The following results (figures 5, 6 and 7) from modelling are confirmed by experimental tests where optimum distance between the 2 heat sources is 4 mm for the laser beam in front of the MAG wire has been determined in quite good relationship to simulation results.

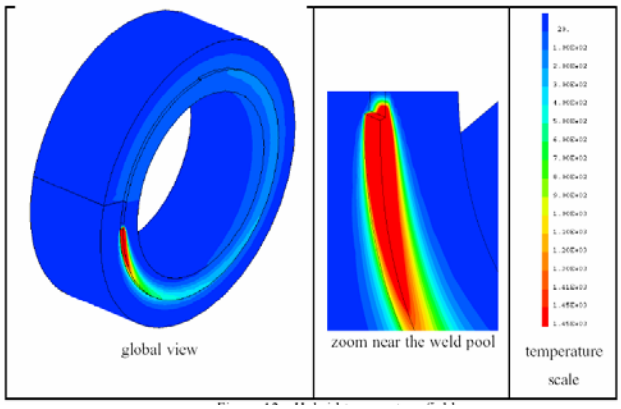

Figure 5: Hybrid temperature field

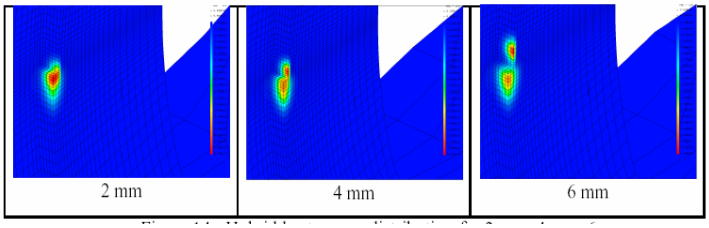

Figure 6: Hybrid heat source distribution for 2, 4, 6 mm

Distance (mm)	Width (mm)	Depth (mm)
2	9.14	5.85
4	10.76	5.95
6	8.96	4.91

Figure 7: Weld bead dimensions

CONCLUSIONS

In order to improve the weldability of narrow gap, welding by hybrid process was modelled by the addition of a CIN heat source, representing the laser process, and a GOLDAK heat source, representing the GMAW process. Thermal simulations were carried out in a eulerian formulation, in quasi-stationary state, to spare computational time. In order to study the influence of the distance between the arc and the laser source (2, 4, 6 mm) on the weld pool dimensions, a parametric study has been performed. Results highlight that there is an optimal distance that widen the width bead.

TASK LEADER

Philippe AUBERT

DEN/DM2S
CEA-Saclay
F-91191 Gif-sur-Yvette Cedex

Tel: 33 1 69 08 37 99
Fax: 33 1 69 08 66 42

e-mail: philippe.aubert@cea.fr

UT-VIV/PFC-HIP

Task Title: IMPROVEMENT OF THE RELIABILITY, PERFORMANCE AND INDUSTRIAL RELEVANCY OF HIP PROCESSES FOR PFC COMPONENTS

INTRODUCTION

In fusion industry, a lot of metallic pieces could be made by forging. However, their fabrication cycle time is long and manufacturers are searching new fabrication techniques to reduce it. In this field, Hot Isostatic Pressing (HIP) is a fabrication technique that appears very interesting because it can be used to fabricate near net shape metallic pieces by densification of metallic powders. Its use could enable a sensible reduction of the fabrication cycle time. However, there is a need to improve the reliability, the performance and the industrial relevancy of this process. To achieve these goals several investigations have been made in the frame of this work in the last few years. To clean large metallic pieces before HIP diffusion welding process, several industrial cleaning processes compatible with the requirement for series production were investigated. Moreover, several anti-diffusion materials were tested to make easier the decanning of the densified pieces after the HIP cycles and thus reduce the final machining cost. Furthermore, computer modelling to predict the final geometry of a piece made with metallic powder were investigated.

In 2007, we focused our effort on the improvement of 316LN solid/powder joints. Parameters investigated are the outgassing conditions of the 316LN powder and the influence of the outgassing conditions on the impact toughness of 316LN dense powder.

2007-2008 ACTIVITIES

Material properties

Solid material used in this study is 316LN stainless steel ITER grade. The chemical composition of the material is given in table 1. Powder used in this study is fabricated by Carpenter and its chemical composition is given in table 2. The size distribution is in the range 63-355µm and the oxygen content is about 145ppm.

Table 1: Chemical composition of 316LN stainless steel solid material

Wt%	C	Ni	Cr	Mo	S	P	Si	Mn	N_2
ITER	<0.03	12-12.5	17-18	2.3-2.7	<0.025	<0.035	<0.5	1.6-2	0.06-0.08
316LN	0.027	12.210	17.530	2.455	0.001	0.024	0.305	1.845	0.069

Table 2: Chemical composition of 316LN stainless steel powder

Wt%	C	Ni	Cr	Mo	S	P	Si	Mn	N_2
316LN	0.023	12.3	17.7	2.56	0.009	0.025	0.41	1.68	0.11

Improvement of the outgassing parameters of 316LN powder

The mechanical properties of the metallic pieces manufactured by powder metallurgy depend mainly on the powder surface contamination such as oxides or carbides. These elements come from the manufacturing process and their quantities can be increased significantly depending on the powder storage conditions or powder handling. They do not disappear totally during the densification process at high temperature but they result in inclusions at the powder particule boundaries (ppb) that may sharply reduce the final mechanical properties of the dense powder material. The negative effect of the ppb depends on the inclusion size, on their number and on their chemical composition. To limit the effect of the ppb and increase the final mechanical properties of consolidated powder it is important to work on the powder outgassing operation before the filling of the canister and the HIP densification cycle.

Outgassing of 316LN powder depends on three parameters. These parameters are the temperature, the pressure and the pressure drop inside the powder bed. Several experiments were made by Bienvenu and al.[1], Nyborg et al. [2] and Tunberg et al. [3] to investigate their influence on the final oxygen content of the stainless steel or steel powders. Experiments were also made by Couturier [4] to study the influence of the pressure and the temperature on the final oxygen content of 316LN powder densified by HIP. The results of his work show that both parameters have an influence on the final oxygen content. Under a primary vacuum (10^{-3} mbar), the oxygen content increases from 200ppm to 235ppm when the temperature rises from 20°C to 250°C. This effect was also observed by Nyborg who showed that the oxide thickness increased on the surface of wet ferritic stainless steel powder when they were heated above 400°C.

These results indicate that the contamination of the metallic powders can be increased if the outgassing pressure and the temperature are not chosen correctly. In this study we investigated the influence of both parameters to reduce the oxygen content of 316LN powders before their consolidation by HIP. The final oxygen content is measured from dense 316LN powder by using chemical analyses and a correlation with the mechanical properties is done by making impact tests.

Experimental set-up

In this study, 316LN powder is heat treated in a special apparatus constituted by a 304L tube coupled to a dry vacuum pump and a mass spectrometer (figure 1). The 304L tube is connected to a small canister that is filled by the 316LN powder after the heat treatment. The 304L tube-canister connection is made with a 10/12mm 304L pipe. After the filling operation the canister is sealed and HIPed at 1100°C under 140MPa during 4 hours.

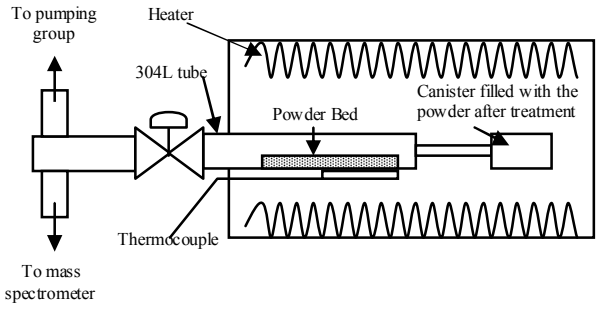

Figure 1: Experimental set-up to heat treat 316LN powder before a full densification by HIP

The vacuum system was designed to limit the pressure drops in order to obtain a low pressure inside the 304L tube. The power of the vacuum group is sufficiently high to obtain a pressure of about 10^{-6}mbar inside the system. At this pressure, the mean free path of the chemical species is very large and it is possible to interpret easily the mass spectra recorded by the mass spectrometer placed near the entrance of the 304L tube. The 304L tube and the canister are treated at the same temperature and at the same time in a large furnace. Moreover, the detection system (from the valve to the mass spectrometer) is wound up with a heater cable to keep the metallic parts outside the furnace at a temperature of about 60°C to avoid cold traps.

The heat treatments were done at 100°C, 300°C, 500°C and 700°C. The heat treatment cycle applied to the powder is presented on figure 2.

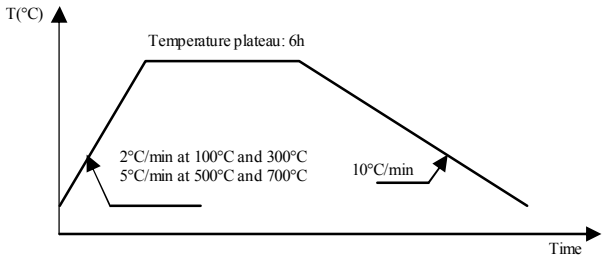

Figure 2: Heat cycle to outgas the 316LN powder

Mass spectrometer recordings are presented on figure 3 to figure 6. On these figures we plotted the time variation of the ratio I/I max associated to the main chemical species degassed by the powder and the outgassing equipment. I is the current obtained by collecting inside a Faraday cage the chemical species previously ionised and filtered by the mass spectrometer. I max is the maximal current intensity associated to each chemical species. Mass spectrometer filters out the chemical species according to their mass and to their electrical charge. Thus it is difficult to make the difference between N_2 and CO because these two molecules have the same mass M (28 UMA). However, as we observe a correlation between signals associated to H_2 (2 UMA), CH_2 (14 UMA) and CO/N_2 (28 UMA) we assume that this last signal is mainly due to CO.

At 300°C (figure 3) we observe that the signals associated to CO, CO_2 and H_2 reach a maximum at 255°C just before the temperature plateau at about 288°C. On the opposite, the signal associated to water is quite flat during most of the temperature rise. At 255°C, the maximum intensities of the recorded signals are correlated to the stop of the temperature rise and not to an optimal outgassing temperature as it will be shown further.

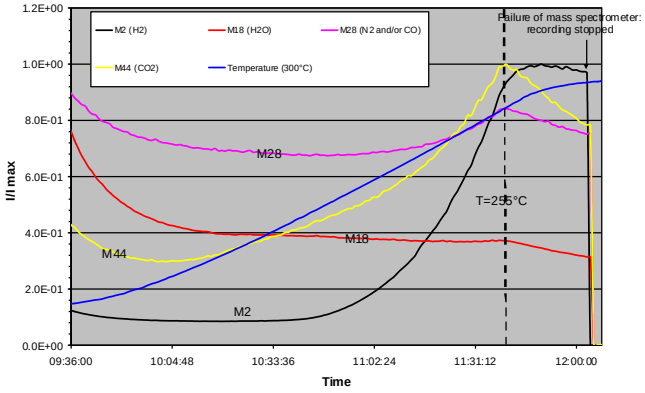

Figure 3: 300°C heat treatment cycle and mass spectrometer records

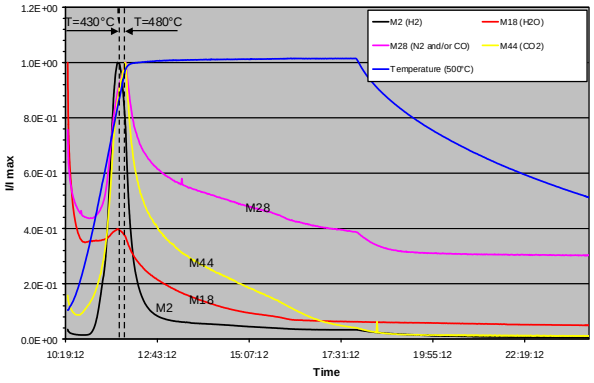

Figure 4: 500°C heat treatment cycle and mass spectrometer records

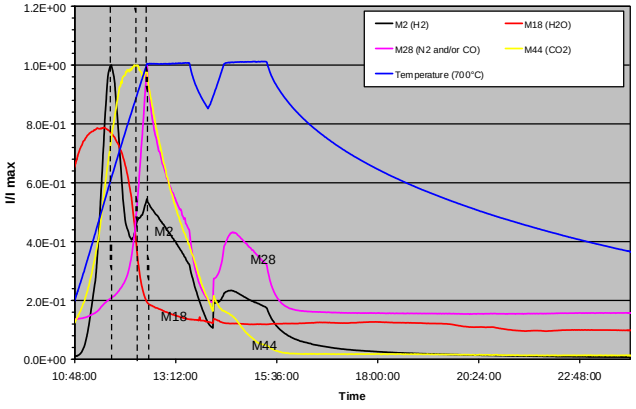

Figure 5: 700°C heat treatment cycle and mass spectrometer records

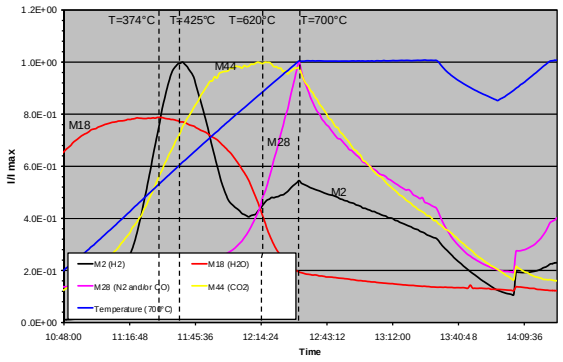

Figure 6: Enlargement of the 700°C heat treatment ramp and mass spectrometer records

At 500°C (figure 4), we observe, as in figure 3, a decrease of the water signal when the temperature of the furnace increases. At about 300°C, the water signal increases and reaches a maximum at around 430°C. Similar observations are done at 700°C where the water signal reaches its maximum at about 375°C (figure 6). We conclude that the optimal outgassing temperature for H_2O is close to 400°C. This result is in good accordance with those given by Nyborg [2] that show that the best outgassing temperature for water is between 300°C and 400°C. Our experiments show also that water outgassing is followed by hydrogen outgassing. The maximum of the hydrogen signal is reached at a slightly higher temperature than water optimal outgassing temperature (around 450°C). Hydrogen species do not come from the bulk material but from a chemical reaction between H_2O and Fe as it has been already observed and described by Nyborg:

$$Fe + 4H_2O \rightarrow Fe_3O_4 + 4H_2$$

Measurements of the oxygen content

To know the effect of the several heat treatment routes on the final oxygen content, chemical analyses were made on densified 316LN powder. The results are presented on table 3. The accuracy of the measurements is about ± 5ppm.

Table 3: Oxygen content from 316LN powder heat treated and densified by HIP

Heat treatment temperature (°C)	Oxygen content (ppm)	Final pressure (mbar)	I H_2O (10^{-10} A)
100	220	$5.3 \cdot 10^{-6}$	2.5
300	200	$1.94 \cdot 10^{-6}$	2.37
500	200	$1.2 \cdot 10^{-6}$	2.06
700	150	$1.5 \cdot 10^{-6}$	1.69
Oxygen content in the powder after fabrication	145		

Chemical analyses show a reduction of the oxygen content when the heat treatment temperature increases. It is particularly interesting to note that a 6 hour heat treatment at 700°C enables to obtain an oxygen content quasi equal to that measured by the powder manufacturer at the end of the fabrication process (145ppm). Powder oxidation that starts at about 500°C seems to have no effect on the oxygen content measured after a heat treatment at 700°C under a high vacuum. This effect is probably due to a reduction of the Fe_3O_4 layer by carbon. This chemical reduction can be correlated to the sharp increase of the CO and CO_2 signals recorded by the mass spectrometer when H_2 (so Fe_3O_4) signal rises (figure 6).

316LN powder impact toughness tests

To make correlations between the several heat treatment routes, the oxygen content and the final mechanical properties of dense 316LN powder, we performed impact toughness tests because they are discriminant to check the quality of the metallic pieces obtained by powder metallurgy. Tests were conducted on impact U notch specimens machined from 316LN dense powder blocks manufactured by HIP (1100°C, 140MPa, and 4h).

Impact specimens have been tested with a 150J pendulum at ambient temperature. The results are presented on table 4. They indicate a small influence of the temperature on the final impact toughness of dense powder. A more significant effect of the heat treatment routes could have been observed by making impact tests at a much lower temperature (77K).

Table 4: Impact toughness measurements performed on dense 316LN powder after several heat treatments

Powder Impact toughness (J/cm²)	100°C	300°C	500°C	700°C
Specimen N°1	184 rupture	192 no rupture	198 rupture	200 no rupture
Specimen N°2	190 rupture	194 rupture	196 rupture	194 no rupture
Mean impact toughness (J/cm²)	187	193	197	197

CONCLUSIONS

In this study we investigated the influence of several heat treatments route to improve the mechanical properties of 316LN powder densified by HIP. Our measurements have demonstrated that a heat treatment at 700°C during 6 hours under a high vacuum (10^{-5}mbar) allows to get an O_2 content equal to the initial concentration of the powder. Our measurements also showed that the maximum temperature for water outgassing is close to 400°C. At this temperature, water outgassing is followed by hydrogen outgassing. Hydrogen does not come from the material itself but from the oxidation of steel as it was already demonstrated by Nyborg. At 20°C, impact toughness results are the same whatever the heat treatment route (around 190J/cm² when the 316LN powder is densified at 1100°C during 4 hours under a pressure equal to 140MPa).

REFERENCES

[1] Y. Bienvenu, T.C. Lu and J.C. Le Flour , "Influence des gaz en métallurgie des poudres métalliques", Annales de Chimie Française, 1989, Vol 14, pp. 83-93

[2] L. Nyborg, I. Olefjord, "Surface analysis of P.M. martensitic steel before and after consolidation, part 2: analysis of compacted material" Powder Metallurgy, vol 31, N°1, pp. 40-44

[3] T. Tunberg, "Powder surface oxidation during production of high alloy PM steels", PhD thesis, Chalmers University of Technology, Göteborg, Sweden, 1995

[4] R. Couturier, "Etude des propriétés mécaniques de l'acier 316LN élaboré par compression isostatique à chaud. Influence des paramètres de fabrication", PhD Thesis, 1999, Ecole Supérieure des Mines de Paris

REPORTS AND PUBLICATIONS

P-E. Frayssines, O. Gillia, B. Riccetti "Improvement of the reliability, performance and industrial relevancy of HIP processes for PFC components" UT-VIV/PFC-HIP, Technical note DTH/DL/2007/96, December 2007

TASK LEADER

Pierre-Eric FRAYSSINES

DRT/LITEN/DTH/LTH
CEA-Grenoble
17 rue des Martyrs
F-38054 Grenoble Cedex 9

Tel: 33 4 38 78 28 59
Fax: 33 4 38 78 54 79

e-mail: pierre-eric.frayssines@cea.fr

UT-VIV/PFC-Hypervapotron

Task Title: NUMERICAL SIMULATION OF SWIRL-TUBE COOLING CONCEPT FOR THE ITER DIVERTOR

INTRODUCTION

This report presents a numerical study of a flow in a swirl tube, a concept suggested as a cooling system of the divertor in the ITER project. Experimental studies of this device were done by CEA/IRFM and measured temperatures are available. These temperatures were measured at two points located inside the solid around the tube. The numerical analysis includes the simultation of both the solid and the flow inside the tube. This is done by the coupling of two codes. One code, SYRTHES (developed by EDF) computes the temperature field within the solid. The other one, NEPTUNE CFD (developed by CEA, EDF and sponsored by AREVA-NP and IRSN) computes the flow. Due to the thermodynamic conditions, the flow boils and this is taken into account by the six equations model of NEPTUNE CFD. Four experimental conditions, where the incident thermal fluxes are 5, 10, 16.83 and 20 MW/m^2 were computed and the numerical results are in agreement with the experimental measurements (they are inside the experimental range error).

2007-2008 ACTIVITIES

In the first section, the swirl concept is presented. The second section gives the thermohydraulic conditions and the solid properties. The third section introduces the coupled computational codes used to model both the heat conduction in the solid and the two-phase flow thermalhydraulics. The fourth section is devoted to a discussion of the simulation results with an experimental comparison. Finally, the last section gives the conclusions.

CONCEPT DESCRIPTION

This study concerns one of the cooling systems of a possible concept of divertor for ITER (figure 1). The divertor is located at the bottom of the ITER toroid and it has to remove a large part of the energy. The cooling system under interest is the swirl flow concept.

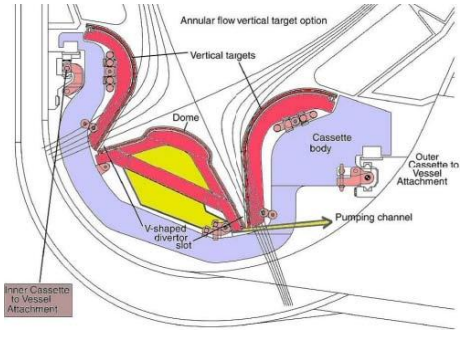

Figure 1: ITER divertor concept

It is a tube with a flow of pressurized water and with a twisted tape located inside in order to improve the heat removing (figure 2). Insertion of twisted tapes in a tube provides a simple passive technique for enhancing the convective heat transfer by introducing swirl into the bulk flow and by disrupting the boundary layer at the tube surface due to repeated changes in the surface geometry. It has been explained that such tapes induce turbulence and superimposed vortex motion (swirl flow) causing a thinner boundary layer and consequently resulting in a high heat transfer coefficient and Nusselt number due to repeated changes in the twisted tape geometry.

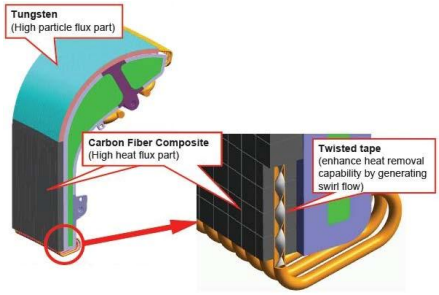

Figure 2: Location of the swirl inside the divertor

An experimental design was operated by the CEA/IRFM [1]. The geometry of the test section is shown on the figure 3.

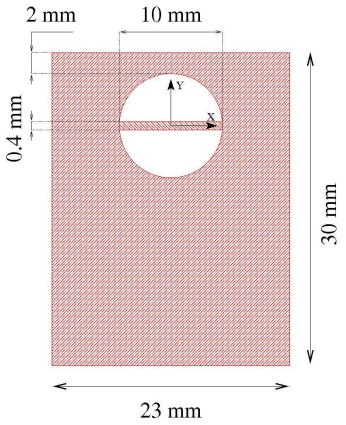

subfigure(Swirl radial cut)

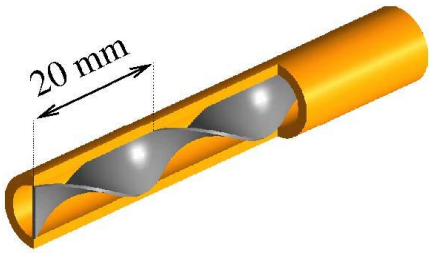

Swirl longitudinal cut

Figure 3: Swirl experiment

THERMOHYDRAULIC CONDITIONS

The water flow conditions are presented here after:
Inlet flow conditions
- Pressure = $33 \cdot 10^5$ Pa,
- Temperature = 388.15 K ,
- Mass flowrate = 0.6688 kg/s (velocity = 10 m/s),
- Saturation temperature = 512.35 K,
- Hydraulic diameter = 5.66 mm,
- Reynolds number = 223 225.

The twisted tape is made up of oxygen free high conductivity copper and the main solid block is in strengthened copper (GLIDCOP). In this study it has been considered that all solids were in GLIDCOP whose properties are listed below:

- Density = 8715 kg/m^3,
- Thermal conductivity = 314 W/m/K,
- Heat capacity = 411 J/kg/K.

The simulations were carried out for 4 Incident Heat Flux (IHF) values (5, 10, 16.83 and 20 MW/m^2).

COMPUTER CODES

The simulations are performed using a system of two coupled computer codes [2]. The local two-phase flow thermalhydraulics is predicted with the NEPTUNE CFD code developped by EDF R&D, CEA, AREVA NP and IRSN [3] while the heat conduction in solid is calculated with the SYRTHES computer code developped by EdF R&D [4].

The coupling procedure [4] allows the exchange of thermal quantities at the fluid/solid interface and parallel calculations. The local wall temperature calculated at the fluid/solid interface is set as a boundary condition for the thermalhydraulics calculation. Because this temperature also depends on the thermalhydraulics behavior, each time step requires several iterations for the fluid temperature to converge towards the solid temperature at the fluid/solid interface.

The NEPTUNE CFD code handles multicomponent multiphase flows by solving a three conservation equation system for each field (fluid component and/or phase). This system was obtained using a Reynolds Averaged Navier-Stokes (RANS) process. The turbulence modelling uses a k-ε model for the liquid phase and a Tchen's theory derived model [5] for the gas phase.

BOILING AND WALL HEAT FLUX MODELS

The boiling modelling is based on the Seiler and al. [6] work, and on the Podowski's approach [7]. This model assumes that the total heat flux Φ is the result of the contributions of 4 different heat transfer mechanisms which can possibly occur simultaneously:

$$\Phi = \Phi_{C1} + \Phi_Q + \Phi_E + \Phi_{C2} \qquad (1)$$

where Φ_{C1} and Φ_{C2} are the classical single phase heat fluxes due to convection in liquid and vapor respectively. Φ_E corresponds to the evaporation heat flux due to the boiling mechanism. Φ_Q is the quenching heat flux representing the heat flux exchange during the transient phase of conduction in liquid which follows a bubble departure. Details of this modelling can be found in [8].

SIMULATION

Meshes

The fluid domain is meshed with 17 280 hexahedrons (figure 4) according to the finite volume discretisation method in NEPTUNE CFD and the solid domain is meshed with 131 154 tetrahedrons (figure 5) according to the finite element discretisation method in SYRTHES.

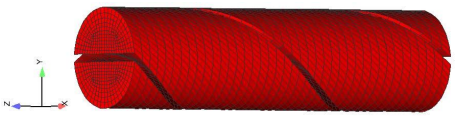

Figure 4: Swirl experiment

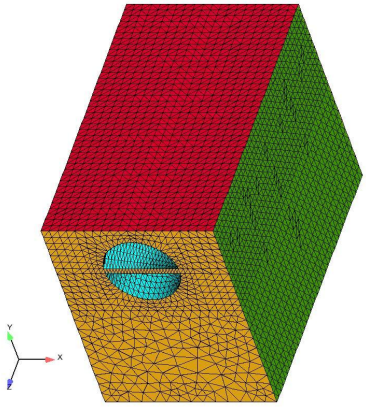

Figure 5: Fluid mesh

Results

In the experiment, the solid temperature is measured at two points A and B. Their locations are given on the figure 6.

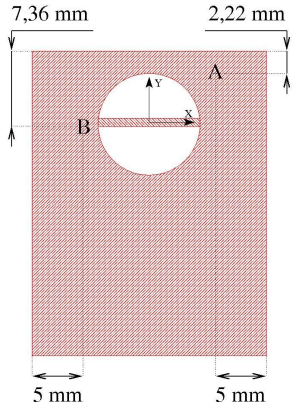

Figure 6: Thermocouples location

The following tables present the comparison between the measured and the computed values. It can also be seen on the figure 7.

Thermocouple A		
IHF (MW/m^2)	T_{Exp} (^{0}C)	T_{Sim} (^{0}C)
5	206	212
10	306	308
16.83	412.8	412.5
20	442.9	455.3

Thermocouple B		
IHF (MW/m^2)	T_{Exp} (^{0}C)	T_{Sim} (^{0}C)
5	161	156
10	202	197
16.83	254.0	252.2
20	268.5	267.9

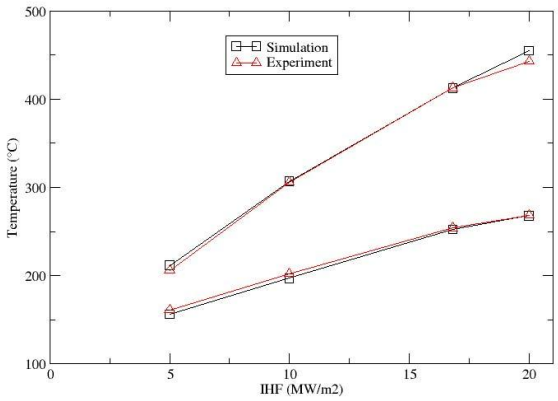

Figure 7: Computed and measured temperatures

The computed values are inside the uncertainty of measurement [1].

In the experiment the burn-out occurs at about 23MW/m^2 (IHF). This is not predicted by the simulation. In addition, an extra simulation has been carried out with an IHF equal to 30 MW/m^2 and the computed temperatures at the two points A and B are respectively equal to 672°C and 360°C which is clearly less than the solid fusion temperature (1080°C).

3D analysis

On the 20 MW/m^2 (IHF) simulation it was observed a void fraction of around 1% close to the swirl tube wall and around 5% at the center of the tube (figure 8). This is in agreement with the different centrifugal forces acting on each phase and moving the vapour to the center.

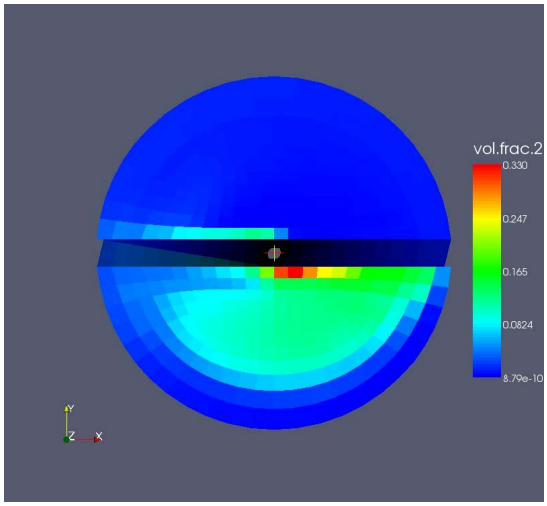

Figure 8: Outlet void fraction (20 MW/m^2)

CONCLUSIONS

This paper presented a numerical simulation of the flow inside a swirl tube, a cooling concept for the divertor in the ITER project. The computations were done with the NEPTUNE_CFD code for four incident heat fluxes. The results were compared to experimental measurements and showed good agreements. Nevertheless improvements should be done in further work in order to predict the burn-out process. A dry-out model should be added in NEPTUNE_CFD, and mesh refinements close to the wall will be necessary.

REFERENCES

[1] F. Escourbiac. 3D Thermalhydraulic simulations of divertor cooling concepts -Input data for simulations of swirl tube geometry. Ref. CFP/NTT-2007.016297, 2007

[2] S. Pascal-Ribot, A. F. Saroli, M. Grandotto, P. Spitz, F. Escourbiac. 3D numerical simulation of hypervapotron cooling concept. Fusion Engineering and Design, 82, 1781-1785 (2007)

[3] A. Guelfi, D. Bestion. M. Boucker, P. Boudier, P. Fillion, M. Grandotto, J.-M. Herard, E. Hervieu, P. Peturaud. NEPTUNE: A new software platform for advanced nuclear thermal hydraulics.
Nuclear Engineering and Design, 156, 281-324 (2007)

[4] I. Rupp and C. Peniguel. SYRTHES: conduction et rayonnement thermique -manuel utilisateur et tutorial de la version 3.3. Technical Report Rapport HI-83/01/038/A, EDF-Chatou, France, 2001

[5] E. Deutsch and O. Simonin Large eddy simulation applied to the motion of particles in stationary homogeneous fluid turbulence. Turbulence Modification in Multiphase Flows, volume 110, pages 35–42, 1991. ASME FED

[6] N. Seiler, O. Simonin, J.-M. Seiler, S. Mimouni and P. Gardin. Advanced results in the modelling and the computation of heat transfer at jet impingement. 5th international Conference of Multiphase Flow, ICMF'04, Yokohama, Japan, 30 May-4 June 2004

[7] R.M Podowski, D.A. Drew, R.T. Lahey, Jr. and M.Z Podowski. A mechanistic model of the ebullition cycle in forced convection subcooled boiling. Eight International Topical Meeting on Nuclear Reactor Thermal-Hydraulics, Kyoto, Japan, 1997

[8] S. Pascal-Ribot, N. Seiler-Marie and M. Grandotto. First Step in Simulations of Hypervapotron Cooling Concept for Fusion Applications. Avignon, France, 2-6 Oct. 2005. NURETH-11

REPORTS AND PUBLICATIONS

Numerical simulation of swirl-tube cooling concept, 25th Soft, Rostock, Germany, 2008 to be published in Fusion Engineering and Design

TASK LEADER

Sylviane PASCAL

DEN/DER/SSTH
CEA-Cadarache
F-13108 Saint-Paul-Lez-Durance Cedex

Tel: 33 4 42 25 22 24
Fax: 33 4 42 25 42 52

e-mail: sylviane.pascal@cea.fr

Task Title: ARTICULATED INSPECTION ARM (AIA)

INTRODUCTION

The Articulated Inspection Arm (AIA) project takes place in the Remote Handling (RH) activities for the next step fusion reactor ITER. The aim of this R&D program is mainly to demonstrate the feasibility of close inspection of the Divertor Cassettes and the Vacuum Vessel first wall of a Tokamak with a long reach multi-link and limited payload carrier called AIA. We assumed that the AIA robot penetrates the first wall using the 6 penetrations evenly distributed around the machine.

Since the beginning of the project, a vacuum and prototype robot module was manufactured and tested in real Tokamak conditions in Tore Supra located in Cadarache facilities. Following promising results on the prototype that validate concepts for operations under ITER relevant vacuum and temperature conditions, the manufacture of the complete AIA robot, deployer, storage cask and video process were achieved in 2007.

The work performed includes the feasibility demonstration of an articulated device demonstrator called Articulated Inspection Arm (AIA).

The AIA has to fulfil the following specifications:

- Elevation: + - 45° range,
- Rotation: +- 90° range,
- Robot total length: 7.4 meters,
- Admissible payload: 10 Kg,
- Temperature: 200 °C during baking – 120°C under working,
- Pressure: $9.7 \cdot 10^{-6}$ Pa – Ultra high vacuum.

2007-2008 ACTIVITIES

ROBOT ACTIVITIES SUMMARY

2007 was an important step in the project roadmap. It was dedicated to:

- The final prototype module qualification under ITER relevant vacuum and temperature conditions (February 2007),

- The tests of the complete AIA robot, deployment trolley system, storage cask and video process (June 2007),

- The robot tuning and deployment scenario rehearsal under ambient conditions (August 2007).

September 2007, 12th: The first complete deployment of the robot in Tore Supra Plasma Vessel under atmospheric conditions was a great success.

The end of the year 2007 was dedicated to the Remote Handling Equipment preparation for a deployment under vacuum and temperature conditions toward the objective to rehearse in 2008 the same trajectory already performed in Tore Supra.

FINAL PROTOTYPE MODULE QUALIFICATION UNDER VACUUM AND TEMPERATURE CONDITION IN ME60 (FEBRUARY 2007)

The February 2007 test campaign was a significant step in the project:

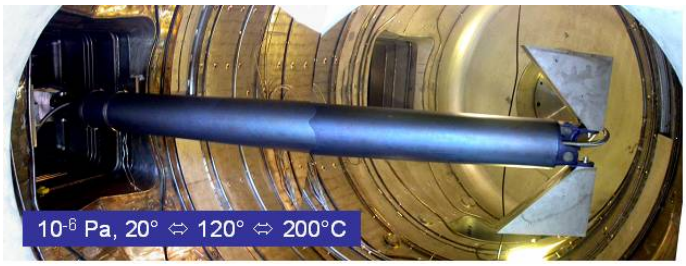

Figure 1: Test campaign on the ITER relevant module under real functioning conditions (February 2007)

- Ultra High Vacuum (10^{-6} Pa),
- Cycles between 200°C for outgassing, 120°C and 20°C,
- Representative load of the following segments (80 kg).

On each 120°C phase, the robot was set in motion for 20 cycles (combinations of rotation motions in both horizontal and vertical planes on the full range allowed in the test room ME60).

The successful issues of this test campaign qualify the entire prototype and also the set of components and technologies developed and selected since the beginning of the project for operations under vacuum and temperature conditions.

THE COMPLETE AIA REMOTE HANDLING EQUIPMENT

The AIA Remote Handling Equipment (RHE) is composed of:

- A Robotic Equipment : a long reach multi-link and limited payload carrier called AIA robot,
- A deployment trolley system supported by a precise guiding system,
- A Tokamak Equipment called the storage cask,
- A video process.

OVERVIEW OF THE AIA ROBOTIC EQUIPMENT CHARACTERISTICS:

Maximal payload	10 kg
Number of modules	5 modules + rail mounted trolley
Arm cantilever length	7.5 m
Wall penetration diameter	Ø 250 mm
Workspace	390m^3
Active degrees of freedom	1 Prismatic + 8 Rotary joints (up to 2 dof per module)
Actuation	DC motors (90 W each)
Rotary joints motion range	In horizontal plane : +/- 90°, in vertical plane : +/- 45°
Prismatic joint motion range	0 to 10 meters
Speed	0.4 to 0.6 rad/s (adaptable)
Accuracy	~ 100 mm radius sphere
Structure	Titanium (TA6V), stainless steel (316L)
Robot weight	~ 300 kg (5 modules : 150 kg + trolley : 150 kg)

OVERVIEW OF THE VIDEO PROCESS CHARACTERISTICS:

Active degrees of freedom	3 rotary joints
Process weight	8.5 kg
Viewing system	CCD color sensor with zoom and LEDs light
Cooling system	N_2 gas cooling system

Figure 2: 5 modules robot first assembly in CEA-LIST Fontenay-aux-Roses facility

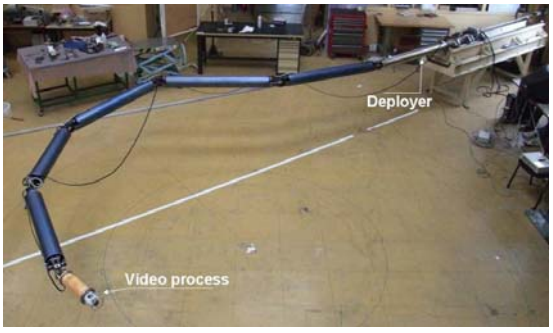

Figure 3: Articulated Inspection Arm (AIA), deployment trolley system and video process in CEA-LIST laboratories (June 2007)

In August 2007, the complete AIA robot assembly is achieved and tested at CEA-LIST Robotics laboratory facilities for:

- Robot mechanical and electronic functional validation,
- Command control setup and validation,
- Robot integration on the deployment system and functional validation,
- Video process integration and functional validation,
- Performances measurements,
- AIA robot qualification under atmospheric conditions in free environment,
- Definition of deployment trajectories in free environment,
- Tuning of security modes.

INTEGRATION OF THE TOKAMAK EQUIPMENT ON TORE SUPRA TOKAMAK

Figure 4: View of the Storage Cask through the dedicated port from inside the Tokamak

AIA DEPLOYMENT UNDER ATMOSPHERIC CONDITIONS (SUMMER 2007)

In September 2007, the Remote Handling Equipment is tested at CEA-IRFM facilities for:

- AIA robot qualification rehearsal under atmospheric conditions in free environment,
- Deployment trajectories rehearsal under atmospheric conditions in free environment (as defined in CEA-LIST labs),
- Deployment trajectories rehearsal under atmospheric conditions on a Tore Supra scale one mock-up for :
  - Trajectory validation,
  - Distance measurements between the robot and the Vacuum Vessel mock-up,
  - Deployment scenario validation before the robot introduction in Tore Supra.
- Security modes rehearsal and validation of safety procedures.

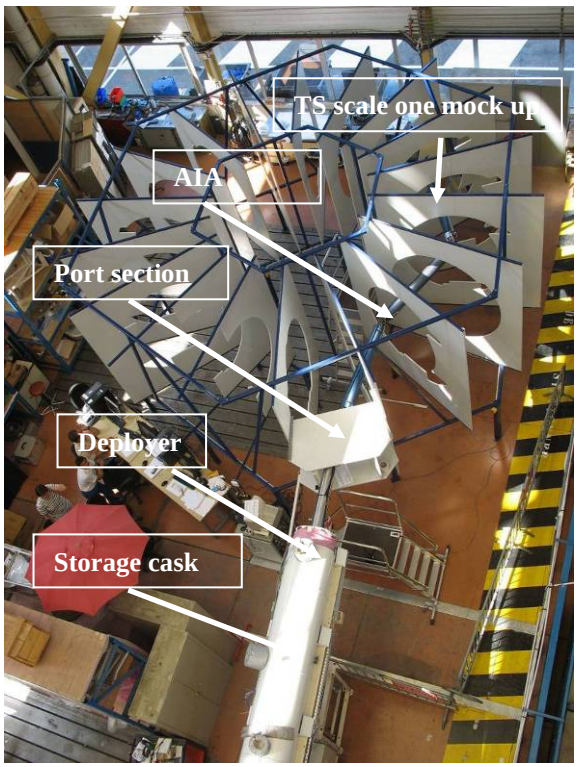

Figure 5: Training on Tore Supra scale one mock-up

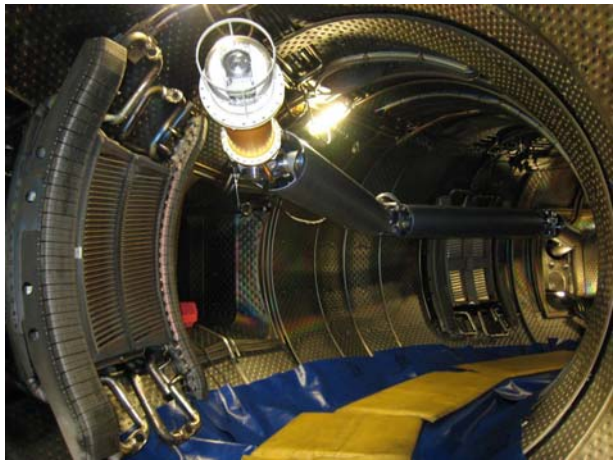

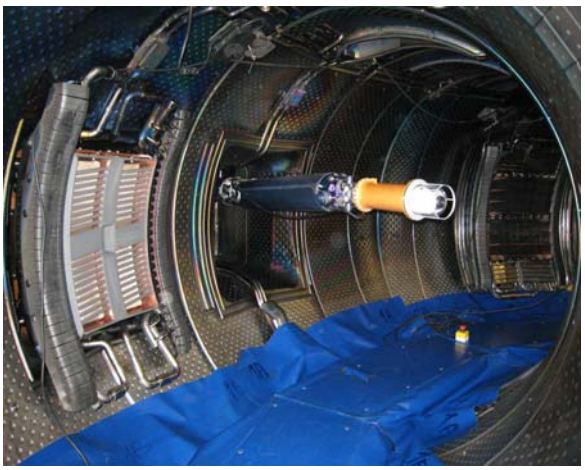

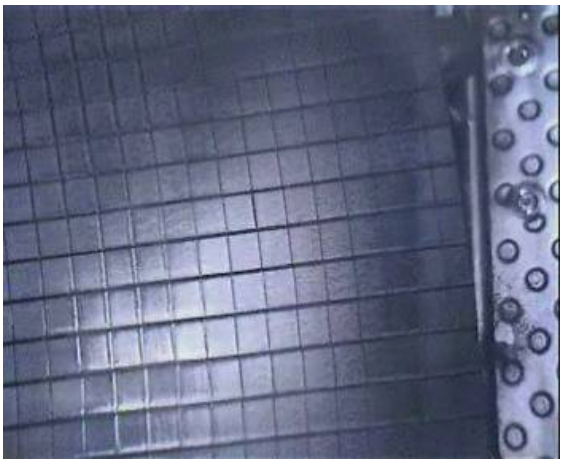

Figure 6: Introduction in Tore Supra In Vessel (September 13th2007) and video capture of the Tokamak PFCs from the AIA video process

The end of the year 2007 was dedicated to the Remote Handling preparation toward the objective of a deployment under vacuum and temperature conditions in Tore Supra in 2008.

CONCLUSIONS

Demonstration of the AIA behaviour and reliability under ambient pressure and temperature conditions in a real Tokamak environment has been achieved in September 2007. The results on this multipurpose robotic device give new perspectives on maintenance and operating activities for a reactor like ITER and aim to enhance operator perception of in-vessel situation, without re-conditioning of the Vessel. (Pollution avoidance, temperature 120°C, pressure UHV (10^{-6} Pa)).
The next step consisted in qualifying the complete Remote Handling Equipment under vacuum and temperature conditions in Tore Supra and rehearsing the previous scenario performed under ambient conditions. This was successfully achieved in September 2008, in operation machine conditions and nearly without perturbation:

- ultra vacuum: $1.4 \cdot 10^{-5}$ Pa,
- temperature: 120°C.

REFERENCES

European Fusion Technology Programme
Task TW0-DTP-1.2
Task TW0-DTP-1.4
Task TW1-TVA-IVP
Task TW2-TVA-IVP
Task TW3-TVR-IVV
Task TW4-TVR-AIA

European Fusion Technology Programme
UT-VIV-AM-AIA, Task TW5-TVR-AIA, May 2005

European Fusion Technology Programme
UT-VIV-AM-AIA, Task TW5-TVR-AIA, 2006

REPORTS AND PUBLICATIONS

Development of an ITER-relevant inspection robot, M. Houry & al., European Nuclear Conference (ENC - 2007), 16/09/2007 - 20/09/2007, Brussel , Belgium

Development of an ITER-relevant inspection robot, L. Gargiulo & al., ISFNT-8, 30/09/2007 – 05/10/2007, Germany, Heidelberg

Development of an inspection robot under ITER-relevant vacuum and temperature conditions, J.-C. Hatchressian & al., IVC-17, 02/07/2007 – 06/07/2007, Stockholm, Sweden

TASK LEADER

Delphine KELLER

DRT/LIST/DTSI
CEA-Fontenay-aux-Roses
BP 6
F-92265 Fontenay-aux-Roses Cedex

Tel: 33 1 46 54 86 84
Fax: 33 1 46 54 89 80

e-mail: delphine.keller@cea.fr

UT-TBM/BB-He

Task Title: HELIUM COMPONENTS TECHNOLOGY PROBLEMS AND OUTLINES OF SOLUTIONS

INTRODUCTION

The CEA is in charge of the generic helium technology for the development of the Gas Cooled Reactor (GCR).
Several main objectives have been determined to verify the feasibility of the very high temperature technology of the GCR: tests and qualifications of the specific high temperature and pressure helium technology processes on small facilities: tribology, thermal insulation, leak tightness, instrumentation, gas purification, He dynamic loop allow to improve the knowledge on the generic technology.

In the HCLL (Helium Cooled Lithium Lead) concept for the fusion reactor blankets, some technological developments are of common interest with the fission Gas Cooled Reactor (GCR). Thus, some experiments have been proposed in the same fields as those undertaken for fusion reactors. The first fields explored are tribology (put in operation in 2003), thermal insulation and leak tightness (put in operation in 2006) and a helium side channel compressor prototype.

In 2007 and 2008 this compressor was qualified with a mix of Helium/Nitrogen gas (80/20) and the helium dynamic loop "HEDYT" has been put in operation. The first objectives of this loop are to achieve the qualification tests of the helium compressor. This facility will also contribute to the validation of heat transfer correlation and pressure drops assessments in helium.

As concern the static benches, HELICOFLEX CEFILAC seal test campaign was completed and the SPG type S seal was qualified on HETIQ (Helium TIghtness Qualification); the test campaign of the concept "Y" thermal barrier have been completed and the "encapsulated" concept of thermal barrier have been qualified on HETHIMO bench (HElium THermal Insulation MOck up).

2007-2008 ACTIVITIES

Qualification of thermal barrier: HETHIMO [2]

The qualification of the concept Y of thermal barrier has been completed by performing the depressurization tests (20 bar/s) to achieve the thermal barrier static qualification.
The second part of the year was used to qualify the other "encapsulated" concept of thermal barrier (figure 1):

- The thermal conductivity of the encapsulated concept thermal barrier have been characterised from 500°C to 850°C and from 20 bar to 80 bar of helium.
- The value of the conductivity of the device has reached 0.50 ± 0.12 W/m.K at 60 bar and 850°C (GFR operation conditions).
- Thermal cycling (50 cycles up and down from 400°C to 850°C He at 25 bar) tests did not damage the structure of the thermal barrier.
- The depressurization tests (-20 bar/s) did not put in evidence any apparent trouble in the device.

Figure 1: On the left view of the "Encapsulated" concept thermal barrier – On the right the HETHIMO facility

Further, activity on HETHIMO has been an in-depth analysis in order to give specifications to the design of such devices.

Qualification of static seals: HETIQ [4]

Helicoflex CEFILAC static seal: during the creep tests the seal is adapted to the score flange and the leak rate is decreased. The leak flowrate is stabilized around $2 \cdot 10^{-4}$ mbar.l.s^{-1} at GFR operation conditions.

In the fatigue tests, 200 cycles have been realised by doing a difference of temperature (50°C) between the two flanges. The leak rate measured during those tests was $1.6 \cdot 10^{-5}$ mbar.l.s^{-1} for operating conditions less severe than GFR's, Helium gas is at 760°C instead of 850°C during the creep tests.

SPG type S seal: at 750°C (temperature of helium gas) and 60 bar He, the leak rate of the tested seal has been estimated around 10^{-6} mbar.l.s^{-1}. The temperature of the flanges and seal is close to 450°C.

- Creep tests which consist in stabilizing the experimental conditions during many days and monitoring the leak rate have been performed at the end of 2007.

- The fatigue tests have been performed at the beginning of 2008.

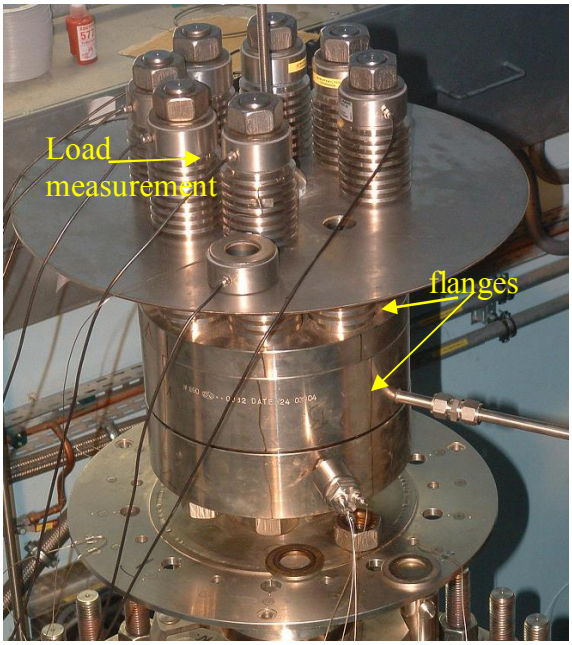

Figure 2: View of the HETIQ seals test device. The Helicoflex seal is set up between the two flanges

Qualification of side channel compressor [1]

The helium side channel compressor (figure 3) has been qualified from 5 bar to 80 bar of helium with different He flow rates in 2006. In 2007/2008, qualification tests with a mix He/N_2 (20/80) instead of pure He gas have been done. Then, this compressor has been put in operation on the new He dynamic loop (HEDYT).

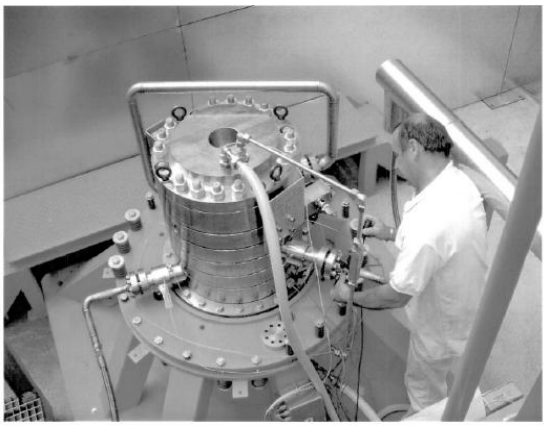

Figure 3: View of the side channel compressor prototype

HEDYT loop [3]

At the end of 2007, HEDYT (figure 4) loop was put in operation. The first tests to be performed on this bench have allowed to achieve the side channel program of qualification. This bench allows to heat helium gas at 850°C, 80 bar with a flowrate of 50 g/s.

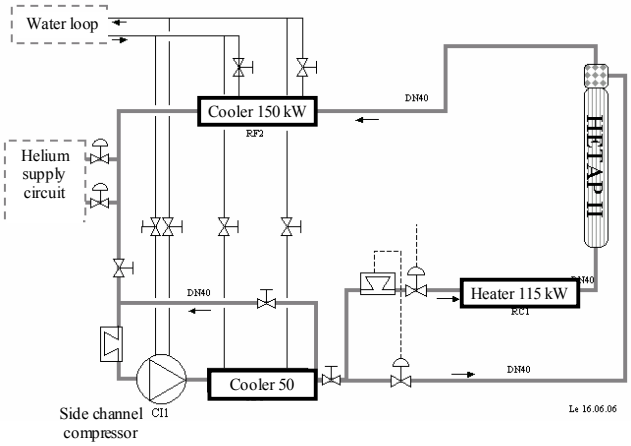

Figure 4: Flow diagram of HEDYT loop

CONCLUSIONS

In 2007, the "Y" concept and "Encapsulated" thermal barriers developed by CEA has been qualified in static operating conditions. The thermal barriers have been characterised in GFR (Gas Fast Reactor) operating conditions (850°C He, 60 bar) and up to (850°C He, 80 bar). The thermal conductivity of the two concepts were evaluated, the estimated values are close to the expected ones (0.5 W.m/K). In 2008, activity has been an in depth analysis in order to give specifications to the design of such devices.

The seals tightness qualification on the HETIQ bench gives results on two concepts HELICOFLEX and S type seals. The type S seal gives good results as concern creep tests, at GFR operating conditions; the leakrate is evaluated at 10^{-6} mbar.l.s^{-1}. In 2008 the test program has been completed with the fatigue tests on this S type seal. As concern the HELICOFLEX seal program in 2008, some improvements on the liner material of the seal were programmed and have been performed and will be qualified in 2009. The HEDYT loop has been put in operation during the second part of 2007. This loop will allow to validate gas correlations for fuel assembly, to study material behaviour at GFR operating conditions, to develop the generic He technology and to qualify gas heat exchanger.

REPORTS AND PUBLICATIONS

[1] L. AYRAULT, "Report on experiments on helium generic technology", CEA Technical note, DTN/STPA/LTCG/ NT 2007- 029

[2] L. AYRAULT, "HETHIMO qualification of encapsulated concept", CEA Technical note, DTN/STPA/LTCG/ NT 2007- 018, Oct. 2007

[3] L. AYRAULT, "HEDYT – Essais de mise en service", CEA Technical note, DTN/STPA/LTCG/ NT 2007- 022, Oct. 2007

[4] L. AYRAULT, "HETIQ - Qualification of type S SPG seal", CEA Technical note, DTN/STPA/LTCG/ NT 2007- 030, Dec. 2007

TASK LEADER

Laurent AYRAULT

DEN/DTN/STPA/LTCG
CEA-Cadarache
F-13108 Saint-Paul-Lez-Durance

Tel : 33 4 42 25 44 72
Fax : 33 4 42 25 66 38

e-mail : laurent.ayrault@cea.fr

UT-S&E-Dust-Suspension

Task Title: OPTICAL CHARACTERIZATION OF DUST IN SUSPENSION EXPERIMENTAL STUDIES OF DUST SUSPENSION

INTRODUCTION

During tokamak operation dust production needs to be characterized and monitored from the operation point of view as well as for safety issues [1-2, 7-9]. In current tokamaks, dust properties studies rely on recovery techniques and outline physical-chemical analyses. In the frame of the ITER program where dust mass inventory limits have been defined, there is a need to develop online techniques to monitor dust quantity on the hot surfaces and more generally in the vacuum vessel [1,3]. Development of ITER relevant Optical Particle Characterization (OPC) techniques, during plasma shutdowns, is nevertheless not a trivial task due to:
i) limited and difficult optical accesses, large distances, vibrations, magnetic field strength;
ii) expected complexity and variety of dusts shapes: homogeneous and layered spheres, cauliflower shapes and flakes, fibres or nanotubes [1-2, 7];
iii) the lack of data on dust composition and the optical properties of mixed materials; *iv)* large size distribution range expected for dusts (with diameter D=10nm~10µm), presence of large flakes (10µm to few millimeters) which should nevertheless rapidly deposit in case of an air ingress for instance.
This report resumes our activity [7] on the development of a non-invasive optical technique to characterize dusts in suspension in ITER vacuum vessel.

2007-2008 ACTIVITIES

The determination of dusts complex refractive index is a crucial task as this parameter has a determinant influence on their scattering properties and it is an input parameter of the light scattering models. Most OPC techniques require knowing in advance the particle refractive index for at least one wavelength. The refractive index spectra of carbonaceous, beryllium, tungsten particles, and their oxides, are totally different each other [7]. The optical properties of the two latter are different each other in the visible-NIR region, but they are similar in the MIR-region [7]. Dusts may be composed of different materials. This can be managed, in some extend, by the scattering models. Materials mixtures can also be modeled by effective medium theories. These theories treat the problem of an inhomogeneous medium as a two-components mixture composed of inclusions embedded in an homogeneous matrix. Our simulations [7] showed that, when considering a carbonaceous particle with an increasing volume fraction of spherical inclusions of tungsten, up to 20-30% of tungsten in volume, the medium refractive index spectra remains somewhat similar to the carbonaceous one. For higher concentrations in tungsten the spectra are totally different from the carbonaceous and the tungsten ones. Another way to determine the refractive index spectra of dusts is to perform experimental analyses. Unfortunately, the determination of the refractive index of powders is also an extremely delicate task. This requires at least obtaining some dusts samples [8, 9]. The procedure is then to measure the spectral hemispheric-reflectivity of dusts (ideally from UV to MIDIR) and to use Kramers-Kronig integral to reconstruct the complex refractive index spectra. An alternative solution will be to use the extinction spectrometry technique itself to recover dust refractive index [7] which a dust sample and a reference technique for the dust size distribution.

Optical diagnoses of dust size distribution and concentration require an accurate modeling of their scattering properties (figure 1). *The Lorenz-Mie Theory (LMT)* was extended during the two last decades to model the scattering of an arbitrary beam by a spherical homogeneous sphere, a multilayered or heterogeneous sphere [3, 4], a spheroid. The predictions of this theory (internal fields, radiation pressure…) are widely and intensively used in all academic and technical fields. For dusts or flakes the use of a spherical particle model is questionable as it generates powerful surface waves and morphological dependence resonances that will be never observed for dusts from tokamaks. The use of a LMT with a layered particle model or the T-Matrix with a cluster particle model could further improve the agreement with these experimental data [7].

The T-Matrix theory [5], based on the Extended Boundary Condition method, allows to calculate the scattering matrix of spheroids, truncated cylinders, "Chebyshev" or cluster of particles. The computational time is quite prohibitive, the particle maximum size-parameter or aspect ratio are also limited. Thus our approach is to produce look-up tables of the T-Matrix results over a large range of parameters. We developed software [7] that automatically generates and rotates clusters of particles, produces the corresponding batch files to run the T-Matrix code, produces statistical results and generates graphs automatically, etc… For the scattering of a "cloud of dusts" the scattering properties are simply averaged over a large number of particles.

The Discrete Dipole Approximation (DDA) is a numerical method which solves the problem of the scattering and absorption by an array of polarizable point dipoles interacting with a monochromatic plane wave [6]. This is limited to soft particles (small size parameter and low refractive index). *Geometrical optics* is not appropriate to model pure wave phenomena and the scattering of particles with a diameter close to the wavelength [11].

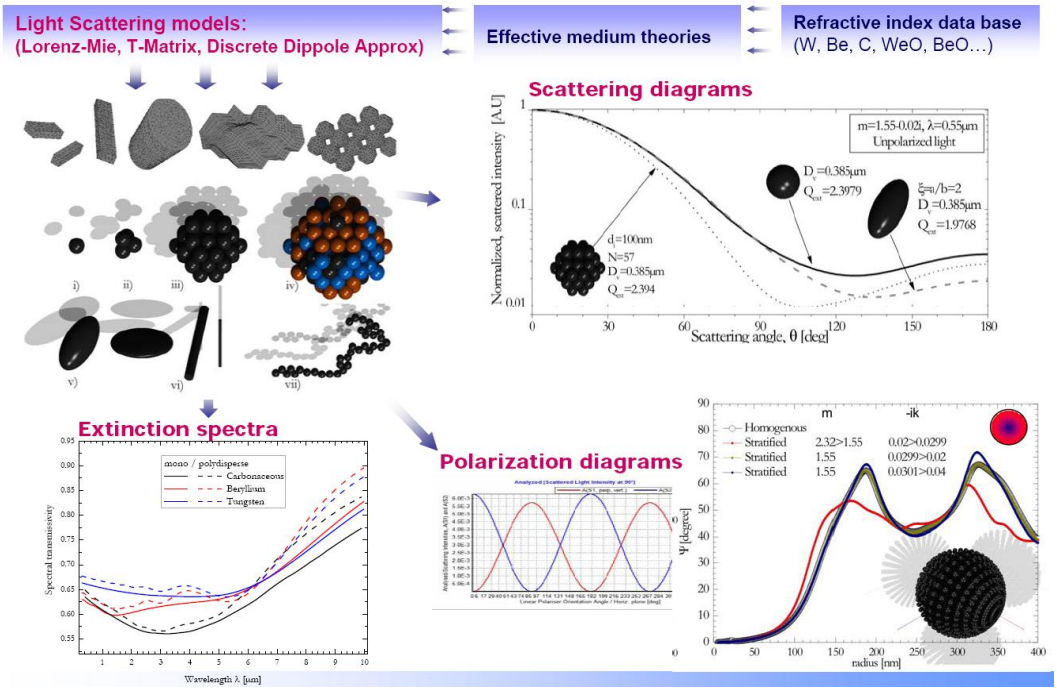

Figure 1: Schematic of the numerical tools developed to predict the scattering properties of dusts

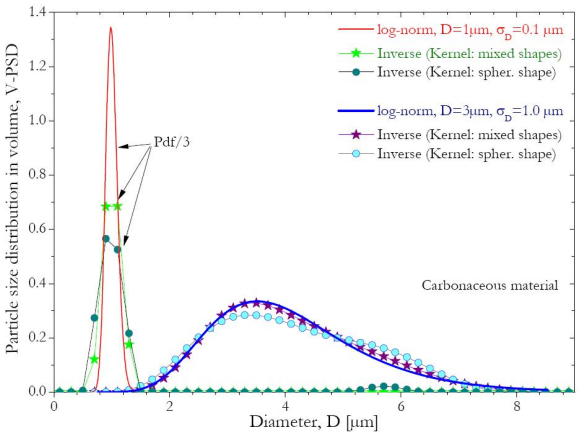

Figure 2: Comparison of initial and reconstructed particle size distributions

Regarding to the constraints imposed for the in-situ characterization of dust, we choose to develop an optical diagnosis based on the measurement of the "turbidity" of the vacuum vessel atmosphere [7, 11]. The corresponding technique will be called further on "light extinction spectrometry". Up to now this technique was mostly used to characterize, in laboratory, liquid suspensions or small droplets in air. However, some studies were devoted to the sizing of crystals or soot aggregates analyses. The challenge here is to extend this technique so as it can satisfy the ITER needs: determination of dust's number concentration and size distribution over a long distance (several meters), only one or two optical accesses, particles having different and complex shapes and compositions. Basically this technique requires passing through the cloud of particles to be analyzed, a collimated and polychromatic beam. The transmitted spectral intensity is collected and directed towards a spectrometer. If the collection of multiple scattered photons is negligible, the beam transmission is given by an exponential decay with arguments: the path length of the beam through the cloud of dusts and the "turbidity of the medium".

The latter depends of an integral quantity which corresponding to the effective extinction cross-section of the particles and the particle number concentration. Mathematically, the problem to solve is a so-called "inhomogeneous Fredholm equation of the first kind". We are looking to extract the particle number concentration and the particle size from the measured transmission and by knowing the calculated kernel (calculated with electromagnetic theories). It is possible to discretize this equation and to obtain a linear algebraic equation. The trivial solution is rejected as it leads to ill conditioned matrices and numerical problems. To stabilize the inversion, based on a Non Negative Least-Square scheme, we use smoothing matrix and a Lagrangian parameter. As an illustration, figure 2 compares the simulated log-normal particle size distribution in volume (V-PSD) and the reconstructed distributions, for different particle shapes and kernels [10, 11].

We performed an intensive bibliographical study to review the various solutions to produce a large band collimated beam: OPO laser, Super Continuum laser, light emitting diodes and thermal sources. We did the same for the detection system: single channel detector with various spectral filters (wheel or linear gradient), monochromator; multichannel spectrometer (CCD, pyroelectric, etc.). For scientific as well as budget reasons we developed a laboratory setup using a thermal source and elliptical mirrors to produce the large band and collimated beam. The spectral analysis is performed with two Fourier Transform (FT) spectrometers working in parallel: a classical FTIR (2.5-16µm) using a Michelson type interferometer and a MEMS based FT-VIS-NIR (0.5-2.6µm) [7]. To validate LES principle it was also necessary to develop a test loop to disperse and generate over a long distance a controlled aerosol of micro and sub micron particles. The system developed uses a Laskin nozzle and a drier to generate aerosols of droplets, crystals or solids particles (depending of the solution atomized), as shown in figure 4.

As an illustration of the experimental results obtained, figure 5 compares the measured and the simulated (using aerosol manufacturer specifications) laser beam transmission for an aerosol of DHES droplets [7].

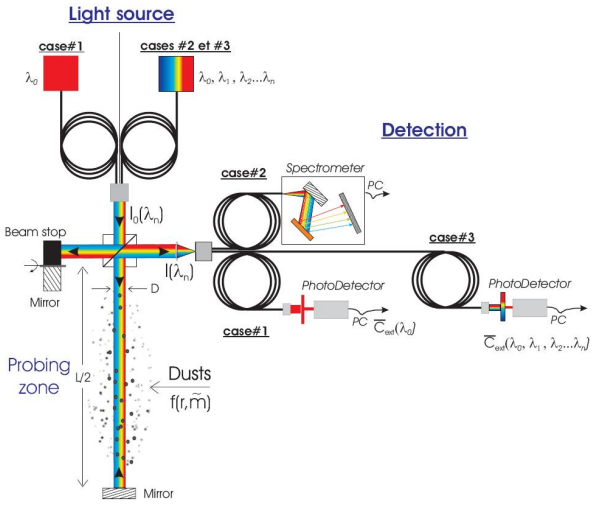

Figure 3: Sketch of the various light extinction spectrometer setups

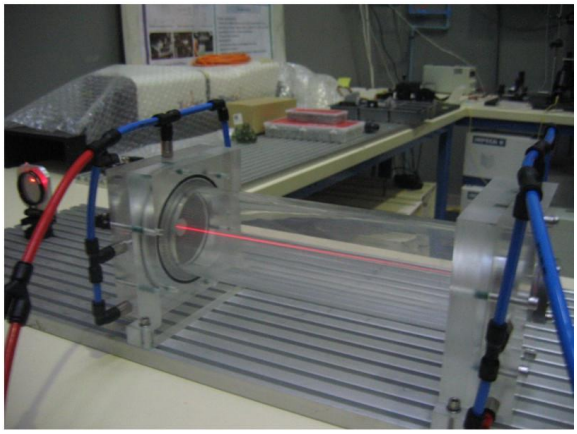

Figure 4: Aerosol test chamber with adjustable length and VIS/Mid-IR windows

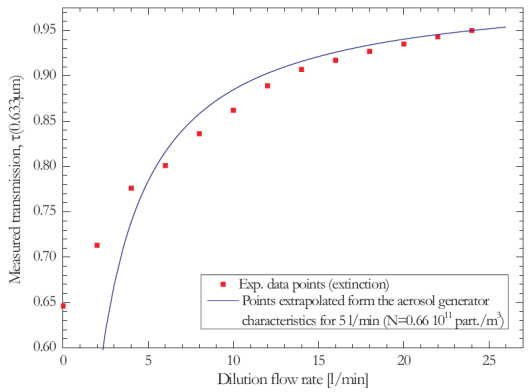

Figure 5: Comparison of laser beam transmission: measured on test chamber and reconstructed from nozzle manufacturer specifications

CONCLUSIONS

Different numerical and theoretical tools were developed to predict the various scattering properties of dust encountered in tokamak, and to inverse the Fredholm integral obtained with collective optical sizing techniques (extinction, diffraction, polarization, etc.). Numerical as well as experimental tests have shown the interest to develop an on-line optical characterization technique based on the principle of the Light extinction Spectrometry [7].

REFERENCES

[1] S. Rosanvallon et al. (2007) Assessment of in-vessel dust measurement and removal Techniques, CEA internal report, NTT-2007.030/TW6-TSS-SEA 5.1 EFDA Task

[2] C. Grisolia et al. (2007), 13th Int. Conf. on Fusion Reactor Material, 10-14 Dec, Nice, France

[3] F. Onofri, G. Gréhan, G. Gouesbet (1995) Appl. Opt. 34 7113

[4] F. Onofri, L. Bergounoux, J.-L. Firpo, J. Mesguish-Ripault (1999) Appl. Opt. 38:4681

[5] Mishchenko M.I., L.D. Travis (1998), J. Quant. Spectrosc. Radiat. Transfer 60 :309

[6] B.T. Draine, P.J. Flatau (1994), J. Opt. Soc. Am. A 11:1491

REPORTS AND PUBLICATIONS

[7] F. Onofri and J. Worms Experimental studies of dust suspension, Convention CEA/ IUSTI-UMR CNRS 6595 n°V 3524.001, Deliverable: 3/3 (Final report)

[8] S. Rosanvallon, C. Grisolia, G. Counsell, S.H. Hong, F. Onofri, J. Worms, J. Winter, B.M. Annaratonee, G. Maddaluno, P. Gasior (2008) Dust control in toka-mak environment, Fusion Engineering and Design 83

[9] S. Rosanvallon, C. Grisolia, P. Delaporte, J. Worms, F. Onofri, S.H. Hong, G. Counsell, J. Winter Dust in ITER: Diagnostics and Removal Techniques, to be published in Journal of Nuclear Materials

[10] F. Onofri, K.F. Ren and C. Grisolia (2008), Development of an in-situ optical diagnostic of dusts in ITER, 14th Int. Symp on Appl. Laser Techniques to Fluid Mechanics, Lisbon, Portugal, July 07–10th

[11] F. Onofri, K.F. Ren and C. Grisolia (2009), Development of an in situ ITER dust diagnostic based on extinction spectroscopy: dedicated light scattering models, to be published in Journal of Nuclear Materials

TASK LEADER

Fabrice ONOFRI

CNRS/University of Provence
IUSTI-UMR 6595, Polytech'Marseille DME
Technopôle Château Gombert
5 rue Enrico Fermi
F-13453 Marseille cedex 13

Tel: 33 4 91 10 68 92
Fax: 33 4 91 10 69 69

e-mail: Fabrice.Onofri@polytech.univ-mrs.fr

UT-S&E-LASER/DEC

Task Title: LASER DECONTAMINATION/TRITIUM REMOVAL - SIMULATIONS OF NEAR-THRESHOLD LASER ABLATION OF METALS

INTRODUCTION

Laser ablation for detritiation and cleaning the inner plasma-facing surfaces of thermonuclear installations is regarded important in the fusion operation. Laser heating and ablation models were developed and applied for simulations of laser heating and ablation of graphite surfaces irradiated by periodically repeating nanosecond laser pulses [1]. A good agreement between the experimental and theoretical results were obtained for nanosecond laser heating and near-threshold laser ablation of technical graphite surface, and the graphite surface with micrometer deposited carbon layer. The laser heating and ablation models developed for graphite were extended to the metal surface, with the metal melting and liquid layer formation being taken into account. Two laser ablation mechanisms (normal vaporization and boiling) were considered.

2007-2008 ACTIVITIES

LASER HEATING AND ABLATION MODELS FOR METALS

The set of the heat equations for electron $T_e(t, \mathrm{r})$ and lattice $T_i(t, \mathrm{r})$ temperatures (time- and space-dependent) in the laser heating of metals can be written as a two-temperature model:

$$c_e^{(vol)} \frac{\partial T_e}{\partial t} = div\left(k_e \nabla T_e\right) - \beta(T_e - T_i) + Q$$
$$c_i^{(vol)} \frac{\partial T_i}{\partial t} = div\left(k_i \nabla T_i\right) + \beta(T_e - T_i) \quad ,$$

where $C_e^{(vol)}$, k_e and $C_i^{(vol)}$, k_i are the specific heat (per unit volume) and thermal conductivity for electron and lattice subsystems, respectively, β is the energy exchange rate between the electrons and lattice, and Q is the energy released in the electron subsystem due to laser radiation absorption. The characteristic time of the electron-lattice relaxation (β-parameter) in metals is in 1 – 100 ps range. Thus, for the nanosecond laser pulses, a lattice temperature is rapidly equalized with the electron temperature and $T = T_e = T_i$ can be introduced. For long pulses (nanosecond and longer), the single heat equation for the common temperature T can be presented as:

$$c^{(vol)}(T)\frac{\partial T}{\partial t} = div\left(k(T)\nabla T\right) + Q(t, r, z) .$$

The laser heating-source term Q can be presented as:

$$Q(t, r, z) = I(t, r) A \alpha \exp(-\alpha z) ,$$

where r and z are the cylindrical coordinates, $I(t, r)$ is the radial distribution of laser intensity on the surface, A is the surface absorptance (the surface reflectivity is $R_S = 1 - A$), and α is the laser absorption coefficient.

If the surface temperature T_S is above the melting temperature T_m , the molten layer formation on the surface should take place. The thickness $d = z_M$ of this layer is increasing during laser heating. Then, after the laser pulse, the molten layer thickness decreases due to its solidification. The Stefan-type boundary condition on the liquid/solid interface $z = z_M$ is applied:

$$k_S \left.\frac{\partial T}{\partial z}\right|_{z=z_M+0} - k_L \left.\frac{\partial T}{\partial z}\right|_{z=z_M-0} = H_f^{(vol)} \frac{dz_M}{dt} ,$$

where k_S and k_L are the thermal conductivity of the solid and liquid state at fusion temperature T_m, $H_f^{(vol)}$ is the specific (per unit of volume) latent heat of melting (fusion) or solidification, depending on the sign of the velocity dz_M/dt of moving liquid/solid interface ($H_f^{(vol)}$ can be somewhat different for the melting and solidification). With this boundary condition, the laser heating of metals can be simulated, at least up to some ablation temperature T_A. Above this temperature, the ablation (due to intensive vaporization/boiling of the metal substance near the surface) should take place. For the two near-threshold ablation regimes, the "boiling regime" and "normal vaporization" were distinguished on the basis of the Stefan-like model with different boundary conditions.

The Stefan-like ablation models for metals

The boiling regime

1D-approximation is quite applicable to consider the laser ablation, on nanosecond or shorter time scales. The corresponding heat equations allow to consider with a good accuracy the surface heating by previous laser pulses with high repetition rate lasers under the initial condition. The calculations of the temperature profile $T_n{}^*(z)$ for the arbitrary pulse number n can be performed with a 3D-laser heating model with the mean thermal properties [1]. For graphite, this model may provide a reasonably good quantitative description of laser heating. For intensive boiling, the Stefan boundary condition on the moving external boundary $z = z_A(t)$ should be written as:

$$k_L(T_S)\left.\frac{\partial T}{\partial z}\right|_{z=z_A(t)} = H_v^{(vol)} v_A(t).$$

Here, $H_v^{(vol)}$ is the volume specific heat of vaporization, or enthalpy jump between the liquid and the gaseous phase of the metal, and $v_A(t) = dz_A(t)/dt$ is the speed of the ablation front. It is more convenient to solve the heat equations in the moving frame with coordinate $\zeta = z - z_A(t)$, where $z_A(t) = \int_0^t v_A(t)\,dt$. The ablation depth h during ablation (for a single n-th laser pulse) can be calculated through the self-consistently found speed of the ablation front, as $h = \int_{t_1}^{t_2} v_A(t)\,dt \equiv z_A(t_2)$.

The normal vaporization regime

Normal surface vaporization is described by the Hertz-Knudsen equation:

$$v_A = (1-\beta)\cdot\frac{P_b}{\rho_L}\left(\frac{m}{2\pi k_B T_S}\right)^{1/2}\exp\left[\frac{H_v^{(mol)}}{R}\left(\frac{1}{T_b}-\frac{1}{T_S}\right)\right].$$

Here, v_A is surface recession velocity, $(1 - \beta)$ is vaporization coefficient close to unity, which is associated with the so-called Knudsen layer near the vaporized surface, P_b is 'boiling pressure' (similar to 1 atm ≈ 0.1 MPa.), T_b is the corresponding boiling temperature, m is metal atomic mass, ρ_L is liquid metal (molten layer) density, $H_v^{(mol)}$ is specific molar latent heat of vaporization, and T_s is surface heating temperature. Also, R = 8.314510 J/(mol K) and k_B is the Boltzmann constant. For normal vaporization regime, the surface temperature is not restricted by the boiling temperature T_b and may be even higher than the boiling temperature, being the result of solution of heat equations with the boundary condition:

$$k_L(T_S)\partial T/\partial\zeta|_{\zeta=0} = H_v^{(vol)} v_A(t).$$

Ablation, due to vaporization mechanism, takes place even before the surface temperature has reached the boiling temperature. In contrast, for the boiling mechanism, the ablation threshold is directly associated with a certain ablation temperature, being the distinguishing feature between the two ablation mechanisms. To distinguish the particular ablation mechanism, the experimental ablation rates should be compared with the corresponding simulation data.

SIMULATIONS OF NEAR-THRESHOLD LASER ABLATION OF METALS

To determine the laser ablation thresholds, the surface modification method, based on detection of the changes in the reflected laser beam from the target resulting from the surface thermal expansion and modification, was applied. Al, Fe, Ni, Cu, Zn, Mo, and Pb metal targets were under study [2, 3]. A Q-switched Nd-YAG laser (532 nm, 5 ns, 0.8 – 80 J/cm^2 laser fluence, 126 μm laser spot diameter, 20 Hz repetition rate) was applied for the ablation threshold measurements. The obtained ablation thresholds are presented in the second column of table 1.

Table 1: Ablation thresholds for different metals at 532 nm wavelength (τ_p = 5 ns)

Metal element	Exp. Ablation threshold (J/cm^2)	F_{th} estimated by $T_A = T_m$	F_{th} estimated by $T_A = T_b$
Al	1.71	0.95	3.74/4.40
Fe	1.00	0.40	0.75/0.89
Ni	0.941	0.42	0.86/1.05
Cu	2.09	0.62	1.48/1.79
Zn	0.980	0.22	0.49/0.66
Mo	2.56	0.77	1.36/1.82
Pb	0.104	0.034	0.19/0.21

Ablation thresholds may be assumed to be associated with the time when the melting temperature is reached by the metal during its laser heating. For all the metals under investigations, the ablation thresholds calculated with the metal melting temperature reached by the end of the laser pulse are systematically much lower than the experimental ones. Thus, in this case, the melting temperature can not play the role of the ablation temperature, and the measured ablation thresholds correspond to temperatures well above the melting threshold. For the boiling temperature being a candidate for the ablation threshold temperature, the discrepancy between the calculated and experimental results can be associated with deviation of the metal absorptance in its liquid state from the reference solid state value. The experimentally measured ablation thresholds are more probably associated with the boiling temperature of the metals.

To compare the boiling regime and the normal vaporization, several calculations were made for the ablation rates to test the codes for the laser ablation of metals. For the same medium parameters, the calculated ablation rates due to normal vaporization are lower than those due to the boiling regime. Correspondingly, the ablation thresholds in the normal vaporization regime are generally much higher than the ablation thresholds calculated in the boiling regime (when it is directly associated with the boiling temperature chosen as an ablation threshold temperature T_A). Figure 1 presents the results of calculations of the ablation rates for both regimes for laser ablation of Cu. The ablation threshold obtained for the boiling is in a good correspondence with the ablation threshold for Cu from table 1. The ablation threshold obtained in the normal vaporization is several times higher. The calculated ablation rates are also quite different.

CONCLUSIONS

The modeling of near-threshold laser ablation of metals by nanosecond and picosecond laser pulses was considered. The formation of the molten layer during laser heating of metals is implemented into the model. The Stefan-like

simulation model of laser ablation is used to estimate the ablation rates. Both vaporization and boiling regimes of laser ablation were implemented into the model. To consider the picosecond laser ablation, two-temperature laser heating equations with different electron and lattice temperatures and with electron-lattice coupling were also implemented. Laser ablation thresholds for metals (Cu, Al, Fe, Zn, Ni, Pb, Mo) were measured experimentally with 532 nm, 5 ns laser pulses in 0.8 – 80 J/cm^2 fluence range. The theoretical analysis of experimentally measured laser ablation thresholds of metals is presented. The quantitative comparison between the calculation results on the ablation rates obtained for different ablation regimes (boiling and normal vaporization) was made. For Cu, the ablation threshold obtained for the boiling regime is in a good correspondence with the experimental one.

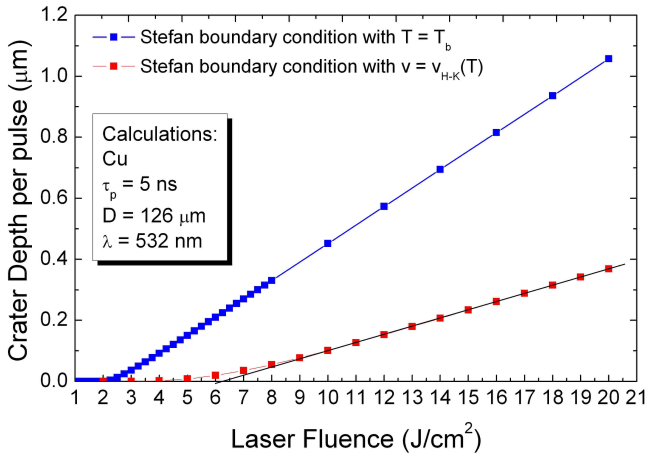

Figure 1: Copper ablation rates calculated for boiling regime (blue curve) and normal vaporization (red curve). 532 nm wavelength, 5 ns laser pulses

REFERENCES

[1] A. Semerok, S. V. Fomichev, J.-M. Weulersse, F. Brygo, P.-Y. Thro, C. Grisolia, *Heating and ablation of tokamak graphite by pulsed nanosecond Nd-YAG lasers*, J. Appl. Phys. 101, 084916 (2007)

[2] A. Semerok, C. Chaléard, V. Detalle, J.-L. Lacour, P. Mauchien, P. Meynadier, C. Nouvellon, B. Sallé, P. Palianov, M. Perdrix, G. Petite, *Experimental investigations of laser ablation efficiency of pure metals with femto, pico and nanosecond pulses*, Appl. Surf. Sci. 138–139, 311 (1999)

[3] A. Semerok, B. Sallé, J.-F. Wagner, G. Petite, *Femtosecond, picosecond and nanosecond laser microablation: Laser plasma and crater investigation*, Laser and Particle Beams 20, 67 (2002)

REPORTS AND PUBLICATIONS

S. V. Fomichev, A. Semerok, *Simulation of near-threshold laser ablation of metals*, CEA report, NT DPC/SCP/207-248, 2007

TASK LEADER

Alexandre SEMEROK

DEN/DPC/SCP/LILM
CEA-Saclay
F-91191 Gif-sur-Yvette Cedex

Tel: 33 1 69 08 65 57
Fax: 33 1 69 08 78 84

e-mail: alexandre.semerok@cea.fr

UT-S&E-LiPbwater

Task Title: MODELISATION OF THE INTERACTION BETWEEN LiPb AND WATER

INTRODUCTION

The work performed on this task has been devoted to the analysis of previous programs. The objective was to enhance the major contributors to this energetic interaction and the potential damages on the surrounding structures.

Due to the replaced operated on the breeding blanket concepts and particularly the replacement of water coolant by Helium, the problem, though less crucial, was still to be investigated with different boundary conditions.

2007-2008 ACTIVITIES

The previous programs were realized in the context of the Water Cooled Lithium Lead TBM design. In Europe, the BLAST, LIFUS and RELA experimental programs were carried out to assess the consequences of injecting pressurized water in a tank filled with LiPb. Calculations with the SIMMER code were performed to model the first seconds of the transient corresponding to the thermal interaction due to the energy released by water droplets in contact with the hot LiPb. The agreement between theoretical and experimental results was pretty good, though the boundary conditions were identified to have a strong influence on the results.

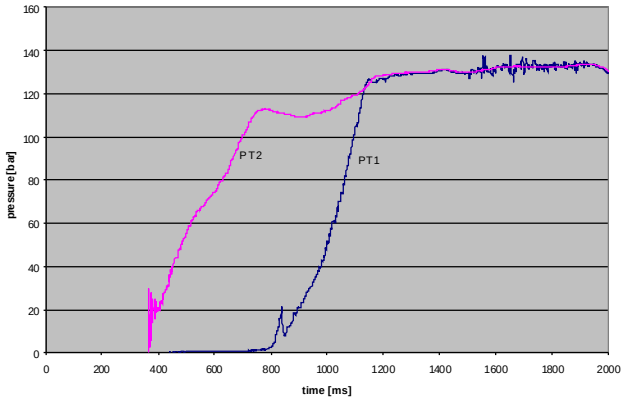

Figure 1: Comparison between experiment (left) and SIMMER calculation (right) for LiPb-water interaction

As shown on figure 1, the agreement between experimental results and SIMMER-III simulation was pretty good. This calculation was made for injection of subcooled water in a tank filled with liquid LiPb at 350 °C, which was performed in the LIFUS facility.

From this analysis it was found that:

- The principal parameters for the input data set are:
  - the modeling of the injector, interaction tank, tube and expansion tank in r/z geometry,
  - the quality of the meshing,
  - the Pb/Li thermo-physical laws.

- The following 3 physical phases were identified:
  - first Pressure peak calculated by SIMMER (thermal peak),
  - pressure stabilization (calculated by SIMMER),
  - second peak (Hydrogen production due to chemical reaction) - not studied with SIMMER.

During meetings held in 2007, the continuation of a Research and Development program was proposed in order to comply with the new breeder blanket designs.

The objective of this program, adapted to the ITER geometry and thermal conditions, is to have a first idea of the expected pressure loads in the Vacuum Vessel due to Pb-Li/water interaction.

A coordinated program was proposed, on different time scale:

Short term proposition:

- based on current knowledge: identify which can be the envelope phenomena to be presented to the Safety Regulators (Preliminary Safety Report),
- represent ITER geometry with SIMMER III 3D with the same modeling assumptions as it was done in LIFUS representation,
- use MELCOR (with Pb-Li reaction model) to model LIFUS experiments and ITER.

Mid term proposition:

- introduce the chemical reaction in SIMMER based on MELCOR and LINT models to get a full representation of the 3 phases,
- taking benefit of the LIFUS results, define an experimental program to better model the Pb-Li interaction phenomena in the ITER conditions.

CONCLUSIONS

The work performed was mainly aimed at defining a work program according to the new specificities of breeding blankets. The possible coordinated program is conditioned to the continuation of an international cooperation in the field of liquid metal water interaction.
The previous works demonstrated that these phenomena were of prime importance for Vacuum Vessel safety concerns and that a precise modeling was necessary in order to have a good idea of the possible damages that such interaction could produce. The reactor design must account for these potential accidental loadings.
A long term program for this technical problem, including both experimental and theoretical approaches, should be set up.

TASK LEADER

Thierry CADIOU

DEN/DER/SESI
CEA-Cadarache
F-13108 Saint-Paul-lez-Durance Cedex

Tel: 33 4 42 25 66 17
Fax: 33 4 42 25 71 87

e-mail: thierry.cadiou@cea.fr

UT-S&E-TRITIUM-IMPACT

Task Title: IMPACT OF CONTAMINATION WITH TRITIUM AT CELL LEVEL

INTRODUCTION

Genetic alteration can result in severe pathologies. However, cells can take advantage of genetic diversity generation, in physiological processes such as meiosis and immunoglobulin diversification. Faithful genome transmission requires the co-ordination of a network of pathways including cell cycle checkpoint, DNA replication, DNA repair/recombination and programmed cell death.

Ionizing radiation produces different kinds of damages among them oxidative stress and DNA double strand breaks (DSB). DSB are the most toxic lesions, which can also be induced by DNA replication arrest. Accumulation of these lesions can trigger cell cycle checkpoints and programmed cell death but non-accurate repair of DSB can lead to genetic rearrangements. DSB can be repaired by different systems, which are mainly homologous recombination (HR) or non-homologous end-joining (NHEJ).

Tritium is present in the environment from different natural or industrial sources: cosmic ray interaction with atmospheric molecules, nuclear reactions in the earth's crust, nuclear testing in the atmosphere, continuous release from nuclear plants, normal and incidental release from tritium production facilities and the nuclear fusion facilities to be developed for energy production [Okada, 1993 #1105]. Crucial environmental concerns are caused by naturally and synthetic radioactive compounds, which may cause either external irradiation or internal contamination. In the case of external exposure, the radioactive source should emit sufficiently penetrating rays to reach targets and to cause biological effects. ^{3}H (0.019 MeV) emits poorly penetrating b-rays, compared to highly penetrating γ-rays (^{137}Cs, 0.662 MeV). However, radioactive compounds emitting rays of low penetration may also bring about biological concerns if they are incorporated in biological tissues, resulting in *in situ* self-irradiation. In addition, because of the low penetration, the disintegration energy could become an amplification factor since the deposition of energy is concentrated in the direct environment of the isotope. Thus, paradoxically, risks are increased when the energy emitted by the contaminant decreases. For instance, ^{3}H-thymidine (0.019 MeV), which deposits 70% of its energy into the nucleus, is more toxic and more efficient to stimulate HR than ^{14}C-thymidine (0.157 MeV), which deposits only 20% of its energy into the nucleus. This underlies the fact that the energy deposited into the nucleus is an essential parametric determinant of cell viability and genetic alteration after contamination with radioactive compounds. In particular, this may be responsible for the toxicity and genetic effects at lower doses.

To produce DNA damages, external irradiation requires sufficient energy to reach the nucleus. In such conditions, Tritium radiation cannot reach the DNA. However, organically bound (OBT) tritium can be incorporated into the cell resulting in an *in situ* chronic irradiation, which is now able to reach the biological target. In this situation, the low penetration of the beam becomes an amplification factor: indeed, when Tritium is incorporated into the nuclear DNA (with tritiated nucleotides), due to the short course of the rays, 70% of the energy is deposited into the nucleus. The impact of Tritium on DNA integrity directly derives from the deposited energy and not from any chemical poisoning since tritium only generates water. However association with another contaminant, which affects cell response, can produce synergistic effects. Moreover, it is also possible that tritium incorporation engages cells in a response that could be inappropriate for a concomitant associated stress.

The goal of this task is to study the impact of contamination with Tritium at the cell level. Homologous recombination (HR) and non-homologous end-joining (NHEJ) are the main processes for DSB repair. Our project aimed to study the impact of contamination with Tritium on cell survival, cell cycle, mutagenesis, HR and NHEJ.

2007-2008 ACTIVITIES

MEASUREMENT OF TRITIUM INCORPORATION TOXICITY (CLONE SURVIVAL)

We incorporated different amount of ^{3}H-thymidine in mammalian cells. Incubation of cells with ^{3}H-thymidine was performed for 24 hours, which corresponds to the maximum incorporation of tritium. This treatment only slightly affected the capacity of cells to form colonies even at the highest incorporated doses (40% at the plateau level).

Importantly, when comparing the survival curves after treatment with ^{3}H-thymidine versus ^{14}C-thymidine, the survival curves exhibits different shapes, consistent with the differences in the deposited energy into the nucleus: 70% with ^{3}H-thymidine and only 20% with ^{14}C-thymidine. While with ^{14}HC-thymidine curves are linear as a function of the incorporated doses, they are biphasic with ^{3}H-thymidine, underlying a low dose effect with this latter contaminant. In addition, at low doses cells defective for HR or for NHEJ both exhibit increased sensitivity; at higher incorporated doses, only NHEJ-defective cells show increased sensitivity to the treatment.

These data reveal a specific role for HR at low doses of ^{3}H-thymidine incorporated. In addition, they show that

tritium incorporated into the nucleus generates DNA double strand breaks, which should be repaired to ensure cell viability.

INDUCTION OF γ-H2AX AND RAD51 FOCI BY ^{3}H-THYMIDINE

Induction of γ-H2AX and Rad51 foci by tritium

Treatment with external ionizing radiation (IR) induces the phosphorylation of the histon H2AX, which is localized at the double strand breaks and is then visualized in foci, by immunofluorescence [5]. The incorporation ^{3}H-thymidine induces 5 to 12 γ-H2AX per cell for doses over 10^5 dpm/10^6 cells. These data confirm our survival experiments performed in NHEJ-deficient cells: the incorporation of high doses of ^{3}H-thymidine generates DNA double strand breaks, which are signaled.
In response to genotoxic stresses Rad51 assemble into nuclear foci, which are considered to represent recombination repair foci [4]. Rad51 foci appeared at doses over $3\cdot10^4$ dpm/10^6 cells and rapidly reached a plateau level at $1\cdot10^5$ dpm/10^6 cells. These data indicate that a part of the damages generate by ^{3}H-thymidine are processed by homologous recombination.

STIMULATION OF HOMOLOGOUS RECOMBINATION (HR)

Using single copy substrates allowing monitoring HR in a chromosomal context, we show that non-lethal doses of ^{3}H-thymidine incorporation result in a tremendous stimulation of RAD51-dependent HR. IR are unable to stimulate HR at such level (10 fold lower), even with highly toxic doses. These data show the involvement of HR for repairing damages into the nucleus induced by tritium.

CONCLUSIONS

Taken together, these data show that tritium incorporation into nucleus, even at doses apparently not toxic (in term of survival) provokes a genotoxic stress. Particularly these data point out at a low dose effect. In contrast with high rate external radiation, few damages are generated and the cell is able to easily manage them. However these damages can generate events of genetic instability resulting from too high HR frequency. These data could thus question the admitted exposition doses to tritium as well as the relative biological efficiency (RBE) generally associated to this isotope, when it is incorporated into nucleus.

REFERENCES

[1] Broome, E. J., Brown, D. L., and Mitchel, R. E. (2002). Dose responses for adaption to low doses of (60)Co gamma rays and (3)H beta particles in normal human fibroblasts. Radiat Res 158, 181-186

[2] Burki, H. J., Bunker, S., Ritter, M., and Cleaver, J. E. (1975). DNA damage from incorporated radioisotopes: influence of the 3H location in the cell. Radiat Res 62, 299-312

[3] Cronkite, E. (1979). Tritium and Other Radionuclide Labeled Organic Compounds Incorporated in Genetic Material (Washington, DC: NCRP)

[4] Haaf, T., Golub, E. I., Reddy, G., Radding, C. M., and Ward, D. C. (1995). Nuclear foci of mammalian Rad51 recombination protein in somatic cells after DNA damage and its localization in synaptonemal complexes. Proc Natl Acad Sci U S A 92, 2298-2302

[5] HRogakou, E. P., Pilch, D. R., Orr, A. H., Ivanova, V. S., and Bonner, W. M. (1998). DNA double-stranded breaks induce histone H2AX phosphorylation on serine 139. J Biol Chem 273, 5858-5868

REPORTS AND PUBLICATIONS

Yannick Saintigny, Stéphane Roche, Delphine Meynard, and Bernard S. Lopez (2008). Homologous recombination is involved in the repair response of mammalian cells to low doses of tritium contamination. *Radiation Res*., 170, 172-183

Fayza Daboussi, Sylvain Courbet, Simone Benhamou, Patricia Kannouche, Margaret Z. Zdzienicka, Michelle Debatisse and Bernard S. Lopez (2008) Homologous recombination defect affects replication fork progression in mammalian cells. *J. Cell Science*, 121, 162-166

Fabien Delacôte and Bernard S. Lopez (2008) Importance Of The Cell Cycle Phase For The Choice Of The Appropriate DSB Repair Pathway, For Genome Stability Maintenance: The Trans-S Double-Strand Break Repair Model. *Cell cycle*, 7, 33-38

Fabien Delacôte, Ludovic Deriano, Sarah Lambert, Pascale Bertrand, Yannick Saintigny and Bernard S. Lopez. (2007) Chronic exposure to sub-lethal soses of rasiation mimetic Zeocin selects for clones deficient in homologous recombination" *Mutation Research Fundamental and Molceular Mechanisms of Mutagenesis*, 615, 125-133

TASK LEADER

Bernard LOPEZ

DSV/IRCM, UMR217 CNRS/CEA, LMR
BP 6
F-92265 Fontenay-aux-Roses Cedex

Tel: 33 1 46 54 88 35
Fax: 33 1 46 54 89 55

e-mail: bernard.lopez@cea.fr

APPENDIX 1 : DIRECTIONS CONTRIBUTION TO THE FUSION PROGRAMME

CEA

DSM

Direction des **S**ciences de la **M**atière

IRFM

Institut de **R**echerche sur la **F**usion par confinement **M**agnétique

Task	Area	Site
CEFDA04-1127	Magnets	Cadarache
CEFDA05-1248	PFC	Cadarache
CEFDA05-1271	Heating	Cadarache
CEFDA05-1293	PFC	Cadarache
CEFDA05-1329	Heating	Cadarache
CEFDA05-1336	Plasma Edge & PWI	Cadarache
CEFDA05-1370	Magnets	Cadarache
CEFDA06-1372	PFC	Cadarache
CEFDA06-1373	PFC	Cadarache
CEFDA06-1376	Remote Part.	Cadarache
CEFDA06-1386	JET Techno	Cadarache
CEFDA06-1401	PFC	Cadarache
CEFDA06-1409	Heating	Cadarache
CEFDA06-1420	Heating	Cadarache
CEFDA06-1422	JET Techno	Cadarache
CEFDA06-1429	Diagnostics	Cadarache
CEFDA06-1438-PP1	Diagnostics	Cadarache
CEFDA06-1438-PP11	Diagnostics	Cadarache
CEFDA06-1438-PP21	Diagnostics	Cadarache
CEFDA06-1438-PP22	Diagnostics	Cadarache
CEFDA06-1483	Design Sup.& Proc.	Cadarache
CEFDA06-1521	Magnets	Cadarache
CEFDA07-1700-1556	Heating	Cadarache
CEFDA07-1700-1572	Heating	Cadarache
CEFDA07-1700-1578	Operation	Cadarache
CEFDA07-1700-1600	Design Sup.& Proc.	Cadarache
CEFDA07-1700-1617	PFC	Cadarache
CEFDA07-1700-1623	Vessel	Cadarache
JW6-FT-3.36	JET Techno	Cadarache
JW6-FT-4.9	JET Techno	Cadarache
TW1-TMS-PFCITE	Magnets	Cadarache
TW5-TPDC-IRRCER-D03	Diagnostics	Cadarache
TW5-TRP-002-D03a	System studies	Cadarache
TW6-THHN-ASD3	Heating	Cadarache
TW6-TMSC-FSTEST	Magnets	Cadarache
TW6-TPP-DUSMEAS-D01a	Plasma Edge & PWI	Cadarache
TW6-TRP-002-D02	System studies	Cadarache
TW6-TRP-006	System studies	Cadarache
TW6-TSL-004	Safety	Cadarache
TW6-TSS-SEA5.1	Safety	Cadarache

INAC

Institut **Na**nosciences et **C**ryogénie

CEFDA06-1515	Cryo	Grenoble
CEFDA07-1700-1565	Cryo	Grenoble
CEFDA07-1700-1603	Magnets	Grenoble
CEFDA07-1700-1606	Magnets	Grenoble

IRFU

Institut de **R**echerche sur les lois **F**ondamentales de l'**U**nivers

CEFDA04-1170	Magnets	Saclay
TW5-TMSF-HTSPER	Magnets	Saclay

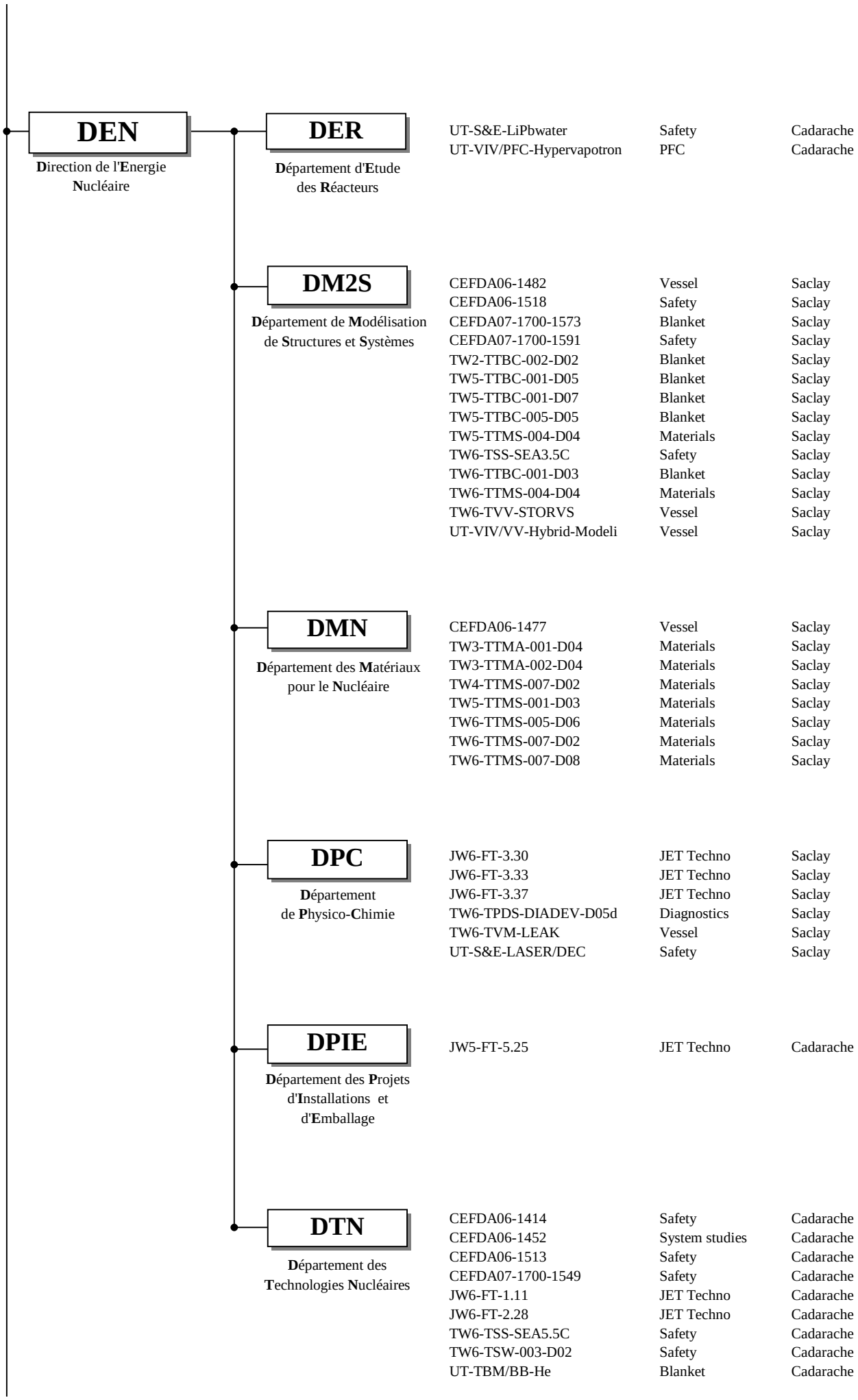
DEN
Direction de l'Energie Nucléaire
DER
Département d'Etude des Réacteurs
UT-S&E-LiPbwater Safety Cadarache
UT-VIV/PFC-Hypervapotron PFC Cadarache
DM2S
Département de Modélisation de Structures et Systèmes
CEFDA06-1482 Vessel Saclay
CEFDA06-1518 Safety Saclay
CEFDA07-1700-1573 Blanket Saclay
CEFDA07-1700-1591 Safety Saclay
TW2-TTBC-002-D02 Blanket Saclay
TW5-TTBC-001-D05 Blanket Saclay
TW5-TTBC-001-D07 Blanket Saclay
TW5-TTBC-005-D05 Blanket Saclay
TW5-TTMS-004-D04 Materials Saclay
TW6-TSS-SEA3.5C Safety Saclay
TW6-TTBC-001-D03 Blanket Saclay
TW6-TTMS-004-D04 Materials Saclay
TW6-TVV-STORVS Vessel Saclay
UT-VIV/VV-Hybrid-Modeli Vessel Saclay
DMN
Département des Matériaux pour le Nucléaire
CEFDA06-1477 Vessel Saclay
TW3-TTMA-001-D04 Materials Saclay
TW3-TTMA-002-D04 Materials Saclay
TW4-TTMS-007-D02 Materials Saclay
TW5-TTMS-001-D03 Materials Saclay
TW6-TTMS-005-D06 Materials Saclay
TW6-TTMS-007-D02 Materials Saclay
TW6-TTMS-007-D08 Materials Saclay
DPC
Département de Physico-Chimie
JW6-FT-3.30 JET Techno Saclay
JW6-FT-3.33 JET Techno Saclay
JW6-FT-3.37 JET Techno Saclay
TW6-TPDS-DIADEV-D05d Diagnostics Saclay
TW6-TVM-LEAK Vessel Saclay
UT-S&E-LASER/DEC Safety Saclay
DPIE
Département des Projets d'Installations et d'Emballage
JW5-FT-5.25 JET Techno Cadarache
DTN
Département des Technologies Nucléaires
CEFDA06-1414 Safety Cadarache
CEFDA06-1452 System studies Cadarache
CEFDA06-1513 Safety Cadarache
CEFDA07-1700-1549 Safety Cadarache
JW6-FT-1.11 JET Techno Cadarache
JW6-FT-2.28 JET Techno Cadarache
TW6-TSS-SEA5.5C Safety Cadarache
TW6-TSW-003-D02 Safety Cadarache
UT-TBM/BB-He Blanket Cadarache

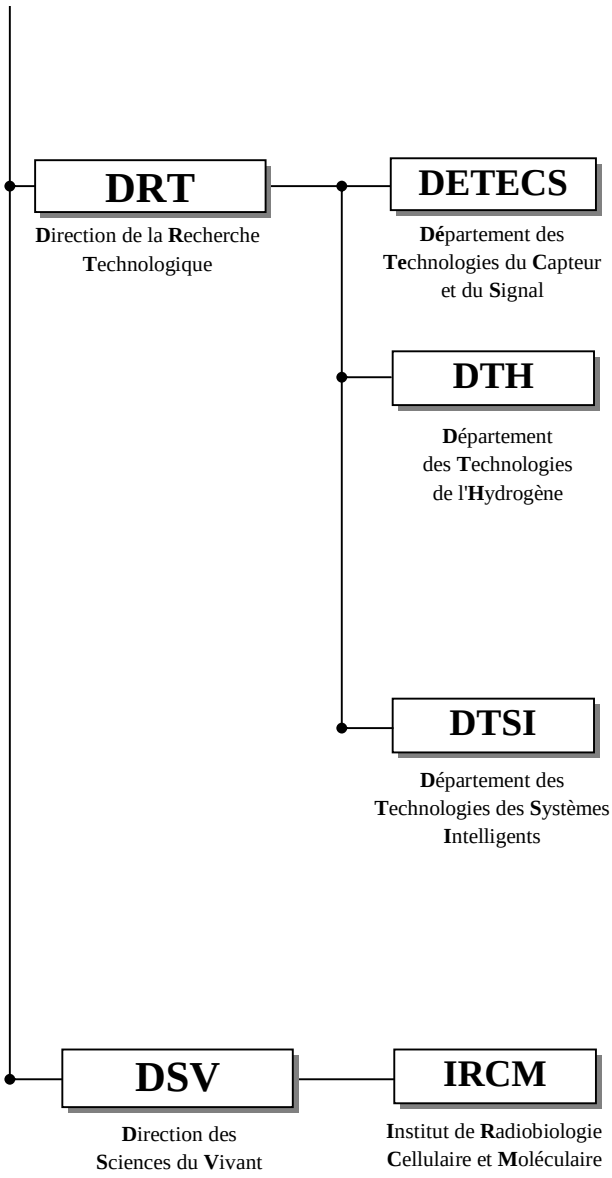

CEFDA04-1202	Vessel	Saclay
CEFDA05-1257	PFC	Grenoble
CEFDA05-1308	PFC	Grenoble
CEFDA05-1309	PFC	Grenoble
CEFDA06-1411	PFC	Grenoble
CEFDA07-1700-1622	PFC	Grenoble
TW5-TTBC-002-D02	Blanket	Grenoble
TW5-TVM-COMADA	PFC	Grenoble
TW6-TTBC-002-D01	Blanket	Grenoble
TW6-TVM-Braze	Vessel	Grenoble
UT-VIV/PFC-HIP	PFC	Grenoble
CEFDA05-1285	System studies	Fontenay
CEFDA05-1359	Materials	Fontenay
TW5-TVR-WHMAN	Remote Handling	Fontenay
UT-VIV/AM-AIA	Remote Handling	Fontenay
UT-S&E-Tritium-Impact	Safety	Fontenay

EXTERNAL COLLABORATIONS

CNRS (French National Centre for Scientific Research)

INPG

UT-S&E-dust-suspension	Safety	Marseille
TW6-TPP-DUSTGEN-D01	Plasma Edge & PWI	Villetaneuse
TW6-TPP-DUSTGEN-D02b	Plasma Edge & PWI	Marseille
TW6-TPP-BETUNCMOD-D01b	Plasma Edge & PWI	Pessac
CEFDA06-1470	Materials	Grenoble

Industrial collaborations

CEFDA07-1700-1542	Vessel	Orbital/ Vonnas

APPENDIX 2 : ALLOCATIONS OF TASKS

EFDA TECHNOLOGY PROGRAMME

		Unit	*Site*
Physics Integration			
Plasma Edge and Plasma Wall Interaction (PWI)			
CEFDA05-1336 CEFDA07-1700-1578	TW5-TPO-ERGITER and TW6-TPO-ELMCONT: Resonant magnetic perturbation (RMPs) for Edge Localized modes (ELMs) suppression in ITER	IRFM	Cadarache
TW6-TPP-BETUNCMOD-D01b	Molecular dynamics simulations of mixed material formation at the ITER divertor Report on the construction of the potentials to study the interactions in the Be-C, Be-W and W-C systems in interaction with D/T and noble gases (Ar, Ne, He) to be used in molecular dynamics simulations	CNRS	Pessac
TW6-TPP-DUSMEAS-D01a	Demonstration of diagnostic techniques for time resolved dust measuremnts in tokamaks	IRFM	Cadarache
TW6-TPP-DUSTGEN-D01	Dust generation rates for the plasma edge/divertor conditions expected for the ITER Q_{DT} = 10 reference scenario with a CFC/W and W divertor target and a Be wall	CNRS	Villetaneuse
TW6-TPP-DUSTGEN-D02b	Evaluation of dust generation mechanisms at the ITER SOL and divertor plasma; Analogy between cluster production by laser ablation and dust generation in ITER	CNRS	Marseille
Heating and Current Drive			
CEFDA05-1271 CEFDA07-1700-1556	TW6-TPHI-ICHDESREW and TW5-TPHI-ITERDES3: Design of the ITER ICRF antenna	IRFM	Cadarache
CEFDA05-1329	TW6-TPHI-ICFS: Faraday shield modelling and RF sheath dissipation	IRFM	Cadarache
CEFDA06-1409	TW6-TPHI-ICRFCOORD2: Coordination of ITER ICRF antenna design R&D activities	IRFM	Cadarache
CEFDA06-1420	TW6-TPHI-ICFSDES1: Faraday shield for design for the ITER ICRF antenna array	IRFM	Cadarache
CEFDA07-1700-1572	TW6-TPHI-RFPFCPOW2: Evaluation of expected power/particle fluxes on ITER PFCs caused by local acceleration of particles in RF fields	IRFM	Cadarache
TW6-THHN-ASD3	SINGAP negative ion accelerator: Study of the beamlet halo, dark currents and verification of electrostatic withstand capability and tolerable stored energy in case of electrical discharges	IRFM	Cadarache
Diagnostics			
CEFDA06-1429	TW6-TPDS-DIASUP1: Support of diagnostic design for ITER Diagnostic port-plug procurement, diagnostic port-plug engineering & integration, & divertor thermography	IRFM	Cadarache
CEFDA06-1438-PP1	TW6-TPDS-DIADES1: Diagnostic design for ITER - PP1: Plasma position reflectometry	IRFM	Cadarache
CEFDA06-1438-PP11	TW6-TPDS-DIADES1: Diagnostic design for ITER - PP11: Visible/IR wide angle viewing system	IRFM	Cadarache

CEFDA06-1438-PP21	TW6-TPDS-DIADES1: Diagnostic design for ITER - PP21: Bolometry	IRFM	Cadarache
CEFDA06-1438-PP22	TW6-TPDS-DIADES1: Diagnostic design for ITER - PP22: Magnetic diagnostics: Development of a fibre optic current sensor suitable for ITER	IRFM	Cadarache
TW5-TPDC-IRRCER-D03	Assessment of IR fibres for thermography applications, Initial gamma induced effects, then neutron irradiations - Fibre selection and provision, Diagnostic preparation and measurements	IRFM	Cadarache
TW6-TPDS-DIADEV-D05d	Theorical and experimental evaluations of laser cleaning methods for diagnostics and mirrors	DPC	Saclay

Remote participation

CEFDA06-1376	TW5-TPR-RPSUP: Support to EFDA remote participation	IRFM	Cadarache

Vessel-In Vessel

Vessel-Blanket and Materials

CEFDA04-1202	TW5-TVV-RFUT: Synthesis of ultrasonic inspection of the vacuum vessel welded mock-ups for ITER : cooperation with RF	DETECS	Saclay
CEFDA06-1477	TW6-TVM-LIP4: Modification of ITER materials documents, assessment of material data and maintenance of a database	DMN	Saclay
CEFDA06-1482	TW6-TVA-IHYB2: Industrialisation and weld quality issues of high productive laser/arc hybrid for thick section welding of ITER grade SS material	DM2S	Saclay
CEFDA07-1700-1542	TW6-TVV-TLDES: Design and manufacture of cosmetic welding heads on EB welds of VV sectors	Orbital	Vonnas
CEFDA07-1700-1623	TW6-TVV-LEAKD1: Leak localisation for in-vessel components	IRFM	Cadarache
TW6-TVM-Braze	Testing of silver free braze materials with Be	DTH	Grenoble
TW6-TVM-LEAK	Investigation of laser-based techniques for leak localization, and demonstration of a laser-based technique for leak detection and localization compatible with ITER requirements	DPC	Saclay
TW6-TVV-STORVS	Storage of stainless steel material for VV	DM2S	Saclay

Plasma Facing Components

CEFDA05-1248	TW5-TVD-ACCEPT: Influence of carbon erosion on the acceptance criteria of the ITER divertor	IRFM	Cadarache
CEFDA05-1257	TW5-TVB-JOINOP: Optimisation of Be/CuCrZr HIP joining for FW panels	DTH	Grenoble
CEFDA05-1293	TW5-TVD-NDTEST1: Upgrade of the SATIR test bed for infrared thermographic inspections - Construction phase	IRFM	Cadarache
CEFDA05-1308	TW5-TVB-DES2: Destructive examination of first wall panels and mock-ups	DTH	Grenoble
CEFDA05-1309	TW5-TVB-INMOCK2: Manufacture of First Wall mock-ups for in-pile experiments	DTH	Grenoble
CEFDA06-1372	TW5-TVD-FABCON: Development of fabrication control methods for the ITER divertor	IRFM	Cadarache

CEFDA06-1373	TW6-TVD-ACCREV: Definition of acceptance criteria for the ITER Divertor	IRFM	Cadarache
CEFDA06-1401	TW6-TVD-SATIR: SATIR tests of vertical target qualification prototypes	IRFM	Cadarache
CEFDA06-1411	TW6-TVB-ACCTEST: Be/CuCrZr HIP joining for ITER FW qualification tests	DTH	Grenoble
CEFDA07-1700-1617	TW6-TVB-FWPROT2: Design of clamped poloidal limiters for ITER	IRFM	Cadarache
CEFDA07-1700-1622	TW6-TVB-HIPJOIN: HIP joining development and application to the FW design of NBI modules	DTH	Grenoble
TW5-TVM-COMADA	Investigations of the effect of creep-fatigue interaction on the mechanical performance and lifetime of CuCrZr	DTH	Grenoble

Remote Handling

TW5-TVR-WHMAN	Development of a linear hydraulic joint for remote handling application	DTSI	Fontenay

Magnet System and Cryogenics

CEFDA04-1127	TW4-TMSC-SAMAN1: Manufacture of subsize samples	IRFM	Cadarache
CEFDA04-1170	TW4-TMSC-RESDEV: Development and testing on new resin solution	IRFU	Saclay
CEFDA05-1370	TW6-TMSC-TFPRO: ITER TF full size prototype conductor	IRFM	Cadarache
CEFDA06-1515	TW6-TES-CRYO-03: Design of the ITER cryoplant and cryodistribution system	INAC	Grenoble
CEFDA06-1521	TW6-TMSC-HEAT1: Heat treatment optimisation of advanced Nb_3Sn strands	IRFM	Cadarache
CEFDA07-1700-1565	TW6-TTFF-VP76: Cryopump valve box and cryo jumper design study	INAC	Grenoble
CEFDA07-1700-1603	TW6-TMSM-CRYOGT: Materials cryogenic testing	INAC	Grenoble
CEFDA07-1700-1606	TW6-TMST-VINCAN: Thermohydraulic analysis for the ITER cryogenic system	INAC	Grenoble
TW1-TMS-PFCITE	Poloidal Field Conductor Insert (PFCI)	IRFM	Cadarache
TW5-TMSF-HTSPER	HTS materials for fusion magnets	IRFU	Saclay
TW6-TMSC-FSTEST	Participation to conductor tests and evaluation of test results	IRFM	Cadarache

Tritium Breeding and Materials

Breeding Blanket

CEFDA07-1700-1573	TW6-TTB-COMON: Technical monitoring and assessment of the KNT/ASSYSTEM contract ESC06-002	DM2S	Saclay

Helium Cooled Lithium Lead (HCLL) Blanket

TW2-TTBC-002-D02	Blanket manufacturing technologies Manufacturing and testing of mock-ups Qualification samples for HCLL and HCPB TBM	DM2S	Saclay

TW5-TTBC-001-D05	TBM design, integration and analysis Finalization of HCLL TBM prototypical mock-up including internal heat system	DM2S	Saclay
TW5-TTBC-001-D07	TBM design, integration and analysis Detailed TBM development workplan up to EM-TBM installation in ITER	DM2S	Saclay
TW5-TTBC-002-D02	Blanket manufacturing technologies Feasibility of the tube forming + HIP fabrication process for the bent part of the FW of HCLL and HCPB TBMs	DTH	Grenoble
TW5-TTBC-005-D05	Process and auxiliary components Modelling of T permeation and behaviour with experimental determination of key modelling parameters	DM2S	Saclay
TW6-TTBC-001-D03	HCLL TBM design and integration analyses	DM2S	Saclay
TW6-TTBC-002-D01	Blanket manufacturing technologies Improvement of the 2-step HIP diffusion welding process for the manufacturing of TBMs subcomponents	DTH	Grenoble

Materials Development

Reduced Activation Ferritic Martensitic (RAFM) Steels

CEFDA06-1470	TW6-TTMS-MODUNI2: DD simulation of the interaction and He cavities in Fe-alpha	INPG	Grenoble
TW4-TTMS-007-D02	Modelisation of irradiation effects Ab initio study of the interaction of Cr atoms & precipitates with He and He-V clusters in α-Fe, and TEM examination of single beam irradiated Fe and Fe-Cr model alloy	DMN	Saclay
TW5-TTMS-001-D03	Irradiation performance Post irradiation experiments of the ARBOR2 irradiation in BOR-60 reactor	DMN	Saclay
TW5-TTMS-004-D04	Qualification fabrication processes Characterization of welding distorsion of simplified welded mock-ups	DM2S	Saclay
TW6-TTMS-004-D04	Qualification fabrication processes Optimisation of filler wire chemistry for Eurofer welds	DM2S	Saclay
TW6-TTMS-005-D06	Material Modelling Improved fatigue life predictions at low strains	DMN	Saclay
TW6-TTMS-007-D02	Modelisation of irradiation effects Comprehensive ab initio study of grain boundaries in α-Fe, equilibrium configurations and migration pathways of He in grain boundaries	DMN	Saclay
TW6-TTMS-007-D08	Material Modelling Ab initio investigation of a screw dislocation in Fe	DMN	Saclay

Advanced Materials

TW3-TTMA-001-D04 TW3-TTMA-002-D04	Effects of irradiation on advanced materials Irradiation of advanced SiC/SiC composites Furioso Experiment	DMN	Saclay

Neutron source

CEFDA05-1359	TW5-TTMI-004a: Preliminary RH handbook for IFMIF	DTSI	Fontenay

Safety and Environment

CEFDA06-1414	TW6-TSL-002: Safety assessment of EU-test blanket modules to support ITER licensing process	DTN	Cadarache
CEFDA06-1513	TW6-TTFD-TR66-2: Design study on ITER HVAC/LAC, depression systems, ADS/VDS and safety tritium monitoring	DTN	Cadarache
CEFDA06-1518 CEFDA07-1700-1591	TW6-TSS-SEA4.5: Feasibility study of possible prevention of hydrogen explosion in ITER by injection of neutral gas - Experiments and calculation for demonstration of inert gas injection feasibility	DM2S	Saclay
CEFDA07-1700-1549	TW6-TSS-SEA5.6b: Validation of the PACTITER computer code and related fusion specific experiments in CORELE loop	DTN	Cadarache
TW6-TSL-004	Collection of data related to Tore Supra operation experience on components failure	IRFM	Cadarache
TW6-TSS-SEA3.5C	In-vessel safety: Small and medium scale experiments on combined hydrogen/dust explosions and mitigation for model development	DM2S	Saclay
TW6-TSS-SEA5.1	In vacuum vessel dust measurement and removal techniques	IRFM	Cadarache
TW6-TSS-SEA5.5C	Cryogenic experiments on the CEA EVITA Facility	DTN	Cadarache
TW6-TSW-003-D02	Study on existing detritiation processes and characterization of tritiated materials, for application to ITER and DEMO	DTN	Cadarache

System studies

Power Plant Conceptual Studies (PPCS)

CEFDA05-1285	TW5-TRP-003: DEMO blanket segmentation and maintenance	DTSI	Fontenay
CEFDA06-1452	TW6-TRP-003: DEMO multi module blanket attachment conceptual design	DTN	Cadarache
TW5-TRP-002-D03a TW6-TRP-002-D02	Analysis of current profile control in tokamak reactor scenarios using realistic treatment of current drive efficiencies	IRFM	Cadarache
TW6-TRP-006	Delivery of the magnet system outline for a DEMO reactor	IRFM	Cadarache

Design Support and Procurement

CEFDA06-1483	TW6-TDS-QA1: Support to the development of the QA system for the ITER EU Domestic Agency and implementation of a quality assurance programme in the european fusion associations for ITER-relevant activities	IRFM	Cadarache
CEFDA07-1700-1600	TW6-TDS-RAMSUP: Contributions to the development of Reliability, Availability and Maintainability (RAM) and Failure Mode, Effects and (FMEA) Analysis for ITER	IRFM	Cadarache

JET technology

CEFDA06-1386	JW6-EP-ICRH-CEA: CEA contribution to RFAD for the JET ICRH ITER-like antenna	IRFM	Cadarache
CEFDA06-1422	JW6-PS-EP2-BET-01: ITER-like FW experiment project: Tile shaping checking	IRFM	Cadarache
JW5-FT-5.25	Human factors experience feedback on JET	DPIE	Cadarache
JW6-FT-1.11	Thermal desorption of flakes	DTN	Cadarache

JW6-FT-2.28	Assessment of industrial process of waste treatment	DTN	Cadarache
JW6-FT-3.30	Laser detritiation system tests in the Berylium handling facility and JET environment	DPC	Saclay
JW6-FT-3.33	In-situ laser induced breakdown spectroscopy of JET deposited layers	DPC	Saclay
JW6-FT-3.36	Multi-colour pyroreflectometer for JET	IRFM	Cadarache
JW6-FT-3.37	Active IR thermography by pulsed-thermal method	DPC	Saclay
JW6-FT-4.9	Glow discharge improvements for JET	IRFM	Cadarache

UNDERLYING TECHNOLOGY PROGRAMME

Vessel/In-Vessel

Vessel-Blanket and Materials

UT-VIV/VV-Hybrid-Modeli	Optimisation of hybrid welding for VV manufacturing	DM2S	Saclay

Plasma Facing Components

UT-VIV/PFC-HIP	Improvement of the reliability, performance and industrial relevancy of HIP processes for PFC components	DTH	Grenoble
UT-VIV/PFC-Hypervapotron	Numerical simulation of swirl-tube cooling concept for the ITER divertor	DER	Cadarache

Remote Handling

UT-VIV/AM-AIA	Articulated inspection arm (AIA)	DTSI	Fontenay

Tritium Breeding and Materials

Breeding Blanket

UT-TBM/BB-He	Helium components technology Problems and outlines of solutions	DTN	Cadarache

Safety and Environment

UT-S&E-dust-suspension	Optical characterization of dust in suspension Experimental studies of dust suspension	CNRS	Marseille
UT-S&E-LASER/DEC	Laser decontamination/Tritium removal Simulations of near-threshold laser ablation of metals	DPC	Saclay
UT-S&E-LiPbwater	Modelisation of the interaction between LiPb and water	DER	Cadarache
UT-S&E-Tritium-Impact	Impact of contamination with tritium at cell level	DRR	Fontenay

APPENDIX 3 : REPORTS AND PUBLICATIONS

EFDA TECHNOLOGY PROGRAMME

Physics Integration

Plasma Edge and Plasma Wall Interaction (PWI)

CEFDA05-1336 CEFDA07-1700-1578	Final Report on the Task: CEFDA05-1336 TW5-TPO-ERGITER: Design studies of Resonant Magnetic Perturbation (RMP) coils for Type I ELMs mitigation in ITER Internal report CEA PHY/NTT-2007.001	M. Bécoulet, E. Nardon, G. Huysmans, W. Zwingmann, P.R. Thomas, M. Lipa, R.A. Moyer, T.E. Evans, V. Chuyanov, Y. Gribov, A. Polevoi, G. Saibene, G. Vayakis, A. Portone, A. Loarte, G. Federici, V. Parail, J. Hastie and C. Gimblett
CEFDA05-1336 CEFDA07-1700-1578	Final Report on the EFDA Task: TW7-TPO-ELMCONT "Evaluation of ELM control coil configuration in ITER, effects on plasma and power loads on PFCs" , Internal report CEA: PHY/NTT-2008.007	M. Bécoulet, E. Nardon, G. Huysmans et al.
TW6-TPP-DUSMEAS-D01a	Assessment of the integration of a dust injector system and electrostatic dust detector in the Tore Supra environment CEA internal report CFP/NTT-2007.075	S. Rosanvallon, T. Boulet and S. Vartanian
TW6-TPP-DUSTGEN-D01	Modelling of carbon dust formation by cluster growth in plasmas J. Nucl. Mater. 363-365, 1190-1194 (2007)	X. Bonnin, G. Lombardi, K. Hassouni, A. Michau, F. Bénédic and C. Arnas
TW6-TPP-DUSTGEN-D01	Growth and heating of carbon nanoparticles in sputtering and hydrocarbon discharges 1st Dust in Fusion Plasmas EPS Workshop, 8-10 July 2007, Warsaw, Poland	C. Arnas, A. Mouberi, C. Dominique, F. Bénédic, D. Monéger, G. Lombardi, X. Bonnin, K. Hassouni, Ch. Brosset and B. Pégourié
TW6-TPP-DUSTGEN-D01	Nanostructure of carbon dust generated in plasmas of different parameters 5th International Conference on the Physics of Dusty Plasmas, Ponta Delgada, Azores, May 18th-23rd, 2008	C. Arnas, A. Mouberi, K. Hassouni, A. Michau, F. Bénédic, G. Lombardi and X. Bonnin
TW6-TPP-DUSTGEN-D01	Carbon dust formation in a cold plasma from cathode sputtering J. Nucl. Mater. (2009), in press	C. Arnas, A. Mouberi, K. Hassouni, A. Michau, G. Lombardi, X. Bonnin, F. Bénédic and B. Pégourié
TW6-TPP-DUSTGEN-D01	Introduction of a new experimental device for simulating parasitic plasmas such as those expected under the divertor dome J. Nucl. Mater. (2009), in press	C. Arnas, A. Mouberi, K. Hassouni, A. Michau, G. Lombardi and X. Bonnin
TW6-TPP-DUSTGEN-D01	Micro-particles in ITER: a comprehensive review 13th International Conference on Fusion Reactor Materials (ICFRM-13), Nice, France, 10-14 December 2007	C. Grisolia, P. Sharpe, J. Winter, C. Arnas, X. Bonnin, S. H. Hong, S. Rosanvallon, M. T. Porfiri, G. Counsell and A. Loarte
TW6-TPP-DUSTGEN-D01	Modelling of carbon dust formation by cluster growth in plasmas 18th International Symposium on Plasma Chemistry, August 26th-31st 2007, Kyoto, Japan	X. Bonnin, G. Lombardi, K. Hassouni, A. Michau, F. Duré, F. Bénédic and C. Arnas
TW6-TPP-DUSTGEN-D01	Modelling of carbon dust formation by cluster growth in plasma 1st Dust in Fusion Plasmas EPS Workshop, 8-10 July 2007, Warsaw, Poland	F. Duré, A. Michau, K. Hassouni, X. Bonnin, G. Lombardi, F. Bénédic and C. Arnas
TW6-TPP-DUSTGEN-D02b	Molecular dynamics study of the role of material properties on nanoparticles formed by rapid expansion of a heated target Applied Surface Science 225, pp 5107-5111, 2009	T. E. Itina
TW6-TPP-DUSTGEN-D02b	Molecular dynamics study of nanoparticle evolution in a background gas under laser ablation conditions Applied Surface Science 225, pp 5116- 5119, 2009	K. Gouriet, L. V. Zhigilei and T. E. Itina

TW6-TPP-DUSTGEN-D02b	Formation of nanoparticles by short and ultra-short laser pulses Conference on High-Power Laser Ablation VII, APR 20-27, 2008 Taos, NM, Proceeding SPIE Vol. 7005 p T50, 2008	K. Gouriet, T. E. Itina, S. Noel et al.
TW6-TPP-DUSTGEN-D02b	Correlation between ablation efficiency and nanoparticle generation during the short-pulse laser ablation of metals Laser Physics 18, pp 374-379, 2008	J. Hermann, S. Noel, T. E.Itina et al.
TW6-TPP-DUSTGEN-D02b	Decomposition of rapidly expanding liquid: Molecular dynamics study Chemical Physics Letters 452, pp 129-132, 2008	T. E. Itina
TW6-TPP-DUSTGEN-D02b	Experimental investigation on laser removal of carbon particles Applied Surface Science (2008), doi:10.1016/j.apsusc.2008.09.045	A.Vatry, M. Naiim Habib, Ph. Delaporte, M. Sentis, D. Grojo, C. Grisolia and S. Rosanvallon
TW6-TPP-DUSTGEN-D02b	Characterisation of carbon and tungsten micro-particles mobilised by laser irradiation in order to develop an ITER dust removal technique Accepted for publication in Journal of Nuclear Materials (2008)	A.Vatry, M. Naiim Habib, Ph. Delaporte, C. Grisolia, D. Grojo, S. Rosanvallon, M. Sentis

Heating and Current Drive

CEFDA05-1271 CEFDA07-1700-1556	TW6-TPHI-ICHDESREW draft report for sub tasks 1.2 & 2.14 CH/NTT-2007.036	P. Mollard and A. Argouarch
CEFDA05-1271 CEFDA07-1700-1556	ITER ICRH antenna – Final report on EFDA task TW6-TPHI-ICHDES-REW CH/NTT-2008.001	G. Agarici, A. Argouarch, J.-P. Martins, P. Mollard and K. Vulliez
CEFDA05-1329	EFDA Task TW6-TPHI-ICFS2 - Final Report CEA internal report PHY/NTT-2007.004	
CEFDA06-1409	Co-ordination of the ITER ICRF Antenna design and R&D Activities EFDA Task TW6-TPHI-ICRFCOORD - (EFDA 06-1409), Final Report CH/NTT-2007.042	G. Agarici
CEFDA06-1420	Faraday Shield Design for the Iter ICRF antenna array Intermediate report for the Task TW6-TPHI-ICFSDES, CFP/NTT-2007.017, May 2007	
CEFDA06-1420	Faraday Shield Design for the Iter ICRF antenna array Final report for the Task TW6-TPHI-ICFSDES, CFP/NTT-2007.082, December 2007	
CEFDA07-1700-1572	EFDA Task TW6-TPHI-RFPCROW- ICRF part - Final Report CEA report PHY/NTT-2008.008	
CEFDA07-1700-1572	EFDA Task TW6-TPHI-RFPCROW- LH part - Final Report CEA report PHY/NTT-2008.020	
TW6-THHN-ASD3	Results of the SINGAP neutral beam accelerator experiment at JAEA Fusion Eng. Des (2009)	H.P.L de Esch et al.
TW6-THHN-ASD3	Aperture Size Effect on Extracted Negative Ion Current Density NIBS (2009)	H.P.L de Esch et al.

Diagnostics

CEFDA06-1429	Diagnostic port plug procurement – Draft Final Report (EFDA Contract 06-1429) D1.2 PEFC/NTT-2007.015 Rev. 0 December 2007	L. Meunier and L. Doceul
CEFDA06-1429	Engineering assessment of diagnostic port integration on ITER Draft Final Report (EFDA Contract 06-1429 D2.2) PEFC/NTT-2007.024 Rev. 0 December 2007	L. Meunier, L. Doceul, J-P. Martins and F. Jullien
CEFDA06-1429	Proposition of a collaborative diagnostics integration management for ITER by using digital mock-up, CAD software & PDM system 25th Symposium on Fusion Technology (2008), to be published in Fusion Engineering and Design	F. Jullien
CEFDA06-1429	CEA engineering activities on the ITER representative diagnostic port plug EQ#01 25th Symposium on Fusion Technology (2008), to be published in Fusion Engineering and Design	L. Meunier

CEFDA06-1429	Study of ITER Equatorial Port Plug handling system and vacuum sealing interface 25th Symposium on Fusion Technology (2008), to be published in Fusion Engineering and Design	J.-P. Martins
CEFDA06-1429	Concept and development of ITER divertor thermography diagnostic 18th Plasma Surface Interactions in Controlled Fusion Devices (2008), to be published in Journal of Nuclear Materials	R. Reichle
CEFDA06-1438-PP11	CEA Draft Final Report on TW6-TPDS-DIADES Procurement Package 11 - Equatorial Visible/IR Wide Angle Viewing System and Integration of Equatorial Port Plug 1 2009 (to be published)	S. Salasca et al.
CEFDA06-1438-PP11	Development of equatorial visible/infrared wide angle viewing system and radial neutron camera for ITER Fusion Eng. Des. (2009), doi:10.1016/j.fusengdes.2008.12.088	S. Salasca et al.
CEFDA06-1438-PP11	Progress of the ITER equatorial vis/IR wide angle viewing system optical design 17th HTPD Conf., Albuquerque (US), May 2008 (to be published in Rev. Sci. Instr.)	M. Davi, Y. Corre, D. Guilhem, F. Jullien, R. Reichle, S. Salasca et al.
CEFDA06-1438-PP11	Concept and Development of Instruments for ITER Thermography in: F.P. Orsitto, et al. (Eds.), Burning Plasma Diagnostics, AIP, New York, 2008, p. 226	R. Reichle, J.-M. Badie, C. Balorin, S. Carpentier, Y. Corre, M. Davi et al.
CEFDA06-1438-PP11	In-vessel components imaging systems: from the present experience towards ITER safe operation Fusion Eng. Des., 2008, in press	J.-M. Travère and Tore Supra Team
CEFDA06-1438-PP11	Draft of the final report on ITER Plasma Position Reflectometry CEA internal report DIAG/NTT-2008.006	R. Sabot, S. heuraux, F. Da Silva and G. Giruzzi
CEFDA06-1438-PP22	Development status of ITER ex-vessel magnetic diagnostic Draft Final Report Contract EFDA 06-1438	
CEFDA06-1438-PP22	Assessment of the equilibrium reconstruction accuracy using ITER magnetic diagnostics Draft Final Report Contract EFDA 06-1438	
CEFDA06-1438-PP22	Overview of ITER Steady State sensors Draft Final Report Contract EFDA 06-1438	
CEFDA06-1438-PP22	Project Plan for ITER ex-vessel magnetic diagnostic Draft Final Report Contract EFDA 06-1438	
CEFDA06-1438-PP22	Design and performance analysis of ITER ex-vessel magnetic diagnostics Fusion Eng. Des. (2009)	Ph. Moreau et al.
TW5-TPDC-IRRCER-D03	Joint Final report for EFDA Tasks TW4-TPDC-IRRCER D16 (SCK-CEN) and TW5-TPDC-IRRCER D3 (CEA) on irradiation tests of IR optical fibres CEA internal report DIAG/NTT-2007.026 (2007)	R. Reichle, B.Brichard, C. Pocheau, M. Jouve, H. Ooms, S. Van Ierschot, S. Martinez
TW5-TPDC-IRRCER-D03	Experimental developments towards an ITER thermography diagnostic Journal of Nuclear Materials, vol. 363-365, (2007) p. 1466-1471	R. Reichle, B. Brichard, F. Escourbiac, J.-L.Gardarein, D. Hernandez, C. Le Niliot, F. Rigollet and J. Serra
TW5-TPDC-IRRCER-D03	Gamma irradiation test of IR optical fibres for ITER thermography in 'Burning Plasma Diagnostics', ed. F.P. Orsitto et al. AIP, New York 2008, pp. 325	R. Reichle et al.
TW6-TPDS-DIADEV-D05d	Simulation of laser cleaning of diagnostic windows and mirrors CEA report, NT DPC/SCP/2007–249, December 2007	A. Semerok and S. V. Fomichev

Remote Participation

CEFDA06-1376	Support tools for EFDA RP Collaboration 6th IAEA TM June 2007 Inuyama-Japan	
CEFDA06-1376	Preliminary report on the progress of the use and expansion or Remote Experiment Participation facilities in Europe RPTC_0235 - 15/02/2008	
CEFDA06-1376	Final report on the status of Remote Experiment Participation Facilities in Europe RPTC_0243 - 29/04/2008	
CEFDA06-1376	Overview of the status of EFDA Remote Experimentation Participation in Fusion Experiments, 25th SOFT, 15-19 September 2008, Rostock, Germany	

Vessel-In Vessel

Vessel-Blanket and Materials

CEFDA04-1202	Automatic ultrasonic system AUGUR SINTEZ/ECHO Report. 2007	
CEFDA04-1202	Inspection of VV welded mock-ups in the frame of RFUT project SYSSC/07 RT0277/ 2008	J. Tirira
CEFDA06-1482	Industrialisation and weld quality issues of high productive laser\arc hybrid for thick section welding of ITER grade SS material – TW6 TVA IHYB – Final report CEA internal report DM2S/DIR/RT/08-0010/A, 14 Dec 08	Ph. Aubert
CEFDA07-1700-1542	TW6-TVV-TLDES Final report Orbital internal report, march 2008	
CEFDA07-1700-1623	EFDA Contract TW6-TVV-LEAKD Deliverable 5 CEA internal report IRFM/STEP/GARV/REF/NTT-2009.003	M. Chantant and J.-C. Hatchressian
TW6-TVM-Braze	Testing of silver free braze materials with Be, Final Report Technical Report DTH/DR/2007/67, December 2007	T. Baffie, E. De Vito, J.-M. Leibold, N. Miloud-Ali, A. Montani, B. Oresic and T. Portra
TW6-TVM-LEAK	Investigation of laser-based techniques for ITER leak localization and selection of the most promising method with regards to ITER requirements NT DPC/SCP 08-257-A, 2008	I. Debecker and A. Pailloux
TW6-TVM-LEAK	Demonstration of laser-based technique for leak detection and localization of ITER vacuum vessel NT DPC/SCP 08-254-A, 2008	J. Cousin and A. Pailloux
TW6-TVV-STORVS	TW6-TVV-STORVS Task, Final Report CEA internal report DEN/DM2S/DIR/RT/08-0004/A, December 2008	P. Aubert

Plasma Facing Components

CEFDA04-1218	Monitoring and analyis of divertor components tested at FE200 CFP/NTT-2007.033	F. Escourbiac
CEFDA05-1248	Influence of the carbon erosion on the acceptance criteria of the ITER divertor EFDA CONTRACT N°05-1248, Final report, CFP/NTT-2007.021, (2007)	J. Schlosser
CEFDA05-1248	Evaluation of the erosion on the CFC tiles of the ITER divertor by means of FE calculations J. Nucl. Mater. (2009), in press	J. Schlosser, C. Lowry, B. Riccardi, E. D'Agata, J. Bouvet and M. Merola
CEFDA05-1257	Optimisation of Be/Cu alloy HIP joining for first wall panels TW5-TVB-JOINOP, final report no. DTH/DL/2007/72	P.-E. Frayssines, O. Gillia, E. De Vito, B. Oresic, J.-M. Leibold and A. Montani
CEFDA05-1293	An operational non-destructive examination technique for ITER Divertor plasma facing components, publication to ICFRM 2007, Nice, France	
CEFDA05-1293	Evaluation of plasma facing components thermal performance by infrared thermography, InfraMation 2008, Reno, USA	

CEFDA05-1308	Destructive examination of first wall panels and mock-ups Be//Cu junction analysis of eight selected mock ups, Intermediate report, DTH/DR/2008/58 (april 2008)	E. De Vito and A. Montani
CEFDA05-1309	Manufacture of first wall mock-ups for In-Pile experiments EFDA 05-1309, TW5-TVB-INMOCK, final report no. DTH/DL/2007/71	P.-E. Frayssines, J.-M. Leibold and B. Oresic
CEFDA06-1372	Development of fabrication control methods for the ITER divertor Final report of EFDA contract 06-1372 CFP/NTT-2008.007	A. Durocher, M. Richou and N. Vignal
CEFDA06-1373	Spécifications techniques pour la maquette W_flat_tile_A à tester au FE200 CEA internal report CFP/NTT-2006.038	F. Escourbiac
CEFDA06-1373	Spécifications techniques pour la maquette W_ mono _A à tester au FE200 CEA internal report CFP/NTT-2007.013	F. Escourbiac
CEFDA06-1373	Spécifications techniques pour la maquette CFC_mono_P1 à tester au FE200 CEA internal report CFP/NTT-2007.020	F. Escourbiac
CEFDA06-1373	Interim report of contract EFDA 06-1373: monitoring and analysis of divertor components tested at FE200 CEA internal report CFP/NTT-2007.037	F. Escourbiac
CEFDA06-1373	Screening and fatigue tests on a CFC_mono_P1 component (CEA94 – CEFDA06/999) NTCF-F IBV R/07.945 A	I. Bobin-Vastra
CEFDA06-1373	Spécifications techniques pour la maquette CFC_mono_P2 à tester au FE200 CEA internal report CFP/NTT-2007.045	F. Escourbiac
CEFDA06-1373	Rapport d'inspection SATIR des Monobloc CFC Ansaldo avant FE200 CEA internal report CFP/NTT-2007.062	N. Vignal
CEFDA06-1373	Rapport d'inspection SATIR des Monobloc CFC Plansee P1 avant /après FE200 CEA internal report CFP/NTT-2007.063	N. Vignal
CEFDA06-1373	Rapport d'inspection SATIR des Monobloc CFC Plansee P2 avant FE200 CEA internal report CFP/NTT-2007.064	N. Vignal
CEFDA06-1373	SATIR inspection report of mock-up CFC_MONO_P2 after FE200 testing CEA internal report CFP/NTT-2007.066	N. Vignal
CEFDA06-1373	Spécifications techniques pour la maquette CFC_mono_A1 à tester au FE200 CEA internal report CFP/NTT-2007.069	F. Escourbiac
CEFDA06-1373	Spécifications techniques pour la maquette CFC_mono_A2 à tester au FE200 CEA internal report CFP/NTT-2007.078	F. Escourbiac
CEFDA06-1373	Spécifications techniques pour la maquette W_mono_P à tester au FE200 CEA internal report CFP/NTT-2008.011	F. Escourbiac
CEFDA06-1373	SATIR inspection report of mock-up CFC_MONO_A 1 and A2 after FE200 testing CEA internal report CFP/NTT-2008.016	N. Vignal
CEFDA06-1373	Final report of contract EFDA 06-1373: monitoring and analysis of divertor components tested at FE200 CEA internal report CFP/NTT-2008.019	F. Escourbiac
CEFDA06-1373	Spécifications techniques pour la maquette W_flat_tile_P à tester au FE200 CEA internal report CFP/NTT-2008.020	F. Escourbiac
CEFDA06-1373	Experimental activity on the definition of acceptance criteria for the ITER Divertor plasma facing components Proceedings SOFT2008 – To be published in Fusion Engineering and Design	F. Escourbiac, S. Constans, N. Vignal, V. Cantone, M. Richou, A. Durocher, B. Riccardi, I. Bobin, J.-L. Jouvelot and M. Merola

CEFDA06-1401	Control of ITER vertical target qualification prototypes by infrared thermography Internal CEA report CFP/PCD-2007.003	
CEFDA06-1401	Visual tests of ITER vertical target qualification prototypes Internal CEA report CFP/PCD-2007.004	
CEFDA06-1401	Quality Plan of SATIR test of vertical target qualification prototypes Internal CEA report CFP/PCD-2007.006	
CEFDA06-1401	Infrared thermography inspection of the ITER vertical target qualification prototypes manufactured by European industry using SATIR Fusion Eng. Des. (2009), doi:10.1016/j.fusengdes.2008.12.095	A. Durocher et al.
CEFDA06-1401	Evaluation of plasma facing components thermal performance by infrared thermography InfraMation workshop 2008, Reno -USA	A. Durocher et al.
CEFDA06-1411	Be/CuCrZr HIP joining optimisation for ITER FW qualification tests, Final report TW6-TVB-ACCTEST, Technical note DTH/DL/2008/113, dec 2008	P.-E. Frayssines, G. Roux, O. Gillia, B. Oresic, J.-M. Leibold, P. Lemoine and A. Montani
CEFDA07-1700-1617	Design of clamped tile concept for ITER poloidal limiters EFDA contract TW6-TVB-FWPROT 3- Subtask2, final report CFP/NTT-2008.001, Jan. 2008	M. Lipa, R. Mitteau et al.
CEFDA07-1700-1622	HIP joining development and application to the FW design of NBI modules, Interim report TW6-TVB-HIPJOIN, Technical note DTH/DL/2008/103, December 2008	P-E. Frayssines, G. Roux, F. Vidotto, B. Oresic, J.-M. Leibold, C. Chabrol and E. De Vito
TW5-TVM-COMADA	TW5-TVM-COMADA, Investigation of the effect of creep fatigue interaction on the mechanical performance and lifetime of CuCrZr - Final Report rapport technique DTH/DL/2007/091, dec. 2007	O. Gillia and P. Lemoine
TW5-TVM-COMADA	Characterization of CuCrZr and CuCrZr/SS joint strength for different blanket components manufacturing conditions International Conference on Fusion Reactor Materials, Nice, France, 2007. To be published in Journal of Nuclear Materials (2009), doi:10.1016/j.jnucmat.2008.12.244	O. Gillia et al.

Remote Handling

TW5-TVR-WHMAN	Results on qualification of a water-hydraulics joint for force feedback applications DTSI/SRI/LPR/06RT018	G. Dubus

Magnet System and Cryogenics

CEFDA04-1127	EFDA contract 04-1127 Final report on manufacture of subsize samples CEA Internal report AIM/NTT-2007.018	N. Dolgetta and J.-L. Duchateau
CEFDA04-1170	Final report to the fusion program contract number FU 06 CT 2004-00158 (EFDA contract number EFDA/04-1170) – CEA internal report RESDEV –T-025-08b – 10/12/2008	F. Rondeaux
CEFDA05-1370	Spécification technique pour la fabrication de longueurs de spirales type ITER note AIM/CCH-2006.001, 10/04/2006	P. Decool
CEFDA05-1370	Rapport contrôle qualité des tubes inox- Tache TFPRO note AIM/RCQ.2006-001, 07/06/2006	J.-L. Maréchal
CEFDA05-1370	Manufacturing of full scale ITER TF conductor prototype lengths (English translation of AIM/CCH-2006.003) note AIM/CCH-2006.004, 23/03/2006	N. Dolgetta
CEFDA05-1370	Task TFPRO: visit to NEXAN-CORTAILLOD (switzerland) to attend the TFPRO cabling, week 5-9/february/07 note AIM/CRM-2007.001, 27/02/2007	N. Dolgetta and P. Decool
CEFDA05-1370	TFPRO Task: visit to NEXAN-JEUMONT to attend the jacketing of TFPRO cables samples, week 26-28/march/2007 note AIM/CRM-2007.002, 30/03/2007	J.-L. Marechal and H. Cloez

CEFDA05-1370	Contract EFDA 05-1370 : Deliverable 3 - Final report on “Cabling and Jacketing of ITER TF Prototype Conductor note AIM/NTT-2007.015	P. Decool, H. Cloez, N. Dolgetta and J.-L. Maréchal
CEFDA06-1515	Detailed analysis of the ITER cryoplant normal and abnormal modes CEA report CC3D/CC3D-2008.001	D. Henry, P. Roussel, P. Reynaud and J.-M. Poncet
CEFDA06-1515	Scale down-loop to simulate the smoothing of ITER heat loads CEA report SBT/CT/08-25	B. Rousset
CEFDA06-1515	Development plan of the ITER cryogenic system CEA report CRYO/NTT 2008.008	J.-Y. Journeaux, J.-M. Poncet
CEFDA06-1521	Final report: Heat treatment optimisation of advanced Nb3Sn strands CEA report AIM/NTT-2008.020	L. Zani, M. Tena, M. Nannini, S. Girard, C. Roux, H. Cloez, J.-P. Serries, P. Decool and A. Torre
CEFDA07-1700-1565	PFD and P&ID of the cryopump cryodistribution and general design of one CVB - First intermediate report of the VP76 task CEA report SBT CT 08 – 18	M. Scannapiego, J.-M. Poncet and P. Reynaud
CEFDA07-1700-1565	PFD of the cryopump cryodistribution, P&ID and general design of one Cold Valve Box (CVB) - Final report of the VP76 task CEA report SBT CT 09 – 8	M. Scannapiego, J.M. Poncet, P.Reynaud
CEFDA07-1700-1565	PFD of the cryopump cryodistribution, P&ID and general design of one Cold Valve Box (CVB) - Final report of the VP76 task - Appendix CEA report SBT CT 09 – 9	M. Scannapiego, J.-M. Poncet, P. Reynaud
CEFDA07-1700-1603	Minutes of meeting Grenoble, France, 13/01/09	
CEFDA07-1700-1603	Thermal contraction measurement with dual extensometers, January 2009 campaign report to be published in 2009	
CEFDA07-1700-1606	Thermohydraulic analysis for the ITER superconducting coils ICEC22 Conference. Seoul July 21-25 2008	R. Vallcorba, Ch. Meuris, B. Rousset, F. Michel, B. Lacroix, S. Nicollet, D. Bessette, H. Rajainmaki and N. Shatil
CEFDA07-1700-1606	Thermohydraulic Analysis for the ITER Cryogenic System. Final report January 2009	
TW5-TMSF-HTSPER	Critical current measurement in HTc Bi2212 ribbons and round wires Presented at ASC 2008 Chicago	J.-M. Rey, A. Allais, J.-L. Duchateau, Ph. Fazilleau, J.-M. Gheller, R. Le Bouter, O. Louchard, L. Quettier and D. Tordera
TW5-TMSF-HTSPER	Losses measurement in HTc Bi2212 ribbons and round wires Presented at ASC 2008 Chicago	J.-M. Rey, L. Quettier, A. Allais, H. Cloez, J.-L. Duchateau, J.-L. Maréchal, L. Zani and S. Girard
TW5-TMSF-HTSPER	HTS Materials on Fusion Magnets, Final Report Deliverable 2, April 2008	
TW6-TMSC-FSTEST	EFDA Task TW6-TMSC-FSTEST: Final Report CEA Internal Note AIM/NTT-2007.020, August 30, 2007	D. Ciazynski, S. Nicollet and N. Pauty

Tritium Breeding and Materials

Breeding Blanket

CEFDA07-1700-1573	Assessment report of ESC06-002/Del. 1 CEA report SEMT/BCCR/RT/07-066/A, September 2008	G. Rampal
CEFDA07-1700-1573	Assessment report of ESC06-002/Del. 2 CEA report SEMT/BCCR/RT/08-008/A, September 2008	G. Rampal
CEFDA07-1700-1573	Assessment report of ESC06-002/Del. 3&4 CEA report SEMT/BCCR/RT/08-018/A, September 2008	G. Rampal
CEFDA07-1700-1573	Synthesis on the follow-up of the ESC06-002 contract CEA report SEMT/BCCR/RT/08-025/A, September 2008	G. Rampal

Helium Cooled Lithium Lead (HCLL) Blanket

TW2-TTBC-002-D02	TBM Manufacturing – Final report, CEA report DEN/DM2S/DIR/RT/08-0009/A, December 2008	P. Aubert
TW5-TTBC-001-D02	Finalization of the conceptual design of the prototypical HCLL TBM mock-up SEMT/BCCR/RT/06-037/A issued 05/2007	G. Rampal
TW5-TTBC-001-D05	Assessments on a Prototypical Mock-up as HCLL TBM qualification test CEA report SEMT/BCCR/RT/08-036/A	G. Rampal and A. Morin
TW5-TTBC-001-D07	The HCLL Test Blanket Module System: Present reference design, System Integration in ITER and R&D Needs Oral presentation to ISFNT-8, Heidelberg, 2007, Engineering and Design 83 (2008) 1157–1162	J.-F. Salavy, G. Aiello, O. David, F. Gabriel, L. Giancarli, C. Girard, N. Jonquères, G. Laffont, S. Madeleine, Y. Poitevin, G. Rampal, I. Ricapito and K. Splichal
TW5-TTBC-001-D07	Ferritic-Martensitic Steel Test Blanket Modules: status and future needs for design criteria requirements and fabrication validation Invited presentation to ICFRM-13, Nice, 2007, tbp in J. Nucl. Mater., 10.1016/j.jnucmat.2008.12.239	J.-F. Salavy, G. Aiello, P. Aubert, L. V. Boccaccini, M. Daichendt, G. De Dinechin, E. Diegele, L. Giancarli, R. Lässer, H. Neuberger, Y. Poitevin, Y. Stephan, G. Rampal and E. Rigal
TW5-TTBC-001-D07	Detailed TBM development workplan up to EM-TBM installation in ITER CEA report, SERMA/RT/06-3816/A, issued March 2008	J.-F. Salavy
TW5-TTBC-002-D02	Feasibility of the tube forming + HIP fabrication process for the bent part of the FW of HCLL and HCPB TBMs EFDA task TW5-TTBC002 Blanket manufacturing technologies, Deliverable 2, final report, report RT DTH DL 2007/69, dec. 2007	M. Reytier, M. Elie, E. Rigal, F. Vidotto and B. Riccetti
TW5-TTBC-005-D05	A 2D finite element modelling of tritium permeation for the HCLL DEMO blanket module Fusion Engineering and Design 82 (2007) 2204–2211	F. Gabriel, Y. Escuriol, F. Dabbene, O. Gastaldi, J.-F. Salavy and L. Giancarli
TW5-TTBC-005-D05	Simulation of tritium permeation - Task TW5-TTBC-005-D05 final report CEA internal report SERMA/LPEC/RT/08-/4451/A, May 2008	F. Gabriel
TW6-TTBC-001-D03	HCLL TBM design and analyses - EFDA task TW6-TTBC-001-D03, del. 3a, 3c & 3e CEA report SEMT/BCCR/RT/07-056/A, February 2008	G. Rampal and G. Aiello
TW6-TTBC-001-D03	Preliminary Assessment of Manufacturing Margins for the HCLL-TBM First Wall CEA report SERMA/LPEC/RT/07-4625/A, November 2007	G. Aiello and F. Gabriel
TW6-TTBC-001-D03	Preliminary analysis of TBM maintenance procedures from a RH point of view CEA report DTSI/SRI/08.321, August 2008	O. David
TW6-TTBC-001-D03	Helium-Cooled Lithium-Lead: TBM Design, integration and analysis CEA report DEN/DTN/STPA/LTCG/2007-031, November 2007	L. Ayrault
TW6-TTBC-002-D01	Improvement of the 2-step HIP diffusion welding process for the manufacturing of TBMs subcomponents EFDA task TW6-TTBC002 Blanket manufacturing technologies, Deliverable 1, final report, RT DTH DL 2007/66, nov. 2007	M. Elie, E. Rigal, F. Vidotto and J.-M. Leibold

Structural Materials development

Reduced Activation Ferritic Martensitic (RAFM) Steels

CEFDA06-1470	Report 1 : Coupling DD code (BCC version) and FEM and application to dislocation-cavity interaction (static case)	
CEFDA06-1470	Report 2 (Final Report): Dislocation-cavity interaction (dynamic case) and comparison with MD simulations	
TW4-TTMS-007-D02	Ab initio study of the interaction of Cr atoms & precipitates with He and He-V clusters in α-Fe, and TEM examination of single beam irradiated Fe and Fe-Cr model allo EFDA subtask 2008 report	
TW5-TTMS-001-D03	Mechanical properties of Reduced Activation steels irradiated in BOR-60 at 325°C up to 78 dpa. Final Report – TW5-TTMS-001-D03 CEA report NT SRMA 2009-3004/A, 2009	
TW5-TTMS-004-D04	Thermomechanical FEA of a representative TBM welded mock-up : comparison with experimental measurements DM2S/SEMT/LTA/RT/08-004/A, TW5-TTMS004-D04, final report	
TW6-TTMS-004-D04	EFDA TW6-TTMS004-Filler Wire Task, Final Report CEA/DEN/DM2S/DIR/RT/08-0008/A, December 2008	
TW6-TTMS-007-D02	Ab initio study of He in grain boundaries in α-Fe EFDA subtask 2007 report	
TW6-TTMS-007-D02	Ab initio study of He in grain boundaries in α-Fe EFDA subtask 2008 report	
TW6-TTMS-007-D02	J. Nucl. Mater. 385, 262 (2009)	
TW6-TTMS-007-D08	J. Computer-Aided Mater. Des. 14, 85 (2007)	
TW6-TTMS-007-D08	Phys. Rev. Lett. 102, 055502 (2009)	

Advanced materials

TW3-TTMA-001-D04 TW3-TTMA-002-D04	Irradiation of SiC/SiC cmpositesand W alloys, Furioso Experiment 7th IEA workshop on SiC/SiC materials, NRG, Petten, The Netherlands, Sept. 18-20, 2007	F. Tavassoli et al.
TW3-TTMA-001-D04 TW3-TTMA-002-D04	SiC_f/SiC composite irradiation programme at CEA EFDA Monitoring meeting, Barcelona, July 26, 2007	F. Tavassoli

Neutron Source

CEFDA05-1359	Overview of the preliminary remote handling handbook for IFMIF Fusion Eng. Des. (2009), doi:10.1016/j.fusengdes.2009.01.089	O. David et al.

Safety and Environment

CEFDA06-1414	Nuclear dosimetry of HCLL and HCPB TBMs CEA internal report DTN/STPA/LPC/2007/41	G. Manon, O. Gastaldi and C. Lacressonnière
CEFDA06-1513	ITER – HVAC- Ventilation and Detritiation System- Requirements Synthesis of design requirements of ITER ventilation and detritiation systems Technical document CEA/DTN/CAD/DTAP/STL/GFDV DO 300	
CEFDA06-1518 CEFDA07-1700-1591	Feasability study of possible prevention of hydrogen combustion in ITER by injection of neutral gas EDFA Task TW6-TSS-SEA4.5 D1, D2 CEA Report DM2S/SFME/LTMF/RT07-059/A (2008)	F. Dabbene
CEFDA07-1700-1549	Development of the PACTITER code and its application to safety analyses of ITER Primary Cooling Water System Fusion Engineering and Design, April 2007, Volume 82, Issue 3, Pages 237-247	L. Di Pace, F. Dacquait, P. Schindler, V. Blet, F. Nguyen, Y. Philibert and B. Larat
CEFDA07-1700-1549	Status of the PACTITER code development CEA Technical Report DTN/SMTM/LMTR/2007-003 February 2007	F. Dacquait
CEFDA07-1700-1549	CuCrZr release rate evaluation in ITER operating conditions CEA Technical Report DTN/SMTM/LMTR/2007-027, February 2007	E. Tevissen and Y. Philibert

CEFDA07-1700-1549	Quality Plan Task Objectives and detailed test matrix CEA Technical report DEN/DTN/SMTM/LMTR/2008-015, May 2008	E. Tevissen and F. Dacquait
CEFDA07-1700-1549	Measurement of stainless steels release in CORELE loop CEA Technical report DEN/DTN/SMTM/LMTR/2008 – 045, December 2008	E. Tevissen and Y. Philibert
CEFDA07-1700-1549	Elements of validation of the PACTITER V3.3 code CEA Technical report DEN/DTN/SMTM/LMTR/2008-46, December 2008	F. Dacquait, F. Herbelet and M. Monin-Baroille
TW6-TSL-004	D01: Final report on toroïdal field magnet CEA report CETS/NTT-2007.002	
TW6-TSL-004	D02: Final report on PFC cooling system, including the in-vessel water leaks analysis CEA report CETS/NTT-2007.003 CEA report CETS/NTT-2007.004	
TW6-TSL-004	D03: Final report on Cryo-plant CEA report CRYO/NTT-2008.006	
TW6-TSS-SEA3.5C	Description of MISTRA facility EDFA Task TW6-TSS-SEA3.5C, D3 CEA Report RT DM2S/SFME/LTMF/RT07-081/B	J. Brinster et al.
TW6-TSS-SEA3.5C	MISTRA experimental results for ITER 2007 test series EDFA Task TW6-TSS-SEA3.5C, D4 CEA Report DM2S/SFME/LEEF/RT09-004/A	D. Abdo et al.
TW6-TSS-SEA5.1	Assessment of in-vessel dust measurement and removal techniques for ITER Delivrable 5 - Final Report, CFP/NTT-2007.030 (2007)	S. Rosanvallon
TW6-TSS-SEA5.1	Dusts in ITER: Diagnostics and Removal Techniques Journal of Nuclear Materials, (2009), doi:10.1016 (2009)	S. Rosanvallon, C. Grisolia, P. Delaporte, F. Onofri, S. Hong, G. Counsell and J. Winter
TW6-TSS-SEA5.5c	Evita, in depth analysis of the experiment and facility CEA Technical note, DTN/STPA/LTCG NT 2007-013, 09/2007	L. Ayrault
TW6-TSW-003-D02	Study on existing detritiation processes and characterisation of tritiated materials for application in ITER and DEMO, Final Report Technical document DTN/STPA/LPC/2007/064, 12/2007	N. Ghirelli and O. Gastaldi

System Studies

Power Plant Conceptual Studies (PPCS)

CEFDA05-1285	Remote Handling Issues DTSI/SRI/LRM/06RT027	J.-P. Martins and Ch. Dechelle
CEFDA05-1285	Selection of Reference Maintenance Concept DTSI/SRI/LRM/07RT041	J. Bonnemaison, Y. Perrot and J.-P. Friconneau
CEFDA05-1285	Contribution to DEMO reactor RH maintenance assessment Fusion Eng. Des. (2009)	J. Bonnemason et al.
CEFDA06-1452	Helium Cooled DEMO design activities - Final deliverable of the contract EFDA/06-1452 CEA technical report NT DTN/STPA/LTCG-2008-030	L. Cachon et al.
CEFDA06-1452	DEMO Multi modules blanket attachment conceptual design - TW6-TRP-003-D01 CEA technical report DTN/STPA/LTCG/2007-028	L. Cachon et al.
TW5-TRP-002-D03a TW6-TRP-002-D02	Analysis of current profile control in tokamak reactor scenarios using realistic treatment of current drive efficiencies CEA Internal report, October 2007	J. Garcia, J.-F. Artaud, V. Basiuk, F. Imbeaux, J. Johner and M. Schneider
TW6-TRP-006	Which superconducting material for the toroidal field system of the fusion DEMO reactor? 2008 J. Phys.: Conf. Ser. 97 012038	J.-L. Duchateau and P. Hertout
TW6-TRP-006	EFDA contract TW –TRP-006 Final report CEA Internal report AIM/NTT-2007.0189	J.-L. Duchateau and P. Hertout

Design Support and procurement

CEFDA06-1483	Support in the Development of the QA System for the ITER EU Domestic Agency and Implementation of a Quality Assurance Programme in the European Fusion Associations for ITER-relevant Activities IRFM Report, ref QUAL/NTT-2007.003 # 01	L. Jourd'Heuil and M. Peyrot
CEFDA07-1700-1600	TW6-TDS-RAMSUP task Quality plan CEA internal report IRFM/QUAL/NTT-2007.005 (2007)	
CEFDA07-1700-1600	Partial report TW6-TDS-RAMSUP- D2.1 on cryogenics CEA internal report IRFM/ SUR/NTT-2008.001	J.-Y. Journeaux and F. Sagot
CEFDA07-1700-1600	Partial report TW6-TDS-RAMSUP- D2.2 on magnets CEA internal report IRFM/ SUR/NTT-2008.002	J.-Y. Journeaux and F. Sagot
CEFDA07-1700-1600	Partial report TW6-TDS-RAMSUP- D3.1 on Cryogenics CEA internal report IRFM/ SUR/NTT-2008.003	J.-Y. Journeaux and F. Sagot
CEFDA07-1700-1600	Partial report TW6-TDS-RAMSUP- D3.2 on magnets CEA internal report IRFM/ SUR/NTT-2008.004	J.-Y. Journeaux and F. Sagot
CEFDA07-1700-1600	Partial report TW6-TDS-RAMSUP- D2.3 on CWS CEA internal report IRFM/ SUR/NTT-2008.006	M. Chantant and F. Sagot
CEFDA07-1700-1600	Partial report TW6-TDS-RAMSUP- D3.3 on CWS CEA internal report IRFM/ SUR/NTT-2008.007	M. Chantant and F. Sagot

JET Technology

CEFDA06-1386	Progress in Arc Safety System Based on Harmonics Detection for ICRH Antennae 17th Topical Conference on Radio Frequency Power in Plasmas (2007)	G. Berger-By, B. Beaumont, G. Lombard, L. Millon, P. Mollard and D. Volpe
CEFDA06-1386	Final report on EFDA Task JW6-OEP-CEA-38A CEA report CH/NTT-2008.002#01 (2008)	G. Berger-By
CEFDA06-1422	JET-ITER-like wall project - Tile shaping checking intermediate report CEA internal report CFP/NTT-2007.010	R. Mitteau
CEFDA06-1422	JET-ITER-like wall project - Tile shaping checking First report for the inner wall guard limiter CEA internal report CFP/NTT-2007.014#02	R. Mitteau
CEFDA06-1422	ITER-like wall project - Tile shaping checking Wide poloidal limiter misaligment cases (tolerance assesment) CEA internal report CFP/NTT-2007.016	R. Mitteau
CEFDA06-1422	ITER-like wall project - Tile shaping checking ICRH side limiters CEA internal report CFP/NTT-2007.035#02	R. Mitteau
CEFDA06-1422	ITER-like wall project - Tile shaping checking Narrow poloidal limiter CEA internal report CFP/NTT-2007.036#01	R. Mitteau
CEFDA06-1422	ITER-like wall project - Tile shaping checking Dump plates CEA internal report CFP/NTT-2007.041	R. Mitteau
CEFDA06-1422	ITER-like wall project - Tile shaping checking Saddle coils and tile carriers CEA internal report CFP/NTT-2007.059	R. Mitteau
CEFDA06-1422	ITER-like wall project - Tile shaping checking ICRH private limiter, cross beam and septum CEA internal report CFP/NTT-2007.070	R. Mitteau
CEFDA06-1422	JET-ITER-like wall project - Tile shaping checking Second interim report CEA internal report CFP/NTT-2007.077	R. Mitteau
CEFDA06-1422	ITER-like wall project - Tile shaping checking A2 protection limiters CEA internal report CFP/NTT-2007.081	R. Mitteau
CEFDA06-1422	ITER-like wall project - Tile shaping checking evidences of HHF on the bottom horizontal LHCD short tile CEA internal report CFP/NTT-2008.002	R. Mitteau
CEFDA06-1422	ITER-like wall project - Tile shaping checking LHCD limiter CEA internal report CFP/NTT-2008.004#01	R. Mitteau

CEFDA06-1422	ITER-like wall project - Tile shaping checking HHF modelling on the dump plates in near null configuration CEA internal report CFP/NTT-2008.021	R. Mitteau
CEFDA06-1422	JET-ITER-like wall project - Tile shaping checking Final report for the task JW6-BEP-CEA-39 CEA internal report CFP/NTT-2008.022	R. Mitteau
CEFDA06-1422	JET-ITER-like wall project - Tile shaping checking phase 1 report of JOI revision contract CEA internal report CFP/NTT-2008.023	R. Mitteau
CEFDA06-1422	ITER-like wall project - Tile shaping checking divertor mode configuration CEA internal report PEFC/NTT-2008.035	C. Portafaix
CEFDA06-1422	ITER-like wall project - Tile shaping checking ICRH poloidal limiters CEA internal report CFP/NTT-2008.041	C. Portafaix
CEFDA06-1422	ITER-like wall project - Tile shaping checking CEA internal report PEFC/NTT-2009.003#01	C. Portafaix
CEFDA06-1422	Tile shape checking of the beryllium tiles for the JET ITER-like Wall 25th Symposium on Fusion Technology (2008), to be published in Fusion Engineering and Design.	R. Mitteau, M. Firdaouss, E. Villedieu, V. Riccardo, P. Lomas, Z. Vizvary, C. Portafaix, P. Thomas, I. Nunes, P. De vries and Y. Stephan
JW5-FT-5.25	Human factors Experience Feedback on JET, 2007.	B. Papin, V. Paulus and M. Tosello
JW6-FT-2.28	Detritiation process for JET waste : Soft housekeeping and metals - Final report CEA Internal report DTN/STPA/LPC/2007-013	K. Liger
JW6-FT-3.30	Laser detritiation system tests in the Berillium Handling Facility and JET environment Report CEA, NT DPC / SCP 08-292-A, December 2008, pp. 1-45	A. Semerok, D. Farcage, P. Dewalle, S. Fomichev, P-Y. Thro, C. Grisolia, P. Coad and A. Widdowson
JW6-FT-3.30	Characterization of aerosols produced by laser-matter interaction Oral presentation on 1st Workshop on the «Dust in Fusion Plasmas», Warsaw, July 8-10, 2007;	P. Dewalle, C. Sortais, S. Pontreau, J. Vendel, J.-M. Weulersse and A. Semerok
JW6-FT-3.33	In situ laser breakdown spectroscopy of JET deposited layers CEA report, NT DPC/SCP/08-293-A, December 2008	J.-M. Weulersse, D. L'Hermite, J.-L. Lacour, F. Le Guern, G. Cheymol, P.-Y. Thro, A. Semerok, C. Grisolia, M. Kempenaars, M. Stamp and N. Bekris
JW6-FT-3.36	Report on JET Fusion Technology Task JW6-FT-3.36 Multicolour Pyroreflectometry for JET DIAG/NTT-2008.033	R. Reichle, D. Hernandez and A. Netchaieff
JW6-FT-3.36	Concept and development of instruments for ITER thermography in 'Burning Plasma Diagnostics', ed. F.P. Orsitto et al. AIP, New York 2008, pp226	R. Reichle et al.
JW6-FT-3.36	Concept and development of ITER divertor thermography diagnostic 18th PSI conf. Toldeo, Espagne, 26-30 May 2008, to be published in Journ. Nucl. Mater. 2009	R. Reichle, Ph. Andrew, B. Brichard, S. Carpentier, Y. Corre, M. Davi, R. Daviot, C. Desgranges, J.-L. Gardarein, E. Gauthier, D. Guilhem, S. Gicquel, A. Herrmann, D. Hernandez, M. Jouve, Ch. Le Niliot, Th. Loarer, A. Martin, J.-P. Martins, J.-B. Migozzi, J.-C. Patterlini, C. Pocheau, F. Rigollet, H. Roche and J.-M. Travere
JW6-FT-3.37	Active IR Thermography by Means of Pulsed Photo-Thermal Method CEA report, NT DPC/SCP 07-245-A, December 2007	A. Semerok, V. Grigorova, D. Farcage, J.-M. Weulersse, P.-Y. Thro, E. Gauthier, H. Roche, Th. Loarer and C. Grisolia

JW6-FT-4.8	Infrared active thermography for surface layer characterization NT DPC / SCP 07-225 indice A DEN/DANS/DPC/SCP/LILM DO 07/049	A. Semerok, X. Courtois, S. Fomichev, D. Farcage and C. Sortais
JW6-FT-4.9	Glow discharge improvement for JET, Final report CEA report PHY/NTT-2007.003, March 2008	D. Douai and D. Garnier

UNDERLYING TECHNOLOGY PROGRAMME

Vessel-In Vessel

Plasma Facing Components

UT-VIV/PFC-HIP	Improvement of the reliability, performance and industrial relevancy of HIP processes for PFC components Technical note DTH/DL/2007/96, Decembre 2007	P.-E. Frayssines, O. Gillia and B. Riccetti
UT-VIV/PFC-Hypervapotron	Numerical simulation of swirl-tube cooling concept 25th SOFT, Rostock, Germany, 2008, to be published in Fusion Engineering and Design	

Remote Handling

UT-VIV/AM-AIA	Development of an ITER-relevant inspection robot European Nuclear Conference (ENC - 2007), 16/09/2007 - 20/09/2007, Brussel , Belgium	M. Houry et al.
UT-VIV/AM-AIA	Development of an ITER-relevant inspection robot ISFNT-8 30/09/2007 – 05/10/2007, Germany, Heidelberg	L. Gargiulo et al.
UT-VIV/AM-AIA	Development of an inspection robot under ITER relevant vacuum and temperature conditions IVC-17, 02/07/2007 – 06/07/2007, Stockholm, Sweden	J.-C. Hatchressian et al.
UT-VIV/AM-AIA	Development of an ITER relevant inspection robot European Nuclear Conference (ENC - 2007), 16/09/2007 - 20/09/2007, Bruxelles , Belgique	M. Houry et al.
UT-VIV/AM-AIA	Development of an ITER relevant inspection robot ISFNT-8, 30/09/2007 – 05/10/2007, Germany, Heidelberg	L. Gargiulo et al.
UT-VIV/AM-AIA	Development of an inspection robot under ITER relevant vacuum and temperature conditions IVC-17, 02/07/2007 – 06/07/2007, Stockholm, Sweden	J.-C. Hatchressian et al.

Tritium Breeding and Materials

Breeding Blanket

UT-TBM/BB-He	Report on experiments on helium generic technology CEA Technical note, DTN/STPA/LTCG/ NT 2007- 029	L. Ayrault
UT-TBM/BB-He	HETHIMO qualication of encap-sulated concept CEA Technical note, DTN/STPA/LTCG/ NT 2007- 018, Oct. 2007	L. Ayrault
UT-TBM/BB-He	HEDYT – Essais de mise en service CEA Technical note, DTN/STPA/LTCG/ NT 2007- 022, Oct. 2007	L. Ayrault
UT-TBM/BB-He	HETIQ - Qualication of type S SPG seal CEA Technical note, DTN/STPA/LTCG/ NT 2007- 030, Dec. 2007	L. Ayrault

Safety and Environment

UT-S&E-Dust-Suspension	Experimental studies of dust suspension Convention CEA/ IUSTI-UMR CNRS 6595 n°V 3524.001, Deliverable: 3/3 (Final report)	F. Onofri and J. Worms
UT-S&E-Dust-Suspension	Dust control in tokamak environment Fusion Engineering and Design 83(10-12):1701-1705 (2008)	S. Rosanvallon, C. Grisolia, G. Counsell, S. H. Hong, F. Onofri, J. Worms, J. Winter, B. M. Annaratonee, G. Maddaluno and P. Gasior
UT-S&E-Dust-Suspension	Dust in ITER: Diagnostics and Removal Techniques, to be published in Journal of Nuclear Materials	S. Rosanvallon, C. Grisolia, P. Delaporte, J. Worms, F. Onofri, S.H. Hong, G. Counsell and J. Winter

UT-S&E-Dust-Suspension	Development of an in situ optical diagnostic of dusts in ITER, 14th Int. Symp on Appl. Laser Techniques to Fluid Mechanics, Lisbon, Portugal, July 07–10th, paper 4.2.4 (2008)	F. Onofri, K. F. Ren and C. Grisolia
UT-S&E-Dust-Suspension	Development of an in situ ITER dust diagnostic based on extinction spectroscopy: dedicated light scattering models, to be published in Journal of Nuclear Materials	F. Onofri, K. F. Ren and C. Grisolia
UT-S&E-LASER/DEC	Simulation of near-threshold laser ablation of metals CEA report, NT DPC/SCP/207-248, 2007	S. V. Fomichev and A. Semerok
UT-S&E-Tritium-Impact	Homologous recombination is involved in the repair response of mammalian cells to low doses of tritium contamination Radiation Res., 170 (2008), 172-183	Y. Saintigny, S. Roche, D. Meynard, and B. S. Lopez
UT-S&E-Tritium-Impact	Homologous recombination defect affects replication fork progression in mammalian cells J. Cell Science, 121 (2008), 162-166	F. Daboussi, S. Courbet, S. Benhamou, P. Kannouche, M. Z. Zdzienicka, M. Debatisse and B. S. Lopez
UT-S&E-Tritium-Impact	Importance Of The Cell Cycle Phase For The Choice Of The Appropriate DSB Repair Pathway, For Genome Stability Maintenance: The Trans-S Double-Strand Break Repair Model Cell cycle, 7 (2008), 33-38	F. Delacôte and B. S. Lopez
UT-S&E-Tritium-Impact	Chronic exposure to sub-lethal soses of rasiation mimetic Zeocin selects for clones deficient in homologous recombination Mutation Research Fundamental and Molceular Mechanisms of Mutagenesis, 615 (2007), 125-133	F. Delacôte, L. Deriano, S. Lambert, P. Bertrand, Y. Saintigny and B. S. Lopez

APPENDIX 4 : CEA TASKS IN ALPHABETICAL ORDER

Task	*Title*	*Prog.*	*Field*	*Area*	*Unit*	*Site*	*Task Leader*	*Page*
CEFDA04-1127	TW4-TMSC-SAMAN1: manufacture of subsize samples	EFDA	MAG	MAG	IRFM	Cadarache	Duchateau J.-L.	157
CEFDA04-1170	TW4-TMSC-RESDEV: Development and testing on new resin solution	EFDA	MAG	MAG	IRFU	Saclay	Rondeaux F.	159
CEFDA04-1202	TW5-TVV-RFUT: Synthesis of ultrasonic inspection of the vacuum vessel welded mock-ups for ITER : cooperation with RF	EFDA	VIV	V/B	DETECS	Saclay	Tirira J.	74
CEFDA05-1248	TW5-TVD-ACCEPT: Influence of carbon erosion on the acceptance criteria of the ITER divertor	EFDA	VIV	PFC	IRFM	Cadarache	Schlosser J.	107
CEFDA05-1257	TW5-TVB-JOINOP: Optimisation of Be/CuCrZr HIP joining for FW panels	EFDA	VIV	PFC	DTH	Grenoble	Frayssines P.-E.	108
CEFDA05-1271 CEFDA07-1700-1556	TW6-TPHI-ICHDESREW and TW5-TPHI-ITERDES3: Design of the ITER ICRF antenna	EFDA	PI	Hea	IRFM	Cadarache	Vulliez K.	29
CEFDA05-1285	TW5-TRP-003: DEMO blanket segmentation and maintenance	EFDA	SS	PPCS	DTSI	Fontenay	Friconneau J.-P.	283
CEFDA05-1293	TW5-TVD-NDTEST1: Upgrade of the SATIR test bed for infrared thermographic inspections - Construction phase	EFDA	VIV	PFC	IRFM	Cadarache	Durocher A.	112
CEFDA05-1308	TW5-TVB-DES2: Destructive examination of first wall panels and mock-ups	EFDA	VIV	PFC	DTH	Grenoble	De Vito E.	116
CEFDA05-1309	TW5-TVB-INMOCK2: Manufacture of First Wall mock-ups for in-pile experiments	EFDA	VIV	PFC	DTH	Grenoble	Frayssines P.E.	120
CEFDA05-1329	TW6-TPHI-ICFS: Faraday shield modelling and RF sheath dissipation	EFDA	PI	Hea	IRFM	Cadarache	Colas L.	32
CEFDA05-1336 CEFDA07-1700-1578	TW5-TPO-ERGITER and TW6-TPO-ELMCONT: Resonant magnetic perturbation (RMPs) for Edge Localized modes (ELMs) suppression in ITER	EFDA	PI	Pl. E	IRFM	Cadarache	Bécoulet M.	13
CEFDA05-1359	TW5-TTMI-004a: Preliminary RH handbook for IFMIF	EFDA	TBM	NS	DTSI	Fontenay	Friconneau J.P.	243
CEFDA05-1370	TW6-TMSC-TFPRO: ITER TF full size prototype conductor	EFDA	MAG	MAG	IRFM	Cadarache	Decool P.	162
CEFDA06-1372	TW5-TVD-FABCON: development of fabrication control methods for the ITER divertor	EFDA	VIV	PFC	IRFM	Cadarache	Durocher A.	123
CEFDA06-1373	TW6-TVD-ACCREV: Definition of acceptance criteria for the ITER Divertor	EFDA	VIV	PFC	IRFM	Cadarache	Escourbiac F.	127
CEFDA06-1376	TW5-TPR-RPSUP: Support to EFDA remote participation	EFDA	PI	RP	IRFM	Cadarache	Balme S.	72
CEFDA06-1386	JW6-EP-ICRH-CEA: CEA contribution to RFAD for the JET ICRH ITER-like antenna	EFDA	JET	JET	IRFM	Cadarache	Berger-By G.	303
CEFDA06-1401	TW6-TVD-SATIR: SATIR tests of vertical target qualification prototypes	EFDA	VIV	PFC	IRFM	Cadarache	Durocher A.	134
CEFDA06-1409	TW6-TPHI-ICRFCOORD2: Coordination of ITER ICRF antenna design R&D activities 2	EFDA	PI	Hea	IRFM	Cadarache	Doceul L.	37
CEFDA06-1411	TW6-TVB-ACCTEST: Be/CuCrZr HIP joining for ITER FW qualification tests	EFDA	VIV	PFC	DTH	Grenoble	Frayssines P.E.	139

Task	*Title*	*Prog.*	*Field*	*Area*	*Unit*	*Site*	*Task Leader*	*Page*
CEFDA06-1414	TW6-TSL-002: Safety assessment of EU-test blanket modules to support ITER licensing process - 3	EFDA	S&E	S&E	DTN	Cadarache	Lacressonnière C.	248
CEFDA06-1420	TW6-TPHI-ICFSDES1: Faraday shield for design for the ITER ICRF antenna array	EFDA	PI	Hea	IRFM	Cadarache	Mitteau R.	39
CEFDA06-1422	JW6-PS-EP2-BET-01: ITER-like FW experiment project: Tile shaping checking	EFDA	JET	JET	IRFM	Cadarache	Mitteau R.	305
CEFDA06-1429	TW6-TPDS-DIASUP1: Support of diagnostic design for ITER Diagnostic port-plug procurement, diagnostic port-plug engineering & integration, & divertor thermography	EFDA	PI	Diag	IRFM	Cadarache	Doceul L.	50
CEFDA06-1438-PP1	TW6-TPDS-DIADES1: Diagnostic design for ITER - PP1: Plasma position reflectometry	EFDA	PI	Diag	IRFM	Cadarache	Sabot R.	54
CEFDA06-1438-PP11	TW6-TPDS-DIADES1: Diagnostic design for ITER - PP11: Visible/IR wide angle viewing system	EFDA	PI	Diag	IRFM	Cadarache	Salasca S.	56
CEFDA06-1438-PP21	TW6-TPDS-DIADES1: Diagnostic design for ITER - PP21: Bolometry	EFDA	PI	Diag	IRFM	Cadarache	Reichle R.	61
CEFDA06-1438-PP22	TW6-TPDS-DIADES1: Diagnostic design for ITER - PP22: Magnetic diagnostics: Development of a fibre optic current sensor suitable for ITER	EFDA	PI	Diag	IRFM	Cadarache	Moreau P.	63
CEFDA06-1452	TW6-TRP-003: DEMO multi module blanket attachment conceptual design	EFDA	SS	PPCS	DTN	Cadarache	Cachon L.	286
CEFDA06-1470	TW6-TTMS-MODUNI2: DD simulation of the interaction and He cavities in Fe-alpha	EFDA	TBM	RAFM	INPG	Grenoble	Fivel M.	214
CEFDA06-1477	TW6-TVM-LIP4: Modification of ITER materials documents, assessment of material data and maintenance of a database	EFDA	VIV	V/B	DMN	Saclay	Tavassoli F.	78
CEFDA06-1482	TW6-TVA-IHYB2: Industrialisation and weld quality issues of high productive laser/arc hybrid for thick section welding of ITER grade SS material	EFDA	VIV	V/B	DM2S	Saclay	Aubert P.	82
CEFDA06-1483	TW6-TDS-QA1: Support to the development of the QA system for the ITER EU Domestic Agency and implementation of a quality assurance programme in the european fusion associations for ITER-relevant activities	EFDA	DSP	DSP	IRFM	Cadarache	Jourd'Heuil L.	294
CEFDA06-1513	TW6-TTFD-TR66-2: Design study on ITER HVAC/LAC, depression systems, ADS/VDS and safety tritium monitoring	EFDA	S&E	S&E	DTN	Cadarache	Gastaldi O.	252
CEFDA06-1515	TW6-TES-CRYO-03: Design of the ITER cryoplant and cryodistribution system	EFDA	MAG	MAG	INAC	Grenoble	Poncet J.-M.	164
CEFDA06-1518 CEFDA07-1700-1591	TW6-TSS-SEA4.5: Feasibility study of possible prevention of hydrogen explosion in ITER by injection of neutral gas - Experiments and calculation for demonstration of inert gas injection feasibility	EFDA	S&E	S&E	DM2S	Saclay	Bengaouer A.	256
CEFDA06-1521	TW6-TMSC-HEAT1: Heat treatment optimisation of advanced Nb_3Sn strands	EFDA	MAG	MAG	IRFM	Cadarache	Zani L.	166
CEFDA07-1700-1542	TW6-TVV-TLDES: Design and manufacture of cosmetic welding heads on EB welds of VV sectors	EFDA	VIV	V/B	Orbital	Vonnas	Mazoyer P.	92
CEFDA07-1700-1549	TW6-TSS-SEA5.6b: Validation of the PACTITER computer code and related fusion specific experiments in CORELE loop	EFDA	S&E	S&E	DTN	Cadarache	Dacquait F.	259
CEFDA07-1700-1565	TW6-TTFF-VP76: Cryopump valve box and cryo jumper design study	EFDA	MAG	MAG	INAC	Grenoble	Poncet J.M.	169
CEFDA07-1700-1572	TW6-TPHI-RFPFCPOW2: Evaluation of expected power/particle fluxes on ITER PFCs caused by local acceleration of particles in RF fields	EFDA	PI	Hea	IRFM	Cadarache	Goniche M.	44
CEFDA07-1700-1573	TW6-TTB-COMON: Technical monitoring and assessment of the KNT/ASSYSTEM contract ESC06-002	EFDA	TBM	BLK	DM2S	Saclay	Rampal G.	188

Task	*Title*	*Prog.*	*Field*	*Area*	*Unit*	*Site*	*Task Leader*	*Page*
CEFDA07-1700-1600	TW6-TDS-RAMSUP: Contributions to the development of Reliability, Availability and Maintainability (RAM) and Failure Mode, Effects and (FMEA) Analysis for ITER	EFDA	DSP	DSP	IRFM	Cadarache	Journeaux J.-Y.	297
CEFDA07-1700-1603	TW6-TMSM-CRYOGT: Materials cryogenic testing	EFDA	MAG	MAG	INAC	Grenoble	Poncet J.M.	171
CEFDA07-1700-1606	TW6-TMST-VINCAN: Tthermohydraulic analysis for the ITER cryogenic system	EFDA	MAG	MAG	INAC	Grenoble	Vallcorba R.	173
CEFDA07-1700-1617	TW6-TVB-FWPROT2: Design of clamped poloidal limiters for ITER	EFDA	VIV	PFC	IRFM	Cadarache	Lipa M.	143
CEFDA07-1700-1622	TW6-TVB-HIPJOIN: HIP joining development and application to the FW design of NBI modules	EFDA	VIV	PFC	DTH	Grenoble	Frayssines P.E.	146
CEFDA07-1700-1623	TW6-TVV-LEAKD1: Leak localisation for in-vessel components	EFDA	VIV	V/B	IRFM	Cadarache	Chantant M.	95
JW5-FT-5.25	Human factors experience feedback on JET	EFDA	JET	JET	DPIE	Cadarache	Tosello M.	308
JW6-FT-1.11	Thermal desorption of flakes	EFDA	JET	JET	DTN	Cadarache	Trabuc P.	311
JW6-FT-2.28	Assessment of industrial process of waste treatment	EFDA	JET	JET	DTN	Cadarache	Liger K.	315
JW6-FT-3.30	Laser detritiation system tests in the Berilium handling facility and JET environment	EFDA	JET	JET	DPC	Saclay	Semerok A.	318
JW6-FT-3.33	In-situ laser induced breakdown spectroscopy of JET deposited layers	EFDA	JET	JET	DPC	Saclay	Weulersse J.M.	321
JW6-FT-3.36	Multi-colour pyroreflectometer for JET	EFDA	JET	JET	IRFM	Cadarache	Reichle R.	323
JW6-FT-3.37	Active IR thermography by pulsed-thermal method	EFDA	JET	JET	DPC	Saclay	Semerok A.	327
JW6-FT-4.9	Glow discharge improvements for JET	EFDA	JET	JET	IRFM	Cadarache	Douai D.	329
TW1-TMS-PFCITE	Poloidal Field Conductor Insert (PFCI)	EFDA	MAG	MAG	IRFM	Cadarache	Ciazynski D.	176
TW2-TTBC-002-D02	Blanket manufacturing technologies Manufacturing and testing of mock-ups Qualification samples for HCLL and HCPB TBM	EFDA	TBM	HCLL	DM2S	Saclay	Aubert P.	190
TW3-TTMA-001-D04 TW3-TTMA-002-D04	Effects of irradiation on advanced materials Irradiation of advanced SiC/SiC composites Furioso Experiment	EFDA	TBM	ADV	DMN	Saclay	Tavassoli F.	240
TW4-TTMS-007-D02	Modelisation of irradiation effects Ab initio study of the interaction of Cr atoms & precipitates with He and He-V clusters in α-Fe, and TEM examination of single beam irradiated Fe and Fe-Cr model alloy	EFDA	TBM	RAFM	DMN	Saclay	Fu C. C.	217
TW5-TMSF-HTSPER	HTS materials for fusion magnets	EFDA	MAG	MAG	IRFU	Saclay	Rey J.M.	180
TW5-TPDC-IRRCER-D03	Assessment of IR fibres for thermography applications, Initial gamma induced effects, then neutron irradiations - Fibre selection and provision, Diagnostic preparation and measurements	EFDA	PI	Diag	IRFM	Cadarache	Reichle R.	65
TW5-TRP-002-D03a TW6-TRP-002-D02	Analysis of current profile control in tokamak reactor scenarios using realistic treatment of current drive efficiencies	EFDA	SS	PPCS	IRFM	Cadarache	Giruzzi G.	289
TW5-TTBC-001-D05	TBM design, integration and analysis Finalization of HCLL TBM prototypical mock-up including internal heat system	EFDA	TBM	HCLL	DM2S	Saclay	Rampal G.	196

Task	*Title*	*Prog.*	*Field*	*Area*	*Unit*	*Site*	*Task Leader*	*Page*
TW5-TTBC-001-D07	TBM design, integration and analysis Detailed TBM development workplan up to EM-TBM installation in ITER	EFDA	TBM	HCLL	DM2S	Saclay	Salavy J.F.	200
TW5-TTBC-002-D02	Blanket manufacturing technologies Feasibility of the tube forming + HIP fabrication process for the bent part of the FW of HCLL and HCPB TBMs	EFDA	TBM	HCLL	DTH	Grenoble	Rigal E.	202
TW5-TTBC-005-D05	Process and auxiliary components Modelling of T permeation and behaviour with experimental determination of key modelling parameters	EFDA	TBM	HCLL	DM2S	Saclay	Gabriel F.	205
TW5-TTMS-001-D03	Irradiation performance Post irradiation experiments of the ARBOR2 irradiation in BOR-60 reactor	EFDA	TBM	RAFM	DMN	Saclay	Henry J.	222
TW5-TTMS-004-D04	Qualification fabrication processes Characterization of welding distorsion of simplified welded mock-ups	EFDA	TBM	RAFM	DM2S	Saclay	Asserin O.	224
TW5-TVM-COMADA	Investigations of the effect of creep-fatigue interaction on the mechanical performance and lifetime of CuCrZr	EFDA	VIV	PFC	DTH	Grenoble	Gillia O.	150
TW5-TVR-WHMAN	Development of a linear hydraulic joint for remote handling application	EFDA	VIV	RH	DTSI	Fontenay	Measson Y.	154
TW6-THHN-ASD3	SINGAP negative ion accelerator: Study of the beamlet halo, dark currents and verification of electrostatic withstand capability and tolerable stored energy in case of electrical discharges	EFDA	PI	Hea	IRFM	Cadarache	Svensson L.	47
TW6-TMSC-FSTEST	Participation to conductor tests and evaluation of test results	EFDA	MAG	MAG	IRFM	Cadarache	Ciazynski D.	184
TW6-TPDS-DIADEV-D05d	Theorical and experimental evaluations of laser cleaning methods for diagnostics and mirrors	EFDA	PI	Diag	DPC	Saclay	Semerok A.	68
TW6-TPP-BETUNCMOD-D01b	Molecular dynamics simulations of mixed material formation at the ITER divertor Report on the construction of the potentials to study the interactions in the Be-C, Be-W and W-C systems in interaction with D/T and noble gases (Ar, Ne, He) to be used in molecular dynamics simulations	EFDA	PI	Pl. E	CNRS	Pessac	Allouche A.	15
TW6-TPP-DUSMEAS-D01a	Demonstration of diagnostic techniques for time resolved dust measuremnts in tokamaks	EFDA	PI	Pl. E	IRFM	Cadarache	Grisolia C.	17
TW6-TPP-DUSTGEN-D01	Dust generation rates for the plasma edge/divertor conditions expected for the ITER QDT = 10 reference scenario with a CFC/W and W divertor target and a Be wall	EFDA	PI	Pl. E	CNRS	Villetaneuse	Bonnin X.	22
TW6-TPP-DUSTGEN-D02b	Evaluation of dust generation mechanisms at the ITER SOL and divertor plasma Analogy between cluster production by laser ablation and dust generation in ITER	EFDA	PI	Pl. E	CNRS	Marseille	Sentis M.	25
TW6-TRP-006	Delivery of the magnet system outline for a DEMO reactor	EFDA	SS	PPCS	IRFM	Cadarache	Duchateau J. L.	292
TW6-TSL-004	Collection of data related to Tore Supra operation experience on components failure	EFDA	S&E	S&E	IRFM	Cadarache	Vallet J.C.	262
TW6-TSS-SEA3.5C	In-vessel safety: Small and medium scale experiments on combined hydrogen/dust explosions and mitigation for model development	EFDA	S&E	S&E	DM2S	Saclay	Tkatschenko I.	267
TW6-TSS-SEA5.1	In vacuum vessel dust measurement and removal techniques	EFDA	S&E	S&E	IRFM	Cadarache	Grisolia C.	270
TW6-TSS-SEA5.5C	Cryogenic experiments on the CEA EVITA Facility	EFDA	S&E	S&E	DTN	Cadarache	Ayrault L.	277
TW6-TSW-003-D02	Study on existing detritiation processes and characterization of tritiated materials, for application to ITER and DEMO	EFDA	S&E	S&E	DTN	Cadarache	Gastaldi O.	279
TW6-TTBC-001-D03	HCLL TBM design and integration analyses	EFDA	TBM	HCLL	DM2S	Saclay	Rampal G.	207

Task	*Title*	*Prog.*	*Field*	*Area*	*Unit*	*Site*	*Task Leader*	*Page*
TW6-TTBC-002-D01	Blanket manufacturing technologies Improvement of the 2-step HIP diffusion welding process for the manufacturing of TBMs subcomponents	EFDA	TBM	HCLL	DTH	Grenoble	Rigal E.	211
TW6-TTMS-004-D04	Qualification fabrication processes Optimisation of filler wire chemistry for Eurofer welds	EFDA	TBM	RAFM	DM2S	Saclay	Aubert P.	226
TW6-TTMS-005-D06	Material Modelling Improved fatigue life predictions at low strains	EFDA	TBM	RAFM	DMN	Saclay	Sauzay M.	230
TW6-TTMS-007-D02	Modelisation of irradiation effects Comprehensive ab initio study of grain boundaries in α-Fe, equilibrium configurations and migration pathways of He in grain boundaries	EFDA	TBM	RAFM	DMN	Saclay	Fu C. C.	233
TW6-TTMS-007-D08	Material Modelling Ab initio investigation of a screw dislocation in Fe	EFDA	TBM	RAFM	DMN	Saclay	Willaime F.	236
TW6-TVM-Braze	Testing of silver free braze materials with Be	EFDA	VIV	V/B	DTH	Grenoble	Baffie T.	97
TW6-TVM-LEAK	Investigation of laser-based techniques for leak localization, and demonstration of a laser-based technique for leak detection and localization compatible with ITER requirements	EFDA	VIV	V/B	DPC	Saclay	Pailloux A.	101
TW6-TVV-STORVS	Storage of stainless steel material for VV	EFDA	VIV	V/B	DM2S	Saclay	Aubert P.	104
UT-S&E-dust-suspension	Optical characterization of dust in suspension Experimental studies of dust suspension	UT	S&E	S&E	CNRS	Marseille	Onofri F.	351
UT-S&E-LASER/DEC	Laser decontamination/Tritium removal Simulations of near-threshold laser ablation of metals	UT	S&E	S&E	DPC	Saclay	Semerok A.	355
UT-S&E-LiPbwater	Modelisation of the interaction between LiPb and water	UT	S&E	S&E	DER	Cadarache	Cadiou T.	358
UT-S&E-Tritium-Impact	Impact of contamination with tritium at cell level	UT	S&E	S&E	DRR	Fontenay	Lopez B.	360
UT-TBM/BB-He	Helium components technology Problems and outlines of solutions	UT	TBM	BLK	DTN	Cadarache	Ayrault L.	348
UT-VIV/AM-AIA	Articulated inspection arm (AIA)	UT	VIV	RH	DTSI	Fontenay	Keller D.	344
UT-VIV/PFC-HIP	Improvement of the reliability, performance and industrial relevancy of HIP processes for PFC components	UT	VIV	PFC	DTH	Grenoble	Frayssines P.E.	336
UT-VIV/PFC-Hypervapotron	Numerical simulation of swirl-tube cooling concept for the ITER divertor	UT	VIV	PFC	DER	Cadarache	Pascal-Ribot S.	340
UT-VIV/VV-Hybrid-Modeli	Optimisation of hybrid welding for VV manufacturing	UT	VIV	V/B	DM2S	Saclay	Aubert P.	344

Programme
EFDA = EFDA Technology Programme
UT = Underlying Technology Programme

Field
PI = Physic Integration
VIV = Vessel - In Vessel
MAG = Magnets & Cryogenics
TBM = Tritium Breeding & Materials
S&E = Safety & Environment
SS = System Studies
DSP = Design Support & Procurement
JET = Joint European Torus

Area
Pl. E = Plasma Edge & PWI
Hea = Heating and Current Drive
Diag = Diagnostics
RP = Remote Participation
V/B = Vessel/Blanket and Materials
PFC = Plasma Facing Components
RH = Remote Handling
MAG = Magnets & Cryogenics
BLK = Blanket
HCLL = Helium Cooled Li-Pb Blanket
MAT = Materials
RAFM = Reduced Activation Ferritic Martensitic stee
ADV = Advanced Materials
NS = Neutron Source
S&E = Safety and environment
PPCS = Power Plant Conceptual Studies
DSP = Design Support & Procurement
JET = Joint European Torus

APPENDIX 5 : CEA SITES

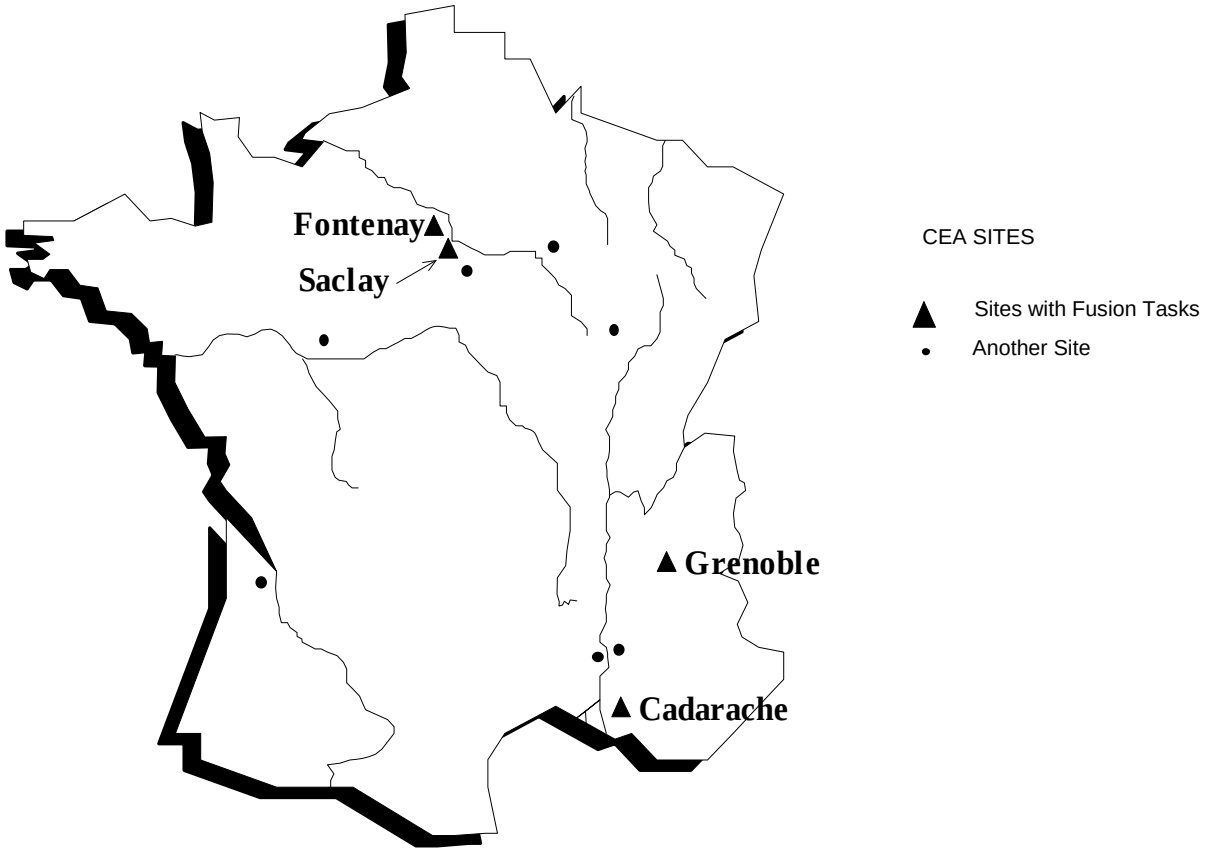

ASSOCIATION EURATOM-CEA CEA/DSM/IRFM
Centre de Cadarache, 13108 Saint-Paul-Lez-Durance, France
TEL 33 4 42 25 46 59 - **FAX** 33 4 42 25 64 21 - **E-MAIL** dirirfm@cea.fr
http://www-fusion-magnetique.cea.fr